Synthesis and Characterization of Histone Deacetylase (HDAC) Inhibitors and PROTACs

Dissertation

zur

Erlangung des Doktorgrades (Dr. rer. nat.)

der

Mathematisch-Naturwissenschaftlichen Fakultät

der

Rheinischen Friedrich-Wilhelms-Universität Bonn

vorgelegt von

Fabian Benedikt Kraft

Master of Science

aus Tübingen

Bonn 2024

Angefertigt mit Genehmigung der Mathematisch-Naturwissenschaftlichen Fakultät

der Rheinischen Friedrich-Wilhelms-Universität Bonn

1. Gutachter: Prof. Dr. Finn K. Hansen

2. Gutachter: Prof. Dr. Gerd Bendas

Tag der Promotion: 08.07.2024

Erscheinungsjahr: 2024

Die vorliegende Arbeit wurde, unter der Leitung von Herrn Prof. Dr. Finn K. Hansen, in der Zeit von Februar 2019 bis August 2020 am Institut für Wirkstoffentwicklung (ehem. Institut für Pharmazie, Fakultät für Biowissenschaften, Pharmazie und Psychologie) der Universität Leipzig sowie von September 2020 bis März 2024 am Pharmazeutischen Institut der Rheinischen Friedrich-Wilhelms-Universität Bonn angefertigt.

„Zwei Dinge sind zu unserer Arbeit nötig. Unermüdliche Ausdauer und die Bereitschaft, etwas, in das man viel Zeit und Arbeit gesteckt hat, wieder wegzuwerfen.“

Albert Einstein (1879-1955)

Preliminary Remarks

Figures, schemes, tables and so forth are numbered consecutively throughout the thesis, using arabic numerals. Well-known active substances are referred to by their common names (e.g. vorinostat). All other chemical substances, including published active substances without established common names, are consecutively numbered within each chapter and may have been used and numbered in more than one chapter. In the running text, chemical substance numbers are written in bold. Unless marked otherwise (e.g. proof of co-authors' contributions of the respective publication or footnotes) figures, schemes, and tables were designed and created by myself. Unless marked otherwise the chapters were all written by myself. References of adapted and reprinted figures/schemes are given in the respective figure/scheme description. Sources of general illustration ideas or theoretical principles depicted in the respective illustration are also given in the respective figure/scheme description.

TABLE OF CONTENTS

Chapter 1 ..... **- 1 -**

Introduction ..... - 2 -

1.1 Preface ..... - 2 -

1.2 Epigenetics – An overview ..... - 3 -

1.3 Histone deacetylases (HDACs) ..... - 5 -

1.3.1 Class I ..... - 7 -

1.3.1.1 HDAC1 and HDAC2 ..... - 7 -

1.3.1.2 HDAC3 ..... - 9 -

1.3.1.3 HDAC8 ..... - 9 -

1.3.2 Class IIa ..... - 10 -

1.3.2.1 HDAC4, 5, 7 and 9 ..... - 10 -

1.3.3 Class IIb ..... - 11 -

1.3.3.1 HDAC6 ..... - 11 -

1.3.3.2 HDAC10 ..... - 13 -

1.3.4 Class IV ..... - 14 -

1.3.5 Deacetylation mechanism of HDACs ..... - 14 -

1.4 HDAC inhibitors ..... - 16 -

1.4.1 FDA approved HDACi ..... - 16 -

1.4.2 Selective HDACi ..... - 18 -

1.4.2.1 Class I selective HDACi ..... - 19 -

1.4.2.2 HDAC6 selective inhibitors ..... - 21 -

1.4.3 HDAC inhibitor prodrugs ..... - 23 -

1.5 Proteolysis Targeting Chimeras (PROTACs) ..... - 24 -

1.5.1 E3-ligase ligands ..... - 26 -

1.5.2 PROTACs targeting histone deacetylases ..... - 27 -

1.6 Scope of Thesis ..... - 32 -

Chapter 2 ..... **- 35 -**

Groebke Blackburn Bienaymé-mediated multi-component synthesis of selective HDAC6 inhibitors with anti-inflammatory properties ..... - 36 -

2.1 Publication Summary ..... - 36 -

2.2 Author Contribution ..... - 38 -

Chapter 3 ..... **- 39 -**

Hydrazide-based class I HDAC inhibitors with HDAC3 preference completely reverse chemoresistance in a synergistic manner in platinum-resistant solid cancer cells ..... - 40 -

3.1 Introduction ..... - 40 -

3.2 Results and Discussion ..... - 43 -

3.2.1 Design and Synthesis of selective HDACi ..... - 43 -

3.2.2 Biological Evaluation ..... - 43 -

3.2.2.1 Physicochemical properties of compound **5** ..... - 46 -

3.2.2.2 Docking studies ..... - 47 -

3.2.2.3 Cellular HDAC activity and cell viability (MTT) assays ..... - 47 -

3.2.2.4 Hydrazide HDACi **5**, **6**, and **8** improve cisplatin cytotoxicity in a synergistic manner ..... - 52 -

3.2.2.5 Compounds **5** and **6** increase cisplatin-induced apoptosis and caspase activation in a synergistic manner ..... - 56 -

3.2.2.6 Compounds **5** and **6** act synergistic with cisplatin by increasing DNA damage and expression of p21 and proapoptotic BIM ..... - 58 -

3.2.2.7 Cytotoxic effect of HDACi **5** and **6** in acute myeloid leukemia cell lines ..... - 60 -

3.3 Conclusion ..... - 61 -

3.4 Experimental Section ..... - 61 -

3.4.1 Experimental procedures ..... - 64 -

3.4.1.1 General procedures ..... - 64 -

3.4.1.2 Compound characterization ..... - 64 -

3.4.2 HDAC enzyme inhibition assay ..... - 68 -

3.4.2.1 Preincubationassay for HDAC1-3 and HDAC6 ..... - 68 -

3.4.2.2 Enzyme assay for HDAC4 and 8 ..... - 69 -

3.4.3 Docking of compounds **5** and **13** in human HDAC3 with *RosettaLigand* ..... - 69 -
3.4.4 Cell Culture ..... - 70 -
3.4.5 HDAC Whole-Cell Assay ..... - 70 -
3.4.6 Cell viability assay ..... - 71 -
3.4.6.1 CellTiter-Glo ..... - 71 -
3.4.6.2 MTT Cell Viability Assay ..... - 71 -
3.4.7 Measurement of Apoptosis Marker and DNA Damage ..... - 72 -
3.4.7.1 Measurement of Apoptotic Nuclei ..... - 72 -
3.4.7.2 Caspase 3/7 Activation Assay ..... - 72 -
3.4.7.3 γH2AX Assay ..... - 72 -
3.4.8 Immunoblot ..... - 73 -
3.4.9 Determination of physiochemical properties ..... - 73 -
Chapter 4 ..... **- 75 -**
Development of class I HDAC selective PROTACs ..... - 76 -
4.1 Introduction ..... - 76 -
4.2 Results and Discussion ..... - 78 -
4.2.1 PROTAC Synthesis ..... - 78 -
4.2.2 Biological Evaluation ..... - 81 -
4.3 Conclusion ..... - 83 -
4.4 Experimental Section ..... - 84 -
4.4.1 General Procedure ..... - 85 -
4.4.2 Compound characterization ..... - 86 -
4.4.3 Biological Evaluation ..... - 100 -
4.4.3.1 HDAC enzyme inhibition assay ..... - 100 -
4.4.3.2 Cell Line and Cell Culture ..... - 100 -
4.4.3.3 Immunoblot ..... - 101 -
Chapter 5 ..... **- 103 -**
Photocaged Histone Deacetylase Inhibitors as Prodrugs in Targeted Cancer Therapy ..... - 104 -
5.1 Publication Summary ..... - 104 -

5.2 Author Contribution ..... - 106 -

6 Summary ..... - 107 -

7 References ..... - 115 -

8 Appendix ..... - 147 -

8.1 Appendix I. Publication I: Groebke Blackburn Bienaymé-mediated multi-component synthesis of selective HDAC6 inhibitors with anti-inflammatory properties ..... - 149 -

8.2 Appendix II. Supporting Information of chapter 3 “Hydrazide-based class I HDAC inhibitors with HDAC3 preference completely reverse chemoresistance in a synergistic manner in platinum-resistant solid cancer cells” ..... - 217 -

8.3 Appendix III. Supporting Information of chapter 4 “Development of HDAC class I selective PROTACs”. ..... - 235 -

8.4 Appendix IV. Publication II: Photocaged Histone Deacetylase Inhibitors as Prodrugs in Targeted Cancer Therapy. ..... - 262 -

Abbreviations

A

Abl Abelson murine leukemia viral oncogene homolog 1

Ac Acetylated

Ada Adenosine deaminase

ADME Absorption-Distributin-Metabolism-Excretion

AMC 7-Amino-4-methylcumarine

AML Acute myeloid leukemia

ATP Adenosine triphosphate

B

BAT Brown adipose tissue

BBB Blood-brain barrier

Bcl B-cell lymphoma

Bcr Breakpoint cluster region

BIM Bcl-2-like protein 11

BSA Bovine serum albumin

C

Calcd Calculated

CaMK Calcium/calmodulin-dependent protein kinase

cAMP Cyclic adenosine monophosphate

Cbz Benzyloxycarbonyl

CD Catalytic domain

cDNA Complementary DNA

CHD Chromodomain helicase DNA-binding

CI Combination index

cIAP Cellular inhibitor of apoptosis

CisR Cisplatin resistant

CML Chronic myeloid leukemia

CMS Compact mass spectrometer

CoA Coenzyme A

CoREST Co-repressor for element-1-silencing transcription factor

CRBN Cereblon

CRM1 Chromosomal region maintenance protein 1

CTCL Cutaneous T-cell lymphoma

CuAAC Cu(I)-catalyzed azide alkyne cycloaddition

D

d (NMR) doublet

Dad Deacetylase-activating domain

DAMP Damage-associated molecular pattern

DC_{50} Half maximal degradation concentration

DFMO Difluormethyl-1,3,4-oxadiazol

DIPEA *N*,*N*-Diisopropylethylamine

D_{max} Maximal extend of degradation

DMEM Dulbecco's Modified Eagle Medium

DMF *N*,*N*-Dimethylformamide

DMNB 4,5-Dimethoxy-2-nitrobenzyl

DMSO Dimethyl sulfoxide

DNA Deoxyribonucleic acid

DNMT DNA methyl transferase

E

EDC 1-Ethyl-3-(3-dimethylaminopropyl)carbodiimide

EDTA Ethylendiaminetetraacetic acid

ELISA Enzyme-linked immunosorbent assay

ELM EGL-27 and MTA1 homology domain

EMA European Medicines Agency

EMT Ephithelial-mesenchymal transition

ERRα Estrogen related receptor α

ESI Electrospray ionization

F

FDA U.S. Food and Drug Administration

FOXP3 Forkhead-Box-Protein P3

FP Foot pocket

FPU Foot pocket unit

G

GAPDH Gyceraldehyde 3-phosphate dehydrogenase

GBB Groebke Blackburn Bienaymé

GPS G-Protein pathway suppressor

H

h (NMR) heptet

HAT Histone acetyltransferase

HATU [*O*-(7-Azabenzotirazol-1-yl)-*N*,*N*,*N*',*N*'-tetramethyluronium-hexafluorophosphate

γH2AX Serine139 phosphorylated histone H2AX

HDAC Histone deacetylase

*h*HDAC Human HDAC

HIF Hypoxia inducible factor

HMT histone methyltransferase

HOBt 1-Hydroxybenzotriazole

HPLC High-performance liquid chromatography

HR+ Hormone-receptor-positive

HRMS High resolution mass spectrometry

HSP Heat shock protein

Hyp Hydroxyproline

I

IC_{50} Half maximal inhibitory concentration

IFN_{γ} Interferon gamma

IKZF Ikaros family zinc finger protein

IL Interleukin

IMiD Immunomodulatory drug

InsP Inositol-phosphates

IPF Idiopathic pulmonary fibrosis

iPrOH *Iso*propanol

L

LC Liquid chromatography

LPS Lipopolysaccharide

LPU Lower pocket unit

LRMS Low resolution mass spectrometry

LSD1 lysine demethylase 1

Lys Lysine

M

m (NMR) multiplet

MAPK Mitogen-activated protein

MBD Methyl-CpG-binding domain

MDM2 Mouse double minute 2 homologue

MeCN acetonitrile

MEF Myocyte enhancer factor

MEF2 Myocyte enhancer factor 2

MeOH Methanol

Mp Melting point

MTA Metastasis-associated protein

MTOC Microtubule-organizing center

MTT 3-(4,5-Dimethylthiazol-2-yl)-2,5-diphenyltetrazolium bromid

N

NCoR Nuclear receptor co-repressor

NES Nuclear export sequence

NF-$_{\kappa}$B nuclear factor kappa-light-chain-enhancer of activated B-cells

NLR Nucleotide-binding oligomerization domain-like receptors

NLRP NLR family pyrin domain containing

NLS Nuclear localization sequence

NMPA Chinese National Medical Products Administration

NMR Nuclear magnetic resonance spectroscopy

NuRD Mi2/nucleosome remodeling deacetylase

NVOC-Cl 6-nitroveratryl chloroformate

P

PAMP Pathogen-associated molecular pattern

PBS Phosphate-buffered saline

Pc Photocaged

PDB Protein data bank

PHD Plant homodomain

Piv Pivalate

PNT Peroxynitrites

POI Protein of interest

PPG Photoremovable protecting group

PPI Protein-Protein interaction

Ppm Parts per million

PROTAC Proteolysis targeting chimeras

PTCL Relapsed or refractory peripheral T-cell lymphoma

PTFE Polytetrafluoroethylene

PTM Post translational modification

PWWP domain Pro-Trp-Trp-Pro domain

Q

q (NMR) quartet

qPCR Real-time polymerase chain reaction

R

RBBP Retinoblastoma binding protein

RF Resistance factor

R_f Retention factor

RIPA buffer Radioimmunoprecipitation assay buffer

RNA Ribonucleic acid

ROS Reactive oxygen species

S

s (NMR) singlet

SAHA Suberoylanilide hydroxamic acid

SAM *S*-adenosyl methionine

SANT Swi3-Ada2-NCoR-TFIIIB domain

SAP Sin3A-associated protein

SAR Structure activity relationship

SD Standard deviation

SDS3 Sin3 histone deacetylase corepressor complex component

SE14 Ser-Glu-tetra-decapeptide repeat domain

SERM selective estrogen receptor modulator

SF Selectivity factor

ShF Shift factor

SIK Salt-inducible kinase

Sin SWI-independent

SIRT Sirtuin

SMRT Silencing mediator for retinoid and thyroid hormone receptor

SWI Switch

T

t (NMR) triplet

TBL Transducin β-like protein

TBTA Tris((1-benzyl-4-triazolyl)methyl)amine

TBTU 2-(1*H*-Benzotriazole-1-yl)-1,1,3,3-tetramethylaminium tetrafluoroborate

TFA Trifluoroacetic acid

TFIIIB Tranfscription factor for polymerase III B

TGF transforming growth factor

TGN Trans-Golgi network

THF Tetrahydrofurane

TLC Thin-layer chromatography

Tle *tert*-Leucine

TLR Toll-like receptor

TNF Tumor necrosis factors

TOF Time of flight

U

UHPLC Ultrahigh performance liquid chromatography

UPS Ubiquitin proteasome system

UV Ultraviolet

V

VHL Von Hippel-Lindau

W

WHO World Health Organization

WT Wildtype

Y

YY1 Ying-Yang 1

Z

ZBG Zinc-binding group

*z*CD Zebrafish catalytic domain

*z*HDAC zebrafish HDAC

ZMAL Cbz-Lys(Ac)-AMC

ZnF-UBP Zinc-finger ubiquitin-binding

Chapter 1

Introduction

1.1 Preface

According to the GLOBOCAN cancer report published by the World Health Organization (WHO), 19.3 million new cases of cancer and almost 10 million cancer-related deaths occurred in 2020 worldwide. It is expected that the number of new cases will rise by 47% until 2040, making cancer one of the leading causes of death in every region of the world.[1] To address this global burden, the continuous development and improvement of therapeutic options are necessary. Nowadays, tumor therapy is based on various therapeutic options and combinations including the surgical removal of the tumor, radiotherapy, and/or chemotherapy.[2] Classic chemotherapeutic agents primarily target rapidly dividing cells, a hallmark of cancer,[3] by unselectively interrupting the cell division or DNA synthesis.[4] However, while effective in killing cancer cells, these agents also affect other fast dividing non-cancer cells, resulting in a high toxicity and undesirable side effects. The discovery of oncogenes and tumor suppressor genes, along with advancements in the exploration of the cellular transduction pathways have paved the way for the development of targeted therapy approaches to treat cancer.[5] In contrast to classic chemotherapeutic agents, such as cisplatin, targeted cancer therapy aims to specifically address proteins that regulate cell proliferation, division, and migration.[6] The clinical success of the Abl-kinase inhibitor imatinib marked a milestone in cancer therapy. For the first time it was possible to hit a specific genetic abnormality, the Bcr-Abl-fusion protein, to treat the chronic myeloid leukemia (CML), thereby transforming it from a life-threatening disease to a manageable condition with largely improved patient survival.[7] Until today, the field of addressable targets continues to expand and has led to the development and approval of numerous drugs across different cancer types. Examples include bortezomib,[8] the first in class proteasome inhibitor, for the first-line treatment of multiple myeloma in combination with lenalidomide or thalidomide[9] or the selective estrogen receptor modulator (SERM) tamoxifen[10] for the treatment of hormone receptor positive breast cancer.

By now, it is well established that both genetic and epigenetic alterations play a crucial role in tumorigenesis. Interestingly, especially mutations in genes encoding for proteins that directly regulate the epigenome occur frequently.[11] The silencing of tumor suppressor genes or the enhanced expression of oncogenes highly influence cellular mechanisms like apoptosis, proliferation, or DNA repair.[12] Furthermore, advances in genomic research have provided insights into the interplay between genetic and epigenetic alterations. Therefore, targeting epigenetic regulatory enzymes through targeted therapy offers the possibility to reverse aberrant gene function and restore normal cellular functions.[13]

1.2 Epigenetics – An overview

In the 1950s, Conrad Waddington suggested the definition of epigenetics as "An epigenetic trait is a stably heritable phenotype resulting from changes in a chromosome without alterations in the DNA sequence."[14] In short, epigenetics is the study of changes in gene expression unrelated to changes in the DNA-sequence. This enables cells, despite having near-identical genetic information stored, to differentiate into specified cells and higher order tissues.[15] One copy of the DNA consists of approximately three million base pairs packaged into 23 chromosomes. The most basic package unit is the nucleosome (see Figure 1). Around 147 base pairs of DNA are wrapped around an octamer core of histone protein. The histones involved, labeled H2A, H2B, H3, and H4, exhibit a positive charge,[16] which interacts with the negatively charged DNA backbone. Additionally, an H1 histone then binds another 20 base pairs of DNA forming the chromatosome with two full DNA turns around the histone core. Two chromatosomes are linked by a DNA-string of around 20 base pairs. The linked chromatosomes are further coiled through histone H1 into the 30-nanometer fiber, which in turn forms 300 nm long higher order structures (chromatin), to be further compressed into the chromosomes.[17] The DNA, in its tightly packed chromatin form, is not accessible for the binding of macromolecules, therefore maintaining cellular mechanisms require continuous regulation of gene expression. The interplay of various factors including architectural proteins, chromatin binding factors, and nucleosome modifications control the access to the DNA. By modulating the structure and accessibility of the chromatin, cells can fine-tune gene expression patterns in response to various signals.[18,19] The state of the chromatin can be roughly divided into two categories: the relaxed, transcriptionally active euchromatin and the condensed, transcriptionally inactive heterochromatin. Transition between those two states is balanced through multiple epigenetic modifications, including DNA methylation[20] and post translational modifications (PTMs) of histones[21] (e.g. methylation and acetylation).[22] Those "epigenetic marks" are covalent modifications that are attached by the so-called "writers" removed by "erasers" and read by "readers".[23] DNA methylation primarily occurs at the C5 position of cytosines on CpG sites and is established by DNA methyl transferases (DNMT), which act as the "writer".[24] The extensive methylation of DNA is associated with transcriptional repression of tumor suppressor genes[25] through the interference with regulatory proteins, thus preventing them from accessing the DNA. On the other hand, hypomethylation is also a regulatory mechanism in the epigenome, where it leads to chromosomal instability and genomic rearrangments.[26] The histones, as the central part of the nucleosome, consist of a structured C-terminal globular region, called the histone fold domain, and an unfolded, flexible N-terminal tail. The histone fold domain is responsible for the formation of the octamer core, which provides the structural stability for the nucleosome.[27] While the majority of histone PTMs are located within the tail domain, they can also occur on the globular core domain. There are well over 100 modifications known, with methylation, acetylation, and phosphorylation being the most

prominent.[21,22,28] The phosphorylation of histones takes place on the hydroxyl-group bearing amino acids serine, threonine and tyrosine. Kinases mediate the transfer of phosphate groups from ATP. The addition introduces a negative charge to the histones, which can affect the chromatin structure and act as a signal for other cellular processes.[29,30]

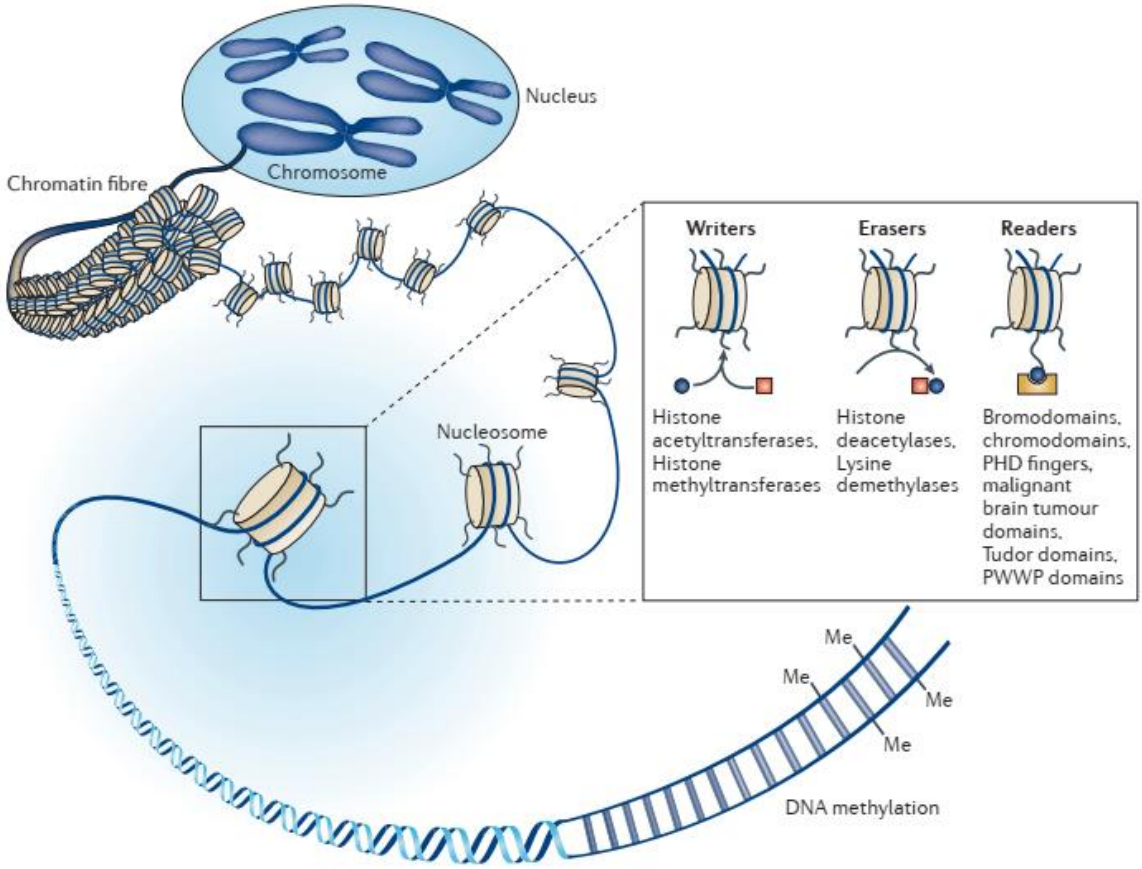


Figure 1. Basic composition of the chromosome. Plant homodomain (PHD) finger; Pro-Trp-Trp-Pro (PWWP) domain. Reprinted with permission from: Arrowsmith, C. H.; Bountra, C.; Fish, P. V.; Lee, K.; Schapira, M. Epigenetic protein families: a new frontier for drug discovery. Nat. Rev. Drug. Discov. **2012**, 11 (5), 384–400.[23] Copyright 2012 Springer Nature Limited.

Histone methylation occurs on the side chains of lysine and arginine residues. The methyl donor metabolite *S*-adenosyl methionine (SAM), derived from the essential amino acid methionine, is used as the co-factor for histone methyltransferases (HMT).[31] The ε-amino group of lysine can be mono-, di- or trimethylated, none of which changes the electronic charge of the side chain. Methylation marks are recognized by various proteins involved in chromatin remodeling and gene regulation.[32] Furthermore, the guanidine moiety of arginine can be mono- and symmetrically/asymmetrically dimethylated, thereby changing the electrostatic interaction between DNA and histones and also regulating other histone modifications. Depending on the level and type of methylation transcriptional processes are activated or represed.[33] Several epigenetic readers of methylated histones have been discovered, including the plant homodomain (PHD) finger motif,

Tudor domain or the Pro-Trp-Trp-Pro (PWWP) domain, which also interacts with the DNA.[23] The proper methylation status has a crucial role in mediating downstream cellular processes and studies have shown that deregulation of the methylation status can cause various diseases like cancer or neurological disorders such as the Sotos syndrome.[34]

The acetylation of histones takes place only on lysine side chains. It is highly regulated by the enzyme families of histone acetyltransferases (HATs, "writers") as well as histone deacetylases (HDACs, "erasers"). Bromodomains are the only known "readers" of acetylated lysine side chains of histones.[13] HATs catalyze the transfer of an acetyl group from the cofactor coenzyme A (CoA) to the ε-amino group of lysine side chains. Lysine acetylation removes the positive charge of the side chain, leading to a weakened interaction between the histones and DNA. The resulting relaxed chromatin structure enables transcription factors to bind to the DNA.[21] On the other hand, the removal of the acetyl group through HDAC enzymes leads to a more condensed chromatin structure, thus inhibiting gene expression.[35] Since HDACs are the focus of this thesis, this target class will be discussed in more detail in the following chapters.

1.3 Histone deacetylases (HDACs)

In 1964, Allfrey et *al*. first described histone acetylation as a highly influential PTM during their research on the role of histones in nuclear functions.[36] This was further elucidated in 1996, when the first human HDACs were identified by Taunton et *al*.[37] They were able to co-crystallize the known HDAC inhibitor (HDACi) trapoxin B with two nuclear proteins with histone deacetylase activity. Today, it is widely recognized that the enzymatic activity is not only limited to acetyl groups on histones but also target a wider variety of acyl groups on different proteins. Despite this expanded understanding, the term "histone deacetylase" remained unchanged and is still used to describe these enzymes.[38] Until now, there are 18 human HDAC (see Figure 2) isoforms known that can be divided onto four classes according to their structural features, sequence homology to HDAC yeast archetype Hda1 and Rpd3, and cellular localization: Class I (HDAC1, 2, 3, and 8), class II (HDAC4, 5, 6, 7, 9, and 10), class III (SIRT1-7), and class IV (HDAC11). Further, the class II enzymes are subdivided into class IIa (HDAC4, 5, 7, and 9) and class IIb (HDAC6 and 10).[39,40] The HDAC isoforms HDAC1-11 rely on a catalytic Zn^{2+}-ion to hydrolyze the acylated lysine, while the so-called sirtuins1-7 use the cofactor NAD^{+} to transfer the acyl group to the C2 position of the ribose moiety.[41,42] The different HDACs target a wide variety of proteins located in cytoplasma, cell nucleus, and mitochondria. Despite their distinct catalytic mechanism, both families of enzymes regulate gene expression and are considered oncoproteins.[43] Interestingly, sirtuins are also

described to act as tumor suppressors.[44] Since the zinc-dependent HDAC isoforms are the main focus of this thesis, sirtuins will not be discussed in more detail.[a]

The remaining eleven HDAC isoforms vary remarkably in their size from 347 amino acids (HDAC11) to 1215 amino acids (HDAC6).[43] The catalytic deacetylase domain shared by the zinc dependent HDAC isoforms has a conserved structure that includes a central β-sheet enveloped by an ensemble of α-helices and interconnecting loops. This arrangement forms a pocket within the domain that is approximately 11 Å deep, hosting the zinc ion. The binding site architecture is nearly identical throughout the different isoforms. The tunnel to the catalytic center consist of mainly hydrophobic amino acids like glycine, phenylalanine, and leucine that can accommodate the carbon chain of the acetyl-lysine. The zinc ion is coordinated by polar residues like histidine and aspartic acid with a water molecule next to it.[45] Depending on the isoform, there are further sub-pockets within the catalytic domain that contribute to isoform-specific functions, allowing them to target distinct substrates.[46]

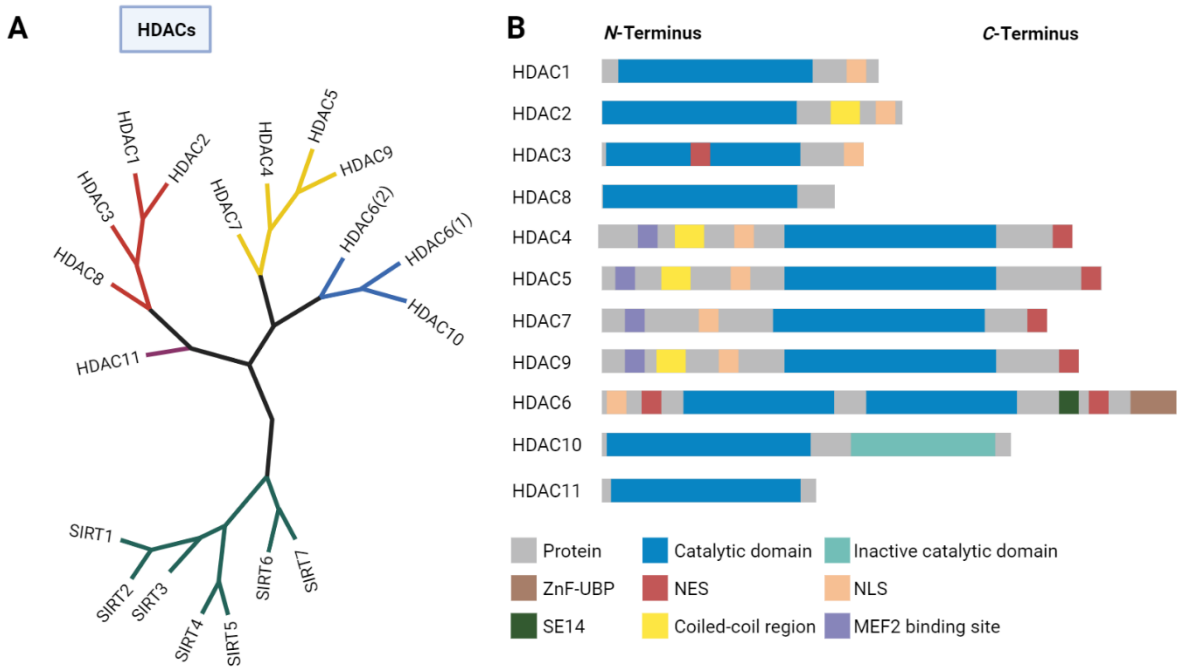


Figure 2. **A**) Evolutionary tree of the histone deacetylases including sirtuins. **B**) Structural and functional domains of the zinc dependent isoforms. Zinc-finger ubiquitin-binding domain (ZnF-UBP); Nuclear export sequence (NES); Nuclear localization sequence (NLS); Ser-Glu-tetra-decapeptide repeat domain (SE14); Myocyte enhancer factor 2 (MEF2). Adapted from Arrowsmith et *al*.[23] and Wagner et *al*.[47] Figure created with BioRender.com

[a] Henceforward, the abbreviation "HDAC" will be only used for the zinc-dependent isoforms of class I, II, and IV.

1.3.1 Class I

1.3.1.1 HDAC1 and HDAC2

The mammalian class I HDACs (HDAC1, HDAC2, HDAC3, and HDAC8) share a high sequence similarity to yeast Rpd3.[48] The HDAC1 and HDAC2 enzymes arose from a gene duplication and show the closest homology in class I.[49] They are localized only in the cell nucleus and occur ubiquitous within and between species. The main target of HDAC1 and HDAC2 are the acetylated lysines of histone tails itself, giving them the most definitive role in the regulation of gene expression by influencing the chromatin structure directly.[50] In addition, they have other important targets involved in gene regulation. For example, the deacylation of the tumor suppressor protein p53 leads to its destabilization and subsequent inactivation.[51] Furthermore, they can interact and enhance the activity of lysine demethylases 1 (LSD1)[52] or reduce the repressive effects of the corepressor Ying-Yang 1 (YY1).[53] Despite their efficient catalytic activity as single enzyme *in vitro*, in the cellular environment they depend on their respective corepressor complexes, where they are recruited interchangeably. The best studied multi-protein complexes are Mi-2/nucleosome remodeling deacetylase (NuRD), co-repressor for element-1-silencing transcription factor (CoREST), and SWI-independent-3A (Sin3A). Apart from Sin3A and Sin3B, HDAC1/2 enzymes are connected via a diverse, but recognizable ELM2-SANT-domain, which serves both as a recruitment and activation domain for the enzymes.[54] The NuRD complex is unique in its ability to combine deacylase and ATP-dependent chromatin remodeling activities. It has been shown that the complex has a regulating role in lineage commitment in embryonic stem cells, as well as in DNA replication and repair.[55] Its core exists as a dimer and is composed of several proteins including HDAC1/2, MTA1/2/3, and RBBP4/7.[56] HDAC1/2 are recruited to the complex via the ELM2-SANT-domain of an MTA corepressor. The C-terminus of MTA interacts with two copies of RBBP, facilitating the interaction of the complex with the histone tails and contributing to its overall binding to chromatin.[57] Notably, the protein-protein interaction (PPI) of the HDAC1:MTA complex is mediated by inositol-phosphates (InsP). Structural analysis has shown that the presence of phosphate groups from InsPs, in at least three adjacent sites, is required to fully activate the NuRD complex.

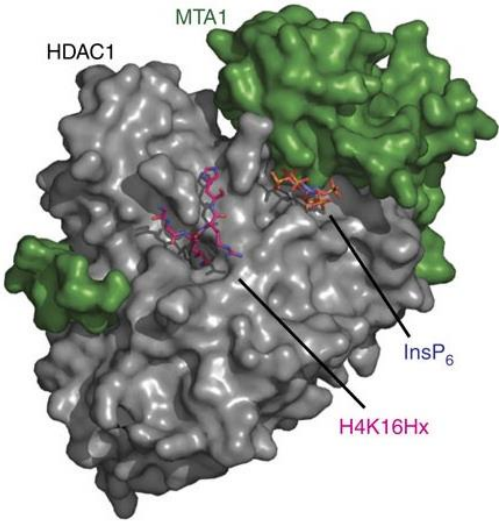


Figure 3. Crystals structure of the HDAC1:MTA1 complex mediated by inositol hexakisphosphate (InsP6) (PDB: 5ICN). The modified histone H4 peptide H4K16Hx interacts with the catalytic center of the HDAC1 enzyme. Adapted from Watson et *al*.[58]

Although there are no structural changes in the HDAC enzymes upon InsP binding, there are alterations in their kinetics and inhibitor binding, suggesting an activation through entropic allostery.[58] In addition, to HDAC1/2 and MTA proteins, the NuRD complex includes other components such as the chromatin remodeler CHD3/4 and methyl-CpG binding domain protein 2/3 (MBD2/3). These interchangeable components further contribute to the enzymatic activity and binding of the complex to histones cores.[59] The CoREST complex consist of a HDAC1/2 enzyme linked to the central REST protein and an additional LSD1 enzyme. It plays a central role in the neuronal gene expression and stem cell development.[60] In contrast to NuRD, the CoREST does not form a dimeric structure. The SANT2 domain, which is also involved in HDAC binding, is thought to be responsible for the DNA binding.[61,62] The SIN3 complex is another transcriptional repressor complex that occurs as a dimer. It has essential influence in embryogenesis and T-cell development.[63] It subsists of SIN3A/B, HDAC1/2, SDS3, and SAP30. Unlike other corepressor complexes, the SIN3 complex does not contain a recognizable ELM2-SAINT domain and the exact mechanism of HDAC binding is still not fully understood and requires further investigation.[54,64] HDAC1/ 2 are heavily involved in various hematopoietic lineages, where they affect cell differentiation, proliferation, lineage commitment determination, and more.[65] There are conflicting results about the interchangeability of the two isoforms.[66] Tissue-specific deletion of one isoform alone produces no distinct deleterious effects, whereas simultaneous deletion of HDAC1 and HDAC2 in the same tissue produces a distinguishable phenotype.[67–69] On the other hand, a global deletion of HDAC1 in mice results in embryonic death, while mice with a global deletion of HDAC2 only lived until the perinatal period.[70] Both enzymes are overexpressed in different kind of cancer, including gastric[71], lung[72], pancreatic[73], prostate cancer[74], as well as Hodgkin's lymphoma.[75] The overexpression of class I HDAC enzymes is typically associated with poor prognosis thus represents an attractive target for the development of new drugs.[76]

1.3.1.2 HDAC3

The HDAC3 enzyme shares around 50% sequence identity with HDAC1 and 2, but unlike them, HDAC3 possesses specific sequences in its protein structure that enable it to move between the nucleus and the cytoplasm.[77,78] The nuclear export signal (NES), present in the central region of HDAC3, facilitates its transportation out of the nucleus into the cytoplasm. Conversely, HDAC3 also contains a nuclear localization signal (NLS) in its C-terminal region to guide it back into the nucleus. The C-terminal region is essential for its enzymatic and transcriptional repression activity.[79] Like HDAC1/2, the catalytic function of HDAC3 requires the formation of a co-repressor complex.[80] The enzyme is uniquely recruited to the homologous silencing mediator for retinoid and thyroid hormone receptor (SMRT) and nuclear receptor co-repressor (NCoR).[81] The core of the complex is formed by two SMRT/NCoR receptors bound to a tetramer of TBL1, which is further associated with two GPS2 proteins. The interaction between HDAC3 and the co-repressors is established through a conserved deacetylase-activating domain (DAD), which includes a SANT motif (see chapter 1.3.1.1).[82] This motif is flanked by an unique amino terminus that is needed for the activation of HDAC3.[83] The interactions between the SANT domain and HDAC3 forms a basic pocket, where, similar to the HDAC1:MTA1 interaction, inositol-phosphates are able to bind.[84] In contrast to the HDAC1 complex, the binding of InsPs is mandatory for the enzymatic activity of HDAC3. Mutation of Arg265 of HDAC3, which forms a salt bridge with a phosphate group of the InsP, leads to a significant loss of activity and abolishment of interactions with SMRT-DAD, while mutation of the equivalent Arg270 in HDAC1 seem to only mildly abolish the activity.[58] HDAC3 is ubiquitously expressed and, depending on its subcelluar localization, involved in the deacylation of e.g. histones, STAT3, and FOXP3.[38] This broad enzymatic activity leads to its involvement in diverse physiological and tissue-dependent processes.[80] For instance, in hepatocytes of mice, the deletion of HDAC3 results in hepatosteatosis, characterized by increased lipogenesis and reduced fatty acid oxidation.[85] This indicates that HDAC3 is essential for maintaining lipid metabolism in the liver. Similarly, in brown adipose tissue (BAT), HDAC3 knockout mice exhibit a worse survival rate when exposed to very low temperatures, underscoring its vital role in thermogenesis and the regulation of core body temperature.[86] Other important tasks are the preservation of the development and remodeling of bones[87], insulin secretion in pancreatic β-cells,[88] and hematopoietic stem cell development[65]. Notably, HDAC3 has a central role in different diseases ranging from cancer[89,90] over inflammatory processes,[91] learning and memory dysfunction[92,93] to neurodegenerative disorders.[94,95]

1.3.1.3 HDAC8

Despite being grouped into class I, HDAC8 is highly distinct from the other three isoforms. It is the unique in its localization on the X-chromosome.[96] Its catalytic activity is independent from co-factors and rather controlled by phosphorylation.[97] Especially the PTM on S39 near the active site

negatively regulates the activity.[98] Notably, HDAC8 displays a distinct substrate preference. *In vivo*, it targets tetrameric histone (H3/H4) with a 40-300-fold higher activity over the corresponding peptide substrates.[99] This indicates that HDAC8's substrate selection is based on a combination of short- and long-range interactions. Moreover, HDAC8 also acts on several other non-histone proteins like cohesin,[100] p53,[101] and estrogen related receptor α (ERRα).[102] Additionally, HDAC8 exhibits a substrate specificity for longer acyl chains such as octanoyl-, dodecanoyl-, and myristoyllysine, suggesting a physiologically relevant fatty acid deacylation activity.[103] These distinct characteristics of HDAC8 highlight its importance in different cellular processes. Malfunction of HDAC8 has been associated with human cancers like metastatic melanoma,[104] and neuroblastoma.[105] Furthermore, mutations in the HDAC8 gene are linked to the Cornelia de Lange syndrome,[100] a developmental disorder.

The class I HDAC enzymes are structurally characterized by a unique internal cavity, the so-called foot pocket (FP), which plays a crucial role in their catalytic activity and substrate recognition.[35] It is approximately 14 Å long (HDAC1) and essential for stabilizing the substrate, thereby facilitating the removal of the acetic acid after cleavage, and supplying water during the catalytic process.[106] Notably, the FPs of HDAC1 and 2 are highly conserved and show similar structural characteristics with comparable substrate specificity. In contrast, HDAC3 exhibits a distinctive feature at the end of its FP, where a serine residue (HDAC1/2) is replaced by a bulkier tyrosine residue. This substitution restricts the available space, potentially influencing substrate specificity and catalytic efficiency.[45,107] Only, HDAC8 diverges from the conventional FP architecture by forming an unique second pocket. Interestingly, the size of the FP depends on the engaging ligand and is promoted by a highly flexible and adaptable N-terminus.[98]

1.3.2 Class IIa

1.3.2.1 HDAC4, 5, 7 and 9

The class IIa (HDAC4, 5, 7, and 9) isoforms share a high level of homology with yeast Hda1 (see Figure 2).[108] The enzymes are commonly found both in the nucleus and in the cytoplasm, regulated by specific regions within their protein structure. Similar to HDAC3, the subcellular localization is controlled by a N-terminal NLS region and a C-terminal NES region.[38] The isoforms are characterized by an extended N-terminus with numerous conserved serine residues acting as a crucial phosphorylation site. Various kinases, including the salt-inducible kinase (SIK)[109] and calcium/calmodulin-dependent protein kinase (CaMK)[110] target these serine residues for phosphorylation. This modification promotes the nuclear export via enhancing the interaction with the chromosomal region maintenance 1 protein (CRM1), a nuclear export factor.[43] Moreover, the proteins of the 14-3-3 family are also involved in this process. They inhibit the interaction of importin α with the NLS region of class IIa HDACs, effectively preventing the transport into the

nucleus. In their unphosphorylated state, class IIa HDACs preferentially localize to the nucleus, enabling the recruitment of HDAC3 in a SMRT/NCoR co-repressor complex. The role of class IIa enzymes in the complexes is still not entirely clear, since they don't show profound deacylase activity like other HDAC isoforms.[111] Additional to the NLS region, the N-terminus also contains a binding site for the myocyte enhancer factor 2 (MEF2) transcription factor. After export to the cytoplasm the HDAC:MEF2 complex dissociates transforming MEF2 from a transcriptional repressor to a transcriptional activator mediating various cellular processes.[110]

Class IIa enzymes have an additional lower pocket that resulted from an exchange of a conserved catalytic tyrosine, found in other HDAC isoforms, with a histidine residue that rotates away from the active center. The additional pocket has been shown to strongly influence the substrate specificity and diminish the enzymatic activity, rendering them approximately 1000-fold weaker than other isoforms.[112] The precise substrates for class IIa HDACs have not been identified so far. Their distinct structural features and very low enzymatic activity imply that they may have specific substrates that are yet to be discovered. Notably, the presence of a histidine residue in the active site exhibits parallels to the classic zinc amidohydrolase thermolysin, where a histidine residue participates in catalysis.[113] This observation raises the possibility of mechanistic similarities between those enzymes. Thus far it seems likely that they mainly act as a scaffolding proteins, with the actual hydrolysis carried out by HDAC3.[38] In contrast to class I HDACs, class IIa enzymes are expressed in a tissue specific manner. HDAC4 is highly expressed in the growth plates of the skeleton and skeleton muscles where they regulate the chondrocyte hypertrophy and skeletogenesis.[114] HDAC5 and HDAC9 are mainly found in heart, muscles, and the brain, suggesting their involvement in cardiac and neural functions.[115] HDAC7 is highly abundant in the vascular endothelium, where it acts as a regulator of blood vessel development during early embryogenesis.[116] Class IIa HDACs are overexpressed in different diseases like thyroid[73] and esophageal cancer[117], Burkitts lymphoma[65] or medulloblastoma.[118]

1.3.3 Class IIb

1.3.3.1 HDAC6

The class IIb HDAC isoforms HDAC6 and HDAC10 are distinct from other class II members in regard to their possession of two deacetylase domains.[119] HDAC6, the largest isoform with 1215 amino acids, is primarily located in the cytoplasm.[120] Its localization is maintained by a Ser-Glu-tetra-decapeptide repeat domain (SE14), which is anchoring the enzyme in the cytoplasm, as well as two CRM1 dependent NES and one NLS (see Figure 2B).[121] The two catalytic domains, CD1 and CD2, of HDAC6 exhibit independent activities. The CD1 has a wider active site than that of the CD2, but shows a high selectivity for substrates with C-terminal lysine residues. This is due to a lysine residue at the entrance to the active site that can serve as a "gatekeeper". As a result, CD1 seems to exhibit an overall weak activity towards peptide substrates, and its biological function

remains elusive.[122] The CD2 domain demonstrates a broader substrate range and is primarily responsible for the biological activity of HDAC6.[123] The CD2 pocket possesses unique structural features at the entrance compared to other isoforms, which arise from the presence of two rigid loops. The L1-loop is primarily characterized by four amino acids (H463, P464, F583, and L712) that create a wide pocket, which can be engaged by HDACi with large, hydrophobic cap-groups. The L2-loop holds a "gatekeeper"–serine residue (S531), which is exclusive to the HDAC6 enzyme.[124] In addition to its distinctive catalytic domains, HDAC6 possesses a zinc-finger ubiquitin-binding domain (ZnF-UBP) in its C-terminus. This domain contains conserved cysteine- and histidine-rich regions that enable HDAC6 to interact with both mono- and polyubiquitin chains.[125,125,126] The striking features of HDAC6 are its specific cellular localization and substrate specificity. While almost all other HDAC isoforms are primarily associated with histone deacylation and chromatin remodeling, HDAC6 regulates the function on many non-histone proteins. Some of its key targets include α-tubulin,[127] heat shock protein 90 (HSP90),[128] and tau,[129] which are involved in maintaining the cytoskeleton and protein homeostasis within the cell. Moreover, HDAC6 exhibits its influence also in the nucleus where it targets important nuclear proteins like FOXP3 and the DNA repair factor KU70.[130] α-Tubulin was the first substrate of HDAC6 to be discovered. Acetylation, especially at lysine 40 of α-tubulin, is a common PTM in the regulation of the transport of cargos along the microtubule network.[131] Additionally, HDAC6's response to transforming growth factor-β1 (TGF-β1) is particularly interesting. Upon TGF-β1 signaling, HDAC6 mediates the deacetylation of α-tubulin, resulting in increased cell motility and the expression of ephithelial-mesenchymal transition (EMT) markers. EMT is a critical cellular process involved in embryonic development, tissue repair, and wound healing. However, dysregulated EMT has been implicated in various pathological conditions. The loss of cell-cell junction leads to increased motility and contributes to the invasive and migratory properties of cancer and fibrotic cells.[132–134] HSP90 was the second identified substrate of HDAC6. Hyperacetylated HSP90 leads to a loss of function through the dissociation from the cochaperone p23. This acetylation-mediated disruption of the HSP90:p23 complex affects the chaperone activity of HSP90, which is essential for the proper folding and stabilization of multiple client proteins.[128] Interestingly, HSP90 and HDAC6 have been found to form a complex, allowing them to detect ubiquitinated cell aggregates.[135] The ubiquitin binding-activity mediates the shuttling of ubiquitinated aggregates to the aggresomes, through the microtubule network, giving HDAC6 a central role in the degradation of misfolded proteins.[136] Another important target of HDAC6 are tau proteins. In healthy tissues, HDAC6 actively shuttles tau proteins for targeted sequestration or degradation. However, in neurodegenerative disorders such as Alzheimer's disease, hyperphosphorylated tau proteins tend to aggregate, thereby leading to the formation of neurofibrillary tangles. Through the inhibition of HDAC6, the HSP90:HDAC6 complex separates,

which subsequently triggers the ubiquitination and degradation of phosphorylated tau proteins.[129,137] Lately, HDAC6 has also been associated with the activation of the NLRP3 inflammasome, which is a crucial component of the innate immune response.[138,139] The activation of the inflammasome is a complex process, which is not fully understood yet. It involves two main stages, the priming and actual activation. During the priming stage, the expression of components of NLRP3, caspase 1, and pro-interleukin-1β (pro-IL-1β) is upregulated. This is accomplished either by the recognition of different pathogen-associated molecular patterns (PAMPs), damage-associated molecular patterns (DAMPs) or through cytokines like tumor necrosis factors (TNF) and IL-1β.[140,141] Additionally, priming with lipopolysaccharide (LPS) shifts the macrophage metabolism from oxidative phosphorylation to glycolysis, further enhancing the IL-1β gene transcription.[142] The activation stage involves the assembly of the NLRP3 inflammasome and consequently the caspase 1 dependent release of IL-1β and IL-18 from their precursor as well as gasdermin D mediated pyroptosis.[140] The NLPR3 activation is triggered by various upstream signals including ATP- and nigericin mediated K^+-efflux[143,144] and Ca^{2+}-flux[145]. HDAC6 has been shown to play an indispensable role by facilitating the microtubule transport of NLRP3 from the trans-Golgi network (TGN) to the microtubule-organizing center (MTOC), where the inflammasome assembles and accumulates.[146] Moreover, after exposure to LPS, HDAC6 promotes the activation of mitogen-activated protein (MAPK) and NF-κB signaling pathways, which ultimately lead to the release of inflammatory cytokines.[147] Inhibition or knockdown of HDAC6 has been shown to suppress these signaling pathways thereby blocking NLRP3 inflammasome activation and the release of interleukins.[148]

Due to its activities, HDAC6 is a key player in multiple diseases. Dysregulation of HDAC6 has been associated with altered motility and invasive properties in cancers like breast carcinoma,[149] pancreatic cancer[150] or neuroblastoma.[151,152] Furthermore, neurodegenerative diseases like Alzheimer's[129] or Parkinson's disease[153] as well as fibrotic diseases[154] and inflammatory processes[138] have been linked to HDAC6.

1.3.3.2 HDAC10

The HDAC10 enzyme is structurally related to HDAC6 and occurs primarily in the cytoplasm (see Figure 2).[155] It comprises a N-terminal catalytic active domain, a leucine-rich domain and a C-terminal catalytic domain that, interestingly, does not exhibit any known catalytic activity.[156] With the exception of the CD1 of HDAC6, all HDAC enzymes have a conserved leucine or methionine at the entrance to their active site, which influences the substrate binding.[122] However, in the case of HDAC10, this residue is replaced by a glutamate. This unique substitution acts as a gatekeeper, which allows HDAC10 to selectively hydrolyze N^8-acetylspermidine.[157] Dysregulation of the polyamine metabolism, in which spermidine plays a vital role, is frequently associated with

hyperproliferative diseases.[158] Recently, spermidine has been connected with the induction of autophagy in cells, resulting in the suppression of necrosis and enhanced longevity of affected cells.[158,159] In this context, inhibiting HDAC10 activity offers the possibility to intercept the spermidine-mediated autophagy pathway and direct cancer cells to undergo apoptosis, potentially providing a new avenue for cancer treatment.[24,160] Furthermore, HDAC10 controls M2 macrophage recruitment,[161] the activity of enzymes involved in stem cell development,[156] and performs regulatory roles through interactions with transcription regulators.[162]

1.3.4 Class IV

HDAC11 is the only member of class IV and highly conserved across species.[48,163] It consists of 347 amino acids, making it the smallest isoform, and shares sequence homology with class I and II HDACs.[164] HDAC11 functions in complexes with other HDAC isoforms to carry out its biological activities.[165] Similar to HDAC8, HDAC11 exhibits substrate specificity for longer acyl chains like myrostoyl lysine.[166] Although there is no X-ray structure of HDAC11 available, homology modeling suggest that the binding of the longer acyl chains occurs in a manner comparable to HDAC8. HDAC11 is expressed in several tissues like the heart,[163] skeletal muscles,[167] brain,[168] and gall bladder.[169] While it is mainly localized in the nucleus, in embryonic astrocyte precursors and mature cells it can also shuttle to the cytoplasm.[38,170] The wide-ranging influence of HDAC11 is evident in its involvement in various physiological and pathological processes such as central nervous system development,[171] immunomodulation,[172] and genomic stability.[173] Recently, HDAC11 has also been linked to obesity disorders[174] and diabetes.[175] Given that HDAC11 knockout mice produce a healthy phenotype, HDAC11 can be a promising target for the treatment of those diseases.[176]

1.3.5 Deacetylation mechanism of HDACs

The first description of the catalytic mechanism of HDACs were provided by Finnin *et al*. in 1999 through the determination of the crystal structure of a HDAC1 homolog from the bacteria *aquifex aeolicus*.[177] Since then, extensive research has further illuminated the structural isoform specificity and its impact on the deacetylation mechanism.[35,38,45] The group of Christianson has contributed immensely to this understanding by investigating the mechanism of the human HDAC6 (*h*HDAC6) CD2 and exploring the CD1 of zebrafish *danio rerio* HDAC6 (*z*HDAC6), which serves as a valid surrogate for studying the human domains.[122,123,178] Given the conservation of the catalytic center between class I and class IIb enzymes, the mechanism can be elucidated using the *z*CD2 domain as an example (Figure 4). The catalytic Zn^{2+}-ion is embedded next to a water molecule in the center of the CD2 (Figure 4A). It is coordinated by two aspartic acid moieties, D612 and D705 as well as a H614, thereby forming a distorted tetrahedral conformation.

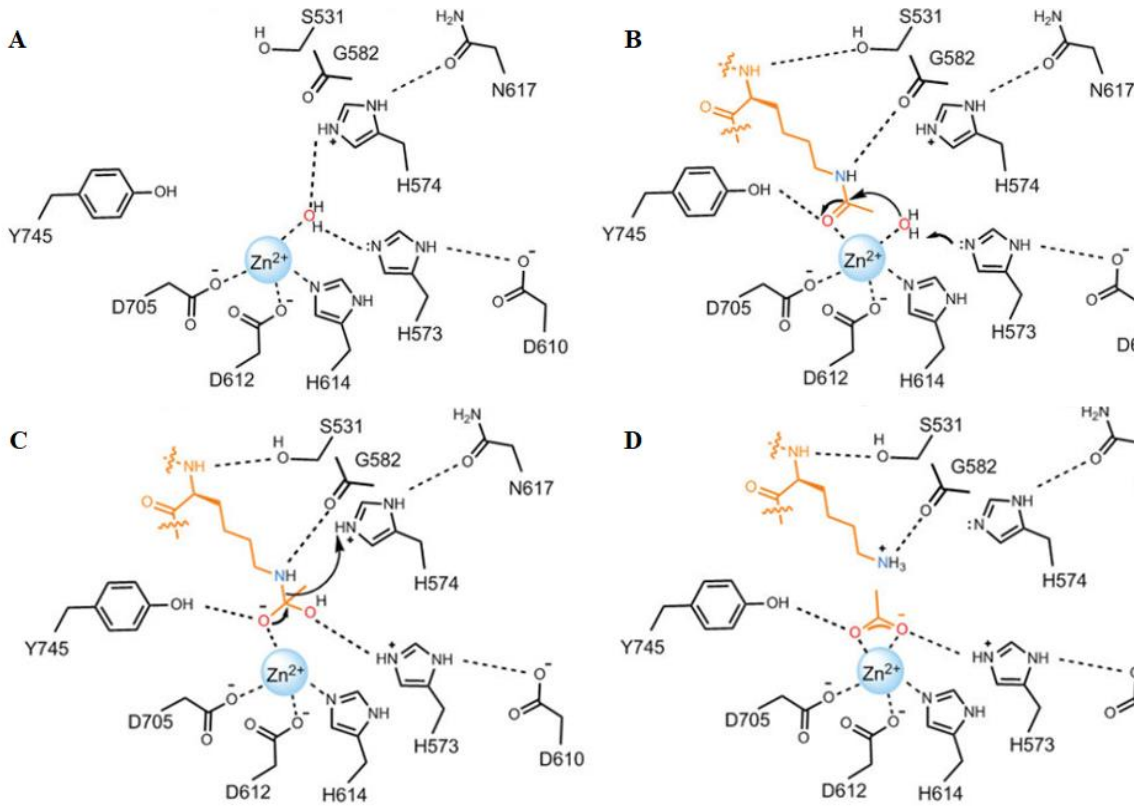


Figure 4. Proposed catalytic mechanism of zHDAC6 CD2 by Christianson *et al*.[123] Amino acids of the enzyme are shown in black, the catalytic Zn^{2+}-ion as a blue sphere, and *N*-acetylated lysine in orange. **A**) Catalytic pocket without substrate. **B**) The acetylated lysine substrate coordinates to the zinc-ion. **C**) Tetrahedral transition state. **D**) Coordination of the acetate leaving group by the enzyme and disengagement of the deacetylated lysine substrate. Adapted with permission from Nature Publishing Group, a division of Macmillan Publishers Limited: Springer Nature, Nature Chemical Biology, Hai, Y.; Christianson, D. W. Histone Deacetylases 6 Structure and Molecular Basis of Catalysis and Inhibition. *Nat. Chem. Biol.* **2016**, 12 (9), 741-747.[123]

An engaging *N*-acetylated lysine substrate (Figure 4B) is stabilized through the coordination with S531, a unique gatekeeper amino acid of HDAC6, the carbonyl group of G582, and Y745. Moreover, the carbonyl group of the acetyl moiety coordinates the Zn^{2+}-ion to form a pentacoordinated metal ion structure. This arrangement enables the adjacent water molecule to perform a nucleophilic attack on the carbonyl carbon-atom, facilitated by the proton uptake of H573 (Figure 4B). The resulting tetrahedral transition state (Figure 4C) is stabilized by coordination of the oxyanion with the zinc-ion and hydrogen bond interaction involving Y745 and H573 (Figure 4C). A proton-transfer from H574 to the ε-aminogroup triggers the collapse of the transition state, leading to the cleavage of the acetyl group from the lysine. Subsequently, the acetate is further stabilized by the Zn^{2+}-ion (Figure 4D) and can exit the active pocket after lysine substrate dissociation, ultimately restoring the enzyme to its resting state (Figure 4A).[123]

1.4 HDAC inhibitors

The widespread influence of HDAC enzymes as well as their overexpression or malfunction in several diseases strongly implicates HDACs as rational targets for drug development. The impact of HDACi on cells varies depending on their selectivity for specific isoforms and the cell types involved.[179] Notably, HDACi exhibit anticancer properties by inducing apoptosis,[180] regulating autophagy,[160] controlling cell migration[134] and angiogenesis,[181] triggering DNA damage,[180] suppressing DNA repair mechanisms,[182] and modulating cellular signaling pathways.[179] Additionally, HDACi have shown anti-inflammatory effects[139] and potential applications in treating neurodegenerative diseases.[129]

1.4.1 FDA approved HDACi

Given that the central basis of the catalytic mechanism revolves around the binding of ε-*N*-acyl-lysine substrates to the Zn^{2+}-ion, replicating this interaction is the logical starting point for drug development. The first pharmacophore model for HDACi was proposed by Jung et *al*. in 1997. This model comprises three key components: a zinc binding group (ZBG), which imitates the binding of the oxyanion transition state (Figure 4C), a linker that fits into the substrate channel, and a cap-group that interacts with the enzyme surface.[183] Trichostatin A (Figure 5) stands out as the first potent and specific HDACi, isolated by Yoshida et *al*. from the bacteria *Streptomyces platensis* in 1990.[184] In this molecule, the hydroxamic acid serves as the ZBG, effectively chelating the Zn^{2+}-ion through a bidentate binding mode which was later confirmed by crystallographic data.[123] The rigid diene linker is a suitable substitute for the C5-carbon-chain of acyl-lysine, while the phenyl ring serves as the cap group.[38] During their analysis of the antiproliferative effects of DMSO, the Breslow group discovered suberoylanilide hydroxamic acid (SAHA), which later became known as vorinostat.[185] Initially, its mode of action was unclear, but structural similarities to trichostatin A eventually revealed that SAHA functions as HDACi. In a significant milestone, in 2006, vorinostat (Zolinza®) became the first HDAC inhibitor to gain approval by the U.S. Food and Drug Administration (FDA) for the treatment of progressive, persistent or recurrent cutaneous T-cell lymphoma (CTCL).[186] This marked a pivotal recognition of the therapeutic potential of HDACi in cancer treatment.

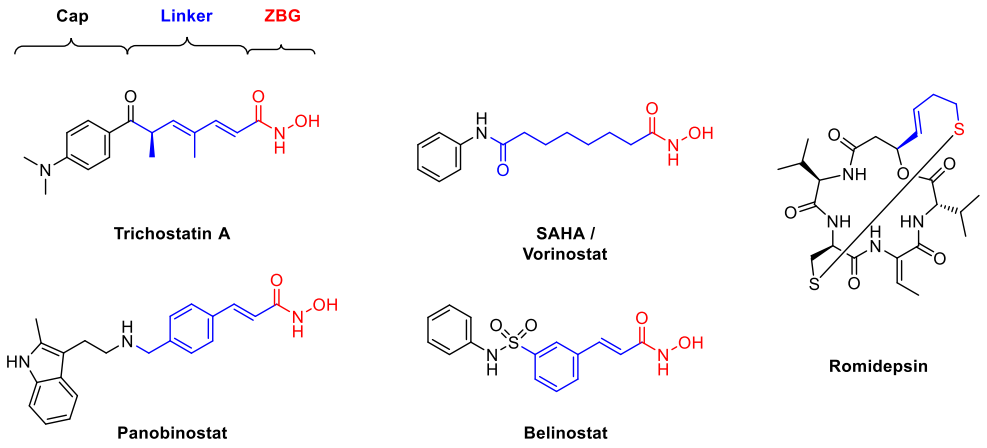


Figure 5. First discovered HDACi Trichostatin A with pharmacophore model and the FDA approved HDACi.[183,184,186]

Romidepsin, a natural product isolated from C*hromobacterium violaceum* in 1994, was identified as an HDAC inhibitor in 1998.[187,188] The prodrug Romidepsin is a class I selective HDACi. It binds the zinc ion of HDACs via a thiol group, which is released upon reduction of the disulfide bond.[189,190] In 2009, romidepsin (Istodax®) became the second FDA approved HDACi for the treatment of CTCL.[191] Another family of HDAC inhibitors, derived from trichostatin A, contains a more rigid linker. In 2014, Belinostat (Beleodaq®) became the third FDA approved HDACi for the treatment of relapsed or refractory peripheral T-cell lymphoma (PTCL).[192] Like vorinostat and panobinostat, it is a non-selective HDACi.[186] In 2015, panobinostat (Farydak®) was approved by the FDA and the European Medicines Agency (EMA) for the treatment of relapsed or refractory multiple myeloma in combination with bortezomib and dexamethasone.[193,194] Moreover, the FDA approved HDACi are under investigation for their chemosensitizing properties and as possible radiosensitizer against different types of cancer, but have not gained approval yet.[195–197] Despite the clinical success of HDACi, the complete scope of their actions within cells remains incompletely understood. While HDACi treatment leads to an increase in global histone acetylation levels, the ensuing gene regulation is complicated, involving both gene downregulation and upregulation. These effects appear to have a pronounced impact on hematological cancers, which could be attributed to their complex hematopoietic origin from stem cells. This makes them potentially more amenable to cellular reprogramming induced by HDACi compared to more differentiated cancer types.[38] In contrast, the underlying mechanisms that limit the effectiveness of HDACi against solid tumors remain poorly understood. Factors that might contribute include tumor resistance mechanisms and dose-limiting toxic effects.[38,198,199] All FDA approved HDACi exhibit severe side effects, including but not limited to low blood cell count, nausea, and fatigue. These adverse effects often necessitate treatment interruptions and limit their clinical utility. Especially the hydroxamic acid bearing inhibitors are known to show mutagenic activity in Ames tests and have been linked to the induction of chromosomal aberrations in rodent cells. This could potentially occur through

the formation of isocyanates via Lossen rearrangement.[200–203] The development of more isoform selective HDACi promises the reduction of these side effects. Such compounds could offer improved therapeutic efficacy with reduced adverse effects. For example, the antiproliferative activities of non-selective HDACi are largely attributed to the inhibition of the class I HDAC isoforms HDAC1, 2, and 3. Targeting these isoforms specificity is likely to be more effective while minimizing undesired side effects associated with the inhibition of various other.[38]

1.4.2 Selective HDACi

To design more selective HDAC inhibitors, several strategies have been explored. One primary approach involves modifying the ZBG, which is a common feature in most HDACi, excluding certain peptide-based inhibitors that predominantly interact with the enzyme surface.[204] Notably, the widely used hydroxamic acid ZBG does not exhibit selectivity across various isoforms. The incorporation of a thiol moiety, as seen in romidepsin, has demonstrated selective inhibition of class I HDAC enzymes.[205,206] Another approach involves utilizing *ortho*-aminoanilides, exemplified by entinostat, and substituted hydrazides such as compound **1** (Figure 6). These compounds have displayed strong selectivity for class I enyzmes.[207,208] As previously discussed, the different HDAC enzymes exhibit distinguished structural features that can be employed to design isoform selective inhibitors. Based on those structural features, Sippl and co-workers presented an extended pharmacophore model, offering a framework to guide the development of HDACi with enhanced isoform specifity.[46] The class I enzymes, especially HDAC1, 2, and 3, have an additional internal cavity perpendicular to the substrate binding tunnel, the so-called foot pocket (FP).[45] This unique structural feature can be used for the design of improved inhibitors. By incorporating a modification known as the foot pocket unit (FPU) onto the ZBG, as seen in hydrazide **1**, additional interactions can be established. This modification improves the inhibitory activity against those isoforms while diminishing the activity towards other isoforms.[209] Class IIa enzymes are distinctive due to their lower pocket, which is a result of a Tyr to His switch in the active site.[112] The gained space allows for the incorporation of a lower pocket unit (LPU) into class IIa selective inhibitors. Notably, branched moieties adjacent to the ZBG, like substituted cyclopropane derivatives (illustrated by compound **2**), possess a geometry conducive to engage this lower pocket.[210] While HDAC6 lacks an additional cavity akin to the aforementioned, its enzyme surface around the CD2 is particularly distinguishable from other isoforms through its wide pocket. Two rigid loops and a "gatekeeper" -serine present a promising opportunity for the introduction of additional interactions that can improve inhibitor binding and selectivity against HDAC6.[123,124]

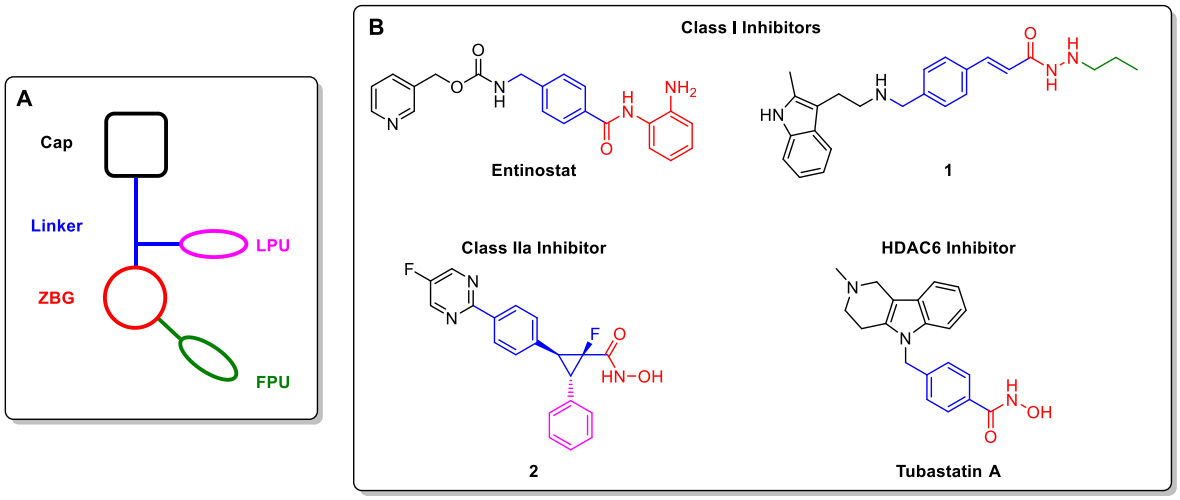


Figure 6. A) Extended pharmacophore model adapted from Sippl et *al.*[46] **B)** Examples for class selective HDACi.[207,208,210,211]

1.4.2.1 Class I selective HDACi

The development of class I selective HDACi can be effectively achieved by selecting an appropriate ZBG. Aminoanilides represent a prominent group of inhibitors in this category, with tucidinostat standing out as a notable example. Tucidinostat is approved by the Chinese National Medical Products Administration (NMPA) for the treatment of PTCL and in combination with the aromatase inhibitor exemestane for the treatment of hormone receptor positive (HR+) breast cancer.[212,213] Accordingly, tucidinostat is the only HDACi, which received regulatory approval for the treatment of a solid cancer entity. Tucidinostat exhibits potent inhibition of HDAC1, 2, and 3 at low nanomolar concentrations while showing no inhibition of HDAC6.[214] Its broad antitumor activity has also led to its evaluation in several clinical studies against various solid and hematological cancers.[215] Other examples of class I selective HDAC inhibitors include mocetinostat and domatinostat (Figure 7).[216,217] Furthermore, as previously mentioned, interaction with the foot pocket leads to increased activity and selectivity for these isoforms. The nature of the FPU used in inhibitor design can also influence enzyme specificity. Large (hetero)aromatic moieties, such as thienyl (compound **3**) or pyridinyl (compound **5**), have been found to confer high selectivity for HDAC1 and 2 over HDAC3. This selectivity arises from the slightly smaller foot pocket of HDAC3, which accommodates these larger FPUs less effectively.[45,218]

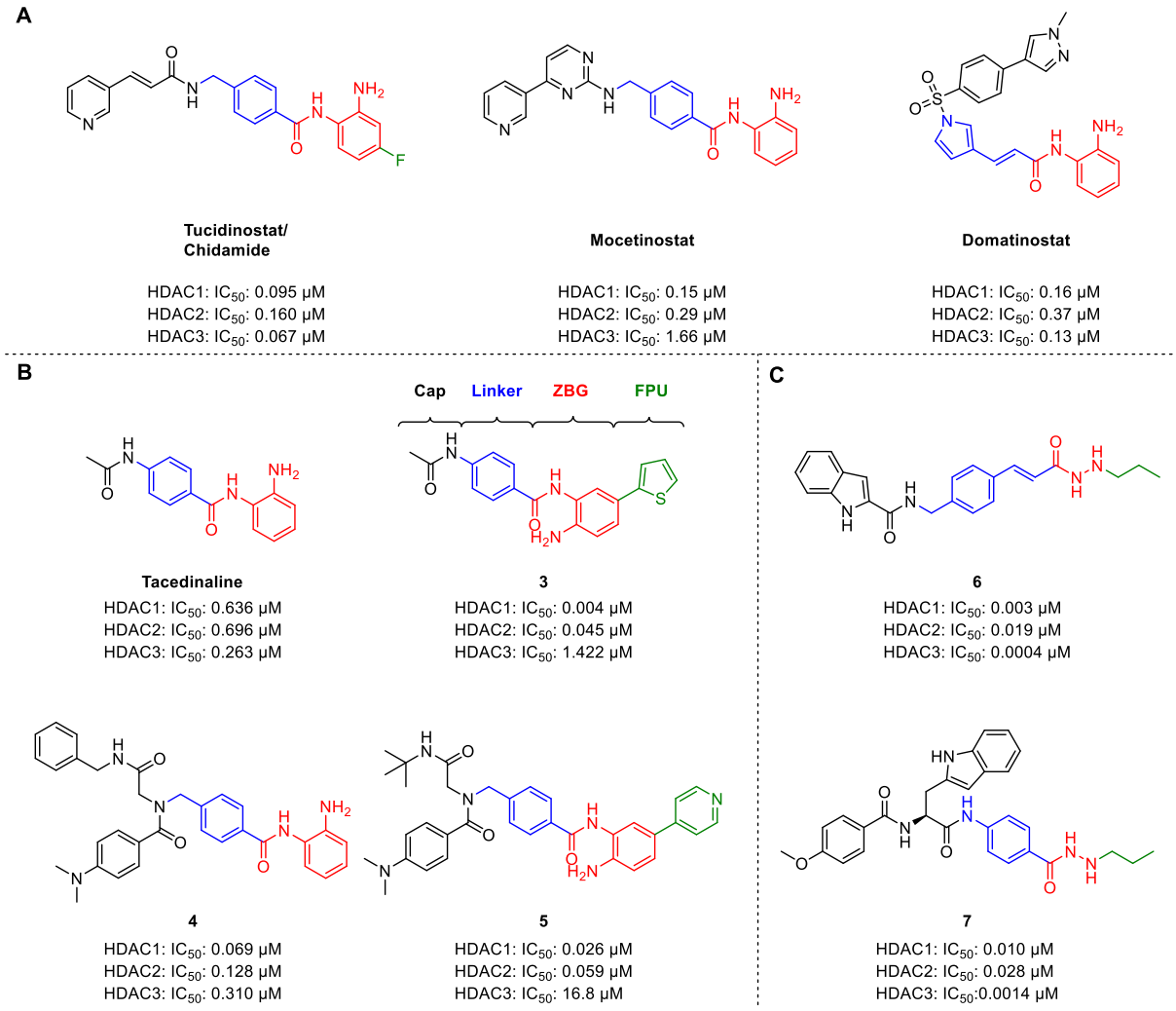


Figure 7. HDAC class I selective inhibitors. **A**) Examples for *ortho*-aminoanilides in clinical studies. Tucidinostat as the only approved class I HDACi. **B**) Example for the isoform-shift in class I through the introduction of a heterocyclic FPU. **C**) Selected substituted hydrazide based HDACi.[214,216–220]

Aminoanilides show distinct binding kinetics compared to hydroxamic acid based HDACi. While compounds like vorinostat and trichostatin A typically engage the enzymes with fast-on/fast-off binding kinetic, *ortho*-aminoanlides mostly demonstrate a slow-binding mechanism.[221] Bressi et *al*. proposed that *ortho*-aminoanilides generally bind with a slow-on, induced-fit mechanism. In the unbound state, the ligand stabilizes itself through an intramolecular hydrogen bound between the *ortho*-amine and the carbonyl oxygen of the ZBG. When the ligand interacts with the enzyme, this hydrogen bond does not necessarily need to be broken for the chelation of the Zn^{2+}-ion. Over time, reorientation of the ZBG enables additional interactions with the amino acids surrounding the zinc ion leading to the formation of a more stable binary enzyme-inhibitor complex.[209] Schäker-Hübner et *al*. further substantiated this concept by demonstrating that regardless of the cap and FPU used, *ortho*-aminoanilides engage HDAC1 in a slow-binding, induced-fit mechanism.[218]

Substituted hydrazides represent a relatively novel class of HDACi (see Figure 6B/7C).[222] Extensive investigations by Chou and coworkers unveiled a series of hydrazide-based compounds, including analogues to panobinostat (e.g. compound **1**, Figure 6B or compound **6** Figure 7C). Contrary to panobinostat, the propyl hydrazide variant displayed a striking selectivity for class I HDAC enzymes with a preference for HDAC3. Importantly, it exhibits superior bioavailability and has demonstrated lower mutagenicity in Ames tests than its parent inhibitor.[207] Furthermore, depending on the p53 status, a known tumor suppressor, hydrazides like **1** and **7** show anticancer properties in different cancer entities.[207,220] Especially, compound **6** stands out as the first hydrazide-based HDACi with *in vivo* antitumor activity against AML.[219] It's worth noting that, like aminoanilides, hydrazides are considered slow-binding inhibitors. However, what sets them apart is their capacity to bind competitively, non-competitively, or exhibit mixed inhibition. The mode of inhibition appears to vary depending on the specific HDAC isoform and the inhibitor in question.[207,223] While the *n*-propyl chain seems to be the best substitution for HDAC3 inhibition, Sippl and coworkers have established a set of HDAC8 selective inhibitors based on a *n*-hexyl substitution.[224] Also, selective HDAC6 inhibitors bearing an ethyl-hydrazide ZBG have been reported (Figure 9, compound **10**).[139] Since HDAC1, 2, and 3 are *in vivo* enzymatically active only within multi-enzyme complexes, and that they exhibit distinct behaviors within different complexes, developing complex-specific inhibitors presents therapeutic value.[54] There is evidence that the *ortho*-aminoanilide entinostat only inhibits HDAC1 and 2 when they are incorporated into the SIN3A/B complex but not when part of NuRD or CoREST.[225] Alternatively, a dual-target inhibitor like domatinostat (Figure 7A), which additionally binds to the LSD1 domain of the CoREST complex, could be a viable approach to achieve improved anticancer activity.[226]

1.4.2.2 HDAC6 selective inhibitors

As previously mentioned, the HDAC6 enzyme addresses non-histone proteins and selective HDAC6i do not show noteworthy cytotoxic properties when used in monotherapy.[227,228] Further, the knock-out of HDAC6 in mice results in a viable phenotype with no relevant deficiencies, indicating a possible use outside of oncology.[229] The structural features of the L1- and L2-loop of the CD2 provide a promising starting point for the development of selective HDAC6i. Moreover, the tunnel leading to the catalytic Zn^{2+}-ion appears to be slightly shorter for HDAC6 compared to class I HDACs. Exploiting these structural aspects, particularly through the use of shorter, phenyl-based linkers with bulky, branched cap groups, can shift the binding mode of inhibitors from the energetically slightly more stable bidentate binding mode (Figure 8A), seen with non-selective inhibitors, to a monodentate binding mode (Figure 8B).[230]

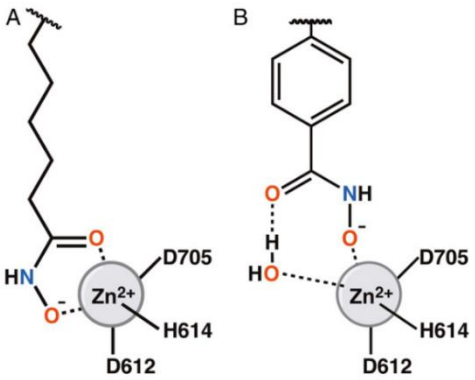


Figure 8. Depiction of the bidendate (**A**) and monodendate (**B**) Zn^{2+}-binding modes of hydroxamic acid based HDACi. Reprinted with permission from: Porter, N. J.; Mahendran, A.; Breslow, R.; Christianson, D. W. Unusual zinc-binding mode of HDAC6-selective hydroxamate inhibitors. Proc. Natl. Acad. Sci. USA **2017**, 114 (51), 13459-13464.[230] Copyright (2017) National Academy of Sciences.

The branch of the cap group should preferably be at the second atom away from the phenyl ring, with both arms being sterically demanding, forming a T-shaped inhibitor structure.[124] This alteration disfavors binding to class I enzymes, thus enhancing selectivity for HDAC6.[230] A selection of HDAC6 inhibitors is summarized in Figure 9. Tubastatin A was rationally designed by Butler et *al*. in 2010 and represents a significant achievement in the design of HDAC inhibitors. It stands out for its exceptional potency for HDAC6, exhibiting remarkable 57-fold preference over HDAC8 and 1000-fold over other isoforms.[231] Tubastatin A has earned recognition as the "gold standard" among HDAC6 selective inhibitors. The inhibitor displays activity against different neurological disorders,[232] hypertension,[233] and is able to reduce the migration capacity of glioblastoma cells.[234] Furthermore, it has been shown that the increased acetylation of α-tubulin through tubastatin A attenuated LPS induced inflammatory effects and protects dopaminergic neurons in Parkinson's disease.[153,235] Nexturastat A contains a less rigid cap group, but nonetheless has a profound selectivity for HDAC6. It has been reported to strongly inhibit the cell growth in murine melanoma cells and multiple myeloma and may be able to overcome resistance to bortezomib.[236,237] Matthias and coworkers found that the aromatic phenyl group of the cap fitted nicely into the L1-loop with the butyl-chain sitting in the L2-loop.[238] This stands in contrast to compound **8**, where the less bulky propyl-chain is pointed towards the L1-loop.[239] Compound **9** has been identified as a highly selective HDAC6 inhibitor, with no observable mutagenicity and cardiotoxicity in Langendorff-isolated rat hearts. As reported by Campiani et *al*., the inhibitor demonstrated the ability to reverse the phenotype in 3D organoid models of TGF-β1 dependent idiopathic pulmonary fibrosis (IPF), a condition that is challenging to treat effectively.[154] In addition to the classic hydroxamic acid, there are other groups that have been explored as ZBG.

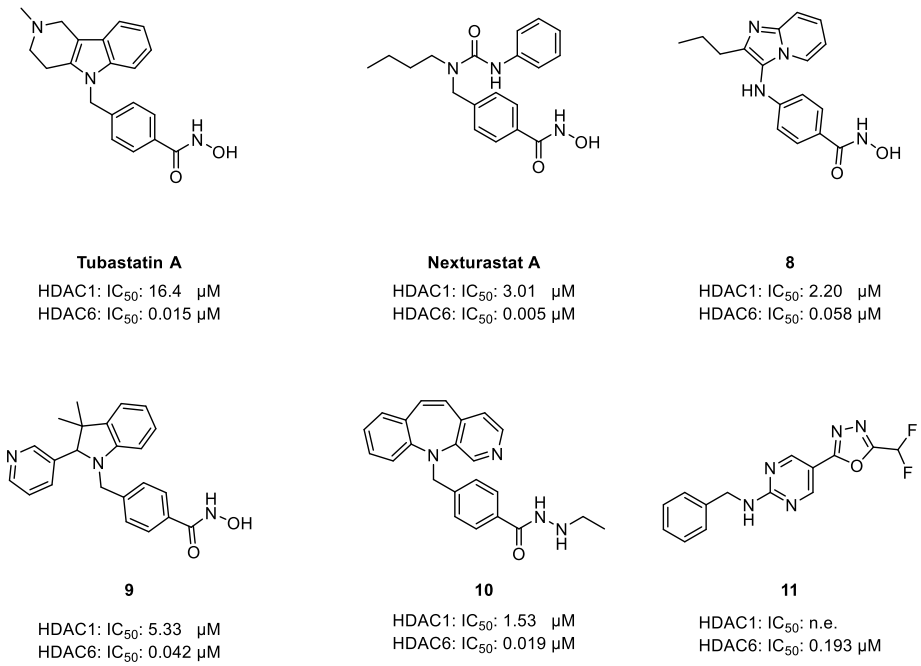


Figure 9. Selected HDAC6 inhibitors with reported activity against HDAC1 and HDAC6.[139,154,231,237,239,240] n.e.: no effect.

For instance, compound **10** represents a significant advancement in this regard, as it is the first selective HDAC6 inhibitor to employ a hydrazide as the ZBG. It outperformed tubastatin A in terms of oral bioavailability, *in vivo* half-life, and blood-brain barrier (BBB) permeability. Furthermore, compound **10** successfully suppresses the LPS/ATP-induced IL-1β release in murine macrophage J774A.1 cells.[154] Additionally, difluoromethyl-1,3,4-oxadiazols (DFMO) derivatives such as compound **12** have some remarkably properties.[241] HDACi featuring DFMO as the ZBG exhibit selectivity primarily for HDAC6 and do not affect other isoforms. Moreover, they operate via a two-step, slow-binding mechanism with an essentially irreversible binding mode. This is due to the hydrolysis of the DFMO group by the zinc-bound water molecule, resulting in the formation of a negatively charged acylhydrazide that coordinates with the zinc-ion.[240]

1.4.3 HDAC inhibitor prodrugs

Prodrugs are molecules that possess minimal or no inherent pharmacological activity but are ingeniously designed to undergo transformation within the body, e.g. through enzymatic or chemical processes, into active drugs. The primary objective of prodrugs is to improve the overall pharmacological profile of the drug. This can involve optimizing factors such as absorption, distribution, metabolism, and excretion (ADME properties), leading to a more effective and safer therapeutic intervention.[242] The high toxicity and limited bioavailability of approved unselective HDACi have sparked the development of different prodrug approaches. For example, Thomas et *al*. modified the hydroxamic acid moiety of vorinostat with β-O-galactoside (Figure 10). Compound **12** was structurally stable under physiological conditions and exhibited reduced cytotoxicity

compared to vorinostat. In the presence of β-galactasidase, an enzyme which occurs ubiquitously across species, the prodrug could be enzymatically converted into the biological active vorinostat.[243] Another approach, reported by Qin and coworkers, involved the modification of vorinostat with a boronic acid containing group (compound **13**). This prodrug is designed to be activated in the presence of specific reactive oxygen species (ROS), such as H_2O_2 or peroxynitrites (PNTs). Notably, these ROS are often found in the microenvironments associated with AML and other cancer entities. This prodrug strategy ensures targeted drug release, allowing for drug activation precisely within disease-specific enviroments.[244,245] In a related approach, the group of Hammond expanded panobinostat with a 1-methyl-2-nitroimidazole (compound **14**). Under normoxic conditions, the prodrug shows only little inhibitory activity against HDACs, but is activated through an enzymatic reduction in hypoxia, a typical environment in tumors and associated with therapy resistance and poor prognosis.[246] The photo-induced activation of a prodrug represents a practical approach for achieving selective drug release within the target tissue. The concept of using a photoremovable protecting group (PPG) for biological applications dates back to 1977, when Engels et *al*. initially described the photorelease of cAMP.[247] In a recent study, Troelsen and colleagues designed a light-sensitive prodrug (compound **15**) by incorporating a 4,5-dimethoxy-2-nitrobenzyl (DMNB) moiety to the ZBG of panobinostat. Notably, compound **15** itself does not exhibit inhibitory activity against HDAC enzymes. Its activation solely occurs upon exposure to light of 405 nm. However, it is worth mentioning that during treatment, a considerable amount of the corresponding carboxamide is formed as a major side product.[248]

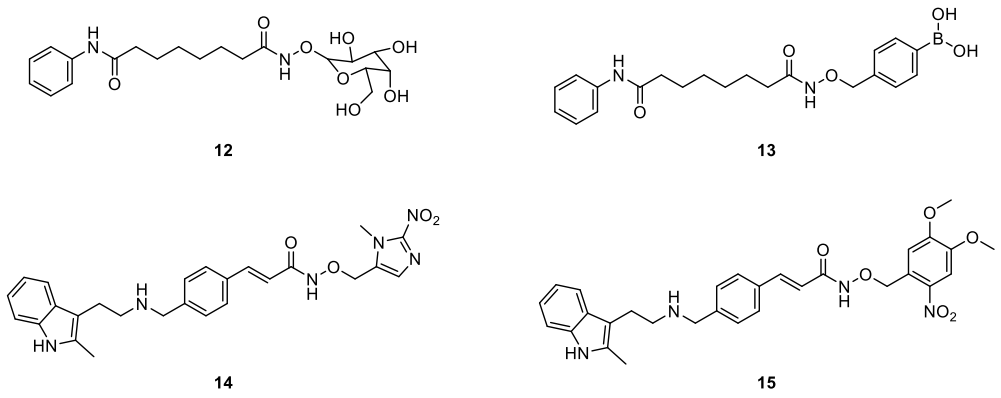


Figure 10. Examples for HDACi prodrugs with different activation principles. [243,244,246,248]

1.5 Proteolysis Targeting Chimeras (PROTACs)

The use of traditional small molecule inhibitors in drug discovery encounters several challenges. Firstly, these inhibitors are often constrained by the availability of suitable binding pockets that can effectively regulate protein function. Additionally, small molecules typically necessitate high systemic exposure to exert a significant impact on biological processes. This, combined with an often only limited selectivity increases the risk of toxic off-target effects. In contrast, the utilization

of the ubiquitin proteasome system (UPS) for targeted protein degradation presents a promising possibility to overcome these limitations.[249] The ubiquitination of proteins is accomplished through three enzymes. First, an E1 ligase activates ubiquitin in the presence of ATP, resulting in the formation of an ubiquitin-E1 thioester. Next, this ubiquitin is transferred to an E2 ligase via another thiol ester linkage, which in turn interacts with an E3 ligase through multiple scaffolding proteins. The E3 ligase is responsible for the final target specificity. Finally, a tertiary complex between the target protein and the E3-ligase complex is formed and the ubiquitin is transferred once more to a lysine residue on the target protein surface. A poly-ubiquitinated protein is then recognized by the proteasome and consequently degraded.[250] Therefore, **Pro**teolysis **Ta**rgeting **C**himeras (PROTACs) represent a groundbreaking approach in drug discovery. They are bifunctional molecules comprising a ligand for the protein of interest (POI) and another ligand for an E3 ubiquitin ligase, which are connected to each other by the so-called "spacer". PROTACs work by redirecting the UPS to target the POI. They bring the POI and the ligase complex into close proximity, facilitating the transfer of ubiquitin to the POI, thereby marking it for degradation (Figure 11).[251]

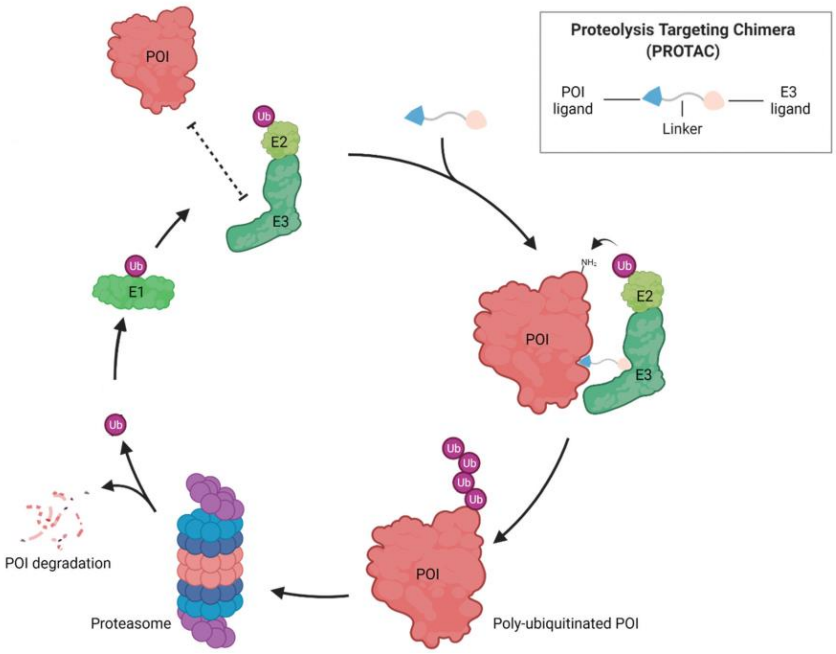


Figure 11. Principle of the mechanism of PROTAC induced targeted protein degradation. Adapted with permission from Royal Society of Chemistry, Chemical Society reviews, Li, K.; Crews, C. M. PROTACs: past, present and future. *Chem. Soc. Rev.* **2022**, *51* (12), 5214–5236.[249]

PROTACs offer several advantages over traditional small molecule inhibitors. Their catalytic mode of action results in a longer lasting effect, allowing for lower drug dosage. Additionally, they tend to be more selective, because they require the formation of a ternary complex for proper ubiquitination of the POI. Since PROTACs do not necessarily have to bind to the active site of a

POI, they are able to target former undruggable proteins. Furthermore, the choice of an appropriate E3 ligase enables tissue-specific degradation, adding an extra layer of selectivity to their mode of action.[252] However, PROTACs have some disadvantages. Being bivalent molecules, they often have a high molecular weight, which can reduce their ability to enter cells, penetrate tissues, and achieve oral bioavailability. Off-target protein degradation can also occur. This off-target effect can involve the degradation of a protein that is not directly bound by the PROTAC, or it can involve the recruitment of neosubstrates by the E3 ligase, leading to their ubiquitination and degradation.[253] The "hook effect" is yet another challenge. At high concentrations, PROTACs can saturate the E3 ligase and target protein without forming a ternary complex, preventing ubiquitination and increasing the risk of binding to lower-affinity off-targets. Furthermore, the PROTAC-protein complex can potentially trigger pharmacological responses distinct from degradation.[254]

1.5.1 E3-ligase ligands

The human genome consists of more than 600 known E3 ligases, of which only a few have been utilized for the design of PROTACs. The pioneering work in small molecule PROTAC development dates back to 2008, when Crews and colleagues used the mouse double minute 2 homologue (MDM2) E3 ligase. They recruited this ligase using the known PPI inhibitor of the MDM2-p53 interaction, nutlin (Figure 12, compound **16**).[255] In 2010, the Hashimoto group reported bestatin (**17**) as the first cellular inhibitor of apoptosis protein 1 (cIAP1). However, the self-ubiquitination of the E3 ligases limited the potential of these early PROTACs.[249,256] After the market removal of thalidomide in the 1960s,[257] extensive studies disclosed thalidomide and its derivatives (**18-20**) as effective immunomodulatory drugs (IMiDs) for the treatment of multiple myeloma.[258] Ito et *al*. confirmed the binding of thalidomide to the E3 ligase cereblon (CRBN) and its consequent inhibition of its endogenous substrate MEIS2.[259] This structural insight paved the way for the application of IMiDs as E3 recruiting ligands, facilitating CRBN-mediated ubiquitination in PROTACs. Furthermore, the von Hippel-Lindau (VHL) protein is the substrate receptor subunit of the Cullin 2 E3 ligase.[260] Dysfunctional VHL proteins are associated with the VHL disease, a rare genetic defect, which increases the risk for a variety of cancers.[261] The best known substrates of VHL are the hypoxia inducible factor 1α (HIF-1α) and HIF-2α. Under normal oxygen conditions, these HIF-α proteins are hydroxylated at the 4-position of a proline, which is recognized by VHL and consequently ubiquitinylated. However, under hypoxia conditions, HIF-α proteins are not hydroxylated, due to the lack of oxygen. Therefore, VHL cannot recognize them, allowing these proteins to activate the transcription of hypoxia-responsive genes.[262] The discovery of small molecule inhibitors for the VHL/HIF-α interaction were centered around the 4-hydroxyproline moiety. In a structure activity relationship (SAR) study, the Ciulli group identified **21** and **22** as two highly potent inhibitors of this PPI.[263]

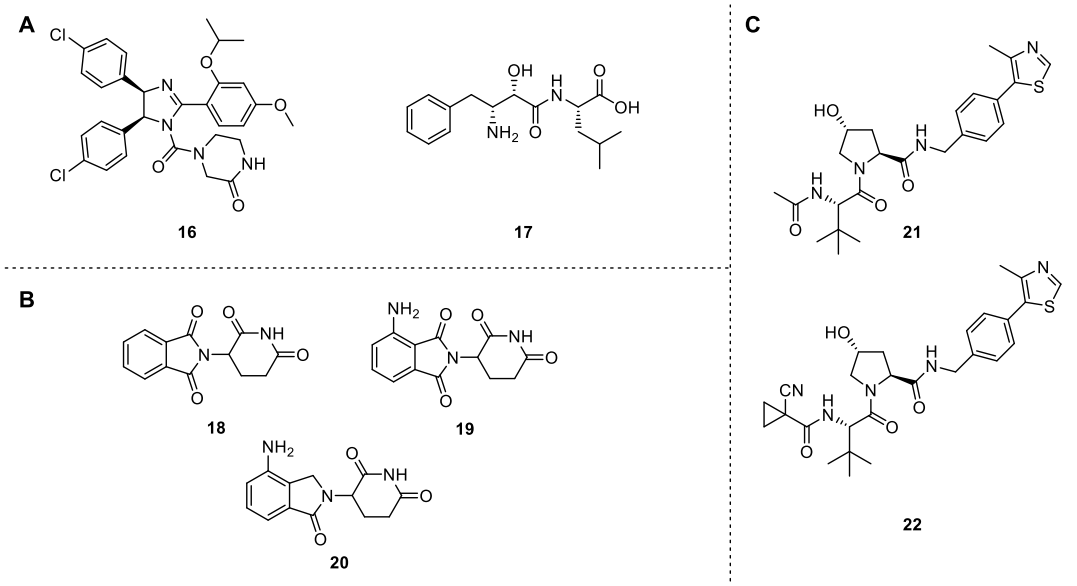


Figure 12. A) MDM2 ligand nutlin-3 (**16**) and the cIAP1 ligand bestatin (**17**), **B**) thalidomide (**18**), pomalidomide (**19**), and lenalidomide (**20**) as CRBN ligands, **C**) inhibitors of the PPI between VHL and HIF-1α VH032 (**21**) and VH298 (**22**).[249,255,257,263]

1.5.2 PROTACs targeting histone deacetylases

The first example of histone deacetylase degradation by PROTACs was published in 2018 by Schiedel et *al*. (Figure 13A).The degrader **23** combined a selective sirtuine 2 (Sirt2) inhibitor with a thalidomide-based E3 ligase ligand. In HeLa cells, compound **24** induced selective Sirt2 degradation in a dose- and time-dependent fashion. Importantly, the degradation of Sirt2 could be rescued by the proteasome inhibitor MG132, confirming that degradation occurred via the UPS.[264] In the same year, Tang and coworkers reported the first PROTAC for a zinc dependent HDAC isoform. Compound **24** consisted of a non-selective HDACi derived from crebinostat, conjugated to pomalidomide (Figure 12B, compound **19**) serving as the E3 ligase recruiting ligand. Unexpectedly, the compound was able to selectively degrade HDAC6 in MCF-7 cells, with a DC_{50} of 0.034 µM and a D_{max} of 70%.[265] To further investigate the role of the ligase recruiting ligand on the degradation profile, Xiong et *al*. synthesized a series of PROTACs with non-selective HDACi related to panobinostat as the POI ligand utilizing different E3 ligase ligands (Figure 13B). Their findings indicated that CRBN-based PROTACs had a preference for degrading HDAC6 and HDAC8 (Figure 13B, compound **25**), whereas VHL-based degraders showed a preference for HDAC3. Interestingly, depending on the attachment point of the VHL ligand, the degradation efficacy could be shifted to a more HDAC3 selective PROTAC (Figure 13B, compound **27**).[266]

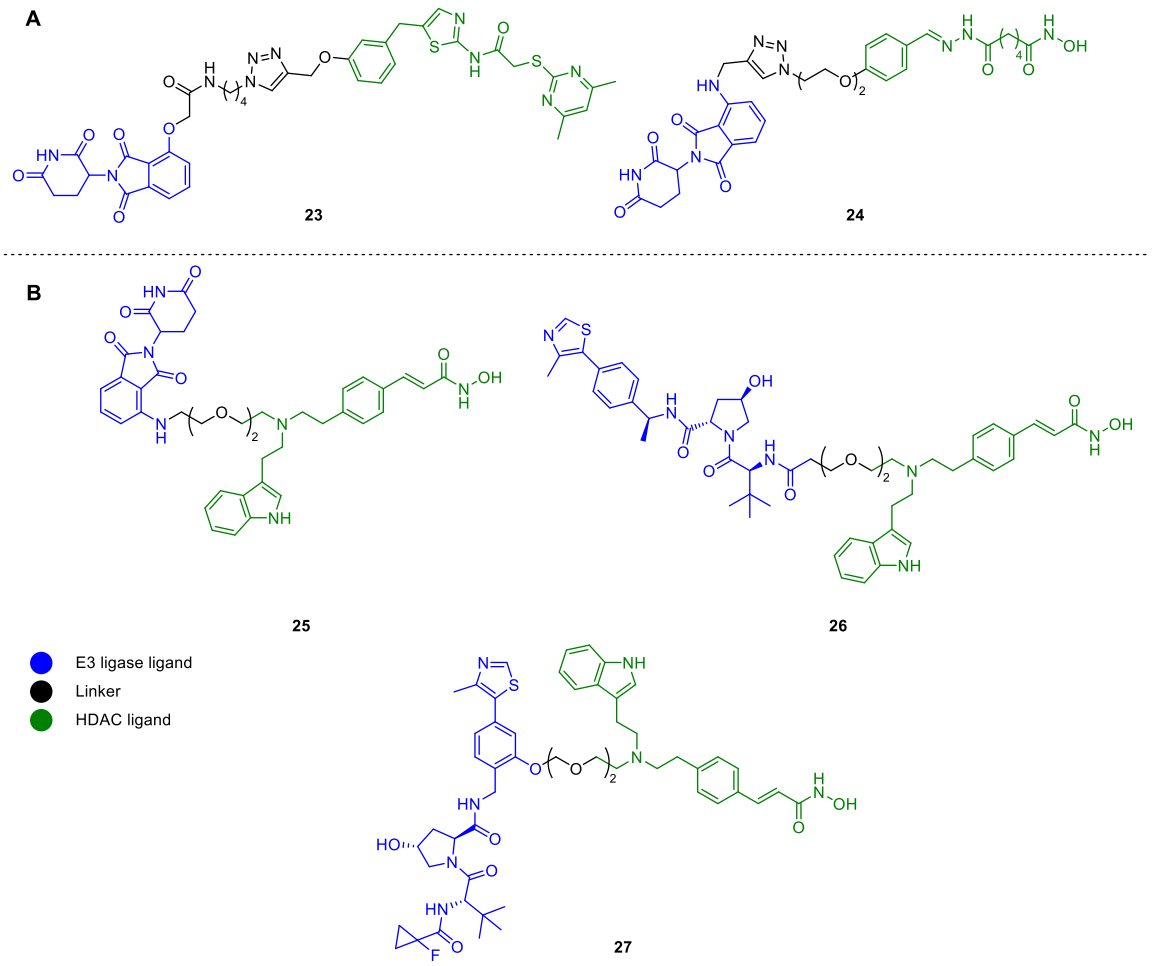


Figure 13. A) First sirtuine and zinc-dependent HDAC PROTACs. **B**) Selected HDAC PROTACs with different E3 ligases for an isoform selective degradation.[264–266]

Changing the POI moiety to other non-selective HDACi did not change the degradation profile drastically. CRBN-based PROTACs still exhibited a more pronounced degradation of HDAC6, while VHL-based PROTACs consistently demonstrate higher degradation activity against class I HDACs across various cell lines.[266] Additional studies conducted by Liao and colleagues further confirmed this preference of VHL-based PROTACs for class I HDACs. When using a class I selective POI moiety, only one CRBN-based PROTAC degraded HDAC3, despite lower inhibitory activities. In contrast, all VHL-based PROTACs effectively degraded HDAC3 at a concentration of 100 nM.[267] Beyond that, Smalley et *al*. tested *ortho*-aminoanilide-based PROTACs against the LSD1-CoREST-HDAC1 complex. In their study, VHL-based PROTACs exhibited an overall higher degradation percentage. Even stronger degradation was observed in the human colon cancer cell line HCT116 compared to E14 mouse embryonic stem cells, indicating a tissue-specific degradation of the respective POI. This is achieved by the careful selection of an appropriate E3 ligase ligand.[268]

The spacer region is a critical component that plays a pivotal role in the proper formation of the ternary complex and is thus a key focus for chemical optimization in PROTAC development.[269] In their chemo-proteomics screen, Xiong et *al*. (Figure 13B) also investigated the influence of the spacer length on the degradation profile, while keeping the E3 ligase ligand and POI ligand consistent. For VHL-recruiting PROTACs, both shorter and longer alkyl chains induced potent degradation of HDAC3, whereas the C4 chain analogue failed to demonstrate degradation. In contrast, PROTACs with a CRBN recruiting ligand exhibited better degradation when shorter spacers were employed with degradation efficiency decreasing as the spacer length increased. Furthermore, longer spacer induced degradation of more HDAC isoforms than the direct analogues with shorter connecting units, as it was seen with two different HDACi regardless of the utilized E3 ligase ligand.[266] Additional research has shown that, in addition of the spacer length, factors such as the attachment point on the E3 ligase ligand and the composition of the spacer itself are also crucial determinants of degradation efficacy in PROTACs.[270,271]

As previously mentioned, the choice of the HDACi essentially influences the selectivity of HDAC-PROTACs. To achieve a more targeted degradation, PROTACs with class selective HDACi scaffolds were developed (Figure 14).[272] For example, the tacedinaline-derived PROTAC **28**, demonstrated the ability to degrade HDAC1 and HDAC2 at low micromolar concentrations. It also compromised the stability of LSD1 as part of the CoREST complex and induced apoptosis. Intriguingly, at concentrations greater than 1 µM, compound **28** exhibited a hook-effect for HDAC3. However, by modifying the linker and VHL ligand in PROTAC **29**, this hook effect was reversed, resulting in the selective degradation of HDAC3 without affecting HDAC1 and HDAC2 levels. It is worth noting that compound **29** did not induce significant cell death in HCT116 cells.[273] In their research focused on understanding the role of HDAC3 in inflammatory processes, the Dekker group identified benzamide **30** as a cereblon recruiting HDAC3 degrader. Despite its potent DC_{50} of 0.32 µM against HDAC3, compound **30** did not have significant effects on the expression of relevant genes in LPS/IFN$_\gamma$ primed RAW 264.7 macrophages. This was in contrast to HDAC inhibitors like entinostat. The lack of gene expression modulation by compound **30** could be attributed to the use of pomalidomide, which is known to have a negative impact on IL expression.[274] In an effort to optimize their approach, Dekker and coworkers developed VHL-based degrader by incorporating a propyl hydrazide as the ZBG. Compound **31** induced HDAC3 degradation in THP-1 cells with a DC_{50} of 0.6 nM and a D_{max} of 90%. Importantly, HDAC1 and HDAC2 remained unaffected. Additionally, in THP-1 cells and human macrophages, the reduction in HDAC3 levels achieved with compound **31** led to decreased expression of pro-inflammatory cytokines like TNFα and IL-6. This effect also prevented the polarization of M0 macrophages into the pro-inflammatory M1-like macrophages.[275]

Based on a known HDAC8 inhibitor Huang et *al*. developed a series of HDAC8 PROTACs. In A549 lung carcinoma cells, compound **31** (Figure 14A) degraded HDAC8 with a DC_{50} of 0.58 μM and D_{max} greater than 95%. Notably, VHL-based degraders also demonstrated effective HDAC8 degradation, but were outperformed by the corresponding CRBN recruiting analogues.[276] It has been observed that the inhibition of the proteasome can lead to increased enzyme levels of class IIa enzymes, suggesting the possibility of their degradation via the UPS.[277] However, PROTACs targeting these isoforms are rare, and so far, only HDAC4 selective PROTACs have been reported. Pioneering work in this area was published by the group of Dominguez (Figure 14B). They developed two series of VHL-based PROTACs. In the first series, which featured a hydroxamic acid as the ZBG, compound **33** demonstrated potent degradation of HDAC4 in double digit nanomolar concentrations. However, it also exhibited a hook effect at 10 μM, while up to 10 μM selective degradation of HDAC4 over other isoforms was observed.[278] Further, compound **33** was evaluated in neuroblastoma and Jurkat cells for potential use against Huntington's disease.[278] In the related study, compound **34** showed potent HDAC4 degradation and, in contrast to compound **33**, only showed minor degradation of HDAC4 at 10 μM.[278]

As mentioned earlier, it is possible to achieve selective HDAC6 degradation using non-selective HDACi through the proper choice of the E3 ligase ligand. Nonetheless, Wu et *al*. developed PROTAC **35** (Figure 13C) by combining pomalidomide with the HDAC6 selective inhibitor nexturastat A. This PROTAC exhibited a low nanomolar DC_{50} value against HDAC6 in multiple myeloma cell line MM.1S. Simultaneously, it led to the degradation of the CRBN neosubstrates IKZF1 and IKZF3, resulting in significant antiproliferative effects. These effects were more pronounced than those observed with the individual HDAC6 inhibitor nexturastat A, IMiD, or their combination.[271] Another HDAC6 selective PROTAC, **36**, was capable of degrading HDAC6 with a DC_{50} of 19 nM in the leukemia cell line HL-60. However, despite its efficacy in degrading HDAC6, compound **36** did not induce antiproliferative effects in AML and B-cell acute lymphoblastic leukemia cell lines.[279] Hansen and coworkers developed the first non-hydroxamate, selective HDAC6 degrader. While compound **37**, exhibited only moderate inhibitory activity, it achieved a DC_{50} of 131 nm with a D_{max} of 84% for HDAC6. Importantly, compound **37** neither reduced cell viability nor led to the degradation of other HDAC isoforms.[280]

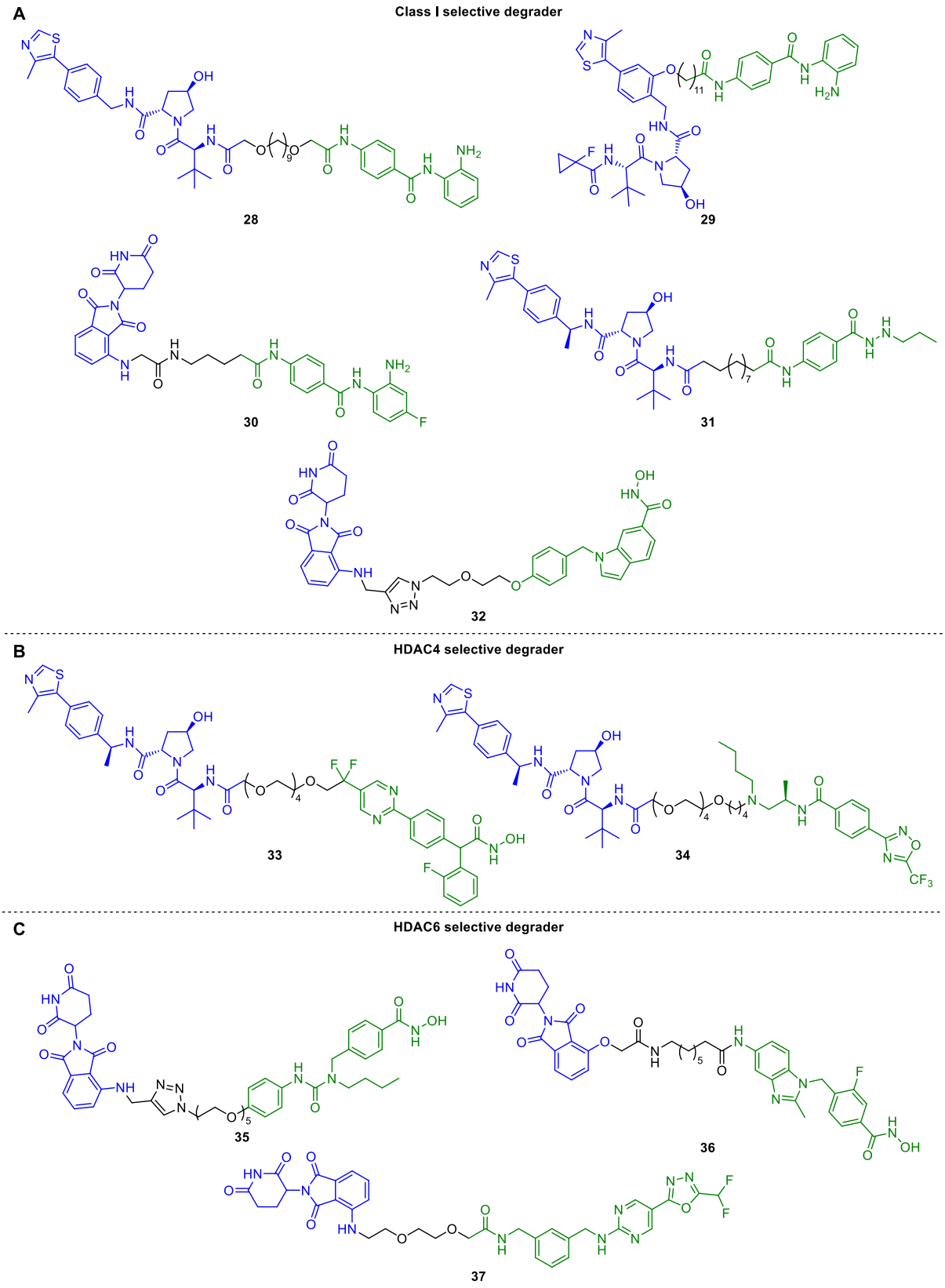


Figure 14. Selected HDAC-PROTACs with isoform selectivity.[271–276,278–280]

1.6 Scope of Thesis

The epigenetic regulation of gene expression is a pivotal process in cell development. For instance, histone modifications directly influence the accessibility of transcription factors to the DNA. In this context, HDACs are crucial for cell differentiation, gene expression, and cell cycle control. The overexpression or malfunction of HDACs has been connected with various diseases.[38] Thus far, five HDACi have gained regulatory approval for the treatment of different kinds of solid or hematological cancers, underlining the potential of HDACi in targeted cancer therapy.[186] However, the high toxicity associated with non-selective HDACi poses a mayor challenge in cancer treatment and limits their therapeutic use beyond oncology. In cancer treatment, the cytotoxicity of HDACi has been primarily attributed to HDAC1, 2, and 3 inhibition.[38] Co-inhibition of other isoforms may only provoke unwanted side effects during cancer therapy. Moreover, other isoforms exhibit a distinguished substrate specificity and regulate other crucial cellular processes. For example, HDAC6 has been associated with neurodegenerative diseases and inflammatory processes. [137] Achieving a more selective inhibition of this isoform holds the promise of expanding the clinical use of HDACi beyond oncology. Therefore, the focus of this thesis is the development of new selective HDACi and HDAC PROTACs

Chapter 2 covers the development of highly selective HDAC6 inhibitors. HDAC6 is a cytoplasmic enzyme which mainly acts on non-histone proteins, influencing cell migration and angiogenesis. Moreover, it has an impact on non-cancer diseases like fibrosis or the activation of the NLRP3 inflammasome. Previously, the HDAC6 preferential inhibitor **MAIP-032** was published and a crystal structure in complex with CD2 domain of HDAC6 from *Danio rerio* was obtained.[239] Although **MAIP-032** displayed promising inhibitory activity against HDAC6, its limited selectivity over HDAC1 (38-fold) hindered its progression as a viable treatment for non-oncological conditions. This project aims to develop more potent and selective HDAC6 inhibitors, leveraging the imidazo[1,2-*a*]pyridine scaffold of **MAIP-032**. To this end, docking studies will explore possible additional interactions of the desired inhibitors with the HDAC6 enzyme. The most promising compounds will be synthesized and undergo testing for their inhibitory activity against multiple HDAC isoforms and their anticancer properties will be assessed. Moreover, the influence of selected HDAC6 inhibitors on the NLRP3-mediated IL1-β release in mouse and human macrophages will be investigated.

Chapter 3 discusses the development of class I HDACi with a substituted hydrazide as the ZBG. The class I HDAC enzymes, in particular HDAC1, 2, and 3 are frequently overexpressed in various types of cancer, rendering them a valuable drug target.[198] Achieving selectivity for class I HDACs is primarily accomplished through the choice of an appropriate ZBG like *ortho*-aminoanilides. Previous studies have explored a series of peptoid-based HDACi with an *ortho*-aminoanilide ZBG, where the HDACi **VK1** demonstrated potent inhibitory activity against HDAC1-3 as well as

chemosensitizing properties, effectively reversing cisplatin resistance in the Cal27CisR cell line.[281] Further modification through the introduction of a 4-pyridinyl FPU resulted in enhanced inhibitory activity against HDAC1 and 2, but also considerably reduced solubility. Substituted hydrazides represent a newer ZBG group of HDACi, which promises potent class I HDAC inhibition while improving physiochemical properties compared to their hydroxamic acid counterparts.[207] In this project, a new generation of peptoid-based HDACi with a substituted hydrazide moiety will be developed and tested for their inhibitory activity against the class I HDAC enzymes. The most promising compounds will be analyzed regarding their anticancer properties in cisplatin sensitive and resistant cell lines, along with synergism studies with cisplatin.

Chapter 4 explores the utilization of PROTACs to degrade HDACs. Targeted protein degradation offers the possibility to circumvent limitations encountered with the classical small molecule inhibitor approach.[252] In this project, VHL recruiting PROTACs, incorporating the most promising class I selective HDACi from chapter 3 as the POI ligand, will be developed. The synthesis of VHL ligands poses challenges. To this end the synthesis will be optimized to establish a fast and straightforward access. Subsequently, different connecting units on the POI ligand will be synthesized to allow the attachment of different types of linkers. The synthesized HDAC-PROTACs will undergo biological evaluation to assess their inhibitory and degradation potency against the class I enzymes HDAC1, 2, and 3.

Chapter 5 scrutinizes the application of light-activatable HDACi prodrugs. The conventional use of HDACi often leads to unwanted side effects, limiting their therapeutic potential. The temporal and tissue specific release of the parent inhibitor promises to diminish unwanted side effects, while preserving the therapeutic benefits of the HDACi. Light-activatable prodrugs were successfully utilized to achieve local drug release in the past.[248] The ZBG, as a central component of HDACi, serves as a promising starting point for the design of HDACi prodrugs. In this project, two light sensitive HDACi prodrugs will be developed. To this end, a DMNB group will be attached to the ZBG of the previously published hydroxamic acid based HDACi **DDK137** and *ortho*-aminoanilide **VK1**. Subsequently, the prodrugs will undergo testing to identify the optimal conditions for successful deprotection. Biological evaluations, including assessments of HDAC inhibitory potency and cytotoxicity on different cell lines, will be conducted to assess their effectiveness.

Chapter 2

Groebke Blackburn Bienaymé-mediated multi-component synthesis of selective HDAC6 inhibitors with anti-inflammatory properties

Fabian B. Kraft, Jana Enns, Irina Honin, Jonas Engelhardt, Andrea Schöler, Shannon T. Smith, Jens Meiler, Linda Schäker-Hübner, Günther Weindl, Finn K. Hansen.

Bioorg. Chem. **2024**, 143, 107072.

Please refer to chapter 8.1 "Appendix I" for the publication's full text and supporting information.

2.1 Publication Summary

HDACs are a class of enzymes that play a pivotal role in diverse cellular processes.[35] Dysfunction or increased expression has been implicated in various disorders, including cancer, inflammatory processes, and neurodegenerative diseases, underscoring the therapeutic potential of targeting HDACs.[93,186,282] This project focuses on HDAC6, a cytoplasmic enzyme, which, despite its name, mainly acts on non-histone proteins like α-tubulin, HSP90, and tau.[137] Notably, by influencing the microtubule transport, HDAC6 has been connected to NLRP3 inflammasome activation in mice.[146] Despite its overexpression in numerous cancers, HDAC6 inhibitors often exhibit limited anticancer efficacy in monotherapy.[228] Moreover, HDAC6 knockout results in a viable phenotype in mice.[229] Thus, targeting selective HDAC6 inhibition shows great potential for minimizing cytotoxic effects and extending applications beyond oncology. This study aimed to design HDAC6 inhibitors with enhanced selectivity and inhibitory activity over other isoforms. In previous work, the imidazo[1,2-*a*]pyridine-capped inhibitor **MAIP-032** (HDAC1 IC_{50}: 2.20 μM; HDAC6 IC_{50}: 0.058 μM; $SF^{1/6}$: 38) was developed and a crystal structure in complex with the CD2 of HDAC6 from *Danio rerio* (PDB: 6CGP) was obtained.[239] Although **MAIP-032** demonstrated a preference for HDAC6 over other isoforms, its inhibitory activity on HDAC1, the main contributor to cytotoxic effects of HDACi, is not sufficient to develop the compound further as a potential treatment of non-oncological diseases.

Based on the available crystal structure, docking studies were conducted to scrutinize possible additional interaction with the HDAC6 binding site, with the L1-loop emerging as the most promising region for further interactions. Altogether 13 inhibitors were synthesized through a four-step protocol with a Groebke Blackburn Bienaymé (GBB) three component reaction as the critical part to form the imidazo[1,2-*a*]pyridine core. All isolated compounds were tested for their inhibitory activity in biochemical HDAC inhibition assays against human HDAC1 and HDAC6. Compounds **8k** (HDAC1 IC_{50}: 5.87 μM; HDAC6 IC_{50}: 0.024 μM; ($SF^{1/6}$): 245) and **8m** (HDAC1

IC_{50}: 3.07 µM; HDAC6 IC_{50}: 0.026 µM; $SF^{1/6}$: 118) emerged as the most potent and selective HDAC6 selective inhibitors, surpassing the lead structure **MAIP-032** in terms of inhibitory potency and selectivity. Cellular target engagement analysis was assessed in U-87 MG glioblastoma cells, confirming HDAC6 selectivity through observing α-tubulin hyperacetylation without affecting histone H3 acetylation. Further, anticancer properties were evaluated through MTT cell viability assays and wound healing assays in U-87 MG cells. While inhibitors **8k**, **8m**, and **tubastatin A** had minimal effects on cell viability, compound **8m** caused a significant reduction in cell migration.

Previously, the influence of HDAC6 on the NLRP3 inflammasome activation and NLRP3-mediated IL-1β release has been reported.[146,283] Despite evidence suggesting the potential of HDAC6 inhibitors to attenuate NLRP3-mediated inflammation, controversies exist regarding their mechanistic role in NLRP3-mediated IL-1β release.[139] To determine the influence of HDAC6 inhibitors on NLPR3 activation, LPS-primed mouse J774A.1 macrophages were treated with **8k**, **8m**, the control substances **MAIP-032** and tubastatin A, with subsequent ATP or nigericin stimulation. While **tubastatin A** and **8k** exhibited reduced nigericin-induced IL-1β release at 50 µM and 100 µM, ATP-induced released remained unaffected. To further investigate the impact of HDAC6 inhibitors on NLRP3 inflammasome activation, human THP-1 macrophages were employed. No HDAC6 inhibitor exhibited an attenuated IL-1β release, while the NLRP3 inhibitor **MCC950** suppressed nigericin induced IL-1β release.

Previous findings demonstrated the interference of tubastatin A with TLR signaling and subsequent inhibition of the NLRP3-inflammasome mediated IL-1β release by human macrophages.[284] **Tubastatin A**, **MAIP-032**, **8k**, and **8m** significantly inhibited LPS-induced *IL1B* mRNA expression and TNF release at 10 µM, with vorinostat completely blocking TLR4-mediated responses.

Additionally, the inhibitory potency on LPS-induced TNF release was evaluated, revealing monophasic concentration-response curves for **tubastatin A**, **MAIP-032**, and **8m**, while **8k** displayed a biphasic curve. The determined IC_{50} values ranged from 4.96 µM to 19.6 µM, with **8k** (19.6 µM) and **8m** (15.8 µM) being comparable to tubastatin A (16.3 µM) but less potent than **MAIP-032** (4.96 µM). Cell viability remained unchanged up to 50 µM, but decreased to 60% at 100 µM for **MAIP-032**, **8k**, and **8m**. The possibility of a biphasic fit suggested that at least two HDAC6-mediated mechanisms might contribute to the inhibition of LPS-induced TNF release.

In conclusion, a set of 13 HDAC6 selective inhibitor with a imidazo[1,2-*a*]pyridine-based cap was developed. The two most potent and selective compounds for HDAC6 (**8k** and **8m)** were further evaluated for their anticancer properties and their influence on the NLRP3 inflammasome activation.

2.2 Author Contribution

Fabian B. Kraft: Conceptualization, data curation, synthesis and structural characterization of all compounds[b], docking studies, and writing - original draft (except section 2.6).

Jana Enns: Cell stimulation, ELISA, Western blotting, RNA isolation, cDNA synthesis, qPCR, cell viability assays, and statistical analysis (THP-1 macrophages, J774A.1 macrophages).

Irina Honin: Immunoblot analysis, MTT and wound healing assays (U-87 MG cells).

Jonas Engelhardt: Cell stimulation, ELISA, Western blotting, and statistical analysis (THP-1 macrophages), writing - review & editing.

Andrea Schöler: Biochemical HDAC inhibition assays.

Shannon T. Smith: Design of computational protocols and supervision.

Jens Meiler: Design of computational protocols and supervision.

Linda Schäker-Hübner: Biochemical HDAC inhibition assays.

Günther Weindl: Conceptualization, formal analysis, funding acquisition, resources, supervision, writing - original draft (section 2.6), writing - review & editing.

Finn K. Hansen: Conceptualization, formal analysis, funding acquisition, project administration, resources, supervision, writing - review & editing.

[b] The compounds **8b**, **8c**, **8e**, **8f**, **8j**, and the respective precursor molecules were synthesized during my master thesis (Multikomponentensynthese von selektiven HDAC6 Inhibitoren von Fabian B. Kraft, **2019**; Universität Leipzig, Fakultät für Chemie und Mineralogie)

Chapter 3

Hydrazide-based class I HDAC inhibitors with HDAC3 preference completely reverse chemoresistance in a synergistic manner in platinum-resistant solid cancer cells

Fabian B. Kraft[#a], Lukas Biermann[#b], Linda Schäker-Hübner[#a], Maria Hanl[a], Alexandra Hamacher[b], Matthias U. Kassack[b,*], Finn K. Hansen[a,*]

[#] These authors contributed equally to this work as first authors.

Chapters 3.1, 3.2.1, 3.2.2, 3.2.2.1, 3.2.2.2, 3.3, and 3.4 were written by Fabian B. Kraft.

Chapters 3.2.2.3 - 3.2.2.7 were written by Lukas Biermann and Prof. Dr. Matthias U. Kassack.

[*] These authors contributed equally to this work as senior authors.

[a] Department of Pharmaceutical and Cell Biological Chemistry, Pharmaceutical institute, University of Bonn, an der Immenburg 4, 53121 Bonn, Germany.

[b] Institute for Pharmaceutical and Medicinal Chemistry, Heinrich Heine University Düsseldorf, 40225 Düsseldorf, Germany.

3.1 Introduction

Epigenetic modifications are alterations to the chromatin structure that regulate gene expression, without changing the DNA sequence itself.[285] These modifications directly contribute to the formation of the phenotype and aberrant epigenetic patterns have been shown to play a prominent role in tumorigenesis and chemoresistance.[286,24,287] The acetylation and deacetylation of the ε-amino group of lysine residues on histones belongs to the best investigated modifications. Histone acetyltransferases (HATs) add an acetyl group to the positively charged amino moiety, which relaxes the chromatin structure and enables transcription factors to bind to the DNA. In contrast, histone deacetylases (HDACs) remove acetyl groups, leading to a more condensed structure and inhibition of gene expression.[35] There are 11 zinc-dependent human HDAC isoforms, which can be divided into four different groups, according to their structural features, homology, and cellular localization: Class I (HDAC1, 2, 3, and 8), class IIa (HDAC4, 5, 7, and 9), class IIb (HDAC6 and 10), and class IV (HDAC11).[40] The class I isoforms HDAC1, 2, and 3 are mainly localized in the nucleus and display high activity towards acetylated histone substrates. Additionally, HDAC1 – 3 operate as constituents of large multi protein complexes like Mi-2/NuRD[288] or NCoR/SMRT,[80] which are involved in the repression of gene expression. Notably, HDAC8 differs from the other class I members in regard to its structure[96] as well as its catalytic preference for longer acyl

chains.[103] In contrast to these class I isoforms, class IIa enzymes are known to shuttle between the cell nucleus and the cytoplasm.[38] As a member of class IIb, HDAC6 is primarily localized in the cytoplasm targeting non-histone proteins like α-tubulin, cortactin, and Hsp90 showing a direct impact on cell migration and the aggresomal degradation pathway.[137] HDAC6 can also translocate to the nucleus where it has comparable functions like HDAC1-3.[289] Additionally, HDAC10, another class IIb isoform, acts as a polyamine deacetylase,[160] while the sole member of class IV, HDAC11, shows a preference for acyl lysine residues with prolonged chain length.[166] Overexpression of HDAC enzymes has been observed in several diseases, including neurodegenerative disorders like Alzheimer's disease,[93] inflammatory processes,[282] and different kinds of cancer.[186] Various HDAC inhibitors (HDACi) have been developed and so far, three non-selective HDACi (e.g. **vorinostat** and **panobinostat**, see Figure 1A) received FDA approval for the treatment of non-solid cancers.[186] Additionally, the class I selective HDACi **tucidinostat** (Figure 15A) was approved by the Chinese National Medical Products Administration (NMPA) for the treatment of the peripheral T-cell lymphoma[290] as well as HR+ breast cancer[291]. The design of HDACi typically follows a pharmacophore model that includes several structural features. It consists of a cap group, which engages the entrance of the catalytic center, a linker that connects the cap group with the zinc-binding-group (ZBG), and the ZBG itself. A more advanced model also includes the foot pocket unit (FPU).[46] It engages the so called foot pocket, an internal cavity, which only occurs in the HDAC class I enzymes.[35]

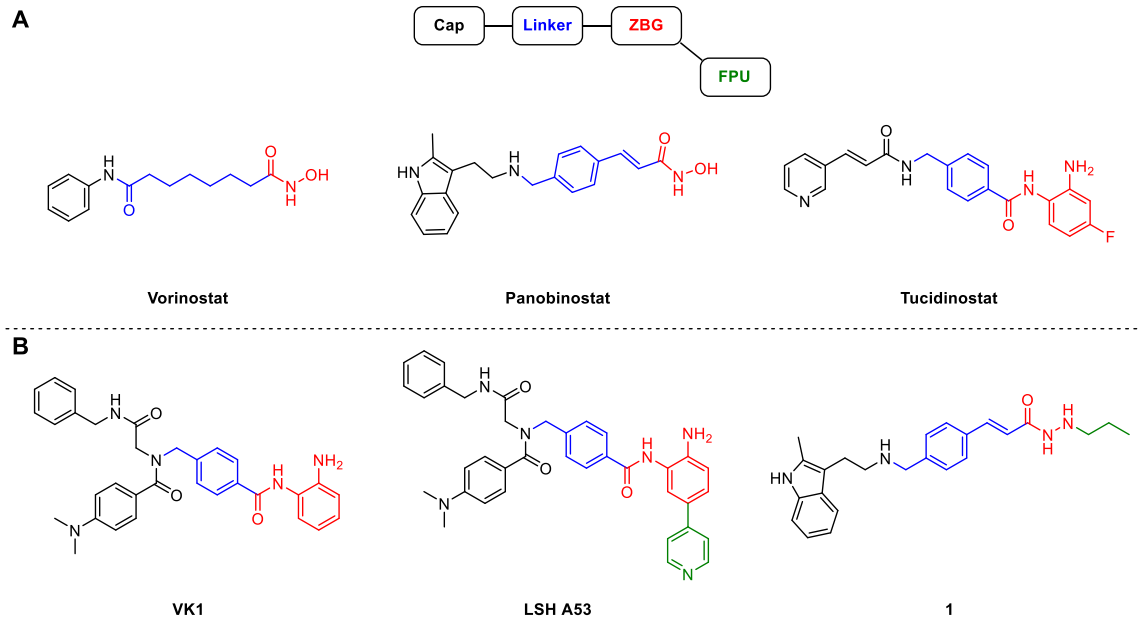


Figure 15. Selected HDACi with pharmacophore model. (**A**) The FDA approved inhibitors **vorinostat, panobinostat**, and the NMPA approved aminoanilide **tucidinostat**. (**B**) Class I selective HDAC inhibitors. **LSH A53** and compound **1** engage the "foot pocket" via a 4-pyridinyl- or propyl-moiety, respectively.

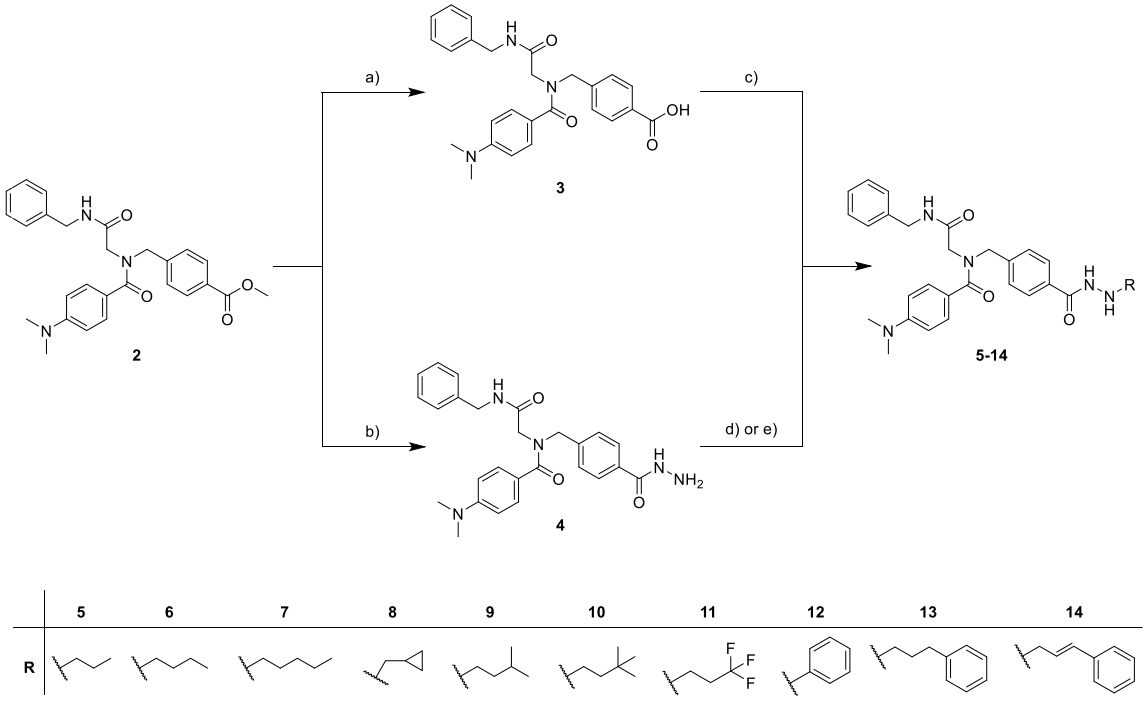
The hydroxamic acid is the most common ZBG, but shows only poor isoform selectivity.[46] In addition, the high toxicity of hydroxamates poses a major challenge for their therapeutic use, as it often leads to interruption of treatment.[194,201,203] In the treatment of cancer, the cytotoxic activity is mainly evoked by the inhibition of the isoforms HDAC1, 2, and 3. The inhibition of other isoforms, most likely, only increases the amount of unwanted side effects. Therefore, more selective inhibitors can lead to an improved safety profile.[94,198,228] To address these problems, alternative ZBGs were developed. For example, o*rtho*-aminoanilides, like **tucidinostat** (Figure 15A), show selectivity for the class I enzymes HDAC1-3.[193,214] In previous studies, we developed a series of peptoid-based HDACi with an *ortho*-aminoanilide ZBG. Compound **VK1** (see Figure 15B) emerged as the hit compound with potent inhibitory activity against HDAC1-3 as well as chemosensitizing properties highlighted by the ability to reverse cisplatin resistance in the Cal27CisR cell line.[281] Based on these results, we modified **VK1** by attaching a 4-pyridinyl FPU to create compound **LSH A53** (Figure 15B). On the one hand, this modification resulted in enhanced activity against HDAC1/2, while almost no inhibition of HDAC3 was observed. On the other hand, the introduction of the 4-pyridinyl FPU led to a considerably reduced solubility (**VK1**: 0.98 µg/mL, **LSH A53**: 0.21 µg/mL, in PBS buffer, pH = 7.4; see Table 2).[218]

Another upcoming new group of class I selective HDACi contain a substituted hydrazide moiety as a ZBG. Based on **panobinostat**, Chou et al.[207] introduced a propyl hydrazide as an alternative ZBG. Their hit compound **1** (Figure 15B) displays potent class I activity with a preference for HDAC3. Depending on the p53 status of the cell line, compound **1** showed promising anti-proliferative effects against different leukemia and prostate tumor cell lines through induction of apoptosis.[207] Additionally, hydrazide-based HDACi exhibit a high oral bioavailability that surpasses those of hydroxamic acid based counterparts.[219]

Overcoming chemoresistance in cancer therapy is still a major medical need.[292] Since epigenetic aberrations contribute to cancer cell resistance,[287] a promising approach to address resistance is the normalization of aberrant acetylation/deacetylation of histone and non-histone proteins in cancer cells by HDACi as we have shown in previous studies.[281,293] Cisplatin-sensitive and -resistant cancer cell pairs (ovarian cancer cell line A2780; head-neck cancer cell line Cal27) were established and applied as models for multiple resistance mechanisms such as decreased platinum uptake, increased efflux, DNA repair, and damage tolerance.[294–297] In this work, we present the synthesis and anticancer evaluation of hydrazide-based class I-selective HDACi. The most potent HDACi **5** showed 6.7-fold preference for HDAC3 over other class I HDAC isoforms, complete reversal of cisplatin resistance and, moreover, a sensitization of the native cancer cells in a highly synergistic manner in combination with cisplatin (shift factor (ShF) = 21).

3.2 Results and Discussion

3.2.1 Design and Synthesis of selective HDACi



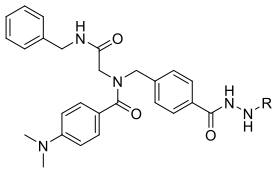
Scheme 1. Synthesis of hydrazide-based HDAC inhibitors. **a**) 2.50 eq. NaOH, THF/MeOH 10/1 *v*/*v*, 40 °C, 24 h 97%; **b**) 10.0 eq. $NH_2NH_2*H_2O$, MeOH, 85 °C, 19 h, quant.; **c**) 1.20 eq. hydrazine-hydrochloride, 1.20 eq. HATU, 1.50 eq. DIPEA, THF/DMF 40/1 *v*/*v*, rt, 90 min to 19 h, 19 – 50%; **d**) 1.00 eq. aldehyde, 2.00 eq. $NaBH_3CN$, 2.00 eq. AcOH, MeOH, rt, 19 h, 23 – 24%; **e**) 1.00 eq. aldehyde, 1.00 eq. $B(OCH_2CF_3)_3$, *i*PrOH/THF 3/1 *v*/*v*, 50 °C, 5 min to rt, 19 h, 1.20 $NaBH_4$, rt, 2 h, 6.00 eq. H_2O, rt, 30 min, 26 – 50%.

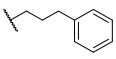
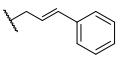
The synthesis of the hydrazide-based HDACi was accomplished via two different strategies (Scheme 1). First, the underlying peptoid scaffold **2** was synthesized *via* an *Ugi* multicomponent reaction, as previously published.[281] Next, the ester was hydrolyzed with sodium hydroxide at slightly elevated temperature to give the carboxylic acid **3** in an excellent yield of 97%. Subsequently, the HATU mediated amide couplings with the respective hydrazine hydrochlorides afforded the target compounds **6**, **7**, and **12** with varying yields. Alternatively, compound **2** was directly boiled with hydrazine monohydrate in methanol. After removal of the solvent under reduced pressure, the unsubstituted hydrazide **4** was isolated in quantitative yield. Reductive aminations with the respective aldehyde resulted in the isolation of the desired products **5**, **8 – 11**, **13**, and **14**.

3.2.2 Biological Evaluation

Following synthesis, compounds **4** – **14** were tested for their *in vitro* inhibitory activity against HDAC1, HDAC2, HDAC3, HDAC4, HDAC6, and HDAC8 using **vorinostat** as well as the class I selective HDACi **VK1** and **entinostat** as controls. The results are summarized in Table 1.

Table 1. Inhibitory activities against human HDAC1 – 4, HDAC6, and HDAC8 of the peptoid-based HDACi **4 – 14**.[c,d]



Code	R	IC$_{50}$ [µM]					
		HDAC1 [a,b]	HDAC2 [a,b]	HDAC3 [a,b]	HDAC4 [b,g]	HDAC6 [b,c]	HDAC8 [d,g]
4		62% @ 10 µM [e]	53% @ 10 µM [e]	57% @ 10 µM [e]	> 10 [d]	55% @ 10 µM [e]	> 10 [d]
5		0.027 ± 0.001	0.141 ± 0.005	0.004 ± 0.00001	> 10 [d]	> 10 [d]	49% @ 10 µM [e]
6		0.037 ± 0.003	0.125 ± 0.020	0.008 ± 0.001	> 10 [d]	> 3.33 [d]	35% @ 10 µM [e]
7		0.065 ± 0.001	0.241 ± 0.020	0.072 ± 0.001	> 10 [d]	> 3.33 [d]	35% @ 10 µM [e]
8		0.065 ± 0.009	0.386 ± 0.043	0.014 ± 0.0003	> 10 [d]	> 10 [d]	43% @ 10 µM [e]
9		0.243 ± 0.011	0.358 ± 0.060	0.199 ± 0.014	> 10 [d]	> 10 [d]	29% @ 10 µM [e]
10		63% @ 10 µM [e]	46% @ 10 µM [e]	> 10 [d]	> 10 [d]	> 10 [d]	> 10 [d]
11		0.133 ± 0.007	0.245 ± 0.030	0.037 ± 0.003	> 10 [d]	> 10 [d]	> 10 [d]
12		17.5 ± 2.71	5.21 ± 0.340	3.82 ± 0.173	> 10 [d]	> 10 [d]	> 10 [d]
13		0.415 ± 0.032	0.871 ± 0.127	1.20 ± 0.043	> 10 [d]	> 3.33 [d]	7.19 ± 0.6
14		37% @ 10 µM [e]	> 10 [d]	32% @ 10 µM [e]	> 10 [d]	> 10 [d]	> 10 [d]
VK1 [f]	-	0.069 ± 0.010	0.128 ± 0.002	0.310 ± 0.009	> 10 [d]	> 10 [d]	> 10 [d]
entinostat [f]	-	0.426 ± 0.059	0.354 ± 0.043	0.311 ± 0.010	> 10 [d]	> 10 [d]	> 10 [d]
vorinostat	-	0.093 ± 0.009	0.191 ± 0.014	0.099 ± 0.013	> 10 [d]	0.031 ± 0.005	5.59 ± 0.31

[a] preincubation of enzyme and inhibitor: 1 h at 25 °C; [b] mean ± standard deviation (SD) of at least two independent experiments; [c] preincubation of enzyme and inhibitor: 15 min at 20 °C; [d] < 25% inhibition at the stated concentration; [e] percent-inhibition (%) at stated concentration [µM]; [f] data taken from Schäker-Hübner *et al.*[218] [g] preincubation of enzyme and inhibitor: 5 min at 37 °C; Data shown are the IC$_{50}$ of pooled data from at least two experiments each carried out in duplicate.

[c] HDAC1, 2, 3, and 6 enzyme assays were performed by Dr. Linda Schäker-Hübner (Rheinische Friedrich-Wilhelms-Universität Bonn, Hansen Group)

[d] HDAC4 and 8 enzyme assays were performed by Lukas Biermann (HHU Düsseldorf, Kassack group).

Overall, most of the newly synthesized compounds (**4** – **14**) showed good inhibitory activity against the class I HDAC isoforms HDAC1–3. However, depending on the respective FPU, their isoform profile as well as potency varies considerably. With IC_{50}-values ranging from 0.004 µM (**5**) to 3.82 µM (**12**) or no inhibition up to 10 µM (**10**) this is particularly true for HDAC3. Further, compounds **5** – **14** showed no relevant inhibition of class II HDACs (HDAC4 and HDAC6). Since substituted hydrazide ZBGs are a known feature of class I selective HDACi, these results are in good agreement with literature.[38,107,220,298] Interestingly though, the unsubstituted hydrazide **4** was able to inhibit HDAC1–3 and HDAC6 to some extent at a concentration of 10 µM, indicating that the unsubstituted hydrazide moiety might be a weak and unselective ZBG. Additionally, HDAC8 inhibition was tested for compounds and controls. With one notable exception (**13**, see below), no relevant inhibition was observed.

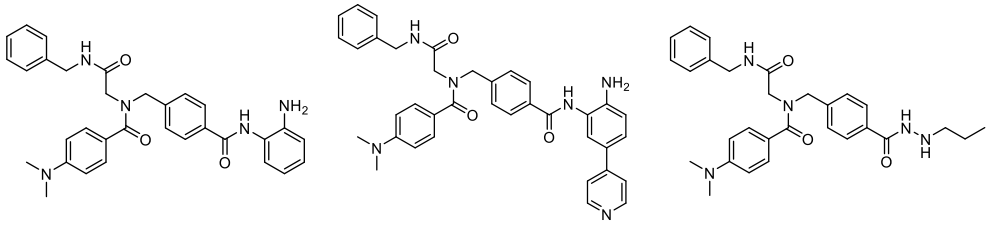
As mentioned above, the propyl hydrazide derivative **5** emerged as the most potent HDAC3 inhibitor of the set with a single digit nanomolar IC_{50}-value (HDAC3 IC_{50} = 0.004 µM). Additionally, **5** showed potent nanomolar inhibitory activity against HDAC1 and HDAC2 (HDAC1 IC_{50} = 0.027 µM; HDAC2 IC_{50} = 0.141 µM). Further, the two compounds **6** and **8**, which feature a slightly larger butyl (**6**) or cyclopropyl FPU (**8**), demonstrated potent HDAC3 inhibition in the low nanomolar range (cpd. **6**: IC_{50} = 0.008 µM; cpd. **8**: IC_{50} = 0.014 µM) as well and potent HDAC1 and HDAC2 inhibition similar to **5** (see Table 1). Interestingly, the 3,3,3-trifluoropropyl hydrazide derivative **11** showed approximately 9-fold reduced HDAC3 inhibition (IC_{50} = 0.037 µM) compared to its non-fluorinated counterpart **5** while HDAC1 and HDAC2 tolerated fluorination comparably well (HDAC1 IC_{50} = 0.133 µM; HDAC2 IC_{50} = 0.245 µM). Similarly, the pentyl hydrazide derivative **7** showed a 18-fold reduced inhibition of HDAC3 (IC_{50} = 0.072 µM) compared to **5** while HDAC1 and HDAC2 inhibition was considerably less affected. In contrast, branched (**9**, **10**) or aromatic FPU (**12**, **13**, and **14**) led to a considerably reduced HDAC1 – 3 inhibition or no inhibition at all. However, size and rigidity of the FPU are key factors concerning HDAC class I inhibition: While the 3-methylbutyl hydrazide derivative **9** demonstrated an **entinostat**-like isoform profile, the 3,3-dimethylbutyl analog **10** showed very low HDAC1 and HDAC2 inhibition at 10 µM and no HDAC3 inhibition up to 10 µM. Similarly, the comparably large and rigid cinnamyl FPU of **14** led to no relevant HDAC inhibition up to 10 µM. In contrast, the more flexible 3-phenylpropyl FPU of compound **13** lead to moderate HDAC1 – 3 inhibition (HDAC1 IC_{50} = 0.415 µM; HDAC2 IC_{50} = 0.871 µM; HDAC3 IC_{50} = 1.20 µM). Notably, compound **13** additionally showed moderate HDAC8 inhibition with a single digit micromolar IC_{50}-value (HDAC8 IC_{50} = 7.19 µM).

Collectively our data show, that especially small, flexible FPUs are suitable for HDAC3 while longer alkyl chains (compare **7** vs. **5**) as well as branched (compare **6** vs. **9** vs. **10**) or rigid, bulky substituents (e.g. **14**) led to considerably reduced HDAC3 inhibition. Accordingly, compounds **5**, **6**, and **8** emerged as the most promising new HDACi of the set.

3.2.2.1 Physicochemical properties of compound 5

In previous studies, peptoid-based HDACi, particularly those incorporating a bulky and rigid FPU, demonstrated remarkably low solubility, limiting their potential use as anticancer agents.[218] To assess the physicochemical characteristics of hydrazide-based HDAC inhibitors, we examined hit compound **5** as a representative. To this end, we determined its lipophilicity ($logD_{7.4}$) and solubility using our previously reported methods.[218] The results are summarized in Table 2. Compared to **VK1** and in contrast to **LSH A53**, compound **5** showed a moderately increased lipophilicity ($logD_{7.4}$) while displaying a considerably improved solubility. This promises a potential improved cellular target engagement of our hydrazide-based inhibitors.

Table 2. Physicochemical properties of **5**, **VK1** and **vorinostat**.[e]



	VK1[a]	**LSH A53**[a]	**5**
$LogD_{7.4}$	3.19	3.16	3.76
Solubility[b,c] **[µg/mL]**	0.98 ± 0.10	0.21 ± 0.03	16.8 ± 0.99

[a] data taken Schäker-Hübner et al.[218] [b] PBS buffer, pH = 7.4; [c] mean ± SD of at least two independent experiments.

[e] Physiochemical properties were determined by Dr. Linda Schäker-Hübner (Rheinische Friedrich-Wilhelms-Universität Bonn, Hansen Group)

3.2.2.2 Docking studies

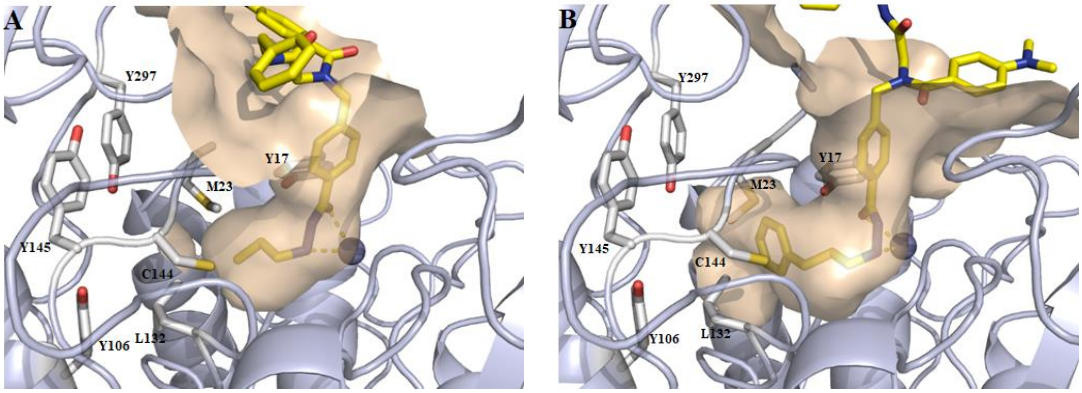


Figure 16. Docking pose of compound **5** (**A**), and **13** (**B**) in the catalytic center of HDAC3 (PDB: 4A69).[84] Ligands are colored yellow, the catalytic Zn^{2+}-ion is shown as a gray sphere. Polar interactions are represented by dashed, yellow lines. Relevant amino acid side chains forming the foot pocket are shown in their respective colors.

For a better understanding of the binding mode, we performed docking studies employing *RosettaLigand*. Exemplary models for compound **5** and **13** in the human HDAC3 enzyme are depicted in Figure 16. Both inhibitors chelate the zinc-ion through interactions with the carbonyl oxygen and the second nitrogen atom of the hydrazide moiety. In the case of compound **5** (Figure 16A), the propyl moiety lightly engages the foot pocket of the HDAC3 enzyme, demonstrating no noticeable clash or interaction with specific amino acids. Conversely, the sterically more demanding 3-phenylpropyl FPU of compound **13** (Figure 16B) penetrates the foot-pocket more profoundly. This results in more obstructive interactions with the foot pocket, potentially contributing to the diminished inhibitory activity of **13** against HDAC3. Contrary, in HDAC1/2, the Y106 residue is replaced by a serine residue. This substitution may account for the more potent inhibition of these isoforms by compound **13**.[299]

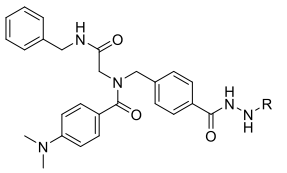
3.2.2.3 Cellular HDAC activity and cell viability (MTT) assays

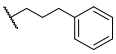
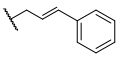
Class I and HDAC6-preferential cellular HDAC assays were performed in A2780 and Cal27 as well as their cisplatin-resistant counterparts A2780CisR and Cal27CisR. Again, the propyl and butyl hydrazides **5** and **6** were the most active compounds (Table 3), although cellular HDAC activity was clearly reduced compared to enzyme HDAC activity (Table 1). Comparing the most potent cellular HDAC inhibition of **5** in Cal27 (0.151 µM) with enzyme HDAC inhibition data of **5**, reduction of cellular HDAC inhibition was 43-fold compared to HDAC3, 5.7-fold compared to HDAC1, and unchanged compared to HDAC2 inhibition. Similar reduced cellular HDAC inhibition was found for the other hydrazides, **VK1**, and **vorinostat** (5-7-fold) but not for **entinostat**. Notably, the *ortho*-aminoanilide **entinostat** gave almost equal enzyme HDAC inhibition and cellular HDAC inhibition (Table 1, Table 3). Further, the hydrazides were up to 3-fold more potent in Cal27 cells than in A2780 cells which was similar for **VK1** but not for

entinostat and **vorinostat**. A reason could be the different HDAC inhibition profile (see Table 1) of the new compound series compared to **entinostat** and **vorinostat**. There were no differences in the cellular HDAC assays comparing respective sensitive and resistant cell lines, assuming that the HDAC expression profile remains similar upon acquisition of cisplatin resistance. Compounds showing no or very weak enzyme HDAC inhibition (**10**, **14**, Table 1) were also inactive or very weak in cellular HDAC inhibition (Table 3). Taken together, the most potent HDAC enzyme inhibitors **5** and **6** (Table 1) perform superior to all other compounds (including reference compounds) in the cellular HDAC assay (Table 3).

Next, the cytotoxic activity was investigated in all four cell lines (Table 4). The most potent HDAC enzyme inhibitors **5** and **6** (Table 1) also show the highest cytotoxicity and were at least 2-fold more potent than the reference HDACi **VK1**, **entinostat**, and **vorinostat** except for A2780 where **entinostat** was equally potent as **5**. Compounds with weak or no HDAC inhibition (**10**, **12**, **14**, Table 1, Table 3), show, as expected, no or weak cytotoxicity (Table 4). For A2780CisR, a cisplatin resistance factor (RF) of 4.5, and for Cal27CisR an RF of 15 was calculated. However, the hydrazides show only small RFs (less than 2, except compound **9** with an RF of 2.5) in Cal27/Cal27CisR. In A2780/A2780CisR however, a resistance against the hydrazides was observed in a similar magnitude as against cisplatin (RF between 2.2 and 6). Platinum-resistant A2780CisR cells thus show some kind of cross-resistance against the hydrazides and reference HDACi (except **vorinostat**) whereas this was much less pronounced (RF < 1, except compound **9**) in Cal27CisR although Cal27CisR cells show a much higher RF against cisplatin.

Table 3. Cellular HDAC inhibition data of compounds **4 – 14** in A2780/A2780CisR and Cal27/Cal27CisR cells using Boc-Lys(ε-Ac)-AMC as selective HDAC1, 2, 3, and 6 substrate.[f]

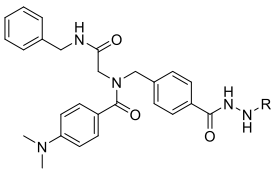


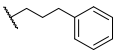
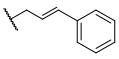
Code	R	IC_{50} [µM]			
		A2780	A2780CisR	Cal27	Cal27CisR
4		33.1 ± 3.3	37.7 ± 5.5	30.9 ± 6.0	35.9 ± 2.5
5		0.235 ± 0.028	0.295 ± 0.056	0.151 ± 0.013	0.155 ± 0.018
6		0.263 ± 0.031	0.268 ± 0.047	0.166 ± 0.010	0.156 ± 0.010
7		0.273 ± 0.031	0.334 ± 0.040	0.264 ± 0.024	0.218 ± 0.015
8		0.722 ± 0.084	0.974 ± 0.145	0.388 ± 0.058	0.392 ± 0.030
9		2.91 ± 0.50	2.08 ± 0.30	0.830 ± 0.104	0.931 ± 0.105
10		n.e.[b]	n.e.[b]	83.4 ± 25.8	43.6 ± 9.6
11		0.691 ± 0.182	0.910 ± 0.196	0.379 ± 0.032	0.385 ± 0.028
12		27.7 ± 9.7	36.0 ± 10.2	21.5 ± 5.1	24.3 ± 2.6
13		2.21 ± 0.43	2.97 ± 0.38	2.46 ± 0.25	1.96 ± 0.18
14		n.e.[a]	n.e.[a]	n.e.[a]	n.e.[a]
VK1	-	1.22 ± 0.08	1.63 ± 0.27	0.327 ± 0.033	0.491 ± 0.052
entinostat	-	0.425 ± 0.043	0.424 ± 0.052	0.539 ± 0.042	0.362 ± 0.029
vorinostat	-	0.628 ± 0.047	0.526 ± 0.066	0.641 ± 0.040	0.877 ± 0.051

The values are the mean of at least two independent experiments, each performed in triplicate.
[a] n.e.: no effect up to 10 µM [b] n.e.: no effect up to 100 µM.

[f] Cellular HDAC assays were performed by Lukas Biermann (HHU Düsseldorf, Kassack group).

Table 4. Cytotoxic activities (MTT assay) of compounds **4 – 14** against A2780/A2780CisR and Cal27/Cal27CisR cell lines.[g]



Code	R	IC_{50} [µM]			
		A2780	A2780CisR	Cal27	Cal27CisR
4		n.e.[a]	n.e.[a]	63.5 ± 6.0	n.e.[a]
5		1.13 ± 0.06	2.46 ± 0.12	0.660 ± 0.050	0.801 ± 0.047
6		0.894 ± 0.036	2.69 ± 0.18	0.688 ± 0.048	0.968 ± 0.128
7		0.675 ± 0.051	3.38 ± 0.33	0.843 ± 0.057	1.50 ± 0.18
8		2.61 ± 0.11	9.08 ± 0.91	1.99 ± 0.11	2.67 ± 0.30
9		4.94 ± 0.79	15.8 ±1.66	3.41 ± 0.81	8.50 ± 3.04
10		70.2 ± 27.83	n.e.[a]	n.e.[a]	n.e.[a]
11		2.25 ± 0.18	8.05 ± 0.49	2.20 ± 0.21	3.14 ± 0.40
12		n.e.[a]	n.e.[a]	60.8 ± 7.3	n.e.[a]
13		5.90 ± 0.42	35.5 ± 26.1	10.3 ± 2.0	21.6 ± 12.6
14		n.e.[a]	n.e.[a]	n.e.[a]	n.e.[a]
VK1	-	4.33 ± 0.32	8.28 ± 0.78	2.00 ± 0.15	2.63 ± 0.31
entinostat	-	1.14 ± 0.04	5.57 ± 0.43	2.96 ± 0.17	3.63 ± 0.30
vorinostat	-	2.32 ± 0.08	3.67 ± 0.15	1.60 ± 0.11	2.78 ± 0.22
cisplatin	-	3.51 ± 0.16	15.8 ± 0.84	1.11 ± 0.08	16.4 ± 1.67

Values are the mean of at least two independent experiments, each performed at least in duplicate.
[a] n.e.: no effect up to 100 µM

[g] MTT assays were performed by Lukas Biermann (HHU Düsseldorf, Kassack group).

Based on enzyme and cellular HDAC inhibition and cytotoxicity assay results (Tables 1-3), the two most potent compounds **5** (propyl) and **6** (butyl) and the cyclopropyl compound **8** were selected for additional biochemical and cellular investigations.

Class IIa (and HDAC8)-preferential cellular HDAC assays confirmed the selectivity of compounds **5**, **6**, and **8** for class I HDACs (Table 2). Selectivity factors (SF, ratio of IC_{50} class IIa-preferential assay (Table 2) and IC_{50} class I-preferential assay (Table 3)) ranged from 12 to 64 in A2780/A2780CisR cells and were lower in Cal27/Cal27CisR ranging from 6-15, except for compound **8** in Cal27CisR where SF was only 3. The class I-selective HDACi **entinostat** gave SF ranging from 16 to 89, whereas the broad-spectrum HDACi **vorinostat** gave SF of 1.3 (Cal27CisR) to 23 (A2780). Taken together, cellular HDAC data confirm a selectivity profile of our novel hydrazides similar to the *ortho*-aminoanilide **entinostat**.

Table 5. Cellular HDAC inhibition data of compounds **5**, **6**, and **8** in A2780/A2780CisR and Cal27/Cal27CisR cells using Boc-Lys(TFA)-AMC as class IIa and HDAC8 selective substrate.[h]

compound	**IC_{50} [µM]**			
	A2780sens	A2780CisR	Cal27sens	Cal27CisR
5	15.1 ± 2.3	12.5 ± 2.2	1.02 ± 0.17	2.32 ± 0.58
6	15.9 ± 3.0	11.0 ± 1.6	1.02 ± 0.18	2.22 ± 0.51
8	8.56 ± 1.53	11.9 ± 3.4	2.97 ± 0.40	1.28 ± 0.74
VK1	49.8 ± 4.9	47.6 ± 4.5	9.34 ± 1.53	6.47 ± 1.40
entinostat	38.0 ± 7.3	36.4 ± 6.4	8.37 ± 1.66	5.99 ± 1.21
vorinostat	14.5 ± 1.5	10.6 ± 2.4	1.49 ± 0.17	1.17 ± 0.19

In addition, class I selective cellular HDAC inhibition of our two frontrunners **5** and **6** was further confirmed in western blot analysis of the acetylation of α-tubulin and histone H3 (Figure 17). Cal27 and Cal27CisR were incubated for 24 h with **5**, **6**, **entinostat**, or **vorinostat**. Only **vorinostat** increased the acetylation of α-tubulin, confirming the inactivity of the hydrazides **5** and **6** against HDAC6 (Table 1). Class I HDAC inhibition of **5** and **6** was confirmed by the observed increase in acetylation of histone H3 in both, Cal27 and Cal27CisR cells. Further, although **entinostat** and **vorinostat** were used in slightly higher concentrations than **5** and **6**, these two hydrazides showed stronger acetylation of histone H3, thus confirming their more potent HDAC inhibition compared to **entinostat** and **vorinosta**t (Table 1). Taken together, biochemical HDAC inhibition assays (Table 1), cellular HDAC assays (Table 3 and Table 5), and western blot analysis confirm the higher

[h] Cellular HDAC assays were performed by Lukas Biermann (HHU Düsseldorf, Kassack group).

potency in class I HDAC inhibition of hydrazides **5** and **6** compared to the reference compounds **entinostat** and **vorinostat**.

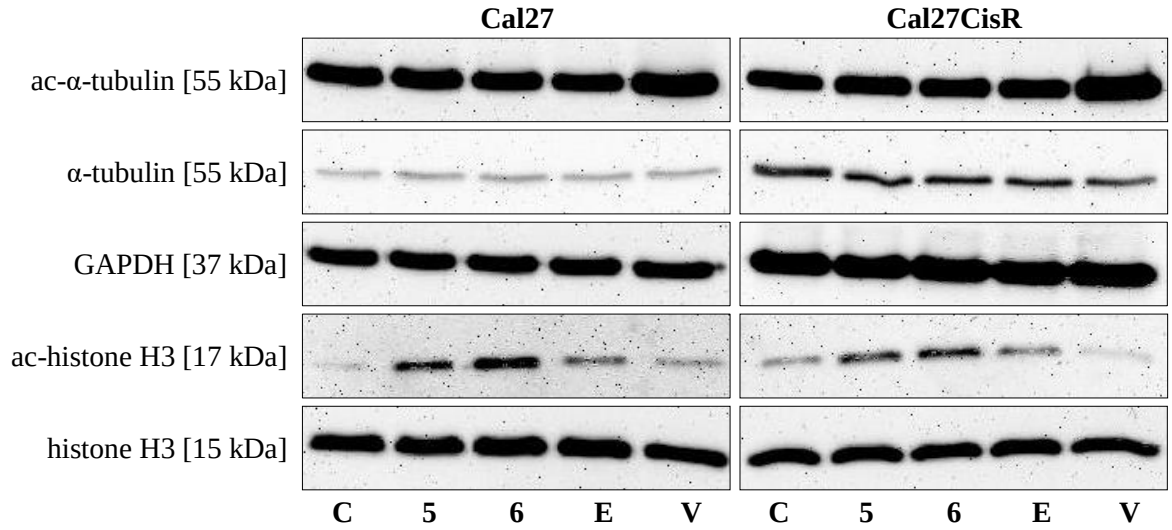


Figure 17. Compound-induced acetylation of α-tubulin and histone H3 in Cal27 and Cal27CisR cells. Displayed are representative immunoblots of two experiments. Cells were incubated for 24 h with 0.316 µM **5**, 0.316 µM **6**, 0.5 µM entinostat (E), or 0.5 µM vorinostat (V). C: untreated control.[i]

3.2.2.4 Hydrazide HDACi 5, 6, and 8 improve cisplatin cytotoxicity in a synergistic manner

In the next step, we evaluated the potential of the HDACi **5**, **6**, and **8** to increase cisplatin cytotoxicity. Native ovarian (A2780) and head-neck (Cal27) cancer cells as well as their cisplatin-resistant counterparts A2780CisR and Cal27CisR were applied. Cells were treated for 48 h with a fixed concentration of HDACi followed by an additional 72 h treatment with increasing concentrations of cisplatin plus the fixed concentration of HDACi. IC_{50} values of cisplatin estimated by this prolonged incubation procedure increased by 2-fold in A2780/A2780CisR and by 15/4-fold in Cal27/Cal27CisR cells compared to IC_{50} values reported in Table 4 with 72 h incubation. Applied HDACi concentrations were derived from IC_{50} values (estimated from IC_{50} values in Table 4) and adjusted in validation experiments in a way that the fixed concentration of HDACi alone should not lead to more than 40% inhibition of proliferation. All hydrazide or reference HDACi led to a significant increase in cisplatin potency (Table 6). Cisplatin resistance in A2780CisR was completely reversed except for HDACi **8** and **VK1** (Table 6). Moreover, HDACi **5** and **6** even led to an oversensitization, i.e. IC_{50} of cisplatin in presence of **5** or **6** in A2780CisR was lower than the IC_{50} of cisplatin in the native cell line A2780. HDACi treatment also led to oversensitization of native A2780 cells. Notably, HDACi **5** and **6** were more efficacious than the reference HDACi, as can be seen from significantly higher ShF (up to 8 for compounds **5** and **6**, only up to 4.5 for reference HDACi).

[i] Western blot analysis was performed by Lukas Biermann (HHU Düsseldorf, Kassack group).

Table 6. IC_{50} values of cisplatin alone and in combination with HDACi **5**, **6**, **8**, **VK1**, **entinostat** or **vorinostat** and shift factors (ShF) in A2780/A2780CisR and Cal27/Cal27CisR cells. HDACi were preincubated 48 h prior to addition of cisplatin. Cisplatin plus HDACi was then incubated for another 72 h. Data are the mean of pooled data from at least three independent experiments, each performed in triplicate. ShF: shift factor, ratio of the IC_{50} values of cisplatin alone and cisplatin in the combination treatment. All ShF were significant ($p < 0.05$), except **.[j]

	Cell line			
	A2780		A2780CisR	
compound	IC_{50}	ShF	IC_{50}	ShF
cisplatin	8.08		38.3	
cisplatin + 5*	4.51	1.79	4.76	8.02
cisplatin + 6*	3.79	2.13	5.29	7.24
cisplatin + 8*	6.03	1.34	14.4	2.66
cisplatin + VK1 (2 µM)	7.09	1.14**	16.2	2.37
cisplatin + entinostat (2 µM)	1.31	6.18	8.47	4.52
cisplatin + vorinostat (2 µM)	2.46	3.29	8.93	4.29

	Cell line			
	Cal27		Cal27CisR	
compound	IC_{50}	ShF	IC_{50}	ShF
cisplatin	17.2		63.5	
cisplatin + 5 (0.316 µM)	2.31	7.43	3.38	18.8
cisplatin + 6 (0.316 µM)	1.90	9.07	3.00	21.2
cisplatin + 8 (0.5 µM)	4.02	4.28	5.16	12.3
cisplatin + VK1 (0.5 µM)	2.03	8.49	7.06	8.99
cisplatin + entinostat (0.5 µM)	3.97	4.33	9.71	6.54
cisplatin + vorinostat (0.5 µM)	3.11	5.53	11.8	5.37

* Concentrations of **5**, **6**, and **8** were in A2780: 0.75 µM, 1 µM, and 2 µM, respectively; in A2780CisR: 2 µM.
** ShF not significant.

Sensitization by hydrazide HDACi against cisplatin was even more pronounced in Cal27/Cal27CisR cells (Table 6). ShF are the highest ever discovered for HDACi in this cellular resistance model leading to complete reversal of cisplatin resistance and moreover even to oversensitization.[293,300,301]

In Cal27CisR, the hydrazides **5**, **6**, and **8** showed stronger sensitization (ShF 12.3-21.2) than the reference HDACi (ShF 5.37-8.99). In native Cal27, ShF were similar for hydrazide and reference HDACi leading to oversensitization of cells against cisplatin. Notably, compounds **5** and **6** showed an almost 2-fold higher ShF than compound **8** (Cal27/Cal27CisR: ShF compound **8**: 4.28/12.3; compound **5**: 7.43/18.8; compound **6**: 9.07/21.2). Figure 18 illustrates the effect of compound **6** on cisplatin sensitization and even oversensitization with an ShF of 21.2.

[j] Synergism studies were performed by Lukas Biermann (HHU Düsseldorf, Kassack group).

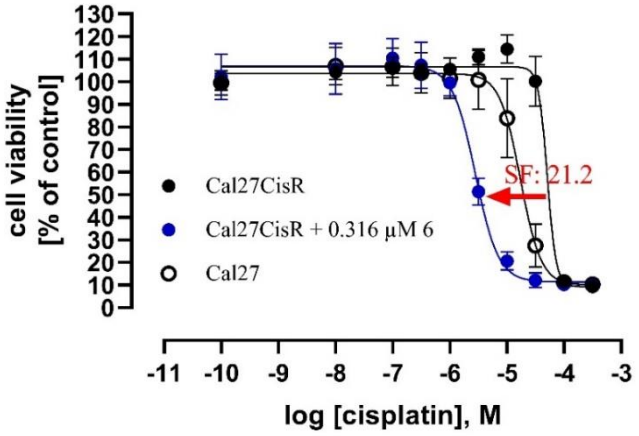


Figure 18. Preincubation with compound **6** for 48 h prior to addition of cisplatin improves cisplatin cytotoxicity in Cal27CisR leading to complete reversal of cisplatin resistance and moreover to oversensitization. IC_{50} values cisplatin: Cal27CisR without compound **6**: 63.5 µM; Cal27CisR with compound **6**: 3.00 µM; Cal27 without compound **6**: 17.2 µM.[k]

Encouraged by these high ShF, we next investigated the two best performing compounds **5** and **6** for synergy in combination with cisplatin. Table 7 shows the concentration-effect analyses of **5** and **6** in the cell line Cal27CisR in comparison to **entinostat**. Presented are combination index (CI) values calculated according to Chou-Talalay.[302] All three compounds are highly synergistic as seen by CI values < 0.2 for certain combinations of concentrations. However, for **entinostat**, only the highest concentrations (0.75 µM **entinostat** plus 10 µM cisplatin) gave a CI of < 0.2 (Table 7) whereas for **5** and **6** CI values of < 0.2 were found at much lower concentrations (red-marked CI values in Table 7). In addition, even at concentrations of 1 µM and 2.5 µM cisplatin, synergism was detected for **5** and **6** but not for **entinostat**.

[k] Synergism studies were performed by Lukas Biermann (HHU Düsseldorf, Kassack group).

Table 7. Combination index (CI) values for combination treatment of cisplatin with compound **5**, **6**, or **entinostat**, respectively, calculated according to Chou-Talalay[302] in Cal27CisR cells. HDACi were preincubated for 48 h followed by 72 h co-treatment with cisplatin.[1]

	HDACi 5 [µM]						**HDACi 6 [µM]**						**entinostat [µM]**					
cisplatin [µM]	0.05	0.15	0.30	0.45	0.60	0.75	0.05	0.15	0.30	0.45	0.60	0.75	0.05	0.15	0.30	0.45	0.60	0.75
1.0	*	*	*	1.48	0.58	0.40	*	*	*	*	0.79	0.46	*	*	*	*	*	*
2.5	*	*	0.40	0.29	0.26	0.25	*	*	0.40	0.19	0.23	0.26	*	*	*	*	*	*
5.0	*	0.32	0.14	0.14	0.15	0.17	*	0.31	0.14	0.10	0.15	0.17	*	*	*	1.10	0.61	0.38
7.5	*	0.19	0.11	0.13	0.13	0.14	*	0.19	0.11	0.10	0.13	0.15	*	*	*	0.40	0.31	0.21
10.0	0.41	0.12	0.10	0.10	0.11	0.13	0.46	0.16	0.10	0.09	0.12	0.13	*	0.57	0.55	0.27	0.21	0.16

[*] fraction affected less than 0.20. Data are the mean of pooled data (MTT assay) from at least three independent experiments, each performed in triplicate. CI were calculated using CompuSyn 1.0 Software. CI > 1.1 indicates antagonism, CI =1 indicates additivity, CI < 0.9 indicates synergism, and CI < 0.2 indicates very strong synergism (marked in red color).[302]

A graphical representation of the synergy is further shown in Figure 19 (LOEWE model of synergy using Combenefit software).[303–305] The synergistic surface is enhanced for compounds **5** and **6** compared to **entinostat**. In summary, the hydrazides **5** and **6** show an outstanding behavior in reversing cisplatin resistance and even leading to oversensitization of native solid cancer cells and display a very strong synergy with cisplatin, clearly exceeding that of **entinostat**.

A) Combination of HDACi **5** with cisplatin

B) Combination of HDACi **6** with cisplatin

C) Combination of **entinostat** with cisplatin

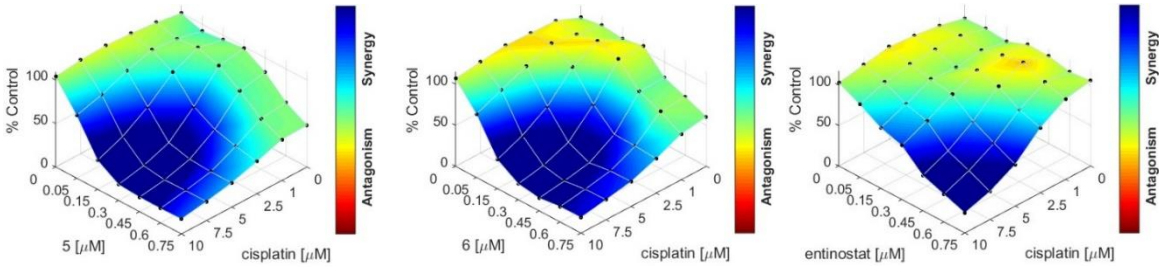


Figure 19. Synergy levels calculated with the LOEWE model using Combenefit software for combination treatments of cisplatin and **5**, **6**, or **entinostat**, respectively, in Cal27CisR cells. The values are the mean of pooled data from at least three independent experiments, each performed in triplicate. HDACi were preincubated for 48 h followed by 72 h co-treatment with cisplatin.[303–305 ,1]

[1] Synergism studies were performed by Lukas Biermann (HHU Düsseldorf, Kassack group).

3.2.2.5 Compounds 5 and 6 increase cisplatin-induced apoptosis and caspase activation in a synergistic manner

Next, we investigated if the cytotoxic effect of compounds **5** and **6** was based on caspase-mediated apoptosis induction. To this end, Cal27 and Cal27CisR cells were incubated for 48 h with HDACi **5**, **6**, or **entinostat** followed by addition of cisplatin for an additional 24 h. Concentrations of the HDACi were the same as used for the shift experiments (Table 6). Cisplatin was used in concentrations reflecting its approximate IC_{50} values (Table 4). The sub G1 fraction of the nuclei was determined by flow cytometry. Figure 20A and 20C show moderate percentage of apoptotic nuclei upon single treatment with cisplatin or the respective HDACi. However, combination treatment leads to a highly significant increase in apoptotic nuclei for all tested HDACi. This increase was synergistic as presented in Figure 20B and 20D. Combination treatment gave significantly higher bars (white bars) than the sum of the single treatments (black bars). HDACi **5** and **6** performed better than **entinostat** in Cal27CisR as can be seen by a higher percentage of apoptotic nuclei for compound **5** and **6** versus **entinostat** (Figure 20D).

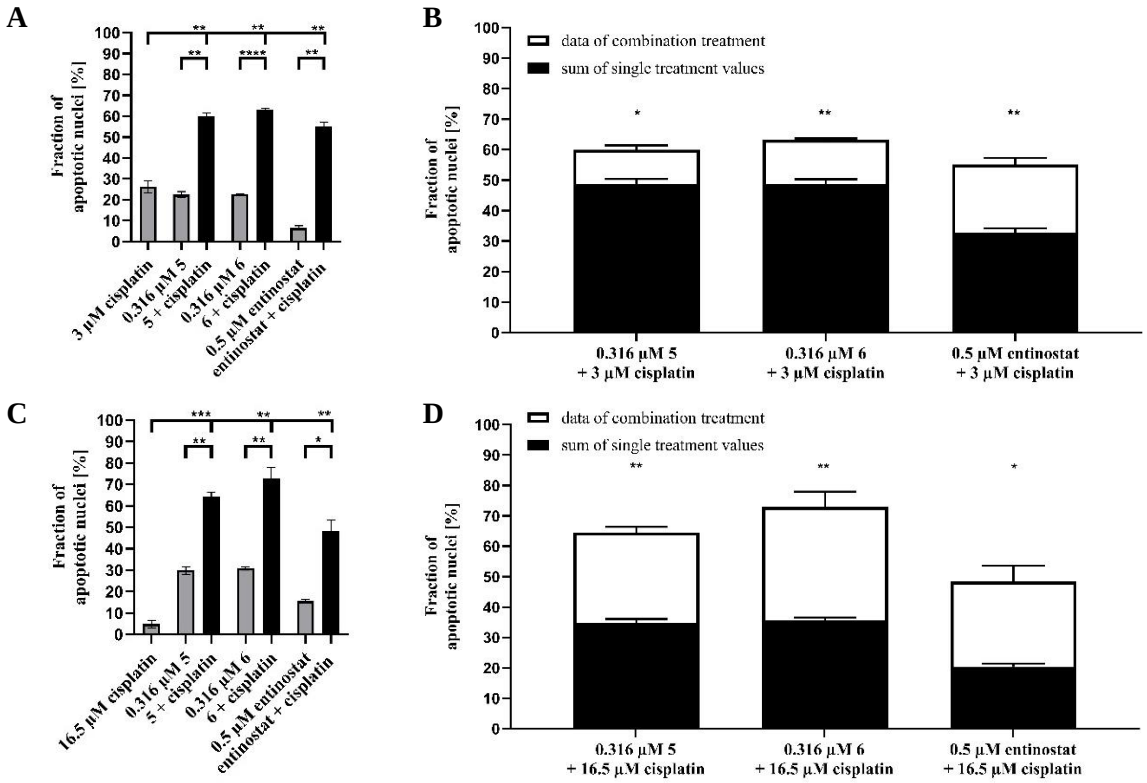


Figure 20. Compound **5** and **6** increase cisplatin-induced apoptosis. (**A**) Cal27 and (**C**) Cal27CisR cells were treated with the HDACi 48 h prior to addition of cisplatin for another 24 h. Determination of the sub G1 fraction of nuclei by flow cytometry served as measure for apoptotic nuclei. The percentage of apoptotic nuclei in the untreated control was subtracted. (**B**) and (**D**) show the synergistic effect of the combination on apoptosis. Black bars illustrate the sum of the single treatment values. White bars show the effect of the combination treatment. Data shown are from a representative experiment out of a set of three, each performed in duplicates. Statistical significance

was tested using a t-test with significance level: * ($p \leq 0.05$); ** ($p \leq 0.01$); *** ($p \leq 0.001$); **** ($p \leq 0.0001$).[m]

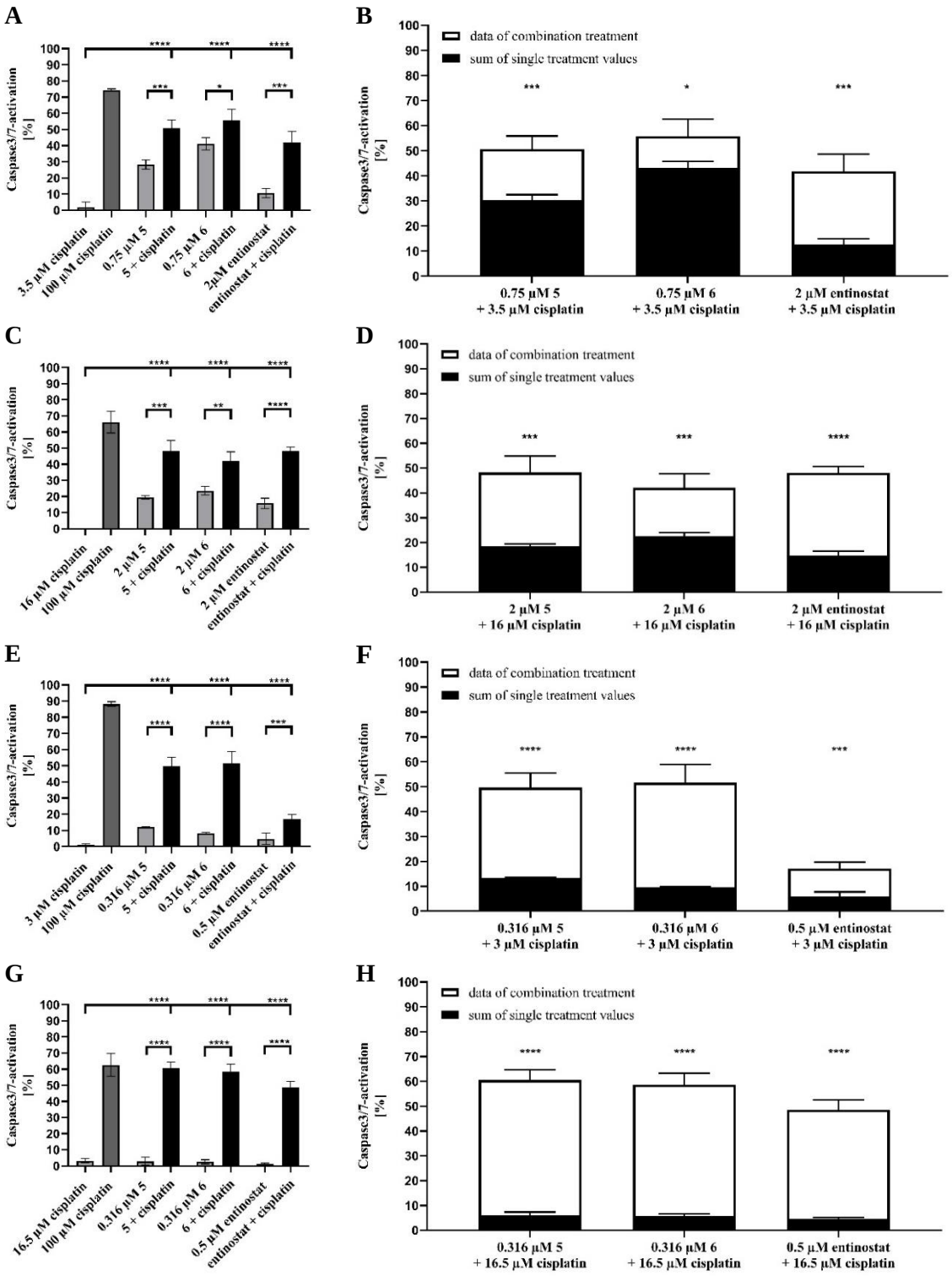


Figure 21. Compounds **5** and **6** increase cisplatin-induced caspase-3/7 activation. (**A**) A2780, (**C**) A2780CisR, (**E**) Cal27 and (**G**) Cal27CisR cells were treated with the HDACi 48 h prior to addition of cisplatin for another 24 h. Determination of caspase activation was monitored by live-cell fluorescence imaging using CellEvent reagent. The percentage of caspase3/7 positive cells in the

[m] Apoptosis studies were performed by Lukas Biermann (HHU Düsseldorf, Kassack group).

untreated control was subtracted. (**B**), (**D**), (**F**) and (**H**) show the synergistic effect of the combination on caspase-3/7 activation. Black bars illustrate the sum of the single treatment values. White bars show the effect of the combination treatment. Data shown are from a representative experiment out of a set of three, each performed in at least triplicates. Statistical significance was tested using a t-test with significance level: * ($p \leq 0.05$); ** ($p \leq 0.01$); *** ($p \leq 0.001$); **** ($p \leq 0.0001$).[n]

Caspase activation was studied by live cell fluorescence imaging in all four cell lines (A2780, A2780CisR, Cal27, Cal27CisR). Cells were incubated as described for the analysis of apoptosis. Concentrations of the HDACi were the same as used for the shift experiments (Table 6). Cisplatin was used in concentrations reflecting its approximate IC_{50} values (Table 4). Figure 21 shows almost no caspase activation under cisplatin treatment alone, except for the positive control 100 µM cisplatin. The control compound **entinostat** alone showed low (around 10%/ 15% in A2780/ A2780CisR cells) or very low (< 5% in Cal27/ Cal27CisR cells) caspase activation whereas compounds **5** and **6** alone showed remarkable caspase activation in A2780 (Figure 21A) and A2780CisR cells (Figure 21C). In Cal27 and Cal27CisR, the inhibitors **5** and **6** also showed low caspase activation if given alone. However, upon combination with cisplatin, caspase activation increased significantly in all cell lines. Particularly in Cal27 but notably even more in Cal27CisR, we found a dramatic increase in caspase activation upon combination treatment (Figure 21E, F).

The increase in caspase activation was synergistic in all four cell lines. There was no difference between the hydrazides **5** and **6** and **entinostat** in the maximum increase in caspase activation in A2780 and A2780CisR. However, compound **5** and **6** performed clearly superior to **entinostat** in Cal27 and Cal27CisR. Of note, the synergy in caspase activation was outstanding in Cal27 and Cal27CisR looking at the difference between the sum of the single treatments (black bars) versus the data for the combination treatments (white bars) in Figure 21F and Figure 21H.

3.2.2.6 Compounds 5 and 6 act synergistic with cisplatin by increasing DNA damage and expression of p21 and proapoptotic BIM

Next, we wanted to investigate prominent proteins inducing cell cycle arrest and apoptosis and the induction of DNA damage as possible mechanism by which HDACi increase cisplatin potency. Cal27 and Cal27CisR cells were incubated for 48 h untreated or treated with HDACi **5**, **6**, or **entinostat** followed by addition of cisplatin (or untreated) for another 24 h. Subsequently, γH2AX formation was measured by immunofluorescence as a marker for DNA damage (Figure 22). Whereas untreated control gave almost no γH2AX signal, 3 µM cisplatin in Cal27 and 16.5 µM in Cal27CisR (concentrations reflect the approximate IC_{50} values from Table 4 gave a small (Figure 22A) or clear increase (Figure 22C) in γH2AX signal. HDACi alone showed very small γH2AX

[n] Apoptosis studies were performed by Lukas Biermann (HHU Düsseldorf, Kassack group).

immunofluorescence, only slightly above control, demonstrating their minor DNA damaging properties. However, combinations of HDACi and cisplatin largely increased γH2AX formation in both, Cal27 and Cal27CisR. Whereas in Cal27 cells the hydrazides **5** and **6** and the *ortho*-aminoanilide **entinostat** gave similar γH2AX signals, in Cal27CisR cells compound **6** was clearly more potent than compound **5** or **entinostat**. Figure 22B and Figure 22D demonstrate the synergistic behavior of the HDACi with cisplatin in increasing DNA damage measured by γH2AX formation.

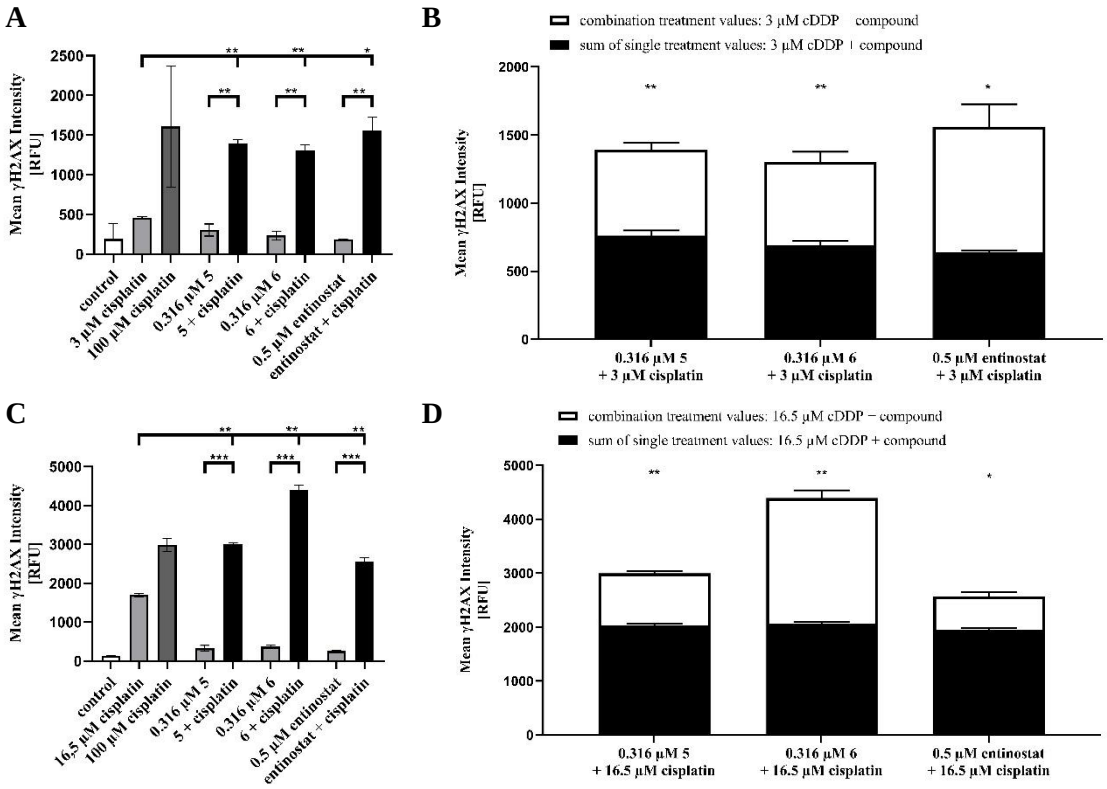


Figure 22. Compounds **5** and **6** enhance cisplatin-induced formation of γH2AX. (**A**) Cal27 and (**C**) Cal27CisR cells were treated with the HDACi 48 h prior to addition of cisplatin for another 24 h. Concentrations of the HDACi were the same as used for the shift experiments (Table 6). Cisplatin was used in concentrations reflecting its IC_{50} values (Table 4). γH2AX formation was analyzed by immunohistochemistry. (**B**) and (**D**) show the synergistic effect of the combination on γH2AX formation. Black bars illustrate the sum of the single treatment values. White bars show the effect of the combination treatment. Data shown are from a representative experiment out of a set of two, each performed in duplicates. Statistical significance was tested using a t-test with significance level: * ($p \leq 0.05$); ** ($p \leq 0.01$); *** ($p \leq 0.001$).[o]

Eventually, Cal27 and Cal27CisR cells were treated as described above for γH2AX analysis, and protein preparations were analyzed by western blotting for changes in p21 and BIM. Figure 23 demonstrates an increase in p21 and BIM upon HDACi treatment. The combination treatment of

[o] Apoptosis studies were performed by Lukas Biermann (HHU Düsseldorf, Kassack group).

HDACi and cisplatin yielded, compared to HDACi treatment alone, a slightly reduced expression of p21 and BIM in Cal27. In Cal27CisR, this was also the case for p21 expression. However, BIM expression in Cal27CisR increased upon combination treatment with the inhibitors **5** and **6**.

Taken together, we could demonstrate that HDACi, particularly **5** and **6**, in combination with cisplatin synergistically increased DNA damage as measured by γH2AX formation and that at least part of the HDACi anticancer effects (in combination with cisplatin) are mediated by increased p21 and BIM.

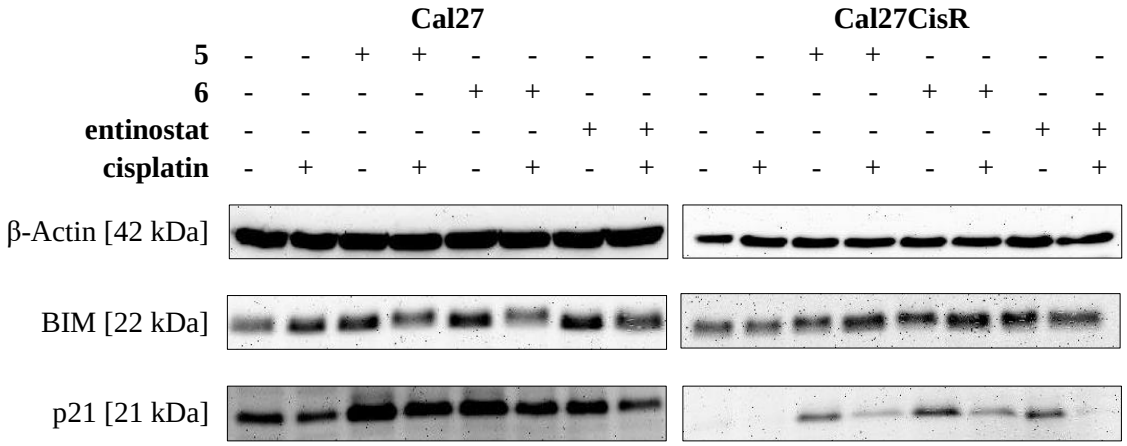


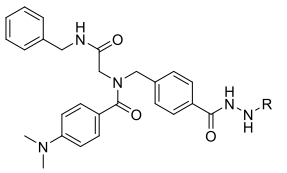
Figure 23. Western blot analysis of p21 and BIM in Cal27 and Cal27CisR cells untreated or treated with HDACi **5**, **6**, or **entinostat** in the absence or presence of cisplatin. Cells were treated with 0.316 µM **5**, 0.316 µM **6**, or 0.5 µM **entinostat** for 48 h prior to addition of cisplatin for another 24 h. Cisplatin was used at 3 µM in Cal27 and at 16.5 µM in Cal27CisR. Displayed are representative immunoblots of at least 3 experiments.[p]

3.2.2.7 Cytotoxic effect of HDACi 5 and 6 in acute myeloid leukemia cell lines

The frontrunners **5** and **6** were eventually tested for their cytotoxic potency at two acute myeloid leukemia (AML) cell lines, MV4-11 which is a p53 WT cell line, and HL-60 which is a p53 null cell line.[207] IC_{50} values were 4-fold / 2-fold lower in MV4-11 and in HL-60, respectively, than in head-neck cancer cells (Cal27). Further, **5** and **6** were 2-fold more potent than **vorinostat** or the *ortho*-aminoanilide **entinostat**. Regardless of the p53 status, hydrazide-based HDACi may thus serve as novel potent epigenetic agents in AML cells.

[p] Western blots were performed by Lukas Biermann (HHU Düsseldorf, Kassack group).

Table 8. Cytotoxicity of **5** and **6** in comparison to **entinostat** in AML cell lines HL-60 (p53-null) and MV4-11 (p53 WT). Data shown are mean +/- SEM, n = 3.[q]



Code	R	IC_{50} [µM]	
		HL-60	MV4-11
5		0.431 ± 0.026	0.194 ± 0.004
6		0.474 ± 0.030	0.212 ± 0.010
entinostat	-	0.939 ± 0.066	0.410 ± 0.034

3.3 Conclusion

3.3 Conclusion

In summary, a set of peptoid-based HDACi with a substituted hydrazide moiety as ZBG was synthesized through an efficient three-step procedure. The isolated compounds were assessed for their *in vitro* inhibitory activity against multiple HDAC isoforms. The two most potent inhibitors **5** and **6**, containing a propyl or butyl FPU, respectively, showed low nanomolar activity against the class I HDAC isoforms HDAC1-3, including single digit nanomolar inhibition of HDAC3. Cellular HDAC assays confirmed their class I selective inhibition. Cytotoxicity assays demonstrated that compounds **5** and **6** were more potent than the reference HDAC inhibitors (**VK1**, **entinostat**, and **vorinostat**) in both native and cisplatin-resistant A2780 and Cal27 cancer cell lines. Further, the potential of the hit compounds **5** and **6** to increase cisplatin cytotoxicity was evaluated. Both compounds completely reversed the cisplatin resistance in A2780CisR (ShF (compound **5**): 8.02, ShF (compound **6**): 7.24) and Cal27CisR cells (ShF (compound **5**): 18.8, ShF (compound **6**): 21.2), even leading to oversensitization of the cells against cisplatin. Furthermore, both compounds were tested for synergy in combination with cisplatin. According to the Chou-Talalay (CI < 0.2) and the LOEWE model, compound **5** and **6** showed very strong synergistic effects in combination with cisplatin, clearly exceeding the synergism of **entinostat**. Moreover, the synergy of the inhibitors **5** and **6** with cisplatin was confirmed in apoptosis assays in Cal27/Cal27CisR cells. In A2780 and A2780CisR cells, compounds **5**, **6**, and **entinostat** showed remarkable caspase 3/7 activation as

[q] MTT assays in HL-60 cells were performed by Lukas Biermann (HHU Düsseldorf, Kassack group). CellTiter-Glo measurements in MV4-11 cells were performed by Dr. Maria Hanl (Rheinische Friedrich-Wilhelms-Universität Bonn, Hansen Group).

single treatment and in combination with cisplatin. In contrast, in Cal27 and Cal27CisR cells, only a low caspase activation was observed in single treatment. However, upon combination with cisplatin the caspase activation increased significantly and compound **5** and **6** clearly outperformed **entinostat**. To clarify the possible mechanism by which the hydrazide-based HDACi **5** and **6** increase the potency of cisplatin, assessments of DNA damage, specifically γH2AX formation, were conducted: While HDACi **5** and **6** alone showed marginal γH2AX immunofluorescence, only slightly surpassing the control, their combination with cisplatin substantially increased γH2AX formation in both Cal27 and Cal27CisR cells. Notably, in Cal27CisR cells, compound **6** demonstrated greater potency than compound **5** or **entinostat** (see Figure 22) in combination with cisplatin underscoring the synergistic effect in increasing DNA damage. Additionally, protein analysis via western blot showed the upregulation of p21 and BIM expression upon treatment with **5** and **6**. However, when **5** and **6** were combined with cisplatin, a slightly reduced expression of p21 and BIM was observed in Cal27. In Cal27CisR, the combination treatment resulted in increased BIM expression, emphasizing the potential role of p21 and BIM in mediating the anticancer effects of hydrazide-based HDACi in synergy with cisplatin. Finally, HDACi **5** and **6** were assessed for their cytotoxic potential against two AML cell lines. Again, compounds **5** and **6** demonstrated potent cytotoxic activities and outperformed **entinostat**, irrespective of the p53 status.

Taken together, the synthesized substituted hydrazides are highly potent class I HDAC selective inhibitors with chemosensitizing properties in cisplatin-resistant solid tumors. Notably, the hit compounds **5** and **6** exhibit remarkly synergy with cisplatin, outperforming the well-established *ortho*-aminoanilide **entinostat** and may serve as lead structures for the development of novel agents for cancer treatment.

3.4 Experimental Section

General Information

Chemicals were obtained from abcr GmbH, Acros Organics, Carbolution Chemicals, Sigma-Aldrich, TCI Chemicals or VWR and used without further purification. Technical grade solvents were distilled prior to use. For all HPLC purposes, acetonitrile in HPLC-grade quality (HiPerSolv CHROMANORM, *VWR*) was used. Water was purified with a PURELAB flex® (*ELGA VEOLIA*). Air-sensitive reactions were carried out under argon atmosphere utilizing standard *Schlenk* techniques. **Thin-layer chromatography (TLC)** was carried out on prefabricated plates (silica gel 60, F_{254}, *Merck*). Components were visualized either by irradiation with ultraviolet light (254 nm or 366 nm) or by staining appropriately. Column Chromatography was carried out on silica gel (60 Å, 40-60 μm, *Acros Organics*). If no solvent is stated an aqueous solution was prepared with demineralized water. Mixtures of two or more solvents are specified as "solvent A"/"solvent B", 3/1, *v*/*v*; meaning that 100 mL of the respective mixture consists of 75 mL of "solvent A" and 25

mL of “solvent B”. The uncorrected melting points were determined using a Büchi Melting Point M-560 apparatus. **Nuclear Magnetic Resonance Spectroscopy (NMR):** Proton (^{1}H), carbon (^{13}C), and fluorine (^{19}F) NMR spectra were recorded either on a *Bruker* Avance III HD 400 MHz at a frequency of 400 MHz (^{1}H), 100 MHz (^{13}C) and 377 MHz (^{19}F), a *Varian/Agilent* Mecury-plus-400 at a frequency of 400 MHz (^{1}H) and 100 MHz (^{13}C), a *Varian/Agilent* Mecury-plus-300 at a frequency of 300 MHz (^{1}H), 75 MHz (^{13}C) and 282 MHz (^{19}F) , a *Bruker* AVANCE 500 MHz at a frequency of 500 MHz (^{1}H) and 126 MHz (^{13}C) or on a *Bruker* AVANCE III HD 600 MHz at a frequency of 600 MHz (^{1}H), 151 MHz (^{13}C) and 565 MHz (^{19}F). The chemical shifts are given in parts per million (ppm). As solvents deuterated chloroform ($CDCl_3$), deuterated methanol (MeOH-d_4) and deuterated dimethyl sulfoxide (DMSO-d_6) were used. The residual solvent signal ($CDCl_3$: ^{1}H NMR: 7.26 ppm, ^{13}C NMR: 77.1 ppm; DMSO-d_6: ^{1}H NMR: 2.50 ppm, ^{13}C NMR: 39.52 ppm; MeOH-d_4: ^{1}H NMR: 3.31 ppm, 4.87 ppm, ^{13}C NMR: 49.00 ppm) was used for calibration. The multiplicity of each signal is reported as singlet (s), doublet (d), triplet (t), quartet (q), multiplet (m) or combinations thereof. Multiplicities and coupling constants are reported as measured and might disagree with the expected values. **Mass Spectrometry: :** High resolution electrospray ionization mass spectra (HRMS-ESI) were acquired with *Bruker Daltonik GmbH* micrOTOF coupled to a an *LC Packings* Ultimate HPLC system and controlled by micrOTOFControl3.4 and HyStar 3.2-LC/MS, with a *BrukerDaltonik GmbH* ESI-qTOF Impact II coupled to a *Dionex* UltiMateTM 3000 UHPLC system and controlled by micrOTOFControl 4.0 and HyStar 3.2-LC/MS or with a micrOTOF-Q mass spectrometer (*Bruker*) with ESI-source coupled with an HPLC Dionex UltiMate 3000 (*Thermo Scientific*). Low resolution electrospray ionisation mass spectra (LRMS-ESI) were acquired with an *Advion* expression® compact mass spectrometer (CMS) coupled with an automated TLC plate reader Plate Express® (*Advion*). **High Performance Liquid Chromatography (HPLC)**: A *Thermo Fisher Scientific* UltiMate™ 3000 UHPLC system with a Nucleodur 100-5 C18 (250 x 4.6 mm, *Macherey Nagel*) with a flow rate of 1 mL/min and a temperature of 25 °C or a 100-5 C18 (100 x 3 mm, *Macherey Nagel*) with a flow rate of 0.5 mL/min and a temperature of 25 °C with an appropriate gradient were used. For preparative purposes a AZURA Prep. 500/1000 gradient system with a Nucleodur 110-5 C18 HTec (250 x 32 mm, *Macherey Nagel*) column with 20 mL/min was used. Detection was implemented by UV absorption measurement at a wavelength of λ = 220 nm and λ = 250 nm. Bidest. H_2O (A) and MeCN (B) were used as eluents with an addition of 0.1% TFA for eluent A. **Purity:** The purity of all final compounds was 95% or higher. Purity was determined via HPLC with the Nucleodur 100-5 C18 (250 x 4.6 mm, *Macherey Nagel*) at 250 nm. After column equilibration for 5 min a linear gradient from 5% A to 95% B in 7 min followed by an isocratic regime of 95% B for 10 min was used.

The following compounds were synthesized according to literature and used without further purification: Methyl-4-({*N*-[2-(benzylamino)-2-oxoethyl]-4-(dimethylamino)-benzamido}-methyl)-benzoate (**2**), 4-({*N*-[2-(benzylamino)-2-oxoethyl]-4-(dimethylamino)-benzamido}-methyl)-benzoic acid (**3**)[218]

3.4.1 Experimental procedures

3.4.1.1 General procedures

General procedure I

To a solution of the hydrazide **4** (1.00 eq.) in MeOH (0.2 M) the respective aldehyde (1.20 eq.) and AcOH (2.00 eq.) were added and stirred at room temperature for 30 min. $NaBH_3CN$ (2.00 eq.) was added and the solution stirred for further 19 h at room temperature. The solvent was removed under reduced pressure and the residue purified by preparative HPLC to give the target compound.

General procedure II

To a solution of the hydrazide **4** (1.00 eq.) in iPrOH (0.1 M) the respective aldehyde (1.00 eq.) and tris(2,2,2-trifluoroethyl) borate (1.00 eq.) were added and stirred for 19 h at room temperature. $NaBH_4$ (2.40 eq.) was added and stirred for further 2 h at room temperature. Afterwards, the reaction was diluted with H_2O (0.1 mL) and stirred for additional 30 min. The solvent was removed under reduced pressure and the residue purified by preparative HPLC to give the target compound.

General procedure III

To a solution of the respective carboxylic acid (1.00 eq.) in THF/DMF (0.1 M, 39/1 *v*/*v*) DIPEA (4.00 eq.) and HATU (1.20 eq.) were added and stirred for 15 min at room temperature. The respective hydrazine (1.20 eq.) or hydrazine hydrochloride (1.50 eq.) was added and stirred for further 4 h. The solvent was removed under reduced pressure and the residue purified by preparative HPLC to give the target compound.

3.4.1.2 Compound characterization

N-[2-(Benzylamino)-2-oxoethyl]-4-(dimethylamino)-*N*-[4-(hydrazinecarbonyl)benzyl]benzamide (**4**)

Ester **2** (0.200 g, 0.435 mmol, 1.00 eq.) was dissolved in 2 mL MeOH. Afterwards, 65 wt-% hydrazine-monohydrate solution (0.339 mL, 0.219 g, 4.35 mmol, 10.0 eq.) in H_2O was added. The flask was capped and heated to 70 °C for 19 h. The solvent was removed under reduced pressure to give the product **4** (0.200 g, 0.435 mmol, quant.) as a white foam. **^{1}H-NMR** (400 MHz, DMSO-d_6) δ = 11.41 (s, 1H), 8.47 (t, *J* = 6.0 Hz, 1H), 7.88 (d, *J* = 8.0 Hz, 2H), 7.47 (d, *J* = 8.0 Hz, 2H), 7.38 – 7.28 (m, 4H), 7.28 – 7.20 (m, 3H), 6.71 – 6.58 (m, 2H), 4.71 (s, 2H), 4.31 (d, *J* = 5.8 Hz, 2H), 3.93 (s, 2H), 2.93 (s, 6H); **^{13}C-NMR** (101 MHz, DMSO-d_6) δ = 171.8, 168.2, 165.8, 158.5,

158.2, 151.2, 142.8, 139.2, 129.3, 128.6, 128.3, 127.9, 127.3, 126.9, 111.0, 42.2; **HRMS-ESI (*m/z*):** $[M+Na]^+$ calcd for $C_{26}H_{29}N_5O_3$: 482.2168, found: 482.2194.

N-[2-(Benzylamino)-2-oxoethyl]-4-(dimethylamino)-*N*-[4-(2-propylhydrazine-1-carbonyl)benzyl]benzamide trifluoroacetate (**5**)

Prepared according to **GP II**, starting from hydrazide **4** (0.100 g, 0.218 mmol, 1.00 eq.), propionaldehyde (15.7 µL, 12.7 mg, 0.218 mmol, 1.00 eq.), tris(2,2,2-trifluroethyl) borate (46.9 µL, 67.1 mg, 0.218 mmol, 1.00 eq.), and $NaBH_4$ (20.0 mg, 0.529 mmol, 2.40 eq.). Compound **5** (67.1 mg, 0.109 mmol, 50%) was isolated as a white lyophilizate. **^{1}H-NMR** (400 MHz, DMSO-d_6) δ = 11.40 (s, 1H), 8.47 (t, *J* = 5.9 Hz, 1H), 7.88 (d, *J* = 8.0 Hz, 2H), 7.47 (d, *J* = 8.0 Hz, 2H), 7.36 – 7.29 (m, 4H), 7.27 – 7.21 (m, 3H), 6.69 – 6.63 (m, 2H), 4.71 (s, 2H), 4.31 (d, *J* = 5.8 Hz, 2H), 3.93 (s, 2H), 3.15 – 3.05 (m, 2H), 2.93 (s, 6H), 1.64 (h, *J* = 7.5 Hz, 2H), 0.94 (t, *J* = 7.5 Hz, 3H); **^{13}C NMR** (101 MHz, DMSO-d_6) δ = 172.2, 168.6, 165.8, 158.8 (q, *J* = 34.8 Hz), 151.7, 143.2, 139.7, 130.1, 129.1, 128.8, 128.4, 127.7, 127.3, 116.6 (d, *J* = 294.0 Hz), 111.5, 52.1, 42.6, 18.6, 11.4; **HRMS-ESI (*m/z*):** $[M+H]^+$ calcd for $C_{29}H_{35}N_5O_3$: 502.2818, found: 502.2822; **HPLC**: t_R = 10.76 min (99.1% purity).

N-[2-(Benzylamino)-2-oxoethyl]-*N*-[4-(2-butylhydrazine-1-carbonyl)benzyl]-4-(dimethylamino)benzamide trifluoroacetate (**6**)

Prepared according to **GP III**, starting from carboxylic acid **3** (0.100 g, 0.224 mmol, 1.00 eq.), butylhydrazine hydrochloride (41.7 mg, 0.336 mmol, 1.50 eq.), HATU (72.7 mg, 0.269 mmol, 1.20 eq), and DIPEA (0.117 mL, 86.8 mg, 0.672 mmol, 3.00 eq.). Compound **6** (39.0 mg, 61.9 µmol, 28%) was isolated as a white lyophilizate. **^{1}H-NMR** (600 MHz, DMSO-d_6) δ = 11.46 (s, 1H), 8.46 (t, *J* = 5.9 Hz, 1H), 7.88 (d, *J* = 7.9 Hz, 2H), 7.47 (d, *J* = 7.9 Hz, 2H), 7.36 – 7.30 (m, 4H), 7.28 – 7.21 (m, 3H), 6.68 – 6.62 (m, 2H), 4.71 (s, 2H), 4.31 (d, *J* = 5.9 Hz, 2H), 3.93 (s, 2H), 3.19 – 3.10 (m, 2H), 2.93 (s, 6H), 1.60 (p, *J* = 7.7 Hz, 2H), 1.37 (h, *J* = 7.4 Hz, 2H), 0.90 (t, *J* = 7.4 Hz, 3H); **^{13}C-NMR** (151 MHz, DMSO-d_6) δ = 171.7, 168.1, 165.3, 158.3 (q, *J* = 35.2 Hz), 151.2, 142.8, 139.2, 129.5, 128.6, 128.3, 127.9, 127.3, 126.8, 116.0 (d, *J* = 292.8 Hz), 111.0, 49.7, 42.1, 26.5, 19.2, 13.5; **HRMS-ESI (*m/z*):** $[M+H]^+$ calcd for $C_{30}H_{37}N_5O_3$: 515.2975, found: 516.2969; **HPLC**: t_R = 10.90 min (> 99.9% purity).

N-[2-(Benzylamino)-2-oxoethyl]-4-(dimethylamino)-*N*-[4-(2-pentylhydrazine-1-carbonyl)benzyl]benzamide trifluoroacetate (**7**)

Prepared according to **GP III**, starting from carboxylic acid **3** (0.100 g, 0.224 mmol, 1.00 eq.), pentylhydrazine dihydrochloride (58.8 mg, 0.336 mmol, 1.50 eq.), HATU (72.7 mg, 0.269 mmol, 1.20 eq.), and DIPEA (0.156 mL, 0.116 g, 0.896 mmol, 4.00 eq.). Compound **7** (27.7 mg, 43.0 µmol, 19%) was isolated as a white lyophilizate. **^{1}H-NMR** (600 MHz, DMSO-d_6) δ = 11.33 –

11.10 (m, 1H), 8.45 (t, *J* = 6.0 Hz, 1H), 7.87 (d, *J* = 7.9 Hz, 2H), 7.46 (d, *J* = 7.9 Hz, 2H), 7.33 (dd, *J* = 8.3, 6.5 Hz, 4H), 7.28 – 7.21 (m, 3H), 6.70 – 6.62 (m, 2H), 4.71 (s, 2H), 4.31 (d, *J* = 5.9 Hz, 2H), 3.92 (s, 2H), 3.08 (t, *J* = 7.7 Hz, 2H), 2.93 (s, 6H), 1.60 (t, *J* = 7.6 Hz, 2H), 1.36 – 1.26 (m, 4H), 0.87 (t, *J* = 7.0 Hz, 3H); **^{13}C-NMR** (151 MHz, DMSO-d_6) δ = 171.7, 168.1, 165.2, 158.2 (q, *J* = 34.2 Hz), 151.2, 142.5, 139.2, 129.8, 128.6, 128.3, 127.8, 127.2, 126.8, 116.3 (d, *J* = 295.3 Hz), 111.0, 50.1, 40.1, 28.1, 24.6, 21.7, 13.7; **HRMS-ESI (*m/z*):** $[M+H]^+$ calcd for $C_{31}H_{39}N_5O_3$: 530.3131, found: 530.3126; **HPLC**: t_R = 11.10 min (99.4% purity).

N-[2-(Benzylamino)-2-oxoethyl]-*N*-{4-[2-(cyclopropylmethyl)hydrazine-1-carbonyl]benzyl}-4-(dimethylamino)benzamide trifluoroacetate (**8**)

Prepared according to **GP II**, starting from hydrazide **4** (0.100 g, 0.218 mmol, 1.00 eq.), cyclopropanecarbaldehyde (16.3 µL, 15.3 mg, 0.218 mmol, 1.00 eq.), tris(2,2,2-trifluroethyl) borate (46.9 µL, 67.1 mg, 0.218 mmol, 1.00 eq.), and $NaBH_4$ (20.0 mg, 0.529 mmol, 2.40 eq.). Compound **8** (62.0 mg, 98.9 µmol, 45%) was isolated as a white lyophilizate. **^{1}H-NMR** (500 MHz, DMSO-d_6) δ = 11.47 (s, 1H), 8.46 (d, *J* = 6.2 Hz, 1H), 7.88 (d, *J* = 7.9 Hz, 2H), 7.47 (d, *J* = 8.0 Hz, 2H), 7.36 – 7.29 (m, 4H), 7.25 (t, *J* = 7.8 Hz, 3H), 6.69 – 6.56 (m, 2H), 4.71 (s, 2H), 4.31 (d, *J* = 5.8 Hz, 2H), 3.93 (s, 2H), 3.05 (d, *J* = 7.3 Hz, 2H), 2.93 (s, 6H), 1.05 (tt, *J* = 7.7, 4.7 Hz, 1H), 0.58 – 0.54 (m, 2H), 0.38 – 0.31 (m, 2H); **^{13}C-NMR** (126 MHz, DMSO-d_6) δ = 171.7, 168.1, 165.2, 158.3 (q, *J* = 34.7 Hz), 151.2, 142.6, 139.2, 129.7, 128.5, 128.2, 127.8, 127.2, 126.8, 122.0, 116.1 (d, *J* = 294.5 Hz), 111.0, 54.8, 42.1, 6.5, 3.5; **HRMS-ESI (*m/z*):** $[M+H]^+$ calcd for $C_{30}H_{35}N_5O_3$: 514.2818, found: 514.2813; **HPLC**: t_R = 10.78 min (95.1% purity).

N-[2-(Benzylamino)-2-oxoethyl]-4-(dimethylamino)-*N*-[4-(2-isopentylhydrazine-1-carbonyl)benzyl]benzamide trifluroacetate (**9**)

Prepared according to **GP II**, starting from hydrazide **4** (0.100 g, 0.218 mmol, 1.00 eq.), 3-methylbutanal (23.6 µL, 18.9 mg, 0.218 mmol, 1.00 eq.), tris(2,2,2-trifluroethyl) borate (46.9 µL, 67.1 mg, 0.218 mmol, 1.00 eq.), and $NaBH_4$ (20.0 mg, 0.529 mmol, 2.40 eq.). Compound **9** (56.5 mg, 87.8 µmol, 40%) was isolated as a white lyophilizate. **^{1}H-NMR** (500 MHz, DMSO-d_6) δ = 11.41 (s, 1H), 8.46 (d, *J* = 6.2 Hz, 1H), 7.88 (d, *J* = 7.9 Hz, 2H), 7.47 (d, *J* = 7.9 Hz, 2H), 7.35 – 7.28 (m, 4H), 7.28 – 7.20 (m, 3H), 6.71 – 6.57 (m, 2H), 4.71 (s, 2H), 4.31 (d, *J* = 5.8 Hz, 2H), 3.93 (s, 2H), 3.20 – 3.08 (m, 2H), 2.93 (s, 6H), 1.71 – 1.62 (m, 1H), 1.58 – 1.47 (m, 2H), 0.90 (s, 3H), 0.88 (s, 3H); **^{13}C-NMR** (126 MHz, DMSO-d_6) δ = 171.7, 168.1, 165.2, 158.3 (q, *J* = 34.9 Hz), 151.2, 142.6, 139.2, 129.7, 128.5, 128.2, 127.8, 127.2, 126.8, 122.0, 116.1 (d, *J* = 293.9 Hz), 111.0, 48.5, 42.1, 33.5, 25.2, 22.2; **HRMS-ESI (*m/z*):** $[M+H]^+$ calcd for $C_{31}H_{39}N_5O_3$: 530.3131, found: 530.3126; **HPLC**: t_R = 11.12 min (98.1% purity).

N-[2-(Benzylamino)-2-oxoethyl]-4-(dimethylamino)-*N*-{4-[2-(3,3-dimethylbutyl)hydrazine-1-carbonyl]benzyl}benzamide trifluroacetate (**10**)

Prepared according to **GP II**, starting from hydrazide **4** (0.100 g, 0.218 mmol, 1.00 eq.), 3,3-dimethylbutanal (27.3 µL, 21.8 mg, 0.218 mmol, 1.00 eq.), tris(2,2,2-trifluroethyl) borate (46.9 µL, 67.1 mg, 0.218 mmol, 1.00 eq.), and $NaBH_4$ (20.0 mg, 0.529 mmol, 2.40 eq.). Compound **10** (52.5 mg, 79.8 µmol, 37%) was isolated as a white lyophilizate. **^{1}H-NMR** (600 MHz, DMSO-d_6) δ = 11.25 (s, 1H), 8.46 (d, *J* = 6.9 Hz, 1H), 7.88 (d, *J* = 7.9 Hz, 2H), 7.46 (d, *J* = 7.9 Hz, 2H), 7.33 (dd, *J* = 8.1, 5.4 Hz, 4H), 7.28 – 7.22 (m, 3H), 6.69 – 6.63 (m, 2H), 4.71 (s, 2H), 4.31 (d, *J* = 5.8 Hz, 2H), 3.93 (s, 2H), 3.14 – 3.07 (m, 2H), 2.93 (s, 6H), 1.55 – 1.49 (m, 2H), 0.90 (s, 9H); **^{13}C-NMR** (151 MHz, DMSO) δ = 171.7, 168.1, 165.2, 158.3 (q, *J* = 34.0 Hz), 151.2, 142.5, 139.2, 129.8, 128.6, 128.3, 127.8, 127.3, 126.8, 122.0, 116.4 (q, *J* = 295.4 Hz), 111.0, 47.0, 42.1, 38.2, 29.4, 29.0; **HRMS-ESI (*m/z*):** $[M+H]^+$ calcd for $C_{32}H_{41}N_5O_3$: 544.3288, found: 544.33282; **HPLC**: t_R = 11.24 min (98.0% purity).

N-[2-(Benzylamino)-2-oxoethyl]-4-(dimethylamino)-*N*-{4-[2-(3,3,3-trifluoropropyl)hydrazine-1-carbonyl]benzyl}benzamide trifluroacetate (**11**)

Prepared according to **GP II**, starting from hydrazide **4** (0.100 g, 0.218 mmol, 1.00 eq.), 3,3,3-trifluoropropanal (17.8 µL, 24.4 mg, 0.218 mmol, 1.00 eq.), tris(2,2,2-trifluroethyl) borate (46.9 µL, 67.1 mg, 0.218 mmol, 1.00 eq.), and $NaBH_4$ (20.0 mg, 0.529 mmol, 2.40 eq.). Compound **11** (43.8 mg, 95.4 µmol, 26%) was isolated as a white lyophilizate. **^{1}H-NMR** (600 MHz, DMSO-d_6) δ = 10.13 (s, 1H), 8.43 (d, *J* = 6.1 Hz, 1H), 7.83 (d, *J* = 7.8 Hz, 2H), 7.39 (d, *J* = 7.9 Hz, 2H), 7.35 – 7.30 (m, 4H), 7.27 – 7.21 (m, 3H), 6.70 – 6.62 (m, 2H), 4.69 (s, 2H), 4.31 (d, *J* = 5.8 Hz, 2H), 3.91 (s, 2H), 3.05 (t, *J* = 7.3 Hz, 2H), 2.93 (s, 6H), 2.52 (s, 2H); **^{13}C-NMR** (151 MHz, DMSO-d_6) δ = 171.7, 168.1, 165.5, 158.2 (q, *J* = 36.9 Hz), 151.1, 141.2, 139.2, 128.9 (q, *J* = 292.2 Hz), 128.6, 128.2, 127.4, 127.2, 126.8, 124.3, 115.5 (d, *J* = 291.0 Hz), 111.0, 43.9 (q, *J* = 3.2 Hz), 42.1, 40.1 31.7 (q, *J* = 27.0 Hz); **^{19}F-NMR** (565 MHz, DMSO-d_6) δ = -64.4 (t, *J* = 11.7 Hz), -75.7; **HRMS-ESI (*m/z*):** $[M+H]^+$ calcd for $C_{29}H_{32}F_3N_5O_3$: 556.2535, found: 556.2530; **HPLC**: t_R = 11.75 min (97.7% purity).

N-[2-(Benzylamino)-2-oxoethyl]-4-(dimethylamino)-*N*-[4-(2-phenylhydrazine-1-carbonyl)benzyl]benzamide (**12**)

Prepared according to **GP III**, starting from carboxylic acid **3** (0.111 g, 0.250 mmol, 1.00 eq.), phenylhydrazine (29.0 µL, 32.0 mg, 0.300 mmol, 1.20 eq.), HATU (0.114 g, 0.300 mmol, 1.20 eq.), and DIPEA (0.347 mL, 0.256 g, 2.00 mmol, 4.00 eq.). Compound **12** (67.8 mg, 0.126 mmol, 50%) was isolated as a white lyophilizate. **^{1}H-NMR** (300 MHz, DMSO-d_6) δ = 10.36 (s, 1H), 8.47 (t, *J* = 6.9 Hz, 1H), 7.92 (d, *J* = 8.0 Hz, 2H), 7.43 (d, *J* = 8.1 Hz, 2H), 7.39 – 7.29 (m, 4H), 7.29 – 7.21 (m, 3H), 7.20 – 7.10 (m, 2H), 6.84 – 6.76 (m, 2H), 6.75 – 6.71 (m, 1H), 6.71 – 6.65 (m, 2H), 4.71 (s, 2H), 4.32 (d, *J* = 5.8 Hz, 2H), 3.93 (s, 2H), 2.94 (s, 6H); **^{13}C-NMR** (75 MHz, DMSO-d_6) δ = 208.1, 171.7, 168.1, 166.0, 151.1, 149.5, 141.3, 139.2, 131.9, 128.7, 128.6, 128.3, 127.6, 127.3,

126.8, 118.6, 112.3, 111.2, 42.1; **HRMS-ESI (*m/z*):** $[M+H]^+$ calcd for $C_{32}H_{33}N_5O_3$: 536.2662, found: 536.2659; **HPLC**: t_R = 12.84 min (99.8% purity).

N-[2-(Benzylamino)-2-oxoethyl]-4-(dimethylamino)-*N*-{4-[2-(3-phenylpropyl)hydrazine-1-carbonyl]benzyl}benzamide trifluroacetate (**13**)

Prepared according to **GP I**, starting from hydrazide **4** (0.100 g, 0.217 mmol, 1.00 eq.), 3-phenylpropanal (34.5 µL, 34.9 mg, 0.260 mmol, 1.20 eq.), acetic acid (13.1 µL, 13.1 mg, 0.217 mmol, 1.00 eq.), and $NaCNBH_3$ (21.5 mg, 0.342 mmol, 2.00 eq.). Compound **13** (34.9 mg, 50.4 µmol, 23%) was isolated as a white lyophilizate. **^{1}H-NMR** (600 MHz, DMSO-d_6) δ = 11.00 (s, 1H), 8.45 (s, 1H), 7.85 (d, *J* = 7.9 Hz, 2H), 7.44 (d, *J* = 7.9 Hz, 2H), 7.35 – 7.30 (m, 4H), 7.28 (d, *J* = 7.5 Hz, 2H), 7.23 (dt, *J* = 8.1, 4.3 Hz, 6H), 7.21 – 7.17 (m, 1H), 6.73 – 6.58 (m, 2H), 4.70 (s, 2H), 4.31 (d, *J* = 5.9 Hz, 2H), 3.92 (s, 2H), 3.05 (t, *J* = 7.5 Hz, 2H), 2.93 (s, 6H), 2.68 (t, *J* = 7.7 Hz, 2H), 1.88 (p, *J* = 7.6 Hz, 2H); **^{13}C-NMR** (151 MHz, DMSO-d_6) δ = 171.7, 168.1, 165.3, 158.2 (q, *J* = 34.4 Hz), 151.2, 142.2, 141.2, 139.2, 130.2, 128.6, 128.3, 128.3, 128.3, 127.7, 127.2, 126.8, 125.9, 116.2 (d, *J* = 294.6 Hz), 49.9, 40.1, 32.1, 27.3; **HRMS-ESI (*m/z*):** $[M+H]^+$ calcd for $C_{35}H_{39}N_5O_3$: 578.3131, found: 578.3126; **HPLC**: t_R = 11.44 min (98.2% purity).

(*E*)-*N*-[2-(Benzylamino)-2-oxoethyl]-*N*-[4-(2-cinnamylhydrazine-1-carbonyl)benzyl]-4-(dimethylamino)benzamide (**14**)

Prepared according to **GP I**, starting from hydrazide **4** (78.8 mg, 0.171 mmol, 1.00 eq.), cinnamaldehyde (21.4 µL, 22.5 mg, 0.171 mmol, 1.00 eq.), acetic acid (20.6 µL, 20.6 mg, 0.342 mmol, 1.00 eq.), and $NaCNBH_3$ (21.5 mg, 0.342 mmol, 2.00 eq.). Compound **14** (28.3 mg, 41.0 µmol, 24%) was isolated as a white lyophilizate. **^{1}H-NMR** (400 MHz, MeOH-d_4) δ = 7.83 (d, *J* = 8.2 Hz, 2H), 7.49 – 7.37 (m, 6H), 7.37 – 7.19 (m, 8H), 6.81 (d, *J* = 15.8 Hz, 1H), 6.74 (d, *J* = 8.8 Hz, 2H), 6.31 (dt, *J* = 15.2, 7.2 Hz, 1H), 4.81 (s, 2H), 4.37 (s, 2H), 4.03 (s, 2H), 3.99 (d, *J* = 7.2 Hz, 2H), 2.99 (s, 6H); **^{13}C-NMR** (101 MHz, MeOH-d_4) δ = 175.5, 170.6, 167.9, 152.8, 143.6, 139.8, 139.6, 137.2, 131.4, 130.1, 129.6, 129.6, 129.1, 128.7, 128.3, 127.8, 123.8, 120.1, 113.1, 54.3, 44.1, 40.8; **HRMS-ESI (*m/z*):** $[M+Na]^+$ calcd for $C_{35}H_{37}N_5O_3$: 598.2794, found: 598.2794; **HPLC**: t_R = 18.72 min (97.3% purity).

3.4.2 HDAC enzyme inhibition assay

3.4.2.1 Preincubationassay for HDAC1-3 and HDAC6

In vitro inhibitory activity against HDAC1-3 and HDAC6 was determined as previously published.[218] In short, serial dilutions of compounds and controls were prepared in assay buffer (50 mM Tris−HCl, pH 8.0, 137 mM NaCl, 2.7 mM KCl, 1.0 mM $MgCl_2$*6 H_2O, 0.1 mg/mL BSA). 5.0 µL of these serial dilutions were transferred into OptiPlate-96 black micro-plates (PerkinElmer). Then, 25 µL assay buffer and 10 µL enzyme solution (human recombinant HDAC1 (BPS

Bioscience, Catalog# 50051); HDAC2 (BPS Bioscience, Catalog# 50052); HDAC3/NcoR2 (BPS Bioscience, Catalog# 50003); HDAC6 (BPS Bioscience, Catalog# 50006) were added. Enzyme and inhibitor were preincubated at 25 °C for 60 minutes (HDAC1-3) or 15 minutes (HDAC6). Afterwards, the fluorogenic substrate ZMAL (Z-Lys(Ac)-AMC[306]; 10 µL; 75 µM in assay buffer) was added. The total assay volume (50 µL, max. 1% DMSO) was incubated at 37 °C for 90 min. Subsequently, 50 µL trypsin solution (0.4 mg/mL trypsin in buffer: 50 mM Tris−HCl, pH 8.0, 100 mM NaCl) was added, followed by additional 30 minutes of incubation at 37 °C. Fluorescence (excitation: 355 nm, emission: 460 nm) was measured using either an Ascent Fluoroskan microplate reader (Thermo Scientific) or a FLUOstar OPTIMA microplate reader (BMG LABTECH). IC_{50}-values were determined by generating normalized dose-response curves using the build-in *"log(inhibitor) vs. response (three parameters)"* equation provided by GraphPad Prism 9.0 for MacOS (GraphPad Software, San Diego, USA). All compounds were tested in duplicates, reported mean IC_{50} values, including standard deviation, are calculated from at least two independent experiments.

3.4.2.2 Enzyme assay for HDAC4 and 8

Both recombinant enzymes were purchased from Reaction Biology Corp. (Malvern, USA). The HDAC activity assay of HDAC4 (catalog no. KDA-21-279) and HDAC8 (catalog no. KDA-21−481) was performed in 96-well plates (Corning, Germany). Briefly, 20 ng of HDAC8 and 2 ng of HDAC4 per reaction were used. Recombinant enzymes were diluted in the assay buffer (50 mM Tris−HCl, pH 8.0, 137 mM NaCl, 2.7 mM KCl, 1 mM MgCl2, 1 mg/mL BSA). This diluted solution (80 µl) was incubated with 10 µl of inhibitors with different concentrations in the assay buffer. After a 5 min incubation step, the reaction was started with 10 µl of 100 µM (HDAC4) or 60 µM (HDAC8) Boc-Lys(TFA)-AMC (Bachem, Germany). The reaction was stopped after 90 min by adding 100 µl of stop solution 16 mg/ mL trypsin, 4 µM panobinostat in 50 mM Tris−HCl, pH 8.0, 100 mM NaCl. Fifteen minutes after the addition of the stop solution, the fluorescence intensity was measured at an excitation wavelength of 355 nm and emission wavelength of 460 nm in a NOVOstar microplate reader (BMG LabTech, Germany).

3.4.3 Docking of compounds 5 and 13 in human HDAC3 with *RosettaLigand*

The crystal structure of human HDAC3 was obtained from the Protein Data Bank (PDB 4A69,[84] www.rcsb.org). Chain C, corresponding to the nuclear receptor corepressor 2, inositol-4-phosphate, and glycerol were deleted. Except for the Zn^{2+}-ion, all heteroatom records were removed. The structure was optimized to the closest local energy minimum using RosettaRelax with coordinate constraint on the backbone and metal ion restraints.[307] Ligand input files for **5** and **13** were created with ChemDraw. An initial 3D conformer with hydrogen atoms was constructed in Chem3D and energetically minimized using the MM2 force field, followed by the production of an ensemble of

1000 low energy conformers with BCL:ConformerGenerator.[308] One conformer was placed in the binding pocket of HDAC3. A constraint file was constructed using the known distance of the zinc binding of *ortho*-aminoanilids.[221] Ligand docking was performed with RosettaLigand (version 3.12) for 5000 models. All models with a negative interface score were subsequently submitted to another round of focused refinement using RosettaLigand. The best scoring models were identified by their predicted binding energy, excluding interactions of the cap group.[309–311]

3.4.4 Cell Culture

MV4-11 cells (DSMZ, Hannover, Germany, ACC 102) were cultured in RPMI (Life Technologies, Darmstadt, Germany, #21875091), containing 10% fetal bovine serum (Sigma Aldrich, St. Louis, MO, USA, #F7524) and 50 U/mL penicillin and 50 µg/mL streptomycin (PAN Biotech GmbH, Aidenbach, Germany, #P06-07100), and were incubated at 37 °C under humidified air with 5% CO_2.

The human ovarian carcinoma cell line A2780 was obtained from European Collection of Cell Cultures (ECACC, UK). The human tongue cell line Cal27 was obtained from the German Collection of Microorganisms and Cell Cultures (DSMZ, Germany). The corresponding cisplatin resistant CisR cell lines Cal27CisR and A2780CisR was generated by exposing the cell lines to weekly cycles of cisplatin in an IC_{50} concentration according to Gosepath et al.[294] and Eckstein et al.[294,312] The human promyeloblast leukemia cell line HL-60 were kindly provided by Helmut Hanenberg, Department of Otorhinolaryngology and Head/ Neck Surgery, Heinrich Heine University, Germany). All cell lines were grown at 37 °C under humidified air supplemented with 5% CO2 in RPMI 1640 (A2780 and HL-60) or DMEM (Cal27) containing 10% heat inactivated fetal calf serum, 120 IU/mL penicillin, and 120 µg/mL streptomycin. The cells were grown to 80% confluency before being used in further assays.

3.4.5 HDAC Whole-Cell Assay

The cellular HDAC assay is based on previously published procedures.[313–315] Briefly, human cancer cell lines A2780, A2780CisR, Cal27 and Cal27CisR were seeded in 96-well tissue culture plates (Corning, Germany) at a density of 25000 c/w, 25000 c/w, 15000 c/w and 15000 c/w in a total volume of 90 µl of culture medium. After 24 hours, cells were incubated for 18 hours with increasing concentrations of test compounds. The reaction was started by adding 10 µl of 3 mM Boc-Lys(ε-Ac)-AMC or 1 mM Boc-Lys(TFA)-AMC (Bachem, Germany) to reach a final concentration of 0.3 or 0.1 mM.[316] Cells were incubated with Boc-Lys(ε-Ac)-AMC or Boc-Lys(TFA)-AMC for 3 h under cell culture conditions. Then, 100 µl/well stop solution (25 mM Tris−HCl (pH 8), 137 mM NaCl, 2.7 mM KCl, 1 mM $MgCl_2$, 1% NP40, 2.0 mg/mL trypsin, 10 µM vorinostat) was added and the reaction was developed for 3 hours under cell culture conditions.

Fluorescence intensity was measured at an excitation wavelength of 320 nm and emission wavelenght of 520 nm in a NOVOstar microplate reader (BMG LabTech, Germany).

3.4.6 Cell viability assay

3.4.6.1 CellTiter-Glo

4000 MV4-11 cells/well were seeded in white 384-well plates (Greiner Bio-One, Kremsmuenster, Austria, #781080). The test compounds were added in increasing concentrations. For this the dilution series were prepared in 200-fold concentration in DMSO and further diluted 10-fold in medium. The final DMSO concentration was 0.5%. The toxicity of compounds was determined after 7 h using the CellTiter-Glo® 2.0 Cell Viability Assay (Promega, Madison, WI, USA, #G9242) according to the manufacturers protocol. Subsequently, the luminescence was measured using a Tecan Spark (Tecan Group AG, Maennedorf, Swiss) and the data were analysed with the four-parameter logistic equation (GraphPad Prism 8.0, San Diego, CA, USA).

3.4.6.2 MTT Cell Viability Assay

The cytotoxic activity of the HDACi and cisplatin was evaluated by an improved MTT assay as previously described.[295,315,317] A2780, A2780CisR, Cal27, Cal27CisR and HL- 60 cell lines were seeded at a density of 8000, 12000, 2500, 2500 and 25000 cells/well (c/w) in 96 well plates (Corning, Germany). After 24 h, cells were exposed to increased concentrations of the test compounds. Incubation was ended after 72 h, and cell survival was determined by addition of MTT (Serva, Germany) solution (5 mg/mL in phosphate buffered saline). The formazan precipitate was dissolved in DMSO (VWR, Germany) or for the HL-60 cells the formed formazan was dissolved by pipetting up and down after addition of 150 µl isopropanol/ concentrated hydrochloric acid (50 ml/ 165 µl). Absorbance was measured at 540 nm and 690 nm or for the HL-60 cell line 595 nm and 690 nm in a ThermoFisher Multiskan FC Microplate Photometer (Thermo Scientific, Germany). To investigate the effect of compound **5**, **6**, **8**, **VK1**, **entinostat** and **vorinostat** on cisplatin-induced cytotoxicity, compounds were added 48 h before cisplatin administration to the cell lines in following density A2780 4000 c/w, A2780CisR 6000 c/w, Cal27 2000 c/w and Cal27CisR 2000 c/w. After 72 h, the cytotoxic effect was determined by the MTT assay as described above, and shift factors were calculated by dividing the IC_{50} value of cisplatin alone by the IC_{50} value of the drug combinations.

Combination Index Analysis. The combined effect of cisplatin and compound **5**, **6** and **entinosta**t was analyzed using the MTT assay. Cell viability was determined from each well relative to the average absorbance of control wells. The combination indexes (CIs) were calculated with the CompuSyn 1.0 software (ComboSyn, Inc., USA) based on the Chou− Talalay method.[318]

3.4.7 Measurement of Apoptosis Marker and DNA Damage

3.4.7.1 Measurement of Apoptotic Nuclei

Cal27 and Cal27CisR cells were seeded at a density of 40000 cells/well in 24-well plates (Sarstedt, Germany). Cells were treated with compound **5**, **6** or **entinostat** and cisplatin alone or in combination for the indicated time points. The supernatant was removed after a centrifugation step, and the cells were lysed in 500 µL of hypotonic lysis buffer (0.1% sodium citrate, 0.1% Triton X-100, 100 µg/mL PI (Sigma, Germany)) at 4 °C in the dark overnight. The percentage of apoptotic nuclei with DNA content in sub-G1 was analyzed by flow cytometry using a CyFlow instrument (Partec, Germany).

3.4.7.2 Caspase 3/7 Activation Assay

Compound-induced activation of caspases 3 and 7 was analyzed using the CellEvent Caspase-3/7 green detection reagent (Thermo Scientific, Germany) according to the manufacturer's instructions. Briefly, A2780, A2780CisR, Cal27 and Cal27CisR cells were seeded in 96-well-plates (Corning, Germany) at a density of 4000 c/w, 6000 c/w,1200c/w and 1200 c/w. Cells were treated with compound **5**, **6** or **entinostat** 48 hours prior to the addition of cisplatin and another incubation period of 24 hours. Then, the medium was removed and 50 µL of the CellEvent Caspase 3/7 green detection reagent (2 µM in PBS supplemented with 1% heatinactivated FBS) was added. Cells were incubated for 30 min at 37 °C in a humidified incubator before imaging by using the Thermo Fisher ArrayScan XTI high content screening (HCS) system (Thermo Fisher Scientific). Hoechst 33342 was used for nuclear staining.

3.4.7.3 γH2AX Assay

The γH2AX DNA damage assay is based on a previously published procedure with minor modifications.[319] Briefly, Cal27 and Cal27CisR cells were seeded in 96-well tissue culture plates (Corning, Germany) at a density of 1500 c/w. The cells were treated with the indicated concentrations of HDACi for 48 hours and then co-incubated with cisplatin and HDACi for 24 hours. Cells were fixed with 3 % formaldehyde solution followed by permeabilization with 0.3 % Triton X-100 in PBS and blocking with blocking buffer (5 % BSA, in PBS-T). Cells were incubated with primary antibody (Cat. No. 05-636, Merk Millipore, Germany) overnight at 4°C and secondary fluorophore-labeled antibody (Cat. No. A-21422, Invitrogen Thermo Fisher Scientific, Germany) for 1 hour in the dark. Cell nuclei were counter stained with Hoechst 33342. Analysis was performed with Thermo Fischer Array Scan XTI (Thermo Fisher Scientific, Germany).

3.4.8 Immunoblot

Cells were treated with the indicated HDACi and cisplatin for 24 hours with only HDACi, 72 hours with only HDACi, HDACi for 48 hours and then co-incubated with cisplatin and HDACi for 24 hours or the vehicle for 24 hours/ 72 hours. Cells were dissolved with a RIPA buffer (50 mM Tris−HCl pH 8.0, 1% Triton X-100, 0.5% sodium deoxycholate, 0.1% SDS, 150 mM sodium chloride, 2 mM EDTA, supplemented with protease inhibitors (cOmplete Mini tablets, Roche Diagnostics, Germany)) and clarified by centrifugation. Equal amounts of total protein (40 µg) were resolved by SDS-PAGE and transferred to poly(vinylidene fluoride) membranes (Merck Millipore). Blots were incubated with antibodies against acetylated α-tubulin, α-tubulin, β-Actin, GAPDH (Santa Cruz Biotechnology, Germany), histone H3, BIM, acetyl histone H3 (Lys18) (Novus Biologicals, USA) and p21 (Cell Signaling Technology, USA). Immunoreactive proteins were visualized using a luminol reagent (Santa Cruz Biotechnology, Germany) with an Intas Imager (Intas, Germany).

Data Analysis. Concentration−effect curves were constructed with Prism 7.0 (GraphPad, USA) by fitting the pooled data of at least two experiments performed in at least duplicates to the four parameter logistic equation. Statistical analysis was performed using the t test.

3.4.9 Determination of physiochemical properties

$LogD_{7.4}$. $LogD_{7.4}$ was determined using the OECD slow-stirring method followed by substance quantification via HPLC/UV as previously described.[218,320,321] In short, a glass vial (20 x 40 mm) was equipped with a magnetic stirring bar (10 mm; PTFE covered, cylindrical), a sample of the respective test substance (0.1 – 1.0 mg), 2.0 mL 1-octanol-saturated PBS buffer (pH = 7.4; 137 mM NaCl, 2.7 mM KCl, 10 mM Na_2HPO_4, 1.8 mM KH_2PO_4) and 2.0 mL PBS-saturated 1-octanol. The vial was firmly sealed, placed on a magnetic stirrer and the biphasic system was left stirring (1000 rpm) at 25 °C for 48 h. 4 h into the experiment all vials were checked for residual suspended solid test substance. Vials with residual solid particles were excluded from the experiment. After 48 h the stirring was stopped, and the phases were separated. The concentration of the test substance in the respective 1-octanol and PBS buffer phase was quantified by comparison with a six-point calibration curve using HPLC/UV detection. As detection wavelength a local maximum between 230 nm and 350 nm was selected individually for each test substance. $LogD_{7.4}$ values were determined by performing three slow-stirring experiments (three independent experimental units). HPLC quantification of each 1-octanol or PBS buffer phase was carried out in duplicates.

Solubility. The solubility of test substances in PBS buffer (pH = 7.4; 137 mM NaCl, 2.7 mM KCl, 10 mM Na_2HPO_4, 1.8 mM KH_2PO_4) was determined using the OECD flask method followed by substance quantification via HPLC/UV as previously described.[218,322] In short, in a glass vial (20x40

mm) was equipped with a magnetic stirring bar (10 mm; PTFE covered, cylindrical), a pulverized sample of the respective test substance (1.5 – 5.0 mg) and 3.0 mL PBS buffer was added. The vial was firmly sealed, placed on a magnetic stirrer and the system was left stirring (1000 rpm) at 25 °C for 72 h. All vials were checked periodically for residual suspended solid test substance. Vials without residual solid particles were excluded from the experiment. After 72 h the stirring was stopped, and the remaining particles were filtered off using a syringe filter (PTFE membrane, pore size: 0.45 µm). The concentration of the test substance in the PBS buffer phase was quantified by comparison with a six-point calibration curve using HPLC/UV detection. The detection wavelength was selected individually for each test substance (local maximum between 230 nm and 350 nm). Solubility was determined by performing two independent experiments. HPLC quantification of each PBS buffer phase was carried out in duplicate.

Chapter 4

Development of class I HDAC selective PROTACs

4.1 Introduction

Targeting HDACs with small molecule inhibitors have long been a valuable approach for targeted cancer therapy. Currently, four HDACi have been approved by the FDA for different non-solid cancers, each demonstrating efficacy but accompanied by multiple, severe side effects. The antiproliferative properties of non-selective HDACi have been linked to the inhibition of the class I HDAC enzymes HDAC1, 2, and 3. To harness the therapeutic potential of HDAC inhibition more effectively, while minimizing off-target effects, selective targeting of these isoforms presents a promising avenue for designing more precise and efficient drugs.[38] Substituted hydrazides represent a rather new class of HDACi that exhibit a strong selectivity for class I HDAC enzymes with a superior bioavailability compared to their hydroxamic acid counterparts.[207] Recognizing the limitations of the classical small molecule inhibitor approaches, the utilization of PROTACs introduced a new way in drug discovery, offering a means to overcome these challenges (see Chapter 1.5).[252] Typically, PROTACs comprise a ligand for the POI and a ligand for an E3 ligase, connected by a linker. By bringing the E3 ligase and the POI into close proximity, they redirect the UPS to target the POI, thereby facilitating the transfer of ubiquitin to the specific POI.[251] PROTACs targeting zinc-dependent HDACs have been first published in 2018.[265] Since then, various PROTACs for the degradation of different HDAC isoforms have been developed.[269] The design of isoform-selective degraders has been accomplished by different approaches. Interestingly, the E3 ligase recruiting ligand influences the selectivity. VHL-based PROTACs repeatedly exhibit higher degradation activity against the class I isoform than CRBN-recruiting degrader (see Chapter 1.5.2 for more detail).[266] Furthermore, the ZBG of HDACi highly influences the isoform selectivity. While there are several cases where a non-selective HDACi incorporated into a PROTAC has resulted in isoform-selective degradation, utilizing selective HDAC inhibitor scaffolds as the POI ligand provides the opportunity for more precise targeted degradation.[266] As previously discussed in chapter 3, the **Hydrazide 5**[r] displays a profound inhibitory activity against class I isoforms, with a preference for HDAC3. In addition, **Hydrazide 5** displayed antiproliferative activity against both cisplatin-sensitive and resistant Cal27 cell lines. In this project, we developed a set of VHL-based PROTACs utilizing the established HDACi scaffold of **Hydrazide 5** as the POI ligand (Figure 24).

[r] **Hydrazide 5** is referred to compound **5** of chapter 3.

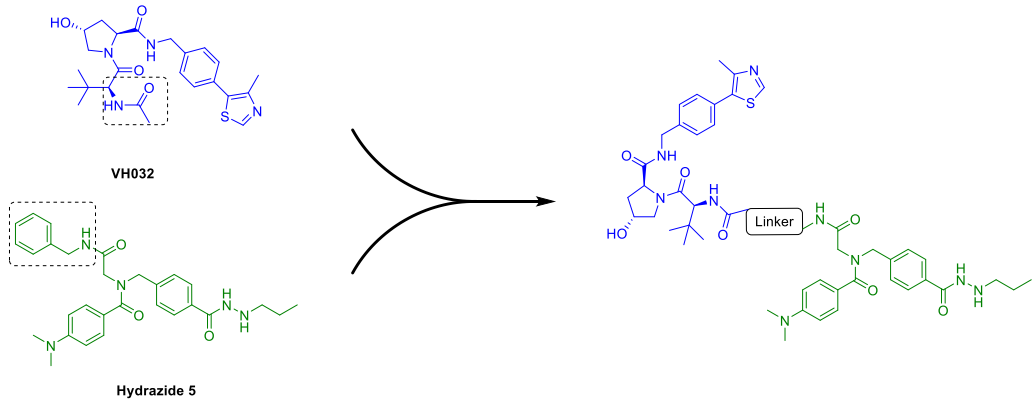


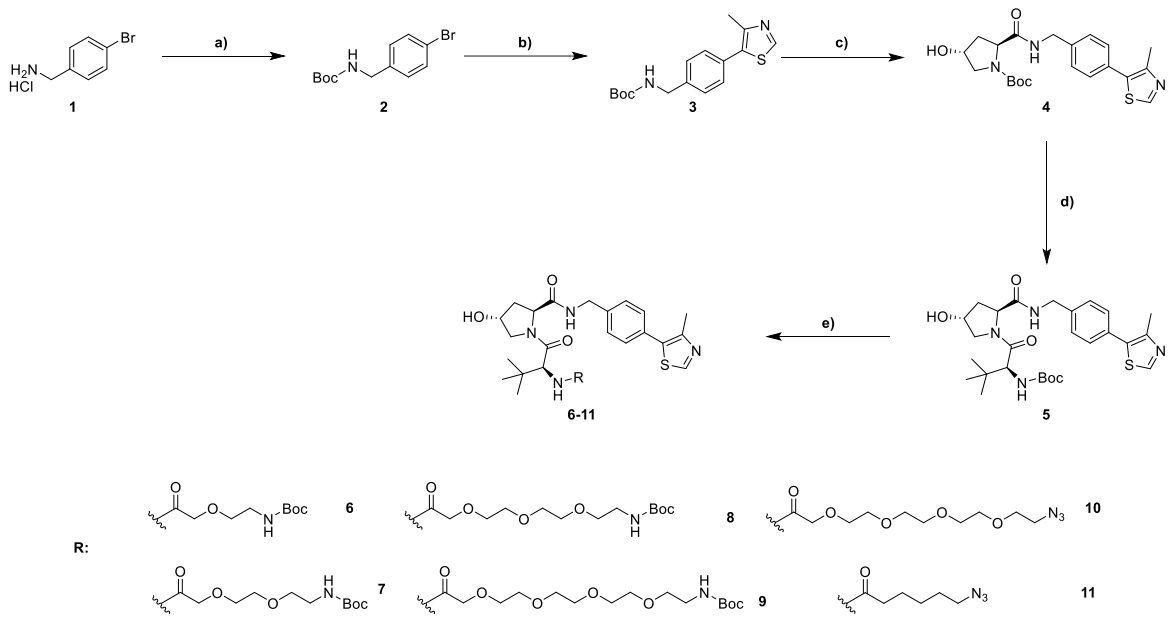
Figure 24. General design of hydrazide-based PROTACs.

To this end, different linkers were attached to the VHL ligand **VH032**, to explore a favorable conformation for the formation of the tertiary complex. The solvent exposed benzyl amide moiety of **Hydrazide 5** served as the attachment point for the linker on the POI ligand.

4.2 Results and Discussion

4.2.1 PROTAC Synthesis

The synthesis of VHL ligands, as described in literature,[323] often contain steps with low yields or troublesome purification procedures. To address these challenges, the synthesis was optimized to provide a fast and straightforward access to the desired Boc-protected ligand **5** (Scheme 2).

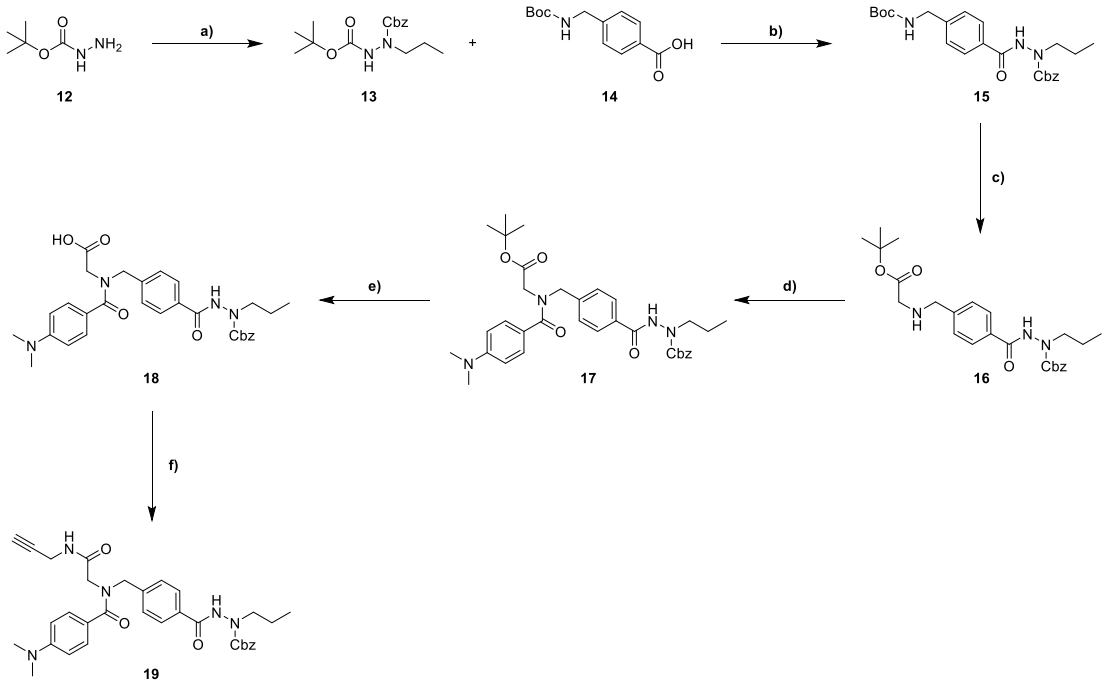


Scheme 2. Synthesis of the VHL ligand and linker attachment. **a)** Boc_2O (1.10 eq.), NEt_3 (2.10 eq.), CH_2Cl_2, rt, 19 h, 96%; **b)** 4-methylthiazole (2.00 eq.), $Pd(OPiv)_2$ (0.10 eq.), Cs_2CO_3 (1.00 eq.), 90 °C, 19 h, 93%; **c)** 4 M HCl in 1,4-dioxane (10.0 eq.), CH_2Cl_2, rt, 2 h; then Boc-Hyp-OH (1.20 eq.), TBTU (1.20 eq.), DIPEA (3.00 eq.), DMF, 84 °C, 19 h, 96%; **d)** 4 M HCl in 1,4-dioxane (10.0 eq.), CH_2Cl_2, rt, 2 h; then Boc-Tle-OH (1.30 eq.), EDC*HCl (1.30 eq.), HOBt*H_2O (1.30 eq.), DIPEA (3.00 eq.), rt, 19 h, 95%; **e)** 4 M HCl in 1,4-dioxane (10.0 eq.), CH_2Cl_2, rt, 2 h; then carboxylic acid (2.00 eq.), DIPEA (3.00 eq.), HATU (2.00 eq.), HOBt*H_2O (2.00 eq.), rt, 19 h, 49 - 92%.

The process began with the use of commercially available 4-bromobenzylamine hydrochloride **1**. In the first step, compound **1** was protected with *tert*-butoxycarbonyl (Boc) under mild conditions, resulting in excellent yields of the desired product. Next, compound **2** underwent a Heck coupling reaction with 4-methylthiazole. Strict temperature control and the use of the catalyst palladium(II) pivalate and Cs_2CO_3 as the base enabled an efficient access to compound **3**. Following this, the Boc group was removed and the benzylamine intermediate was submitted to an amide coupling with Boc-Hyp-OH, mediated by TBTU at elevated temperature. Compound **4** was isolated in near quantitative yield. In the final step of the synthesis, another EDC and HOBT mediated amide coupling was performed. As a result, the VHL ligand **5** was isolated in 95% yield and an overall yield of 81%. Next, six different type of linkers were attached by an amide coupling of the

respective carboxylic acid to the previously prepared E3 ligase ligand **5**. To this end, compound **5** was first deprotected using 4 M HCl in 1,4-dioxane. After activation of the respective carboxylic acid with HATU and HOBt*H_2O, the amide couplings proceeded over 19 h at room temperature to give the target compounds **6**-**11** in up to 92% yield.

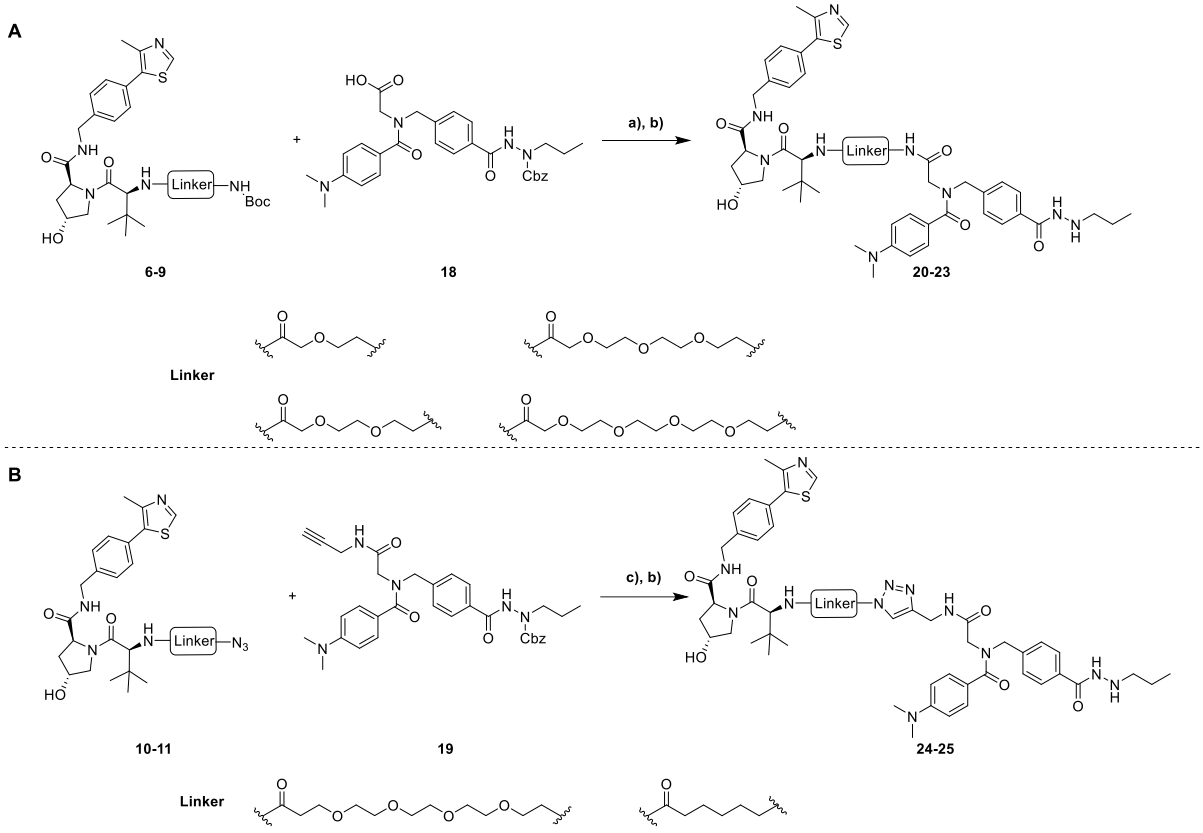
The POI ligand was synthesized based on the submonomer pathway previously published by Mackwitz et *al*. (Scheme 3).[324] Initially, *tert*-butyl carbazate **12** underwent reductive amination with propionic aldehyde. The resulting monoalkylated product was used without further purification to Cbz protect the second nitrogen atom yielding compound **13**. Subsequently, Boc deprotection followed by amide coupling with the benzoic acid **14** afforded compound **15** in a high yield of 90%. After another acidolytic Boc deprotection, the benzyl amine intermediate was reacted with *tert*-butyl bromoacetate to produce compound **16**, which was then acylated with 4-(dimethylamino)benzoyl chloride to form **17** in 74% yield. The *tert*-butyl group was removed under acidic conditions to obtain the corresponding carboxylic acid **18** in quantitative yield. Furthermore, another amide coupling between compound **18** and propargyl amine, using EDC*HCl and HOBT*H_2O as mediators, resulted in the formation of compound **19**.



Scheme 3. Synthesis of the precursor for the POI ligand. **a)** Propionic aldehyde (1.20 eq.), $MgSO_4$, THF, 50 °C, 2 h; then $NaBH_4$ (2.00 eq.), rt, 2 h; then Cbz-Cl (1.10 eq.), pyridine (1.20 eq.), 0 °C, rt, 19 h, 44%; **b**) 4 M HCl in 1,4-dioxane (10.0 eq.), CH_2Cl_2, rt, 2 h; then compound **14** (1.50 eq.), HATU (1.50 eq.), DIPEA (4.00 eq.), DMF, rt, 19 h, 90%; **c**) 4 M HCl in 1,4-dioxane (10.0 eq.), CH_2Cl_2, rt, 2 h; *tert*-butylbromoacetat (1.10 eq.), DIPEA (3.00 eq.), CH_2Cl_2, rt, 3 d, 58%; **d**) 4-(dimethylamino)benzoyl chloride (1.10 eq.), NEt_3 (1.25 eq.), CH_2Cl_2, rt, 2 h, 74%;

e) TFA/CH_2Cl_2 1/1, *v*/*v*, 2h, quant.; **f**) propargyl amine (1.10 eq.), EDC*HCl (1.10 eq.), HOBt*H_2O (1.10 eq.), CH_2Cl_2, rt, 19 h, 60%.

Next, the POI precursors **18** and **19** were either coupled with compound **6**-**9** through anamide coupling after Boc deprotection, or with compound **10** and **11** via a 1,3-dipolar Cu(I)-catalyzed azide alkyne cycloaddition (CuAAC). Finally, the Cbz protecting group was removed in a nucleophilic fashion using 2-mercaptoethanol and K_3PO_4 to yield the respective PROTACs **20**-**25** (Scheme 4). All PROTACs were purified to > 95% purity and structurally characterized (see chapter 4.4.2 and chapter 8.3 for further information).

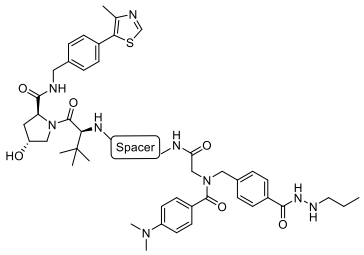


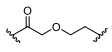
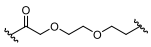
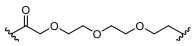
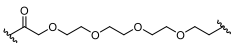
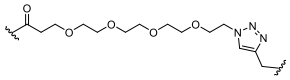
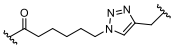
Scheme 4. Final steps of the PROTAC synthesis via amide coupling (**A**) or CuAAC (**B**) and subsequent Cbz removal. **a**) 4 M HCl in 1,4-dioxane (10.0 eq.), CH_2Cl_2, rt, 2 h; then EDC*HCl (1.10 eq.), HATU (1.10 eq.) HOBt*H_2O (1.10 eq.), DIPEA (6.00 eq.), 30% - 47%; **b**) 2-mercaptoethanol (2.00 eq.), K_3PO_4 (4.00 eq.), DMF, 75 °C, 3 d, 7% - 27%; **c**) TBTA (0.20 eq.), 0.1 M $CuSO_4$ (0.20 eq.), 0.1 M ascorbic acid (0.20 eq.), H_2O/*tert*-butanol/DMF (1:1:0.3), rt, 1 h, 38 - 46%.

4.2.2 Biological Evaluation

All synthesized PROTACs were screened in biochemical assays against human HDAC1, 2, and 3 (Table 9). Unexpectedly, all compounds failed to show inhibition at HDAC1 and 2, despite the confirmed activity of the parent compound **Hydrazide 5**. However, the compounds exhibited micromolar inhibition of HDAC3 with compound **21** displaying the lowest value (HDAC3: IC_{50} = 5.78 µM).

Table 9. *In vitro* HDAC inhibition of PROTACs **20**-**25**.[s]



Code	Spacer	IC_{50} [µM]		
		HDAC1 [a,b]	HDAC2 [a,b]	HDAC3 [a,b]
20		> 10 [d]	> 10 [d]	8.97 ± 0.709
21		> 3.33 [d]	> 10 [d]	5.79 ± 0.867
22		> 10 [d]	> 10 [d]	14.4 ± 1.93
23		> 10 [d]	> 10 [d]	13.1 ± 0.446
24		> 10 [d]	> 10 [d]	8.61 ± 0.557
25		> 10 [d]	> 10 [d]	10.4 ± 1.22
	Hydrazide 5 [e]	0.027 ± 0.001	0.141 ± 0.005	0.004 ± 0.00001
	Vorinostat	0.100 ± 0.009	0.185 ± 0.001	0.091 ± 0.009

[a] preincubation of enzyme and inhibitor: 1 h at 20 °C; [b] mean ± standard deviation (SD) of at least two independent experiments; [c] preincubation of enzyme and inhibitor: 15 min at 20 °C; [d] < 25% inhibition at the stated concentration; [e] data taken from chapter 3.2.2.

We continued to investigate the effects of the compounds **20**-**25** on HDAC1-4 and 6 levels by immunoblot analysis in the well-established breast cancer cell line MCF-7. The PROTACs were tested at 5 µM after 24 h of incubation time using the established HDAC class I degrader **JPS016** as a control (Figure 25).[273]

[s] HDAC enzyme assays were performed by Dr. Linda Schäker-Hübner (Rheinische Friedrich-Wilhelms-Universität Bonn, Hansen Group).

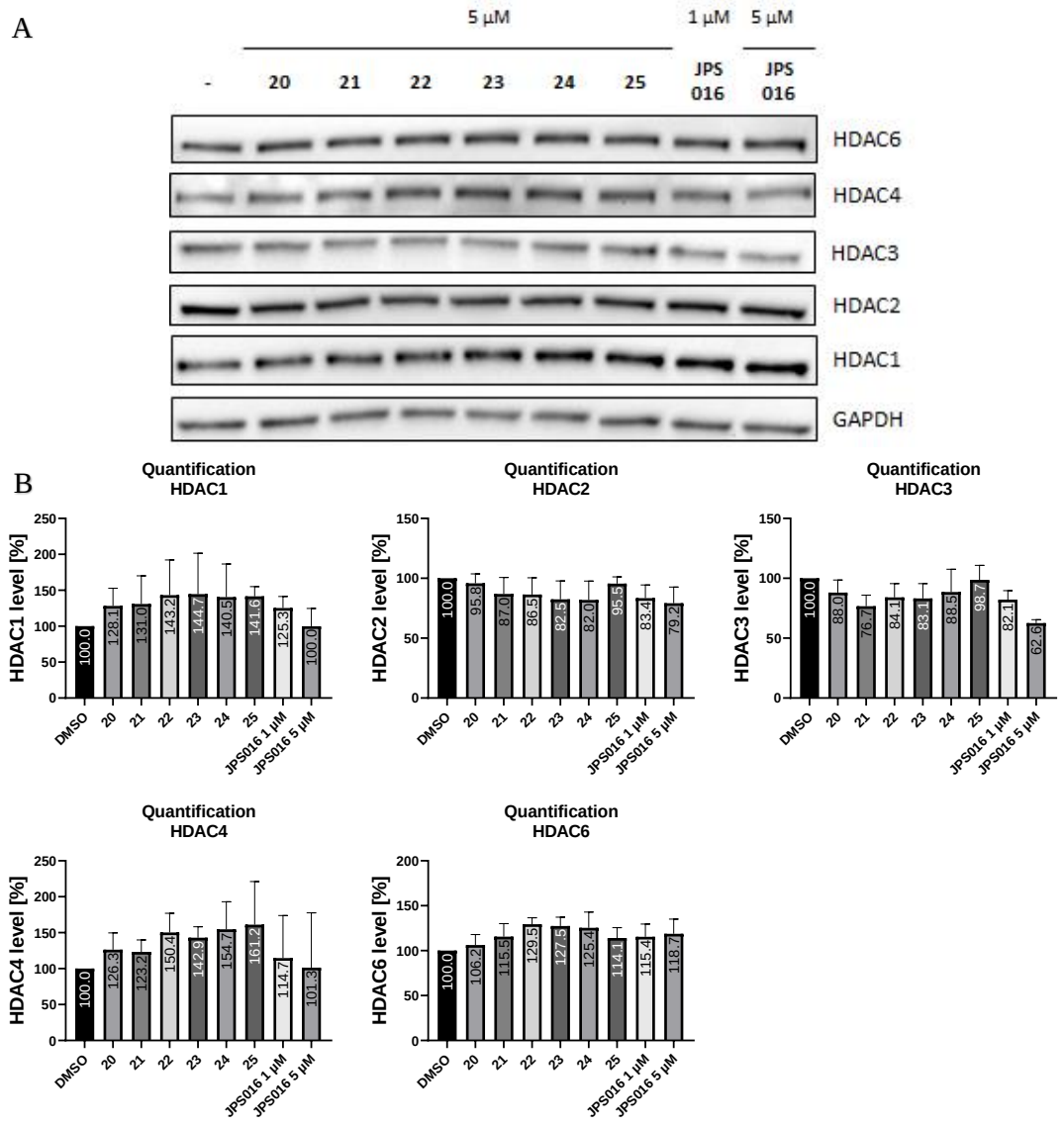


Figure 25. Representative immunoblot analysis (**A**) and quantification (**B**) of HDAC1-4 and 6 levels. MCF-7 cells were incubated for 24 h with the indicated compounds and concentrations. GAPDH was used as the loading control.[t]

The PROTACs only showed limited degradation of HDAC2 and 3. Overall, compound **21** emerged as the most potent degrader, displaying a D_{max} of 13% and 23% against HDAC2 and 3, respectively. Additionally, we observed an unprecedented increase in enzyme levels of HDAC1, 4, and 6 with our compounds as well as the control degrader.

[t] Immunoblot analysis were performed by Felix Feller (Rheinische Friedrich-Wilhelms-Universität Bonn, Hansen Group).

4.3 Conclusion

In summary, a small set of VHL-recruiting HDAC-PROTACs was synthesized and assessed concerning their potential to degrade selected HDAC isoforms. The synthesis of the VHL-recruiting ligand was optimized to enhance purification efficiency and yields, resulting in the isolation of precursor **5** with an overall yield of 81% (14% reported in literature[325]). The well-established peptoid-based class I HDACi, **Hydrazide 5** (chapter 3), was chosen as the POI ligand. Six HDAC PROTACs featuring variations in their spacer structures were synthesized and subjected to biological evaluation. While no inhibition of HDAC1 and 2 was observed, all compounds inhibited HDAC3 with single or double-digit micromolar IC_{50} values.

The selection of attachment points on both the POI-ligand and VHL-ligand sites significantly influences the formation of the tertiary complex between the target protein and the E3-ligase complex. This factor is critical for achieving effective target degradation. In the context of this project, replacing the benzyl group of the cap from **Hydrazide 5** with an exit vector appears to negatively impact the binding of HDAC enzymes. Exploring an alternative site for the exit vector within the cap group, such as the aminophenyl moiety, holds the potential for enhanced degradation. Additionally, transitioning from a *para*- to a *meta*-substitution may further facilitate the desired complex formation (Figure 26).

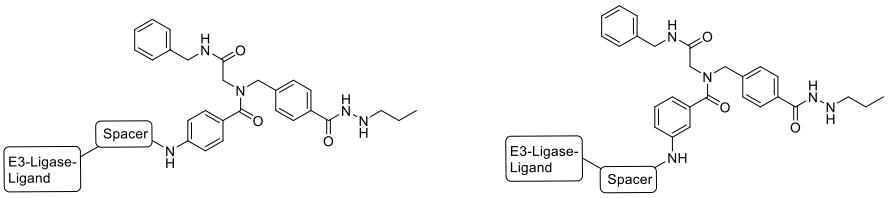


Figure 26. Possible design of future hydrazide-based HDAC PROTACs.

4.4 Experimental Section

General Information

Chemicals were obtained from abcr GmbH, Acros Organics, Carbolution Chemicals, Sigma-Aldrich, TCI Chemicals or VWR and used without further purification. Technical grade solvents were distilled prior to use. For all HPLC purposes, acetonitrile in HPLC-grade quality (HiPerSolv CHROMANORM, *VWR*) was used. Water was purified with a PURELAB flex® (ELGA VEOLIA). Air-sensitive reactions were carried out under argon atmosphere utilizing standard *Schlenk* techniques. **Thin-layer chromatography (TLC)** was carried out on prefabricated plates (silica gel 60, F_{254}, *Merck*). Components were visualized either by irradiation with ultraviolet light (254 nm or 366 nm) or by staining appropriately. Column Chromatography was carried out on silica gel (60 Å, 40-60 µm, *Acros Organics*). If no solvent is stated an aqueous solution was prepared with demineralized water. Mixtures of two or more solvents are specified as "solvent A"/"solvent B", 3/1, *v*/*v*; meaning that 100 mL of the respective mixture consists of 75 mL of "solvent A" and 25 mL of "solvent B". The uncorrected melting points were determined using a Büchi Melting Point M-560 apparatus. **Nuclear Magnetic Resonance Spectroscopy (NMR):** Proton (^{1}H), carbon (^{13}C), and fluorine (^{19}F) NMR spectra were recorded either on a *Bruker* Avance III HD 400 MHz at a frequency of 400 MHz (^{1}H), 100 MHz (^{13}C) and 377 MHz (^{19}F), a *Varian/Agilent* Mecury-plus-400 at a frequency of 400 MHz (^{1}H) and 100 MHz (^{13}C), a *Varian/Agilent* Mecury-plus-300 at a frequency of 300 MHz (^{1}H), 75 MHz (^{13}C) and 282 MHz (^{19}F) , a Bruker AVANCE 500 MHz at a frequency of 500 MHz (^{1}H) and 126 MHz (^{13}C) or on a Bruker AVANCE III HD 600 MHz at a frequency of 600 MHz (^{1}H), 151 MHz (^{13}C) and 565 MHz (^{19}F). The chemical shifts are given in parts per million (ppm). As solvents deuterated chloroform ($CDCl_3$), deuterated methanol (MeOH-d_4) and deuterated dimethyl sulfoxide (DMSO-d_6) were used. The residual solvent signal ($CDCl_3$: ^{1}H NMR: 7.26 ppm, ^{13}C NMR: 77.1 ppm; DMSO-d_6: ^{1}H NMR: 2.50 ppm, ^{13}C NMR: 39.52 ppm; MeOH-d_4: ^{1}H NMR: 3.31 ppm, 4.87 ppm, ^{13}C NMR: 49.00 ppm) was used for calibration. The multiplicity of each signal is reported as singlet (s), doublet (d), triplet (t), quartet (q), heptet (h), multiplet (m) or combinations thereof. Multiplicities and coupling constants are reported as measured and might disagree with the expected values. **Mass Spectrometry: :** High resolution electrospray ionization mass spectra (HRMS-ESI) were acquired with *Bruker Daltonik GmbH* micrOTOF coupled to a an *LC Packings* Ultimate HPLC system and controlled by micrOTOFControl3.4 and HyStar 3.2-LC/MS, with a *BrukerDaltonik GmbH* ESI-qTOF Impact II coupled to a *Dionex* UltiMateTM 3000 UHPLC system and controlled by micrOTOFControl 4.0 and HyStar 3.2-LC/MS or with a micrOTOF-Q mass spectrometer (*Bruker*) with ESI-source coupled with an HPLC Dionex UltiMate 3000 (*Thermo Scientific*). Low resolution electrospray ionisation mass spectra (LRMS-ESI) were acquired with an *Advion* expression® compact mass spectrometer (CMS) coupled with an automated TLC plate reader Plate Express® (*Advion*).

High Performance Liquid Chromatography (HPLC): A *Thermo Fisher Scientific* UltiMate™ 3000 UHPLC system with a Nucleodur 100-5 C18 (250 x 4.6 mm, *Macherey Nagel*) with a flow rate of 1 mL/min and a temperature of 25 °C or a 100-5 C18 (100 x 3 mm, *Macherey Nagel*) with a flow rate of 0.5 mL/min and a temperature of 25 °C with an appropriate gradient were used. For preparative purposes a AZURA Prep. 500/1000 gradient system with a Nucleodur 110-5 C18 HTec (250 x 32 mm, *Macherey Nagel*) column with 20 mL/min was used. Detection was implemented by UV absorption measurement at a wavelength of λ = 220 nm and λ = 250 nm. Bidest. H_2O (A) and MeCN (B) were used as eluents with an addition of 0.1% TFA for eluent A. **Purity:** The purity of all final compounds was 95% or higher. Purity was determined via HPLC with the Nucleodur 100-5 C18 (250 x 4.6 mm, *Macherey Nagel*) at 250 nm. After column equilibration for 5 min a linear gradient from 5% A to 95% B in 7 min followed by an isocratic regime of 95% B for 10 min was used.

4.4.1 General Procedure

General Procedure I

Compound **5** (0.100 g, 0.188 mmol, 1.00 eq.) was dissolved in CH_2Cl_2 (0.4 mL). 4 M HCl in 1,4-dioxane (0.470 mL, 1.88 mmol, 10.0 eq.) was added and stirred for 2 h at room temperature. Afterwards, the solvent was removed under reduced pressure, the remaining hydrochloride salt was dried in high vacuum and subsequently dissolved in DMF (0.2 mL) and DIPEA (98.5 µL, 98.5 µg, 0.556 µmol, 3.00 eq.).

In a separate flask, the respective carboxylic acid (0.376 mmol, 2.00 eq.) was dissolved in DMF (0.2 mL) and DIPEA (0.143 g, 0.556 mmol, 3.00 eq.) Next, HATU (0.143 g, 0.376 mmol, 2.00 eq.) and HOBt*H_2O (57.6 mg, 0.376 mmol, 2.00 eq.) was added and the solution stirred for 30 min at rt. The previously prepared solution of the hydrochloride salt was added to the solution and stirred for 19 h at room temperature. The solvent was removed under reduced pressure. The residue was dissolved in ethyl acetate (15 mL) and washed with $NaHCO_3$ (15 mL). The inorganic layer was extracted with ethyl acetate (3 x 20 mL), the combined organic layers were washed with sat. NaCl (20 mL) solution and dried over Na_2SO_4. The solvent was removed under reduced pressure and the crude product purified by column chromatography.

General Procedure II

The respective Boc-protected amine (1.00 eq. – 1.73 eq.) was dissolved in CH_2Cl_2 (0.4 M). 4 M HCl in 1,4-dioxane (10.0 eq, to the Boc-amine) was added and stirred for 2 h at room temperature. Afterwards, the solvent was removed under reduced pressure, the remaining hydrochloride salt was dried in high vacuum and subsequently dissolved in DMF (0.2 mL) and DIPEA (17.0 µL, 12.6 mg, 97.5 µmol, 1.00 eq.).

In a separate flask, compound **18** (50.0 mg, 97.5 µmol, 1.00 eq.) was dissolved in DMF (0.6 mL). EDC*HCl (20.5 mg, 0.107 mmol, 1.10 eq.), HATU (40.7 mg, 0.107 mmol, 1.10 eq.), HOBt*H_2O (16.4 mg, 0.107 mmol, 1.10 eq.) and DIPEA (0.102 mL, 75.6 mg, 0,585 mmol, 6.00 eq.) were added and the solution stirred for 30 min at room temperature. The previously prepared solution of the hydrochloride salt was added to the solution and stirred for 19 h at room temperature. The solvent was removed under reduced pressure. The oily residue was purified by preparative HPLC to yield the target compound.

General Procedure III

The reaction was conducted under argon atmosphere.

The respective Cbz-protected hydrazide (1.00 eq.) was dissolved in DMF (0.1 mL). Next, K_3PO_4 (4.00 eq.) and 2-mercaptoethanol (2.00 eq.) was added, the flask capped, and stirred for 3 d at 75 °C. The solvent was removed under reduced pressure and the oily residue dissolved in CH_2Cl_2 (10 mL). It was washed with H_2O (10 mL) and the inorganic layer extracted with CH_2Cl_2 (3 x 10 mL). The combined organic layers were washed with sat. NaCl-solution (20 mL) and dried over Na_2SO_4. The solvent was removed under reduced pressure. The oily residue was purified by preparative HPLC to yield the target compound.

4.4.2 Compound characterization

tert-Butyl (4-bromobenzyl)carbamate (**2**)

(4-Bromophenyl)methanamine hydrochloride (2.22 g, 10.0 mmol, 1.00 eq.) was suspended in CH_2Cl_2 (20 mL). NEt_3 (2.90 mL, 2.12 g, 10,0 mmol, 2.10 eq.) was added and cooled to 0 °C. Di-*tert*-butyl dicarbonate (2.40 g, 11.0 mmol, 1.10 eq.) was added and the solution stirred for 19 h at rt. H_2O (20 mL) was added and the layers separated. The organic layer was washed with 1 M HCl (2 x 15 mL), sat. NaCl (15 mL) and dried over Na_2SO_4. The solvent was removed under reduced pressure to yield the target compound **2** (2.75 g, 9.61 mmol, 96%) as a white solid. $\mathbf{R_f}$ (cyclohexane/ethyl acetate 4/1, *v*/*v*): 0.33, **^{1}H NMR** (500 MHz, $CDCl_3$) δ = 7.49 – 7.37 (m, 2H), 7.18 – 7.10 (m, 2H), 4.87 (s, 1H), 4.25 (d, *J* = 5.8 Hz, 2H), 1.45 (s, 9H). Reported data match the literature.[325]

tert-Butyl [4-(4-methylthiazol-5-yl)benzyl]carbamate (**3**)

Under argon atmosphere, compound **2** (1.00 g, 3.49 mmol, 1.00 eq), $Pd(OPiv)_2$ (0.108 g, 0.349 mmol, 0.10 eq.), and Cs_2CO_3 (1.13 g, 3.49 mmol, 1.00 eq.) were suspended in dry DMF (11.5 mL). Next, 4-methylthiazole (0.635 mL, 0.692 g, 6.98 mmol, 2.00 eq.) was added and the flask capped. It was stirred for 19 h at 90 °C. The solvent was removed under reduced pressure. The residue was dissolved in ethyl acetate (20 mL) and filtered through Celite®. It was washed with H_2O (30 mL) and the inorganic layer extracted with ethyl acetate (3 x 30 mL). The combined

organic layers were washed with sat. NaCl (20 mL) solution and dried over Na_2SO_4. The solvent was removed under reduced pressure and the oily residue purified by column chromatography (cyclohexane/ethyl acetate 4/1 to 1/2, *v*/*v*) yielding the target compound **3** (0.993 g, 3.26 mmol, 93%) as a yellow solid. $\mathbf{R_f}$ (cyclohexane/ethyl acetate 1/1, *v*/*v*): 0.5; **^{1}H NMR** (400 MHz, $CDCl_3$) δ = 8.68 (s, 1H), 7.43 – 7.38 (m, 2H), 7.34 (d, *J* = 8.0 Hz, 2H), 4.94 (s, 1H), 4.35 (d, *J* = 5.9 Hz, 2H), 2.53 (s, 3H), 1.47 (s, 9H). Reported data match the literature.[325]

tert-Butyl (2*S*,4*R*)-4-hydroxy-2-{[4-(4-methylthiazol-5-yl)benzyl]carbamoyl}pyrrolidine-1-carboxylate (**4**)

Compound **3** (1.18 g, 3.89 mmol, 1.00 eq.) was dissolved in CH_2Cl_2 (10 mL). 4 M HCl in 1,4-dioxane (9.7 mL, 38.9 mmol, 10.0 eq) was added and stirred for 2 h at room temperature. Afterwards, the solvent was removed under reduced pressure, the remaining hydrochloride salt was dried in high vacuum and subsequently dissolved in DMF (6 mL) and DIPEA (0.720 mL, 0.505 g, 3.90 mmol, 1.00 eq.).

In a separate flask, (2*S*,4*R*)-1-(*tert*-butoxycarbonyl)-4-hydroxypyrrolidine-2-carboxylic acid (1.08 g, 4.67 mmol, 1.20 eq.) was dissolved in DMF (8 mL). TBTU (1.50 g, 4.67 mmol, 1.20 eq.) and DIPEA (2.00 mL, 1.52 g, 11.7 mmol, 3.00 eq.) were added and stirred for 30 min at room temperature. The previously prepared solution of the hydrochloride salt was added to the solution and stirred for 19 h at 84 °C. The solvent was removed under reduced pressure. The residue was dissolved in ethyl acetate (20 mL) and washed with sat. $NaCO_3$ solution (20 mL). The inorganic layer was extracted with ethyl acetate (3 x 20 mL), the combined organic layers washed with sat. NaCl solution (25 mL) and dried over Na_2SO_4. The solvent was removed under reduced pressure and the oily residue purified by column chromatography (CH_2Cl_2/MeOH 1/0 to 94/6, *v*/*v*) yielding the target compound **4** (1.56 g, 3.74 mmol, 96%) as a yellow solid. $\mathbf{R_f}$ (CH_2Cl_2/MeOH 9/1, *v*/*v*): 0.40; **^{1}H NMR** (500 MHz, DMSO-d_6) δ = 8.97 (s, 1H), 8.52 – 8.39 (m, 1H), 7.45 – 7.33 (m, 4H), 4.43 – 4.30 (m, 1H), 4.29 – 4.14 (m, 3H), 3.65 – 3.58 (m, 1H), 3.51 (s, 1H), 3.47 – 3.36 (m, 1H), 3.33 – 3.10 (m, 2H), 2.44 (s, 3H), 2.13 – 1.98 (m, 2H), 1.94 – 1.82 (m, 1H), 1.29 – 1.23 (m, 9H). Reported data match the literature.[325]

tert-Butyl [(*S*)-1-((2*S*,4*R*)-4-hydroxy-2-{[4-(4-methylthiazol-5-yl)benzyl]carbamoyl}pyrrolidin-1-yl)-3,3-dimethyl-1-oxobutan-2-yl]carbamate (**5**)

Compound **4** (0.140 g, 0.335 mmol, 1.00 eq.) was dissolved in CH_2Cl_2 (1 mL). 4 M HCl in 1,4-dioxane (0.837 mL, 3.35 mmol, 10.0 eq) was added and stirred for 2 h at room temperature. Afterwards, the solvent was removed under reduced pressure, the remaining hydrochloride salt was dried in high vacuum.

In a separate flask, (*S*)-2-[(*tert*-butoxycarbonyl)amino]-3,3-dimethylbutanoic acid (0.101 g, 0.435 mmol, 1.30 eq.) was dissolved in CH_2Cl_2 (3.5 mL). EDC*HCl (83.6 mg, 0.435 mmol, 1.30 eq.), DIPEA (0.173 mL, 0.129 mg, 1.00 mmol, 3.00 eq.) and HOBt*H_2O (66.1 mg, 0.435 mmol, 1.30 eq.) were added and stirred for 10 min at room temperature. The solution was added to the hydrochloride salt and stirred for 19 h at room temperature. The solvent was removed under reduced pressure and the oily residue purified by column chromatography (CH_2Cl_2/MeOH 96/4, *v*/*v*) yielding the target compound **5** (0.169 g, 0.318 mmol, 95%) as a white solid. $\mathbf{R_f}$ (CH_2Cl_2/MeOH 96/4, *v*/*v*): 0.30; **^{1}H NMR** (500 MHz, DMSO-d_6) δ = 9.13 (s, 1H), 8.97 (s, 1H), 8.54 (t, *J* = 6.0 Hz, 1H), 7.43 – 7.36 (m, 4H), 6.77 – 6.31 (m, 1H), 5.11 (s, 1H), 4.49 – 4.31 (m, 3H), 4.26 – 4.20 (m, 1H), 4.18 – 4.13 (m, 1H), 3.70 – 3.57 (m, 2H), 2.44 (s, 3H), 2.08 – 1.85 (m, 1H), 1.38 (s, 9H), 0.93 (s, 9H). Reported data match the literature.[325]

tert-Butyl [2-(2-{[(*S*)-1-((2*S*,4*R*)-4-hydroxy-2-{[4-(4-methylthiazol-5-yl)benzyl]carbamoyl}pyrrolidin-1-yl)-3,3-dimethyl-1-oxobutan-2-yl]amino}-2-oxoethoxy)ethyl]carbamate (**6**)

Synthesized according to **General Procedure I**.

The crude mixture was purified by column chromatography (CH_2Cl_2/MeOH 96/4 to 94/6, *v*/*v*) yielding compound **6** (95.3 mg, 0.151 mmol, 80%) as a white solid. $\mathbf{R_f}$ (CH_2Cl_2/MeOH 9/1, *v*/*v*): 0.44; **^{1}H NMR** (600 MHz, DMSO-d_6) δ = 8.98 (s, 1H), 8.57 (t, *J* = 6.1 Hz, 1H), 7.40 (s, 5H), 6.89 – 6.81 (m, 1H), 5.13 (d, *J* = 3.6 Hz, 1H), 4.56 (d, *J* = 9.6 Hz, 1H), 4.47 – 4.32 (m, 2H), 4.28 – 4.22 (m, 1H), 3.94 (d, *J* = 5.5 Hz, 1H), 3.71 – 3.64 (m, 1H), 3.65 – 3.59 (m, 1H), 3.51 (s, 4H), 3.47 (t, *J* = 5.8 Hz, 2H), 2.44 (s, 3H), 2.10 – 2.01 (m, 1H), 1.96 – 1.87 (m, 1H), 1.36 (s, 9H), 0.95 (s, 9H); **^{13}C NMR** (151 MHz, DMSO-d_6) δ = 171.7, 169.1, 168.5, 155.6, 151.4, 147.7, 139.4, 131.1, 129.7, 128.7, 127.5, 77.6, 69.8, 69.3, 68.8, 58.7, 56.5, 41.7, 37.9, 35.6, 28.2, 26.2, 18.1, 16.7, 15.9; **LRMS-ESI** (**m/z**): $[M+H]^+$ calcd for $C_{31}H_{45}N_5O_7S$: 632.3 found: 632.3.

tert-Butyl (2-{2-[2-({(*S*)-1-[(2*S*,4*R*)-4-hydroxy-2-{[4-(4-methylthiazol-5-yl)benzyl]carbamoyl}pyrrolidin-1-yl]-3,3-dimethyl-1-oxobutan-2-yl}amino)-2-oxoethoxy]ethoxy}ethyl)carbamate (**7**)

Synthesized according to **General Procedure I**.

The crude mixture was purified by column chromatography (CH_2Cl_2/MeOH 96/4 to 93/7, *v*/*v*) yielding compound **7** (61.9 mg, 91.5 µmol, 49%) as a colorless oil. $\mathbf{R_f}$ (CH_2Cl_2/MeOH 9/1, *v*/*v*): 0.50; **^{1}H NMR** (600 MHz, MeOH-d_4) δ = 8.89 – 8.87 (m, 1H), 8.59 (s, 1H), 7.69 (d, *J* = 9.4 Hz, 1H), 7.49 – 7.39 (m, 4H), 6.66 (t, *J* = 6.0 Hz, 1H), 4.72 (d, *J* = 9.2 Hz, 1H), 4.61 – 4.49 (m, 2H), 4.38 – 4.33 (m, 1H), 4.07 – 4.02 (m, 1H), 3.89 – 3.79 (m, 1H), 3.74 – 3.69 (m, 2H), 3.64 – 3.62 (m, 6H), 3.59 – 3.49 (m, 2H), 3.28 – 3.18 (m, 2H), 2.49 – 2.47 (m, 3H), 2.26 – 2.18 (m, 1H), 2.18 –

2.07 (m, 1H), 1.46 – 1.39 (m, 9H), 1.06 – 1.01 (m, 9H); **^{13}C NMR** (151 MHz, MeOH-d_4) δ = 174.3, 172.2, 171.7, 158.4, 152.9, 149.1, 140.2, 133.4, 131.6, 130.4, 129.0, 80.2, 72.4, 71.5, 71.3, 71.2, 71.0, 60.8, 58.1, 43.8, 41.3, 38.9, 37.2, 30.8, 28.8, 27.0, 15.8; **LRMS-ESI** (**m/z**): $[M+H]^+$ calcd for $C_{33}H_{49}N_5O_8S$: 676.3 found: 676.3.

tert-Butyl {(*S*)-13-[(2*S*,4*R*)-4-hydroxy-2-{[4-(4-methylthiazol-5-yl)benzyl]carbamoyl}pyrrolidine-1-carbonyl]-14,14-dimethyl-11-oxo-3,6,9-trioxa-12-azapentadecyl}carbamate (**8**)

Synthesized according to **General Procedure I**.

The crude mixture was purified by column chromatography (CH_2Cl_2/MeOH 96/4 to 93/7, *v*/*v*) yielding compound **8** (0.109 g, 0.151 µmol, 80%) as a colorless oil. **R_f** (CH_2Cl_2/MeOH 9/1, *v*/*v*): 0.50; **^{1}H NMR** (500 MHz, DMSO-d_6) δ = 8.98 (s, 1H), 8.57 (t, *J* = 6.0 Hz, 1H), 8.31 (s, 1H), 7.49 – 7.34 (m, 5H), 6.71 (s, 1H), 5.13 (d, *J* = 3.6 Hz, 1H), 4.56 (d, *J* = 9.6 Hz, 1H), 4.48 – 4.33 (m, 3H), 4.31 – 4.22 (m, 1H), 3.97 (s, 1H), 3.69 – 3.65 (m, 1H), 3.61 (td, *J* = 5.0, 4.6, 2.1 Hz, 2H), 3.59 – 3.52 (m, 3H), 3.51 (d, *J* = 1.8 Hz, 4H), 3.35 (t, *J* = 6.1 Hz, 2H), 3.04 (q, *J* = 6.1 Hz, 2H), 2.44 (s, 3H), 2.09 – 2.02 (m, 1H), 1.95 – 1.87 (m, 1H), 1.36 (s, 9H), 0.95 (s, 9H); **^{13}C NMR** (126 MHz, DMSO-d_6) δ = 171.6, 169.1, 168.5, 155.5, 151.3, 147.7, 139.4, 131.0, 129.7, 128.6, 127.4, 79.1, 77.5, 70.4, 69.7, 69.6 (d, *J* = 4.3 Hz), 69.5, 69.1, 68.8, 58.7, 56.4, 55.6, 41.6, 37.8, 35.6, 28.1, 26.1, 15.8; **LRMS-ESI** (**m/z**): $[M+H]^+$ calcd for $C_{35}H_{53}N_5O_9S$: 720.4 found: 720.3.

tert-Butyl {(*S*)-16-[(2*S*,4*R*)-4-hydroxy-2-{[4-(4-methylthiazol-5-yl)benzyl]carbamoyl}pyrrolidine-1-carbonyl]-17,17-dimethyl-14-oxo-3,6,9,12-tetraoxa-15-azaoctadecyl}carbamate (**9**)

Synthesized according to **General Procedure I**.

The crude mixture was purified by column chromatography (CH_2Cl_2/MeOH 96/4 to 93/7, *v*/*v*) yielding compound **9** (0.132 g, 0.173 µmol, 92%) as a colorless oil. **R_f** (CH_2Cl_2/MeOH 9/1, *v*/*v*): 0.60; **^{1}H NMR** (500 MHz, DMSO-d_6) δ = 8.97 (s, 1H), 8.56 (t, *J* = 5.9 Hz, 1H), 8.31 – 8.29 (m, 1H), 7.43 – 7.37 (m, 4H), 6.69 (s, 1H), 5.14 – 5.07 (m, 1H), 4.57 (d, *J* = 9.6 Hz, 1H), 4.49 – 4.33 (m, 3H), 4.29 – 4.21 (m, 1H), 3.97 (s, 1H), 3.71 – 3.64 (m, 1H), 3.64 – 3.43 (m, 14H), 3.36 (t, *J* = 6.2 Hz, 2H), 3.05 (q, *J* = 5.9 Hz, 2H), 2.44 (s, 3H), 2.11 – 2.00 (m, 1H), 1.96 – 1.87 (m, 1H), 1.37 (s, 9H), 0.95 (s, 9H); **^{13}C NMR** (126 MHz, DMSO-d_6) δ = 171.5, 169.1, 168.5, 155.5, 151.3, 147.7, 139.4, 131.1, 129.7, 128.6, 127.4, 79.1, 77.5, 70.4, 69.8, 69.7, 69.7, 69.6, 69.5, 69.4, 69.1, 68.8, 58.7, 56.5, 55.6, 41.7, 37.8, 35.6, 28.2, 26.1, 15.8; **LRMS-ESI** (**m/z**): $[M+H]^+$ calcd for $C_{37}H_{57}N_5O_{10}S$: 764.4 found: 764.3.

(2*S*,4*R*)-1-[(*S*)-1-azido-17-(tert-butyl)-15-oxo-3,6,9,12-tetraoxa-16-azaoctadecan-18-oyl]-4-hydroxy-*N*-[4-(4-methylthiazol-5-yl)benzyl]pyrrolidine-2-carboxamide (**10**)

Synthesized according to **General Procedure I**.

The crude mixture was purified by column chromatography (CH_2Cl_2/MeOH 96/4 to 94/6, *v*/*v*) yielding compound **10** (92.6 mg, 0.131 mmol, 70%) as a colorless waxy oil. $\mathbf{R_f}$ (CH_2Cl_2/MeOH 94/6, *v*/*v*): 0.30; **^{1}H NMR** (600 MHz, DMSO-d_6) δ = 8.98 (s, 1H), 8.54 (t, *J* = 6.1 Hz, 1H), 7.89 (d, *J* = 9.4 Hz, 1H), 7.42 (d, *J* = 8.2 Hz, 2H), 7.38 (d, *J* = 8.3 Hz, 2H), 5.11 (d, *J* = 3.6 Hz, 1H), 4.55 (d, *J* = 9.4 Hz, 1H), 4.46 – 4.40 (m, 2H), 4.37 – 4.32 (m, 1H), 4.25 – 4.19 (m, 1H), 3.69 – 3.66 (m, 1H), 3.63 (s, 1H), 3.62 – 3.57 (m, 3H), 3.58 – 3.54 (m, 2H), 3.54 – 3.52 (m, 1H), 3.52 – 3.47 (m, 8H), 3.48 – 3.45 (m, 1H), 3.38 (t, *J* = 4.9 Hz, 2H), 2.59 – 2.50 (m, 2H), 2.44 (s, 3H), 2.39 – 2.30 (m, 1H), 2.07 – 1.99 (m, 1H), 1.95 – 1.86 (m, 1H), 0.94 (s, 9H); **^{13}C NMR** (151 MHz, DMSO-d_6) δ = 171.9, 169.9, 169.5, 151.4, 147.7, 139.5, 131.1, 129.6, 128.6, 127.4, 69.8, 69.8, 69.7, 69.7, 69.5, 69.2, 68.9, 66.9, 58.7, 56.3, 56.3, 50.0, 41.6, 37.9, 35.7, 35.3, 26.3, 15.9; **LRMS-ESI** (**m/z**): $[M+H]^+$ calcd for $C_{33}H_{49}N_7O_8S$: 704.3 found: 704.3.

(2*S*,4*R*)-1-[(*S*)-2-(6-azidohexanamido)-3,3-dimethylbutanoyl]-4-hydroxy-*N*-[4-(4-methylthiazol-5-yl)benzyl]pyrrolidine-2-carboxamide (**11**)

Synthesized according to **General Procedure I**.

The crude mixture was purified by column chromatography (CH_2Cl_2/MeOH 99/1 to 94/6, *v*/*v*) yielding compound **11** (56.4 mg, 99.0 µmol, 53%) as a colorless waxy oil. $\mathbf{R_f}$ (CH_2Cl_2/MeOH 9/1, *v*/*v*): 0.50; **^{1}H NMR** (600 MHz, $CDCl_3$) δ = 8.73 (s, 1H), 7.37 – 7.31 (m, 4H), 6.22 (d, *J* = 8.8 Hz, 1H), 5.29 (s, 1H), 4.56 – 4.50 (m, 3H), 4.35 – 4.30 (m, 1H), 4.06 – 4.01 (m, 1H), 3.63 (s, 2H), 2.50 (s, 3H), 2.49 – 2.43 (m, 1H), 2.21 – 2.17 (m, 2H), 2.14 – 2.08 (m, 1H), 1.64 – 1.59 (m, 2H), 1.58 – 1.54 (m, 2H), 1.51 – 1.43 (m, 2H), 1.41 (d, *J* = 6.7 Hz, 1H), 1.39 – 1.32 (m, 2H), 0.93 (s, 9H). **^{13}C NMR** (151 MHz, $CDCl_3$) δ = 173.5, 171.9, 171.0, 150.7, 148.1, 138.4, 132.0, 130.8, 129.6, 128.2, 70.1, 58.7, 57.6, 56.8, 53.6, 51.3, 43.3, 43.0, 36.3, 35.2, 28.6, 26.5, 25.1, 18.7, 17.4, 16.0; **LRMS-ESI** (**m/z**): $[M+H]^+$ calcd for $C_{28}H_{39}N_7O_4S$: 570.3 found: 570.3.

1-Benzyl 2-(*tert*-butyl) 1-propylhydrazine-1,2-dicarboxylate (**13**)

tert-Butyl carbazate (1.32 g, 10.0 mmol, 1.00 eq.) was dissolved in THF (25 mL). Propionic aldehyde (0.860 mL, 0.697 g, 12.0 mmol, 1.20 eq.) was added and the solution stirred for 2 h at 50 °C. Afterwards, it was cooled to 0 °C, $NaBH_4$ (1.13 g, 30.0 mmol, 3.00 eq.) was added, warmed to room temperature and stirred for 16 h at this temperature. The reaction was stopped through the addition of 10 mL H_2O. THF was removed under reduced pressure and the inorganic layer was extracted with CH_2Cl_2 (3 x 20 mL). The combined organic layers where washed with sat. NaCl (20 mL) solution and dried over Na_2SO_4. The solvent was removed under reduced pressure and the oily residue dissolved in 20 mL THF. Pyridine (0.968 mL, 0.949 g, 12.0 mmol, 1.20 eq.) and benzyl chloroformate (1.54 mL, 1.88 g, 11.0 mmol, 1.10 eq.) were added. It was warmed to room

temperature and stirred for 16 h at this temperature. The reaction was stopped through the addition of sat. Na_2CO_3 (20 mL) solution. THF was removed under reduced pressure and the inorganic layer was extracted witch CH_2Cl_2 (3 x 20 mL). The combined organic layers were washed with sat. NaCl (20 mL) solution and dried over Na_2SO_4. After removal of the solvent under reduced pressure and the crude product purified by column chromatography (cyclohexane/ethyl acetate 4/1, *v*/*v*) yielding **13** (1.37 g, 4.44 mmol, 44%) as a white solid. $\mathbf{R_f}$ (cyclohexane/ethyl acetate 4/1, *v*/*v*): 0.48; **mp.:** ~30 °C; **^{1}H NMR** (600 MHz, $CDCl_3$) δ = 7.39 – 7.28 (m, 4H), 6.43 (m, 1H), 5.23 – 5.02 (m, 2H), 3.45 (m, 2H), 1.60 (q, *J* = 7.5 Hz, 2H), 1.43 (m, 9H), 0.89 (m, 3H); **^{13}C NMR** (151 MHz, $CDCl_3$) δ = 156.2, 136.2, 128.6, 128.2, 128.0, 81.6, 68.0, 52.4, 51.9 28.3, 21.0, 20.7, 11.3; **LRMS-ESI** (**m/z**): $[M+H]^+$ calcd for $C_{16}H_{24}N_2O_4$: 309.2 found: 309.2.

Benzyl 2-(4-{[(*tert*-butoxycarbonyl)amino]methyl}benzoyl)-1-propylhydrazine-1-carboxylate (**15**)

Compound **13** (1.20 g, 3.89 mmol, 1.00 eq.) was dissolved in CH_2Cl_2 (10 mL). 4 M HCl in 1,4-dioxane (9.70 mL, 38.9 mmol, 10.0 eq) was added and stirred for 2 h at room temperature. Afterwards, the solvent was removed under reduced pressure, the remaining hydrochloride salt was dried in high vacuum and subsequently dissolved in DMF (3 mL) and DIPEA (1.38 mL, 1.05 g, 7.80 mmol, 2.00 eq.). In a separate flask, 4-{[(*tert*-butoxycarbonyl)amino]methyl}benzoic acid (1.46 g, 5.83 mmol, 1.50 eq.) was dissolved in DMF (4 mL). Next, HATU (2.22 g, 5.83 mmol, 1.50 eq.) and DIPEA (1.38 mL, 1.05 g, 7.80 mmol, 2.00 eq.) were added and the solution stirred for 30 min at room temperature. The previously prepared solution of the hydrochloride salt was added to the solution and stirred for 19 h at room temperature. The solvent was removed under reduced pressure. The residue dissolved in ethyl acetate (20 mL) and washed with $NaHCO_3$ (20 mL). The inorganic layer was extracted with ethyl acetate (3 x 20 mL), the combined organic layers were washed with sat. NaCl (20 mL) solution and dried over Na_2SO_4. The solvent was removed under reduced pressure and the crude product purified by column chromatography (cyclohexane/ethyl acetate 2/1 to 1/1, *v*/*v*) yielding **15** (1.64 g, 3.71 mmol, 95%) as a white solid. $\mathbf{R_f}$ (cyclohexane/ethyl acetate 1/1, *v*/*v*): 0.55; **^{1}H NMR** (500 MHz, 90 °C, DMSO-d_6) δ = 10.37 (s, 1H), 7.92 – 7.85 (m, 1H), 7.79 (d, *J* = 7.7 Hz, 2H), 7.42 – 7.24 (m, 6H), 5.12 (d, *J* = 3.2 Hz, 2H), 4.20 (t, *J* = 6.1 Hz, 2H), 3.49 (t, *J* = 7.1 Hz, 2H), 1.59 (q, *J* = 7.3 Hz, 2H), 1.41 (s, 9H), 0.99 – 0.86 (m, 2H); **^{13}C NMR** (126 MHz, 90 °C DMSO-d_6) δ = 166.6, 165.2, 155.3, 150.5, 143.8, 136.3, 130.7, 127.8, 127.3, 127.0, 126.8, 126.5, 120.1, 77.6, 66.3, 51.1, 43.2, 27.9, 20.0, 10.6; **LRMS-ESI** (**m/z**): $[M+H]^+$ calcd for $C_{24}H_{31}N_3O_5$: 442.2 found: 442.2.

Benzyl 2-[4-({[2-(*tert*-butoxy)-2-oxoethyl]amino}methyl)benzoyl]-1-propylhydrazine-1-carboxylate (**16**)

Compound **15** (1.32 g, 2.99 mmol, 1.00 eq) was dissolved in CH_2Cl_2 (7.5 mL). 4 M HCl in 1,4-dioxane (7.50 mL, 29.9 mmol, 10.0 eq) was added and stirred for 2 h at room temperature. Afterwards, the solvent was removed under reduced pressure, the remaining hydrochloride salt was dried in high vacuum and dissolved in CH_2Cl_2 (6 mL) and DIPEA (1.56 mL, 1.16 g, 8.97 mmol, 3.00 eq.). *tert*-Butylbromoacetate (0.486 mL, 0.624 g, 3.29 mmol, 1.10 eq.) was added and the solution stirred for 3 d at room temperature. H_2O (15 mL) was added, the layers separated and the inorganic layer extracted with CH_2Cl_2 (3 x 15 mL). The combined organic layers were washed with sat. NaCl (20 mL) and dried over Na_2SO_4. The solvent was removed under reduced pressure and the crude product purified by column chromatography (cyclohexane/ethyl acetate 1/2, *v*/*v*) yielding **16** (0.798 g, 1.75 mmol, 58%) as a yellow oil. $\mathbf{R_f}$ (cyclohexane/ethyl acetate 1/2, *v*/*v*): 0.36; **^{1}H NMR** (600 MHz, DMSO-d_6) δ = 10.67 – 10.59 (m, 1H), 7.79 (d, *J* = 8.0 Hz, 2H), 7.47 – 7.36 (m, 3H), 7.29 (d, *J* = 4.2 Hz, 3H), 5.20 – 5.03 (m, 2H), 3.76 (s, 3H), 3.47 (s, 2H), 3.18 (s, 2H), 1.55 (h, *J* = 7.3 Hz, 2H), 1.41 (s, 9H), 0.95 – 0.86 (m, 3H); **^{13}C NMR** (151 MHz, DMSO-d_6) δ = 171.3, 165.5, 155.7, 144.7, 136.6, 130.7, 128.2, 127.9, 127.6, 127.4, 127.0, 80.1, 66.5, 51.6, 50.8, 50.2, 27.8, 20.3, 11.1; **LRMS-ESI** (**m/z**): $[M+H]^+$ calcd for $C_{25}H_{33}N_3O_5$: 456.6 found: 456.6.

Benzyl 2-[4-({*N*-[2-(*tert*-butoxy)-2-oxoethyl]-4-(dimethylamino)benzamido}methyl)benzoyl]-1-propylhydrazine-1-carboxylate (**17**)

Compound **16** (0.170 g, 0.373 mmol, 1.00 eq.) and NEt_3 (90.9 µL, 66.0 mg, 0.652 mmol, 1.75 eq.) were dissolved in CH_2Cl_2 (2 mL). 4-(Dimethylamino)benzoyl chloride (0.103 g, 0.559 mmol, 1.50 eq.) was added and the solution stirred for 19 h at room temperature. Next, NaOH (1 M, 1 mL) was added and stirred for 10 min. The layers were separated and the inorganic layer extracted with CH_2Cl_2 (3 x 5 mL). The combined organic layers were washed with sat. NaCl solution (3 x 15 mL) and dried over Na_2SO_4. The solvent was removed under reduced pressure and the oily residue purified by column chromatography (cyclohexane/ethyl acetate 1/1, *v*/*v*) yielding **17** (0.181 g, 0.300 mmol, 80%) as a white solid. $\mathbf{R_f}$ (cyclohexane/ethyl acetate 1/1, *v*/*v*): 0.30; **^{1}H NMR** (600 MHz, DMSO-d_6) δ = 10.75 – 10.61 (m, 1H), 7.85 (s, 2H), 7.48 – 7.37 (m, 3H), 7.36 – 7.23 (m, 5H), 6.67 (d, *J* = 8.3 Hz, 2H), 5.17 (s, 1H), 5.09 (s, 1H), 4.68 (s, 2H), 3.93 (s, 2H), 3.48 (s, 2H), 2.92 (s, 6H), 1.56 (h, *J* = 7.3 Hz, 2H), 1.39 (s, 9H), 0.96 – 0.81 (m, 3H); **^{13}C NMR** (151 MHz, DMSO-d_6) δ = 171.7, 165.3, 155.7, 151.4, 141.7, 136.6, 131.1, 128.4, 128.2, 127.8, 127.6, 127.5, 127.0, 111.0, 80.7, 66.9, 66.5, 51.6, 50.8, 40.1, 27.6, 20.3, 11.1; **LRMS-ESI** (**m/z**): $[M+H]^+$ calcd for $C_{34}H_{42}N_4O_6$: 602.3 found: 602.3.

N-(4-{2-[(Benzyloxy)carbonyl]-2-propylhydrazine-1-carbonyl}benzyl)-*N*-[4-(dimethylamino)benzoyl]glycine (**18**)

Compound **17** (0.111 g, 0.185 mmol, 1.00 eq) was dissolved in CH_2Cl_2 (1 mL). Trifluoracetic acid (1 mL) was added and the solution stirred for 2 h at room temperature. It was diluted with CH_2Cl_2

(10 mL) and washed with H_2O (10 mL). The inorganic layer was extracted with CH_2Cl_2 (3 x 10 mL). The combined organic layers were washed with sat. NaCl (15 mL) and dried over Na_2SO_4. The solvent was removed under reduced pressure yielding the target compound **18** as a white solid. $\mathbf{R_f}$ (CH_2Cl_2/MeOH 9/1, *v*/*v*): 0.45; **^{1}H NMR** (600 MHz, DMSO-d_6) δ = 12.72 (s, 1H), 10.86 – 10.68 (m, 1H), 7.87 (s, 2H), 7.47 – 7.36 (m, 3H), 7.28 (dd, *J* = 16.8, 6.4 Hz, 5H), 6.67 (s, 2H), 5.18 – 5.06 (m, 2H), 4.69 (s, 2H), 3.95 (s, 2H), 3.47 (s, 2H), 2.92 (s, 6H), 1.55 (h, *J* = 7.3 Hz, 2H), 0.89 (t, *J* = 7.6 Hz, 3H); **^{13}C NMR** (151 MHz, DMSO-d_6) δ = 171.7, 165.3, 155.7, 151.3, 141.7, 136.6, 131.1, 128.4, 128.2, 127.9, 127.6, 127.5, 127.0, 111.0, 66.8, 66.5, 50.9, 40.1, 20.7, 20.3, 11.1; **LRMS-ESI** (**m/z**): $[M-H]^-$ calcd for $C_{30}H_{34}N_4O_6$: 545.2 found: 545.1.

Benzyl 2-(4-{[4-(dimethylamino)-*N*-[2-oxo-2-(prop-2-yn-1-ylamino)ethyl]benzamido]methyl}benzoyl)-1-propylhydrazine-1-carboxylate (**19**)

Compound **18** (0.164 g, 0.300 mmol, 1.00 eq.) was dissolved in CH_2Cl_2 (0.6 mL). EDC*HCl (86.3 mg, 0.450 mmol, 1.20 eq.), DMAP (11.0 mg, 9.00 µmol, 0.30 eq.), and propargylamine (28.6 µL, 24.8 mg, 0.450 mmol, 1.20 eq.) were added and the solution stirred for 19 h. Next, 1 M HCl (15 mL) was added and the layers separated. The inorganic layer was extracted with CH_2Cl_2 (3 x 15 mL). The combined organic layers were washed with sat. NaCl solution (15 mL) and dried over Na_2SO_4. The solvent was removed under reduced pressure and the oily residue purified by column chromatography (cyclohexane/ethyl acetate 1/6, *v*/*v*) yielding the target compound **19** (99.8 mg, 0.171 mmol, 57%) as a yellow solid. $\mathbf{R_f}$ (cyclohexane/ethyl acetate 1/4, *v*/*v*): 0.34; **^{1}H NMR** (600 MHz, DMSO-d_6) δ = 10.78 – 10.59 (m, 1H), 8.40 (s, 1H), 7.83 (d, *J* = 8.6 Hz, 2H), 7.40 (d, *J* = 8.0 Hz, 3H), 7.37 – 7.21 (m, 6H), 6.68 (d, *J* = 8.3 Hz, 2H), 5.23 – 5.07 (m, 2H), 4.66 (s, 2H), 3.90 (dd, *J* = 5.5, 2.5 Hz, 2H), 3.86 (s, 2H), 3.48 (s, 2H), 3.14 (s, 1H), 2.93 (s, 6H), 1.55 (h, *J* = 7.3 Hz, 2H), 0.90 (t, *J* = 7.6 Hz, 3H); **^{13}C NMR** (151 MHz, DMSO-d_6) δ = 171.7, 167.9, 165.3, 155.7, 151.2, 141.7, 136.6, 131.1, 128.6, 128.4, 128.2, 127.8, 127.7, 127.5, 127.0, 111.0, 80.8, 73.2, 66.9, 66.5, 51.6, 50.9, 40.1, 27.9, 20.3, 11.1; **LRMS-ESI** (**m/z**): $[M+H]^+$ calcd for $C_{33}H_{37}N_5O_5$: 584.4 found: 584.3.

Benzyl 2-(4-{(*S*)-2-[4-(dimethylamino)benzoyl]-12-[(2*S*,4*R*)-4-hydroxy-2-{[4-(4-methylthiazol-5-yl)benzyl]carbamoyl}pyrrolidine-1-carbonyl]-13,13-dimethyl-4,10-dioxo-8-oxa-2,5,11-triazatetradecyl}benzoyl)-1-propylhydrazine-1-carboxylate trifluoroacetate (**Cbz-20**[u])

Synthesized according to **General Procedure II.**

Starting from compound **6** (78.9 mg 0.125 mmol, 1.28 eq.) and 4 M HCl in 1,4-dioxane (0.310 mL, 1.25 mmol, 12.8 eq.), compound **Cbz-20** (37.7 mg, 32.1 µmol, 34%) was isolated as a white lyophilisate. **^{1}H NMR** (500 MHz, DMSO-d_6) δ = 10.72 – 10.59 (m, 1H), 9.01 – 8.95 (m, 1H), 8.60

[u] The numbering refers to the Cbz-protected precursor of the respective final PROTAC.

– 8.50 (m, 1H), 8.12 (s, 1H), 7.83 (d, *J* = 8.5 Hz, 2H), 7.50 – 7.43 (m, 1H), 7.43 – 7.21 (m, 13H), 6.70 (d, *J* = 8.3 Hz, 2H), 5.20 – 5.03 (m, 2H), 4.66 (d, *J* = 6.1 Hz, 2H), 4.56 (d, *J* = 9.5 Hz, 1H), 4.48 – 4.42 (m, 1H), 4.39 – 4.31 (m, 2H), 4.29 – 4.22 (m, 1H), 4.03 – 3.92 (m, 2H), 3.90 – 3.81 (m, 2H), 3.70 – 3.57 (m, 2H), 3.55 – 3.41 (m, 4H), 3.37 – 3.22 (m, 2H), 2.93 (s, 6H), 2.44 (s, 3H), 2.09 – 2.00 (m, 1H), 1.96 – 1.85 (m, 1H), 1.55 (h, *J* = 7.3 Hz, 2H), 0.93 – 0.86 (m, 12H); **^{13}C NMR** (126 MHz, DMSO-d_6) δ = 171.6, 171.6, 169.1, 168.5, 168.1, 165.3, 158.2 (d, *J* = 37.7 Hz), 155.7, 151.4, 151.0, 147.6, 141.7, 139.4, 136.6, 131.1, 129.6, 128.8, 128.6, 128.5, 128.2, 128.0, 127.7, 127.4, 127.0, 115.2 (d, *J* = 289.6 Hz), 111.2, 69.7, 69.6, 69.4, 68.8, 66.5, 58.7, 56.4, 55.8, 50.9, 41.7, 38.5, 37.8, 36.0, 35.6, 26.1, 20.2, 15.8, 11.1; **LC-MS** (**ESI**) (**m/z**): $[M+H]^+$ calcd for $C_{56}H_{69}N_9O_{10}S$: 1060.5 found: 1060.5.

Benzyl 2-(4-{(*S*)-2-[4-(dimethylamino)benzoyl]-15-((2*S*,4*R*)-4-hydroxy-2-{[4-(4-methylthiazol-5-yl)benzyl]carbamoyl}pyrrolidine-1-carbonyl)-16,16-dimethyl-4,13-dioxo-8,11-dioxa-2,5,14-triazaheptadecyl}benzoyl)-1-propylhydrazine-1-carboxylate trifluoroacetate (**Cbz-21**)

Synthesized according to **General Procedure II**.

Starting from compound **7** (65.9 mg 97.5 µmol, 1.00 eq.) and 4 M HCl in 1,4-dioxane (0.244 mL, 0.975 mmol, 10.0 eq.), compound **Cbz-21** (36.0 mg, 29.5 µmol, 30%) was isolated as a white lyophilisate. **^{1}H NMR** (600 MHz, DMSO-d_6) δ = 10.77 – 10.59 (m, 1H), 9.02 – 8.97 (m, 1H), 8.55 (t, *J* = 6.1 Hz, 1H), 7.83 (d, *J* = 8.8 Hz, 2H), 7.46 – 7.36 (m, 7H), 7.35 – 7.32 (m, 5H), 7.31 – 7.21 (m, 3H), 6.69 (d, *J* = 8.4 Hz, 2H), 5.16 (s, 1H), 5.09 (s, 1H), 4.64 (d, *J* = 7.7 Hz, 2H), 4.57 (d, *J* = 9.5 Hz, 1H), 4.44 (t, *J* = 8.2 Hz, 1H), 4.38 – 4.31 (m, 2H), 4.29 – 4.22 (m, 1H), 4.00 – 3.91 (m, 2H), 3.85 (s, 2H), 3.70 – 3.57 (m, 4H), 3.57 – 3.54 (m, 2H), 3.46 – 3.42 (m, 2H), 3.26 (p, *J* = 5.8 Hz, 2H), 2.92 (s, 6H), 2.46 – 2.42 (m, 3H), 2.10 – 2.02 (m, 1H), 1.93 – 1.87 (m, 1H), 1.55 (h, *J* = 7.3 Hz, 2H), 0.93 – 0.86 (m, 12H); **^{13}C NMR** (151 MHz, DMSO-d_6) δ = 171.7, 171.6, 169.2, 168.6, 168.1, 165.3, 158.3 (q, *J* = 37.7 Hz), 155.7, 151.5, 151.0, 147.6, 141.8, 139.4, 136.6, 129.7, 128.9, 128.7, 128.6, 128.4, 128.2, 128.1, 127.7, 127.6, 127.4, 127.0, 115.2 (q, *J* = 289.5 Hz), 111.2, 70.4, 69.8, 69.6, 69.4, 69.1, 68.8, 66.9, 66.5, 58.7, 56.5, 55.7, 51.6, 50.9, 41.7, 38.6, 36.1, 35.7, 26.1, 20.7, 20.3, 15.8, 11.1; **LC-MS** (**ESI**) (**m/z**): $[M+H]^+$ calcd for $C_{58}H_{73}N_9O_{11}S$: 1104.6 found: 1104.5.

Benzy 2-(4-{(*S*)-2-[4-(dimethylamino)benzoyl]-18-((2*S*,4*R*)-4-hydroxy-2-{[4-(4-methylthiazol-5-yl)benzyl]carbamoyl}pyrrolidine-1-carbonyl)-19,19-dimethyl-4,16-dioxo-8,11,14-trioxa-2,5,17-triazaicosyl}benzoyl)-1-propylhydrazine-1-carboxylate trifluoroacetate (**Cbz-22**)

Synthesized according to **General Procedure II**.

Starting from compound **8** (0.101 mg 0.146 mmol, 1.40 eq.) and 4 M HCl in 1,4-dioxane (0.350 mL, 1.46 mmol, 14.0 eq.), compound **Cbz-22** (49.4 mg, 39.1 µmol, 40%) was isolated as a white lyophilisate. **^{1}H NMR** (600 MHz, DMSO-d_6) δ = 10.73 – 10.63 (m, 1H), 9.01 – 8.96 (m, 1H), 8.57

(t, *J* = 6.1 Hz, 1H), 8.00 (s, 1H), 7.83 (d, *J* = 8.5 Hz, 2H), 7.42 – 7.37 (m, 7H), 7.34 (s, 5H), 7.30 (d, *J* = 4.6 Hz, 2H), 7.28 – 7.24 (m, 1H), 6.70 (d, *J* = 8.3 Hz, 2H), 5.16 (s, 1H), 5.09 (s, 1H), 4.67 – 4.61 (m, 2H), 4.56 (d, *J* = 9.6 Hz, 1H), 4.44 (t, *J* = 8.2 Hz, 1H), 4.41 – 4.34 (m, 2H), 4.29 – 4.23 (m, 1H), 3.95 (s, 2H), 3.84 (s, 2H), 3.69 – 3.64 (m, 2H), 3.63 – 3.57 (m, 3H), 3.55 (ddd, *J* = 9.0, 5.0, 2.6 Hz, 3H), 3.53 – 3.50 (m, 2H), 3.47 (t, *J* = 6.4 Hz, 1H), 3.40 (t, *J* = 5.8 Hz, 2H), 3.23 (q, *J* = 5.7 Hz, 2H), 2.93 (s, 6H), 2.45 – 2.43 (m, 3H), 2.09 – 2.02 (m, 1H), 1.94 – 1.87 (m, 1H), 1.54 (p, *J* = 7.3 Hz, 2H), 0.96 – 0.85 (m, 12H); **^{13}C NMR** (151 MHz, DMSO-d_6) δ = 171.7, 171.6, 171.3, 169.5, 169.1, 168.6, 168.5, 168.1, 167.8, 165.3, 158.3 (q, *J* = 37.8 Hz), 155.7, 151.5, 151.0, 147.6, 141.7, 139.5, 136.6, 131.2, 131.1, 129.6, 128.9, 128.7, 128.6, 128.4, 128.2, 128.1, 127.8, 127.7, 127.6, 127.5, 127.0, 115.2 (q, *J* = 289.4 Hz), 111.2, 70.4, 69.8, 69.6, 69.6, 69.0, 68.8, 66.5, 58.7, 56.5, 55.7, 50.9, 41.7, 38.6, 37.9, 35.7, 26.2, 20.3, 15.8, 11.1; **LC-MS** (**ESI**) (**m/z**): $[M+H]^+$ calcd for $C_{60}H_{77}N_9O_{12}S$: 1148.5 found: 1148.6.

Benzyl 2-(4-{(*S*)-2-[4-(dimethylamino)benzoyl]-21-((2*S*,4*R*)-4-hydroxy-2-{[4-(4-methylthiazol-5-yl)benzyl]carbamoyl}pyrrolidine-1-carbonyl)-22,22-dimethyl-4,19-dioxo-8,11,14,17-tetraoxa-2,5,20-triazatricosyl}benzoyl)-1-propylhydrazine-1-carboxylate trifluoroacetate (**Cbz-23**)

Synthesized according to **General Procedure II**.

Starting from compound **9** (0.129 mg 0.169 mmol, 1.73 eq.) and 4 M HCl in 1,4-dioxane (0.430 mL, 1.69 mmol, 17.3 eq.), compound **Cbz-23** (47.3 mg, 45.6 µmol, 47%) was isolated as a white lyophilisate. **^{1}H NMR** (600 MHz, DMSO-d_6) δ = 10.73 – 10.60 (m, 1H), 8.99 (s, 1H), 8.57 (t, *J* = 6.1 Hz, 1H), 8.01 (s, 1H), 7.89 – 7.77 (m, 2H), 7.42 – 7.37 (m, 7H), 7.37 – 7.31 (m, 6H), 7.30 (d, *J* = 4.8 Hz, 2H), 7.26 (s, 1H), 6.70 (d, *J* = 8.3 Hz, 2H), 5.13 (d, *J* = 44.5 Hz, 2H), 4.68 – 4.61 (m, 2H), 4.56 (d, *J* = 9.5 Hz, 1H), 4.45 (t, *J* = 8.2 Hz, 1H), 4.42 – 4.33 (m, 2H), 4.29 – 4.22 (m, 1H), 3.96 (s, 2H), 3.84 (s, 2H), 3.70 – 3.63 (m, 1H), 3.63 – 3.61 (m, 1H), 3.62 – 3.56 (m, 3H), 3.57 (s, 1H), 3.56 – 3.52 (m, 2H), 3.54 – 3.50 (m, 2H), 3.51 – 3.45 (m, 4H), 3.40 (t, *J* = 5.9 Hz, 2H), 3.23 (q, *J* = 5.7 Hz, 2H), 2.93 (s, 6H), 2.44 (s, 3H), 2.08 – 2.03 (m, 1H), 1.93 – 1.88 (m, 1H), 1.55 (h, *J* = 7.3 Hz, 2H), 0.98 – 0.85 (m, 12H); **^{13}C NMR** (151 MHz, DMSO-d_6) δ = 171.7, 171.6, 171.3, 169.5, 169.1, 168.6, 168.5, 168.1, 167.8, 165.3, 158.3 (q, *J* = 37.7 Hz), 155.7, 151.5, 151.1, 147.6, 141.7, 139.5, 136.6, 131.2, 129.6, 128.9, 128.7, 128.6, 128.4, 128.2, 127.9, 127.8, 127.7, 127.6, 127.5, 127.0, 115.3 (q, *J* = 289.6 Hz), 111.2, 70.4, 69.8, 69.8, 69.7, 69.6, 69.5, 69.0, 68.8, 66.9, 66.5, 58.7, 56.5, 55.7, 50.9, 41.7, 38.6, 37.9, 36.1, 35.7, 26.2, 20.7, 20.3, 15.8, 11.1; **LC-MS** (**ESI**) (**m/z**): $[M+H]^+$ calcd for $C_{62}H_{81}N_9O_{13}S$: 1193.4 found: 1193.1.

Benzyl 2-(4-{[4-(dimethylamino)-*N*-(2-{[(1-{(*S*)-17-[(2*S*,4*R*)-4-hydroxy-2-{[4-(4-methylthiazol-5-yl)benzyl]carbamoyl}pyrrolidine-1-carbonyl]-18,18-dimethyl-15-oxo-3,6,9,12-tetraoxa-16-azanonadecyl}-1H-1,2,3-triazol-4-yl)methyl]amino}-2-oxoethyl)benzamido]methyl}benzoyl)-1-propylhydrazine-1-carboxylate trifluoroacetate (**Cbz-24**)

Compound **10** (78.8 mg, 0.112 mmol, 1.30 eq.) was dissolved in DMF (0.5 mL). It was diluted with H_2O/*tert*-butanol (4.3 mL *v*/*v*, 1/1). Subsequently, compound **19** (50.0 mg, 82.7 µmol, 1.00 eq.) in DMF (0.5 mL), TBTA (9.2 mg, 17 µmol, 0.2 eq.) in DMF (0.5 mL), 0.1 M $CuSO_4$ (0.171 mL, 17.1 µmol, 0.2 eq), and 0.1 M ascorbic acid (0.171 mL, 17.1 µmol, 0.2 eq) was added and stirred for 1 h at room temperature. The solvent was removed under reduced pressure and the oily residue purified by preparative HPLC. The target compound **Cbz-24** (55.2 mg, 39.4 µmol, 46%) was isolated as a white lyophilisate. **^{1}H NMR** (600 MHz, DMSO-d_6) δ = 10.68 (m, 1H), 9.00 (s, 1H), 8.54 (t, *J* = 6.1 Hz, 1H), 8.46 (s, 1H), 7.90 – 7.89 (m, 1H), 7.88 (s, 1H), 7.83 (d, *J* = 8.3 Hz, 2H), 7.45 – 7.36 (m, 7H), 7.36 – 7.24 (m, 6H), 6.69 (d, *J* = 8.4 Hz, 2H), 5.16 (s, 1H), 5.09 (s, 1H), 4.67 (s, 2H), 4.55 (d, *J* = 9.4 Hz, 1H), 4.50 (t, *J* = 5.3 Hz, 2H), 4.46 – 4.40 (m, 2H), 4.34 (t, *J* = 5.2 Hz, 3H), 4.22 (m 1H), 3.87 (s, 2H), 3.80 (t, *J* = 5.3 Hz, 2H), 3.69 – 3.54 (m, 4H), 3.51 (dd, *J* = 5.9, 3.4 Hz, 2H), 3.48 – 3.43 (m, 10H), 2.93 (s, 6H), 2.54 (m, 1H), 2.44 (s, 3H), 2.39 – 2.32 (m, 1H), 2.10 – 1.99 (m, 1H), 1.96 – 1.86 (m, 1H), 1.55 (h, *J* = 7.3 Hz, 2H), 0.93 (s, 12H); **^{13}C NMR** (151 MHz, DMSO-d_6) δ = 171.9, 171.6, 169.9, 169.5, 168.1, 165.3, 158.3 (q, *J* = 38.0 Hz), 155.7, 151.5, 151.0, 147.5, 141.7, 139.5, 136.6, 131.2, 131.1, 129.6, 128.8, 128.6, 128.6, 128.4, 128.2, 128.0, 127.7, 127.6, 127.4, 127.0, 123.2, 115.2 (d, *J* = 288.6 Hz), 111.3, 69.7, 69.7, 69.6, 69.5, 69.4, 68.9, 68.8, 66.9, 66.5, 62.5, 58.7, 56.3, 50.9, 49.3, 41.7, 37.9, 35.7, 35.3, 34.2, 26.3, 20.7, 20.3, 15.8, 13.8, 11.1; **LC-MS** (**ESI**) (**m/z**): $[M+H]^+$ calcd for $C_{66}H_{86}N_{12}O_{13}S$: 1287.6 found: 1287.6.

Benzyl 2-[4-({4-(dimethylamino)-*N*-[2-({[1-(6-{[(*S*)-1-((2*S*,4*R*)-4-hydroxy-2-{[4-(4-methylthiazol-5-yl)benzyl]carbamoyl}pyrrolidin-1-yl)-3,3-dimethyl-1-oxobutan-2-yl]amino}-6-oxohexyl)-1H-1,2,3-triazol-4-yl]methyl}amino)-2-oxoethyl]benzamido}methyl)benzoyl]-1-propylhydrazine-1-carboxylate (**Cbz-25**)

Compound **11** (38.8 mg, 68.2 µmol, 1.00 eq.) was dissolved in DMF (0.3 mL). It was diluted with H_2O/*tert*-butanol (3.4 mL *v*/*v*, 1/1). Subsequently, compound **19** (40.0 mg, 68.2 µmol, 1.00 eq.) in DMF (0.3 mL), TBTA (7.2 mg, 14 µmol, 0.2 eq.) in DMF (0.3 mL), 0.1 M $CuSO_4$ (0.136 mL, 13.6 µmol, 0.2 eq), and 0.1 M ascorbic acid (0.136 mL, 13.6 µmol, 0.2 eq) was added and stirred for 1 h at room temperature. The solvent was removed under reduced pressure and the oily residue purified by preparative HPLC. The target compound **Cbz-25** (32.8 mg, 25.9 µmol, 38%) was isolated as a white lyophilisate. **^{1}H NMR** (600 MHz, DMSO-d_6) δ = 10.75 – 10.60 (m, 1H), 8.99 (s, 1H), 8.54 (t, *J* = 6.1 Hz, 1H), 8.45 (s, 1H), 7.90 (s, 1H), 7.84 (d, *J* = 9.2 Hz, 3H), 7.44 – 7.35 (m, 7H), 7.34 – 7.22 (m, 5H), 6.67 (d, *J* = 8.4 Hz, 2H), 5.16 (s, 1H), 5.09 (s, 1H), 4.67 (t, *J* = 7.2 Hz,

3H), 4.54 (d, *J* = 9.4 Hz, 1H), 4.46 – 4.40 (m, 2H), 4.37 – 4.27 (m, 5H), 4.25 – 4.19 (m, 1H), 3.87 (s, 2H), 3.70 – 3.63 (m, 2H), 3.53 – 3.42 (m, 2H), 2.93 (s, 6H), 2.44 (s, 3H), 2.27 – 2.20 (m, 1H), 2.15 – 2.09 (m, 1H), 2.06 – 2.00 (m, 1H), 1.94 – 1.88 (m, 1H), 1.79 (p, *J* = 7.3 Hz, 2H), 1.59 – 1.45 (m, 4H), 1.22 (p, *J* = 7.5 Hz, 2H), 0.97 – 0.85 (m, 12H); **^{13}C NMR** (151 MHz, DMSO-d_6) δ = 171.9, 171.7, 169.7, 168.1, 165.3, 158.3 (q, *J* = 37.8 Hz), 155.7, 151.5, 151.0, 147.6, 141.8, 139.5, 136.6, 131.2, 129.6, 128.8, 128.6, 128.6, 128.4, 128.2, 128.0, 127.9, 127.8, 127.7, 127.6, 127.4, 127.0, 122.7, 115.3 (q, *J* = 289.6 Hz), 111.2, 68.9, 66.9, 66.5, 58.7, 56.3, 51.6, 50.9, 49.2, 42.3, 41.7, 37.9, 35.2, 34.6, 34.3, 29.5, 26.4, 26.4, 25.5, 24.8, 20.3, 15.9, 11.1; **LC-MS** (**ESI**) (**m/z**): $[M+H]^+$ calcd for $C_{61}H_{76}N_{12}O_9S$: 1153.6 found: 1153.6.

(2*S*,4*R*)-1-{(*S*)-12-(*tert*-butyl)-1-[4-(dimethylamino)phenyl]-1,4,10-trioxo-2-[4-(2-propylhydrazine-1-carbonyl)benzyl]-8-oxa-2,5,11-triazatridecan-13-oyl}-4-hydroxy-*N*-[4-(4-methylthiazol-5-yl)benzyl]pyrrolidine-2-carboxamide trifluoroacetate (**20**)

Synthesized according to **General Procedure III**.

Starting from compound **Cbz-20** (33.1 mg, 28.2 µmol, 1.00 eq.), compound **20** (6.1 mg, 5.9 µmol, 21%) was isolated as a white lyophilisate. **^{1}H NMR** (600 MHz, DMSO) δ = 8.97 (s, 1H), 8.55 (t, *J* = 6.0 Hz, 1H), 7.77 (d, *J* = 8.1 Hz, 2H), 7.50 – 7.41 (m, 3H), 7.41 – 7.36 (m, 4H), 7.33 (d, *J* = 7.7 Hz, 2H), 6.68 (d, *J* = 8.4 Hz, 2H), 4.67 (s, 2H), 4.55 (d, *J* = 9.4 Hz, 1H), 4.44 (d, *J* = 8.2 Hz, 1H), 4.43 – 4.31 (m, 2H), 4.27 – 4.20 (m, 1H), 4.02 – 3.90 (m, 2H), 3.69 (d, *J* = 6.9 Hz, 2H), 3.67 – 3.64 (m, 1H), 3.60 (d, *J* = 10.8 Hz, 1H), 3.54 (t, *J* = 6.8 Hz, 2H), 3.52 – 3.47 (m, 2H), 3.34 – 3.25 (m, 2H), 2.92 (s, 6H), 2.85 – 2.78 (m, 2H), 2.61 (t, *J* = 6.8 Hz, 2H), 2.43 (s, 3H), 2.11 – 1.96 (m, 1H), 1.92 – 1.85 (m, 1H), 1.72 (p, *J* = 7.2 Hz, 2H), 0.92 – 0.87 (m, 12H**); ^{13}C NMR** (151 MHz, DMSO) δ = 171.7, 169.1, 168.5, 168.1, 158.1 (q, *J* = 36.5 Hz), 152.9, 152.2, 151.4, 151.2, 147.7, 141.4, 139.4, 131.1, 129.6, 128.8, 128.6, 128.6, 128.1, 127.4, 125.5, 122.3, 115.6 (d, *J* = 292.0 Hz), 111.0, 69.6, 69.4, 68.8, 60.9, 58.7, 56.5, 55.8, 46.9, 41.7, 38.5, 38.1, 37.9, 35.6, 33.9, 30.9, 26.2, 21.0, 15.9, 10.7; **HPLC**: t_R = 11.80 min (97.8% purity); **HR-MS** (**ESI**) (**m/z**): $[M+H]^+$ calcd for $C_{48}H_{63}N_9O_8S$: 926.4599 found: 926.4596.

(2*S*,4*R*)-1-{(*S*)-15-(*tert*-butyl)-1-[4-(dimethylamino)phenyl]-1,4,13-trioxo-2-[4-(2-propylhydrazine-1-carbonyl)benzyl]-8,11-dioxa-2,5,14-triazahexadecan-16-oyl}-4-hydroxy-*N*-[4-(4-methylthiazol-5-yl)benzyl]pyrrolidine-2-carboxamide trifluoroacetate (**21**)

Synthesized according to **General Procedure III**.

Starting from compound **Cbz-21** (37.7 mg, 30.9 µmol, 1.00 eq.), compound **21** (7.7 mg, 7.1 µmol, 23%) was isolated as a white lyophilisate.**^{1}H NMR** (600 MHz, DMSO) δ = 8.97 (s, 1H), 8.53 (t, *J* = 6.1 Hz, 1H), 7.77 (d, *J* = 8.0 Hz, 2H), 7.48 – 7.29 (m, 10H), 6.68 (d, *J* = 8.4 Hz, 2H), 4.65 (s, 3H), 4.56 (d, *J* = 9.5 Hz, 1H), 4.45 – 4.36 (m, 1H), 4.37 – 4.27 (m, 2H), 4.28 – 4.20 (m, 1H), 3.96

(d, *J* = 2.6 Hz, 2H), 3.87 (s, 2H), 3.72 – 3.64 (m, 3H), 3.63 – 3.51 (m, 6H), 3.47 – 3.42 (m, 2H), 3.31 – 3.21 (m, 2H), 2.92 (s, 6H), 2.43 (s, 3H), 2.09 – 2.02 (m, 1H), 1.94 – 1.86 (m, 1H), 1.73 (h, *J* = 7.2 Hz, 2H), 0.98 – 0.86 (m, 12H); **^{13}C NMR** (151 MHz, DMSO) δ = 171.6, 171.6, 169.2, 168.6, 158.2 (q, *J* = 37.2 Hz), 152.9, 152.2, 151.4, 151.1, 147.7, 141.4, 139.4, 131.1, 129.7, 128.8, 128.6, 128.1, 127.4, 125.5, 122.4, 115.4 (q, *J* = 290.3 Hz), 111.1, 70.4, 69.5, 69.4, 69.1, 68.8, 58.7, 56.5, 55.7, 46.9, 41.6, 38.6, 38.1, 37.9, 36.1, 35.7, 33.9, 30.9, 26.1, 21.0, 15.9, 10.7; **HPLC**: t_R = 12.01 min (99.7% purity); **HR-MS** (**ESI**) (**m/z**): $[M+H]^+$ calcd for $C_{50}H_{67}N_9O_9S$: 970.4861 found: 970.4855.

(2*S*,4*R*)-1-{(*S*)-18-(*tert*-butyl)-1-[4-(dimethylamino)phenyl]-1,4,16-trioxo-2-[4-(2-propylhydrazine-1-carbonyl)benzyl]-8,11,14-trioxa-2,5,17-triazanonadecan-19-oyl}-4-hydroxy-*N*-[4-(4-methylthiazol-5-yl)benzyl]pyrrolidine-2-carboxamide trifluoroacetate (**22**)

Starting from compound **Cbz-22** (45.1 mg, 35.7 µmol, 1.00 eq.), compound **22** (2.9 mg, 2.6 µmol, 7%) was isolated as a white lyophilisate. **^{1}H NMR** (600 MHz, DMSO) δ = 8.97 (s, 1H), 8.56 (t, *J* = 6.0 Hz, 1H), 7.78 (d, *J* = 8.0 Hz, 2H), 7.48 – 7.42 (m, 2H), 7.39 (s, 5H), 7.35 – 7.31 (m, 2H), 6.68 (d, *J* = 8.4 Hz, 2H), 4.65 (s, 2H), 4.55 (d, *J* = 9.5 Hz, 1H), 4.44 (t, *J* = 8.1 Hz, 1H), 4.41 – 4.32 (m, 2H), 4.30 – 4.22 (m, 1H), 3.95 (s, 2H), 3.85 (s, 2H), 3.75 – 3.63 (m, 3H), 3.60 – 3.48 (m, 10H), 3.39 (t, *J* = 5.9 Hz, 2H), 3.22 (q, *J* = 5.7 Hz, 2H), 2.92 (s, 6H), 2.86 – 2.78 (m, 1H), 2.61 (t, *J* = 6.8 Hz, 1H), 2.43 (s, 3H), 2.10 – 1.96 (m, 2H), 1.93 – 1.86 (m, 1H), 1.73 (h, *J* = 7.2 Hz, 2H), 0.95 – 0.88 (m, 12H); **^{13}C NMR** (151 MHz, DMSO) δ = 171.7, 169.1, 168.5, 158.0 (d, *J* = 35.4 Hz), 152.9, 152.2, 151.4, 151.2, 147.7, 141.4, 139.4, 131.1, 129.6 (d, *J* = 8.2 Hz), 128.8, 128.6, 128.1, 127.4, 125.5, 122.4, 111.0, 70.4, 69.8, 69.6, 69.6, 69.0, 68.8, 60.9, 58.7, 56.5, 55.7, 46.9, 41.7, 38.6, 38.1, 37.9, 36.1, 35.7, 35.1, 33.9, 30.9, 26.1, 25.1, 22.0, 21.0, 15.9, 13.9, 10.7; **HPLC**: t_R = 12.01 min (95.0% purity); **HR-MS** (**ESI**) (**m/z**): $[M+H]^+$ calcd for $C_{52}H_{71}N_9O_{10}S$: 1014.5123 found: 1014.5119.

(2*S*,4*R*)-1-{(*S*)-21-(*tert*-butyl)-1-[4-(dimethylamino)phenyl]-1,4,19-trioxo-2-[4-(2-propylhydrazine-1-carbonyl)benzyl]-8,11,14,17-tetraoxa-2,5,20-triazadocosan-22-oyl}-4-hydroxy-*N*-[4-(4-methylthiazol-5-yl)benzyl]pyrrolidine-2-carboxamide trifluoroacetate (**23**)

Synthesized according to **General Procedure III**.

Starting from compound **Cbz-23** (44.4 mg, 34.0 µmol, 1.00 eq.), compound **23** (9.1 mg, 7.8 µmol, 23%) was isolated as a white lyophilisate. **^{1}H NMR** (600 MHz, DMSO) δ = 8.97 (s, 1H), 8.56 (t, *J* = 6.1 Hz, 1H), 7.78 (d, *J* = 8.1 Hz, 2H), 7.47 – 7.42 (m, 2H), 7.42 – 7.36 (m, 5H), 7.36 – 7.29 (m, 2H), 6.68 (d, *J* = 8.4 Hz, 2H), 4.68 – 4.62 (m, 2H), 4.56 (d, *J* = 9.6 Hz, 1H), 4.44 (t, *J* = 8.2 Hz, 1H), 4.40 (d, *J* = 6.4 Hz, 0H), 4.39 – 4.33 (m, 2H), 4.27 – 4.22 (m, 1H), 3.95 (s, 2H), 3.85 (s, 2H), 3.71 – 3.65 (m, 3H), 3.63 – 3.58 (m, 3H), 3.58 – 3.48 (m, 7H), 3.48 (s, 3H), 3.39 (d, *J* = 5.8 Hz, 4H), 3.23 (q, *J* = 5.7 Hz, 2H), 2.92 (s, 6H), 2.83 – 2.79 (m, 1H), 2.61 (t, *J* = 6.8 Hz, 1H), 2.43 (s,

3H), 2.08 – 2.02 (m, 1H), 1.93 – 1.86 (m, 1H), 1.73 (h, *J* = 7.2 Hz, 2H), 0.95 – 0.88 (m, 12H); **^{13}C NMR** (151 MHz, DMSO) δ = 171.7, 169.5, 169.1, 168.6, 168.1, 167.8, 158.1 (d, *J* = 35.3 Hz), 152.9, 152.2, 151.4, 151.2, 147.7, 141.4, 139.4, 131.1, 129.7, 128.9, 128.7, 128.6, 128.1, 127.4, 125.5, 122.4, 121.9, 111.0, 70.4, 69.8, 69.8, 69.7, 69.6, 69.5, 69.0, 68.9, 67.0, 60.9, 58.7, 56.5, 55.7, 47.0, 41.7, 38.6, 38.1, 37.9, 36.1, 35.7, 33.9, 30.9, 26.2, 21.0, 15.9, 10.7; **HPLC**: t_R = 11.79 min (96.9% purity); **HR-MS** (**ESI**) (**m/z**): $[M+H]^+$ calcd for $C_{54}H_{75}N_9O_{11}S$: 1058.5385 found: 1058.5370.

(2*S*,4*R*)-1-((*S*)-17-(*tert*-butyl)-1-{4-[(2-{4-(dimethylamino)-*N*-[4-(2-propylhydrazine-1-carbonyl)benzyl]benzamido}acetamido)methyl]-1H-1,2,3-triazol-1-yl}-15-oxo-3,6,9,12-tetraoxa-16-azaoctadecan-18-oyl)-4-hydroxy-*N*-[4-(4-methylthiazol-5-yl)benzyl]pyrrolidine-2-carboxamide (**24**)

Synthesized according to **General Procedure III**.

Starting from compound **Cbz-24** (35.7 mg, 25.5 µmol, 1.00 eq.), compound **24** (4.6 mg, 4.0 µmol, 16%) was isolated as a white lyophilisate. **^{1}H NMR** (600 MHz, DMSO) δ = 8.97 (s, 1H), 8.54 (t, *J* = 6.1 Hz, 1H), 7.90 – 7.85 (m, 2H), 7.78 (d, *J* = 7.9 Hz, 2H), 7.45 (d, *J* = 8.0 Hz, 2H), 7.41 (d, *J* = 8.4 Hz, 2H), 7.38 (d, *J* = 8.4 Hz, 2H), 7.32 (d, *J* = 8.4 Hz, 2H), 6.69 – 6.61 (m, 2H), 5.11 (d, *J* = 3.6 Hz, 1H), 4.68 (s, 2H), 4.54 (d, *J* = 9.4 Hz, 1H), 4.50 (t, *J* = 5.2 Hz, 2H), 4.45 – 4.38 (m, 2H), 4.33 (d, *J* = 5.7 Hz, 2H), 4.25 – 4.18 (m, 1H), 3.88 (s, 2H), 3.80 (t, *J* = 5.3 Hz, 2H), 3.70 (t, *J* = 6.9 Hz, 2H), 3.68 – 3.64 (m, 1H), 3.63 – 3.53 (m, 3H), 3.50 (dd, *J* = 5.9, 3.4 Hz, 2H), 3.48 – 3.42 (m, 10H), 3.30 (s, 4H), 2.92 (s, 6H), 2.55 – 2.53 (m, 1H), 2.44 (s, 3H), 2.37 – 2.30 (m, 1H), 2.05 – 1.99 (m, 1H), 1.93 – 1.88 (m, 1H), 1.73 (h, *J* = 7.2 Hz, 2H), 0.94 – 0.89 (m, 12H); **^{13}C NMR** (151 MHz, DMSO) δ = 171.9, 171.7, 169.9, 169.5, 168.1, 152.9, 152.2, 151.4, 151.3, 147.7, 141.5, 139.5, 131.1, 129.6, 128.6, 127.4, 123.2, 111.0, 69.7, 69.7, 69.7, 69.6, 69.5, 69.4, 68.8, 68.8, 66.9, 58.7, 56.3, 56.3, 49.3, 47.0, 41.6, 37.9, 35.6, 35.3, 34.2, 26.3, 21.0, 15.9, 10.7; ; **HPLC**: t_R = 11.58 min (> 99.9% purity); **HR-MS** (**ESI**) (**m/z**): $[M+H]^+$ calcd for $C_{58}H_{80}N_{12}O_{11}S$: 1153.5868 found: 1153.5866.

(2*S*,4*R*)-1-[(*S*)-2-(6-{4-[(2-{4-(dimethylamino)-*N*-[4-(2-propylhydrazine-1-carbonyl)benzyl]benzamido}acetamido)methyl]-1H-1,2,3-triazol-1-yl}hexanamido)-3,3-dimethylbutanoyl]-4-hydroxy-*N*-[4-(4-methylthiazol-5-yl)benzyl]pyrrolidine-2-carboxamide (**25**)

Synthesized according to **General Procedure III**.

Starting from compound **Cbz-25** (26.9 mg, 21.2 µmol, 1.00 eq.), compound **25** (5.9 mg, 5.8 µmol, 27%) was isolated as a white lyophilisate. **^{1}H NMR** (600 MHz, DMSO) δ = 8.97 (s, 1H), 8.53 (t, *J* = 6.1 Hz, 1H), 7.90 (s, 1H), 7.83 (d, *J* = 9.4 Hz, 1H), 7.78 (d, *J* = 7.9 Hz, 2H), 7.45 (d, *J* = 8.0 Hz, 2H), 7.41 (d, *J* = 8.2 Hz, 2H), 7.38 (d, *J* = 8.3 Hz, 2H), 7.31 (d, *J* = 8.3 Hz, 2H), 6.69 – 6.59 (m,

2H), 5.11 (d, *J* = 3.6 Hz, 1H), 4.68 (s, 2H), 4.53 (d, *J* = 9.4 Hz, 1H), 4.46 – 4.39 (m, 2H), 4.32 (dt, *J* = 14.2, 8.4 Hz, 5H), 4.21 (dd, *J* = 15.8, 5.5 Hz, 1H), 3.91 – 3.85 (m, 2H), 3.70 (t, *J* = 6.9 Hz, 2H), 3.66 – 3.60 (m, 2H), 3.56 – 3.52 (m, 1H), 2.92 (s, 6H), 2.84 – 2.79 (m, 1H), 2.63 – 2.58 (m, 1H), 2.44 (s, 3H), 2.40 – 2.34 (m, 1H), 2.28 – 2.19 (m, 1H), 2.15 – 2.07 (m, 1H), 2.06 – 1.99 (m, 1H), 1.93 – 1.87 (m, 1H), 1.79 (p, *J* = 7.3 Hz, 2H), 1.73 (p, *J* = 7.2 Hz, 2H), 1.55 – 1.43 (m, 2H), 0.94 – 0.88 (m, 12H); **^{13}C NMR** (151 MHz, DMSO) δ = 171.9, 171.7, 169.7, 168.1, 153.0, 152.2, 151.4, 151.3, 147.7, 141.5, 139.5, 131.1, 129.6, 128.6, 127.4, 125.6, 122.7, 110.9, 68.8, 60.9, 58.7, 56.3, 49.2, 47.0, 41.7, 38.1, 38.0, 35.2, 34.6, 33.9, 30.9, 29.5, 26.4, 25.5, 24.8, 21.0, 15.9, 10.7; **HPLC**: t_R = 11.80 min (96.2% purity); **HR-MS** (**ESI**) (**m/z**): $[M+H]^+$ calcd for $C_{53}H_{70}N_{12}O_7S$: 1019.5289 found: 1019.5292.

4.4.3 Biological Evaluation

4.4.3.1 HDAC enzyme inhibition assay

In vitro inhibitory activity against HDAC1-3 was determined as previously published.[218] In short, serial dilutions of compounds and controls were prepared in assay buffer (50 mM Tris−HCl, pH 8.0, 137 mM NaCl, 2.7 mM KCl, 1.0 mM $MgCl_2$*6 H_2O, 0.1 mg/mL BSA). 5.0 µL of these serial dilutions were transferred into OptiPlate-96 black micro-plates (PerkinElmer). Then, 25 µL assay buffer and 10 µL enzyme solution (human recombinant HDAC1 (BPS Bioscience, Catalog# 50051); HDAC2 (BPS Bioscience, Catalog# 50052); HDAC3/NcoR2 (BPS Bioscience, Catalog# 50003); HDAC6 (BPS Bioscience, Catalog# 50006) were added. Enzyme and inhibitor were preincubated at 25 °C for 60 minutes (HDAC1-3) or 15 minutes (HDAC6). Afterwards, the fluorogenic substrate ZMAL (Z-Lys(Ac)-AMC[306]; 10 µL; 75 µM in assay buffer) was added. The total assay volume (50 µL, max. 1% DMSO) was incubated at 37 °C for 90 min. Subsequently, 50 µL trypsin solution (0.4 mg/mL trypsin in buffer: 50 mM Tris−HCl, pH 8.0, 100 mM NaCl) was added, followed by additional 30 minutes of incubation at 37 °C. Fluorescence (excitation: 355 nm, emission: 460 nm) was measured using either an Ascent Fluoroskan microplate reader (Thermo Scientific) or a FLUOstar OPTIMA microplate reader (BMG LABTECH). IC_{50}-values were determined by generating normalized dose-response curves using the build-in *"log(inhibitor) vs. response (three parameters)"* equation provided by GraphPad Prism 9.0 for MacOS (GraphPad Software, San Diego, USA). All compounds were tested in duplicates, reported mean IC_{50} values, including standard deviation, are calculated from at least two independent experiments.

4.4.3.2 Cell Line and Cell Culture

The human breast cancer cell line MCF-7 was obtained from Leibnitz Institute DSMZ GmbH. The cell lines were cultivated in DMEM medium supplemented with 10% (*v*/*v*) fetal bovine serum, 2 mM L-glutamine and 50 U/mL penicillin and 50 µg/mL streptomycin and incubated at 37 °C under humidified air with 5% CO_2 to 80–90% confluency before being used in further assays.

4.4.3.3 Immunoblot

MCF-7 cells (0.7×10^6 cells/mL) were seeded to cell culture flasks and after 48 h treated with the indicated concentration of compound or vehicle (DMSO) for the given time. Cell lysis was performed with Cell Extraction Buffer (10 mM Tris, pH 7.4, 100 mM NaCl, 1 mM EDTA, 1 mM EGTA, 1 mM NaF, 20 mM $Na_4P_2O_7$, 2 mM Na_3VO_4, 1% Triton™ ×-100, 10% glycerol, 0.1% SDS, 0.5% deoxycholate; Catalog# FNN0011, Thermo Fisher Scientific Inc., Waltham, MA, USA) and addition of Halt Protease Inhibitor Cocktail (100×) (Catalog# 78429, Life Technologies GmbH, Carlsbad, CA, USA) and phenylmethanesulfonyl fluoride (Catalog# 10837091001, Sigma-Aldrich, St. Louis, MO, USA) according to manufacturer instructions. Protein content was determined by Pierce™ BCA Protein Assay Kit (Catalog# 23225, Thermo Fisher Scientific Inc., Waltham, MA, USA) according to manufacturer guidelines. Samples were denatured by Laemmli 2× Concentrate (Catalog# S3401-10VL, Sigma-Aldrich, St. Louis, MO, USA), and Precision Plus Protein Unstained Standard was used as molecular weight marker (Catalog# 1610363, Bio-Rad, Hercules, CA, USA). SDS-PAGE was performed with 10% Mini-PROTEAN TGX Stain-Free Gel (Catalog# 458035, Bio-Rad, Hercules, CA, USA) at 200 V for 50 min (Catalog# 458035, Bio-Rad). Afterwards, proteins were transferred with the Trans-Blot Turbo Transfer System (Catalog# 1704150, Bio-Rad, Hercules, CA, USA) to Immobilon-FL PVDF membranes (Catalog# IPFL00005, Millipore Merck, Burlington, MA, USA) at 1.0 A for 30 min and incubated with 5% milk-powder solution for 1 h at room temperature under slight agitation. Subsequently, the membranes were incubated with anti-HDAC1 (Catalog# 5356S, Cell Signaling Technology, Denver, MA, USA), anti-HDAC2 (Catalog# 9959S, Cell Signaling Technology, Denver, MA, USA), anti-HDAC3 (Catalog# 85057S, Cell Signaling Technology, Denver, MA, USA), anti-HDAC4 (Catalog#7628S, Cell Signaling Technology, Denver, MA, USA), anti-HDAC6 (Catalog#7558S, Cell Signaling Technology, Denver, MA, USA), or anti-GAPDH (Catalog# T0004, Affinity Biosciences, Cincinnati, OH, USA) antibody solutions in 1:1000–1:20000 dilutions at 4 °C, overnight. Incubation with HRP-conjugated secondary anti-mouse (Catalog# sc-516102, Santa Cruz, Dallas, TX, USA) and anti-rabbit (Catalog# HAF008, R&D Systems, Inc., Minneapolis, MN, USA) antibody solution was performed for 1.5 h, and membranes were developed with clarity western ECL substrate (Catalog# 1705061, Bio-Rad, Hercules, CA, USA). The ChemiDoc XRS+ System (Catalog# 1708265, Bio-Rad, Hercules, CA, USA) was used for detection and Image Lab Software 6.1 (Bio-Rad, Hercules, CA, USA) for quantification. GraphPad Prism (GraphPad Software, San Diego, CA, USA) was used for normalization, statistical analysis and bar graph creation.

Chapter 5

Photocaged Histone Deacetylase Inhibitors as Prodrugs in Targeted Cancer Therapy

Fabian B. Kraft, Maria Hanl, Felix Feller, Linda Schäker-Hübner, and Finn K. Hansen.

Pharmaceuticals **2023**, 16(3), 356.

Please refer to chapter 8.4 "Appendix IV" for the publication's full text and supporting information.

5.1 Publication Summary

HDACs represent a class of enzymes that directly influence the chromatin structure, thereby playing crucial roles in essential cellular processes such as gene transcription, cell proliferation, differentiation, and migration.[38] There are 18 human HDAC isoforms, of which eleven feature a catalytic center with a Zn^{2+}-ion. These enzymes are often overexpressed in various diseases, including cancer, inflammatory conditions, and neurodegenerative disorders, rendering them valuable targets for drug development.[93,139,186] Currently, the FDA has granted approval for four HDACi for the treatment of hematological cancers.[186] A typical HDACi molecule comprises two key components: a cap group and a ZBG, connected by a linker. Despite concerns related to mutagenicity and genotoxicity, three of the FDA-approved HDACi employ hydroxamic acids as their ZBG.[203] Moreover, all FDA approved HDACi can cause severe side effects, presumably due to off-target effects, often leading to treatment interruption.[35] One way to circumvent unwanted side effects is the selective activation of the drug in the target tissue. Light-activatable prodrugs offer the possibility to control the release of an active drug with spatio-temporal accuracy. It has been successfully utilized e.g. in photodynamic therapy to locally produce radicals and reactive oxygen species or through the introduction of a photoremovable protecting group (PPG) to a small molecule inhibitor or PROTAC.[326–328]

Since the ZBG is the main warhead of HDACi, attaching a cleavable moiety to the ZBG is a promising starting point for the design of HDACi prodrugs. In this project, two light sensitive HDACi prodrugs were developed, based on the previously published hydroxamic acid DDK137 (**I**) and the *ortho*-aminoanilide VK1 (**II**),[281,324] using a DMNB based PPG to mask the ZBG. The photocaged (pc) prodrug **pc-I** was synthesized through several steps. Initially, commercially available 6-nitroveratralaldehyde was reduced to the corresponding benzyl alcohol. The alcohol was then subjected to a *Mitsunobu* reaction with *N*-hydroxyphtalimide, resulting in the protected hydroxylamine **4**. After deprotection of the phtalimide group with hydrazine followed by subsequent amide coupling with the carboxylic acid precursor **6**, which was synthesized according

to literature,[324] the prodrug **pc-I** was obtained. Additionally, the prodrug **pc-II** was isolated after treating compound **II** with 6-nitroveratryl chloroformate (NVOC-Cl) in the presence of pyridine.

The photo-uncaging of the prodrugs **pc-I** and **pc-II** was quantified using high-performance liquid chromatography (HPLC). A solution of each prodrug in DMSO was exposed to light with a wavelength of 365 nm. After 10 minutes of irradiation, prodrug **pc-I** underwent deprotection to yield its parent inhibitor **I** in 82% conversion. On the other hand, prodrug **pc-II** decomposed upon light exposure and did not release its parent inhibitor. Therefore, the subsequent biological evaluation focused on **pc-I**. The *in vitro* inhibitory activity was assessed against HDAC1, as a member of class I, and HDAC6, as a member of class IIb. Prior to irradiation, prodrug **pc-I** exhibited low inhibitory activity against both isoforms. After irradiation with UV light, the inhibitory activity significantly increased, by 121-fold for HDAC1 and 37-fold for HDAC6, respectively. In a whole-cell HDAC inhibition assay conducted in the malignant melanoma cell line MV-3, the phototreated prodrug **pc-I** demonstrated significant inhibition of HDAC activity comparable to the parent compound **I**. In contrast, untreated prodrug **pc-I** had no observable effects on HDAC activity. Furthermore, to assess target engagement, immunoblot analysis was performed. The analysis revealed that both the light-activated prodrug **pc-I** and compound **I**, but not untreated **pc-I**, were capable of inducing hyperacetylation of acetylated α-tubulin, which serves as a marker of HDAC6 inhibition, and acetylated histone H3, a marker of HDAC1-3 inhibition. In MTT cell viability assays in MV-3 cells and ovarian cancer A2780 cells, irradiated **pc-I** showed pronounced antiproliferative activities. Not activated **pc-I** exhibited less than 25% viability reduction at 25 µM in both cell lines, confirming its inactivity in a cellular environment. Moreover, apoptosis analysis revealed that treatment with activated **pc-I** and compound **I** led to a significant increase in early and late apoptotic cells in a caspase 3/7-dependent fashion.

In summary, two light activatable prodrugs of previously published HDACi were synthesized. Prodrug **pc-I** was further evaluated for its biological properties and capability to selectively release the parent inhibitor. The compound demonstrated promise for the further development of light-activatable HDACi prodrugs, with the potential to minimize unwanted side effects.

5.2 Author Contribution

Fabian B. Kraft: Study design, synthesis and characterization of all compounds except compound **II**, data analysis and paper writing with input from all authors.

Maria Hanl: MTT, apoptosis, and Caspase-Glo 3/7 assays.

Felix Feller: Whole-cell HDAC inhibition assays and immunoblot experiments.

Linda Schäker-Hübner: Synthesis of compound **II**, biochemical HDAC inhibition assays.

Finn K. Hansen: Study design, data analysis, and supervision.

6 Summary

In 2020, the World Health Organization reported 19.3 million new cases of cancer worldwide, establishing it as a leading cause of death in 112 out of 183 countries.[1] The understanding that both genetic and epigenetic alterations play a pivotal role in tumorigenesis is now well established. Mutations in genes encoding for proteins, which directly regulate the epigenome are particularly common and have a significant impact on cellular processes such as apoptosis, proliferation, and DNA repair.[11,12] HDACs are epigenetic "erasers", which modulate histone and non-histone proteins by removing acyl-groups of ε-*N*-lysine moieties.[23,35] There are 18 human HDAC isoforms,[40] which vary in shape, size, and substrate specificity. Depending on the isoform, they influence processes like stem cell development, cytoskeleton dynamics, and protein homeostasis.[50,127,128] The extensive impact of HDACs coupled with their overexpression or malfunction in several diseases strongly implicates HDACs as valuable targets for drug development. HDACi offer the possibility to reverse aberrant transcription of genes and restore normal cellular functions. Notably, several experimental and approved HDACi have demonstrated anticancer properties or are currently under investigation as possible anti-inflammatory drugs, as well as a potential treatment for neurodegenerative disorders.[38] Currently, the FDA has approved four non-selective HDACi for the treatment of hematological cancers.[38] However, all FDA-approved HDACi are known to cause severe side effects, including but not limited to low blood cell count, nausea, and fatigue, often leading to treatment interruption.[200–202] In contrast, the development of more isoform selective HDACi holds the promise of reducing these side effects and offering improved therapeutic efficacy with fewer adverse consequences. For instance, the antiproliferative activities of non-selective HDACi are primarily attributed to the inhibition of the class I HDAC isoforms HDAC1, 2, and 3, while the inhibition of HDAC6 fails to show anticancer properties in monotherapy, but potentially influences inflammatory processes.[38,154] In addition to more selective inhibitors, the utilization of prodrugs may also present an opportunity for more effective and safe therapeutic interventions: Hydroxamic acids, the most common ZBG among HDACi, are associated with mutagenicity and chromosomal aberrations. Since the ZBG as the central warhead of HDACi is crucial for target binding, masking the ZBG can attenuate the toxicity of the inhibitor until the parent drug is selectively released in the target tissue. Various approaches for HDACi prodrugs have been explored, e.g. activation under typical tumor conditions like hypoxia or through external stimulation like light with a specific wavelength.[246,248]

The first project (chapter 2) focused on HDAC6, a cytoplasmic enzyme known for acting on non-histone proteins. Despite its role in cancer, HDAC6 inhibitors often show limited efficacy in monotherapy, thereby prompting the pursuit of selective HDAC6 inhibitors for reduced cytotoxic effects and broader therapeutic applications outside of oncology. Based on the crystal structure of the previously published inhibitor **MAIP-032** in complex with the CD2 of HDAC6 from *Danio rerio* (PDB: 6CGP)[239], docking studies were performed to scrutinize possible additional interactions with the HDAC6 binding site, whereby the L1 loop emerged as the most promising region for further interactions. Subsequently, 13 inhibitors were synthesized, utilizing a Groebke Blackburn Bienaymé (GBB) three-component reaction as the key step to form the imidazo[1,2-*a*]pyridine core.

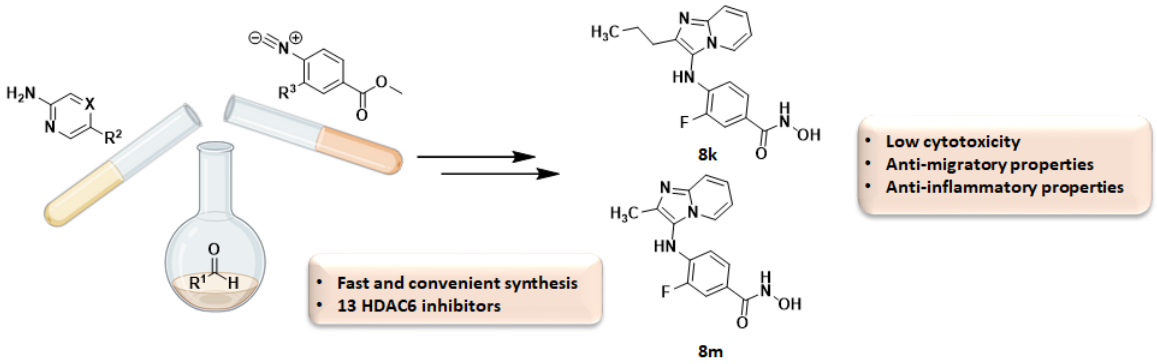


Figure 27. Basic approach and results of the project presented in chapter 2. Figure created with BioRender.com

The subsequent biochemical HDAC inhibition assays led to the identification of the compounds **8k** (HDAC1 IC_{50}: 5.87 µM; HDAC6 IC_{50}: 0.024 µM; $SF^{1/6}$: 245) and **8m** (HDAC1 IC_{50}: 3.07 µM; HDAC6 IC_{50}: 0.026 µM; $SF^{1/6}$: 118) as the most potent and selective HDAC6 inhibitors, surpassing **MAIP-032** both in its inhibitory potency and selectivity over HDAC1. Cellular target engagement analysis in U-87 MG glioblastoma cells confirmed HDAC6 selectivity through α-tubulin hyperacetylation without affecting histone H3 acetylation up to 10 µM. Additionally, anti-cancer properties were assessed in U-87 MG cells, revealing that the inhibitors **8k**, **8m**, and **tubastatin** A had minimal effects on cell viability, yet compound **8m** significantly reduced cell migration.

Besides, the study explored the influence of selected HDAC6 inhibitors on the activation of the NLRP3 inflammasome. Mouse J774A.1 macrophages treated with **8k**, **8m**, **MAIP-032**, and **tubastatin A** exhibited reduced nigericin-induced IL-1β release, with no effect on ATP-induced release. Human THP-1 macrophages showed no attenuation of IL-1β release by any HDAC6 inhibitor, while the NLRP3 inhibitor **MCC950** suppressed nigericin-induced IL-1β release.

Further investigations concerning the impact of HDAC6 inhibitors on the TLR-mediated priming of human THP-1 macrophages revealed that tubastatin A, **MAIP-032**, **8k**, and **8m** inhibited LPS-induced IL-1β mRNA expression and TNF release at 10 µM. Moreover, the investigation of the

inhibitory potency of the inhibitors on the LPS-induced TNF release demonstrated monophasic concentration-response curves for **tubastatin A**, **MAIP-032**, and **8m**. Interestingly, compound **8k** displayed a biphasic curve, suggesting the possibility of at least two HDAC6-mediated mechanisms contributing to the inhibition. The obtained IC_{50} values ranged from 4.96 µM to 19.6 µM, with **8k** and **8m** showing a comparable inhibitory activity as tubastatin A, but being less potent than **MAIP-032** (4.96 µM).

In summary, a set of HDAC6 selective inhibitors was synthesized. From this set, **8k** and **8m** emerged as the most potent and selective candidates. These compounds exhibit superior inhibitory activity and selectivity compared to **MAIP-032**. Furthermore, the inhibitors influenced the activation of the NLRP3 inflammasome by interfering with the TLR-mediated priming pathway, highlighting the potential of HDAC6 selective inhibitors to treat NLRP3 inflammasome driven diseases.

In the second project (chapter 3), class I HDAC selective inhibitors were developed and investigated for their anticancer properties and synergism with cisplatin. Starting from the previously published HDACi **VK1**, the ZBG was modified to achieve additional interaction with the FPU of class I HDAC enzymes. To this end, two distinct synthetic strategies were employed, both based on the Ugi multicomponent reaction, to generate peptoid-based HDACi with a substituted hydrazide moiety as the ZBG. Altogether, 11 novel HDACi were synthesized and assessed for their *in vitro* inhibitory activity against the HDAC isoforms HDAC1-4, 6, and 8.

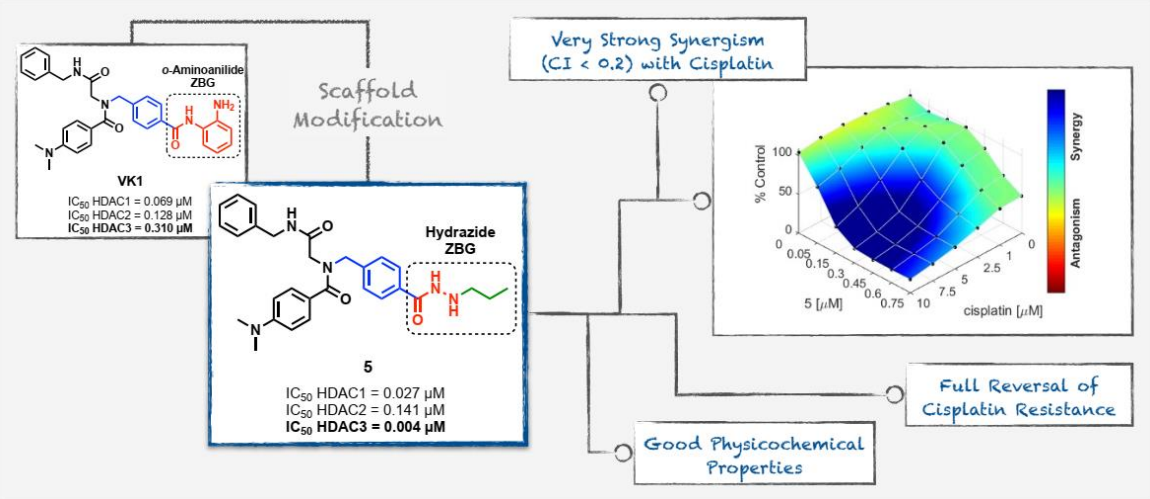


Figure 28. Basic approach and results of the project presented in chapter 3.

The two most potent inhibitors **5** (HDAC3 IC_{50}: 0.004 µM) and **6** (HDAC3 IC_{50}: 0.008 µM) containing a propyl or butyl FPU, respectively, showed low nanomolar inhibitory activity against the class I HDAC isoforms HDAC1-3, including single digit nanomolar inhibition of HDAC3. Importanty, both compounds outperformed the established class I HDACi **VK1** and **entinostat**. No

relevant inhibition of the other HDAC isoforms was observed. Additionally, compound **5** had a 17-fold improved solubility compared to **VK1**, making it potentially better suited as an anticancer agent. The following whole-cell HDAC inhibition assays and western blot analysis of hyperacetylation of α-tubulin (HDAC6 inhibition marker) and histone H3 (HDAC1-3 inhibition marker) confirmed the class I selectivity in a cellular environment. Measurement of cell viability through MTT assays demonstrated higher potency of compounds **5** and **6** compared to reference HDACi (**VK1**, **entinostat**, and **vorinostat**) in both native and cisplatin-resistant A2780 and Cal27 cancer cell lines.

Next, the potential of the hit compounds **5** and **6** to increase cisplatin cytotoxicity was evaluated. Both compounds completely reversed the cisplatin resistance in A2780CisR (ShF (compound **5**): 8.02, ShF (compound **6**): 7.24) and Cal27CisR cells (ShF (compound **5**): 18.8, ShF (compound **6**): 21.2), even leading to oversensitization of the cells against cisplatin. The ShF of compound **5** and **6** are the highest ever discovered for HDACi in this cellular resistance model.

Furthermore, both compounds were tested for synergy in combination with cisplatin. According to the Chou-Talalay model, compound **5** and **6** exhibited very strong synergistic effects (CI < 0.2) in combination cisplatin, clearly exceeding the synergism of **entinostat** and **VK1**. The observed synergy was further confirmed in apoptosis assays in Cal27/Cal27CisR cells, in which combination treatments with cisplatin resulted in a highly significant increase in apoptotic nuclei.

Caspase 3/7 activation assays demonstrated remarkable activation in A2780 and A2780CisR cells for compounds **5**, **6**, and **entinostat**, both in single and combination treatments with cisplatin. In Cal27 and Cal27CisR cells, low caspase activation was observed in single treatment, but the combination with cisplatin significantly increased caspase activation, with compounds **5** and **6** outperforming **entinostat**.

In conclusion, the developed substituted hydrazides represent highly potent class I HDAC selective inhibitors with chemosensitizing properties in cisplatin-resistant solid tumors. Compounds **5** and **6** exhibit very strong synergism with cisplatin outperforming the well-established inhibitors **entinostat** and **VK1**. Taken together, compounds **5** and **6** are promising candidates for the development of novel anticancer agents.

In the third project (chapter 4), the application of targeted protein degradation of HDACs utilizing PROTACs was explored. To this end, a small set of VHL recruiting HDAC degrading PROTACs was synthesized. The synthesis of VHL ligands, as described in literature,[325] remains troublesome. To address these challenges, the synthesis was optimized to enhance the purification efficiency and yields, resulting in the isolation of the VHL ligand precursor **5** in 81% overall yield (lit.[325]: 14%).

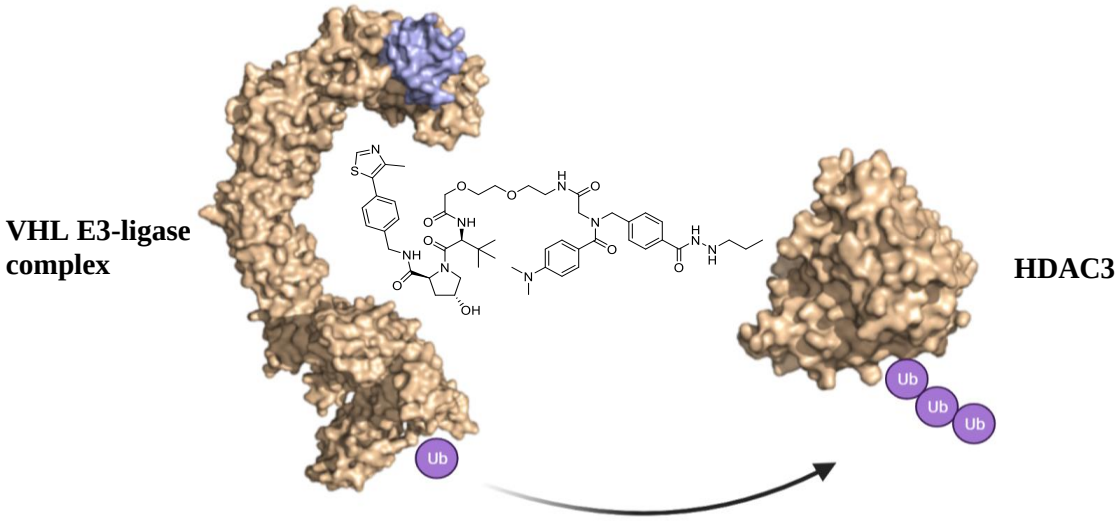


Figure 29. Basic principle of the project presented in chapter 4. Figure created with BioRender.com

Based on the in chapter 3 developed class I HDAC inhibitor **Hydrazide 5**[v], six HDAC PROTACs featuring variations in their linker structures were synthesized. Despite the low nanomolar HDAC inhibitory activity of the parent inhibitor **Hydrazide 5**, the synthesized PROTACs demonstrated only micromolar inhibition of HDAC3, while HDAC1 and 2 were unaffected. Subsequent immunoblot analysis to investigate the degradation efficacy of the PROTACs in MCF-7 cells, revealed limited degradation of HDAC2 and 3, with compound **21** emerging as the most efficient degrader of the set (HDAC2: D_{max} = 13%; HDAC3: D_{max} = 23%).

While the designed PROTACs did not exhibit potent degradation of the target proteins, compound **21** presents a promising lead structure for the further development of class I HDAC degrader. Further investigations into the optimal attachment points of both the VHL ligand and the POI ligand hold the promise of enhancing tertiary complex formation, a crucial factor for the efficient degradation of the target protein.

[v] **Hydrazide 5** is referred to compound **5** of chapter 3.

The fourth project (chapter 5) deals with the development of two light activatable HDACi prodrugs. Utilizing prodrugs represents a promising approach to circumvent unwanted side effects, while preserving therapeutic efficacy. Derived from the previously published hydroxamic acid **DDK137** (**I**) and *ortho*-aminoanilide **VK1** (**II**), the prodrugs **pc-I** and **pc-II** were synthesized through a multi-step process to incorporate a light-cleavable moiety on the ZBG of the respective inhibitors.

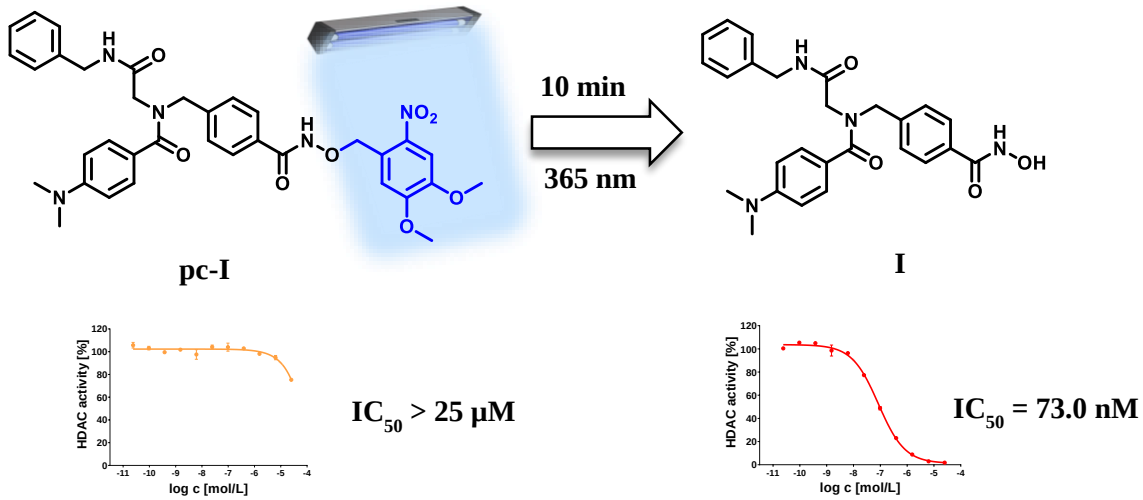


Figure 30. Basic approach and results of the project presented in chapter 5. Figure created with BioRender.com

Quantification of the photo-uncaging using analytical HPLC revealed that **pc-I** underwent deprotection after 10 min exposure to 365 nm UV light, yielding its parent inhibitor **I** in 82% conversion, while **pc-II** did not release its parent inhibitor. The subsequent *in vitro* inhibitory activity assessments against HDAC1 (class I) and HDAC6 (class IIb) showed low activity of prodrug **pc-I** before irradiation. However, after UV light exposure its inhibitory activity significantly increased by 121-fold for HDAC1 and 37-fold for HDAC6. In a whole-cell HDAC inhibition assay in the malignant melanoma cell line MV-3, phototreated **pc-I** demonstrated significant HDAC inhibitory activity (Figure 30) comparable to the parent compound **I**, while untreated **pc-I** showed no observable effects.

Furthermore, immunoblot analysis confirmed intracellular target engagement, showing that both activated **pc-I** and compound **I** increased the levels of acetylated α-tubulin (HDAC6 inhibition marker) and acetylated histone H3 (HDAC1-3 inhibition marker). Moreover, MTT cell viability assays in MV-3 cells and ovarian cancer A2780 cell line revealed pronounced antiproliferative activities for irradiated **pc-I**, while non-activated **pc-I** exhibited only minor effects on cell viability. These results further confirmed the utility of the light activatable prodrug in a cellular environment. Additionally, apoptosis assays demonstrated that activated **pc-I** and compound **I** induced a significant increase in early and late apoptotic cells in a caspase 3/7-dependent fashion.

In conclusion, in the fourth project two light-activatable HDACi prodrugs, **pc-I** and **pc-II**, derived from **DDK137** and **VK1** were developed. The prodrug **pc-I** efficiently released its parent inhibitor upon exposure to UV light at 365 nm. *In vitro* assessments showed a substantial increase in inhibitory activity for HDAC1 and HDAC6 and antiproliferative activity after exposure to UV light. To conclude, the approach of selectively releasing the parent inhibitor using light activation holds potential for reducing unwanted side effects, thereby opening avenues for the advancement of light-activatable HDACi prodrugs.

7 References

References

(1) Sung, H.; Ferlay, J.; Siegel, R. L.; Laversanne, M.; Soerjomataram, I.; Jemal, A.; Bray, F. Global Cancer Statistics 2020: GLOBOCAN Estimates of Incidence and Mortality Worldwide for 36 Cancers in 185 Countries. *CA-Cancer J. Clin.* **2021**, *71* (3), 209-249. DOI: 10.3322/caac.21660.

(2) Cancer.Net. *Types of Oncologists*. https://www.cancer.net/navigating-cancer-care/cancer-basics/cancer-care-team/types-oncologists (accessed 2023-06-06).

(3) Hanahan, D.; Weinberg, R. A. Hallmarks of cancer: the next generation. *Cell* **2011**, *144* (5), 646-674. DOI: 10.1016/j.cell.2011.02.013.

(4) Baudino, T. A. Targeted Cancer Therapy: The Next Generation of Cancer Treatment. *Curr. Drug Discov. Technol.* **2015**, *12* (1), 3–20. DOI: 10.2174/1570163812666150602144310.

(5) Strebhardt, K.; Ullrich, A. Paul Ehrlich's magic bullet concept: 100 years of progress. *Nat. Rev. Cancer* **2008**, *8* (6), 473–480. DOI: 10.1038/nrc2394.

(6) National Cancer Institute. *Targeted Therapy for Cancer*. https://www.cancer.gov/about-cancer/treatment/types/targeted-therapies (accessed 2023-06-07).

(7) Druker, B. J.; Tamura, S.; Buchdunger, E.; Ohno, S.; Segal, G. M.; Fanning, S.; Zimmermann, J.; Lydon, N. B. Effects of a selective inhibitor of the Abl tyrosine kinase on the growth of Bcr-Abl positive cells. *Nat. Med.* **1996**, *2* (5), 561–566. DOI: 10.1038/nm0596-561.

(8) Bonvini, P.; Zorzi, E.; Basso, G.; Rosolen, A. Bortezomib-mediated 26S proteasome inhibition causes cell-cycle arrest and induces apoptosis in CD-30+ anaplastic large cell lymphoma. *Leukemia* **2007**, *21* (4), 838–842. DOI: 10.1038/sj.leu.2404528.

(9) Piechotta, V.; Jakob, T.; Langer, P.; Monsef, I.; Scheid, C.; Estcourt, L. J.; Ocheni, S.; Theurich, S.; Kuhr, K.; Scheckel, B.; Adams, A.; Skoetz, N. Multiple drug combinations of bortezomib, lenalidomide, and thalidomide for first-line treatment in adults with transplant-ineligible multiple myeloma: a network meta-analysis. *Cochrane Database Syst. Rev.* **2019**, *2019* (11), CD013487. DOI: 10.1002/14651858.CD013487.

(10) National Cancer Institute. *Tamoxifen Citrate*. https://www.cancer.gov/about-cancer/treatment/drugs/tamoxifencitrate (accessed 2023-06-07).

(11) Halaburkova, A.; Cahais, V.; Novoloaca, A.; Da Araujo, M. G. S.; Khoueiry, R.; Ghantous, A.; Herceg, Z. Pan-cancer multi-omics analysis and orthogonal experimental assessment of epigenetic driver genes. *Genome Res.* **2020**, *30* (10), 1517–1532. DOI: 10.1101/gr.268292.120.

(12) Plass, C.; Pfister, S. M.; Lindroth, A. M.; Bogatyrova, O.; Claus, R.; Lichter, P. Mutations in regulators of the epigenome and their connections to global chromatin patterns in cancer. *Nat. Rev. Genet.* **2013**, *14* (11), 765–780. DOI: 10.1038/nrg3554.

(13) Cheng, Y.; He, C.; Wang, M.; Ma, X.; Mo, F.; Yang, S.; Han, J.; Wei, X. Targeting epigenetic regulators for cancer therapy: mechanisms and advances in clinical trials. *Sig. Transduct Target Ther.* **2019**, *Dec*, 17:14:62. DOI: 10.1038/s41392-019-0095-0.

(14) Berger, S. L.; Kouzarides, T.; Shiekhattar, R.; Shilatifard, A. An operational definition of epigenetics. *Genes Dev.* **2009**, *23* (7), 781–783. DOI: 10.1101/gad.1787609.

(15) Carter, B.; Zhao, K. The epigenetic basis of cellular heterogeneity. *Nat. Rev. Genet.* **2021**, *22* (4), 235–250. DOI: 10.1038/s41576-020-00300-0.

(16) Bradbury, E. M. K. E. Van Holde. Chromatin. Series in molecular biology. Springer-Verlag, New York. 1988. 530 pp. *J. Mol. Recognit.* **1989**, *2* (3). DOI: 10.1002/jmr.300020308.

(17) Annunziato, A. *DNA Packaging: Nucleosomes and Chromatin.* https://www.nature.com/scitable/topicpage/dna-packaging-nucleosomes-and-chromatin-310/ (accessed 2023-06-12).

(18) Klemm, S. L.; Shipony, Z.; Greenleaf, W. J. Chromatin accessibility and the regulatory epigenome. *Nat. Rev. Genet.* **2019**, *20* (4), 207–220. DOI: 10.1038/s41576-018-0089-8.

(19) Cramer, P. Organization and regulation of gene transcription. *Nature* **2019**, *573* (7772), 45–54. DOI: 10.1038/s41586-019-1517-4.

(20) Shen, L.; Waterland, R. A. Methods of DNA methylation analysis. *Curr. Opin. Clin. Nutr. Metab. Care* **2007**, *10* (5), 576–581. DOI: 10.1097/MCO.0b013e3282bf6f43.

(21) Bannister, A. J.; Kouzarides, T. Regulation of chromatin by histone modifications. *Cell Res.* **2011**, *21* (3), 381–395. DOI: 10.1038/cr.2011.22.

(22) Dai, Z.; Ramesh, V.; Locasale, J. W. The evolving metabolic landscape of chromatin biology and epigenetics. *Nat. Rev. Genet.* **2020**, *21* (12), 737–753. DOI: 10.1038/s41576-020-0270-8.

(23) Arrowsmith, C. H.; Bountra, C.; Fish, P. V.; Lee, K.; Schapira, M. Epigenetic protein families: a new frontier for drug discovery. *Nat. Rev. Drug. Discov.* **2012**, *11* (5), 384–400. DOI: 10.1038/nrd3674.

(24) Allis, C. D.; Jenuwein, T. The molecular hallmarks of epigenetic control. *Nat. Rev. Genet.* **2016**, *17* (8), 487-500. DOI: 10.1038/nrg.2016.59.

(25) Baylin, S. B.; Jones, P. A. A decade of exploring the cancer epigenome - biological and translational implications. *Nat. Rev. Cancer* **2011**, *11* (10), 726–734. DOI: 10.1038/nrc3130.

(26) Gaudet, F.; Hodgson, J. G.; Eden, A.; Jackson-Grusby, L.; Dausman, J.; Gray, J. W.; Leonhardt, H.; Jaenisch, R. Induction of tumors in mice by genomic hypomethylation. *Science* **2003**, *300* (5618), 489–492. DOI: 10.1126/science.1083558.

(27) Tekel, S. J.; Haynes, K. A. Molecular structures guide the engineering of chromatin. *Nucleic Acids Res.* **2017**, *45* (13), 7555-7570. DOI: 10.1093/nar/gkx531.

(28) Tan, M.; Luo, H.; Lee, S.; Jin, F.; Yang, J. S.; Montellier, E.; Buchou, T.; Cheng, Z.; Rousseaux, S.; Rajagopal, N.; Lu, Z.; Ye, Z.; Zhu, Q.; Wysocka, J.; Ye, Y.; Khochbin, S.; Ren,

B.; Zhao, Y. Identification of 67 histone marks and histone lysine crotonylation as a new type of histone modification. *Cell* **2011**, *146* (6), 1016–1028. DOI: 10.1016/j.cell.2011.08.008.

(29) Oki, M.; Aihara, H.; Ito, T. Role of histone phosphorylation in chromatin dynamics and its implications in diseases. *Subcell Biochem* **2007**, *41*, 319–336.

(30) Dawson, M. A.; Bannister, A. J.; Göttgens, B.; Foster, S. D.; Bartke, T.; Green, A. R.; Kouzarides, T. JAK2 phosphorylates histone H3Y41 and excludes HP1alpha from chromatin. *Nature* **2009**, *461* (7265), 819–822. DOI: 10.1038/nature08448.

(31) Sanderson, S. M.; Gao, X.; Dai, Z.; Locasale, J. W. Methionine metabolism in health and cancer: a nexus of diet and precision medicine. *Nat. Rev. Cancer* **2019**, *19* (11), 625–637. DOI: 10.1038/s41568-019-0187-8.

(32) Black, J. C.; van Rechem, C.; Whetstine, J. R. Histone lysine methylation dynamics: establishment, regulation, and biological impact. *Mol. Cell* **2012**, *48* (4), 491–507. DOI: 10.1016/j.molcel.2012.11.006.

(33) Litt, M.; Qiu, Y.; Huang, S. Histone arginine methylations: their roles in chromatin dynamics and transcriptional regulation. *Biosci. Rep.* **2009**, *29* (2), 131–141. DOI: 10.1042/BSR20080176.

(34) Hyun, K.; Jeon, J.; Park, K.; Kim, J. Writing, erasing and reading histone lysine methylations. *Exp. Mol. Med* **2017**, *49* (4), e324. DOI: 10.1038/emm.2017.11.

(35) Roche, J.; Bertrand, P. Inside HDACs with more selective HDAC inhibitors. *Eur. J. Med. Chem.* **2016**, *121*, 451-483. DOI: 10.1016/j.ejmech.2016.05.047.

(36) Allfrey, G.; Faulkner R.; Mirsky, A. E. Acetylation and methylation of histones and their possible role in the regulation of RNA synthesis. *Proc. Natl. Acad. Sci. USA* **1964**, *51* (5), 786–794. DOI: 10.1073/pnas.51.5.786.

(37) Taunton, J.; Hassig, C. A.; Schreiber, S. L. A mammalian histone deacetylase related to the yeast transcriptional regulator Rpd3p. *Science* **1996**, *272* (5260), 408–411. DOI: 10.1126/science.272.5260.408.

(38) Ho, T. C. S.; Chan, A. H. Y.; Ganesan, A. Thirty Years of HDAC Inhibitors: 2020 Insight and Hindsight. *J. Med. Chem.* **2020**, *63* (21), 12460–12484. DOI: 10.1021/acs.jmedchem.0c00830.

(39) Leipe, D. D.; Landsman, D. Histone deacetylases, acetoin utilization proteins and acetylpolyamine amidohydrolases are members of an ancient protein superfamily. *Nucleic Acids Res.* **1997**, *25* (18), 3693–3697. DOI: 10.1093/nar/25.18.3693.

(40) Park, S.-Y.; Kim, J.-S. A short guide to histone deacetylases including recent progress on class II enzymes. *EMM* **2020**, *52* (2), 204-212. DOI: 10.1038/s12276-020-0382-4.

(41) Yoshida, M.; Kudo, N.; Kosono, S.; Ito, A. Chemical and structural biology of protein lysine deacetylases. *Proc. Jpn. Acad. Ser. B Phys. Biol. Sci.* **2017**, *93* (5), 297–321. DOI: 10.2183/pjab.93.019.

(42) Jiang, Y.; Liu, J.; Di Chen; Yan, L.; Zheng, W. Sirtuin Inhibition: Strategies, Inhibitors, and Therapeutic Potential. *Trends Pharmacol. Sci.* **2017**, *38* (5), 459–472. DOI: 10.1016/j.tips.2017.01.009.

(43) Li, G.; Tian, Y.; Zhu, W.-G. The Roles of Histone Deacetylases and Their Inhibitors in Cancer Therapy. *Front. Cell Dev. Biol.* **2020**, *8*, 576946. DOI: 10.3389/fcell.2020.576946.

(44) Kugel, S.; Sebastián, C.; Fitamant, J.; Ross, K. N.; Saha, S. K.; Jain, E.; Gladden, A.; Arora, K. S.; Kato, Y.; Rivera, M. N.; Ramaswamy, S.; Sadreyev, R. I.; Goren, A.; Deshpande, V.; Bardeesy, N.; Mostoslavsky, R. SIRT6 Suppresses Pancreatic Cancer through Control of Lin28b. *Cell* **2016**, *165* (6), 1401–1415. DOI: 10.1016/j.cell.2016.04.033.

(45) Micelli, C.; Rastelli, G. Histone deacetylases: structural determinants of inhibitor selectivity. *Drug Discov. Today* **2015**, *20* (6), 718–735. DOI: 10.1016/j.drudis.2015.01.007.

(46) Melesina, J.; Simoben, C. V.; Praetorius, L.; Bülbül, E. F.; Robaa, D.; Sippl, W. Strategies To Design Selective Histone Deacetylase Inhibitors. *ChemMedChem* **2021**, *16* (9), 1336–1359. DOI: 10.1002/cmdc.202000934.

(47) Wagner, F. F.; Weïwer, M.; Lewis, M. C.; Holson, E. B. Small molecule inhibitors of zinc-dependent histone deacetylases. *Neurotherapeutics* **2013**, *10* (4), 589-604. DOI: 10.1007/s13311-013-0226-1.

(48) Yang, X.-J.; Seto, E. The Rpd3/Hda1 family of lysine deacetylases: from bacteria and yeast to mice and men. *Nat. Rev. Mol. Cell Biol.* **2008**, *9* (3), 206–218. DOI: 10.1038/nrm2346.

(49) Hess, L.; Moos, V.; Lauber, A. A.; Reiter, W.; Schuster, M.; Hartl, N.; Lackner, D.; Boenke, T.; Koren, A.; Guzzardo, P. M.; Gundacker, B.; Riegler, A.; Vician, P.; Miccolo, C.; Leiter, S.; Chandrasekharan, M. B.; Vcelkova, T.; Tanzer, A.; Jun, J. Q.; Bradner, J.; Brosch, G.; Hartl, M.; Bock, C.; Bürckstümmer, T.; Kubicek, S.; Chiocca, S.; Bhaskara, S.; Seiser, C. A toolbox for class I HDACs reveals isoform specific roles in gene regulation and protein acetylation. *PLoS genetics* **2022**, *18* (8), e1010376. DOI: 10.1371/journal.pgen.1010376.

(50) Milazzo, G.; Mercatelli, D.; Di Muzio, G.; Triboli, L.; Rosa, P. de; Perini, G.; Giorgi, F. M. Histone Deacetylases (HDACs): Evolution, Specificity, Role in Transcriptional Complexes, and Pharmacological Actionability. *Genes* **2020**, *11* (5), 556. DOI: 10.3390/genes11050556.

(51) Ito, A.; Kawaguchi, Y.; Lai, C.-H.; Kovacs, J. J.; Higashimoto, Y.; Appella, E.; Yao, T.-P. MDM2-HDAC1-mediated deacetylation of p53 is required for its degradation. *EMBO J.* **2002**, *21* (22), 6236–6245. DOI: 10.1093/emboj/cdf616.

(52) Nalawansha, D. A.; Pflum, M. K. H. LSD1 Substrate Binding and Gene Expression Are Affected by HDAC1-Mediated Deacetylation. *ACS Chem. Biol.* **2017**, *12* (1), 254–264. DOI: 10.1021/acschembio.6b00776.

(53) Yao, Y. L.; Yang, W. M.; Seto, E. Regulation of transcription factor YY1 by acetylation and deacetylation. *Mol. Cell. Biol.* **2001**, *21* (17), 5979–5991. DOI: 10.1128/MCB.21.17.5979-5991.2001.

(54) Millard, C. J.; Watson, P. J.; Fairall, L.; Schwabe, J. W. R. Targeting Class I Histone Deacetylases in a "Complex" Environment. *Trends Pharmacol. Sci.* **2017**, *38* (4), 363–377. DOI: 10.1016/j.tips.2016.12.006.

(55) Lai, A. Y.; Wade, P. A. Cancer biology and NuRD: a multifaceted chromatin remodelling complex. *Nat. Rev. Cancer* **2011**, *11* (8), 588–596. DOI: 10.1038/nrc3091.

(56) Allen, H. F.; Wade, P. A.; Kutateladze, T. G. The NuRD architecture. *Cell. Mol. Life Sci.* **2013**, *70* (19), 3513–3524. DOI: 10.1007/s00018-012-1256-2.

(57) Millard, C. J.; Varma, N.; Saleh, A.; Morris, K.; Watson, P. J.; Bottrill, A. R.; Fairall, L.; Smith, C. J.; Schwabe, J. W. R. The structure of the core NuRD repression complex provides insights into its interaction with chromatin. *eLife* **2016**, *5*, e13941. DOI: 10.7554/eLife.13941.

(58) Watson, P. J.; Millard, C. J.; Riley, A. M.; Robertson, N. S.; Wright, L. C.; Godage, H. Y.; Cowley, S. M.; Jamieson, A. G.; Potter, B. V. L.; Schwabe, J. W. R. Insights into the activation mechanism of class I HDAC complexes by inositol phosphates. *Nat. Comm* **2016**, *7*, 11262. DOI: 10.1038/ncomms11262.

(59) Zhang, W.; Aubert, A.; Gomez de Segura, J. M.; Karuppasamy, M.; Basu, S.; Murthy, A. S.; Diamante, A.; Drury, T. A.; Balmer, J.; Cramard, J.; Watson, A. A.; Lando, D.; Lee, S. F.; Palayret, M.; Kloet, S. L.; Smits, A. H.; Deery, M. J.; Vermeulen, M.; Hendrich, B.; Klenerman, D.; Schaffitzel, C.; Berger, I.; Laue, E. D. The Nucleosome Remodeling and Deacetylase Complex NuRD Is Built from Preformed Catalytically Active Sub-modules. *J. Mol. Bio.* **2016**, *428* (14), 2931–2942. DOI: 10.1016/j.jmb.2016.04.025.

(60) Andrés, M. E.; Burger, C.; Peral-Rubio, M. J.; Battaglioli, E.; Anderson, M. E.; Grimes, J.; Dallman, J.; Ballas, N.; Mandel, G. CoREST: a functional corepressor required for regulation of neural-specific gene expression. *Proc. Natl. Acad. Sci. USA* **1999**, *96* (17), 9873–9878. DOI: 10.1073/pnas.96.17.9873.

(61) Kim, S.-A.; Chatterjee, N.; Jennings, M. J.; Bartholomew, B.; Tan, S. Extranucleosomal DNA enhances the activity of the LSD1/CoREST histone demethylase complex. *Nucleic Acids Res.* **2015**, *43* (10), 4868–4880. DOI: 10.1093/nar/gkv388.

(62) Yang, M.; Gocke, C. B.; Luo, X.; Borek, D.; Tomchick, D. R.; Machius, M.; Otwinowski, Z.; Yu, H. Structural basis for CoREST-dependent demethylation of nucleosomes by the human LSD1 histone demethylase. *Mol. Cell* **2006**, *23* (3), 377–387. DOI: 10.1016/j.molcel.2006.07.012.

(63) Cowley, S. M.; Iritani, B. M.; Mendrysa, S. M.; Xu, T.; Cheng, P. F.; Yada, J.; Liggitt, H. D.; Eisenman, R. N. The mSin3A chromatin-modifying complex is essential for embryogenesis and T-cell development. *Mol. Cell. Biol.* **2005**, *25* (16), 6990–7004. DOI: 10.1128/MCB.25.16.6990-7004.2005.

(64) Clark, M. D.; Marcum, R.; Graveline, R.; Chan, C. W.; Xie, T.; Chen, Z.; Ding, Y.; Zhang, Y.; Mondragón, A.; David, G.; Radhakrishnan, I. Structural insights into the assembly of the

histone deacetylase-associated Sin3L/Rpd3L corepressor complex. *Proc. Natl. Acad. Sci. USA* **2015**, *112* (28), E3669-78. DOI: 10.1073/pnas.1504021112.

(65) Wang, P.; Wang, Z.; Liu, J. Role of HDACs in normal and malignant hematopoiesis. *Mol. Cancer* **2020**, *19* (1), 5. DOI: 10.1186/s12943-019-1127-7.

(66) Kelly, R. D. W.; Cowley, S. M. The physiological roles of histone deacetylase (HDAC) 1 and 2: complex co-stars with multiple leading parts. *Biochem. Soc. Trans.* **2013**, *41* (3), 741–749. DOI: 10.1042/BST20130010.

(67) Dovey, O. M.; Foster, C. T.; Conte, N.; Edwards, S. A.; Edwards, J. M.; Singh, R.; Vassiliou, G.; Bradley, A.; Cowley, S. M. Histone deacetylase 1 and 2 are essential for normal T-cell development and genomic stability in mice. *Blood.* **2013**, *121* (8), 1335–1344. DOI: 10.1182/blood-2012-07-441949.

(68) Ma, P.; Pan, H.; Montgomery, R. L.; Olson, E. N.; Schultz, R. M. Compensatory functions of histone deacetylase 1 (HDAC1) and HDAC2 regulate transcription and apoptosis during mouse oocyte development. *Proc Natl Acad Sci USA* **2012**, *109* (8), E481-489. DOI: 10.1073/pnas.1118403109.

(69) LeBoeuf, M.; Terrell, A.; Trivedi, S.; Sinha, S.; Epstein, J. A.; Olson, E. N.; Morrisey, E. E.; Millar, S. E. Hdac1 and Hdac2 act redundantly to control p63 and p53 functions in epidermal progenitor cells. *Dev. Cell.* **2010**, *19* (6), 807–818. DOI: 10.1016/j.devcel.2010.10.015.

(70) Montgomery, R. L.; Davis, C. A.; Potthoff, M. J.; Haberland, M.; Fielitz, J.; Qi, X.; Hill, J. A.; Richardson, J. A.; Olson, E. N. Histone deacetylases 1 and 2 redundantly regulate cardiac morphogenesis, growth, and contractility. *Genes Dev.* **2007**, *21* (14), 1790–1802. DOI: 10.1101/gad.1563807.

(71) Song, J.; Noh, J. H.; Lee, J. H.; Eun, J. W.; Ahn, Y. M.; Kim, S. Y.; Lee, S. H.; Park, W. S.; Yoo, N. J.; Lee, J. Y.; Nam, S. W. Increased expression of histone deacetylase 2 is found in human gastric cancer. *APMIS* **2005**, *113* (4), 264–268. DOI: 10.1111/j.1600-0463.2005.apm_04.x.

(72) Sasaki, H.; Moriyama, S.; Nakashima, Y.; Kobayashi, Y.; Kiriyama, M.; Fukai, I.; Yamakawa, Y.; Fujii, Y. Histone deacetylase 1 mRNA expression in lung cancer. *Lung Cancer.* **2004**, *46* (2), 171–178. DOI: 10.1016/j.lungcan.2004.03.021.

(73) Giaginis, C.; Damaskos, C.; Koutsounas, I.; Zizi-Serbetzoglou, A.; Tsoukalas, N.; Patsouris, E.; Kouraklis, G.; Theocharis, S. Histone deacetylase (HDAC)-1, -2, -4 and -6 expression in human pancreatic adenocarcinoma: associations with clinicopathological parameters, tumor proliferative capacity and patients' survival. *BMC Gastroeterol* **2015**, *15*, 148. DOI: 10.1186/s12876-015-0379-y.

(74) Weichert, W.; Röske, A.; Gekeler, V.; Beckers, T.; Stephan, C.; Jung, K.; Fritzsche, F. R.; Niesporek, S.; Denkert, C.; Dietel, M.; Kristiansen, G. Histone deacetylases 1, 2 and 3 are highly

expressed in prostate cancer and HDAC2 expression is associated with shorter PSA relapse time after radical prostatectomy. *Br. J. Cancer* **2008**, *98* (3), 604–610. DOI: 10.1038/sj.bjc.6604199.
(75) Adams, H.; Fritzsche, F. R.; Dirnhofer, S.; Kristiansen, G.; Tzankov, A. Class I histone deacetylases 1, 2 and 3 are highly expressed in classical Hodgkin's lymphoma. *Expert Opin. Ther. Targets* **2010**, *14* (6), 577–584. DOI: 10.1517/14728221003796609.
(76) Barneda-Zahonero, B.; Parra, M. Histone deacetylases and cancer. *Mol. Oncol* **2012**, *6* (6), 579–589. DOI: 10.1016/j.molonc.2012.07.003.
(77) Takami, Y.; Nakayama, T. N-terminal region, C-terminal region, nuclear export signal, and deacetylation activity of histone deacetylase-3 are essential for the viability of the DT40 chicken B cell line. *J. Biol. Chem.* **2000**, *275* (21), 16191–16201. DOI: 10.1074/jbc.M908066199.
(78) Escaffit, F.; Vaute, O.; Chevillard-Briet, M.; Segui, B.; Takami, Y.; Nakayama, T.; Trouche, D. Cleavage and cytoplasmic relocalization of histone deacetylase 3 are important for apoptosis progression. *Mol. Cell. Biochem.* **2007**, *27* (2), 554–567. DOI: 10.1128/MCB.00869-06.
(79) Yang, W.-M.; Tsai, S.-C.; Wen, Y.-D.; Fejer, G.; Seto, E. Functional domains of histone deacetylase-3. *J. Biol. Chem.* **2002**, *277* (11), 9447–9454. DOI: 10.1074/jbc.M105993200.
(80) Emmett, M. J.; Lazar, M. A. Integrative regulation of physiology by histone deacetylase 3. *Nat. Rev. Mol. Cell Biol.* **2019**, *20* (2), 102-115. DOI: 10.1038/s41580-018-0076-0.
(81) Oberoi, J.; Fairall, L.; Watson, P. J.; Yang, J.-C.; Czimmerer, Z.; Kampmann, T.; Goult, B. T.; Greenwood, J. A.; Gooch, J. T.; Kallenberger, B. C.; Nagy, L.; Neuhaus, D.; Schwabe, J. W. R. Structural basis for the assembly of the SMRT/NCoR core transcriptional repression machinery. *Nat. Struct. Mol. Biol.* **2011**, *18* (2), 177–184. DOI: 10.1038/nsmb.1983.
(82) Ishizuka, T.; Lazar, M. A. The nuclear receptor corepressor deacetylase activating domain is essential for repression by thyroid hormone receptor. *Mol. Endocrinol.* **2005**, *19* (6), 1443–1451. DOI: 10.1210/me.2005-0009.
(83) Yu, J.; Li, Y.; Ishizuka, T.; Guenther, M. G.; Lazar, M. A. A SANT motif in the SMRT corepressor interprets the histone code and promotes histone deacetylation. *EMBO J.* **2003**, *22* (13), 3403–3410. DOI: 10.1093/emboj/cdg326.
(84) Watson, P. J.; Fairall, L.; Santos, G. M.; Schwabe, J. W. R. Structure of HDAC3 bound to co-repressor and inositol tetraphosphate. *Nature* **2012**, *481* (7381), 335–340. DOI: 10.1038/nature10728.
(85) Sun, Z.; Miller, R. A.; Patel, R. T.; Chen, J.; Dhir, R.; Wang, H.; Zhang, D.; Graham, M. J.; Unterman, T. G.; Shulman, G. I.; Sztalryd, C.; Bennett, M. J.; Ahima, R. S.; Birnbaum, M. J.; Lazar, M. A. Hepatic Hdac3 promotes gluconeogenesis by repressing lipid synthesis and sequestration. *Nat. Med.* **2012**, *18* (6), 934–942. DOI: 10.1038/nm.2744.
(86) Emmett, M. J.; Lim, H.-W.; Jager, J.; Richter, H. J.; Adlanmerini, M.; Peed, L. C.; Briggs, E. R.; Steger, D. J.; Ma, T.; Sims, C. A.; Baur, J. A.; Pei, L.; Won, K.-J.; Seale, P.; Gerhart-Hines,

Z.; Lazar, M. A. Histone deacetylase 3 prepares brown adipose tissue for acute thermogenic challenge. *Nature* **2017**, *546* (7659), 544–548. DOI: 10.1038/nature22819.

(87) Bradley, E. W.; Carpio, L. R.; van Wijnen, A. J.; McGee-Lawrence, M. E.; Westendorf, J. J. Histone Deacetylases in Bone Development and Skeletal Disorders. *Physiol Rev.* **2015**, *95* (4), 1359–1381. DOI: 10.1152/physrev.00004.2015.

(88) Lundh, M.; Galbo, T.; Poulsen, S. S.; Mandrup-Poulsen, T. Histone deacetylase 3 inhibition improves glycaemia and insulin secretion in obese diabetic rats. *Diabetes Obes. Metab.* **2015**, *17* (7), 703–707. DOI: 10.1111/dom.12470.

(89) Zhang, X.; Zhao, X.; Fiskus, W.; Lin, J.; Lwin, T.; Rao, R.; Zhang, Y.; Chan, J. C.; Fu, K.; Marquez, V. E.; Chen-Kiang, S.; Moscinski, L. C.; Seto, E.; Dalton, W. S.; Wright, K. L.; Sotomayor, E.; Bhalla, K.; Tao, J. Coordinated silencing of MYC-mediated miR-29 by HDAC3 and EZH2 as a therapeutic target of histone modification in aggressive B-Cell lymphomas. *Cancer cell* **2012**, *22* (4), 506–523. DOI: 10.1016/j.ccr.2012.09.003.

(90) Falkenberg, K. J.; Johnstone, R. W. Histone deacetylases and their inhibitors in cancer, neurological diseases and immune disorders. *Nat. Rev. Drug Discov.* **2014**, *13* (9), 673–691. DOI: 10.1038/nrd4360.

(91) Leus, N. G.; Zwinderman, M. R.; Dekker, F. J. Histone deacetylase 3 (HDAC 3) as emerging drug target in NF-κB-mediated inflammation. *Curr. Opin. Che. Biol.* **2016**, *33*, 160–168. DOI: 10.1016/j.cbpa.2016.06.019.

(92) Amin, S. A.; Adhikari, N.; Kotagiri, S.; Jha, T.; Ghosh, B. Histone deacetylase 3 inhibitors in learning and memory processes with special emphasis on benzamides. *Eur. J. Med. Chem.* **2019**, *166*, 369–380. DOI: 10.1016/j.ejmech.2019.01.077.

(93) Kilgore, M.; Miller, C. A.; Fass, D. M.; Hennig, K. M.; Haggarty, S. J.; Sweatt, J. D.; Rumbaugh, G. Inhibitors of class 1 histone deacetylases reverse contextual memory deficits in a mouse model of Alzheimer's disease. *Neuropsychopharmacol.* **2010**, *35* (4), 870-880. DOI: 10.1038/npp.2009.197.

(94) Adhikari, N.; Jha, T.; Ghosh, B. Dissecting Histone Deacetylase 3 in Multiple Disease Conditions: Selective Inhibition as a Promising Therapeutic Strategy. *J. Med. Chem.* **2021**, *64* (13), 8827-8869. DOI: 10.1021/acs.jmedchem.0c01676.

(95) D'Mello, S. R. Histone deacetylase-3: Friend and foe of the brain. *Exp. Biol. Med.* **2020**, *245* (13), 1130–1141. DOI: 10.1177/1535370220928278.

(96) Chakrabarti, A.; Oehme, I.; Witt, O.; Oliveira, G.; Sippl, W.; Romier, C.; Pierce, R. J.; Jung, M. HDAC8: a multifaceted target for therapeutic interventions. *Trends Pharmacol Sci.* **2015**, *36* (7), 481–492. DOI: 10.1016/j.tips.2015.04.013.

(97) Hu, E.; Chen, Z.; Fredrickson, T.; Zhu, Y.; Kirkpatrick, R.; Zhang, G. F.; Johanson, K.; Sung, C. M.; Liu, R.; Winkler, J. Cloning and characterization of a novel human class I histone

deacetylase that functions as a transcription repressor. *J. Biol. Chem.* **2000**, *275* (20), 15254–15264. DOI: 10.1074/jbc.M908988199.

(98) Somoza, J. R.; Skene, R. J.; Katz, B. A.; Mol, C.; Ho, J. D.; Jennings, A. J.; Luong, C.; Arvai, A.; Buggy, J. J.; Chi, E.; Tang, J.; Sang, B.-C.; Verner, E.; Wynands, R.; Leahy, E. M.; Dougan, D. R.; Snell, G.; Navre, M.; Knuth, M. W.; Swanson, R. V.; McRee, D. E.; Tari, L. W. Structural snapshots of human HDAC8 provide insights into the class I histone deacetylases. *Structure* **2004**, *12* (7), 1325–1334. DOI: 10.1016/j.str.2004.04.012.

(99) Castañeda, C. A.; Wolfson, N. A.; Leng, K. R.; Kuo, Y.-M.; Andrews, A. J.; Fierke, C. A. HDAC8 substrate selectivity is determined by long- and short-range interactions leading to enhanced reactivity for full-length histone substrates compared with peptides. *J. Biol. Chem.* **2017**, *292* (52), 21568–21577. DOI: 10.1074/jbc.M117.811026.

(100) Deardorff, M. A.; Bando, M.; Nakato, R.; Watrin, E.; Itoh, T.; Minamino, M.; Saitoh, K.; Komata, M.; Katou, Y.; Clark, D.; Cole, K. E.; Baere, E. de; Decroos, C.; Di Donato, N.; Ernst, S.; Francey, L. J.; Gyftodimou, Y.; Hirashima, K.; Hullings, M.; Ishikawa, Y.; Jaulin, C.; Kaur, M.; Kiyono, T.; Lombardi, P. M.; Magnaghi-Jaulin, L.; Mortier, G. R.; Nozaki, N.; Petersen, M. B.; Seimiya, H.; Siu, V. M.; Suzuki, Y.; Takagaki, K.; Wilde, J. J.; Willems, P. J.; Prigent, C.; Gillessen-Kaesbach, G.; Christianson, D. W.; Kaiser, F. J.; Jackson, L. G.; Hirota, T.; Krantz, I. D.; Shirahige, K. HDAC8 mutations in Cornelia de Lange syndrome affect the cohesin acetylation cycle. *Nature* **2012**, *489* (7415), 313–317. DOI: 10.1038/nature11316.

(101) Olson, D. E.; Udeshi, N. D.; Wolfson, N. A.; Pitcairn, C. A.; Sullivan, E. D.; Jaffe, J. D.; Svinkina, T.; Natoli, T.; Lu, X.; Paulk, J.; McCarren, P.; Wagner, F. F.; Barker, D.; Howe, E.; Lazzaro, F.; Gale, J. P.; Zhang, Y.-L.; Subramanian, A.; Fierke, C. A.; Carr, S. A.; Holson, E. B. An unbiased approach to identify endogenous substrates of "histone" deacetylase 8. *ACS Chem. Biol.* **2014**, *9* (10), 2210–2216. DOI: 10.1021/cb500492r.

(102) Wilson, B. J.; Tremblay, A. M.; Deblois, G.; Sylvain-Drolet, G.; Giguère, V. An acetylation switch modulates the transcriptional activity of estrogen-related receptor alpha. *Mol. Endocrinol.* **2010**, *24* (7), 1349–1358. DOI: 10.1210/me.2009-0441.

(103) Aramsangtienchai, P.; Spiegelman, N. A.; He, B.; Miller, S. P.; Dai, L.; Zhao, Y.; Lin, H. HDAC8 Catalyzes the Hydrolysis of Long Chain Fatty Acyl Lysine. *ACS Chem. Biol.* **2016**, *11* (10), 2685-2692. DOI: 10.1021/acschembio.6b00396.

(104) Goutas, D.; Theocharis, S.; Tsourouflis, G. Unraveling the Epigenetic Role and Clinical Impact of Histone Deacetylases in Neoplasia. *Diagnostics* **2021**, *11* (8), 1346. DOI: 10.3390/diagnostics11081346.

(105) Witt, O.; Deubzer, H. E.; Lodrini, M.; Milde, T.; Oehme, I. Targeting histone deacetylases in neuroblastoma. *Curr. Pharm Des.* **2009**, *15* (4), 436–447. DOI: 10.2174/138161209787315774.

(106) Wambua, M. K.; Nalawansha, D. A.; Negmeldin, A. T.; Pflum, M. K. H. Mutagenesis studies of the 14 Å internal cavity of histone deacetylase 1: insights toward the acetate-escape

hypothesis and selective inhibitor design. *J. Med. Chem.* **2014**, *57* (3), 642-650. DOI: 10.1021/jm401837e.

(107) Chou, C. J.; Herman, D.; Gottesfeld, J. M. Pimelic diphenylamide 106 is a slow, tight-binding inhibitor of class I histone deacetylases. *J. Biol. Chem.* **2008**, *283* (51), 35402–35409. DOI: 10.1074/jbc.M807045200.

(108) Yang, X.-J.; Grégoire, S. Class II histone deacetylases: from sequence to function, regulation, and clinical implication. *Mol. Cell. Biol.* **2005**, *25* (8), 2873–2884. DOI: 10.1128/MCB.25.8.2873-2884.2005.

(109) Walkinshaw, D. R.; Weist, R.; Kim, G.-W.; You, L.; Xiao, L.; Nie, J.; Li, C. S.; Zhao, S.; Xu, M.; Yang, X.-J. The tumor suppressor kinase LKB1 activates the downstream kinases SIK2 and SIK3 to stimulate nuclear export of class IIa histone deacetylases. *J. Biol. Chem.* **2013**, *288* (13), 9345–9362. DOI: 10.1074/jbc.M113.456996.

(110) McKinsey, T. A.; Zhang, C. L.; Lu, J.; Olson, E. N. Signal-dependent nuclear export of a histone deacetylase regulates muscle differentiation. *Nature* **2000**, *408* (6808), 106–111. DOI: 10.1038/35040593.

(111) Grozinger, C. M.; Schreiber, S. L. Regulation of histone deacetylase 4 and 5 and transcriptional activity by 14-3-3-dependent cellular localization. *Proc. Natl. Acad. Sci. USA* **2000**, *97* (14), 7835–7840. DOI: 10.1073/pnas.140199597.

(112) Lahm, A.; Paolini, C.; Pallaoro, M.; Nardi, M. C.; Jones, P.; Neddermann, P.; Sambucini, S.; Bottomley, M. J.; Lo Surdo, P.; Carfí, A.; Koch, U.; Francesco, R. de; Steinkühler, C.; Gallinari, P. Unraveling the hidden catalytic activity of vertebrate class IIa histone deacetylases. *Proc. Natl. Acad. Sci. USA* **2007**, *104* (44), 17335–17340. DOI: 10.1073/pnas.0706487104.

(113) Tronrud, D. E.; Roderick, S. L.; Matthews, B. W. Structural basis for the action of thermolysin. *Matrix Suppl.* **1992**, *1*, 107–111.

(114) Vega, R. B.; Matsuda, K.; Oh, J.; Barbosa, A. C.; Yang, X.; Meadows, E.; McAnally, J.; Pomajzl, C.; Shelton, J. M.; Richardson, J. A.; Karsenty, G.; Olson, E. N. Histone deacetylase 4 controls chondrocyte hypertrophy during skeletogenesis. *Cell* **2004**, *119* (4), 555–566. DOI: 10.1016/j.cell.2004.10.024.

(115) Müller, B. M.; Jana, L.; Kasajima, A.; Lehmann, A.; Prinzler, J.; Budczies, J.; Winzer, K.-J.; Dietel, M.; Weichert, W.; Denkert, C. Differential expression of histone deacetylases HDAC1, 2 and 3 in human breast cancer--overexpression of HDAC2 and HDAC3 is associated with clinicopathological indicators of disease progression. *BMC cancer* **2013**, *13*, 215. DOI: 10.1186/1471-2407-13-215.

(116) Chang, S.; Young, B. D.; Li, S.; Qi, X.; Richardson, J. A.; Olson, E. N. Histone deacetylase 7 maintains vascular integrity by repressing matrix metalloproteinase 10. *Cell* **2006**, *126* (2), 321–334. DOI: 10.1016/j.cell.2006.05.040.

(117) Zeng, L.-S.; Yang, X.-Z.; Wen, Y.-F.; Mail, S.-J.; Wang, M.-H.; Zhang, M.-Y.; Zheng, X. F. S.; Wang, H.-Y. Overexpressed HDAC4 is associated with poor survival and promotes tumor progression in esophageal carcinoma. *Aging* **2016**, *8* (6), 1236–1249. DOI: 10.18632/aging.100980.

(118) Milde, T.; Oehme, I.; Korshunov, A.; Kopp-Schneider, A.; Remke, M.; Northcott, P.; Deubzer, H. E.; Lodrini, M.; Taylor, M. D.; Deimling, A. von; Pfister, S.; Witt, O. HDAC5 and HDAC9 in medulloblastoma: novel markers for risk stratification and role in tumor cell growth. *Clin. Cancer Res.* **2010**, *16* (12), 3240–3252. DOI: 10.1158/1078-0432.CCR-10-0395.

(119) Blackwell, L.; Norris, J.; Suto, C. M.; Janzen, W. P. The use of diversity profiling to characterize chemical modulators of the histone deacetylases. *Life Sci.* **2008**, *82* (21-22), 1050–1058. DOI: 10.1016/j.lfs.2008.03.004.

(120) Grozinger, C. M.; Hassig, C. A.; Schreiber, S. L. Three proteins define a class of human histone deacetylases related to yeast Hda1p. *Proc. Natl. Acad. Sci. USA* **1999**, *96* (9), 4868–4873. DOI: 10.1073/pnas.96.9.4868.

(121) Bertos, N. R.; Gilquin, B.; Chan, G. K. T.; Yen, T. J.; Khochbin, S.; Yang, X.-J. Role of the tetradecapeptide repeat domain of human histone deacetylase 6 in cytoplasmic retention. *J. Biol. Chem.* **2004**, *279* (46), 48246–48254. DOI: 10.1074/jbc.M408583200.

(122) Osko, J. D.; Christianson, D. W. Structural Basis of Catalysis and Inhibition of HDAC6 CD1, the Enigmatic Catalytic Domain of Histone Deacetylase 6. *Biochem.* **2019**, *58* (49), 4912-4924. DOI: 10.1021/acs.biochem.9b00934.

(123) Hai, Y.; Christianson, D. W. Histone deacetylase 6 structure and molecular basis of catalysis and inhibition. *Nature Chem. Bio.* **2016**, *12* (9), 741–747. DOI: 10.1038/nchembio.2134.

(124) Porter, N. J.; Osko, J. D.; Diedrich, D.; Kurz, T.; Hooker, J. M.; Hansen, F. K.; Christianson, D. W. Histone Deacetylase 6-Selective Inhibitors and the Influence of Capping Groups on Hydroxamate-Zinc Denticity. *J. Med.Chem.* **2018**, *61* (17), 8054-8060. DOI: 10.1021/acs.jmedchem.8b01013.

(125) Seigneurin-Berny, D.; Verdel, A.; Curtet, S.; Lemercier, C.; Garin, J.; Rousseaux, S.; Khochbin, S. Identification of components of the murine histone deacetylase 6 complex: link between acetylation and ubiquitination signaling pathways. *Mol. Cell Biol.* **2001**, *21* (23), 8035–8044. DOI: 10.1128/MCB.21.23.8035-8044.2001.

(126) Hook, S. S.; Orian, A.; Cowley, S. M.; Eisenman, R. N. Histone deacetylase 6 binds polyubiquitin through its zinc finger (PAZ domain) and copurifies with deubiquitinating enzymes. *PNAS* **2002**, *99* (21), 13425-13430. DOI: 10.1073/pnas.172511699.

(127) Hubbert, C.; Guardiola, A.; Shao, R.; Kawaguchi, Y.; Ito, A.; Nixon, A.; Yoshida, M.; Wang, X.-F.; Yao, T.-P. HDAC6 is a microtubule-associated deacetylase. *Nature* **2002**, *417* (6887), 455-458. DOI: 10.1038/417455a.

(128) Kovacs, J. J.; Murphy, P. J. M.; Gaillard, S.; Zhao, X.; Wu, J.-T.; Nicchitta, C. V.; Yoshida, M.; Toft, D. O.; Pratt, W. B.; Yao, T.-P. HDAC6 regulates Hsp90 acetylation and chaperone-dependent activation of glucocorticoid receptor. *Mol. Cell. Biochem.* **2005**, *18* (5), 601–607. DOI: 10.1016/j.molcel.2005.04.021.

(129) Fan, S.-J.; Huang, F.-I.; Liou, J.-P.; Yang, C.-R. The novel histone de acetylase 6 inhibitor, MPT0G211, ameliorates tau phosphorylation and cognitive deficits in an Alzheimer's disease model. *Cell Death Dis.* **2018**, *9* (6), 655. DOI: 10.1038/s41419-018-0688-5.

(130) Kaur, S.; Rajoria, P.; Chopra, M. HDAC6: A unique HDAC family member as a cancer target. *Cell Oncol.* **2022**, *45* (5), 779–829. DOI: 10.1007/s13402-022-00704-6.

(131) Cabrero, J. R.; Serrador, J. M.; Barreiro, O.; Mittelbrunn, M.; Naranjo-Suárez, S.; Martín-Cófreces, N.; Vicente-Manzanares, M.; Mazitschek, R.; Bradner, J. E.; Avila, J.; Valenzuela-Fernández, A.; Sánchez-Madrid, F. Lymphocyte chemotaxis is regulated by histone deacetylase 6, independently of its deacetylase activity. *Mol. Biol. Cell.* **2006**, *17* (8), 3435–3445. DOI: 10.1091/mbc.e06-01-0008.

(132) Zhu, S.; Goldschmidt-Clermont, P. J.; Dong, C. Transforming growth factor-beta-induced inhibition of myogenesis is mediated through Smad pathway and is modulated by microtubule dynamic stability. *circ. Res.* **2004**, *94* (5), 617–625. DOI: 10.1161/01.RES.0000118599.25944.D5.

(133) Zavadil, J.; Böttinger, E. P. TGF-beta and epithelial-to-mesenchymal transitions. *Oncogene* **2005**, *24* (37), 5764–5774. DOI: 10.1038/sj.onc.1208927.

(134) Shan, B.; Yao, T.-P.; Nguyen, H. T.; Zhuo, Y.; Levy, D. R.; Klingsberg, R. C.; Tao, H.; Palmer, M. L.; Holder, K. N.; Lasky, J. A. Requirement of HDAC6 for transforming growth factor-beta1-induced epithelial-mesenchymal transition. *J. Biol. Chem.* **2008**, *283* (30), 21065–21073. DOI: 10.1074/jbc.M802786200.

(135) Boyault, C.; Zhang, Y.; Fritah, S.; Caron, C.; Gilquin, B.; Kwon, S. H.; Garrido, C.; Yao, T.-P.; Vourc'h, C.; Matthias, P.; Khochbin, S. HDAC6 controls major cell response pathways to cytotoxic accumulation of protein aggregates. *Genes De.* **2007**, *21* (17), 2172–2181. DOI: 10.1101/gad.436407.

(136) Kawaguchi, Y.; Kovacs, J. J.; McLaurin, A.; Vance, J. M.; Ito, A.; Yao, T. P. The deacetylase HDAC6 regulates aggresome formation and cell viability in response to misfolded protein stress. *Cell* **2003**, *115* (6), 727–738. DOI: 10.1016/s0092-8674(03)00939-5.

(137) Brindisi, M.; Saraswati, A. P.; Brogi, S.; Gemma, S.; Butini, S.; Campiani, G. Old but Gold: Tracking the New Guise of Histone Deacetylase 6 (HDAC6) Enzyme as a Biomarker and Therapeutic Target in Rare Diseases. *J. Med. Chem.* **2020**, *63* (1), 23-39. DOI: 10.1021/acs.jmedchem.9b00924.

(138) Chang, P.; Li, H.; Hu, H.; Li, Y.; Wang, T. The Role of HDAC6 in Autophagy and NLRP3 Inflammasome. *Front. Immunol.* **2021**, *12*, 763831. DOI: 10.3389/fimmu.2021.763831.

(139) Yue, K.; Sun, S.; Jia, G.; Qin, M.; Hou, X.; Chou, C. J.; Huang, C.; Li, X. First-in-Class Hydrazide-Based HDAC6 Selective Inhibitor with Potent Oral Anti-Inflammatory Activity by Attenuating NLRP3 Inflammasome Activation. *J. Med. Chem.* **2022**, *65* (18), 12140–12162. DOI: 10.1021/acs.jmedchem.2c00853.

(140) Swanson, K. V.; Deng, M.; Ting, J. P.-Y. The NLRP3 inflammasome: molecular activation and regulation to therapeutics. *Nat. Rev. Immonol* **2019**, *19* (8), 477–489. DOI: 10.1038/s41577-019-0165-0.

(141) Bauernfeind, F. G.; Horvath, G.; Stutz, A.; Alnemri, E. S.; MacDonald, K.; Speert, D.; Fernandes-Alnemri, T.; Wu, J.; Monks, B. G.; Fitzgerald, K. A.; Hornung, V.; Latz, E. Cutting edge: NF-kappaB activating pattern recognition and cytokine receptors license NLRP3 inflammasome activation by regulating NLRP3 expression. *J. Immunol.* **2009**, *183* (2), 787–791. DOI: 10.4049/jimmunol.0901363.

(142) Tannahill, G. M.; Curtis, A. M.; Adamik, J.; Palsson-McDermott, E. M.; McGettrick, A. F.; Goel, G.; Frezza, C.; Bernard, N. J.; Kelly, B.; Foley, N. H.; Zheng, L.; Gardet, A.; Tong, Z.; Jany, S. S.; Corr, S. C.; Haneklaus, M.; Caffrey, B. E.; Pierce, K.; Walmsley, S.; Beasley, F. C.; Cummins, E.; Nizet, V.; Whyte, M.; Taylor, C. T.; Lin, H.; Masters, S. L.; Gottlieb, E.; Kelly, V. P.; Clish, C.; Auron, P. E.; Xavier, R. J.; O'Neill, L. A. J. Succinate is an inflammatory signal that induces IL-1β through HIF-1α. *Nature* **2013**, *496* (7444), 238–242. DOI: 10.1038/nature11986.

(143) Muñoz-Planillo, R.; Kuffa, P.; Martínez-Colón, G.; Smith, B. L.; Rajendiran, T. M.; Núñez, G. K^+ efflux is the common trigger of NLRP3 inflammasome activation by bacterial toxins and particulate matter. *Immunity* **2013**, *38* (6), 1142–1153. DOI: 10.1016/j.immuni.2013.05.016.

(144) Perregaux, D.; Gabel, C. A. Interleukin-1 beta maturation and release in response to ATP and nigericin. Evidence that potassium depletion mediated by these agents is a necessary and common feature of their activity. *J. Biol. Chem.* **1994**, *269* (21), 15195–15203.

(145) Murakami, T.; Ockinger, J.; Yu, J.; Byles, V.; McColl, A.; Hofer, A. M.; Horng, T. Critical role for calcium mobilization in activation of the NLRP3 inflammasome. *Proc. Natl. Acad. Sci. USA* **2012**, *109* (28), 11282–11287. DOI: 10.1073/pnas.1117765109.

(146) Magupalli, V. G.; Negro, R.; Tian, Y.; Hauenstein, A. V.; Di Caprio, G.; Skillern, W.; Deng, Q.; Orning, P.; Alam, H. B.; Maliga, Z.; Sharif, H.; Hu, J. J.; Evavold, C. L.; Kagan, J. C.; Schmidt, F. I.; Fitzgerald, K. A.; Kirchhausen, T.; Li, Y.; Wu, H. HDAC6 mediates an aggresome-like mechanism for NLRP3 and pyrin inflammasome activation. *Science* **2020**, *369* (6510), eaas8995. DOI: 10.1126/science.aas8995.

(147) Oliveira, R. G. de; Campos Castilho, G. R. de; da Cunha, A. L.; Miyajima, F.; Oliveira Martins, D. T. de. Dilodendron bipinnatum Radlk. inhibits pro-inflammatory mediators through the induction of MKP-1 and the down-regulation of MAPKp38/JNK/NF-κB pathways and COX-

2 in LPS-activated RAW 264.7 cells. *J. Ethnopharmacol.* **2017**, *202*, 127–137. DOI: 10.1016/j.jep.2017.02.026.

(148) Zhang, W.-B.; Yang, F.; Wang, Y.; Jiao, F.-Z.; Zhang, H.-Y.; Wang, L.-W.; Gong, Z.-J. Inhibition of HDAC6 attenuates LPS-induced inflammation in macrophages by regulating oxidative stress and suppressing the TLR4-MAPK/NF-κB pathways. *Biomed. Pharmacother.* **2019**, *117*, 109166. DOI: 10.1016/j.biopha.2019.109166.

(149) Lee, Y.-S.; Lim, K.-H.; Guo, X.; Kawaguchi, Y.; Gao, Y.; Barrientos, T.; Ordentlich, P.; Wang, X.-F.; Counter, C. M.; Yao, T.-P. The cytoplasmic deacetylase HDAC6 is required for efficient oncogenic tumorigenesis. *Cancer Res.* **2008**, *68* (18), 7561–7569. DOI: 10.1158/0008-5472.CAN-08-0188.

(150) Li, D.; Sun, X.; Zhang, L.; Yan, B.; Xie, S.; Liu, R.; Liu, M.; Zhou, J. Histone deacetylase 6 and cytoplasmic linker protein 170 function together to regulate the motility of pancreatic cancer cells. *Protein Cell* **2014**, *5* (3), 214–223. DOI: 10.1007/s13238-013-0010-3.

(151) Li, T.; Zhang, C.; Hassan, S.; Liu, X.; Song, F.; Chen, K.; Zhang, W.; Yang, J. Histone deacetylase 6 in cancer. *J. Hematol. Oncol.* **2018**, *11* (1), 111. DOI: 10.1186/s13045-018-0654-9.

(152) Zhang, L.; Liu, N.; Xie, S.; He, X.; Zhou, J.; Liu, M.; Li, D. HDAC6 regulates neuroblastoma cell migration and may play a role in the invasion process. *Cancer Biol. Ther.* **2014**, *15* (11), 1561–1570. DOI: 10.4161/15384047.2014.956632.

(153) Yan, S.; Wei, X.; Jian, W.; Qin, Y.; Liu, J.; Zhu, S.; Jiang, F.; Lou, H.; Zhang, B. Pharmacological Inhibition of HDAC6 Attenuates NLRP3 Inflammatory Response and Protects Dopaminergic Neurons in Experimental Models of Parkinson's Disease. *Front. Aging. Neurosci.* **2020**, *12*, 78. DOI: 10.3389/fnagi.2020.00078.

(154) Campiani, G.; Cavella, C.; Osko, J. D.; Brindisi, M.; Relitti, N.; Brogi, S.; Saraswati, A. P.; Federico, S.; Chemi, G.; Maramai, S.; Carullo, G.; Jaeger, B.; Carleo, A.; Benedetti, R.; Sarno, F.; Lamponi, S.; Rottoli, P.; Bargagli, E.; Bertucci, C.; Tedesco, D.; Herp, D.; Senger, J.; Ruberti, G.; Saccoccia, F.; Saponara, S.; Gorelli, B.; Valoti, M.; Kennedy, B.; Sundaramurthi, H.; Butini, S.; Jung, M.; Roach, K. M.; Altucci, L.; Bradding, P.; Christianson, D. W.; Gemma, S.; Prasse, A. Harnessing the Role of HDAC6 in Idiopathic Pulmonary Fibrosis: Design, Synthesis, Structural Analysis, and Biological Evaluation of Potent Inhibitors. *J. Med. Chem.* **2021**, *64* (14), 9960-9988. DOI: 10.1021/acs.jmedchem.1c00184.

(155) Tong, J. J.; Liu, J.; Bertos, N. R.; Yang, X.-J. Identification of HDAC10, a novel class II human histone deacetylase containing a leucine-rich domain. *Nucleic Acids Res.* **2002**, *30* (5), 1114–1123. DOI: 10.1093/nar/30.5.1114.

(156) Cheng, F.; Zheng, B.; Wang, J.; Zhao, G.; Yao, Z.; Niu, Z.; He, W. Histone deacetylase 10, a potential epigenetic target for therapy. *Biosci. Rep.* **2021**, *41* (6). DOI: 10.1042/BSR20210462.

(157) Hai, Y.; Shinsky, S. A.; Porter, N. J.; Christianson, D. W. Histone deacetylase 10 structure and molecular function as a polyamine deacetylase. *Nature Comm.* **2017**, *8*, 15368. DOI: 10.1038/ncomms15368.

(158) Casero, R. A.; Marton, L. J. Targeting polyamine metabolism and function in cancer and other hyperproliferative diseases. *Nat. Rev. Drug Discov.* **2007**, *6* (5), 373–390. DOI: 10.1038/nrd2243.

(159) Eisenberg, T.; Knauer, H.; Schauer, A.; Büttner, S.; Ruckenstuhl, C.; Carmona-Gutierrez, D.; Ring, J.; Schroeder, S.; Magnes, C.; Antonacci, L.; Fussi, H.; Deszcz, L.; Hartl, R.; Schraml, E.; Criollo, A.; Megalou, E.; Weiskopf, D.; Laun, P.; Heeren, G.; Breitenbach, M.; Grubeck-Loebenstein, B.; Herker, E.; Fahrenkrog, B.; Fröhlich, K.-U.; Sinner, F.; Tavernarakis, N.; Minois, N.; Kroemer, G.; Madeo, F. Induction of autophagy by spermidine promotes longevity. *Nat. Cell Biol.* **2009**, *11* (11), 1305–1314. DOI: 10.1038/ncb1975.

(160) Shinsky, S. A.; Christianson, D. W. Polyamine Deacetylase Structure and Catalysis: Prokaryotic Acetylpolyamine Amidohydrolase and Eukaryotic HDAC10. *Biochemistry* **2018**, *57* (22), 3105–3114. DOI: 10.1021/acs.biochem.8b00079.

(161) Li, Y.; Zhang, X.; Zhu, S.; Dejene, E. A.; Peng, W.; Sepulveda, A.; Seto, E. HDAC10 Regulates Cancer Stem-Like Cell Properties in KRAS-Driven Lung Adenocarcinoma. *Cancer Res.* **2020**, *80* (16), 3265–3278. DOI: 10.1158/0008-5472.CAN-19-3613.

(162) Park, B. L.; Kim, Y. J.; Cheong, H. S.; Lee, S. O.; Han, C. S.; Yoon, J.-H.; Park, J. H.; Chang, H. S.; Park, C.-S.; Lee, H.-S.; Shin, H. D. HDAC10 promoter polymorphism associated with development of HCC among chronic HBV patients. *Biochem. Biophys. Res. commun.* **2007**, *363* (3), 776–781. DOI: 10.1016/j.bbrc.2007.09.026.

(163) Gao, L.; Cueto, M. A.; Asselbergs, F.; Atadja, P. Cloning and functional characterization of HDAC11, a novel member of the human histone deacetylase family. *J. Biol. Chem.* **2002**, *277* (28), 25748–25755. DOI: 10.1074/jbc.M111871200.

(164) Chen, H.; Xie, C.; Chen, Q.; Zhuang, S. HDAC11, an emerging therapeutic target for metabolic disorders. *Front. Edenocrinol.* **2022**, *13*, 989305. DOI: 10.3389/fendo.2022.989305.

(165) Cheng, F.; Lienlaf, M.; Perez-Villarroel, P.; Wang, H.-W.; Lee, C.; Woan, K.; Woods, D.; Knox, T.; Bergman, J.; Pinilla-Ibarz, J.; Kozikowski, A.; Seto, E.; Sotomayor, E. M.; Villagra, A. Divergent roles of histone deacetylase 6 (HDAC6) and histone deacetylase 11 (HDAC11) on the transcriptional regulation of IL10 in antigen presenting cells. *Mol. Immunol.* **2014**, *60* (1), 44–53. DOI: 10.1016/j.molimm.2014.02.019.

(166) Kutil, Z.; Novakova, Z.; Meleshin, M.; Mikesova, J.; Schutkowski, M.; Barinka, C. Histone Deacetylase 11 Is a Fatty-Acid Deacylase. *ACS Chem. Biol.* **2018**, *13* (3), 685–693. DOI: 10.1021/acschembio.7b00942.

(167) Hurtado, E.; Núñez-Álvarez, Y.; Muñoz, M.; Gutiérrez-Caballero, C.; Casas, J.; Pendás, A. M.; Peinado, M. A.; Suelves, M. HDAC11 is a novel regulator of fatty acid oxidative metabolism in skeletal muscle. *FEBS J* **2021**, *288* (3), 902–919. DOI: 10.1111/febs.15456.

(168) Liu, H.; Hu, Q.; Kaufman, A.; D'Ercole, A. J.; Ye, P. Developmental expression of histone deacetylase 11 in the murine brain. *J. Neurosci. Res.* **2008**, *86* (3), 537–543. DOI: 10.1002/jnr.21521.

(169) Boltz, T. A.; Khuri, S.; Wuchty, S. Promoter conservation in HDACs points to functional implications. *BMC genomics* **2019**, *20* (1), 613. DOI: 10.1186/s12864-019-5973-x.

(170) Tiwari, S.; Dharmarajan, S.; Shivanna, M.; Otteson, D. C.; Belecky-Adams, T. L. Histone deacetylase expression patterns in developing murine optic nerve. *BMC Dev. Biol.* **2014**, *14*, 30. DOI: 10.1186/1471-213X-14-30.

(171) Yue, L.; Sharma, V.; Horvat, N. P.; Akuffo, A. A.; Beatty, M. S.; Murdun, C.; Colin, C.; Billington, J. M. R.; Goodheart, W. E.; Sahakian, E.; Zhang, L.; Powers, J. J.; Amin, N. E.; Lambert-Showers, Q. T.; Darville, L. N.; Pinilla-Ibarz, J.; Reuther, G. W.; Wright, K. L.; Conti, C.; Lee, J. Y.; Zheng, X.; Ng, P. Y.; Martin, M. W.; Marshall, C. G.; Koomen, J. M.; Levine, R. L.; Verma, A.; Grimes, H. L.; Sotomayor, E. M.; Shao, Z.; Epling-Burnette, P. K. HDAC11 deficiency disrupts oncogene-induced hematopoiesis in myeloproliferative neoplasms. *Blood* **2020**, *135* (3), 191–207. DOI: 10.1182/blood.2019895326.

(172) Yanginlar, C.; Logie, C. HDAC11 is a regulator of diverse immune functions. *Biochem. Biophys. Acta. Gene. Regul. Mech.* **2018**, *1861* (1), 54–59. DOI: 10.1016/j.bbagrm.2017.12.002.

(173) Bagui, T. K.; Sharma, S. S.; Le Ma; Pledger, W. J. Proliferative status regulates HDAC11 mRNA abundance in nontransformed fibroblasts. *Cell cycle* **2013**, *12* (21), 3433–3441. DOI: 10.4161/cc.26433.

(174) Bhaskara, S. Histone deacetylase 11 as a key regulator of metabolism and obesity. *EBioMedicine* **2018**, *35*, 27–28. DOI: 10.1016/j.ebiom.2018.08.008.

(175) Sun, L.; Marin de Evsikova, C.; Bian, K.; Achille, A.; Telles, E.; Pei, H.; Seto, E. Programming and Regulation of Metabolic Homeostasis by HDAC11. *EBioMedicine* **2018**, *33*, 157–168. DOI: 10.1016/j.ebiom.2018.06.025.

(176) Huang, J.; Wang, L.; Dahiya, S.; Beier, U. H.; Han, R.; Samanta, A.; Bergman, J.; Sotomayor, E. M.; Seto, E.; Kozikowski, A. P.; Hancock, W. W. Histone/protein deacetylase 11 targeting promotes Foxp3+ Treg function. *Sci. Rep.* **2017**, *7* (1), 8626. DOI: 10.1038/s41598-017-09211-3.

(177) Finnin, M. S.; Donigian, J. R.; Cohen, A.; Richon, V. M.; Rifkind, R. A.; Marks, P. A.; Breslow, R.; Pavletich, N. P. Structures of a histone deacetylase homologue bound to the TSA and SAHA inhibitors. *Nature* **1999**, *401* (6749), 188–193. DOI: 10.1038/43710.

(178) Osko, J. D.; Christianson, D. W. Structural determinants of affinity and selectivity in the binding of inhibitors to histone deacetylase 6. *Bioorg. Med. Chem. Lett.* **2020**, *30* (8), 127023. DOI: 10.1016/j.bmcl.2020.127023.

(179) Eckschlager, T.; Plch, J.; Stiborova, M.; Hrabeta, J. Histone Deacetylase Inhibitors as Anticancer Drugs. *Int. J. Mol. Sci.* **2017**, *18* (7), 1414. DOI: 10.3390/ijms18071414.

(180) Jenke, R.; Reßing, N.; Hansen, F. K.; Aigner, A.; Büch, T. Anticancer Therapy with HDAC Inhibitors: Mechanism-Based Combination Strategies and Future Perspectives. *Cancers* **2021**, *13* (4), 643. DOI: 10.3390/cancers13040634.

(181) Li, W.; Sun, Z. Mechanism of Action for HDAC Inhibitors-Insights from Omics Approaches. *Int. J. Mol. Sci.* **2019**, *20* (7), 1616. DOI: 10.3390/ijms20071616.

(182) Miller, K. M.; Tjeertes, J. V.; Coates, J.; Legube, G.; Polo, S. E.; Britton, S.; Jackson, S. P. Human HDAC1 and HDAC2 function in the DNA-damage response to promote DNA nonhomologous end-joining. *Nat. Struct. Mol. Biol.* **2010**, *17* (9), 1144–1151. DOI: 10.1038/nsmb.1899.

(183) Jung, M.; Hoffmann, K.; Brosch, G.; Loidl, P. Analogues of trichostatin a and trapoxin B as histone deacetylase inhibitors. *Bioorg. Med. Chem. Lett.* **1997**, *7* (13), 1655–1658. DOI: 10.1016/S0960-894X(97)00284-9.

(184) Yoshida, M.; Kijima, M.; Akita, M.; Beppu, T. Potent and specific inhibition of mammalian histone deacetylase both in vivo and in vitro by trichostatin A. *J. Biol. Chem.* **1990**, *265* (28), 17174–17179.

(185) Marks, P. A.; Breslow, R. Dimethyl sulfoxide to vorinostat:Development of this histone deacetylase inhibitor as an anticancer drug. *Nat. Biotechnol.* **2007**, *25* (1), 84–90. DOI: 10.1038/nbt1272.

(186) Cappellacci, L.; Perinelli, D. R.; Maggi, F.; Grifantini, M.; Petrelli, R. Recent Progress in Histone Deacetylase Inhibitors as Anticancer Agents. *Curr. Med. Chem.* **2020**, *27* (15), 2449-2493. DOI: 10.2174/0929867325666181016163110.

(187) Manal, M.; Chandrasekar, M. J. N.; Gomathi Priya, J.; Nanjan, M. J. Inhibitors of histone deacetylase as antitumor agents: A critical review. *Bioorg. Chem.* **2016**, *67*, 18–42. DOI: 10.1016/j.bioorg.2016.05.005.

(188) Nakajima, H.; Kim, Y. B.; Terano, H.; Yoshida, M.; Horinouchi, S. FR901228, a potent antitumor antibiotic, is a novel histone deacetylase inhibitor. *Exp. Cell Res.* **1998**, *241* (1), 126–133. DOI: 10.1006/excr.1998.4027.

(189) Porter, N. J.; Christianson, D. W. Structure, mechanism, and inhibition of the zinc-dependent histone deacetylases. *Curr. Opin. Struct. Biol.* **2019**, *59*, 9–18. DOI: 10.1016/j.sbi.2019.01.004.

(190) Shigematsu, N.; Ueda, H.; Takase, S.; Tanaka, H.; Yamamoto, K.; Tada, T. FR901228, a novel antitumor bicyclic depsipeptide produced by Chromobacterium violaceum No. 968. II. Structure determination. *J. Antibiot.* **1994**, *47* (3), 311–314. DOI: 10.7164/antibiotics.47.311.

(191) Foss, F.; Duvic, M.; Lerner, A.; Waksman, J.; Whittaker, S. Clinical Efficacy of Romidepsin in Tumor Stage and Folliculotropic Mycosis Fungoides. *Clin. Lymphoma Myeloma Leuk.* **2016**, *16* (11), 637–643. DOI: 10.1016/j.clml.2016.08.009.

(192) Finn, P. W.; Loza, E.; Carstensen, E. The Discovery and Development of Belinostat. In *Successful drug discovery*, 1. Auflage; Fischer, J., Childers, W. E., Eds.; Wiley-VCH Verlag GmbH & Co. KGaA, 2017; pp 31–57. DOI: 10.1002/9783527800315.ch3.

(193) Atadja, P. Development of the pan-DAC inhibitor panobinostat (LBH589): successes and challenges. *Cancer let.* **2009**, *280* (2), 233–241. DOI: 10.1016/j.canlet.2009.02.019.

(194) San-Miguel, J. F.; Hungria, V. T. M.; Yoon, S.-S.; Beksac, M.; Dimopoulos, M. A.; Elghandour, A.; Jedrzejczak, W. W.; Günther, A.; Nakorn, T. N.; Siritanaratkul, N.; Corradini, P.; Chuncharunee, S.; Lee, J.-J.; Schlossman, R. L.; Shelekhova, T.; Yong, K.; Tan, D.; Numbenjapon, T.; Cavenagh, J. D.; Hou, J.; LeBlanc, R.; Nahi, H.; Qiu, L.; Salwender, H.; Pulini, S.; Moreau, P.; Warzocha, K.; White, D.; Bladé, J.; Chen, W.; La Rubia, J. de; Gimsing, P.; Lonial, S.; Kaufman, J. L.; Ocio, E. M.; Veskovski, L.; Sohn, S. K.; Wang, M.-C.; Lee, J. H.; Einsele, H.; Sopala, M.; Corrado, C.; Bengoudifa, B.-R.; Binlich, F.; Richardson, P. G. Panobinostat plus bortezomib and dexamethasone versus placebo plus bortezomib and dexamethasone in patients with relapsed or relapsed and refractory multiple myeloma: a multicentre, randomised, double-blind phase 3 trial. *Lancet Oncol.* **2014**, *15* (11), 1195-1206. DOI: 10.1016/S1470-2045(14)70440-1.

(195) Gallagher, S. J.; Gunatilake, D.; Beaumont, K. A.; Sharp, D. M.; Tiffen, J. C.; Heinemann, A.; Weninger, W.; Haass, N. K.; Wilmott, J. S.; Madore, J.; Ferguson, P. M.; Rizos, H.; Hersey, P. HDAC inhibitors restore BRAF-inhibitor sensitivity by altering PI3K and survival signalling in a subset of melanoma. *Int. J. Cancer* **2018**, *142* (9), 1926–1937. DOI: 10.1002/ijc.31199.

(196) *ClinicalTrials.gov*. https://clinicaltrials.gov/search?term=panobinostat&cond=cancer&aggFilters=status:not%20rec%20act (accessed 2023-08-28).

(197) Oki, Y.; Younes, A.; Copeland, A.; Hagemeister, F.; Fayad, L. E.; McLaughlin, P.; Shah, J.; Fowler, N.; Romaguera, J.; Kwak, L. W.; Pro, B. Phase I study of vorinostat in combination with standard CHOP in patients with newly diagnosed peripheral T-cell lymphoma. *Br. J. Haematol.* **2013**, *162* (1), 138–141. DOI: 10.1111/bjh.12326.

(198) Hogg, S. J.; Beavis, P. A.; Dawson, M. A.; Johnstone, R. W. Targeting the epigenetic regulation of antitumour immunity. *Nat. Rev. Drug. Discov.* **2020**, *19* (11), 776-800. DOI: 10.1038/s41573-020-0077-5.

(199) Lee, J.-H.; Choy, M. L.; Marks, P. A. Mechanisms of resistance to histone deacetylase inhibitors. *Adv. Cancer Res.* **2012**, *116*, 39–86. DOI: 10.1016/B978-0-12-394387-3.00002-1.

(200) O'Connor, O. A. Clinical experience with the novel histone deacetylase inhibitor vorinostat (suberoylanilide hydroxamic acid) in patients with relapsed lymphoma. *Br J Cancer* **2006**, *95* (S1), S7-S12. DOI: 10.1038/sj.bjc.6603464.

(201) Eleutherakis-Papaiakovou, E.; Kanellias, N.; Kastritis, E.; Gavriatopoulou, M.; Terpos, E.; Dimopoulos, M. A. Efficacy of Panobinostat for the Treatment of Multiple Myeloma. *J. Oncol.* **2020**, *2020* (13), 7131802. DOI: 10.1155/2020/7131802.

(202) Kerr, J. S.; Galloway, S.; Lagrutta, A.; Armstrong, M.; Miller, T.; Richon, V. M.; Andrews, P. A. Nonclinical safety assessment of the histone deacetylase inhibitor vorinostat. *Int. J. toxicol.* **2010**, *29* (1), 3–19. DOI: 10.1177/1091581809352111.

(203) Shen, S.; Kozikowski, A. P. Why Hydroxamates May Not Be the Best Histone Deacetylase Inhibitors--What Some May Have Forgotten or Would Rather Forget? *Chem. Med. Chem.* **2016**, *11* (1), 15-21. DOI: 10.1002/cmdc.201500486.

(204) Jones, P.; Steinkühler, C. From natural products to small molecule ketone histone deacetylase inhibitors: development of new class specific agents. *curr. Pharm. Des.* **2008**, *14* (6), 545–561. DOI: 10.2174/138161208783885317.

(205) Furumai, R.; Matsuyama, A.; Kobashi, N.; Lee, K.-H.; Nishiyama, M.; Nakajima, H.; Tanaka, A.; Komatsu, Y.; Nishino, N.; Yoshida, M.; Horinouchi, S. FK228 (depsipeptide) as a natural prodrug that inhibits class I histone deacetylases. *Cancer Res.* **2002**, *62* (17), 4916–4921.

(206) Kim, B.; Ratnayake, R.; Lee, H.; Shi, G.; Zeller, S. L.; Li, C.; Luesch, H.; Hong, J. Synthesis and biological evaluation of largazole zinc-binding group analogs. *Bioorg. Chem.* **2017**, *25* (12), 3077–3086. DOI: 10.1016/j.bmc.2017.03.071.

(207) Li, X.; Jiang, Y.; Peterson, Y. K.; Tongqiang, X.; Himes, R. A.; Xin, L.; Yin, G.; Inks, E. S.; Dolloff, N.; Halene, S.; Chan, S. S. L.; Chou, C. J. Design of hydrazide-bearing HDACIs based on panobinostat and their p53 and FLT3-ITD dependency in anti-leukemia activity. *J. Med. Chem.* **2020**, *63*, 5501-5525. DOI: 10.1021/acs.jmedchem.0c00442.

(208) Connolly, R. M.; Rudek, M. A.; Piekarz, R. Entinostat: a promising treatment option for patients with advanced breast cancer. *Future Oncol.* **2017**, *13* (13), 1137–1148. DOI: 10.2217/fon-2016-0526.

(209) Bressi, J. C.; Jennings, A. J.; Skene, R.; Wu, Y.; Melkus, R.; Jong, R. de; O'Connell, S.; Grimshaw, C. E.; Navre, M.; Gangloff, A. R. Exploration of the HDAC2 foot pocket: Synthesis and SAR of substituted N-(2-aminophenyl)benzamides. *Bioorg. Med. Chem. Lett.* **2010**, *20* (10), 3142–3145. DOI: 10.1016/j.bmcl.2010.03.091.

(210) Luckhurst, C. A.; Breccia, P.; Stott, A. J.; Aziz, O.; Birch, H. L.; Bürli, R. W.; Hughes, S. J.; Jarvis, R. E.; Lamers, M.; Leonard, P. M.; Matthews, K. L.; McAllister, G.; Pollack, S.; Saville-Stones, E.; Wishart, G.; Yates, D.; Dominguez, C. Potent, Selective, and CNS-Penetrant Tetrasubstituted Cyclopropane Class IIa Histone Deacetylase (HDAC) Inhibitors. *ACS Med. Chem. Lett.* **2016**, *7* (1), 34–39. DOI: 10.1021/acsmedchemlett.5b00302.

(211) Yardley, D. A.; Ismail-Khan, R. R.; Melichar, B.; Lichinitser, M.; Munster, P. N.; Klein, P. M.; Cruickshank, S.; Miller, K. D.; Lee, M. J.; Trepel, J. B. Randomized phase II, double-blind, placebo-controlled study of exemestane with or without entinostat in postmenopausal women with locally recurrent or metastatic estrogen receptor-positive breast cancer progressing on treatment with a nonsteroidal aromatase inhibitor. *JCO* **2013**, *31* (17), 2128–2135. DOI: 10.1200/JCO.2012.43.7251.

(212) Shenzhen Chipscreen Biosciences, Ltd. Chipscreen Biosciences Announces CFDA Approval of Chidamide (Epidaza) for PTCLs in China, Jan 9, 2015. https://www.prnewswire.com/news-releases/chipscreen-biosciences-announces-cfda-approval-of-chidamide-epidaza-for-ptcls-in-china-300017763.html (accessed 2023-09-01).

(213) Zhang, Q.; Wang, T.; Geng, C.; Zhang, Y.; Zhang, J.; Ning, Z.; Jiang, Z. Exploratory clinical study of chidamide, an oral subtype-selective histone deacetylase inhibitor, in combination with exemestane in hormone receptor-positive advanced breast cancer. *Chin. J. Cancer Res.* **2018**, *30* (6), 605–612. DOI: 10.21147/j.issn.1000-9604.2018.06.05.

(214) Ning, Z.-Q.; Li, Z.-B.; Newman, M. J.; Shan, S.; Wang, X.-H.; Pan, D.-S.; Zhang, J.; Dong, M.; Du, X.; Lu, X.-P. Chidamide (CS055/HBI-8000): a new histone deacetylase inhibitor of the benzamide class with antitumor activity and the ability to enhance immune cell-mediated tumor cell cytotoxicity. *Cancer Chemother. Pharmacol.* **2012**, *69* (4), 901-909. DOI: 10.1007/s00280-011-1766-x.

(215) *ClinicalTrials.gov*. https://clinicaltrials.gov/search?intr=tucidinostat&page=3 (accessed 2023-09-01).

(216) Fournel, M.; Bonfils, C.; Hou, Y.; Yan, P. T.; Trachy-Bourget, M.-C.; Kalita, A.; Liu, J.; Lu, A.-H.; Zhou, N. Z.; Robert, M.-F.; Gillespie, J.; Wang, J. J.; Ste-Croix, H.; Rahil, J.; Lefebvre, S.; Moradei, O.; Delorme, D.; Macleod, A. R.; Besterman, J. M.; Li, Z. MGCD0103, a novel isotype-selective histone deacetylase inhibitor, has broad spectrum antitumor activity in vitro and in vivo. *Mol. Cancer Res.* **2008**, *7* (4), 759–768. DOI: 10.1158/1535-7163.MCT-07-2026.

(217) Pinkerneil, M.; Hoffmann, M. J.; Kohlhof, H.; Schulz, W. A.; Niegisch, G. Evaluation of the Therapeutic Potential of the Novel Isotype Specific HDAC Inhibitor 4SC-202 in Urothelial Carcinoma Cell Lines. *Target. Oncol.* **2016**, *11* (6), 783–798. DOI: 10.1007/s11523-016-0444-7.

(218) Schäker-Hübner, L.; Haschemi, R.; Büch, T.; Kraft, F. B.; Brumme, B.; Schöler, A.; Jenke, R.; Meiler, J.; Aigner, A.; Bendas, G.; Hansen, F. K. Balancing Histone Deacetylase (HDAC) Inhibition and Drug-likeness: Biological and Physicochemical Evaluation of Class I Selective HDAC Inhibitors. *ChemMedChem* **2022**, *17* (9), e202100755. DOI: 10.1002/cmdc.202100755.

(219) Jiang, Y.; Xu, J.; Yue, K.; Huang, C.; Qin, M.; Chi, D.; Yu, Q.; Zhu, Y.; Hou, X.; Xu, T.; Li, M.; Chou, C. J.; Li, X. Potent Hydrazide-Based HDAC Inhibitors with a Superior

Pharmacokinetic Profile for Efficient Treatment of Acute Myeloid Leukemia In Vivo. *J. Med. Chem.* **2022**, *65* (1), 285–302. DOI: 10.1021/acs.jmedchem.1c01472.

(220) Li, X.; Peterson, Y. K.; Inks, E. S.; Himes, R. A.; Li, J.; Zhang, Y.; Kong, X.; Chou, C. J. Class I HDAC Inhibitors Display Different Antitumor Mechanism in Leukemia and Prostatic Cancer Cells Depending on Their p53 Status. *J. Med. Chem.* **2018**, *61* (6), 2589-2603. DOI: 10.1021/acs.jmedchem.8b00136.

(221) Lauffer, B. E. L.; Mintzer, R.; Fong, R.; Mukund, S.; Tam, C.; Zilberleyb, I.; Flicke, B.; Ritscher, A.; Fedorowicz, G.; Vallero, R.; Ortwine, D. F.; Gunzner, J.; Modrusan, Z.; Neumann, L.; Koth, C. M.; Lupardus, P. J.; Kaminker, J. S.; Heise, C. E.; Steiner, P. Histone deacetylase (HDAC) inhibitor kinetic rate constants correlate with cellular histone acetylation but not transcription and cell viability. *J. Biol. Chem.* **2013**, *288* (37), 26926-26943. DOI: 10.1074/jbc.M113.490706.

(222) Banerjee, S.; Badya, S. K.; Adhikari, N.; Jha, T.; Ghosh, B. Hydrazides as potential HDAC inhibitors: Structure-activity relationships and biological implications. *Curr. Top. Med. Chem.* **2023**, *23* (25), 2343–2372. DOI: 10.2174/1568026623666230405124207.

(223) McClure, J. J.; Zhang, C.; Inks, E. S.; Peterson, Y. K.; Li, J.; Chou, C. J. Development of Allosteric Hydrazide-Containing Class I Histone Deacetylase Inhibitors for Use in Acute Myeloid Leukemia. *J. Med. Chem.* **2016**, *59* (21), 9942–9959. DOI: 10.1021/acs.jmedchem.6b01385.

(224) Sun, P.; Wang, J.; Khan, K. S.; Yang, W.; Ng, B. W.-L.; Ilment, N.; Zessin, M.; Bülbül, E. F.; Robaa, D.; Erdmann, F.; Schmidt, M.; Romier, C.; Schutkowski, M.; Cheng, A. S.-L.; Sippl, W. Development of Alkylated Hydrazides as Highly Potent and Selective Class I Histone Deacetylase Inhibitors with T cell Modulatory Properties. *J. Med. Chem.* **2022**, 16313-16337. DOI: 10.1021/acs.jmedchem.2c01132.

(225) Becher, I.; Dittmann, A.; Savitski, M. M.; Hopf, C.; Drewes, G.; Bantscheff, M. Chemoproteomics reveals time-dependent binding of histone deacetylase inhibitors to endogenous repressor complexes. *ACS Chem. Biol.* **2014**, *9* (8), 1736–1746. DOI: 10.1021/cb500235n.

(226) Zhijun, H.; Shusheng, W.; Han, M.; Jianping, L.; Li-Sen, Q.; Dechun, L. Pre-clinical characterization of 4SC-202, a novel class I HDAC inhibitor, against colorectal cancer cells. *Tumor Biol.* **2016**, *37* (8), 10257–10267. DOI: 10.1007/s13277-016-4868-6.

(227) Zhang, X.-H.; Qin-Ma; Wu, H.-P.; Khamis, M. Y.; Li, Y.-H.; Ma, L.-Y.; Liu, H.-M. A Review of Progress in Histone Deacetylase 6 Inhibitors Research: Structural Specificity and Functional Diversity. *J. Med. Chem.* **2021**, *64* (3), 1362-1391. DOI: 10.1021/acs.jmedchem.0c01782.

(228) Depetter, Y.; Geurs, S.; Vreese, R. de; Goethals, S.; Vandoorn, E.; Laevens, A.; Steenbrugge, J.; Meyer, E.; Tullio, P. de; Bracke, M.; D'hooghe, M.; Wever, O. de. Selective

pharmacological inhibitors of HDAC6 reveal biochemical activity but functional tolerance in cancer models. *Int. J. Cancer* **2019**, *145* (3), 735–747. DOI: 10.1002/ijc.32169.

(229) Zhang, Y.; Kwon, S.; Yamaguchi, T.; Cubizolles, F.; Rousseaux, S.; Kneissel, M.; Cao, C.; Li, N.; Cheng, H.-L.; Chua, K.; Lombard, D.; Mizeracki, A.; Matthias, G.; Alt, F. W.; Khochbin, S.; Matthias, P. Mice lacking histone deacetylase 6 have hyperacetylated tubulin but are viable and develop normally. *Mol. Cell. Biol.* **2008**, *28* (5), 1688–1701. DOI: 10.1128/MCB.01154-06.

(230) Porter, N. J.; Mahendran, A.; Breslow, R.; Christianson, D. W. Unusual zinc-binding mode of HDAC6-selective hydroxamate inhibitors. *Proc. Natl. Acad. Sci. USA* **2017**, *114* (51), 13459-13464. DOI: 10.1073/pnas.1718823114.

(231) Butler, K. V.; Kalin, J.; Brochier, C.; Vistoli, G.; Langley, B.; Kozikowski, A. P. Rational design and simple chemistry yield a superior, neuroprotective HDAC6 inhibitor, tubastatin A. *J. Am. Chem. Soc.* **2010**, *132* (31), 10842–10846. DOI: 10.1021/ja102758v.

(232) Shen, S.; Svoboda, M.; Zhang, G.; Cavasin, M. A.; Motlova, L.; McKinsey, T. A.; Eubanks, J. H.; Bařinka, C.; Kozikowski, A. P. Structural and in Vivo Characterization of Tubastatin A, a Widely Used Histone Deacetylase 6 Inhibitor. *ACS Med. Chem. Lett.* **2020**, *11* (5), 706–712. DOI: 10.1021/acsmedchemlett.9b00560.

(233) Chi, Z.; Byeon, H.-E.; Seo, E.; Nguyen, Q.-A. T.; Lee, W.; Jeong, Y.; Choi, J.; Pandey, D.; Berkowitz, D. E.; Kim, J. H.; Lee, S. Y. Histone deacetylase 6 inhibitor tubastatin A attenuates angiotensin II-induced hypertension by preventing cystathionine γ-lyase protein degradation. *Pharmacol. Res.* **2019**, *146*, 104281. DOI: 10.1016/j.phrs.2019.104281.

(234) Urdiciain, A.; Erausquin, E.; Meléndez, B.; Rey, J. A.; Idoate, M. A.; Castresana, J. S. Tubastatin A, an inhibitor of HDAC6, enhances temozolomide-induced apoptosis and reverses the malignant phenotype of glioblastoma cells. *J. Oncol.* **2019**, *54* (5), 1797–1808. DOI: 10.3892/ijo.2019.4739.

(235) Song, Y.; Qin, L.; Yang, R.; Yang, F.; Kenechukwu, N. A.; Zhao, X.; Zhou, X.; Wen, X.; Li, L. Inhibition of HDAC6 alleviating lipopolysaccharide-induced p38MAPK phosphorylation and neuroinflammation in mice. *Pharmaceutical Biol.* **2019**, *57* (1), 263–268. DOI: 10.1080/13880209.2018.1563620.

(236) Bergman, J. A.; Woan, K.; Perez-Villarroel, P.; Villagra, A.; Sotomayor, E. M.; Kozikowski, A. P. Selective histone deacetylase 6 inhibitors bearing substituted urea linkers inhibit melanoma cell growth. *J. Med. Chem.* **2012**, *55* (22), 9891–9899. DOI: 10.1021/jm301098e.

(237) Sun, X.; Xie, Y.; Sun, X.; Yao, Y.; Li, H.; Li, Z.; Yao, R.; Xu, K. The selective HDAC6 inhibitor Nexturastat A induces apoptosis, overcomes drug resistance and inhibits tumor growth in multiple myeloma. *Biosci. Rep.* **2019**, *39* (3), BSR20181916. DOI: 10.1042/BSR20181916.

(238) Miyake, Y.; Keusch, J. J.; Wang, L.; Saito, M.; Hess, D.; Wang, X.; Melancon, B. J.; Helquist, P.; Gut, H.; Matthias, P. Structural insights into HDAC6 tubulin deacetylation and its selective inhibition. *Nat. Chem. Bio.* **2016**, *12* (9), 748–754. DOI: 10.1038/nchembio.2140.

(239) Mackwitz, M. K. W.; Hamacher, A.; Osko, J. D.; Held, J.; Schöler, A.; Christianson, D. W.; Kassack, M. U.; Hansen, F. K. Multicomponent Synthesis and Binding Mode of Imidazo[1,2-a]pyridine-Capped Selective HDAC6 Inhibitors. *Org. Let.* **2018**, *20*, 3255-3258. DOI: 10.1021/acs.orglett.8b01118.

(240) König, B.; Watson, P. R.; Reßing, N.; Cragin, A. D.; Schäker-Hübner, L.; Christianson, D. W.; Hansen, F. K. Difluoromethyl-1,3,4-oxadiazoles Are Selective, Mechanism-Based, and Essentially Irreversible Inhibitors of Histone Deacetylase 6. *J. Med. Chem.* **2023**, *66* (19), 13821–13837. DOI: 10.1021/acs.jmedchem.3c01345.

(241) Çakır, I.; Hadley, C. K.; Pan, P. L.; Bagchi, R. A.; Ghamari-Langroudi, M.; Porter, D. T.; Wang, Q.; Litt, M. J.; Jana, S.; Hagen, S.; Lee, P.; White, A.; Lin, J. D.; McKinsey, T. A.; Cone, R. D. Histone deacetylase 6 inhibition restores leptin sensitivity and reduces obesity. *Nat. Metab.* **2022**, *4* (1), 44–59. DOI: 10.1038/s42255-021-00515-3.

(242) Rautio, J.; Kumpulainen, H.; Heimbach, T.; Oliyai, R.; Oh, D.; Järvinen, T.; Savolainen, J. Prodrugs: design and clinical applications. *Nat. Rev. Drug. Discov.* **2008**, *7* (3), 255–270. DOI: 10.1038/nrd2468.

(243) Thomas, M.; Rivault, F.; Tranoy-Opalinski, I.; Roche, J.; Gesson, J.-P.; Papot, S. Synthesis and biological evaluation of the suberoylanilide hydroxamic acid (SAHA) beta-glucuronide and beta-galactoside for application in selective prodrug chemotherapy. *Bioorg. Med. Chem. Lett.* **2007**, *17* (4), 983-986. DOI: 10.1016/j.bmcl.2006.11.042.

(244) Liao, Y.; Xu, L.; Ou, S.; Edwards, H.; Luedtke, D.; Ge, Y.; Qin, Z. H2O2/Peroxynitrite-Activated Hydroxamic Acid HDAC Inhibitor Prodrugs Show Antileukemic Activities against AML Cells. *ACS Med. Chem. Lett.* **2018**, *9* (7), 635-640. DOI: 10.1021/acsmedchemlett.8b00057.

(245) Rautio, J.; Meanwell, N. A.; Di, L.; Hageman, M. J. The expanding role of prodrugs in contemporary drug design and development. *Nat. Rev. Drug. Discov.* **2018**, *17* (8), 559-587. DOI: 10.1038/nrd.2018.46.

(246) Skwarska, A.; Calder, E. D. D.; Sneddon, D.; Bolland, H.; Odyniec, M. L.; Mistry, I. N.; Martin, J.; Folkes, L. K.; Conway, S. J.; Hammond, E. M. Development and pre-clinical testing of a novel hypoxia-activated KDAC inhibitor. *Cell Chem. Biol.* **2021**, *28*, 1258-1270.e.13. DOI: 10.1016/j.chembiol.2021.04.004.

(247) Engels, J.; Schlaeger, E. J. Synthesis, structure, and reactivity of adenosine cyclic 3',5'-phosphate benzyl triesters. *J. Med. Chem.* **1977**, *20* (7), 907–911. DOI: 10.1021/jm00217a008.

(248) Troelsen, K. S.; Calder, E. D. D.; Skwarska, A.; Sneddon, D.; Hammond, E. M.; Conway, S. J. Zap-Pano: a Photocaged Prodrug of the KDAC Inhibitor Panobinostat. *ChemMedChem* **2021**, *16*, 3691-3700. DOI: 10.1002/cmdc.202100403.

(249) Li, K.; Crews, C. M. PROTACs: past, present and future. *Chem. Soc. Rev.* **2022**, *51* (12), 5214–5236. DOI: 10.1039/d2cs00193d.

(250) Nandi, D.; Tahiliani, P.; Kumar, A.; Chandu, D. The ubiquitin-proteasome system. *J. Biosci.* **2006**, *31* (1), 137–155. DOI: 10.1007/BF02705243.

(251) Sakamoto, K. M.; Kim, K. B.; Kumagai, A.; Mercurio, F.; Crews, C. M.; Deshaies, R. J. Protacs: chimeric molecules that target proteins to the Skp1-Cullin-F box complex for ubiquitination and degradation. *Proc. Natl. Acad. Sci. USA* **2001**, *98* (15), 8554–8559. DOI: 10.1073/pnas.141230798.

(252) Khan, S.; He, Y.; Zhang, X.; Yuan, Y.; Pu, S.; Kong, Q.; Zheng, G.; Zhou, D. PROteolysis TArgeting Chimeras (PROTACs) as emerging anticancer therapeutics. *Oncogene* **2020**, *39*, 4909–4927. DOI: 10.1038/s41388-020-1336-y.

(253) Moreau, K.; Coen, M.; Zhang, A. X.; Pachl, F.; Castaldi, M. P.; Dahl, G.; Boyd, H.; Scott, C.; Newham, P. Proteolysis-targeting chimeras in drug development: A safety perspective. *Br. J. Pharmacol.* **2020**, *177* (8), 1709–1718. DOI: 10.1111/bph.15014.

(254) Paiva, S.-L.; Crews, C. M. Targeted protein degradation: elements of PROTAC design. *Curr. Opin. Chem. Biol.* **2019**, *50*, 111–119. DOI: 10.1016/j.cbpa.2019.02.022.

(255) Schneekloth, A. R.; Pucheault, M.; Tae, H. S.; Crews, C. M. Targeted intracellular protein degradation induced by a small molecule: En route to chemical proteomics. *Bioorg. Med. Chem. Lett.* **2008**, *18* (22), 5904–5908. DOI: 10.1016/j.bmcl.2008.07.114.

(256) Itoh, Y.; Ishikawa, M.; Naito, M.; Hashimoto, Y. Protein knockdown using methyl bestatin-ligand hybrid molecules: design and synthesis of inducers of ubiquitination-mediated degradation of cellular retinoic acid-binding proteins. *J. Am. Chem. Soc.* **2010**, *132* (16), 5820–5826. DOI: 10.1021/ja100691p.

(257) Lee, J.; Lee, Y.; Jung, Y. M.; Park, J. H.; Yoo, H. S.; Park, J. Discovery of E3 Ligase Ligands for Target Protein Degradation. *Molecules* **2022**, *27* (19), 6515. DOI: 10.3390/molecules27196515.

(258) Singhal, S.; Mehta, J.; Desikan, R.; Ayers, D.; Roberson, P.; Eddlemon, P.; Munshi, N.; Anaissie, E.; Wilson, C.; Dhodapkar, M.; Zeddis, J.; Barlogie, B. Antitumor activity of thalidomide in refractory multiple myeloma. *N. Engl. J. Med.* **1999**, *341* (21), 1565–1571. DOI: 10.1056/NEJM199911183412102.

(259) Ito, T.; Ando, H.; Suzuki, T.; Ogura, T.; Hotta, K.; Imamura, Y.; Yamaguchi, Y.; Handa, H. Identification of a primary target of thalidomide teratogenicity. *Science* **2010**, *327* (5971), 1345–1350. DOI: 10.1126/science.1177319.

(260) Cardote, T. A. F.; Gadd, M. S.; Ciulli, A. Crystal Structure of the Cul2-Rbx1-EloBC-VHL Ubiquitin Ligase Complex. *Structure* **2017**, *25* (6), 901-911. DOI: 10.1016/j.str.2017.04.009.

(261) Kaelin, W. G. The von Hippel–Lindau Tumor Suppressor Protein. *Annu. Rev. Cancer Biol.* **2018**, *2* (1), 91–109. DOI: 10.1146/annurev-cancerbio-030617-050527.

(262) Kaelin, W. G.; Ratcliffe, P. J. Oxygen sensing by metazoans: the central role of the HIF hydroxylase pathway. *Mol. Cell.* **2008**, *30* (4), 393–402. DOI: 10.1016/j.molcel.2008.04.009.
(263) Diehl, C. J.; Ciulli, A. Discovery of small molecule ligands for the von Hippel-Lindau (VHL) E3 ligase and their use as inhibitors and PROTAC degraders. *Chem. Soc. Rev.* **2022**, *51* (19), 8216–8257. DOI: 10.1039/d2cs00387b.
(264) Schiedel, M.; Herp, D.; Hammelmann, S.; Swyter, S.; Lehotzky, A.; Robaa, D.; Oláh, J.; Ovádi, J.; Sippl, W.; Jung, M. Chemically Induced Degradation of Sirtuin 2 (Sirt2) by a Proteolysis Targeting Chimera (PROTAC) Based on Sirtuin Rearranging Ligands (SirReals). *J. Med. Chem.* **2018**, *61* (2), 482-491. DOI: 10.1021/acs.jmedchem.6b01872.
(265) Yang, K.; Song, Y.; Xie, H.; Wu, H.; Wu, Y.-T.; Leisten, E. D.; Tang, W. Development of the first small molecule histone deacetylase 6 (HDAC6) degraders. *Bioorg. Med. Chem. Lett.* **2018**, *28* (14), 2493–2497. DOI: 10.1016/j.bmcl.2018.05.057.
(266) Xiong, Y.; Donovan, K. A.; Eleuteri, N. A.; Kirmani, N.; Yue, H.; Razov, A.; Krupnick, N. M.; Nowak, R. P.; Fischer, E. S. Chemo-proteomics exploration of HDAC degradability by small molecule degraders. *Cell Chem. Biol.* **2021**, *28* (10), 1514-1527.e4. DOI: 10.1016/j.chembiol.2021.07.002.
(267) Xiao, Y.; Wang, J.; Zhao, L. Y.; Chen, X.; Zheng, G.; Zhang, X.; Liao, D. Discovery of histone deacetylase 3 (HDAC3)-specific PROTACs. *Chem. Commun.* **2020**, *56* (68), 9866-9869. DOI: 10.1039/d0cc03243c.
(268) Smalley, J. P.; Adams, G. E.; Millard, C. J.; Song, Y.; Norris, J. K. S.; Schwabe, J. W. R.; Cowley, S. M.; Hodgkinson, J. T. PROTAC-mediated degradation of class I histone deacetylase enzymes in corepressor complexes. *Chem. Commun.* **2020**, *56* (32), 4476–4479. DOI: 10.1039/d0cc01485k.
(269) Fischer, F.; Alves Avelar, L. A.; Murray, L.; Kurz, T. Designing HDAC-PROTACs: lessons learned so far. *Future Med. Chem.* **2022**, *14* (3), 143–166. DOI: 10.4155/fmc-2021-0206.
(270) Yang, K.; Wu, H.; Zhang, Z.; Leisten, E. D.; Nie, X.; Liu, B.; Wen, Z.; Zhang, J.; Cunningham, M. D.; Tang, W. Development of Selective Histone Deacetylase 6 (HDAC6) Degraders Recruiting Von Hippel-Lindau (VHL) E3 Ubiquitin Ligase. *ACS Med. Chem. Lett.* **2020**, *11* (4), 575–-581. DOI: 10.1021/acsmedchemlett.0c00046.
(271) Wu, H.; Yang, K.; Zhang, Z.; Leisten, E. D.; Li, Z.; Xie, H.; Liu, J.; Smith, K. A.; Novakova, Z.; Barinka, C.; Tang, W. Development of Multifunctional Histone Deacetylase 6 Degraders with Potent Antimyeloma Activity. *J. Med. Chem.* **2019**, *62* (15), 7042-7057. DOI: 10.1021/acs.jmedchem.9b00516.
(272) Patel, U.; Smalley, J. P.; Hodgkinson, J. T. PROTAC chemical probes for histone deacetylase enzymes. *RSC Chem. Biol.* **2023**, *4* (9), 623–634. DOI: 10.1039/d3cb00105a.
(273) Smalley, J. P.; Baker, I. M.; Pytel, W. A.; Lin, L.-Y.; Bowman, K. J.; Schwabe, J. W. R.; Cowley, S. M.; Hodgkinson, J. T. Optimization of Class I Histone Deacetylase PROTACs

Reveals that HDAC1/2 Degradation is Critical to Induce Apoptosis and Cell Arrest in Cancer Cells. *J. Med. Chem.* **2022**, *65* (7), 5642-5659. DOI: 10.1021/acs.jmedchem.1c02179.

(274) Cao, F.; Weerd, S. de; Chen, D.; Zwinderman, M. R. H.; van der Wouden, P. E.; Dekker, F. J. Induced protein degradation of histone deacetylases 3 (HDAC3) by proteolysis targeting chimera (PROTAC). *Eur. J. Med. Chem.* **2020**, *208*, 112800. DOI: 10.1016/j.ejmech.2020.112800.

(275) Zhao, C.; Chen, S.; Chen, D.; Río-Bergé, C.; Zhang, J.; van der Wouden, P. E.; Daemen, T.; Dekker, F. J. Histone Deacetylase 3-Directed PROTACs Have Anti-inflammatory Potential by Blocking Polarization of M0-like into M1-like Macrophages. *Angew. Chem. Int. Ed.* **2023**, e202310059. DOI: 10.1002/anie.202310059.

(276) Huang, J.; Zhang, J.; Xu, W.; Wu, Q.; Zeng, R.; Liu, Z.; Tao, W.; Chen, Q.; Wang, Y.; Zhu, W.-G. Structure-Based Discovery of Selective Histone Deacetylase 8 Degraders with Potent Anticancer Activity. *J. Med. Chem.* **2023**, *66* (2), 1186–1209. DOI: 10.1021/acs.jmedchem.2c00739.

(277) Li, X.; Song, S.; Liu, Y.; Ko, S.-H.; Kao, H.-Y. Phosphorylation of the histone deacetylase 7 modulates its stability and association with 14-3-3 proteins. *J. Biol. Chem.* **2004**, *279* (33), 34201–34208. DOI: 10.1074/jbc.M405179200.

(278) Macabuag, N.; Esmieu, W.; Breccia, P.; Jarvis, R.; Blackaby, W.; Lazari, O.; Urbonas, L.; Eznarriaga, M.; Williams, R.; Strijbosch, A.; van de Bospoort, R.; Matthews, K.; Clissold, C.; Ladduwahetty, T.; Vater, H.; Heaphy, P.; Stafford, D. G.; Wang, H.-J.; Mangette, J. E.; McAllister, G.; Beaumont, V.; Vogt, T. F.; Wilkinson, H. A.; Doherty, E. M.; Dominguez, C. Developing HDAC4-Selective Protein Degraders To Investigate the Role of HDAC4 in Huntington's Disease Pathology. *J. Med. Chem.* **2022**, *65* (18), 12445–12459. DOI: 10.1021/acs.jmedchem.2c01149.

(279) Sinatra, L.; Yang, J.; Schliehe-Diecks, J.; Dienstbier, N.; Vogt, M.; Gebing, P.; Bachmann, L. M.; Sönnichsen, M.; Lenz, T.; Stühler, K.; Schöler, A.; Borkhardt, A.; Bhatia, S.; Hansen, F. K. Solid-Phase Synthesis of Cereblon-Recruiting Selective Histone Deacetylase 6 Degraders (HDAC6 PROTACs) with Antileukemic Activity. *J. Med. Chem.* **2022**, *65* (24), 16860–16878. DOI: 10.1021/acs.jmedchem.2c01659.

(280) Keuler, T.; König, B.; Bückreiß, N.; Kraft, F. B.; König, P.; Schäker-Hübner, L.; Steinebach, C.; Bendas, G.; Gütschow, M.; Hansen, F. K. Development of the first non-hydroxamate selective HDAC6 degraders. *Chem. Commun.* **2022**, *58* (79), 11087–11090. DOI: 10.1039/d2cc03712b.

(281) Krieger, V.; Hamacher, A.; Cao, F.; Stenzel, K.; Gertzen, C. G. W.; Schäker-Hübner, L.; Kurz, T.; Gohlke, H.; Dekker, F. J.; Kassack, M. U.; Hansen, F. K. Synthesis of Peptoid-Based Class I-Selective Histone Deacetylase Inhibitors with Chemosensitizing Properties. *J. Med. Chem.* **2019**, *62* (24), 11260-11279. DOI: 10.1021/acs.jmedchem.9b01489.

(282) Cao, F.; Zwinderman, M. R. H.; Dekker, F. J. The Process and Strategy for Developing Selective Histone Deacetylase 3 Inhibitors. *Molecules* **2018**, *23* (3), 551. DOI: 10.3390/molecules23030551.

(283) Aldana-Masangkay, G. I.; Sakamoto, K. M. The role of HDAC6 in cancer. *J. Biomed. Biotechnol.* **2011**, *2011*, 875-885. DOI: 10.1155/2011/875824.

(284) Bockstiegel, J.; Wurnig, S. L.; Engelhardt, J.; Enns, J.; Hansen, F. K.; Weindl, G. Pharmacological inhibition of HDAC6 suppresses NLRP3 inflammasome-mediated IL-1β release. *Biochem. Pharmacol.* **2023**, *215*, 115693. DOI: 10.1016/j.bcp.2023.115693.

(285) Topart, C.; Werner, E.; Arimondo, P. B. Wandering along the epigenetic timeline. *Clin. Epigenetics* **2020**, *12* (97), 1-13. DOI: 10.1186/s13148-020-00893-7.

(286) Biswas, S.; Rao, C. M. Epigenetics in cancer: Fundamentals and Beyond. *Pharmacol. Ther.* **2017**, *173*, 118-134. DOI: 10.1016/j.pharmthera.2017.02.011.

(287) Morel, D.; Jeffery, D.; Aspeslagh, S.; Almouzni, G.; Postel-Vinay, S. Combining epigenetic drugs with other therapies for solid tumours - past lessons and future promise. *Nat. Rev. Clin. Oncol.* **2020**, *17* (2), 91–107. DOI: 10.1038/s41571-019-0267-4.

(288) Zhang, Y.; Li, Y. The Expanding Mi-2/NuRD Complexes: A Schematic Glance. *Proteomics Insights* **2010**, *3*, PRI.S6329. DOI: 10.4137/PRI.S6329.

(289) Liu, Y.; Peng, L.; Seto, E.; Huang, S.; Qiu, Y. Modulation of histone deacetylase 6 (HDAC6) nuclear import and tubulin deacetylase activity through acetylation. *JBC* **2012**, *287* (34), 29168-29174. DOI: 10.1074/jbc.M112.371120.

(290) Ito, Y.; Makita, S.; Tobinai, K. Development of new agents for peripheral T-cell lymphoma. *Expert Opin. Biol. Ther.* **2019**, *19* (3), 197-209. DOI: 10.1080/14712598.2019.1572746. Published Online: Jan. 29, 2019.

(291) Ning, Z. Why ACE—overview of the development of the subtype-selective histone deacetylase inhibitor chidamide in hormone receptor positive advanced breast cancer. *Transl. Breast Cancer Res.* **2020**, *1*, 1-10. DOI: 10.21037/tbcr.2020.03.06.

(292) Vaidya, F. U.; Sufiyan Chhipa, A.; Mishra, V.; Gupta, V. K.; Rawat, S. G.; Kumar, A.; Pathak, C. Molecular and cellular paradigms of multidrug resistance in cancer. *Cancer Rep.* **2022**, *5* (12), e1291. DOI: 10.1002/cnr2.1291. Published Online: Oct. 13, 2020.

(293) Alves Avelar, L. A.; Schrenk, C.; Sönnichsen, M.; Hamacher, A.; Hansen, F. K.; Schliehe-Diecks, J.; Borkhardt, A.; Bhatia, S.; Kassack, M. U.; Kurz, T. Synergistic induction of apoptosis in resistant head and neck carcinoma and leukemia by alkoxyamide-based histone deacetylase inhibitors. *Eur. J. Med. Chem.* **2021**, *211*, 113095. DOI: 10.1016/j.ejmech.2020.113095.

(294) Gosepath, E. M.; Eckstein, N.; Hamacher, A.; Servan, K.; Jonquieres, G. von; Lage, H.; Györffy, B.; Royer, H. D.; Kassack, M. U. Acquired cisplatin resistance in the head-neck cancer cell line Cal27 is associated with decreased DKK1 expression and can partially be reversed by overexpression of DKK1. *Int. J. Cancer* **2008**, *123* (9), 2013–2019. DOI: 10.1002/ijc.23721.

(295) Engelke, L. H.; Hamacher, A.; Proksch, P.; Kassack, M. U. Ellagic Acid and Resveratrol Prevent the Development of Cisplatin Resistance in the Epithelial Ovarian Cancer Cell Line A2780. *J Cancer* **2016**, *7* (4), 353–363. DOI: 10.7150/jca.13754.

(296) Gandin, V.; Hoeschele, J. D.; Margiotta, N. Special Issue "Cisplatin in Cancer Therapy: Molecular Mechanisms of Action 3.0". *Int. J. Mol. Sci* **2023**, *24* (9), 7917. DOI: 10.3390/ijms24097917.

(297) Pchejetski, D.; Alfraidi, A.; Sacco, K.; Alshaker, H.; Muhammad, A.; Monzon, L. Histone deacetylases as new therapy targets for platinum-resistant epithelial ovarian cancer. *J. Cancer res. Clin. Oncol.* **2016**, *142* (8), 1659–1671. DOI: 10.1007/s00432-015-2064-5.

(298) Bradner, J. E.; West, N.; Grachan, M. L.; Greenberg, E. F.; Haggarty, S. J.; Warnow, T.; Mazitschek, R. Chemical phylogenetics of histone deacetylases. *Nat. Chem. Bio.* **2010**, *6* (3), 238-243. DOI: 10.1038/nchembio.313.

(299) Maolanon, A. R.; Madsen, A. S.; Olsen, C. A. Innovative Strategies for Selective Inhibition of Histone Deacetylases. *Cell chemical biology* **2016**, *23* (7), 759–768. DOI: 10.1016/j.chembiol.2016.06.011.

(300) Krieger, V.; Hamacher, A.; Gertzen, C. G. W.; Senger, J.; Zwinderman, M. R. H.; Marek, M.; Romier, C.; Dekker, F. J.; Kurz, T.; Jung, M.; Gohlke, H.; Kassack, M. U.; Hansen, F. K. Design, Multicomponent Synthesis, and Anticancer Activity of a Focused Histone Deacetylase (HDAC) Inhibitor Library with Peptoid-Based Cap Groups. *J. Med. Chem.* **2017**, *60* (13), 5493–5506. DOI: 10.1021/acs.jmedchem.7b00197.

(301) Stenzel, K.; Hamacher, A.; Hansen, F. K.; Gertzen, C. G. W.; Senger, J.; Marquardt, V.; Marek, L.; Marek, M.; Romier, C.; Remke, M.; Jung, M.; Gohlke, H.; Kassack, M. U.; Kurz, T. Alkoxyurea-Based Histone Deacetylase Inhibitors Increase Cisplatin Potency in Chemoresistant Cancer Cell Lines. *J. Med. Chem.* **2017**, *60* (13), 5334–5348. DOI: 10.1021/acs.jmedchem.6b01538.

(302) Chou, T. C.; Talalay, P. Quantitative analysis of dose-effect relationships: the combined effects of multiple drugs or enzyme inhibitors. *Adv. enzyme Regul.* **1984**, *22*, 27–55. DOI: 10.1016/0065-2571(84)90007-4.

(303) Loewe, S.; Muischnek, H. Über Kombinationswirkungen. *Archiv f. experiment. Pathol. u. Pharmakol* **1926**, *114* (5-6), 313–326. DOI: 10.1007/BF01952257.

(304) Loewe, S. The problem of synergism and antagonism of combined drugs. *Arzneimittel-Forschung* **1953**, *3* (6), 285–290.

(305) Di Veroli, G. Y.; Fornari, C.; Wang, D.; Mollard, S.; Bramhall, J. L.; Richards, F. M.; Jodrell, D. I. Combenefit: an interactive platform for the analysis and visualization of drug combinations. *Bioinformatics* **2016**, *32* (18), 2866–2868. DOI: 10.1093/bioinformatics/btw230.

(306) Kraft, F. B.; Hanl, M.; Feller, F.; Schäker-Hübner, L.; Hansen, F. K. Photocaged Histone Deacetylase Inhibitors as Prodrugs in Targeted Cancer Therapy. *Pharmaceuticals* **2023**, *16* (3), 356. DOI: 10.3390/ph16030356.

(307) Nivón, L. G.; Moretti, R.; Baker, D. A Pareto-optimal refinement method for protein design scaffolds. *PloS one* **2013**, *8* (4), e59004. DOI: 10.1371/journal.pone.0059004.

(308) Kothiwale, S.; Mendenhall, J. L.; Meiler, J. BCL:Conf: small molecule conformational sampling using a knowledge based rotamer library. *Cheminform* **2015**, *7*, 1–15. DOI: 10.1186/s13321-015-0095-1.

(309) DeLuca, S.; Khar, K.; Meiler, J. Fully Flexible Docking of Medium Sized Ligand Libraries with RosettaLigand. *PloS one* **2015**, *10* (7), e0132508. DOI: 10.1371/journal.pone.0132508.

(310) Kaufmann, K. W.; Meiler, J. Using RosettaLigand for small molecule docking into comparative models. *PloS one* **2012**, *7* (12), e50769. DOI: 10.1371/journal.pone.0050769.

(311) Meiler, J.; Baker, D. ROSETTALIGAND: protein-small molecule docking with full side-chain flexibility. *Proteins* **2006**, *65* (3), 538-548. DOI: 10.1002/prot.21086.

(312) Eckstein, N.; Servan, K.; Girard, L.; Di Cai; Jonquieres, G. von; Jaehde, U.; Kassack, M. U.; Gazdar, A. F.; Minna, J. D.; Royer, H.-D. Epidermal growth factor receptor pathway analysis identifies amphiregulin as a key factor for cisplatin resistance of human breast cancer cells. *J. Biol. Chem.* **2008**, *283* (2), 739–750. DOI: 10.1074/jbc.M706287200.

(313) Ciossek, T.; Julius, H.; Wieland, H.; Maier, T.; Beckers, T. A homogeneous cellular histone deacetylase assay suitable for compound profiling and robotic screening. *Anal. Biochem.* **2008**, *372* (1), 72-81. DOI: 10.1016/j.ab.2007.07.024. Published Online: Aug. 2, 2007.

(314) Bonfils, C.; Kalita, A.; Dubay, M.; Siu, L. L.; Carducci, M. A.; Reid, G.; Martell, R. E.; Besterman, J. M.; Li, Z. Evaluation of the pharmacodynamic effects of MGCD0103 from preclinical models to human using a novel HDAC enzyme assay. *Clinc. Cancer Res.* **2008**, *14* (11), 3441–3449. DOI: 10.1158/1078-0432.CCR-07-4427.

(315) Marek, L.; Hamacher, A.; Hansen, F. K.; Kuna, K.; Gohlke, H.; Kassack, M. U.; Kurz, T. Histone deacetylase (HDAC) inhibitors with a novel connecting unit linker region reveal a selectivity profile for HDAC4 and HDAC5 with improved activity against chemoresistant cancer cells. *J. Med. Chem.* **2013**, *56* (2), 427–436. DOI: 10.1021/jm301254q.

(316) Hoffmann, K.; Brosch, G.; Loidl, P.; Jung, M. A non-isotopic assay for histone deacetylase activity. *Nucleic Acids Res.* **1999**, *27* (9), 2057–2058. DOI: 10.1093/nar/27.9.2057.

(317) Bandolik, J. J.; Hamacher, A.; Schrenk, C.; Weishaupt, R.; Kassack, M. U. Class I-Histone Deacetylase (HDAC) Inhibition is Superior to pan-HDAC Inhibition in Modulating Cisplatin Potency in High Grade Serous Ovarian Cancer Cell Lines. *Int. J. Mol. Sci* **2019**, *20* (12). DOI: 10.3390/ijms20123052.

(318) Chou, T.-C. Drug combination studies and their synergy quantification using the Chou-Talalay method. *Cancer Res.* **2010**, *70* (2), 440–446. DOI: 10.1158/0008-5472.CAN-09-1947.

(319) Ziegler, V.; Albers, A.; Fritz, G. Lovastatin protects keratinocytes from DNA damage-related pro-apoptotic stress responses stimulated by anticancer therapeutics. *Biochimica et biophysica acta* **2016**, *1863* (6 Pt A), 1082–1092. DOI: 10.1016/j.bbamcr.2016.02.009.
(320) *Test No. 123: Partition Coefficient (1-Octanol/Water): Slow-Stirring Method*; OECD, 2022. DOI: 10.1787/9789264015845-en.
(321) Bruijn, J. de; Busser, F.; Seinen, W.; Hermens, J. Determination of octanol/water partition coefficients for hydrophobic organic chemicals with the "slow-stirring" method. *Enviro Toxic and Chemistry* **1989**, *8* (6), 499–512. DOI: 10.1002/etc.5620080607.
(322) *Test No. 105: Water Solubility*; OECD, 1995. DOI: 10.1787/9789264069589-en.
(323) Sosič, I.; Bricelj, A.; Steinebach, C. E3 ligase ligand chemistries: from building blocks to protein degraders. *Chem. Soc. Rev.* **2022**, *51*, 3487-3534. DOI: 10.1039/d2cs00148a.
(324) Mackwitz, M. K. W.; Hesping, E.; Antonova-Koch, Y.; Diedrich, D.; Woldearegai, T. G.; Skinner-Adams, T.; Clarke, M.; Schöler, A.; Limbach, L.; Kurz, T.; Winzeler, E. A.; Held, J.; Andrews, K. T.; Hansen, F. K. Structure-Activity and Structure-Toxicity Relationships of Peptoid-Based Histone Deacetylase Inhibitors with Dual-Stage Antiplasmodial Activity. *ChemMedChem* **2019**, *14* (9), 912–926. DOI: 10.1002/cmdc.201800808.
(325) Steinebach, C.; Voell, S. A.; Vu, L. P.; Bricelj, A.; Sosič, I.; Schnakenburg, G.; Gütschow, M. A Facile Synthesis of Ligands for the von Hippel–Lindau E3 Ligase. *Synthesis* **2020**, *52*, A-G. DOI: 10.1055/s-0040-1707400.
(326) Horbert, R.; Pinchuk, B.; Davies, P.; Alessi, D.; Peifer, C. Photoactivatable Prodrugs of Antimelanoma Agent Vemurafenib. *ACS Chem. Biol.* **2015**, *10* (9), 2099-2107. DOI: 10.1021/acschembio.5b00174.
(327) Naro, Y.; Darrah, K.; Deiters, A. Optical Control of Small Molecule-Induced Protein Degradation. *J. Am. Chem. Soc.* **2020**, *142* (5), 2193–2197. DOI: 10.1021/jacs.9b12718.
(328) Huang, Z. A review of progress in clinical photodynamic therapy. *TCRT* **2005**, *4* (3), 283-293. DOI: 10.1177/153303460500400308.

8 Appendix

This section contains the full-length publications of the chapters 2 and 5, including the supporting information. Furthermore, this appendix contains the NMR spectra of newly synthesized compounds and HPLC chromatograms of all final compounds reported in chapter 3 and 4. Please note that the copyright of the publications belongs to the publishers of the respective journals, as indicated by the copyright statements denoted before each paper.

8.1 Appendix I. Publication I: Groebke Blackburn Bienaymé-mediated multi-component synthesis of selective HDAC6 inhibitors with anti-inflammatory properties

The following pages include the article “Groebke Blackburn Bienaymé-mediated multi-component synthesis of selective HDAC6 inhibitors with anti-inflammatory properties” as it was published in Bioorganic Chemistry by Elsevier.

The article is reprinted with permission from:

Kraft, F. B.; Enns, J.; Honin, I.; Engelhardt, J.; Schöler, A.; Smith, S. T.; Meiler, J.; Schäker-Hübner, L.; Weindl, G.; Hansen, F. K. Groebke Blackburn Bienaymé-mediated multi-component synthesis of selective HDAC6 inhibitors with anti-inflammatory properties. *Bioorg. Chem.* **2024**, *143*, 107072.

Copyright 2023. Elsevier Inc.

Bioorganic Chemistry 143 (2024) 107072



Contents lists available at ScienceDirect

Bioorganic Chemistry

journal homepage: www.elsevier.com/locate/bioorg



Groebke Blackburn Bienaymé-mediated multi-component synthesis of selective HDAC6 inhibitors with anti-inflammatory properties

Fabian B. Kraft [a], Jana Enns [b], Irina Honin [a], Jonas Engelhardt [b], Andrea Schöler [c], Shannon T. Smith [d], Jens Meiler [c,d], Linda Schäker-Hübner [a], Günther Weindl [b], Finn K. Hansen [a,*]

[a] Department of Pharmaceutical and Cell Biological Chemistry, Pharmaceutical Institute, University of Bonn, An der Immenburg 4, 53121 Bonn, Germany
[b] Department of Pharmacology and Toxicology, Pharmaceutical Institute, University of Bonn, Gerhard-Domagk-Str.3, 53121 Bonn, Germany
[c] Institute for Drug Discovery, Medicinal Faculty, University Leipzig, Brüderstraße 34, 04103 Leipzig, Germany
[d] Center for Structural Biology, Vanderbilt University, Nashville, TN 37240, USA

ARTICLE INFO

Keywords:
Histone deacetylase
Cancer
NLRP3 inflammasome
Inflammation
HDAC6

ABSTRACT

Histone deacetylases (HDACs) are a class of enzymes that cleave acyl groups from lysine residues of histone and non-histone proteins. There are 18 human HDAC isoforms with different cellular targets and functions. Among them, HDAC6 was found to be overexpressed in different types of cancer. However, when used in monotherapy, HDAC6 inhibition by selective inhibitors fails to show pronounced anti-cancer effects. The HDAC6 enzyme also addresses non-histone proteins like α-tubulin and cortactin, making it important for cell migration and angiogenesis. Recently, the NLRP3 inflammasome was identified as an important regulator of inflammation and immune responses and, importantly, HDAC6 is critically involved the activation of the inflammasome. We herein report the design, synthesis and biological evaluation of a library of selective HDAC6 inhibitors. Starting from the previously published crystal structure of **MAIP-032** in complex with CD2 of zHDAC6, we performed docking studies to evaluate additional possible interactions of the cap group with the L1-loop pocket. Based on the results we synthesized 13 novel HDAC6 inhibitors *via* the *Groebke-Blackburn-Bienaymé* three component reaction as the key step. Compounds **8k** (HDAC1 IC_{50}: 5.87 μM; HDAC6 IC_{50}: 0.024 μM; selectivity factor ($SF^{1/6}$): 245) and **8m** (HDAC1 IC_{50}: 3.07 μM; HDAC6 IC_{50}: 0.026 μM; $SF^{1/6}$: 118) emerged as the most potent and selective inhibitors of HDAC6 and outperformed the lead structure **MAIP-032** (HDAC1 IC_{50}: 2.20 μM; HDAC6 IC_{50}: 0.058 μM; $SF^{1/6}$: 38) both in terms of inhibitory potency and selectivity. Subsequent immunoblot analysis confirmed the high selectivity of **8k** and **8m** for HDAC6 in a cellular environment. While neither **8k** and **8m** nor the selectivity HDAC6 inhibitor tubastatin A showed antiproliferative effects in the U-87 MG glioblastoma cell line, compound **8m** attenuated cell migration significantly in wound healing assays in U-87 MG cells. Moreover, in macrophages compounds **8k** and **8m** demonstrated significant inhibition of LPS-induced *IL1B* mRNA expression and TNF release. These findings suggest that our imidazo[1,2-*a*]pyridine-capped HDAC6 inhibitors may serve as promising candidates for the development of drugs to effectively treat NLRP3 inflammasome-driven inflammatory diseases.

1. Introduction

Histone deacetylases (HDACs) are a class of enzymes, which remove acetyl groups from histone and non-histone proteins [1]. There are 18 human HDAC isoforms known, which can be divided into four classes, according to their structural features, homology, and cellular localization. Class I, II and IV HDACs possess a Zn^{2+} ion in their catalytic center. The remaining seven isoforms belong to the class III, the sirtuin family, which depend on the cofactor NAD^{+} for their enzymatic activity [2–4]. HDACs have a direct influence on important cellular processes like cell

Abbreviations: CD, Catalytical domain; FDA, U.S. Food and Drug Administration; GBB, Groebke Blackburn Bienaymé; HDAC, Histone deacetylase; HSP90, Heat shock protein 90; IL1-b, Interleukin-1-beta; LDH, Lactate dehydrogenase; LPS, Lipopolysaccharaide; NLRP, Nucleotide-binding oligomerization domain; SEM, Standard error of the mean; SF, Selectivity factor; TLR, Toll like receptor; TNF, Tumor necrosis factor.

* Corresponding author.
E-mail address: finn.hansen@uni-bonn.de (F.K. Hansen).

https://doi.org/10.1016/j.bioorg.2023.107072
Received 9 October 2023; Received in revised form 19 December 2023; Accepted 27 December 2023
Available online 2 January 2024
0045-2068/© 2023 Elsevier Inc. All rights reserved.

proliferation [5] and migration [6]. The upregulation of HDAC enzymes has been implicated in a range of diseases, establishing them as valuable therapeutic targets [7–9]. Promising results have emerged from both preclinical and clinical studies demonstrating the efficacy of HDAC inhibition [10–13]. Notably, four non-selective HDAC inhibitors (HDACi) have obtained FDA approval for different hematological malignancies (Fig. 1A) [9,14].

Despite their success, those HDACi exhibit serious side effects, often leading to treatment interruption [12,15]. One way to circumvent unwanted side effects is the design of more selective inhibitors [16]. The HDAC6 enzyme, a member of class IIb, is mainly localized in the cytoplasm [17]. Unlike class I enzymes, HDAC6 addresses non-histone proteins like the cytoskeletal proteins α-tubulin, cortactin, and tau [18–20]. This makes HDAC6 a key player in various cellular processes, including tumor cell migration and angiogenesis [6] as well as in non-cancer diseases like fibrosis or Alzheimer [21]. In addition, HDAC6 plays a crucial role in the refolding of misfolded proteins by activating Hsp90 and facilitating their targeted degradation through aggresome formation [18]. Despite being overexpressed in several cancer types, selective HDAC6 inhibition fails to show anti-cancer properties when used in monotherapy [22] and HDAC6 knock-out mice produce a viable phenotype [23,24]. This indicates a possible use of HDAC6 inhibitors beyond of oncology. Recently, HDAC6 has also been connected with the activation of the NLRP3 inflammasome. By acting as a dynein adaptor for microtubule transport, HDAC6 is crucial for inflammasome formation in mice, making it a potential therapeutic target for NLRP3 driven inflammatory diseases [25]. The NLRP3 inflammasome is a cytoplasmic complex involved in innate immunity and inflammation [26]. When activated, NLRP3 triggers the generation and release of pro-inflammatory cytokines like interleukin (IL)-1β, which plays a significant role in the development of chronic inflammatory diseases, including gout, rheumatoid arthritis, and inflammatory bowel disease [27]. Consequently, inhibition of the NLRP3 inflammasome has become a target for anti-inflammatory therapy [28,29]. HDAC10, the closest paralog of HDAC6, is implicated in various cellular processes, including cell cycle regulation and apoptosis, and is primarily acting as polyamine deacetylase [30]. Recent findings highlight that HDAC10 alleviates intracerebral hemorrhage (ICH)-induced injury by down-regulating the inflammatory response induced by NLRP3 inflammasomes through the protein tyrosine phosphatase, nonreceptor type 22 (PTPN22) pathway [31]. Additionally, according to a recent preprint, HDAC10 adversely modulates NLRP3 inflammasome activation by switching NLRP3 modification from acetylation to ubiquitination [32].

HDAC6 is the largest isoform, composed of 1215 amino acids [33]. It consists of two catalytic domains (CD1 and CD2), which both exhibit deacetylase activity although with different substrate preferences. While the CD1 domain shows a high selectivity for substrates with C-terminal lysine residues [34], the CD2 domain demonstrates a broader substrate range and is primarily responsible for the biological activity of HDAC6 inhibitors [35]. HDAC6 possesses unique structural features at the entrance to its catalytic pocket. Compared to other isoforms, these differences arise from the presence of two rigid loops. The L1-loop is primarily characterized by four amino acids (H463, P464, F583, and L712) that create a wide pocket, which can be engaged by HDACi with large, hydrophobic cap-groups. The L2-loop holds a "gatekeeper"–serine residue (S531), which is exclusive to the HDAC6 enzyme. Interactions with this residue are contributing to HDAC6 selectivity [36]. We recently reported the design and biological evaluation of imidazo[1,2-*a*]pyridine-capped HDAC6 preferential inhibitors [37]. Compound **MAIP-032** (Fig. 1) showed the highest preference for HDAC6 over HDAC1, with a selectivity factor (SF) of 38. A crystal structure of HDAC6 CD2 domain from *Danio rerio* complexed with **MAIP-032** (PDB code 6CGP) [37] was obtained and revealed important interaction with the enzyme. Briefly, the Zn^{2+}-ion is complexed by the hydroxamic acid in a monodentate binding mode, while the bridging secondary amino-group forms a hydrogen bond with the aforementioned gatekeeper S531. Interestingly, the propyl side chain is oriented to the L1-loop, while the heteroaromatic cap-group is oriented away from it. This stands in contrast to other, sterically demanding HDAC6 inhibitors, where the (hetero)aromatic cap-groups point towards the L1-pocket [36]. This distinctive binding mode forms a promising foundation for further optimization of **MAIP-032**.

While **MAIP-032** displayed promising inhibitory activity against HDAC6, its selectivity was only 38-fold over HDAC1. Given that HDAC1

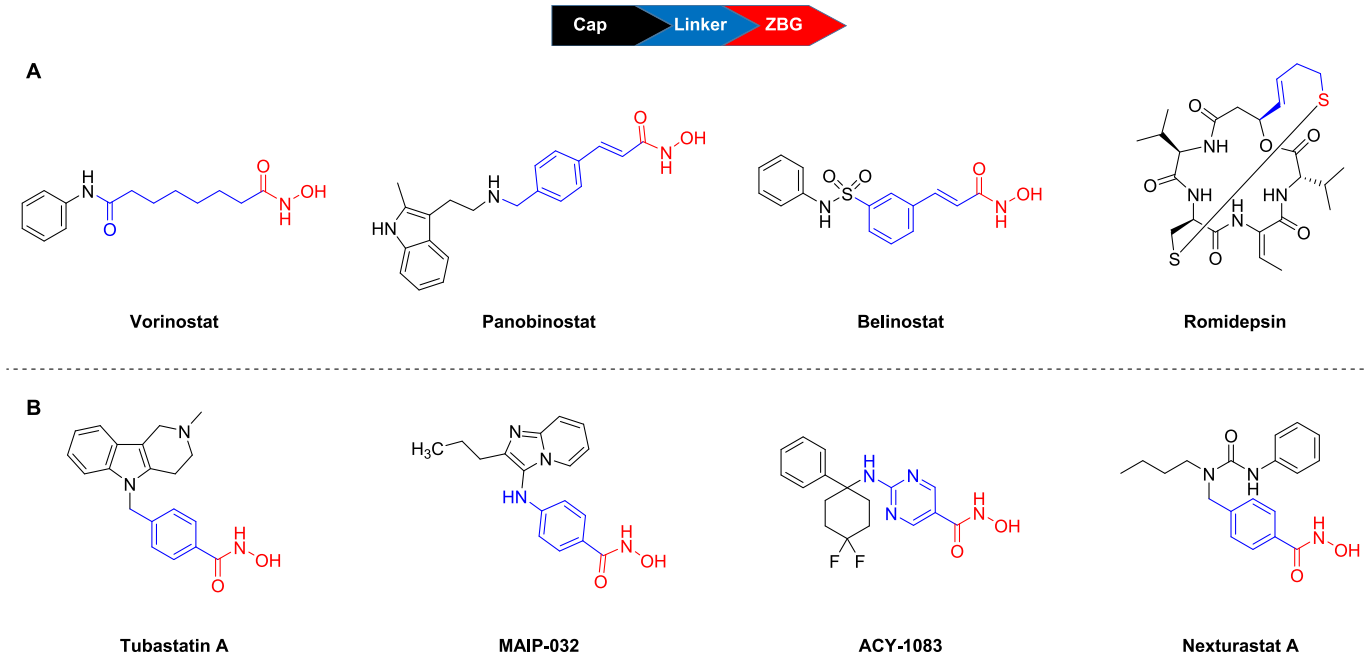


Fig. 1. Selected HDACi including the pharmacophore model. Cap, linker, and ZBG are highlighted in black, blue, and red, respectively. A) FDA approved HDACi. Romidepsin binds via an *in situ* generated thiol. B) Selected HDAC6 preferential HDACi [10]. (For interpretation of the references to colour in this figure legend, the reader is referred to the web version of this article.)

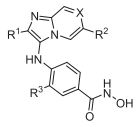
is the primary contributor to the cytotoxic effects of HDAC inhibitors (HDACi), this limited selectivity falls short for advancing this compound as a viable treatment for non-oncological conditions, such as inflammation. Thus, the aim of this study was to perform a structure guided optimization campaign to develop highly selective HDAC6 inhibitors based on the imidazo[1,2-*a*]pyridine scaffold. In this work, we report the design, synthesis, and biological evaluation of the second generation of imidazo[1,2-*a*]pyridine-capped HDAC6 inhibitors.

2. Results and discussion

2.1. Docking studies

Based on the crystal structure of the HDAC6 CD2 domain in complex with **MAIP-032**, we hypothesized that modifications of the alkyl side chain can lead to enhanced interactions with the L1-loop and consequently to improved HDAC6 inhibitory activities. We first performed docking studies using *RosettaLigand* to investigate the scope of possible side chain lengths. Exemplary models for compounds **8a**, **8f**, and **8k** (for compound numbering see Table 1) are depicted in Fig. 2 (for further information, see Supporting Information). All compounds showed a monodentate zinc-binding mode and a hydrogen bond interaction with the gatekeeper S531 as it was already observed for **MAIP-032** [37]. The methyl group of compound **8a** is slightly pointing away from the L1-loop indicating that the shortened side chain can lead to more flexibility in the cap orientation of the inhibitor. The longer pentyl side chain of compound **8f** seems to clash with the amino acids H500 and P501 of the L1-loop. The introduction of a fluorine atom in the linker in compound **8k** did not lead to any noteworthy changes compared to **MAIP-032**. However, it has recently been well elucidated that a fluorine atom in *meta*-position to the hydroxamic acid can increase the binding affinity due to the pi-pi interactions of the linker and additional interactions between the fluorine and the gatekeeper S531 [38].

Table 1
Inhibitory activities of synthesized hydroxamic acids **8a–m**, **MAIP-032**, tubastatin A, and vorinostat against human HDAC1 and 6 isoforms.



Entry	R^1	R^2	R^3	HDAC1 IC_{50} [μM]	HDAC6 IC_{50} [μM]	SF[a]
8a (X = CH)	Methyl	H	H	2.746 ± 0.254	0.046 ± 0.004	60
8b (X = CH)	Ethyl	H	H	2.903 ± 0.191	0.075 ± 0.0004	39
8c (X = CH)	Isobutyl	H	H	3.705 ± 0.081	0.099 ± 0.005	37
8d (X = CH)	Cyclopropyl	H	H	2.515 ± 0.196	0.106 ± 0.016	24
8e (X = CH)	Butyl	H	H	3.294 ± 0.133	0.120 ± 0.001	27
8f (X = CH)	Pentyl	H	H	1.154 ± 0.071	0.081 ± 0.008	14
8g (X = CH)	$CH_2CH_2CF_3$	H	H	2.837 ± 0.049	0.230 ± 0.023	12
8h (X = CH)	Propyl	Methyl	H	2.554 ± 0.166	0.093 ± 0.003	27
8i (X = CH)	Propyl	Ethyl	H	1.356 ± 0.011	0.082 ± 0.017	16
8j (X = N)	Propyl	H	H	2.999 ± 0.393	0.115 ± 0.018	26
8k (X = CH)	Propyl	H	F	5.872 ± 0.981	0.024 ± 0.003	245
8l (X = CH)	Propyl	H	Methyl	19.77 ± 0.948	0.589 ± 0.001	34
8m (X = CH)	Methyl	H	F	3.068 ± 0.144	0.026 ± 0.001	118
Vorinostat	/	/	/	0.089 ± 0.001	0.029 ± 0.002	3
MAIP-032[b] (X = CH)	Propyl	H	H	2.20 ± 0.33	0.058 ± 0.012	38
Tubastatin A[b]	/	/	/	2.49 ± 0.14	0.014 ± 0.001	178

[a] Selectivity factor (SF) = IC_{50} (HDAC1)/ IC_{50} (HDAC6); [b] Data taken from Mackwitz et al. [37].

2.2. Design and synthesis

The target compounds were synthesized by a four-step procedure, with a *Groebke-Blackburn-Bienaymé* (GBB) [39] three component reaction as the key step to form the imidazo[1,2-*a*]pyridine core (Scheme 1). The synthesis required commercially available aldehydes and amidine components as well as isocyanides. The isocyanides were synthesized from their respective anilines in two steps. Initially, the anilines were formylated with formic acid in ethyl acetate to give the formamides **1**–**3** in 94 % to quantitative yields. Next, they were dehydrated with phenyl phosphordichloridate to generate the individual isocyanides. The GBB reaction was performed either by addition of acetic acid with microwave assistance or with scandium(III) triflate as a catalyst at room temperature. In the final step, the hydroxamic acids **8a-m** were prepared *via* hydroxylaminolysis of the esters **7a-m**.

All final compounds were characterized by ^{1}H-, ^{13}C-NMR spectroscopy as well as HRMS and HPLC analysis. The measured NMR spectra were in agreement with the expected values and all test compounds showed >95 % purity. Furthermore, in case of the fluorinated derivatives **8g**, **8k**, and **8m**, ^{19}F-NMR spectra clearly confirmed successful fluorination. The NMR spectra and HPLC chromatograms are provided in the Supporting Information.

2.3. Inhibitory activity against human HDAC isoforms

First, all synthesized hydroxamic acids were evaluated in biochemical HDAC inhibition assays for their inhibitory activity against human HDAC1 and HDAC6 isoforms using ZMAL as substrate [40]. The results are summarized in Table 1.

We started the structural modification on the side chain R^1 of the cap group to improve the interaction with the L1-loop. As expected from our docking studies, shorter alkyl chains showed a better inhibitory activity and selectivity profile for HDAC6. Inhibitor **8a** (IC_{50} (HDAC6) = 0.046 μM), with the shortest side chain, showed a comparable HDAC6 activity to the reference inhibitor **MAIP-032** (IC_{50} (HDAC6) = 0.058 μM) but also a lower HDAC1 inhibition, thus resulting in an increased selectivity. Prolonging the chain further, the HDAC6 inhibitory activity declined up to 0.120 μM (SF: 27) for the butyl group (**8e**). Remarkably, the compound **8f**, with a pentyl side chain, exhibited an increased inhibitory activity against both isoforms. In contrast to our expectations, the 3,3,3-trifluoropropyl derivative (**8g**) displayed nearly fourfold lower inhibition of HDAC6 and threefold lower selectivity compared to **MAIP-032**. This suggests that the additional, hypothesized interactions with the L1-pocket, might not be feasible in this case. Similarly, the introduction of branched (**8c**) or short, cyclic (**8d**) side chain both resulted in a decreased HDAC6 inhibitory activity. Next, we aimed to optimize the heterocyclic cap group. To achieve this, we introduced alkyl chains at the 6-position (**8h** and **8i**), which failed to improve HDAC6 inhibition, but increased HDAC1 inhibition. Furthermore, the pyrazine-based inhibitor **8j** exhibited an overall lower activity compared to **MAIP-032**. Next, we modified the linker to improve the hydrogen bond interaction of the bridging secondary amino group with S531. Initially, the introduction of a methyl group at the 3-position (**8l**) on the linker substantially attenuated the inhibition on both isoforms. However, when a fluorine atom was introduced (**8k**), we observed a twofold increase in

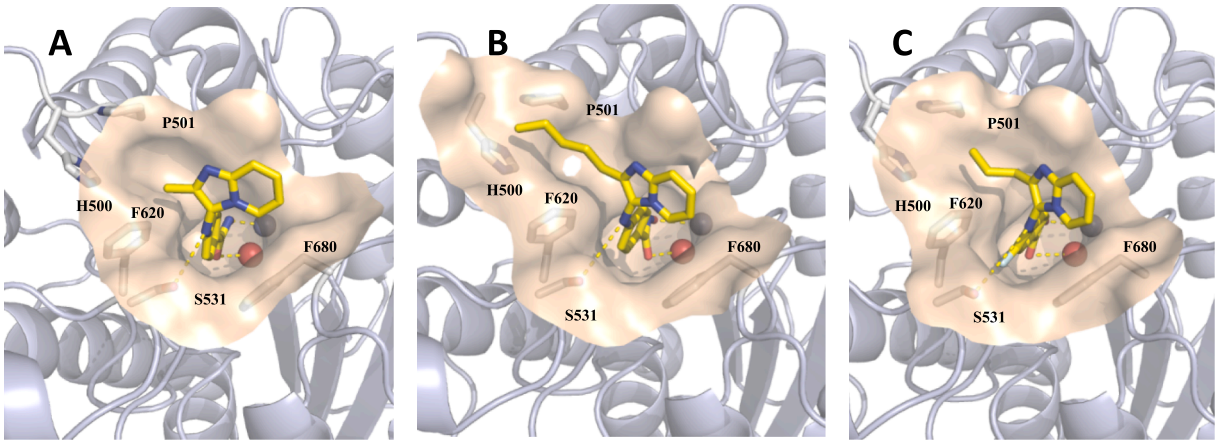
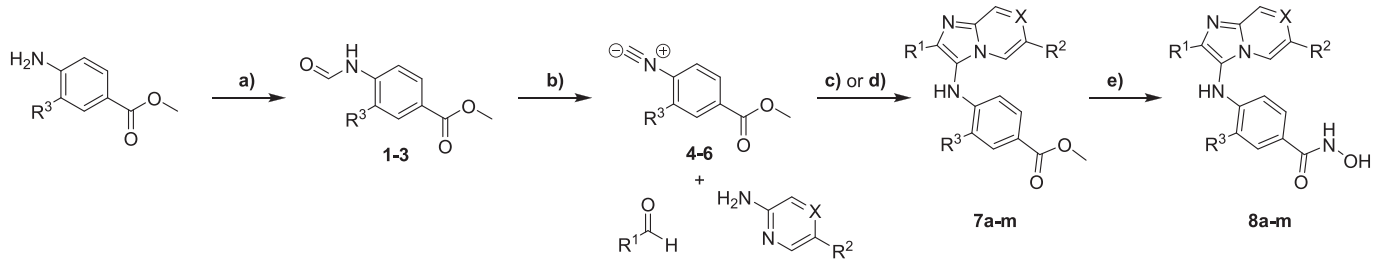


Fig. 2. Docking pose of **8a** (A), **8f** (B), and **8k** (C) in the CD2 of *danio rerio* HDAC6 (PDB: 6CGP) [37]. Ligands are colored yellow, the catalytic Zn^{2+}-ion and water molecule are shown as a gray and red sphere, respectively. Polar interactions are represented by dashed, yellow lines. (For interpretation of the references to colour in this figure legend, the reader is referred to the web version of this article.)



Scheme 1. Synthesis of imidazopyridine-capped HDAC inhibitors. a) CHOOH (20.0 eq), ethyl acetate, rt, 3 d; 94 % – quant.; b) $PhOPOCl_2$ (1.20 eq.), NEt_3 (3.00 eq.), CH_2Cl_2, 0 °C to rt, 90 min, 61–94 %; c) AcOH (2.00 eq.), MeOH, MW (110 W), 85 °C, 3 h, 27–84 %; d) $Sc(OTf)_3$ (5 mol-%), MeOH/CH_2Cl_2 1/1 (*v*/*v*), rt, 3 d, 62 %; e) NH_2OH_2 (50 % in H_2O, 30.0 eq.), NaOH (10.0 eq.), MeOH/CH_2Cl_2 1/2 (*v*/*v*), 0 °C to rt, 90 min, 21–92 %.

HDAC6 activity and remarkable sixfold improvement in selectivity over HDAC1 (IC_{50} (HDAC6) = 0.024 μM; SF: 245). Notably, **8k** outperformed the selectivity profile of the gold standard selective HDAC6 inhibitor tubastatin A (SF: 178). Encouraged by these findings, we proceeded to combine the methyl side chain with the fluorinated linker, resulting in the synthesis of inhibitor **8m**. Interestingly, compound **8m** (IC_{50} (HDAC6) = 0.026 nM; SF: 118) showed comparable HDAC6 inhibition to **8k**, but displayed also better HDAC1 activity, which consequently led to a lower selectivity. The most important structure–activity relationships from our previous work [37] and this series of compounds are summarized in Fig. 3.

With the two most promising compound **8k** and **8m**, we continued to test their activity against additional HDAC isoforms (see Table 2). The inhibitor **8k** showed a very high selectivity of $SF^{2/6}$: 460 (HDAC2) and $SF^{3/6}$: 919 (HDAC3), which is 1.7- and 2.1-fold higher than in the case of **8m**. Finally, **8k** and **8m** were screened for their inhibitory activity against HDAC10, the closest paralog of HDAC6. Both compounds showed only moderate inhibition of HDAC10, further supporting that **8k**

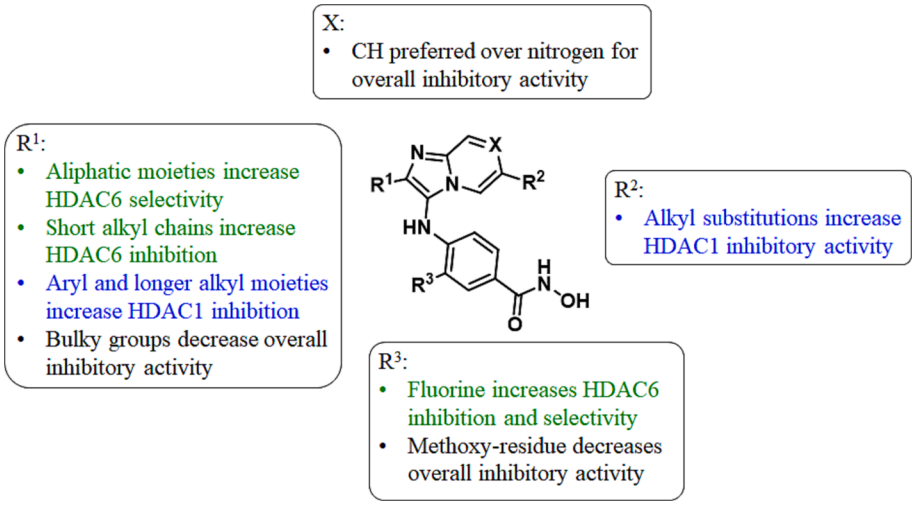
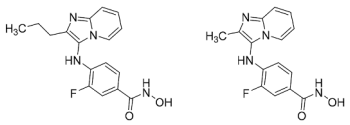


Fig. 3. Structure-activity relationships of imidazo[1,2–a]pyridine based HDACi.

Table 2
Extended isoform profiling of hit compounds **8k** and **8m** against human HDAC1,2,3 and HDAC6.



8k **8m**

Entry	HDAC1 IC_{50} [μM]	HDAC2 IC_{50} [μM]	HDAC3 IC_{50} [μM]	HDAC6 IC_{50} [μM]	HDAC10 IC_{50} [μM]	$SF^{1/6}$	$SF^{2/6}$	$SF^{3/6}$	$SF^{10/6}$
8k	5.872 ± 0.981	11.04 ± 0.594	22.06 ± 3.019	0.024 ± 0.003	1.11 ± 0.07	245	460	919	46
8m	3.068 ± 0.144	6.858 ± 0.238	11.03 ± 1.531	0.026 ± 0.001	0.562 ± 0.046	118	264	424	22
Vorinostat	0.089 ± 0.001	0.202 ± 0.001	0.128 ± 0.004	0.029 ± 0.002	n.d.	3	7	4	n.d.
Quisinostat	n.d.	n.d.	n.d.	n.d.	0.005 ±0.0004	n.d.	n.d.	n.d.	n.d.

n.d.: not determined.

(HDAC10 IC_{50}: 1.11 μM) and **8m** (HDAC10 IC_{50}: 0.562 μM) are selective HDAC6 inhibitors.

2.4. Cellular HDAC inhibition and anticancer effects in the U-87 MG glioblastoma cell line

Motivated by the potent and selective inhibition of HDAC6 in biochemical HDAC assays, we decided to investigate the properties of the hit compounds **8k** and **8m** in more detail. To assess the cellular target engagement of compounds **8k** and **8m** for HDAC6, we treated the glioblastoma cell line U-87 MG with **8k**, **8m**, tubastatin A, and vorinostat for 24 h. The following western blot analysis showed α-tubulin hyperacetylation (Ac-α-tubulin), a well-known indicator of HDAC6 inhibition (Fig. 4) in the case of **8k**, **8m**, tubastatin A, as well as vorinostat. In contrast, the acetylation status of histone H3 (Ac-H3) remained unaffected following the treatment with **8k**, **8m**, and tubastatin A while the unselective HDAC inhibitor vorinostat induced significant hyperacetylation of histone H3. Since Ac-H3 serves as a marker for class I HDAC inhibition, these results confirm the HDAC6 selectivity of **8k** and **8m** in a cellular environment.

Next, we evaluated the anticancer properties of **8k** and **8m**. To this end, we analyzed the antiproliferative activity of **8k** and **8m** in a MTT assay in the glioblastoma cell line U-87 MG using tubastatin A and vorinostat as control compounds. The results are summarized in Table 3. As expected, the HDAC6 selective inhibitors **8k**, **8m**, and tubastatin A had only minor effects on the cell viability with IC_{50} values ranging from 16.1 to 24.7 μM, while vorinostat demonstrated more potent antiproliferative activity (IC_{50} (U-87 MG) = 4.60 μM). This is in accordance with recent studies by us and others that indicate low single-agent cytotoxic properties of selective HDAC6 inhibitors [22,41].

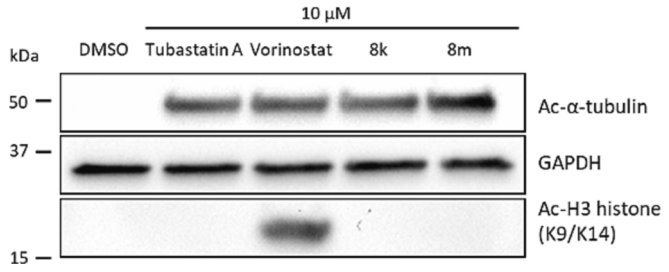


Fig. 4. Representative immunoblot analysis of acetylatedα–tubulin and histone H3. U-87 MG cells were incubated for 24 h with 10 μM of tubastatin A, vorinostat, 8 k, and 8 m. Afterwards, cell lysates were immunoblotted with anti-acetyl-α-tubulin and anti-acetyl-histone H3 (K9/K14) antibodies. GAPDH was used as a loading control.

Table 3
Antiproliferative activity of **8k** and **8m** against the glioblastoma cell line U-87 MG.[a]

Entry	U-87 MG IC_{50} [μM]
8k	19.5 ± 3.26
8m	16.1 ± 1.54
Tubastatin A	24.7 ± 2.12
Vorinostat	4.60 ± 0.44

[a] Stated IC_{50} values were determined from the mean of at least three independent experiments in duplicates.

2.5. Wound healing assay in the U-87 MG cell line

HDAC6 plays a crucial role in cell migration by regulating processes such as microtubule dynamics, cytoskeletal remodeling, and cell signaling. The U-87 MG cell line has proven effective in prior research for investigating the anti-migratory properties of selective HDAC6 inhibitors [42]. We thus used this cell line to investigate the anti-migratory potential of tubastatin A, vorinostat, **8k**, and **8m** in wound healing assays. To this end, the cells were pretreated with 10 μM of the respective HDAC6i and cell migration was followed over 48 h and compared to the DMSO treated control cells. The results are presented in Fig. 5. Tubastatin A, vorinostat, and **8k** had no significant effects on cell migration, while **8m** attenuated cell migration significantly.

2.6. NLRP3-mediated IL1-β release

Although selective HDAC6 inhibitors hold great potential as anticancer agents when used in combination therapies e.g. with proteasome inhibitors, there is growing evidence that HDAC6 inhibitors may offer therapeutic benefits in various diseases beyond oncology. In addition to its involvement in various other cellular processes, HDAC6 has recently been implicated in NLRP3 inflammasome-related inflammatory responses [25,43,44]. Consequently, selective HDAC6 inhibitors present a promising new option for the treatment of diseases associated with the NLRP3 inflammasome. However, the underlying mechanisms are poorly understood and the mechanistic role of HDAC6 in NLRP3-mediated IL-1β release remains controversial. It has been reported that HDAC6 inhibitors have been reported to attenuate NLRP3-mediated inflammation [44–46], however, other studies demonstrate that tubastatin A shows no effect on ATP-induced IL-1β release in mouse cells [47]. To determine effects of HDAC6 inhibition on NLPR3 inflammasome activation, lipopolysaccharide (LPS)-primed THP-1 macrophages were incubated with tubastatin A, **MAIP-032**, and the two most potent inhibitors **8k** and **8m**

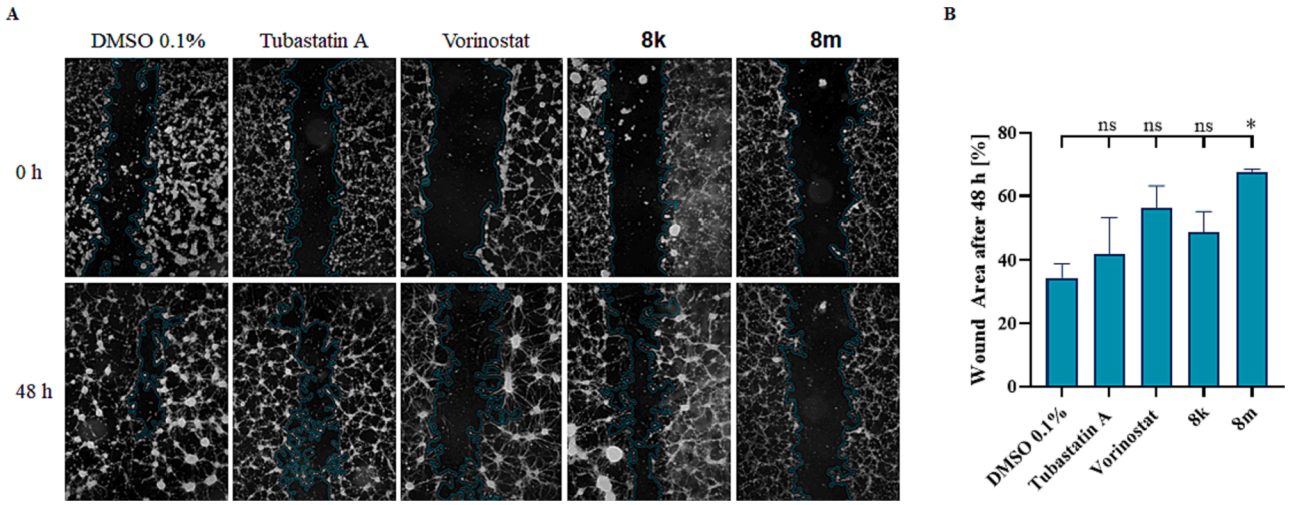


Fig. 5. Wound healing assay in U-87 MG cells which were treated with selected HDACi (10 μM) or vehicle (0.1 % DMSO). (A) Representative images taken immediately after scratching (0 h) and after 48 h. (B) Quantification of remaining wound area compared to the initial wound area. Mean + SEM, n = 3. Significances were determined by one-way ANOVA followed by Dunnett's multiple comparisons test and are indicated by asterisks (ns = not significant; *P ≤ 0.05).

at concentrations ranging from 0.01 to 100 μM, followed by stimulation with ATP or nigericin. However, none of the HDAC6 inhibitors demonstrated a decrease in IL-1β release (Fig. S1, Supporting Information). Consistent with our previous findings [48], the NLRP3 inflammasome inhibitor MCC90 suppressed IL-1β release induced by nigericin, but it did not show inhibitory effects in the presence of ATP. Similar results were observed when LDH release was determined to monitor pyroptosis. This indicates that HDAC6 is dispensable for IL-1β release during NLRP3 inflammasome activation in human macrophages which confirms our recent findings [49]. Since studies have demonstrated that HDAC6 inhibitors suppress the activation of the NLRP3 inflammasome in mice [25], we next used mouse J774A.1 macrophages. Tubastatin A and **8k** reduced nigericin- but not ATP-induced IL-1β release at 50 and 100 μM, respectively (Fig. S2, Supporting Information). As expected, MCC950 completely blocked IL-1β release. Notably, in our experimental setting, J774.1 macrophages released 30-times higher IL-1β levels compared to previous studies using immortalized mouse bone marrow-derived macrophages [25]. This indicates, that HDAC6 inhibitors show only a weak inhibitory effect on NLRP3 inflammasome activation in mouse cells that release high levels of IL-1β.

Previously, we demonstrated that inhibition of HDAC6 by tubastatin A interferes with TLR signaling, which inhibits NLRP3-inflammasome mediated IL-1β release by human macrophages [49]. Thus, we tested whether HDAC6 inhibitors block the release of IL-1β by suppressing TLR-mediated priming in THP-1 macrophages. Tubastatin A, as well as **MAIP-032**, **8k**, and **8m** significantly inhibited LPS-induced *IL1B* mRNA expression and TNF release at 10 μM (Fig. 6A). In line with our previous observations [49], vorinostat completely blocked TLR4-mediated responses, suggesting that inhibition of other HDACs contributes to this effect. We confirmed that vorinostat but not the selective HDAC6 inhibitors induced histone-H3 acetylation (Ac-H3) in THP-1 macrophages with **8k** and **8m** being highly selective (Fig. 6B).

Next, we analyzed the inhibitory potency of the HDAC6 inhibitors on LPS-induced TNF release (Fig. 6C). To determine whether the data for the tested inhibitors, tubastatin A, **MAIP-032**, **8k**, and **8m**, were better represented by a monophasic or biphasic inhibitory concentration-response curve, we conducted a comparative analysis of both models. Tubastatin A, **MAIP-032** and **8m** were best fitted by a monophasic model, while a biphasic model was preferred for **8k**. However, for better comparison all inhibitors were fitted to monophasic inhibitory concentration-response curves with IC_{50} values ranging from 4.96 to 19.6 μM (Table 4).

IC_{50} values of **8k** (19.6 μM) and **8m** (15.8 μM) were similar to tubastatin A (16.3 μM), but all three compounds appear to be less potent than **MAIP-032** (4.96 μM). Cell viability in the presence of the HDAC6 inhibitors remained unchanged up to 50 μM and was reduced to 60 % at 100 μM for **MAIP-032**, **8k**, and **8m** (Fig. 6D). The possibility of a biphasic fit indicates that at least two HDAC6-mediated mechanisms contribute to the inhibition of LPS-induced TNF release. HDAC6 inhibitors affect TLR signaling by modulating acetylation of several proteins involved in this pathway, among other mechanisms [43]. However, the specific mechanistic details remain poorly understood. Further studies are warranted to clarify the underlying mechanisms behind the inhibitory role of HDAC6 in TLR-mediated priming.

3. Conclusions

In this study, starting from a co-crystal structure of the preferential HDAC6 inhibitor **MAIP-032**, we performed a structure-based optimization campaign to yield a series of inhibitors with improved potency and selectivity. The synthesis of 13 novel inhibitors was achieved using a highly efficient *Groebke Blackburn Bienaymé* three component reaction as the key step. While the variation of the propyl group of **MAIP-032** showed only a slight improvement in HDAC6 selectivity (e.g. compound **8a**), the fluorination of the benzyl linker in *meta*-position to the hydroxamic acid significantly enhanced potency and selectivity (compounds **8k** and **8m**). Compound **8k** outperformed the gold standard selective HDAC6 inhibitor, tubastatin A, in terms of selectivity. Importantly, **8k** and **8m** exhibit notable selectivity over HDAC10, the closest paralog of HDAC6. This finding is crucial as inhibiting HDAC10 can potentially counteract the anti-inflammatory processes mediated by the inhibition of HDAC6 [31,32]. While neither **8k** and **8m** nor tubastatin A demonstrated pronounced antiproliferative effects in the U-87 MG glioblastoma cell line, compound **8m** effectively attenuated cell migration in wound healing assays. Additionally, tubastatin A, **MAIP-032**, **8k**, and **8m** showed significant inhibition of LPS-induced *IL1B* mRNA expression and TNF release in macrophages, thereby indicating that our imidazo[1,2-*a*]pyridine-capped HDAC6 inhibitors could be a suitable starting to develop drugs to treat NLRP3 inflammasome driven inflammatory diseases.

4. Experimental section

4.1. General information & chemistry

Chemicals were obtained from abcr GmbH, Acros Organics,

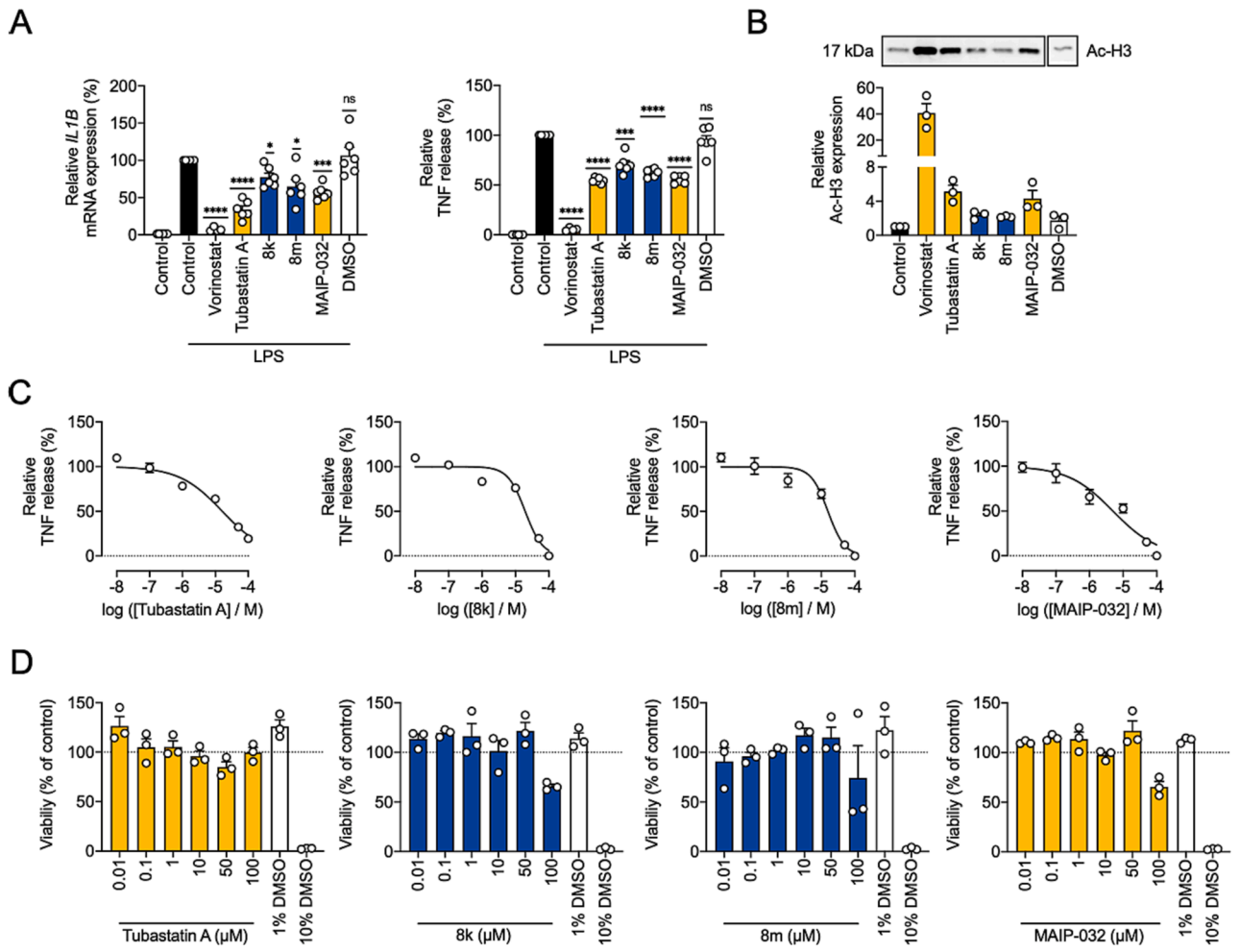
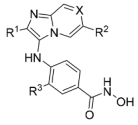


Fig. 6. (A) Human THP-1 macrophages were incubated with indicated HDAC inhibitors (10 μM) or vehicle (0.1 %, v/v, DMSO) for 24 h. Subsequently, cells were incubated with LPS (100 ng/ml) for 3 h. Supernatants were assayed for TNF release by ELISA. *IL1B* gene expression was normalized to the housekeeping gene *GAPDH*. LPS induced TNF release and *IL1B* gene expression was set to 100 %. Other values were calculated accordingly. Mean + SEM, n = 4–6. One sample *t* test against 100 %. ns = not significant, *P ≤ 0.05, ***P ≤ 0.001, ****P ≤ 0.0001. (B) Human THP-1 macrophages were incubated with indicated HDAC inhibitors (10 μM) or vehicle (0.1 %, v/v, DMSO) for 24 h. Cell lysates were analyzed for acetyl-histone-H3 expression by western blot. Acetyl-histone-H3 protein levels were normalized to the respective total protein amount and values were referenced to the control (control set to a value of 1). Mean + SEM, n = 3. (C) Human THP-1 macrophages were incubated with increasing concentrations of indicated HDAC inhibitors for 24 h. Subsequently, cells were incubated with LPS (100 ng/ml) for 3 h. Supernatants were assayed for TNF release by ELISA. LPS induced TNF release was set to 100 %. Other values were calculated accordingly. Mean ± SEM, n = 3–4. Curves were fitted to a monophasic model with variable slope. (D) Human THP-1 macrophages were incubated with increasing concentrations of indicated HDAC inhibitors for 24 h. DMSO (1 % and 10 %, v/v) served as controls. Cytotoxicity was determined by MTT assay. Mean + SEM, n = 3.

Table 4
Inhibitory activities of **8k**, **8m**, MAIP-032, and tubastatin A against LPS-induced TNF release by THP-1 macrophages.[a]



Entry	R^1	R^2	R^3	IC_{50} [μM] (95 % CI)
8k (X = CH)	Propyl	H	F	19.6 (15.4–25.2)
8m (X = CH)	Methyl	H	F	15.8 (11.0–22.3)
MAIP-032 (X = CH)	Propyl	H	H	4.96 (2.34–9.97)
Tubastatin A	/	/	/	16.3 (10.6–24.2)

[a] Stated IC_{50} values were determined from the mean of at least three independent experiments.

Carbolution Chemicals, Fluorochem, Sigma-Aldrich, TCI Chemicals or VWR and used without further purification. Technical grade solvents were distilled prior to use. For all HPLC purposes, acetonitrile in HPLC-grade quality (HiPerSolv CHROMANORM, *VWR*) was used. Water was purified with a PURELAB flex® (*ELGA VEOLIA*). Air-sensitive reactions were carried out under argon atmosphere utilizing standard *Schlenk* techniques. If no solvent is stated an aqueous solution was prepared with demineralized water. Mixtures of two or more solvents are specified as "solvent A"/"solvent B", 3/1, *v/v*; meaning that 100 mL of the respective mixture consists of 75 mL of "solvent A" and 25 mL of "solvent B". **Thin-layer chromatography (TLC)** was carried out on prefabricated plates (silica gel 60, F_{254}, *Merck*). Components were visualized either by irradiation with ultraviolet light (254 nm or 366 nm) or by staining appropriately. **Column Chromatography:** If not stated otherwise, column chromatography was carried out on silica gel (60 Å, 40–60 μm, *Acros Organics*). **Melting Point (mp.):** The uncorrected melting points were determined using a *Büchi* Melting Point M-560 apparatus. **Nuclear Magnetic Resonance Spectroscopy (NMR):** Proton (^1H), carbon (^{13}C), and fluorine (^{19}F) NMR spectra were recorded either on Bruker Avance

III HD 400 MHz at a frequency of 400 MHz (^{1}H), 100 MHz (^{13}C) and 377 MHz (^{19}F), a *Varian/Agilent* Mecury-plus-400 at a frequency of 400 MHz (^{1}H) and 100 MHz (^{13}C), a *Varian/Agilent* Mecury-plus-300 at a frequency of 300 MHz (^{1}H), 75 MHz (^{13}C) and 282 MHz (^{19}F), a *Bruker* AVANCE 500 MHz at a frequency of 500 MHz (^{1}H) and 126 MHz (^{13}C) or on a *Bruker* AVANCE III HD 600 MHz at a frequency of 600 MHz (^{1}H), 151 MHz (^{13}C) and 565 MHz (^{19}F). The chemical shifts are given in parts per million (ppm). As solvents deuterated chloroform ($CDCl_3$), deuterated methanol (MeOH-d_4) and deuterated dimethyl sulfoxide (DMSO-d_6) were used. The residual solvent signal ($CDCl_3$: ^{1}H NMR: 7.26 ppm, ^{13}C NMR: 77.1 ppm; DMSO-d_6: ^{1}H NMR: 2.50 ppm, ^{13}C NMR: 39.52 ppm; MeOH-d_4: ^{1}H NMR: 3.31 ppm, 4.87 ppm, ^{13}C NMR: 49.00 ppm) was used for calibration. The multiplicity of each signal is reported as singulet (s), doublet (d), triplet (t), quartet (q), pentet (p), sextet (sext), multiplet (m) or combinations thereof. Multiplicities and coupling constants are reported as measured and might disagree with the expected values. **Mass Spectrometry:** High resolution electrospray ionization mass spectra (HRMS-ESI) were acquired with *Bruker Daltonik GmbH* micrOTOF coupled to a an *LC Packings* Ultimate HPLC system and controlled by micrOTOFControl3.4 and HyStar 3.2-LC/MS, with a *BrukerDaltonik GmbH* ESI-qTOF Impact II coupled to a *Dionex* UltiMateTM 3000 UHPLC system and controlled by micrOTOFControl 4.0 and HyStar 3.2-LC/MS or with a micrOTOF-Q mass spectrometer (*Bruker*) with ESI-source coupled with an HPLC Dionex UltiMate 3000 (*Thermo Scientific*). Low resolution electrospray ionisation mass spectra (LRMS-ESI) were acquired with an *Advion* expression® compact mass spectrometer (CMS) coupled with an automated TLC plate reader Plate Express® (*Advion*). **High Performance Liquid Chromatography (HPLC)**: A *Thermo Fisher Scientific* UltiMate^{TM} 3000 UHPLC system with a Nucleodur 100-5 C18 (250 × 4.6 mm, *Macherey Nagel*) with a flow rate of 1 mL/min and a temperature of 25 °C or a 100-5 C18 (100 × 3 mm, Macherey Nagel) with a flow rate of 0.5 mL/min and a temperature of 25 °C with an appropriate gradient were used. For preparative purposes a AZURA Prep. 500/1000 gradient system (*Knauer*) with a Nucleodur 110-5 C18 HTec (150 × 32 mm, *Macherey Nagel*) column with 20 mL/min was used. Detection was implemented by UV absorption measurement at a wavelength of λ = 220 nm and λ = 250 nm. Bidest·H_2O (A) and MeCN (B) were used as eluents with an addition of 0.1 % TFA for eluent A. **Purity:** The purity of all final compounds was 95 % or higher. Purity was determined via HPLC with the Nucleodur 100-5 C18 (250 × 4.6 mm, *Macherey Nagel*) at 250 nm. After column equilibration for 5 min a linear gradient from 5% A to 95% B in 7 min followed by an isocratic regime of 95 % B for 10 min was used.

4.2. Experimental procedures (chemistry)

4.2.1. General procedures

General procedure I (GP I): The respective amine (1.00 eq) was dissolved in formic acid (20.0 eq.) and ethyl acetate (1.5 mL). The solution was stirred for three days at room temperature before the solvent was removed under reduced pressure. The residue was dissolved in ethyl acetate (50 mL) and washed with H_2O (50 mL). The inorganic layer was extracted with ethyl acetate (3 × 20 mL). The combined organic layers were washed with sat. $NaHCO_3$-solution (20 mL) and sat. NaCl-solution (20 mL) and dried over Na_2SO_4. After evaporation of the solvent under reduced pressure the respective formamide was isolated and used without further purification.

General procedure II (GP II): The respective formamide (1.00 eq.) was dissolved in CH_2Cl_2 (0.25 M) and NEt_3 (3.00 eq.) was added. The solution was cooled to 0 °C and phenyl phosphordichloridate (1.20 eq) was added dropwise over 5 min. The ice bath was removed and the solution stirred for 90 min at rt. The solvent was removed under reduced pressure and the residue purified by column chromatography (Al_2O_3 neutral BROCKMANN Grade I, CyH/CH_2Cl_2 1:4, *v/v*).

General procedure III (GP III): The respective amidine (1.00 eq.) and aldehyde (1.10 eq.) were dissolved in MeOH (0.3 M). Acetic acid (2.00 eq.) was added, and the solution stirred for 30 min at rt. Next, the respective isocyanate (1.00 eq.) was added, and the suspension submitted to microwave irritation (110 W) for 3 h at 85 °C. Afterwards, the solvent was removed under reduced pressure and the residue was purified by column chromatography.

General procedure IV (GP IV): The respective ester (1.00 eq.) was dissolved in CH_2Cl_2/MeOH (0.25 M, 1:2, *v/v*) and cooled to 0 °C. Hydroxyl amine (50% in H_2O, 30.0 eq.,) and NaOH (10.0 eq.) were added and the reaction mixture was stirred for 30 min at 0 °C followed by 60 min at rt. Subsequently, the solvent was removed under reduced pressure and the residue was taken up in a small amount of water. The pH value of the aqueous solution adjusted to 7–8 using 1 M HCl, the precipitated solid filtrated, washed with Et_2O (3 × 5 mL) and dried *in vacuo*.

4.2.2. Compound characterization

Methyl-4-formamidobenzoate (**1**)

Prepared according to **GP I**. Starting from methyl-4-aminobenzoate (3.12 g, 20.6 mmol, 1.00 eq.). Compound **1** (3.69 g, 20.6 mmol, quant.) was isolated as a beige solid. **R_f** (CyH/EE 2:1, *v/v*) = 0.12; **^{1}H NMR** (300 MHz, $CDCl_3$) δ = 8.84 (d, J = 11.2 Hz, 1H), 8.44 (d, J = 1.6 Hz, 1H), 8.14 (s, 1H), 8.09–7.97 (m, 3H), 7.74–7.57 (m, 2H), 7.47 (s, 1H), 7.20–7.07 (m, 1H), 3.91 (s, 2H), 3.90 (s, 3H); **LRMS-ESI (*m/z*):** $[M + H]^+$ calcd for $C_9H_9NO_3$: 180.1, found: 180.1. Analytical data match with literature [37].

Methyl-3-fluoro-4-formamidobenzoate (**2**)

Prepared according to **GP I**. Starting from methyl-3-fluoro-4-aminobenzoate (1.69 g, 10.0 mmol, 1.00 eq.). Compound **2** (1.86 g, 9.43 mmol, 94%) was isolated as a beige solid. **R_f** (CyH/EE 2:1, *v/v*) = 0.3; **mp.** 154–156 °C; **^{1}H NMR** (300 MHz, $CDCl_3$) δ = 8.90–8.80 (m, 1H), 8.58–8.40 (m, 1H), 7.89–7.66 (m, 3H), 7.36–7.28 (m, 1H), 3.91 (s, 3H); **^{13}C NMR** (101 MHz, $CDCl_3$) δ = 165.7, 161.0, 158.9, 151.4 (d, J = 244.3 Hz), 129.8 (d, J = 10.3 Hz), 126.9–126.5 (m), 121.2, 118.1–117.6 (m), 117.3, 116.5–115.9 (m), 52.8–52.2 (m); **^{19}F NMR** (282 MHz $CDCl_3$) δ = −128.8 – −128.9 (m), −130.8 – −131.2 (m); **LRMS-ESI (*m/z*):** $[M + Na]^+$ calcd for $C_9H_8FNO_3$: 220.0, found: 220.0.

Methyl-4-formamido-3-methylbenzoate (**3**)

Prepared according to **GP I**. Starting from methyl-4-amino-3-methylbenzoate (0.825 g, 5.00 mmol, 1.00 eq.). Compound **3** (0.935 g, 4.83 mmol, 97%) was isolated as a white solid. **R_f** (CyH/EE 1:1, *v/v*) = 0.44; **mp.** 120–122 °C; **^{1}H NMR** (600 MHz, $CDCl_3$) δ = 8.72 (d, J = 11.1 Hz, 1H), 8.50 (d, J = 1.7 Hz, 0H), 8.20 (d, J = 8.3 Hz, 0H), 7.98–7.84 (m, 3H), 7.30 (s, 1H), 7.21 (d, J = 8.3 Hz, 1H), 3.90 (d, J = 7.1 Hz, 3H), 2.33 (d, J = 6.4 Hz, 3H); **^{13}C NMR** (151 MHz, $CDCl_3$) δ = 166.8, 166.6, 162.5, 159.1, 139.3, 139.2, 132.9, 132.0, 129.0, 128.8, 128.0, 127.1, 126.7, 126.3, 121.3, 118.1, 53.1, 52.1,17.7; **LRMS-ESI (*m/z*):** $[M + H]^+$ calcd for $C_{10}H_{12}NO_3$: 194.1 found: 194.1.

Methyl-4-isocyanobenzoate (**4**)

Prepared according to **GP II**. Starting from formamide **1** (1.06 g, 5.92 mmol, 1.00 eq.). Compound **4** (0.899 g, 5.59 mmol, 94%) was isolated as a dark green solid. **R_f** (CyH/CH_2Cl_2 1:4, *v/v*) = 0.68; **mp.** ~30 °C; **^{1}H NMR** (300 MHz, $CDCl_3$) δ = 8.14–8.02 (m, 2H), 7.50–7.38 (m, 2H), 3.94 (s, 3H); **LRMS-ESI (*m/z*):** $[M + H]^+$ calcd for $C_9H_8NO_2$: 162.1, found: 162.0. Analytical data match with literature [37].

Methyl-3-fluoro-4-isocyanobenzoate (**5**)

Prepared according to **GP II**. Starting from formamide **2** (0.986 g, 4.99 mmol, 1.00 eq.). Compound **5** (0.548 g, 3.06 mmol, 61%) was isolated as a brown solid. **R_f** (CyH/CH_2Cl_2 1:4, *v/v*) = 0.68, **mp.** ~30 °C; **^{1}H NMR** (300 MHz, $CDCl_3$) δ = 7.89–7.87 (m, 1H), 7.86–7.83 (m, 1H), 7.53–7.44 (m, 1H), 3.95 (s, 3H); **^{13}C NMR** (101 MHz, $CDCl_3$) δ = 173.3, 164.7, 157.2 (d, J = 258.4 Hz), 132.9 (d, J = 6.5 Hz), 128.1, 126.0 (d, J = 4.0 Hz), 118.0 (d, J = 20.3 Hz), 53.0; **^{19}F NMR** (377 MHz, $CDCl_3$) δ = −116.6 (d, J = 5.2 Hz); **LRMS-ESI (*m/z*):** $[M + K]^+$ calcd for $C_9H_6FNO_2$: 218.0, found: 218.0.

Methyl-4-isocyano-3-methylbenzoate (**6**)

Prepared according to **GP II**. Starting from formamide **3** (0.560 g,

3.00 mmol, 1.00 eq.). Compound **6** (0.431 g, 2.46 mmol, 82%) was isolated as a white solid. $\mathbf{R_f}$ (CyH/CH_2Cl_2 1:4, *v/v*) = 0.70; **mp.** ~30 °C; **^{1}H NMR** (600 MHz, $CDCl_3$) δ = 7.97 (s, 1H), 7.88 (dd, J = 8.2, 1.9 Hz, 1H), 7.40 (d, J = 8.3 Hz, 1H), 3.92 (s, 3H), 2.48 (s, 3H); **^{13}C NMR** (151 MHz, $CDCl_3$) δ = 168.7, 165.9, 135.4, 131.9, 130.8, 130.4–129.7 (m), 128.1, 126.7, 52.6, 18.7; **LRMS-ESI (*m/z*):** $[M + H]^+$ calcd for $C_{10}H_9NO_2$: 176.1, found: 176.1.

Methyl-4-[(2-methylimidazo[1,2-*a*]pyridin-3-yl)amino]benzoate (**7a**)

Prepared according to **GP III**. Starting from 2-aminopyridine (0.103 g, 1.10 mmol, 1.00 eq.), acetaldehyde (5 M in THF, 0.240 mL, 52.8 mg, 1.20 mmol, 1.10 eq.), isonitrile **4** (0.181 g, 1.10 mmol, 1.00 eq.), and acetic acid (0.125 mL, 0.132 g, 2.20 mmol, 2.00 eq.). The crude mixture was purified by column chromatography (CyH/EE 2:1 to 0:1 *v/v*). Compound **7a** (0.164 g, 0.583 mmol, 53%) was isolated as a brown solid. $\mathbf{R_f}$ (CyH/EE 1:4, *v/v*) = 0.10; **mp.** 187–189 °C; **^{1}H NMR** (500 MHz, DMSO-d_6) δ = 8.49 (s, 1H), 7.88 (dt, J = 6.8, 1.2 Hz, 1H), 7.79–7.74 (m, 2H), 7.49 (dt, J = 9.0, 1.1 Hz, 1H), 7.22 (ddd, J = 9.0, 6.7, 1.3 Hz, 1H), 6.86 (td, J = 6.7, 1.1 Hz, 1H), 6.52 (d, J = 8.4 Hz, 2H), 3.76 (s, 3H), 2.22 (s, 3H); **^{13}C NMR** (126 MHz, DMSO-d_6) δ = 166.0, 150.7, 141.5, 137.1, 131.3, 124.0, 122.6, 119.0, 118.0, 116.5, 112.3, 111.7, 51.4, 12.7; **LRMS-ESI (*m/z*):** $[M + H]^+$ calcd for $C_{16}H_{15}N_3O_2$: 282.1, found: 282.2.

Methyl 4-[(2-ethylimidazo[1,2-*a*]pyridin-3-yl)amino]benzoate (**7b**)

Prepared according to **GP III**. Starting from 2-aminopyridine (0.103 g, 1.10 mmol, 1.00 eq.), propionaldehyde (0.128 mL, 0.104 g, 1.20 mmol, 1.09 eq.), isonitrile **4** (0.181, 1.10, 1.00.), and acetic acid (0.125, 0.132, 2.20 mmol, 2.00 eq.). The crude mixture was purified by column chromatography (CyH/EE 2:1 to 1:4 *v/v*). Compound **7b** (0.166 g, 0.562 mmol, 51%) was isolated as a green solid. $\mathbf{R_f}$ (CyH/EE 1:1, *v/v*) = 0.10; **mp.** 160–162 °C; **^{1}H NMR** (400 MHz, DMSO-d_6) δ = 8.01–7.88 (m, 2H), 7.58 (d, J = 8.1 Hz, 2H), 7.15 (d, J = 8.1 Hz, 2H), 7.13–7.08 (m, 1H), 6.71–6.59 (m, 1H), 4.32 (s, 2H), 3.89 (s, 3H), 2.80 (t, J = 7.6 Hz, 2H), 1.82 (q, J = 7.5 Hz, 2H), 0.99 (t, J = 7.3 Hz, 3H); **^{13}C NMR** (101 MHz, DMSO-d_6) δ = 166.1, 150.9, 142.5, 141.6, 131.3, 124.0, 122.7, 119.0, 117.2, 116.7, 112.3, 111.8, 51.5, 20.1, 13.5; **HRMS-ESI (*m/z*):** $[M + H]^+$ calcd for $C_{17}H_{17}N_3O_2$: 296,1404, found: 296,1399.

Methyl 4-[(2-isobutylimidazo[1,2-*a*]pyridin-3-yl)amino]benzoate (**7c**)

Prepared according to **GP III**. Starting from 2-aminopyridine (0.103 g, 1.10 mmol, 1.00 eq.), isovaleraldehyde, isonitrile **4** (0.181 g, 1.10 mmol, 1.00 eq.), and acetic acid (0.125 mL, 0.132 g, 2.20 mmol, 2.00 eq.). The crude mixture was purified by column chromatography (CyH/EE 2:1 to 1:2 *v/v*). Compound **7c** (0.234 g, 0.723 mmol, 66%) was isolated as a brown solid. $\mathbf{R_f}$ (CyH/EE 1:1, *v/v*) = 0.14; **mp.** 72–74C; **^{1}H NMR** (400 MHz, DMSO-d_6) δ = 8.51 (s, 1H), 7.83 (d, J = 6.7 Hz, 1H), 7.75 (d, J = 8.5 Hz, 2H), 7.52 (d, J = 9.0 Hz, 1H), 7.31–7.16 (m, 1H), 6.91–6.80 (m, 1H), 6.49 (d, J = 8.4 Hz, 2H), 3.75 (s, 3H), 2.45 (d, J = 7.1 Hz, 2H), 2.06 (hept, J = 6.7 Hz, 1H), 0.85 (d, J = 6.6 Hz, 6H); **^{13}C NMR** (75 MHz, DMSO-d_6) δ = 166.5, 151.2, 142.1, 141.1, 131.7, 124.5, 123.1, 119.4, 118.7, 117.2, 112.8, 112.2, 51.9, 36.3, 28.2, 23.0; **HRMS-ESI (*m/z*):** $[M + H]^+$ calcd for $C_{19}H_{21}N_3O_2$: 324.1712, found: 324.1709.

Methyl 4-[(2-cyclopropylimidazo[1,2-*a*]pyridin-3-yl)amino]benzoate (**7d**)

Prepared according to **GP III**. Starting from 2-aminopyridine (0.103 g, 1.10 mmol, 1.00 eq.), (89.0 μL, 83.4 mg, 1.17 mmol, 1.06 eq.) cyclopropanal, isonitrile **4** (0.181 g, 1.10 mmol, 1.00 eq.), and acetic acid (0.125 mL, 0.132 g, 2.20 mmol, 2.00 eq.). The crude mixture was purified by column chromatography (CyH/EE 2:1 to 1:3 *v/v*). Compound **7d** (0.282 g, 0.917 mmol, 84%) was isolated as a brown solid. $\mathbf{R_f}$ (CyH/EE 1:2, *v/v*) = 0.18; **mp.** 194–196 °C; **^{1}H NMR** (400 MHz, DMSO-d_6) δ = 8.58 (s, 1H), 7.85 (dt, J = 6.8, 1.2 Hz, 1H), 7.77 (d, 2H), 7.51–7.41 (m, 1H), 7.25–7.15 (m, 1H), 6.87–6.80 (m, 1H), 6.55 (d, J = 8.3 Hz, 2H), 3.76 (s, 3H), 1.87 (ddt, J = 9.8, 8.1, 4.3 Hz, 1H), 0.89 (dtd, J = 17.6, 5.9, 3.4 Hz, 4H); **^{13}C NMR** (101 MHz, DMSO-d_6) δ = 166.1, 150.9, 142.3, 141.6, 131.3, 124.0, 122.4, 119.0, 117.5, 116.4, 112.4, 111.7, 51.5, 8.0, 7.9; **HRMS-ESI (*m/z*):** $[M + H]^+$ calcd for $C_{18}H_{17}N_3O_2$: 308.1399, found: 308.1399.

Methyl 4-[(2-butylimidazo[1,2-*a*]pyridin-3-yl)amino]benzoate (**7e**)

Prepared according to **GP III**. Starting from 2-aminopyridine (0.103 g, 1.10 mmol, 1.00 eq.), valeraldehyde (0.161 mL, 0.129 g, 1.20 mmol, 1.09 eq.), isonitrile **4** (0.181 g, 1.10 mmol, 1.00 eq.), and acetic acid (0.125 mL, 0.132 g, 2.20 mmol, 2.00 eq.). The crude mixture was purified by column chromatography (CyH/EE 2:1 to 1:2 *v/v*). Compound **7e** (0.142 g, 0.439 mmol, 40%) was isolated as a brown solid. $\mathbf{R_f}$ (CyH/EE 1:1, *v/v*) = 0.20; **mp.** 98–100 °C; **^{1}H NMR** (400 MHz, DMSO-d_6) δ = 8.50 (s, 1H), 7.87 (d, J = 6.7 Hz, 1H), 7.76 (d, J = 8.5 Hz, 2H), 7.51 (d, J = 9.0 Hz, 1H), 7.28–7.18 (m, 1H), 6.91–6.82 (m, 1H), 6.50 (d, J = 8.3 Hz, 2H), 3.75 (s, 3H), 2.58 (q, J = 7.6 Hz, 2H), 1.19 (t, J = 7.5 Hz, 3H); **^{13}C NMR** (101 MHz, DMSO-d_6) δ = 166.1, 150.9, 142.5, 141.6, 131.3, 124.0, 122.7, 119.0, 117.2, 116.7, 112.3, 111.8, 51.5, 20.1, 13.5; **HRMS-ESI (*m/z*):** $[M + H]^+$ calcd for $C_{19}H_{21}N_3O_2$: 324.1712, found: 324.1714.

Methyl 4-[(2-pentylimidazo[1,2-*a*]pyridin-3-yl)amino]benzoate (**7f**)

Prepared according to **GP III**. Starting from 2-aminopyridine (0.103 g, 1.10 mmol, 1.00 eq.), hexanal (0.142 mL, 0.129 g, 1.20 mmol, 1.09 eq.), isonitrile **4** (0.181 g, 1.10 mmol, 1.00 eq.), and acetic acid (0.125 mL, 0.132 g, 2.20 mmol, 2.00 eq.). The crude mixture was purified by column chromatography (CyH/EE 2:1 to 1:2 *v/v*). Compound **7f** (0.159 g, 0.471 mmol, 43%) was isolated as a brown solid. $\mathbf{R_f}$ (CyH/EE 1:1, *v/v*) = 0.28; **mp.** 55–57 °C; **^{1}H NMR** (300 MHz, DMSO-d_6) δ = 8.50 (s, 1H), 7.88–7.82 (m, 1H), 7.75 (d, J = 8.9 Hz, 2H), 7.54–7.47 (m, 1H), 7.26–7.17 (m, 1H), 6.89–6.81 (m, 1H), 6.49 (d, J = 8.4 Hz, 2H), 3.75 (s, 3H), 2.56 (t, J = 7.5 Hz, 2H), 1.70–1.57 (m, 2H), 1.26–1.18 (m, 4H), 0.81–0.74 (m, 3H); **^{13}C NMR** (75 MHz, DMSO-d_6) δ = 166.1, 150.9, 141.6, 141.4, 131.2, 124.0, 122.6, 119.0, 117.7, 116.7, 112.3, 111.8, 51.4, 31.0, 28.1, 26.5, 21.8, 13.8; **HRMS-ESI (*m/z*):** $[M + H]^+$ calcd for $C_{20}H_{23}N_3O_2$: 338.1869, found: 338.1870.

Methyl 4-{[2-(3,3,3-trifluoropropyl)imidazo[1,2-*a*]pyridin-3-yl]amino}benzoate (**7g**)

Prepared according to **GP III**. Starting from 2-aminopyridine (0.103 g, 1.10 mmol, 1.00 eq.), 4,4,4-trifluorbutanal (0.116 mL, 0.139 g, 1.20 mmol, 1.09 eq.), isonitrile **4** (0.181 g, 1.10 mmol, 1.00 eq.), and acetic acid (0.125 mL, 0.132 g, 2.20 mmol, 2.00 eq.). The crude mixture was purified by column chromatography (CyH/EE 2:1 to 0:1 *v/v*). Compound **7g** (0.185 g, 0.509 mmol, 47%) was isolated as an orange solid. $\mathbf{R_f}$ (CyH/EE 1:1, *v/v*) = 0.11; **mp.** 183–185 °C; **^{1}H NMR** (400 MHz, DMSO-d_6) δ = 8.55 (s, 1H), 7.90 (dt, J = 6.8, 1.2 Hz, 1H), 7.83–7.72 (m, 2H), 7.55 (dt, J = 9.0, 1.1 Hz, 1H), 7.27 (ddd, J = 9.0, 6.7, 1.3 Hz, 1H), 6.90 (td, J = 6.8, 1.2 Hz, 1H), 6.53 (d, J = 8.3 Hz, 2H), 3.76 (s, 3H), 2.82 (dd, J = 9.9, 6.0 Hz, 2H), 2.74–2.59 (m, 2H); **^{13}C NMR** (101 MHz, DMSO-d_6) δ = 166.0, 150.5, 141.7, 137.9, 131.3, 127.3 (q, J = 276.8 Hz), 124.5, 122.9, 119.3, 118.0, 116.8, 112.4, 112.2, 51.5, 31.7 (q, J = 27.7 Hz), 19.5; **^{19}F {^{1}H} NMR** (377 MHz, DMSO-d_6) δ = −65.2 (s); **HRMS-ESI (*m/z*):** $[M + H]^+$ calcd for $C_{18}H_{16}F_3N_3O_2$: 364.1273, found: 364.1273.

Methyl 4-[(6-methyl-2-propylimidazo[1,2-*a*]pyridin-3-yl)amino]benzoate (**7h**)

Prepared according to **GP III**. Starting from 5-methyl-2-aminopyridine (0.119 g 1.10 mmol, 1.00 eq.), butanal (0.108 mL, 86.5 mg, 1.20 mmol, 1.10 eq.), isonitrile **4** (0.181 g, 1.10 mmol, 1.00 eq.), and acetic acid (0.125 mL, 0.132 g, 2.20 mmol, 2.00 eq.). The crude mixture was purified by column chromatography (CyH/EE 1:2 to 1:9 *v/v*). Compound **7h** (0.150 g, 0.464 mmol, 42%) was isolated as a brown solid. $\mathbf{R_f}$ (CyH/EE 1:2, *v/v*) = 0.18; **mp.** 175–176 °C; **^{1}H NMR** (400 MHz, DMSO-d_6) δ = 8.45 (s, 1H), 7.79–7.68 (m, 3H), 7.28 (s, 1H), 6.70 (dd, J = 6.9, 1.6 Hz, 1H), 6.49 (d, J = 8.3 Hz, 2H), 3.75 (s, 3H), 2.54–2.51 (m, 1H), 2.34 (s, 3H), 1.64 (sext, J = 7.4 Hz, 2H), 0.85 (t, J = 7.4 Hz, 3H); **^{13}C NMR** (101 MHz, DMSO-d_6) δ = 166.1, 151.0, 142.0, 140.8, 134.5, 131.2, 122.0, 118.9, 117.2, 115.1, 114.2, 112.2, 51.4, 28.7, 21.8, 20.7, 13.9; **HRMS-ESI (*m/z*):** $[M + H]^+$ calcd for $C_{19}H_{21}N_3O_2$: 324.1714, found: 324.1750.

Methyl 4-[(6-ethyl-2-propylimidazo[1,2-*a*]pyridin-3-yl)amino]

benzoate (**7i**)

Prepared according to **GP III**. Starting from 5-ethyl-2-aminopyridine (0.134 g, 1.10 mmol, 1.00 eq.), butanal (0.108 mL, 86,5 mg, 1.20 mmol, 1.10 eq.), isonitrile **4** (0.181 g, 1.10 mmol, 1.00 eq.), and acetic acid (0.125 mL, 0.132 g, 2.20 mmol, 2.00 eq.). The crude mixture was purified by column chromatography (CyH/EE 1:2 to 1:9 *v/v*). Compound **7i** (0.157 g, 0.465 mmol, 42%) was isolated as a brown solid. **R_f** (CyH/EE 1:2, *v/v*) = 0.18; **mp.** 161–163 °C; **^{1}H NMR** (400 MHz, DMSO-d_6) δ = 8.46 (s, 1H), 7.80–7.70 (m, 3H), 7.29 (s, 1H), 6.75 (dd, J = 7.0, 1.7 Hz, 1H), 6.49 (d, J = 8.3 Hz, 2H), 3.75 (s, 3H), 2.68–2.61 (m, 2H), 2.53 (d, J = 7.3 Hz, 2H), 1.64 (h, J = 7.4 Hz, 2H), 1.21 (t, J = 7.5 Hz, 3H), 0.85 (t, J = 7.4 Hz, 3H); **^{13}C NMR** (75 MHz, DMSO-d_6) δ = 166.1, 151.0, 142.0, 140.9, 140.6, 131.2, 122.2, 118.9, 117.2, 113.7, 113.2, 112.3, 51.4, 28.7, 27.6, 21.8, 14.6, 13.9; **HRMS-ESI** (*m/z*): [M + H]$^+$ calcd for $C_{20}H_{23}N_3O_2$: 338.1869, found: 338.1906.

Methyl 4-[(2-propylimidazo[1,2-*a*]pyrazin-3-yl)amino]benzoate (**7j**)

Prepared according to **GP III**. Starting from 2-aminopyrazine (0.143 g, 1.50 mmol, 1.00 eq.), (0.149 mL, 0.119 g, 1.65 mmol, 1.10 eq.) butanal, isonitrile **4** (0.241 g, 1.50 mmol, 1.00 eq.), and acetic acid (0.171 mL, 0.180 g, 3.00 mmol, 2.00 eq.). The crude mixture was purified by column chromatography (CH_2Cl_2/MeOH 1:0 to 95:5 *v/v*). Compound **7j** (0.185 g, 0.596 mmol, 40%) was isolated as a yellow solid. **R_f** (CH_2Cl_2/MeOH 99:1, *v/v*) = 0.20; **mp.** 161–163 °C; **^{1}H NMR** (300 MHz, DMSO-d_6) δ = 8.98 (d, J = 1.5 Hz, 1H), 8.69 (s, 1H), 7.95 (dd, J = 4.5, 1.5 Hz, 1H), 7.84 (d, J = 4.5 Hz, 1H), 7.80–7.74 (m, 2H), 6.57–6.49 (m, 2H), 3.76 (s, 3H), 2.61 (t, J = 7.9 Hz, 2H), 1.68 (sext, J = 7.4 Hz, 2H), 0.85 (t, J = 7.3 Hz, 3H); **^{13}C NMR** (101 MHz, DMSO-d_6) δ = 166.0, 150.0, 143.8, 142.2, 137.1, 131.3, 129.0, 119.7, 119.5, 116.2, 112.6, 51.5, 28.7, 21.5, 13.8; **HRMS-ESI (*m/z*)**: [M + H]$^+$ calcd for $C_{17}H_{18}N_4O_2$: 311.1508, found: 311.1505.

Methyl-3-fluoro-4-[(2-propylimidazo[1,2-*a*]pyridin-3-yl)amino] benzoate (**7k**)

Prepared according to **GP III**. Starting from 2-aminopyridine (0.143 g, 1.50 mmol, 1.00 eq.), (0.149 mL, 0.143 g, 1.65 mmol, 1.10 eq.) butanal, isonitrile **5** (0.296 g 1.65 mmol, 1.10 eq.), and acetic acid (0.171 mL, 0.180 g, 3.00 mmol, 2.00 eq.). The crude mixture was purified by column chromatography ($CHCl_3$/MeOH 1:0 to 99:1 *v/v*). Compound **7k** (0.184 g, 0.562 mmol, 37%) was isolated as a brown solid. **R_f** ($CHCl_3$) = 0.18; **mp.** 182–184 °C; **^{1}H NMR** (400 MHz, DMSO-d_6) δ = 8.47 (s, 1H), 7.93 (d, J = 6.8 Hz, 1H), 7.68 (dd, J = 12.3, 1.9 Hz, 1H), 7.58–7.46 (m, 2H), 7.29–7.18 (m, 1H), 6.91–6.81 (m, 1H), 6.19–6.05 (m, 1H), 3.78 (s, 3H), 2.57–2.51 (m, 2H), 1.66 (sext, J = 7.4 Hz, 2H), 0.86 (t, J = 7.4 Hz, 3H); **^{13}C NMR** (101 MHz, DMSO-d_6) δ = 165.3, 150.0 (d, J = 241.1 Hz), 141.7 (d, J = 12.1 Hz), 139.1 (d, J = 11.6 Hz), 127.1, 124.2, 122.8, 119.2 (d, J = 6.1 Hz), 116.7, 116.1, 115.9, 112.6 (d, J = 3.7 Hz), 111.8, 51.8, 28.7, 21.7, 14.0; **^{19}F NMR** (377 MHz, DMSO-d_6) δ = −133.1 (t, J = 12.4 Hz); **HRMS-ESI** (*m/z*): [M + H]$^+$ calcd for $C_{18}H_{18}FN_3O_2$: 328.1461, found: 328.1459.

Methyl-3-methyl-4-[(2-propylimidazo[1,2-*a*]pyridin-3-yl)amino] benzoate (**7l**)

2-Aminopyridine (94.0 mg, 1.00 mmol, 1.00 eq.) was dissolved in 3 mL MeOH/CH_2Cl_2 (1/1, *v/v*). butanal (91.0 μL, 79.3 mg, 1.10 mmol, 1.10 eq.), isonitrile **6** (0.175 g, 1.00 mmol, 1.00 eq.) and scandium(III) triflate (24.6 mg, 50.0 μmol, 5 mol-%) were added and stirred for three days at room temperature. The solvent was removed under reduced pressure and the crude mixture purified by column chromatography (CyH/EE 1:1 to 1:4 *v/v*). Compound **7l** (0.200 g, 0.618 mmol, 62%) was isolated as a white solid. **R_f** (CyH/EE 1:2, *v/v*) = 0.20; **mp.** 204–206 °C; **^{1}H NMR** (600 MHz, $CDCl_3$) δ = 7.90–7.83 (m, 1H), 7.71 (dt, J = 6.7, 1.2 Hz, 1H), 7.65 (dd, J = 8.5, 2.0 Hz, 1H), 7.59 (dt, J = 9.1, 1.1 Hz, 1H), 7.20 (ddd, J = 9.1, 6.7, 1.3 Hz, 1H), 6.76 (td, J = 6.7, 1.2 Hz, 1H), 6.05 (d, J = 8.5 Hz, 1H), 5.61 (s, 1H), 3.84 (s, 3H), 2.66 (t, J = 7.6 Hz, 2H), 2.43 (s, 3H), 1.75 (h, J = 7.4 Hz, 2H), 0.92 (t, J = 7.4 Hz, 3H); **^{13}C NMR** (151 MHz, $CDCl_3$) δ = 167.2, 147.6, 143.2, 142.8, 132.6, 129.7, 124.7, 122.3, 121.5, 121.1, 117.5, 117.4, 112.2, 111.0, 51.9, 29.3, 22.5, 17.5, 14.3; **LRMS-ESI** (*m/z*): [M + H]$^+$ calcd for $C_{19}H_{21}N_3O_2$: 324.2, found: 324.2.

Methyl 3-fluoro-4-[(2-methylimidazo[1,2-*a*]pyridin-3-yl)amino] benzoate (**7m**)

Prepared according to **GP III**. Starting from 2-aminopyridine (0.181 g, 1.81 mmol, 1.00 eq.), acetaldehyde (5 M in THF, 0.400 mL, 88.1 mg, 2.00 mmol, 1.10 eq.), isonitrile **5** (0.353 g, 2.00 mmol, 1.10 eq.), and acetic acid (0.207 mL, 0.217 g, 3.62 mmol, 2.00 eq.). The crude mixture was purified by column chromatography (CyH/EE 1:3 to 1:19 *v/v*). Compound **7m** (0.144 g, 0.481 mmol, 27%) was isolated as a brown solid. **R_f** (CyH/EE 1/3) = 0.10; **mp.** ~147 °C (decomposition); **^{1}H NMR** (600 MHz, DMSO-d_6) δ = 8.46 (d, J = 2.2 Hz, 1H), 7.95 (dt, J = 6.8, 1.2 Hz, 1H), 7.68 (dd, J = 12.3, 1.9 Hz, 1H), 7.54 (dd, J = 8.5, 1.9 Hz, 1H), 7.50 (dt, J = 9.0, 1.1 Hz, 1H), 7.24 (ddd, J = 9.1, 6.7, 1.3 Hz, 1H), 6.86 (td, J = 6.7, 1.2 Hz, 1H), 6.16 (t, J = 8.6 Hz, 1H), 3.78 (s, 3H), 2.22 (s, 3H); **^{13}C NMR** (151 MHz, DMSO-d_6) δ = 165.3 (d, J = 2.7 Hz), 150.0 (d, J = 241.0 Hz), 141.6, 138.9 (d, J = 11.5 Hz), 137.5, 127.1 (d, J = 2.5 Hz), 124.2, 122.8, 119.2 (d, J = 6.1 Hz), 116.9, 116.5, 116.0 (d, J = 19.3 Hz), 112.6 (d, J = 3.6 Hz), 111.7, 51.8, 12.7; **^{19}F NMR** (565 MHz, DMSO-d_6) δ = −133.9–−134.0 (m); **LRMS-ESI** (*m/z*): [M + H]$^+$ calcd for $C_{16}H_{14}FN_3O_2$: 300.1, found: 300.1.

N-Hydroxy-4-[(2-methylimidazo[1,2-*a*]pyridin-3-yl)amino]benzamide trifluoroacetate (**8a**)

Prepared according to **GP IV.** Starting from (0.100 g, 0.355 mmol, 1.00 eq.) ester **7a**, hydroxyl amine (50% in H_2O, 0.680 mL, 0.336 g, 10.7 mmol, 30.0 eq.), and NaOH (0.140 g, 3.55 mmol, 10.0 eq.). The formed participate was further purified via preparative HPLC. Compound **8a** (29.4 mg, 74.2 μmol, 21%) was isolated as a white lyophilizate. **HPLC**: t_R = 10.12 min (96.0% purity); **R_f** (CH_2Cl_2/MeOH 9:1, *v/v*) = 0.25; **^{1}H NMR** (500 MHz, DMSO-d_6) δ = 10.96 (s, 1H), 8.66 (s, 1H), 8.34 (dt, J = 6.8, 1.1 Hz, 1H), 7.98 (dt, J = 9.0, 1.2 Hz, 1H), 7.92 (ddd, J = 9.0, 6.9, 1.2 Hz, 1H), 7.64–7.60 (m, 2H), 7.43 (td, J = 6.9, 1.2 Hz, 1H), 6.73–6.66 (m, 2H), 2.37 (s, 3H); **^{13}C NMR** (126 MHz, DMSO-d_6) δ = 164.1, 158.2 (q, J = 32.2 Hz), 147.3, 137.2, 132.6, 128.6, 128.5, 124.8, 123.7, 120.6, 116.8 (q, J = 297.2 Hz), 116.7, 112.9, 112.4, 9.4; **HRMS-ESI** (*m/z*): [M + H]$^+$ calcd for $C_{15}H_{14}N_4O_2$: 283.1195, found: 283.1187.

4-[(2-Ethylimidazo[1,2-*a*]pyridin-3-yl)amino]-*N*-hydroxybenzamide (**8b**)

Prepared according to **GP IV.** Starting from ester **7b** (80.0 mg, 0.271 mmol, 1.00 eq.), hydroxyl amine (50% in H_2O, 0.540 mL 0.268 g, 8.13 mmol, 30.0 eq.), and NaOH (0.109 g, 2.72 mmol, 10.0 eq.). Compound **8b** (52.8 mg, 0.178 mmol, 66%) was isolated as a white solid. **HPLC**: t_R = 10.20 min (98.5% purity); **R_f** (CH_2Cl_2/MeOH 9:1, *v/v*) = 0.30; **mp.** 173 °C–175 °C; **^{1}H NMR** (300 MHz, DMSO-d_6) δ = 10.87 (s, 1H), 8.81 (s, 1H), 8.24 (s, 1H), 7.90–7.81 (m, 1H), 7.57 (d, J = 8.4 Hz, 2H), 7.51 (d, J = 9.0 Hz, 1H), 7.27–7.16 (m, 1H), 6.91–6.80 (m, 1H), 6.44 (d, J = 8.4 Hz, 2H), 2.59 (q, J = 7.5 Hz, 2H), 1.19 (t, J = 7.5 Hz, 3H); **^{13}C NMR** (101 MHz, DMSO-d_6) δ = 164.5, 149.1, 142.5, 141.5, 128.6, 123.9, 122.7, 122.4, 117.7, 116.7, 112.0, 111.7, 20.1, 13.6; HRMS-ESI (*m/z*): [M + H]$^+$ calcd for $C_{16}H_{16}N_4O_2$: 297.1362, found: 297.1352.

Methyl 4-[(2-isobutylimidazo[1,2-*a*]pyridin-3-yl)amino]benzoate (**8c**)

Prepared according to **GP IV.** Starting from ester **7c** (80.0 mg, 0.247 mmol, 1.00 eq.), hydroxyl amine (50% in H_2O, 0.492 mL, 0.245 g, 7.41 mmol, 30.0 eq.), and NaOH (98.8 mg, 2.47 mmol, 10.0 eq.). Compound **8c** (64.8 mg, 0.200 mmol, 81%) was isolated as a white solid. **HPLC**: t_R = 10.66 min (96.6% purity); **R_f** (CH_2Cl_2/MeOH 9:1, *v/v*) = 0.46; **mp.** 171 °C–173 °C; **^{1}H NMR** (300 MHz, DMSO-d_6) δ = 10.88 (s, 1H), 8.82 (s, 1H), 8.27 (s, 1H), 7.81 (d, J = 6.7 Hz, 1H), 7.56 (d, J = 8.4 Hz, 2H), 7.53–7.47 (m, 1H), 7.28–7.14 (m, 1H), 6.93–6.75 (m, 1H), 6.43 (d, J = 8.3 Hz, 2H), 2.46 (d, J = 7.9 Hz, 2H), 2.14–1.98 (m, 1H), 0.85 (d, J = 6.6 Hz, 6H); **^{13}C NMR** (101 MHz, DMSO-d_6) δ = 164.5, 148.9, 141.5, 140.7, 128.6, 123.9, 122.7, 122.3, 118.7, 116.7, 112.1, 111.7, 35.9, 27.8, 22.6; **HRMS-ESI** (*m/z*): [M + H]$^+$ calcd for $C_{18}H_{20}N_4O_2$: 325.1665, found: 325.1665.

4-[(2-Cyclopropylimidazo[1,2-*a*]pyridin-3-yl)amino]-*N*-

hydroxybenzamide (**8d**)

Prepared according to **GP IV.** Starting from ester **7d** (67.3 mg, 0.220 mmol, 1.00 eq.), hydroxyl amine (50% in H_2O, 0.438 mL, 0.217 g, 6.60 mmol, 30.0 eq.), and NaOH (88.0 mg, 2.20 mmol, 10.0 eq.). Compound **8d** (47.0 mg, 0.132 mmol, 60%) was isolated as a yellow solid. **HPLC**: t_R = 10.32 min (99.0% purity); **R_f** (CH_2Cl_2/MeOH 9:1, *v/v*) = 0.28; **mp.** 179–181 °C; **^{1}H NMR** (400 MHz, DMSO-d_6) δ = 10.75 (s, 1H), 9.02 (s, 1H), 8.35 (s, 1H), 7.84 (dd, J = 6.7, 1.3 Hz, 1H), 7.59 (d, J = 8.3 Hz, 2H), 7.45 (dd, J = 9.0, 1.2 Hz, 1H), 7.19 (ddd, J = 8.7, 6.8, 1.4 Hz, 1H), 6.83 (td, J = 6.8, 1.2 Hz, 1H), 6.53–6.44 (m, 2H), 1.88 (tt, J = 8.2, 5.0 Hz, 1H), 0.97–0.80 (m, 4H); **^{13}C NMR** (101 MHz, DMSO-d_6) δ = 164.5, 149.1, 142.2, 141.5, 128.6, 123.9, 122.4, 122.4, 118.0, 116.4, 112.1, 111.6, 8.1, 7.9; HRMS-ESI (*m/z*): $[M + H]^+$ calcd for $C_{17}H_{16}N_4O_2$: 309.1352, found: 309.1347.

4-[(2-Butylimidazo[1,2-*a*]pyridin-3-yl)amino]-*N*-hydroxybenzamide (**8e**)

Prepared according to GP IV. Starting from ester **7e** (69.6 mg, 0.215 mmol, 1.00 eq.), hydroxyl amine (50% in H_2O, 0.428 mL, 0.214 g, 6.45 mmol, 30.0 eq.), and NaOH (86.0 mg, 2.15 mmol, 10.0 eq.). Compound **8e** (63.6 mg 0.196 mmol, 91%) was isolated as a white solid. **HPLC**: t_R = 10.71 min (96.8% purity); **R_f** (CH_2Cl_2/MeOH 9:1, *v/v*) = 0.48; **mp.** 155 °C–157 °C; **^{1}H NMR** (400 MHz, DMSO-d_6) δ = 10.90 (s, 1H), 8.82 (s, 1H), 8.24 (s, 1H), 7.83 (d, J = 6.8 Hz, 1H), 7.57 (d, J = 8.4 Hz, 2H), 7.50 (d, J = 9.0 Hz, 1H), 7.21 (t, J = 7.9 Hz, 1H), 6.85 (t, J = 6.7 Hz, 1H), 6.43 (d, J = 8.4 Hz, 2H), 2.57 (t, J = 7.5 Hz, 2H), 1.62 (p, J = 7.5 Hz, 2H), 1.27 (sext, J = 7.1 Hz, 2H), 0.82 (t, J = 7.4 Hz, 3H); **^{13}C NMR** (101 MHz, DMSO-d_6) δ = 164.4, 149.0, 141.5, 141.4, 128.6, 123.9, 122.7, 122.3, 118.1, 116.7, 112.0, 111.7, 30.7, 26.3, 21.9, 13.7; HRMS-ESI (*m/z*): $[M + H]^+$ calcd for $C_{18}H_{20}N_4O_2$: 325.1665, found: 325.1667.

N-Hydroxy-4-[(2-pentylimidazo[1,2-*a*]pyridin-3-yl)amino]benzamide (**8f**)

Prepared according to **GP IV.** Starting from ester **7f** (60.0 mg, 0.177 mmol, 1.00 eq.), hydroxyl amine (50% in H_2O, 0.353 mL, 0.176 g, 5.31 mmol, 30.0 eq.), and NaOH (70.8 mg, 1.77 mmol, 10.0 eq.). Compound **8f** (53.8 mg, 0.159 mmol, 90%) was isolated as a white solid. **HPLC**: t_R = 10.95 min (95.0% purity); **R_f** (CH_2Cl_2/MeOH 9:1, *v/v*) = 0.50; **mp.** 155 °C–157 °C; **^{1}H NMR** (400 MHz, DMSO-d_6) δ = 10.88 (s, 1H), 8.79 (s, 1H), 8.25 (s, 1H), 7.83 (d, J = 6.8 Hz, 1H), 7.57 (d, J = 8.3 Hz, 2H), 7.50 (d, J = 9.1 Hz, 1H), 7.21 (t, J = 7.8 Hz, 1H), 6.85 (t, J = 6.7 Hz, 1H), 6.43 (d, J = 8.2 Hz, 2H), 2.57 (t, J = 7.5 Hz, 2H), 1.70–1.58 (m, 2H), 1.29–1.15 (m, 4H), 0.84–0.71 (m, 3H); **^{13}C NMR** (101 MHz, DMSO-d_6) δ = 164.5, 149.1, 141.5, 141.4, 128.6, 123.9, 122.6, 122.3, 118.2, 116.7, 112.0, 111.7, 31.0, 28.2, 26.6, 21.9, 13.8; HRMS-ESI (*m/z*): $[M + H]^+$ calcd for $C_{19}H_{22}N_4O_2$: 339.1821, found: 339.1826.

N-Hydroxy-4-{[2-(3,3,3-trifluoropropyl)imidazo[1,2-*a*]pyridin-3-yl]amino}benzamide (**8g**)

Prepared according to **GP IV.** Starting from ester **7g** (82.1 mg, 0.226 mmol, 1.00 eq.), hydroxyl amine (50% in H_2O, 0.438 mL, 0.217 g, 6.60 mmol, 30.0 eq.), and NaOH (90.4 mg 2.26 mmol, 10.0 eq.). Compound **8g** (50.3 mg, 0.138 mmol, 61%) was isolated as a yellow solid. **HPLC**: t_R = 10.66 min (95.4% purity); **R_f** (CH_2Cl_2/MeOH 9:1, *v/v*) = 0.30, **mp.** > 148 °C (decomposition); **^{1}H NMR** (300 MHz, DMSO-d_6) δ = 10.91 (s, 1H), 8.83 (s, 1H), 8.31 (s, 1H), 7.88 (d, J = 6.7 Hz, 1H), 7.66–7.49 (m, 3H), 7.26 (dd, J = 9.0, 6.7 Hz, 1H), 6.89 (t, J = 6.7 Hz, 1H), 6.48 (d, J = 8.3 Hz, 2H), 2.88–2.77 (m, 2H), 2.76–2.55 (m, 2H); **^{13}C NMR** (101 MHz, DMSO-d_6) δ = 164.5, 148.7, 141.6, 137.9, 128.7, 127.3 (d, J = 277.2 Hz), 124.5, 122.9, 122.7, 118.5, 116.8, 112.5–111.9 (m), 31.9 (q, J = 27.6 Hz), 19.5 (q, J = 3.5 Hz); **^{19}F NMR** (282 MHz, DMSO) δ = −65.2 (dd, J = 12.6, 9.6 Hz); HRMS-ESI (*m/z*): $[M + H]^+$ calcd for $C_{17}H_{15}F_3N_4O_2$: 365.1225, found: 365.1236.

N-Hydroxy-4-[(6-methyl-2-propylimidazo[1,2-*a*]pyridin-3-yl)amino]benzamide (**8h**)

Prepared according to **GP IV.** Starting from ester **7h** (82.5 mg, 0.255 mmol, 1.00 eq.), hydroxyl amine (50% in H_2O, 0.484 mL, 0.240 g, 7.65 mmol, 30.0 eq.), and NaOH (0.102 g, 2.55 mmol, 10.0 eq.). Compound **8h** (75.9 mg, 0.234 mmol, 92%) was isolated as a beige solid. **HPLC**: t_R = 10.74 min (97.4% purity); **R_f** (CH_2Cl_2/MeOH 9:1, *v/v*) = 0.24; **mp.** 195–197 °C; **^{1}H NMR** (400 MHz, DMSO-d_6) δ = 10.89 (s, 1H), 8.82 (s, 1H), 8.22 (s, 1H), 7.71 (d, J = 6.8 Hz, 1H), 7.56 (d, J = 8.4 Hz, 2H), 7.27 (s, 1H), 6.69 (dd, J = 6.9, 1.6 Hz, 1H), 6.42 (d, J = 8.3 Hz, 2H), 2.56–2.51 (m, 2H), 2.33 (s, 3H), 1.64 (p, J = 7.4 Hz, 2H), 0.85 (t, J = 7.4 Hz, 3H); **^{13}C NMR** (101 MHz, DMSO-d_6) δ = 164.6, 149.2, 141.9, 140.8, 134.4, 128.6, 122.3, 122.0, 117.7, 115.1, 114.1, 112.0, 28.7, 21.9, 20.7, 14.0; HRMS-ESI (*m/z*): $[M + H]^+$ calcd for $C_{18}H_{20}N_4O_2$: 325.1665, found: 325.1675.

4-[(6-Ethyl-2-propylimidazo[1,2-*a*]pyridin-3-yl)amino]-*N*-hydroxybenzamide (**8i**)

Prepared according to **GP IV.** Starting from ester **7i** (80.0 mg, 0.237 mmol, 1.00 eq.), hydroxyl amine (50% in H_2O, 0.471 mL, 0.233 g, 7.11 mmol, 30.0 eq.), and NaOH (94.8 mg, 2.37 mmol, 10.0 eq.). Compound **8i** (72.8 mg, 0.215 mmol, 91%) was isolated as a beige solid. **HPLC**: t_R = 10.95 min (96.8% purity); **R_f** (CH_2Cl_2/MeOH 9:1, *v/v*) = 0.24; **mp.** 205–207 °C; **^{1}H NMR** (400 MHz, DMSO-d_6) δ = 10.88 (s, 1H), 8.82 (s, 1H), 8.21 (s, 1H), 7.73 (d, J = 6.9 Hz, 1H), 7.56 (d, J = 8.4 Hz, 2H), 7.27 (s, 1H), 6.73 (dd, J = 7.0, 1.7 Hz, 1H), 6.43 (d, J = 8.3 Hz, 2H), 2.64 (q, J = 7.5 Hz, 2H), 2.53 (d, J = 7.3 Hz, 2H), 1.64 (h, J = 7.4 Hz, 2H), 1.20 (t, J = 7.5 Hz, 3H), 0.85 (t, J = 7.4 Hz, 3H); **^{13}C NMR** (101 MHz, DMSO-d_6) δ = 164.5, 149.2, 142.0, 140.9, 140.4, 128.6, 122.3, 122.2, 117.7, 113.7, 113.0, 112.0, 28.8, 27.6, 21.9, 14.6, 14.0; HRMS-ESI (*m/z*): $[M + H]^+$ calcd for $C_{19}H_{22}N_4O_2$: 339.1821, found: 339.1826.

N-Hydroxy-4-[(2-propylimidazo[1,2-*a*]pyrazin-3-yl)amino]benzamide (**8j**)

Prepared according to **GP IV.** Starting from ester **7j** (0.115 g, 0.371 mmol, 1.00 eq.), hydroxyl amine (50% in H_2O, 0.734 mL, 0.367 g, 11.1 mmol, 30.0 eq.), and NaOH (0.148 mg, 3.71 mmol, 10.0 eq.). Compound **8j** (60.1 mg, 0.193 mmol, 52%) was isolated as a white solid. **HPLC**: t_R = 10.32 min (95.8% purity); **R_f** (CH_2Cl_2/MeOH 9:1, *v/v*) = 0.28; **mp.** 193 °C–195 °C; **^{1}H NMR** (400 MHz, DMSO-d_6) δ = 10.90 (s, 1H), 8.97 (s, 1H), 8.79 (s, 1H), 8.43 (d, J = 3.1 Hz, 1H), 7.97–7.88 (m, 1H), 7.84 (d, J = 4.1 Hz, 1H), 7.64–7.51 (m, 2H), 6.51–6.41 (m, 2H), 2.65–2.58 (m, 2H), 1.76–1.63 (m, 2H), 0.91–0.82 (m, 3H); **^{13}C NMR** (101 MHz, DMSO-d_6) δ = 164.4, 148.1, 143.7, 142.1, 137.0, 128.9, 128.6, 122.8, 120.2, 116.1, 112.4, 28.7, 21.6, 13.9; HRMS-ESI (*m/z*): $[M + H]^+$ calcd for $C_{16}H_{17}N_5O_2$: 312.1460, found: 312.1463.

3-Fluoro-*N*-hydroxy-4-[(2-propylimidazo[1,2-*a*]pyridin-3-yl)amino]benzamide (**8k**)

Prepared according to **GP IV.** Starting from ester **7k** (80.0 mg, 0.244 mmol, 1.00 eq.), hydroxyl amine (50% in H_2O, 0.484 mL, 0.242 g, 7.32 mmol, 30.0 eq.), and NaOH (98.0 mg, 2.44 mmol, 10.0 eq.). Compound **8k** (61.6 mg, 0.188 mmol, 77%) was isolated as a white solid. **HPLC**: t_R = 10.56 min (97.0% purity); **R_f** (CH_2Cl_2/MeOH 9:1, *v/v*) = 0.40; **mp.** 189–191 °C; **^{1}H NMR** (300 MHz, DMSO-d_6) δ = 11.02 (s, 1H), 8.93 (s, 1H), 8.21 (s, 1H), 7.91 (d, J = 6.8 Hz, 1H), 7.59 (d, J = 12.7 Hz, 1H), 7.52 (d, J = 8.9 Hz, 1H), 7.35 (d, J = 8.4 Hz, 1H), 7.23 (t, J = 7.8 Hz, 1H), 6.86 (t, J = 6.8 Hz, 1H), 6.06 (t, J = 8.6 Hz, 1H), 2.59–2.53 (m, 2H), 1.66 (q, J = 7.4 Hz, 2H), 0.86 (t, J = 7.3 Hz, 3H); **^{13}C NMR** (101 MHz, DMSO-d_6) δ = 163.3, 150.1 (d, J = 240.3 Hz), 141.7, 141.6, 137.0 (d, J = 11.5 Hz), 124.2, 124.1, 122.8, 122.5 (d, J = 5.4 Hz), 117.1, 116.6, 114.1 (d, J = 19.4 Hz), 112.5 (d, J = 3.8 Hz), 111.7, 28.7, 21.7, 14.0; **^{19}F NMR** (282 MHz, DMSO-d_6) δ = −133.4 (t, J = 10.7 Hz); HRMS-ESI (*m/z*): $[M + H]^+$ calcd for $C_{17}H_{17}FN_4O_2$: 329.1414, found: 329.1413.

N-Hydroxy-3-methyl-4-[(2-propylimidazo[1,2-*a*]pyridin-3-yl)amino]benzamide (**8l**)

Prepared according to **GP IV.** Starting from ester **7l** (0.100 g, 0.309 mmol, 1.00 eq.), hydroxyl amine (50% in H_2O, 0.614 mL, 0.304 g, 9.27 mmol, 30.0 eq.), and NaOH (0.124 g, 3.09 mmol, 10.0 eq.). Compound **8l** (73.7 mg, 0.227 mmol, 73%) was isolated as a white solid. **HPLC**: t_R = 10.41 min (98.6% purity); **R_f** (CH_2Cl_2/MeOH 9:1, *v/v*) = 0.35; **mp.** 250 °C (decomposition); **^{1}H NMR** (600 MHz, DMSO-d_6) δ = 10.83 (s, 1H), 8.76 (s, 1H), 7.83 (dt, J = 6.8, 1.2 Hz, 1H), 7.57 (d, J = 2.1 Hz, 1H), 7.53–7.48 (m, 2H), 7.31 (dd, J = 8.5, 2.1 Hz, 1H), 7.21 (ddd, J = 9.0, 6.6, 1.3 Hz, 1H), 6.83 (td, J = 6.7, 1.1 Hz, 1H), 5.82 (d, J = 8.4 Hz, 1H),

2.55 (t, $J = 7.5$ Hz, 2H), 2.37 (s, 3H), 1.67 (h, $J = 7.4$ Hz, 2H), 0.87 (t, $J = 7.4$ Hz, 3H); **^{13}C NMR** (151 MHz, DMSO-d_6) $\delta = 165.1, 147.4, 142.1, 142.0, 130.1, 126.5, 124.3, 123.2, 122.7, 122.5, 118.9, 117.1, 112.0, 110.5, 29.3, 22.2, 18.3, 14.5$; HRMS-ESI ($m/z$): $[M + H]^+$ calcd for $C_{18}H_{20}N_4O_2$: 325.1665, found: 325.1660.

3-Fluoro-*N*-hydroxy-4-[(2-methylimidazo[1,2-*a*]pyridin-3-yl) amino]benzamide (**8m**)

Prepared according to **GP IV.** Starting from ester **7m** (80.0 mg, 0.267 mmol, 1.00 eq.), hydroxyl amine (50% in H_2O, 0.644 mL, 0.251 g, 8.01 mmol, 30.0 eq.), and NaOH (0.107 g, 2.67 mmol, 10.0 eq.). Compound **8m** (48.0 mg, 0.160 mmol, 60%) was isolated as a white solid. **HPLC**: $t_R = 10.19$ min (96.1% purity); **R_f** (CH_2Cl_2/MeOH 9:1, v/v) = 0.30; **mp.** ~145 °C (decomposition); **^{1}H NMR** (600 MHz, DMSO-d_6) $\delta = 11.00$ (s, 1H), 8.92 (s, 1H), 8.20 (d, $J = 2.2$ Hz, 1H), 7.93 (dt, $J = 6.8, 1.2$ Hz, 1H), 7.59 (dd, $J = 12.6, 1.9$ Hz, 1H), 7.49 (dt, $J = 9.1, 1.2$ Hz, 1H), 7.36 (dd, $J = 8.4, 1.9$ Hz, 1H), 7.23 (ddd, $J = 9.0, 6.7, 1.3$ Hz, 1H), 6.86 (td, $J = 6.7, 1.2$ Hz, 1H), 6.08 (t, $J = 8.6$ Hz, 1H), 2.22 (s, 3H); **^{13}C NMR** (151 MHz, DMSO-d_6) $\delta = 163.2, 150.1$ (d, $J = 240.2$ Hz), 141.6, 137.5, 136.8 (d, $J = 11.6$ Hz), 124.2, 124.1, 122.8, 122.6 (d, $J = 5.4$ Hz), 117.4, 116.4, 114.0 (d, $J = 19.4$ Hz), 112.4 (d, $J = 3.5$ Hz), 111.7, 12.7; **^{19}F NMR** (565 MHz, DMSO-d_6) $\delta = -133.4$ (t, $J = 10.8$ Hz); HRMS-ESI (m/z): $[M + H]^+$ calcd for $C_{15}H_{13}FN_4O_2$: 301.1101, found: 301.1097.

4.3. HDAC enzyme inhibition assay

In vitro inhibitory activities against HDAC1 − 3 and HDAC6 were measured using a previously published protocol.50 In short, 3-fold serial dilutions of test compounds and controls were prepared in assay buffer (50 mM Tris-HCl (pH 8.0), 137 mM NaCl, 2.7 mM KCl, 1.0 mM $MgCl_2{\cdot}6$ H2O, and 0.1 mg/mL BSA). These serial dilutions (5.0 µL) were transferred into 96-well microplates (OptiPlate-96F, black, PerkinElmer). 35 µL of the fluorogenic substrate ZMAL (Z-Lys(Ac)-AMC [40]; 21.43 µM in assay buffer) and 10 µL of human recombinant HDAC enzyme solution (HDAC1 - BPS Bioscience, Catalog# 50051; HDAC2 - BPS Bioscience, Catalog# 50052; HDAC3/NcoR2 - BPS Bioscience, Catalog# 50003; HDAC6 - BPS Bioscience, Catalog# 50006) were added. The total assay volume of 50 µL (max. 1% DMSO) was incubated at 37 °C for 90 min. Subsequently, 50 µL trypsin solution (0.4 mg/mL trypsin in buffer: 50 mM Tris-HCl (pH 8.0), 100 mM NaCl) was added, followed by 30 min of incubation at 37 °C. Fluorescence (excitation, 355 nm; emission, 460 nm) was measured using a FLUOstar OPTIMA microplate reader (BMG LABTECH). All compounds were tested in duplicates. Reported mean IC_{50}-values, including standard deviation, were calculated from at least two independent experiments.

In vitro inhibitory activity against HDAC10 was performed by Reaction Biology. In short, 10 µL of reaction buffer (20 mM Na_2HPO_4 (pH 8.0), 100 mM NaCl, 0.25 mM EDTA, 10 mM Mesna, 0.01 % Brij35, 1% DMSO) and/or 10 µL enzyme solution (human full-length HDAC10 (aa2-669end, Accession # NM_032019.5), N-terminal GST-TEV-tag, expressed in Sf9 insect cells) was delivered into wells of 3573 Corning Black react plates. Subsequently, compound dilutions (in 100% DMSO) were delivered into the enzyme mixture and pre-incubated for 20 min. Next, 10 µL of substrate mixture (Ac-spermidine-AMC) was delivered to all reaction wells and incubated for 1 h at 30 °C. The reaction was stopped by the addition of borate buffer (pH 9.5) and NDA (167 µM final). Results was determined by endpoint measurement (Ex/Em = 355/460 nm).

4.4. Cell biological evaluation

4.4.1. THP-1 macrophages and J774A.1 macrophages

4.4.1.1. Cell culture. Human THP-1 cells (ACC 16, DSMZ-German Collection of Microorganisms and Cell Cultures GmbH, Braunschweig, Germany) were used from passages 10 to 25 and cultured in RPMI 1640 (2653669, Thermo Fisher Scientific, Darmstadt, Germany), supplemented with 100 U/ml penicillin, 100 µg/ml streptomycin (P4333, Sigma-Aldrich, Taufkirchen, Germany) and 10 % heat-inactivated fetal bovine serum (FBS; S0615, Sigma-Aldrich). For differentiation of THP-1 monocytes into THP-1 macrophages, cells were seeded into 24-well plates at a density of 4×10^5 cells/well in growth medium. Phorbol 12-myristate 13-acetate (P1585, Sigma-Aldrich) as added to the completed RPMI 1640 medium (25 ng/ml). After 48 h, adherent cells were washed with PBS (phosphate buffered saline; P04-53500, PanBiotech, Aidenbach, Germany) and incubated with PMA-free RPMI 1640 for 24 h. Mouse J774A.1 macrophages (CLS Cell Lines Service GMbH, Eppelheim, Germany) were used from passages 39 to 60 and cultured in DMEM (P04-03596, Pan-Biotech) containing 10% heat-inactivated FBS (S0615, Sigma-Aldrich) and 1 % L-glutamine. 2×10^5 cells/well were seeded into 24 well-plates and rested 24 h before stimulation. Cells were maintained at 37 °C in a humidified atmosphere of 5 % CO_2 and 95 % air and regularly tested negative for mycoplasma contamination (VenorGeM Classic Mycoplasma PCR detection kit, 11–8100, Minerva Biolabs, Berlin, Germany).

4.4.1.2. Cell stimulation. For inflammasome activation studies, THP-1 macrophages were primed with 100 ng/ml LPS (LPS EB ultrapure, from *Escherchia coli* O111:B4, InvivoGen, Toulouse France) for 3 h. Afterwards, cells were incubated with different concentrations of tubastatin A (S804906, Selleckchem, Houston, Texas, USA), MAIP-032, **8k** and **8m** for 1 h and then stimulated with 5 mM ATP (adenosine 5́-triphosphate, NU-1010-100G, Jena Bioscience, Jena, Germany) or 10 µM nigericin (4312/10, Tocris Bioscience, Bristol, United Kingdom) for 3 h. For J774A.1 macrophages, cells were stimulated for 4.5 h with 1 µg/ml LPS, followed by incubation with tubastatin A or **8k**. Afterwards, cells were stimulated with 2 mM ATP for 1 h or 10 µM nigericin for 3 h. For inflammasome priming studies, THP-1 macrophages were pre-incubated 24 h with tubastatin A, **MAIP-032**, **8k** and **8m**. Subsequently, medium was removed, and cells were stimulated with 100 ng/ml LPS for 3 h. The pan-HDAC inhibitor vorinostat (10 µM, synthesized according to literature [51]), NLRP3 inhibitor MCC950 (10 µM, 5479, Tocris Bioscience) and DMSO (Dimethylsulfoxide, RNBL6559, Sigma-Aldrich) were used as controls.

4.4.1.3. ELISA. Supernatants were collected and analyzed for human TNF (355053–003, Thermo Fisher Scientific), human IL-1β (316234–006, Thermo Fisher Scientific) and mouse IL-1β (P329282, DuoSet; R&D Systems) secretion following the manufacturer's instructions.

4.4.1.4. Western blotting. Western blot analysis was performed as previously described by us [49]. Membranes were incubated overnight at 4 °C with anti-acetyl-histone H3 (1:20,000) (06–599, Merck KGaA, Darmstadt, Germany) antibody and afterwards probed with anti-rabbit HRP-conjugated antibody (1:2000) (7074, Cell Signaling Technology, Leiden, The Netherlands) for 1 h and visualized by ECL solution (Clarity Max Western ECL Substrate; 1705062; Bio-Rad, Feldkirchen, Germany) and ChemiDoc imaging system (Bio-Rad). Protein expression was normalized to total protein amount and analyzed using Image Lab 6.1 (Bio-Rad).

4.4.1.5. RNA isolation, cDNA synthesis and qPCR. Total RNA isolation, cDNA synthesis and quantitative real-time RT-PCR (qRT-PCR) were performed as described previously [49,52,53]. Primers (synthesized by Eurofins, Ebersberg, Germany) with the following sequences were used: *GAPDH*, 5′-CTCTCTGCTCCTCCTGTTCGAC-3′ and 5′-TGAGCGATGTGGCTCGGCT-3′; IL1B, 5′-TGGAGCAACAAGTGGTGT-3′ and 5′-TTGGGATCTACACTCTCCAGC-3′. Fold difference in gene expression was normalized to the housekeeping gene GAPDH showing the most constant expression levels.

4.4.1.6. Cell viability assays. Cell viability was determined using MTT and LDH assay as described [49]. Absorbance was measured at 492 nm using a microplate reader (Mitras^2 LB 943, Berthold Technologies GmbH & Co. KG, Bad Wildbad, Germany).

4.4.1.7. Statistical analysis. Unless otherwise specified, all experiments were performed at least three times. TNF-ELISA and mRNA experiments were performed in four to six independent experiments with duplicates. Significant differences were assessed by one sample *t* test against 100%. Data are expressed as means + SEM considered significant at $^*P \leq 0.05$, $^{**}P \leq 0.01$, $^{***}P \leq 0.001$, $^{****}P \leq 0.0001$. Extra sum-of-squares F test was used to evaluate whether inhibitory concentration–response curves were best represented by a monophasic or biphasic model. The monophasic model was preferred unless the extra sum-of-squares F test had a value $P < 0.05$. All IC_{50} values were fitted using a monophasic model with variable slope (four parameters). The parameters are presented as mean with 95 % confidence interval. Statistical evaluation was performed using GraphPad Prism 9 (GraphPad software, San Diego, USA).

4.4.2. U-87 MG glioblastoma cell line

4.4.2.1. Cell line and cell culture. The human glioblastoma cell line U-87 MG was cultivated in DMEM medium supplemented with 100 U/mL penicillin, 100 U/mL streptomycin, 2 mM L-glutamine and 10% fetal bovine serum in at a humidified atmosphere at 37 °C containing 5% CO_2. Mycoplasma contamination was routinely excluded by PCR.

4.4.2.2. Cell viability assay. MTT (3-(4,5-dimethylthiazol-2-yl)-2,5-diphenyltetrazolium bromide; Catalog# A2231; *BioChemica*, Applichem GmbH, Darmstadt, Germany) was employed to measure cell viability. A total of 6,000 U-87 MG cells were seeded in duplicates in 96-well plates (*Starlab GmbH*, Hamburg, Germany) with each well containing 90 µL of volume. These cells were subsequently stimulated with dilution series of different compounds. Following an incubation period of 72 h, 20 µL of freshly prepared MTT solution (5 mg/mL) was added for 1 h at 37 °C and 5% CO_2. After removing the supernatant, the formazan dye was solubilized in 200 µL DMSO (*Sigma-Aldrich*, Steinheim, Germany). The absorbance of the plates was then measured at 570 nm using a Multiskan microplate photometer (*Thermo Fisher Scientific*, Waltham, MA, USA) with background subtraction at 690 nm. The acquired data was normalized to DPBS, considering 100% viability, and analyzed using nonlinear regression to determine IC_{50} values (*GraphPad* Prism 8, San Diego, CA, USA).

4.4.2.3. Immunoblot analysis. U-87 MG cells were seeded to cell culture flasks and allowed to adhere for 24 h. After that cells were treated with a concentration of 10 µM of HDACi or vehicle (DMSO) for additional 24 h. For cell lysis the cells were initially washed with PBS and detached using a scraper. The cells were then centrifuged at 1,200 rpm for 4 min at 4 °C, followed by two additional washing steps. Afterwards, the cell pellet was resuspended in 100 µL of freshly prepared lysis buffer and incubated on ice for 30 min with vortexing every 10 min. The lysis buffer consisted of Invitrogen cell extraction buffer (10 mM Tris, pH 7.4, 100 mM NaCl, 1 mM EDTA, 1 mM EGTA, 1 mM NaF, 20 mM $Na_4P_2O_7$, 2 mM Na_3VO_4, 1% Triton™ ×-100, 10% glycerol, 0.1% SDS, 0.5% deoxycholate; Catalog# FNN0011, *Thermo Fisher Scientific Inc.*, Waltham, MA, USA), supplemented with 0.1 mM PMSF (Catalog# 10837091001, *Sigma-Aldrich*, St. Louis, MO, USA) and Halt™ Protease Inhibitor (100x) (Catalog# 78429, *Life Technologies GmbH* Carlsbad, CA, USA). Finally, the samples were centrifuged at 14,000 rpm and 4 °C for 30 min and the supernatant was collected. Protein quantification was performed by using BCA protein assay reagents (Catalog# 23225, *Thermo Fisher Scientific Inc.*, Waltham, MA, USA). Lysates were mixed with Laemmli sample buffer 2x concentrate (Catalog# S3401-10VL, *Sigma-Aldrich*, St. Louis, MO, USA) to a protein concentration of 1.25 µg/µL and denatured at 95 °C for 5 min. Subsequently, SDS-PAGE was performed with 12% Mini-PROTEAN TGX stain-free gels (Catalog# 4568045, *Bio-Rad*, Hercules, CA, USA) at 200 V for 45 min. Proteins were then transferred to a Trans-Blot Turbo®-PVDF membrane (Catalog# 1704156, *Bio-Rad*, Hercules, CA, USA) with the Trans-Blot Turbo Transfer System (Catalog# 1704150, *Bio-Rad*, Hercules, CA, USA) at 1.0 A for 30 min. The membrane was blocked with a solution of 5 % milk powder in TBST (Tris-buffered saline-Tween 20 0.2 %) for 60 min at room temperature. After three washing cycles for 10 min with TBST, the membrane was incubated with the respective antibody at room temperature for 60 min and 4 °C overnight. For detection of GAPDH and the acetylation levels of Histone H3 and α-Tubulin, antibodies specific for GAPDH (Catalog# T0004, *Affinity Biosciences*, Cincinnati, OH, USA; 1:20,000 dilution), acetyl-Histone H3 (K9/K14) (Catalog# 9677S, *Cell Signaling Technology*, Denver, MA, USA; 1:1000 dilution) and acetyl-α-Tubulin (Lys40) (Catalog#5335, *Cell Signaling Technology*, Denver, MA, USA: 1:1000 dilution) were used as primary antibodies. The membrane was rinsed again three times before applying the secondary antibody for 1.5 h at room temperature. As secondary antibody HRP-conjugated anti-mouse IgGκ binding protein (Catalog# sc-516102, *Santa Cruz*, Dallas, TX, USA; 1:10,000 dilution) and HRP-conjugated anti-rabbit IgG antibody (Catalog# HAF008, *R&D Systems, Inc.*, Minneapolis, MN, USA; 1:10,000 dilution) were employed. After washing off the secondary antibody, protein bands were detected via chemiluminescence using Clarity Western ECL substrate (Catalog# 1705061, *Bio-Rad*, Hercules, CA, USA). Detection and analysis were performed with ChemiDox XRS + System (Catalog# 1708265, *Bio-Rad*, Hercules, CA, USA) and Image Lab software v. 6.1 (*Bio-Rad*, Hercules, CA, USA).

4.4.2.4. Wound healing assay. In total 3×10^5 U-87 MG cells/well were seeded in a 24-well plate (*Starlab GmbH*, Hamburg, Germany). After 24 h the cell culture medium was replaced with serum free medium and cells were treated with 10 µM of the respective HDACi. Following a 24-hour preincubation period, the cell monolayer was gently scratched across the centre of each well with a sterile 200 µL pipette tip. Subsequently, cells were carefully washed once with PBS and a fresh serum–free medium containing the same inhibitor was added. The scratched cells were then incubated at 37 °C and 5% CO_2. The process of wound healing was monitored for 48 h at regular intervals with 10fold magnification with a Axiovert 200 microscope (*Carl Zeiss Microscopy*, Jena, Germany). The acquired images were analyzed with ImageJ (*Tiago Ferreira*, Wayne Rasband), ZEN® 3.0 blue edition (*Carl Zeiss Microscopy*, Oberkochen, Germany) and evaluated with *GraphPad* Prism 8 (San Diego, CA, USA). Wound closure was quantified as relative area (%) compared to initial area. GraphPad Prism Version 8 was used for statistical analysis. One-way ANOVA followed by Dunnett's multiple comparisons test was applied for statistical analysis. ns: not significant; $^*P \leq 0.05$, $^{**}P \leq 0.01$, $^{***}P \leq 0.001$.

*4.4.3. Docking of **8a**, **8f**, and **8k** in zHDAC6 with RosettaLigand*

The crystal structure of the catalytic domain 2 (CD2) of HDAC6 from *danio reriro* (PDB: 6CGP) [37] was obtained from the Protein Data Bank (PDB, https://www.rcsb.org). All heteroatom records were removed, except for the metal ions (one zinc ion and two potassium ions) and the catalytic water molecule next to the zinc ion. The structure was optimized to the closest local energy minimum using RosettaRelax with coordinate constraint on the backbone and metal ion restraints [54]. Ligand input files for **8a**, **8f**, and **8k** were created with ChemDraw. An initial 3D conformer with hydrogen atoms was constructed in Chem3D and energetically minimized using the MM2 force field, followed by the production of an ensemble of 1000 low energy conformers with BCL: ConformerGenerator [55]. One conformer was placed in the binding pocket of HDAC6 CD2. A constraint file was constructed using the known distance of the zinc binding of hydroxamic acids [36]. Ligand docking was performed with RosettaLigand (version 3.12) for 5000

models. Those models were clustered according to their similarity in their binding mode. The depicted models are the best scoring models from the cluster with the lowest delta-RMDS values [56–58].

CRediT authorship contribution statement

Fabian B. Kraft: Conceptualization, Data curation, Investigation, Writing – original draft. **Jana Enns:** Investigation. **Irina Honin:** Investigation. **Jonas Engelhardt:** Investigation. **Andrea Schöler:** Investigation. **Shannon T. Smith:** Supervision. **Jens Meiler:** Supervision. **Linda Schäker-Hübner:** Investigation. **Günther Weindl:** Conceptualization, Formal analysis, Funding acquisition, Supervision, Resources, Writing – review & editing. **Finn K. Hansen:** Conceptualization, Formal analysis, Funding acquisition, Project administration, Resources, Supervision, Writing – review & editing.

Declaration of competing interest

The authors declare that they have no known competing financial interests or personal relationships that could have appeared to influence the work reported in this paper.

Acknowledgments

FKH and GW acknowledge partial funding by the Deutsche Forschungsgemeinschaft (DFG, German Research Foundation)–GRK2873 (494832089).

Appendix A. Supplementary data

Supplementary data to this article can be found online at https://doi.org/10.1016/j.bioorg.2023.107072.

References

[1] J. Roche, P. Bertrand, Inside HDACs with more selective HDAC inhibitors, Eur. J. Med. Chem. 121 (2016) 451–483, https://doi.org/10.1016/j.ejmech.2016.05.047.
[2] S.-Y. Park, J.-S. Kim, A short guide to histone deacetylases including recent progress on class II enzymes, EMM 52 (2) (2020) 204–212, https://doi.org/10.1038/s12276-020-0382-4.
[3] M. Yoshida, N. Kudo, S. Kosono, A. Ito, Chemical and structural biology of protein lysine deacetylases, Proc. Jpn. Acad. Ser. B Phys. Biol. Sci. 93 (5) (2017) 297–321, https://doi.org/10.2183/pjab.93.019.
[4] Y. Jiang, J. Liu, D. Chen, L. Yan, W. Zheng, Sirtuin inhibition: strategies, inhibitors, and therapeutic potential, Trends Pharmacol. Sci. 38 (5) (2017) 459–472, https://doi.org/10.1016/j.tips.2017.01.009.
[5] P. Wang, Z. Wang, J. Liu, Role of HDACs in normal and malignant hematopoiesis, Mol. Cancer 19 (1) (2020) 1–27, https://doi.org/10.1186/s12943-019-1127-7.
[6] D. Kaluza, J. Kroll, S. Gesierich, T.-P. Yao, R.A. Boon, E. Hergenreider, M. Tjwa, L. Rössig, E. Seto, H.G. Augustin, A.M. Zeiher, S. Dimmeler, C. Urbich, Class IIb HDAC6 regulates endothelial cell migration and angiogenesis by deacetylation of cortactin, EMBO J. 30 (20) (2011) 4142–4156, https://doi.org/10.1038/emboj.2011.298.
[7] M. Kilgore, C.A. Miller, D.M. Fass, K.M. Hennig, S.J. Haggarty, J.D. Sweatt, G. Rumbaugh, Inhibitors of class 1 histone deacetylases reverse contextual memory deficits in a mouse model of Alzheimer's disease, Neuropsychopharmacology 35 (4) (2010) 870–880, https://doi.org/10.1038/npp.2009.197.
[8] F. Cao, M.R.H. Zwinderman, F.J. Dekker, The process and strategy for developing selective histone deacetylase 3 inhibitors, Molecules 23 (3) (2018) 551, https://doi.org/10.3390/molecules23030551.
[9] L. Cappellacci, D.R. Perinelli, F. Maggi, M. Grifantini, R. Petrelli, Recent progress in histone deacetylase inhibitors as anticancer agents, Curr. Med. Chem. 27 (15) (2020) 2449–2493, https://doi.org/10.2174/0929867325666181016163110.
[10] T.C.S. Ho, A.H.Y. Chan, A. Ganesan, Thirty years of HDAC inhibitors: 2020 insight and hindsight, J. Med. Chem. 63 (21) (2020) 12460–12484, https://doi.org/10.1021/acs.jmedchem.0c00830.
[11] N. Ibrahim, E.I. Buchbinder, S.R. Granter, S.J. Rodig, A. Giobbie-Hurder, C. Becerra, A. Tsiaras, E. Gjini, D.E. Fisher, F.S. Hodi, A phase I trial of panobinostat (LBH589) in patients with metastatic melanoma, Cancer Med. 5 (11) (2016) 3041–3050, https://doi.org/10.1002/cam4.862.
[12] San-Miguel, J. F.; Hungria, V. T. M.; Yoon, S.-S.; Beksac, M.; Dimopoulos, M. A.; Elghandour, A.; Jedrzejczak, W. W.; Günther, A.; Nakorn, T. N.; Siritanaratkul, N.; Corradini, P.; Chuncharunee, S.; Lee, J.-J.; Schlossman, R. L.; Shelekhova, T.; Yong, K.; Tan, D.; Numbenjapon, T.; Cavenagh, J. D.; Hou, J.; LeBlanc, R.; Nahi, H.; Qiu, L.; Salwender, H.; Pulini, S.; Moreau, P.; Warzocha, K.; White, D.; Bladé, J.; Chen, W.; La Rubia, J. de; Gimsing, P.; Lonial, S.; Kaufman, J. L.; Ocio, E. M.; Veskovski, L.; Sohn, S. K.; Wang, M.-C.; Lee, J. H.; Einsele, H.; Sopala, M.; Corrado, C.; Bengoudifa, B.-R.; Binlich, F.; Richardson, P. G. Panobinostat plus bortezomib and dexamethasone versus placebo plus bortezomib and dexamethasone in patients with relapsed or relapsed and refractory multiple myeloma: a multicentre, randomised, double-blind phase 3 trial. Lancet Oncol. 2014, 15 (11), 1195-1206. DOI: 10.1016/S1470-2045(14)70440-1.
[13] Z. Ning, Why ACE—overview of the development of the subtype-selective histone deacetylase inhibitor chidamide in hormone receptor positive advanced breast cancer, Transl. Breast Cancer Res. 1 (2020) 1–10, https://doi.org/10.21037/tbcr.2020.03.06.
[14] H.-Z. Lee, V.E. Kwitkowski, P.L. Del Valle, M.S. Ricci, H. Saber, B.A. Habtemariam, J. Bullock, E. Bloomquist, Y. Li Shen, X.-H. Chen, J. Brown, N. Mehrotra, S. Dorff, R. Charlab, R.C. Kane, E. Kaminskas, R. Justice, A.T. Farrell, R. Pazdur, FDA approval: belinostat for the treatment of patients with relapsed or refractory peripheral T-cell lymphoma, Clin. Cancer Res. 21 (12) (2015) 2666–2670, https://doi.org/10.1158/1078-0432.CCR-14-3119.
[15] E. Eleutherakis-Papaiakovou, N. Kanellias, E. Kastritis, M. Gavriatopoulou, E. Terpos, M.A. Dimopoulos, Efficacy of panobinostat for the treatment of multiple myeloma, J. Oncol. 2020 (2020) 1–12, https://doi.org/10.1155/2020/7131802.
[16] S.J. Hogg, P.A. Beavis, M.A. Dawson, R.W. Johnstone, Targeting the epigenetic regulation of antitumour immunity, Nat. Rev. Drug. Discov. 19 (11) (2020) 776–800, https://doi.org/10.1038/s41573-020-0077-5.
[17] Y. Liu, L. Peng, E. Seto, S. Huang, Y. Qiu, Modulation of histone deacetylase 6 (HDAC6) nuclear import and tubulin deacetylase activity through acetylation, JBC 287 (34) (2012) 29168–29174, https://doi.org/10.1074/jbc.M112.371120.
[18] M. Brindisi, A.P. Saraswati, S. Brogi, S. Gemma, S. Butini, G. Campiani, Old but gold: tracking the new guise of histone deacetylase 6 (HDAC6) enzyme as a biomarker and therapeutic target in rare diseases, J. Med. Chem. 63 (1) (2020) 23–39, https://doi.org/10.1021/acs.jmedchem.9b00924.
[19] C. Cook, Y. Carlomagno, T.F. Gendron, J. Dunmore, K. Scheffel, C. Stetler, M. Davis, D. Dickson, M. Jarpe, M. DeTure, L. Petrucelli, Acetylation of the KXGS motifs in tau is a critical determinant in modulation of tau aggregation and clearance, Hum. Mol. Genet. 23 (1) (2014) 104–116, https://doi.org/10.1093/hmg/ddt402.
[20] C. Hubbert, A. Guardiola, R. Shao, Y. Kawaguchi, A. Ito, A. Nixon, M. Yoshida, X.-F. Wang, T.-P. Yao, HDAC6 is a microtubule-associated deacetylase, Nature 417 (6887) (2002) 455–458, https://doi.org/10.1038/417455a.
[21] G. Campiani, C. Cavella, J.D. Osko, M. Brindisi, N. Relitti, S. Brogi, A.P. Saraswati, S. Federico, G. Chemi, S. Maramai, G. Carullo, B. Jaeger, A. Carleo, R. Benedetti, F. Sarno, S. Lamponi, P. Rottoli, E. Bargagli, C. Bertucci, D. Tedesco, D. Herp, J. Senger, G. Ruberti, F. Saccoccia, S. Saponara, B. Gorelli, M. Valoti, B. Kennedy, H. Sundaramurthi, S. Butini, M. Jung, K.M. Roach, L. Altucci, P. Bradding, D. W. Christianson, S. Gemma, A. Prasse, Harnessing the role of HDAC6 in idiopathic pulmonary fibrosis: design, synthesis, structural analysis, and biological evaluation of potent inhibitors, J. Med. Chem. 64 (14) (2021) 9960–9988, https://doi.org/10.1021/acs.jmedchem.1c00184.
[22] Depetter, Y.; Geurs, S.; Vreese, R. de; Goethals, S.; Vandoorn, E.; Laevens, A.; Steenbrugge, J.; Meyer, E.; Tullio, P. de; Bracke, M.; D'hooghe, M.; Wever, O. de. Selective pharmacological inhibitors of HDAC6 reveal biochemical activity but functional tolerance in cancer models. Int. J. Cancer 2019. DOI: 10.1002/ijc.32169.
[23] O. Witt, H.E. Deubzer, T. Milde, I. Oehme, HDAC family: What are the cancer relevant targets? Cancer Let. 277 (1) (2009) 8–21, https://doi.org/10.1016/j.canlet.2008.08.016.
[24] Y. Zhang, S. Kwon, T. Yamaguchi, F. Cubizolles, S. Rousseaux, M. Kneissel, C. Cao, N. Li, H.-L. Cheng, K. Chua, D. Lombard, A. Mizeracki, G. Matthias, F.W. Alt, S. Khochbin, P. Matthias, Mice lacking histone deacetylase 6 have hyperacetylated tubulin but are viable and develop normally, Mol. Cell. Biol. 28 (5) (2008) 1688–1701, https://doi.org/10.1128/MCB.01154-06.
[25] V.G. Magupalli, R. Negro, Y. Tian, A.V. Hauenstein, G. Di Caprio, W. Skillern, Q. Deng, P. Orning, H.B. Alam, Z. Maliga, H. Sharif, J.J. Hu, C.L. Evavold, J. C. Kagan, F.I. Schmidt, K.A. Fitzgerald, T. Kirchhausen, Y. Li, H. Wu, HDAC6 mediates an aggresome-like mechanism for NLRP3 and pyrin inflammasome activation, Science 369 (2020) 6510, https://doi.org/10.1126/science.aas8995.
[26] K.V. Swanson, M. Deng, J.-P.-Y. Ting, The NLRP3 inflammasome: molecular activation and regulation to therapeutics, Nat. Rev. Immonol 19 (8) (2019) 477–489, https://doi.org/10.1038/s41577-019-0165-0.
[27] C.A. Dinarello, Interleukin-1 in the pathogenesis and treatment of inflammatory diseases, Blood 117 (14) (2011) 3720–3732, https://doi.org/10.1182/blood-2010-07-273417.
[28] R.C. Coll, K. Schroder, P. Pelegrín, NLRP3 and pyroptosis blockers for treating inflammatory diseases, Trends Pharmacol. Sci. 43 (8) (2022) 653–668, https://doi.org/10.1016/j.tips.2022.04.003.
[29] M.S.J. Mangan, E.J. Olhava, W.R. Roush, H.M. Seidel, G.D. Glick, E. Latz, Targeting the NLRP3 inflammasome in inflammatory diseases, Nat. Rev. Drug Discov. 17 (8) (2018) 588–606, https://doi.org/10.1038/nrd.2018.97.
[30] C. Lambona, C. Zwergel, R. Fioravanti, S. Valente, A. Mai, Histone deacetylase 10: A polyamine deacetylase from the crystal structure to the first inhibitors, Curr. Opin. Struct. Biol. 82 (2023) 102668, https://doi.org/10.1016/j.sbi.2023.102668.
[31] L. Wang, S. Zheng, L. Zhang, H. Xiao, H. Gan, H. Chen, X. Zhai, P. Liang, J. Zhao, Y. Li, Histone deacetylation 10 alleviates inflammation after intracerebral hemorrhage via the PTPN22/NLRP3 pathway in rats, Neuroscience 432 (2020) 247–259, https://doi.org/10.1016/j.neuroscience.2020.02.027.
[32] Yang, M.; Qin, Z.; Lin, Y.; Lv, X.; Sun, C.; Cheng, Y.; Xuan, H.; Cui, X.; Ma, W.; Han, L. HDAC10 negatively regulates NLRP3 inflammasome activation by switching NLRP3 modification from acetylation to ubiquitination. Preprint from Research

Square, 2023; This content is a preprint and has not been peer-reviewed. DOI: 10.21203/rs.3.rs-2792906/v1.
[33] C.M. Grozinger, C.A. Hassig, S.L. Schreiber, Three proteins define a class of human histone deacetylases related to yeast Hda1p, Proc. Natl. Acad. Sci. USA 96 (9) (1999) 4868–4873, https://doi.org/10.1073/pnas.96.9.4868.
[34] J.D. Osko, D.W. Christianson, Structural basis of catalysis and inhibition of HDAC6 CD1, the enigmatic catalytic domain of histone deacetylase 6, Biochemistry 58 (49) (2019) 4912–4924, https://doi.org/10.1021/acs.biochem.9b00934.
[35] Y. Hai, D.W. Christianson, Histone deacetylase 6 structure and molecular basis of catalysis and inhibition, Nature Chem. Biol. 12 (9) (2016) 741–747, https://doi.org/10.1038/nchembio.2134.
[36] N.J. Porter, J.D. Osko, D. Diedrich, T. Kurz, J.M. Hooker, F.K. Hansen, D. W. Christianson, Histone deacetylase 6-selective inhibitors and the influence of capping groups on hydroxamate-zinc denticity, J. Med. Chem. 61 (17) (2018) 8054–8060, https://doi.org/10.1021/acs.jmedchem.8b01013.
[37] M.K.W. Mackwitz, A. Hamacher, J.D. Osko, J. Held, A. Schöler, D.W. Christianson, M.U. Kassack, F.K. Hansen, Multicomponent synthesis and binding mode of imidazo[1,2-a]pyridine-capped selective HDAC6 inhibitors, Org. Let. 20 (2018) 3255–3258, https://doi.org/10.1021/acs.orglett.8b01118.
[38] G. Sandrone, C.D. Cukier, K. Zrubek, M. Marchini, B. Vergani, G. Caprini, G. Fossati, C. Steinkühler, A. Stevenazzi, Role of fluorination in the histone deacetylase 6 (HDAC6) selectivity of benzohydroxamate-based inhibitors, ACS Med. Chem. Lett. 12 (11) (2021) 1810–1817, https://doi.org/10.1021/acsmedchemlett.1c00425.
[39] K. Groebke, L. Weber, F. Mehlin, Synthesis of imidazo[1,2-a] annulated pyridines, pyrazines and pyrimidines by a novel three-component condensation, Synlett 1998 (6) (1998) 661–663, https://doi.org/10.1055/s-1998-1721.
[40] F.B. Kraft, M. Hanl, F. Feller, L. Schäker-Hübner, F.K. Hansen, Photocaged histone deacetylase inhibitors as prodrugs in targeted cancer therapy, Pharmaceuticals 16 (3) (2023) 356, https://doi.org/10.3390/ph16030356.
[41] N. Reßing, M. Sönnichsen, J.D. Osko, A. Schöler, J. Schliehe-Diecks, A. Skerhut, A. Borkhardt, J. Hauer, M.U. Kassack, D.W. Christianson, S. Bhatia, F.K. Hansen, Multicomponent synthesis, binding mode, and structure-activity relationship of selective histone deacetylase 6 (HDAC6) inhibitors with bifurcated capping groups, J. Med. Chem. 63 (18) (2020) 10339–10351, https://doi.org/10.1021/acs.jmedchem.9b01888.
[42] J.-R. Liu, C.-W. Yu, P.-Y. Hung, L.-W. Hsin, J.-W. Chern, High-selective HDAC6 inhibitor promotes HDAC6 degradation following autophagy modulation and enhanced antitumor immunity in glioblastoma, Biochem. Pharmacol. 2019 (163) (2019) 458–471, https://doi.org/10.1016/j.bcp.2019.03.023. Published Online: Mar. 15.
[43] P. Chang, H. Li, H. Hu, Y. Li, T. Wang, The role of HDAC6 in autophagy and NLRP3 inflammasome, Front. Immunol. 12 (2021) 763831, https://doi.org/10.3389/fimmu.2021.763831.
[44] K. Yue, S. Sun, G. Jia, M. Qin, X. Hou, C.J. Chou, C. Huang, X. Li, First-in-class hydrazide-based HDAC6 selective inhibitor with potent oral anti-inflammatory activity by attenuating NLRP3 inflammasome activation, J. Med. Chem. 65 (18) (2022) 12140–12162, https://doi.org/10.1021/acs.jmedchem.2c00853.
[45] S. Yan, X. Wei, W. Jian, Y. Qin, J. Liu, S. Zhu, F. Jiang, H. Lou, B. Zhang, Pharmacological inhibition of HDAC6 attenuates NLRP3 inflammatory response and protects dopaminergic neurons in experimental models of Parkinson's disease, Front. Aging. Neurosci. 12 (2020) 78–92, https://doi.org/10.3389/fnagi.2020.00078.
[46] Q. Chen, Y. Wang, F. Jiao, P. Cao, C. Shi, M. Pei, L. Wang, Z. Gong, HDAC6 inhibitor ACY1215 inhibits the activation of NLRP3 inflammasome in acute liver failure by regulating the ATM/F-actin signalling pathway, J. Cell. Mol. Med. 25 (15) (2021) 7218–7228, https://doi.org/10.1111/jcmm.16751.
[47] I. Hwang, E. Lee, S.-A. Jeon, J.-W. Yu, Histone deacetylase 6 negatively regulates NLRP3 inflammasome activation, Biochem. Biophys. Res. Commun. 467 (4) (2015) 973–978, https://doi.org/10.1016/j.bbrc.2015.10.033.
[48] Bockstiegel, J.; Engelhardt, J.; Weindl, G. P2X7 receptor activation leads to NLRP3-independent IL-1β release by human macrophages. Cell Commun. Signal. CCS 2023, 21 (1), 335. DOI: 10.1186/s12964-023-01356-1. Published Online: Nov. 23, 2023.
[49] J. Bockstiegel, S.L. Wurnig, J. Engelhardt, J. Enns, F.K. Hansen, G. Weindl, Pharmacological inhibition of HDAC6 suppresses NLRP3 inflammasome-mediated IL-1β release, Biochem. Pharmacol. 215 (2023) 115693, https://doi.org/10.1016/j.bcp.2023.115693.
[50] L. Schäker-Hübner, R. Warstat, H. Ahlert, P. Mishra, F.B. Kraft, J. Schliehe-Diecks, A. Schöler, A. Borkhardt, B. Breit, S. Bhatia, M. Hügle, S. Günther, F.K. Hansen, 4-Acyl pyrrole capped HDAC inhibitors: A new scaffold for hybrid inhibitors of BET proteins and histone deacetylases as antileukemia drug leads, J. Med. Chem. 64 (19) (2021) 14620–14646, https://doi.org/10.1021/acs.jmedchem.1c01119.
[51] L.K. Gediya, P. Chopra, P. Purushottamachar, N. Maheshwari, V.C.O. Njar, A new simple and high-yield synthesis of suberoylanilide hydroxamic acid and its inhibitory effect alone or in combination with retinoids on proliferation of human prostate cancer cells, J. Med. Chem. 48 (15) (2005) 5047–5051, https://doi.org/10.1021/jm058214k.
[52] G. Müller, C. Lübow, G. Weindl, Lysosomotropic beta blockers induce oxidative stress and IL23A production in Langerhans cells, Autophagy 16 (8) (2020) 1380–1395, https://doi.org/10.1080/15548627.2019.1686728.
[53] C. Lübow, J. Bockstiegel, G. Weindl, Lysosomotropic drugs enhance pro-inflammatory responses to IL-1β in macrophages by inhibiting internalization of the IL-1 receptor, Biochem. Pharmacol. 175 (2020) 113864, https://doi.org/10.1016/j.bcp.2020.113864.
[54] L.G. Nivón, R. Moretti, D. Baker, A Pareto-optimal refinement method for protein design scaffolds, PloS One 8 (4) (2013) e59004.
[55] S. Kothiwale, J.L. Mendenhall, J. Meiler, BCL:Conf: small molecule conformational sampling using a knowledge based rotamer library, Cheminform 7 (2015) 1–15, https://doi.org/10.1186/s13321-015-0095-1.
[56] S. DeLuca, K. Khar, J. Meiler, Fully flexible docking of medium sized ligand libraries with rosettaligand, PloS One 10 (7) (2015) e0132508.
[57] K.W. Kaufmann, J. Meiler, Using RosettaLigand for small molecule docking into comparative models, PloS One 7 (12) (2012) e50769.
[58] J. Meiler, D. Baker, ROSETTALIGAND: protein-small molecule docking with full side-chain flexibility, Proteins 65 (3) (2006) 538–548, https://doi.org/10.1002/prot.21086.

Groebke Blackburn Bienaymé-mediated multi-component synthesis of selective HDAC6 inhibitors with anti-inflammatory properties

Fabian B. Kraft, [a] Jana Enns,[b] Irina Honin,[a] Jonas Engelhardt,[b] Andrea Schöler,[c] Shannon Smith,[d] Jens Meiler, [c,d] Linda Schäker-Hübner,[a] Günther Weindl,[b] Finn K. Hansen[a]*

[a] Department of Pharmaceutical and Cell Biological Chemistry, Pharmaceutical Institute, University of Bonn, An der Immenburg 4, 53121 Bonn, Germany; [b] Department of Pharmacology and Toxicology, Pharmaceutical Institute, University of Bonn, Gerhard-Domagk-Str.3, 53121 Bonn, Germany; [c] Institute for Drug Discovery, Medicinal Faculty, University Leipzig, Brüderstraße 34, 04103 Leipzig, Germany;[d] Center for Structural Biology, Vanderbilt University,Nashville, TN 37240, USA; *Correspondence: finn.hansen@uni-bonn.de

Table of content

1 General Information & Chemistry S2
2 Supplemental figures S4
3 Docking Protocols S6
4 NMR Spectra S9
5 HPLC-Chromatograms S44
6 Dose-Response-Curves of the *In Vitro* HDAC Inhibition Assay S51

1 General Information & Chemistry

Chemicals were obtained from abcr GmbH, Acros Organics, Carbolution Chemicals, Fluorochem, Sigma-Aldrich, TCI Chemicals or VWR and used without further purification. Technical grade solvents were distilled prior to use. For all HPLC purposes, acetonitrile in HPLC-grade quality (HiPerSolv CHROMANORM, *VWR*) was used. Water was purified with a PURELAB flex® (*ELGA VEOLIA*). Air-sensitive reactions were carried out under argon atmosphere utilizing standard *Schlenk* techniques. If no solvent is stated an aqueous solution was prepared with demineralized water. Mixtures of two or more solvents are specified as "solvent A"/"solvent B", 3/1, *v*/*v*; meaning that 100 mL of the respective mixture consists of 75 mL of "solvent A" and 25 mL of "solvent B". **Thin-layer chromatography (TLC)** was carried out on prefabricated plates (silica gel 60, F_{254}, *Merck*). Components were visualized either by irradiation with ultraviolet light (254 nm or 366 nm) or by staining appropriately. **Column Chromatography:** If not stated otherwise, column chromatography was carried out on silica gel (60 Å, 40-60 µm, *Acros Organics*). **Melting Point (mp.):** The uncorrected melting points were determined using a *Büchi* Melting Point M-560 apparatus. **Nuclear Magnetic Resonance Spectroscopy (NMR):** Proton (^{1}H), carbon (^{13}C), and fluorine (^{19}F) NMR spectra were recorded either on Bruker Avance III HD 400 MHz at a frequency of 400 MHz (^{1}H), 100 MHz (^{13}C) and 377 MHz (^{19}F), a *Varian/Agilent* Mecury-plus-400 at a frequency of 400 MHz (^{1}H) and 100 MHz (^{13}C), a *Varian/Agilent* Mecury-plus-300 at a frequency of 300 MHz (^{1}H), 75 MHz (^{13}C) and 282 MHz (^{19}F) , a *Bruker* AVANCE 500 MHz at a frequency of 500 MHz (^{1}H) and 126 MHz (^{13}C) or on a *Bruker* AVANCE III HD 600 MHz at a frequency of 600 MHz (^{1}H), 151 MHz (^{13}C) and 565 MHz (^{19}F). The chemical shifts are given in parts per million (ppm). As solvents deuterated chloroform ($CDCl_3$), deuterated methanol (MeOH-d_4) and deuterated dimethyl sulfoxide (DMSO-d_6) were used. The residual solvent signal ($CDCl_3$: ^{1}H NMR: 7.26 ppm, ^{13}C NMR: 77.1 ppm; DMSO-d_6: ^{1}H NMR: 2.50 ppm, ^{13}C NMR: 39.52 ppm; MeOH-d_4: ^{1}H NMR: 3.31 ppm, 4.87 ppm, ^{13}C NMR: 49.00 ppm) was used for calibration. The multiplicity of each signal is reported as singulet (s), doublet (d), triplet (t), quartet (q), pentet (p), sextet (sext), multiplet (m) or combinations thereof. Multiplicities and coupling constants are reported as measured and might disagree with the expected values. **Mass Spectrometry:** High resolution electrospray ionization mass spectra (HRMS-ESI) were acquired with *Bruker Daltonik GmbH* micrOTOF coupled to a an *LC Packings* Ultimate HPLC system and controlled by micrOTOFControl3.4 and HyStar 3.2-LC/MS, with a *BrukerDaltonik GmbH* ESI-qTOF Impact II coupled to a *Dionex* UltiMateTM 3000 UHPLC system and controlled

by micrOTOFControl 4.0 and HyStar 3.2-LC/MS or with a micrOTOF-Q mass spectrometer (*Bruker*) with ESI-source coupled with an HPLC Dionex UltiMate 3000 (*Thermo Scientific*). Low resolution electrospray ionisation mass spectra (LRMS-ESI) were acquired with an *Advion* expression® compact mass spectrometer (CMS) coupled with an automated TLC plate reader Plate Express® (*Advion*). **High Performance Liquid Chromatography (HPLC)**: A *Thermo Fisher Scientific* UltiMate^{TM} 3000 UHPLC system with a Nucleodur 100-5 C18 (250 x 4.6 mm, *Macherey Nagel*) with a flow rate of 1 mL/min and a temperature of 25 °C or a 100-5 C18 (100 x 3 mm, *Macherey Nagel*) with a flow rate of 0.5 mL/min and a temperature of 25 °C with an appropriate gradient were used. For preparative purposes a AZURA Prep. 500/1000 gradient system (*Knauer*) with a Nucleodur 110-5 C18 HTec (150 x 32 mm, *Macherey Nagel*) column with 20 mL/min was used. Detection was implemented by UV absorption measurement at a wavelength of λ = 220 nm and λ = 250 nm. Bidest. H_2O (A) and MeCN (B) were used as eluents with an addition of 0.1% TFA for eluent A. **Purity:** The purity of all final compounds was 95% or higher. Purity was determined via HPLC with the Nucleodur 100-5 C18 (250 x 4.6 mm, *Macherey Nagel*) at 250 nm. After column equilibration for 5 min a linear gradient from 5% A to 95% B in 7 min followed by an isocratic regime of 95% B for 10 min was used.

2 Supplemental figures

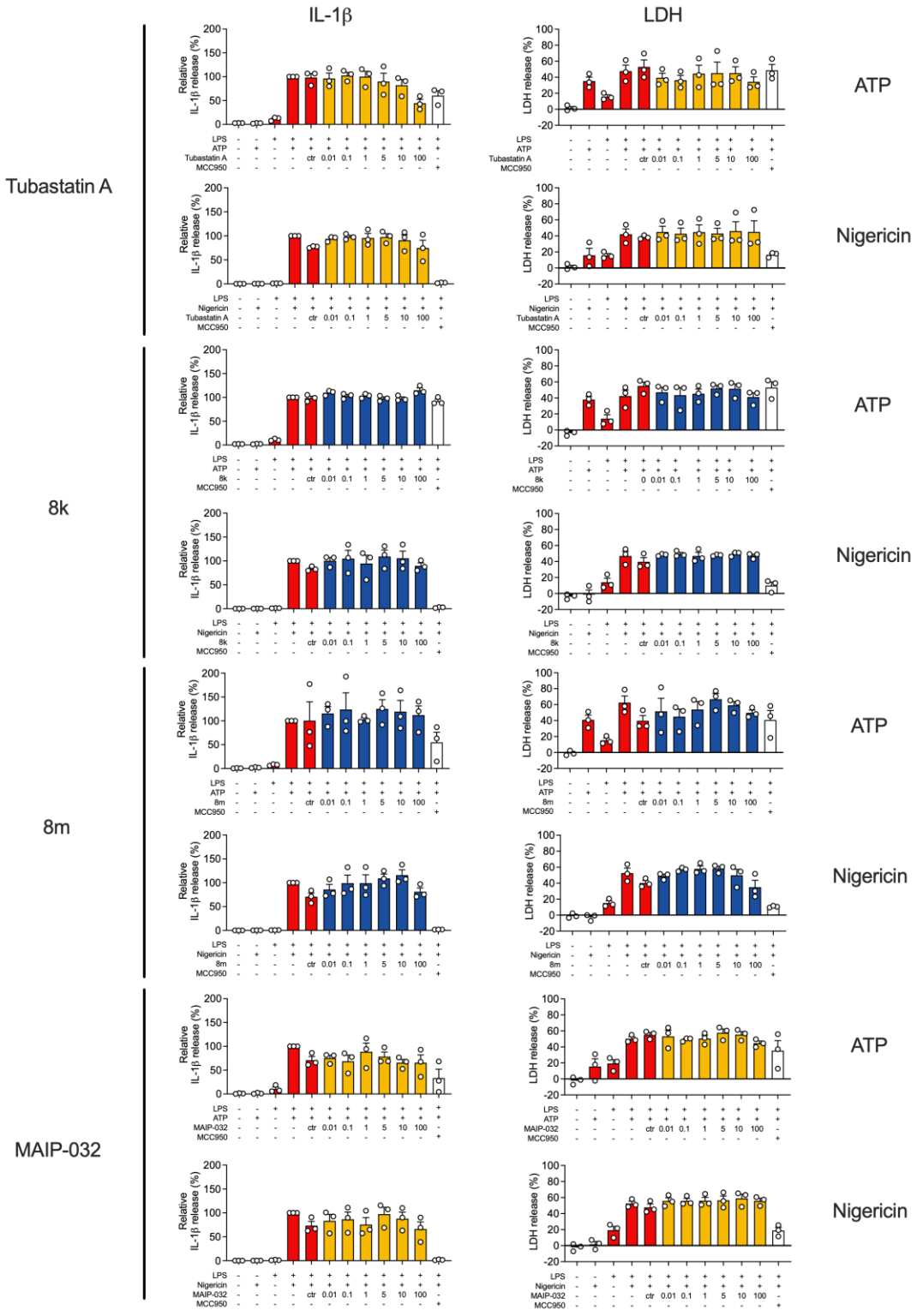


Figure S1. Human THP-1 macrophages were incubated with LPS (100 ng/ml) for 3 h. Increasing concentrations of

indicated HDAC inhibitors (depicted in µM) or NLRP3 inhibitor MCC950 (10 µM) were added 1 h before incubation with ATP (5 mM) or nigericin (10 µM) for 3 h. DMSO (1%, *v*/*v*) was used as solvent control. Mean + SEM, n=3.

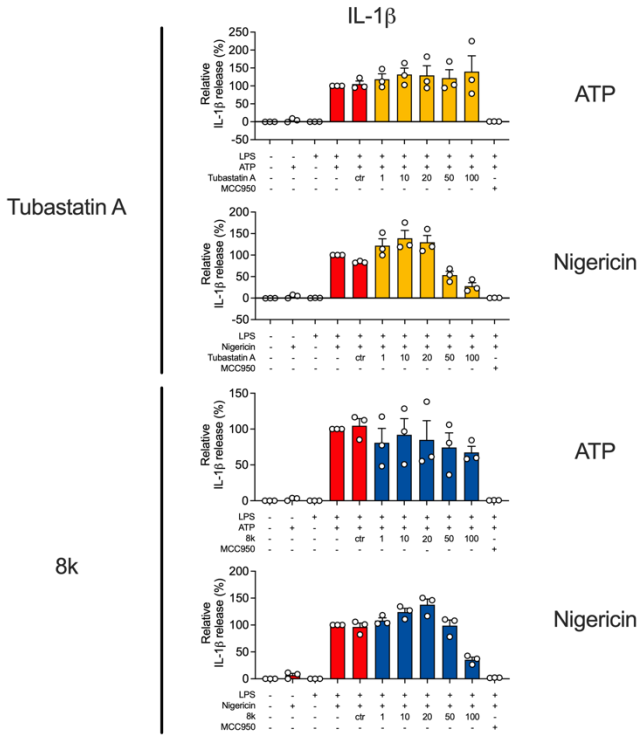


Figure S2. Mouse J774A.1 macrophages were incubated with LPS (1 µg/ml) for 4.5 h. Increasing concentrations of indicated HDAC inhibitors (depicted in µM) or NLRP3 inhibitor MCC950 (10 µM) were added 1 h before incubation with ATP (2 mM) for 1 h or nigericin (10 µM) for 3 h. DMSO (1%, *v*/*v*) was used as solvent control. Supernatants were assayed for IL-1β release by ELISA. Mean + SEM, n=3.

3 Docking Protocols

Rosetta version 3.12 was used. The following commands were executed throughout the modeling process:

- Relax input starting structures:

```
rosetta/source/bin/relax.linuxgccrelease -s 6CGP_prepared.pdb rosetta/source/database/ -
constrain_relax_to_start_coords -in:auto_setup_metals -nstruct 25 -out:prefix relaxed_ -ignore_unrecognized_res
-overwrite -ignore_waters False
```

- Options for RosettaLigand:

```
-in:file:extra_res_fa ligand.params

-packing

        -ex1

        -ex2

         -no_optH false

         -flip_HNQ true

         -ignore_ligand_chi true

-parser

          -protocol dock.xml

-mistakes

            -restore_pre_talaris_2013_behavior true

-constraints:cst_file constraint_HAcid_water.cst

-out:path:all ../output/
```

- RosettaScripts protocol for executing RosettaLigand:

```
<ROSETTASCRIPTS>

                <SCOREFXNS>

                        <ScoreFunction name="ligand_soft_rep" weights="ligand_soft_rep">

                         </ScoreFunction>

                        <ScoreFunction name="hard_rep" weights="ligand">

                        </ScoreFunction>

                </SCOREFXNS>

                <LIGAND_AREAS>
```

```
        <LigandArea name="inhibitor_dock_sc" chain="X" cutoff="6.0"
        add_nbr_radius="true" all_atom_mode="false"/>

        <LigandArea name="inhibitor_final_sc" chain="X" cutoff="6.0"
        add_nbr_radius="true" all_atom_mode="false"/>

        <LigandArea name="inhibitor_final_bb" chain="X" cutoff="7.0"
add_nbr_radius="false"

        all_atom_mode="true" Calpha_restraints="0.3"/>

</LIGAND_AREAS>

<INTERFACE_BUILDERS>

        <InterfaceBuilder name="side_chain_for_docking"
        ligand_areas="inhibitor_dock_sc"/> <InterfaceBuilder name="side_chain_for_final"
        ligand_areas="inhibitor_final_sc"/>

        <InterfaceBuilder name="backbone" ligand_areas="inhibitor_final_bb"
        extension_window="3"/>

</INTERFACE_BUILDERS>

<MOVEMAP_BUILDERS>

        <MoveMapBuilder name="docking" sc_interface="side_chain_for_docking"

        minimize_water="false"/>

        <MoveMapBuilder name="final" sc_interface="side_chain_for_final"
        bb_interface="backbone" minimize_water="false"/>

 </MOVEMAP_BUILDERS>

<SCORINGGRIDS ligand_chain="X" width="15">

<ClassicGrid grid_name="classic" weight="1.0"/>

</SCORINGGRIDS>

<MOVERS>

        <StartFrom name="startFrom" chain="X">

        <Coordinates x="-21.09" y="21.43" z="24.28"/>

        </StartFrom>

        <ConstraintSetMover name="constraint" add_constraints="true" cst_file="./
        constraint_HAcid_water.cst "/>

        <Transform name="transform" chain="X" box_size="7.0" move_distance="0.2"
        angle="20" cycles="500" repeats="1" temperature="5"/>

        <HighResDocker name="high_res_docker" cycles="6" repack_every_Nth="3"
        scorefxn="ligand_soft_rep" movemap_builder="docking"/>
```

```
                    <FinalMinimizer name="final" scorefxn="hard_rep" movemap_builder="final"/>
                    <ClearConstraintsMover name="clearconstraints"/>

                    <InterfaceScoreCalculator name="add_scores" chains="X" scorefxn="hard_rep"
                    native="../ligand_prep/6cgp_crystal.pdb"/></MOVERS>

            <PROTOCOLS>

                    <Add mover_name="startFrom"/>

                    <Add mover_name="constraint"/>

                    <Add mover_name="transform"/>

                    <Add mover_name="high_res_docker"/>

                     <Add mover_name="final"/>

                    <Add mover_name="clearconstraints"/>

                     <Add mover_name="add_scores"/>

            </PROTOCOLS>

</ROSETTASCRIPTS>
```

- Executing RosettaLigand:

```
cat ./listof_pdbs_6CGP | parallel -j 10 bash run_dock_parallel.sh

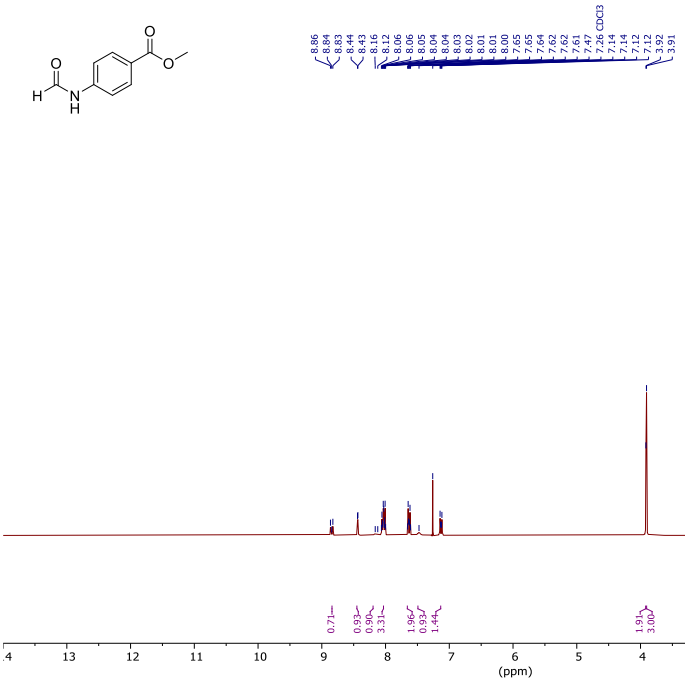
- run_dock_parallel.sh file:

PDB=$1

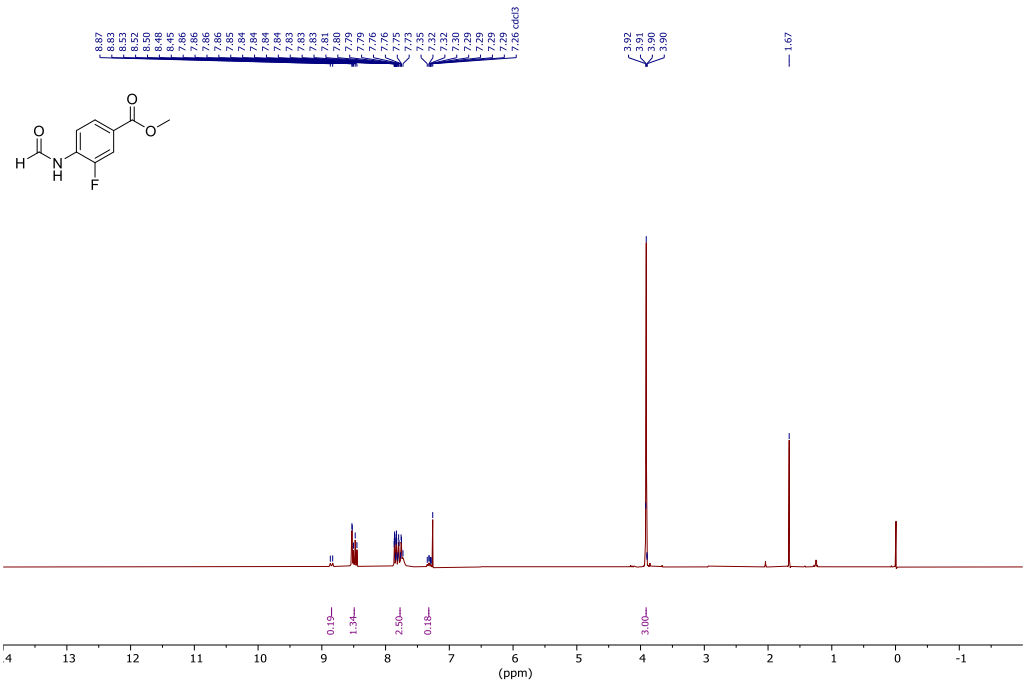
rosetta/source/bin/rosetta_scripts.linuxgccrelease -s ${PDB} -database rosetta/database/

-ignore_waters False -in:auto_setup_metals @option.txt -nstruct 20
```

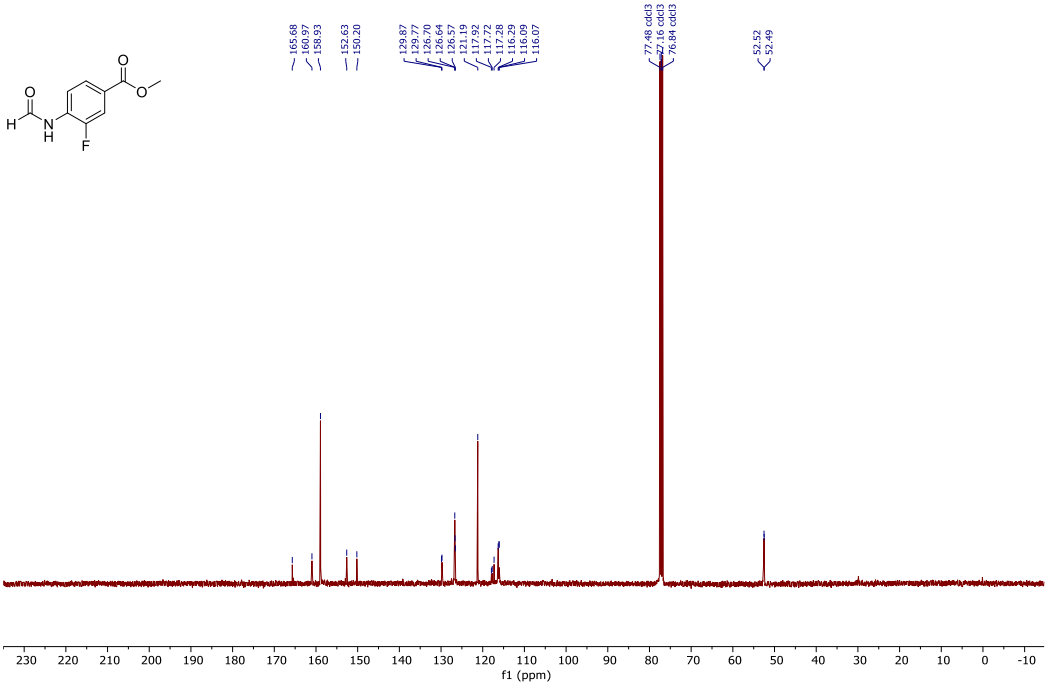
4 NMR Spectra



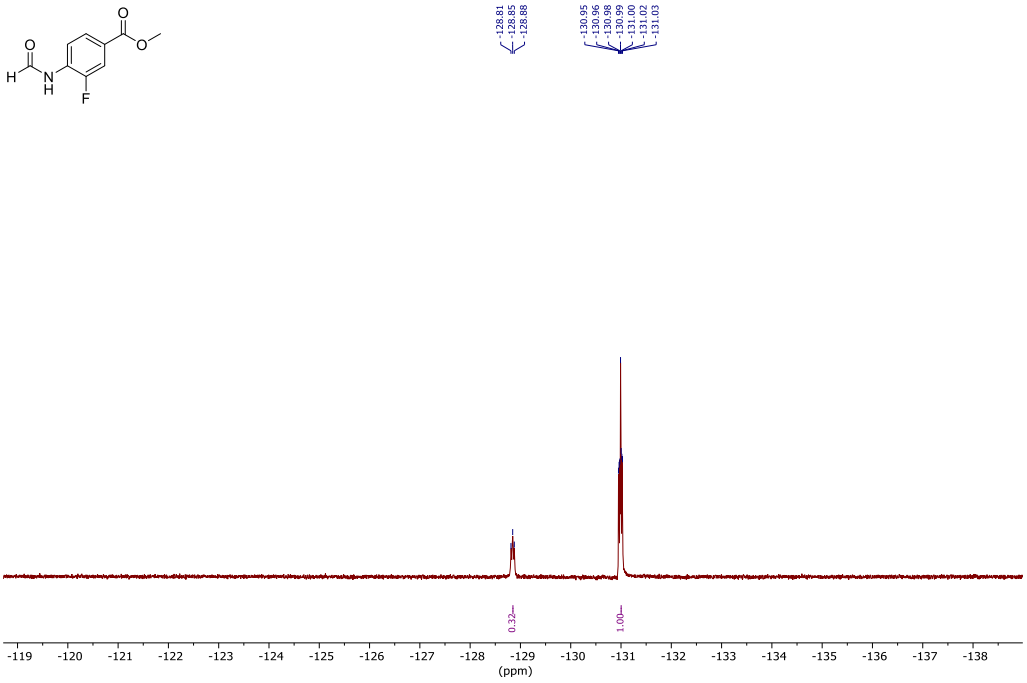
^{1}H-NMR (300 MHz, $CDCl_3$) of compound **1**.



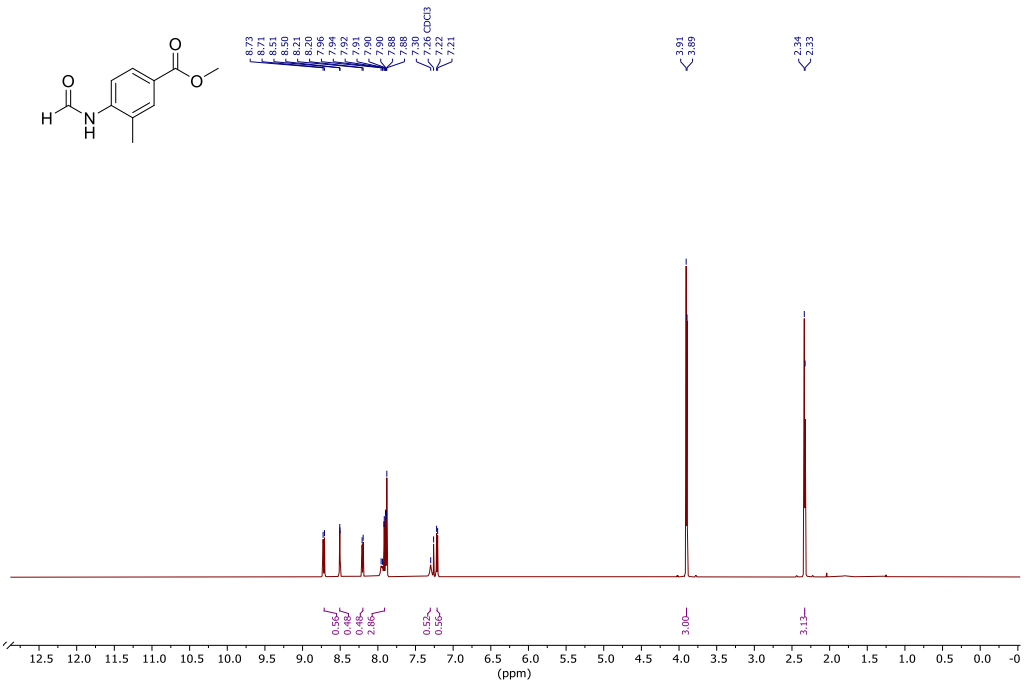
^{1}H-NMR (300 MHz, $CDCl_3$) of compound **2**.



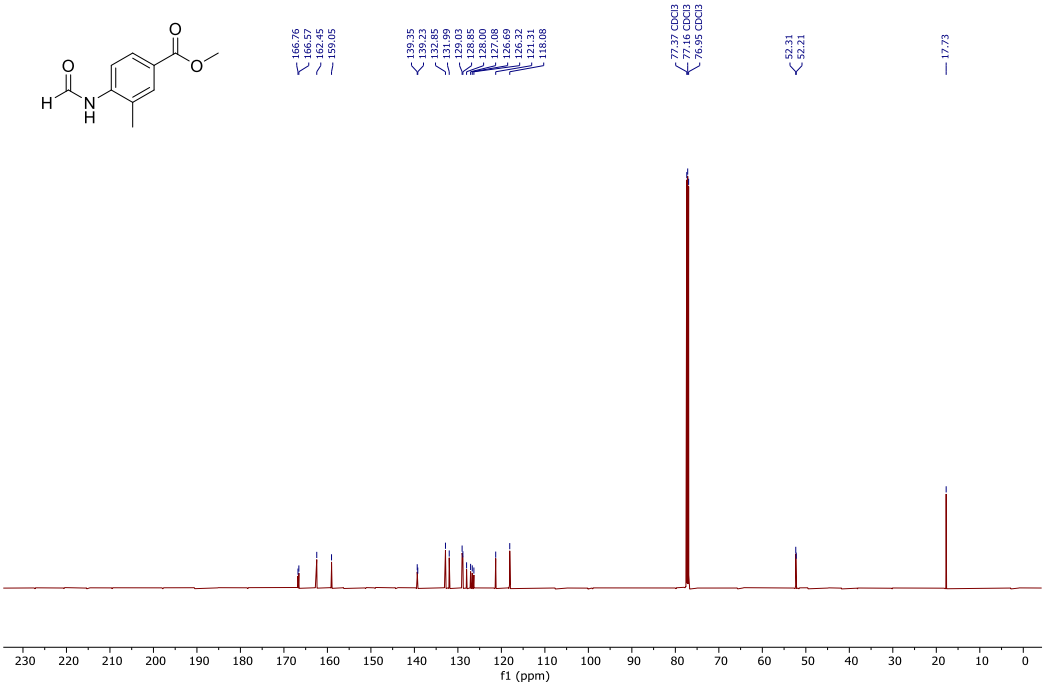
^{13}C-NMR (101 MHz, $CDCl_3$) of compound **2.**



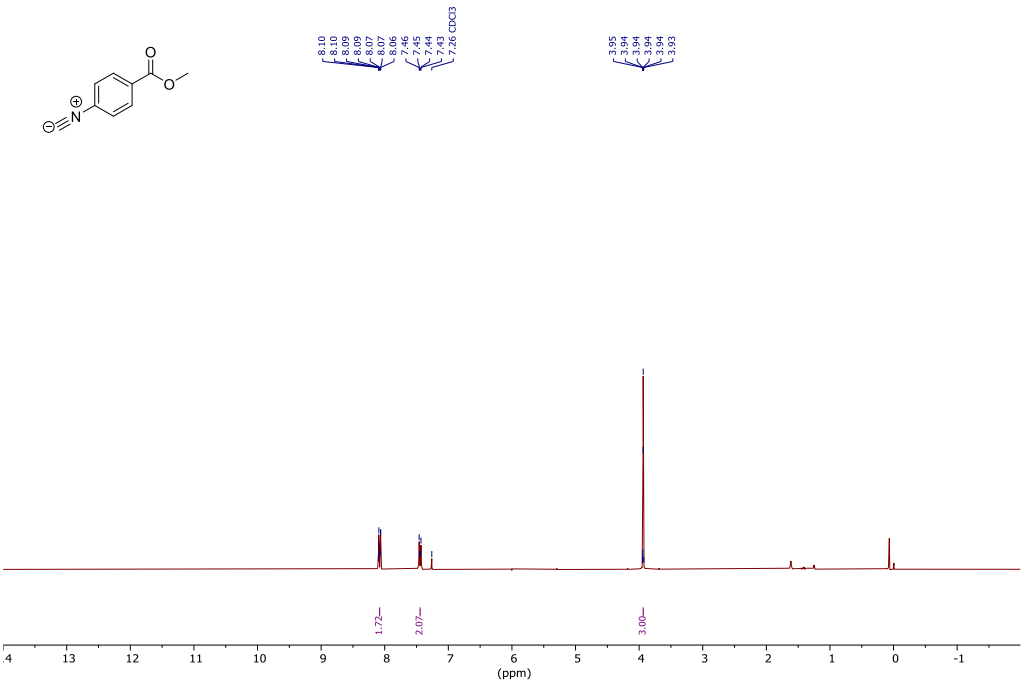
^{19}F-NMR (282 MHz, $CDCl_3$) of compound **2**.



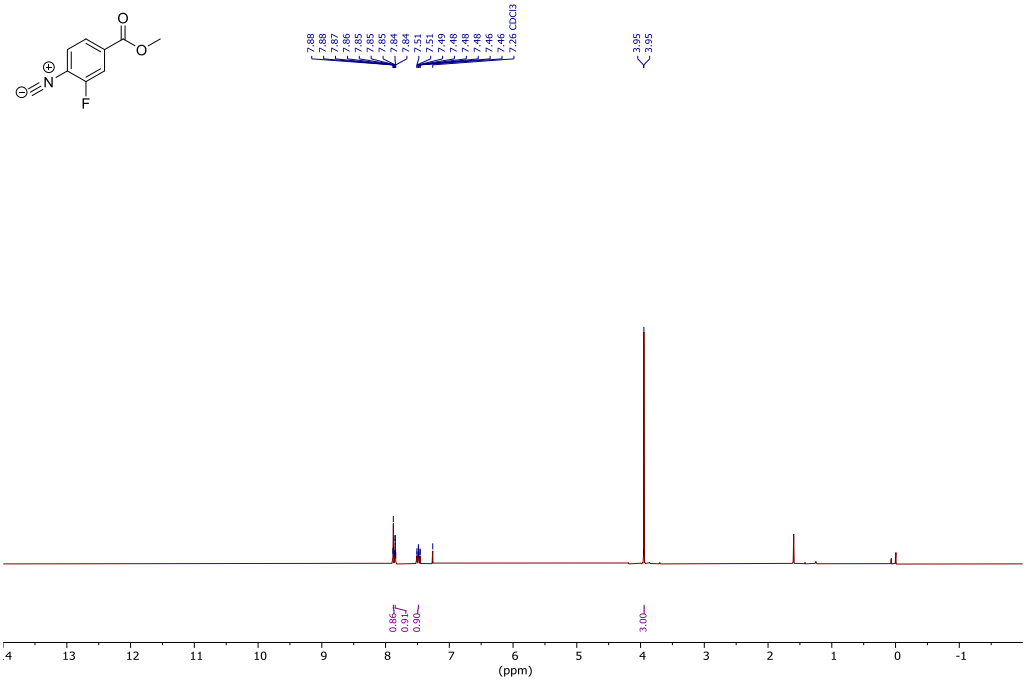
^{1}H-NMR (600 MHz, DMSO-d_6) of compound **3**.



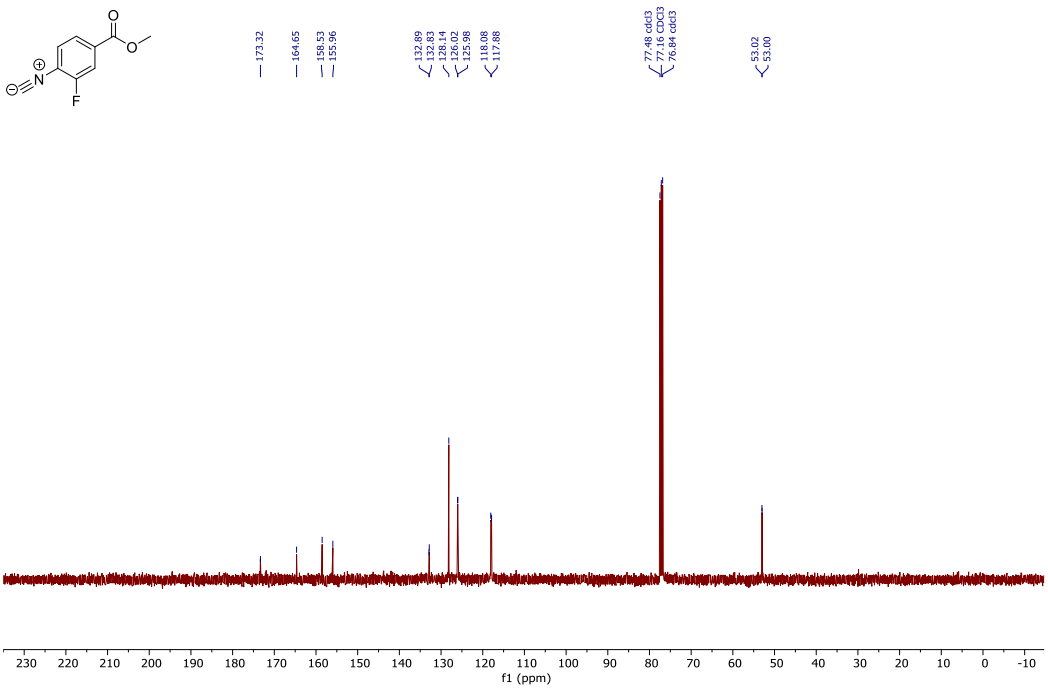
^{13}C-NMR (151 MHz, DMSO-d_6) of compound **3**.



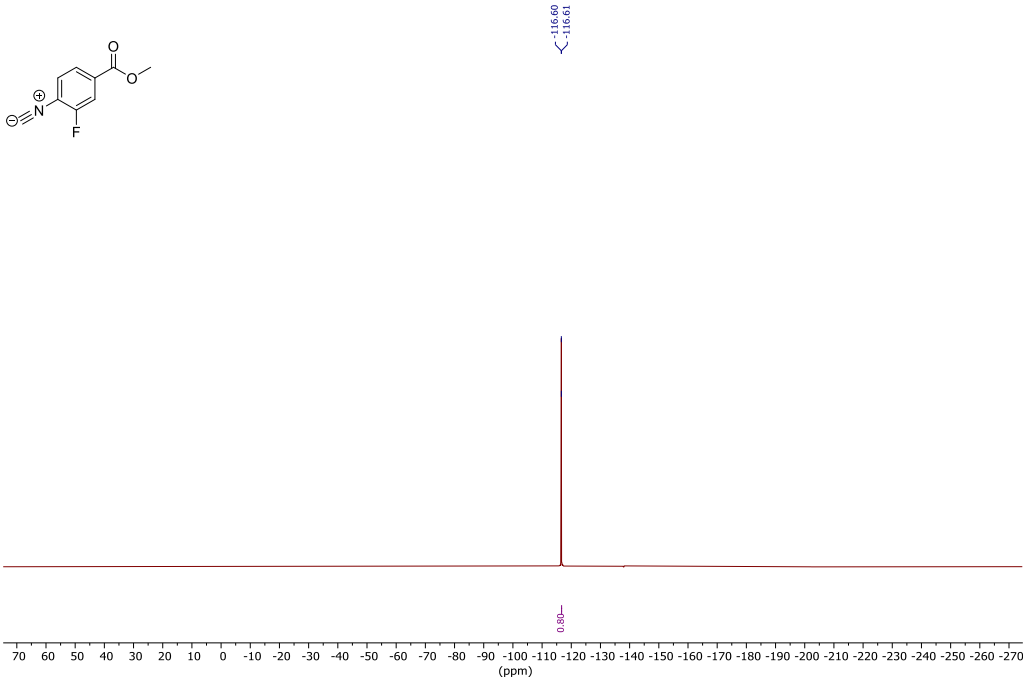
^{1}H-NMR (300 MHz, $CDCl_3$) of compound **4**.



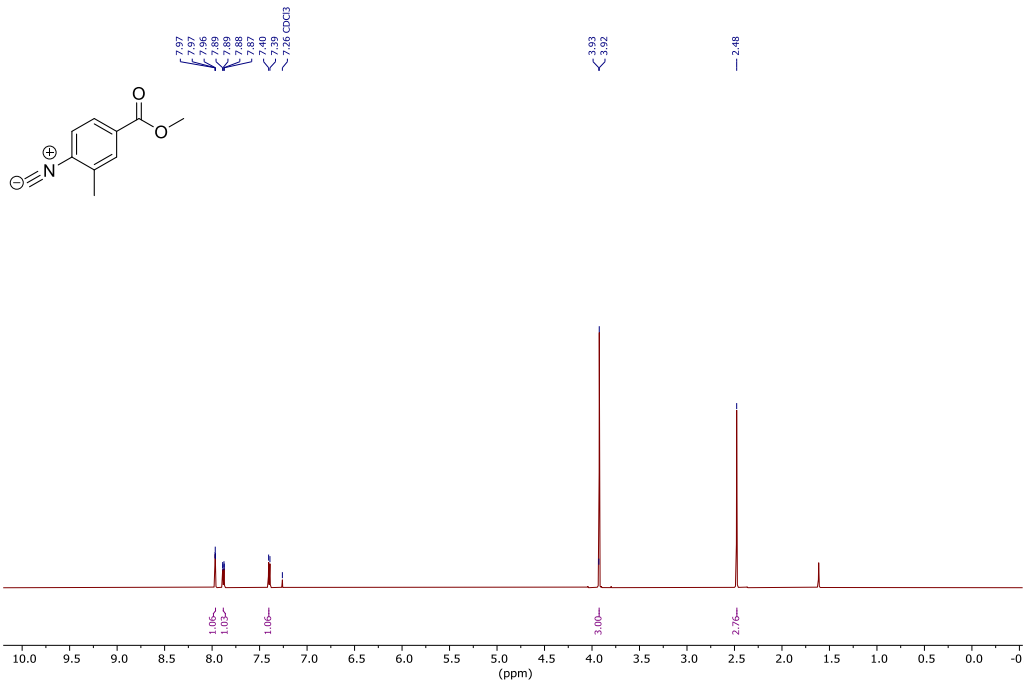
^{1}H-NMR (300 MHz, $CDCl_3$) of compound **5**.



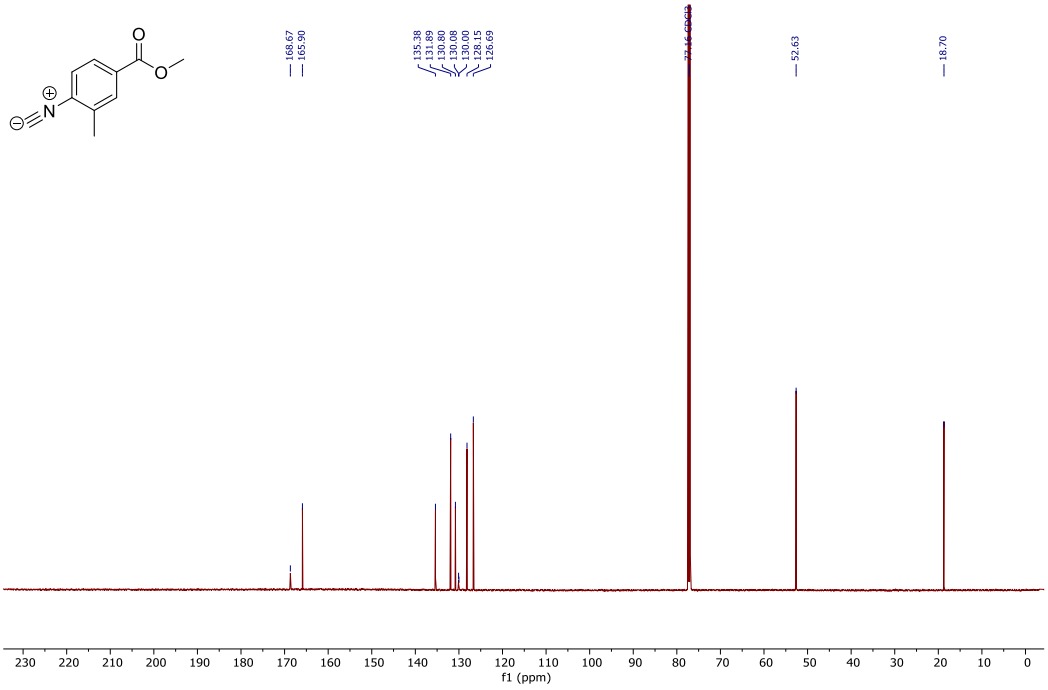
^{13}C-NMR (101 MHz, $CDCl_3$) of compound **5**.



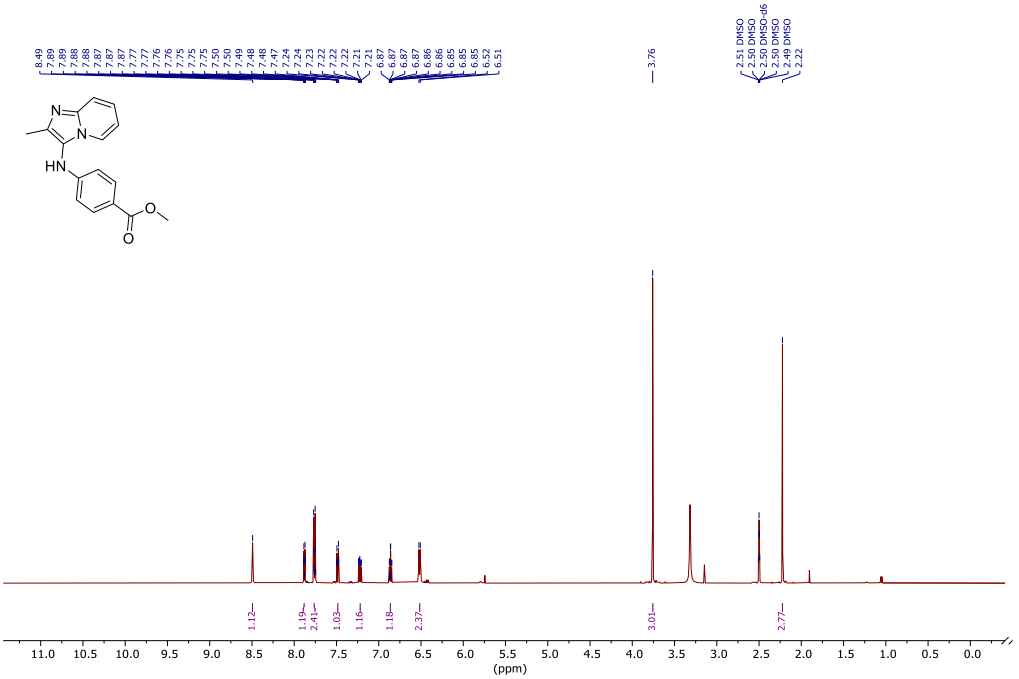
^{19}F-NMR (377 MHz, $CDCl_3$) of compound **5**.



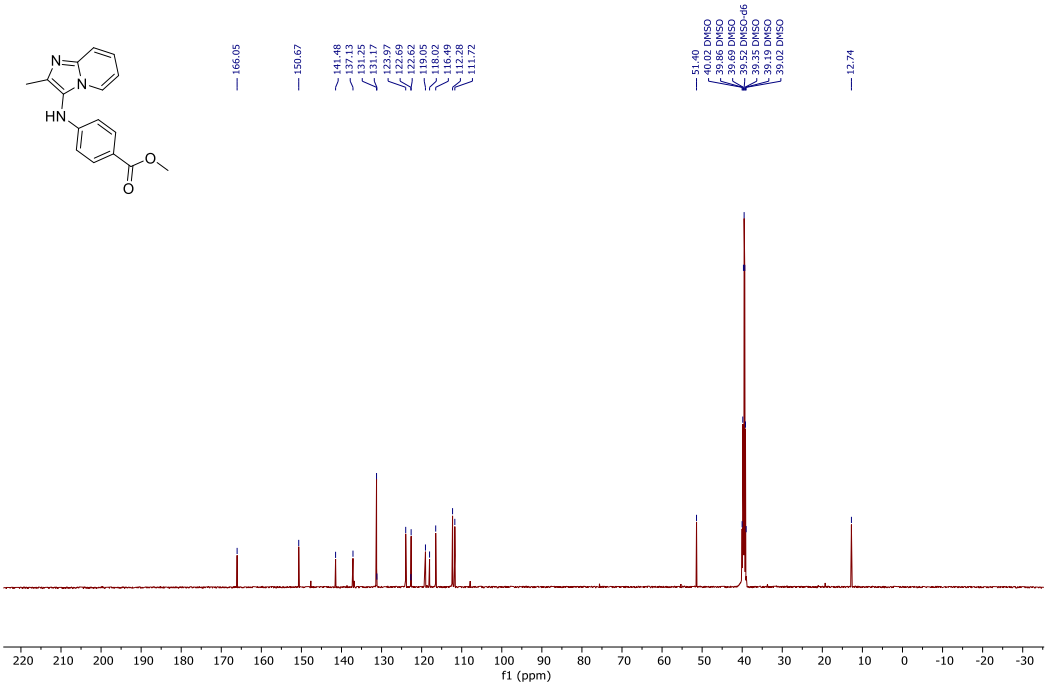
^{1}H-NMR (600 MHz, DMSO-d_6) of compound **6**.



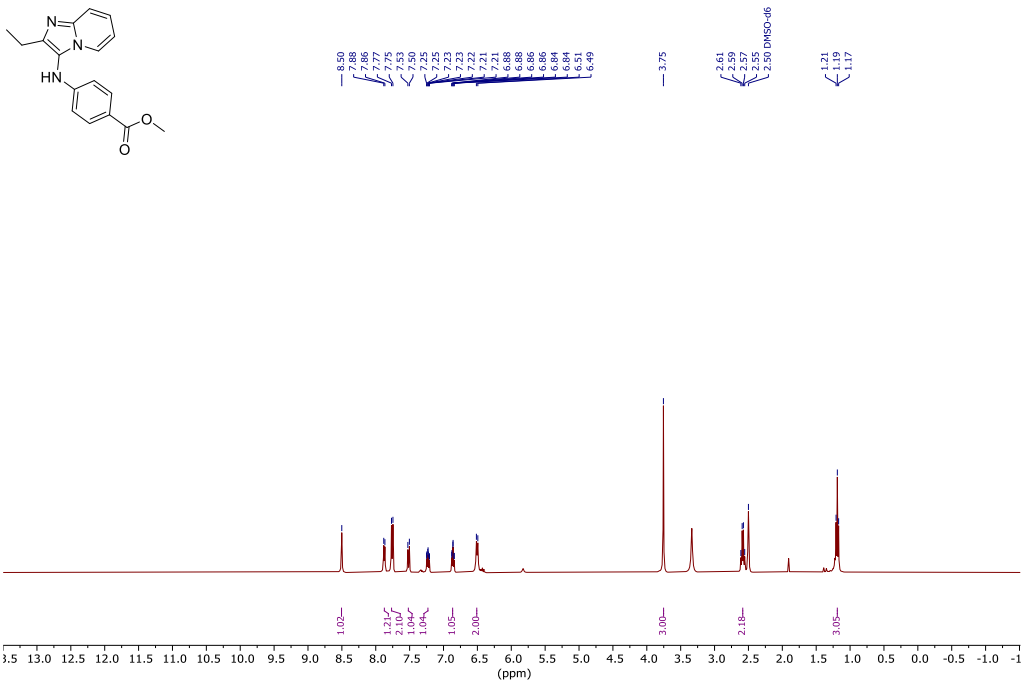
^{13}C-NMR (151 MHz, DMSO-d_6) of compound **6**.



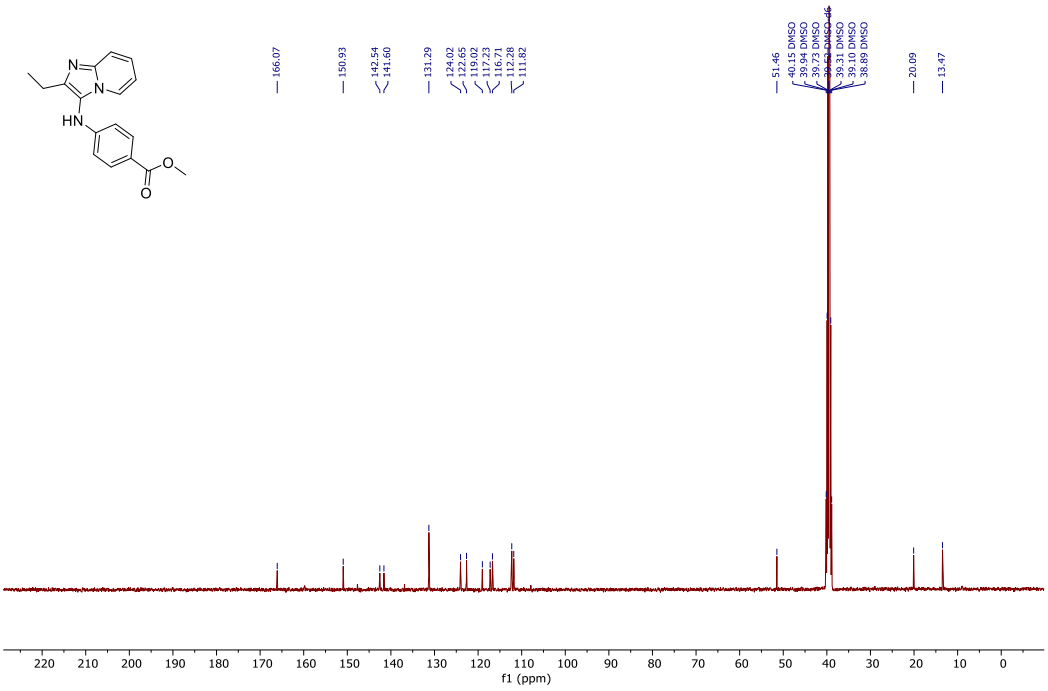
^{1}H-NMR (500 MHz, DMSO-d_6) of compound **7a**.



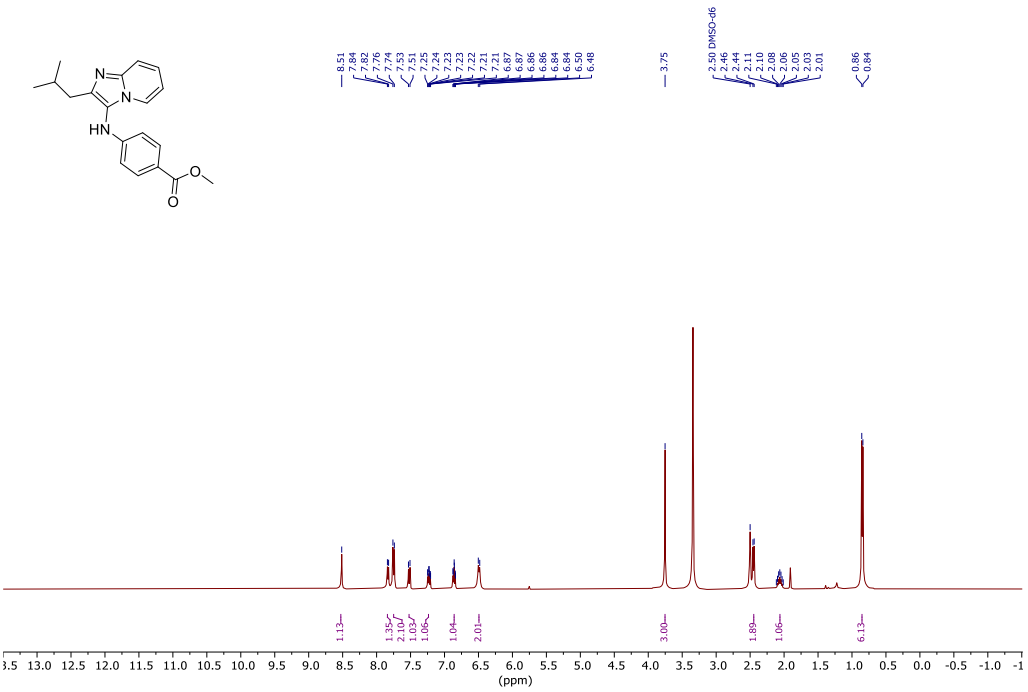
^{13}C-NMR (126 MHz, DMSO-d_6) of compound **7a**.



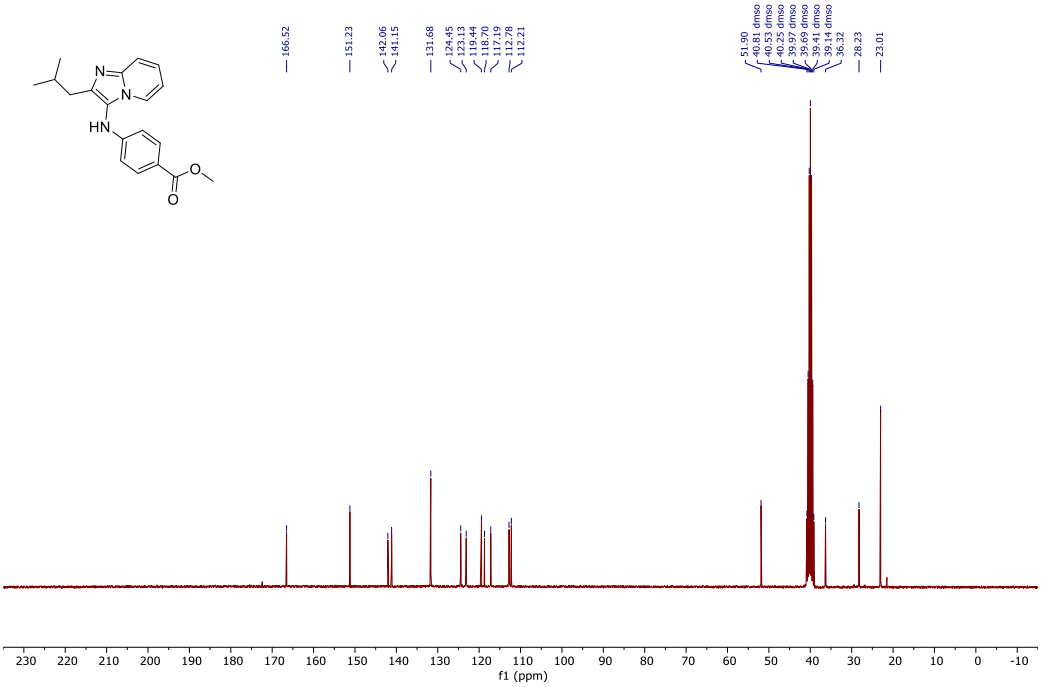
^{1}H-NMR (400 MHz, DMSO-d_6) of compound **7b**.



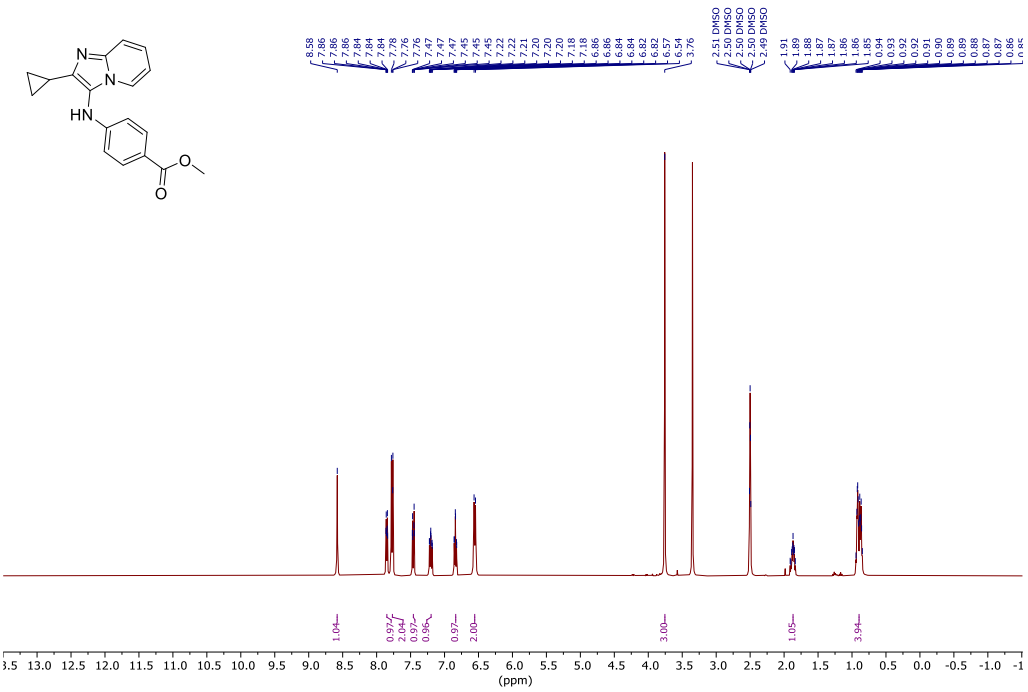
^{13}C-NMR (101 MHz, DMSO-d_6) of compound **7b**.



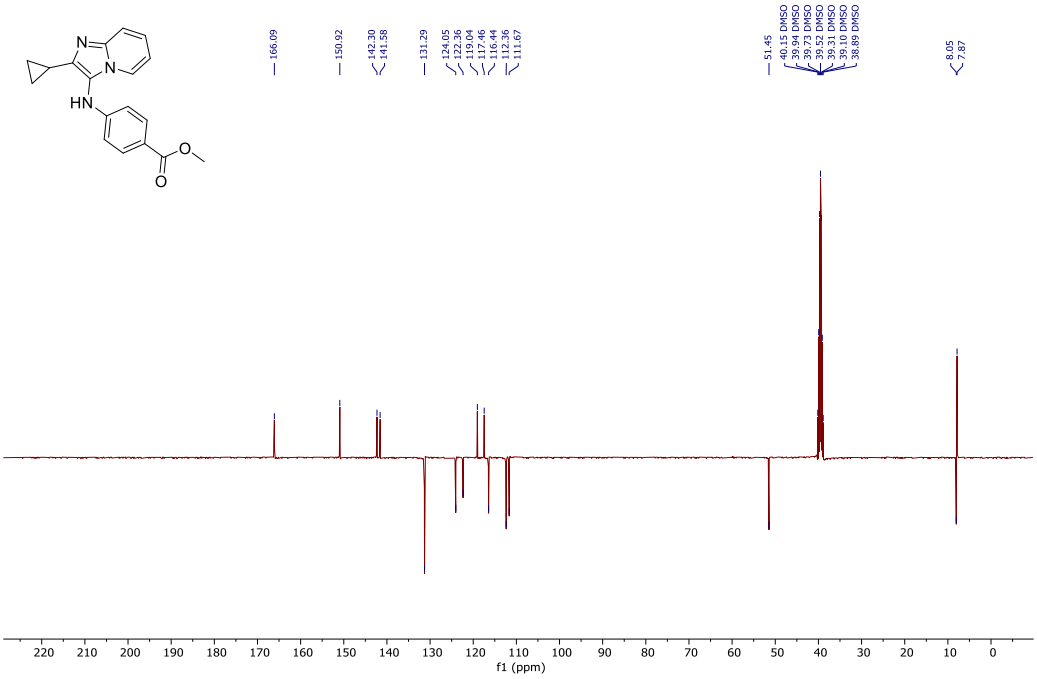
^{1}H-NMR (400 MHz, DMSO-d_6) of compound **7c**.



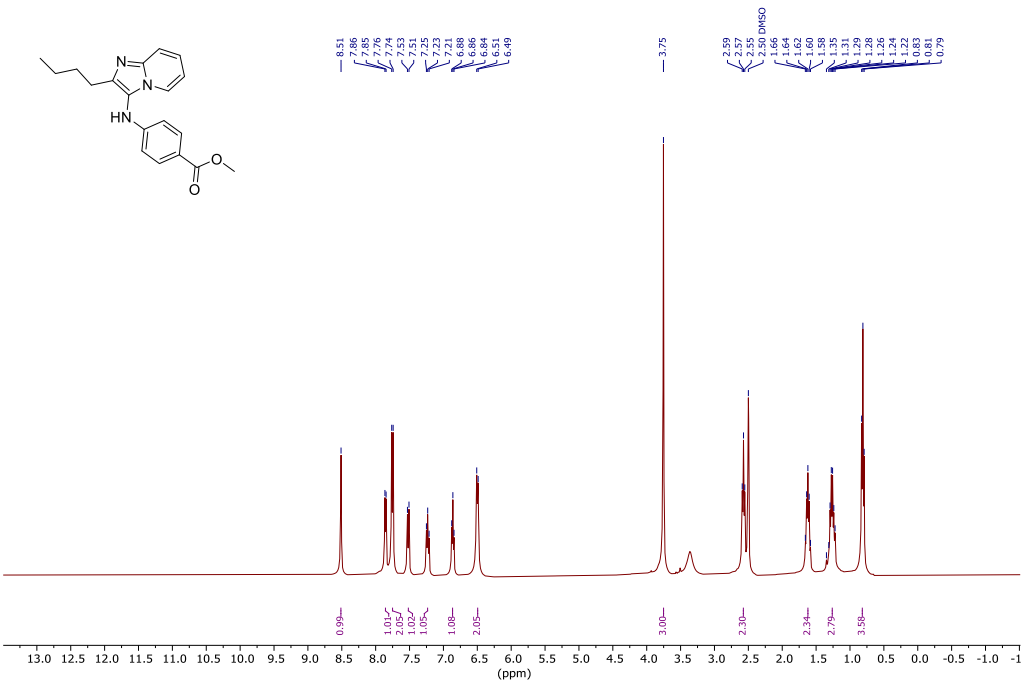
^{13}C-NMR (75 MHz, DMSO-d_6) of compound **7c**.



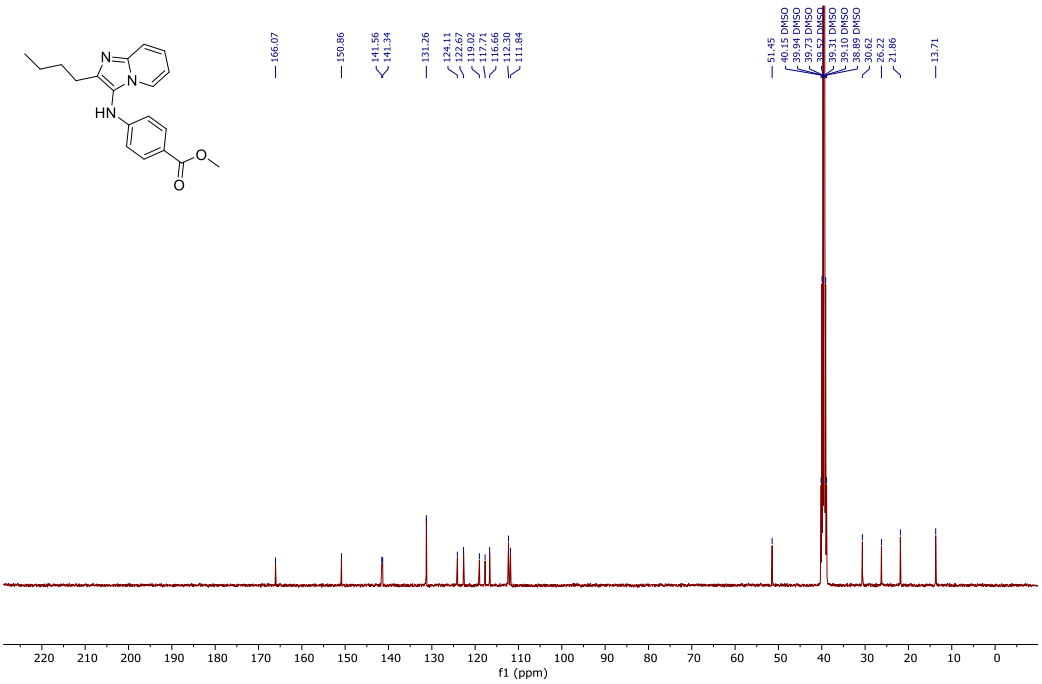
^{1}H-NMR (400 MHz, DMSO-d_6) of compound **7d**.



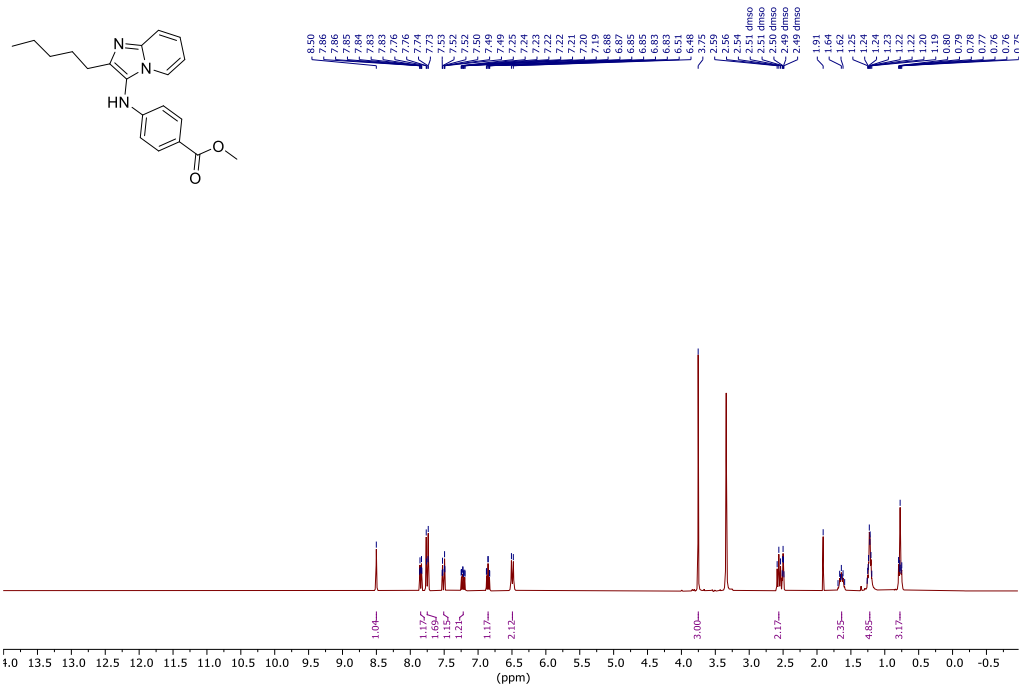
^{13}C-NMR APT (101 MHz, DMSO-d_6) of compound **7d**.



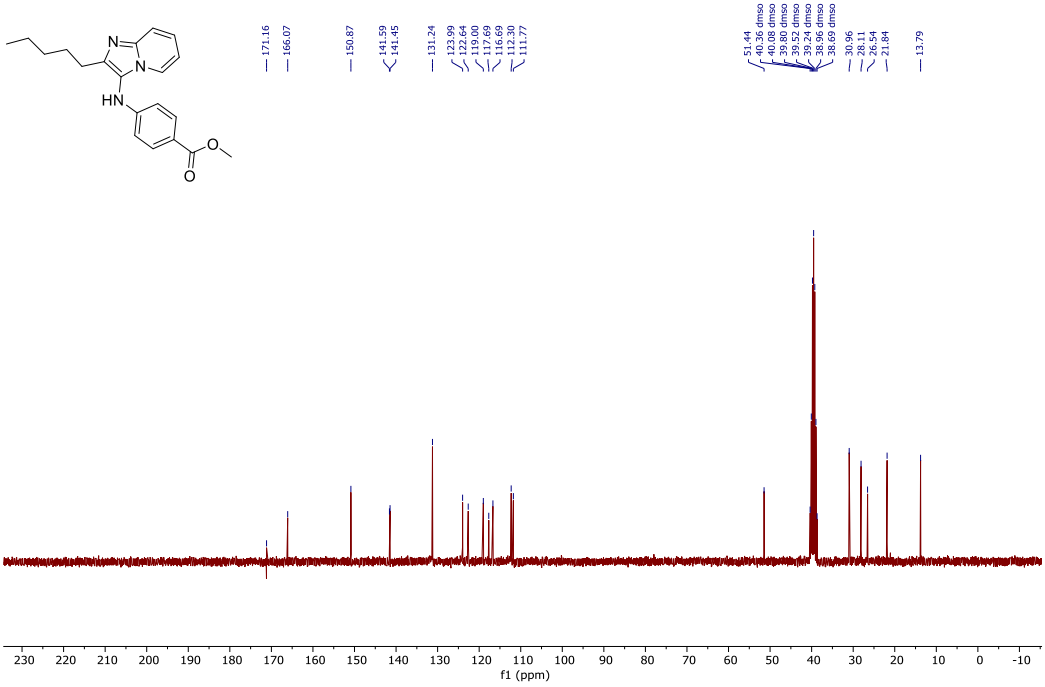
^{1}H-NMR (400 MHz, DMSO-d_6) of compound **7e**.



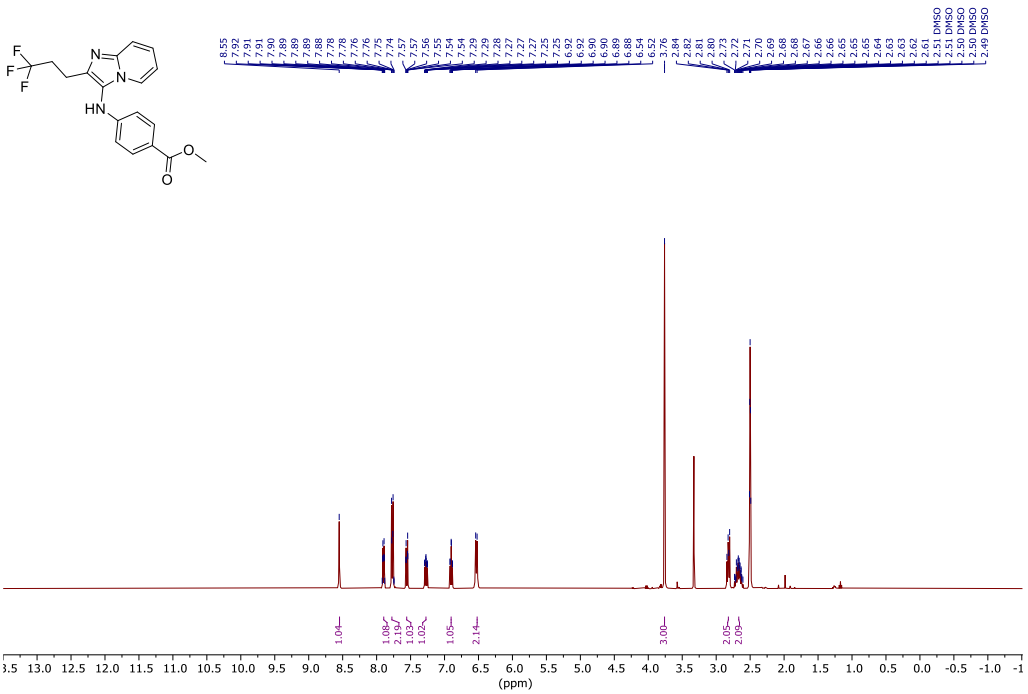
^{13}C-NMR (75 MHz, DMSO-d_6) of compound **7e**.



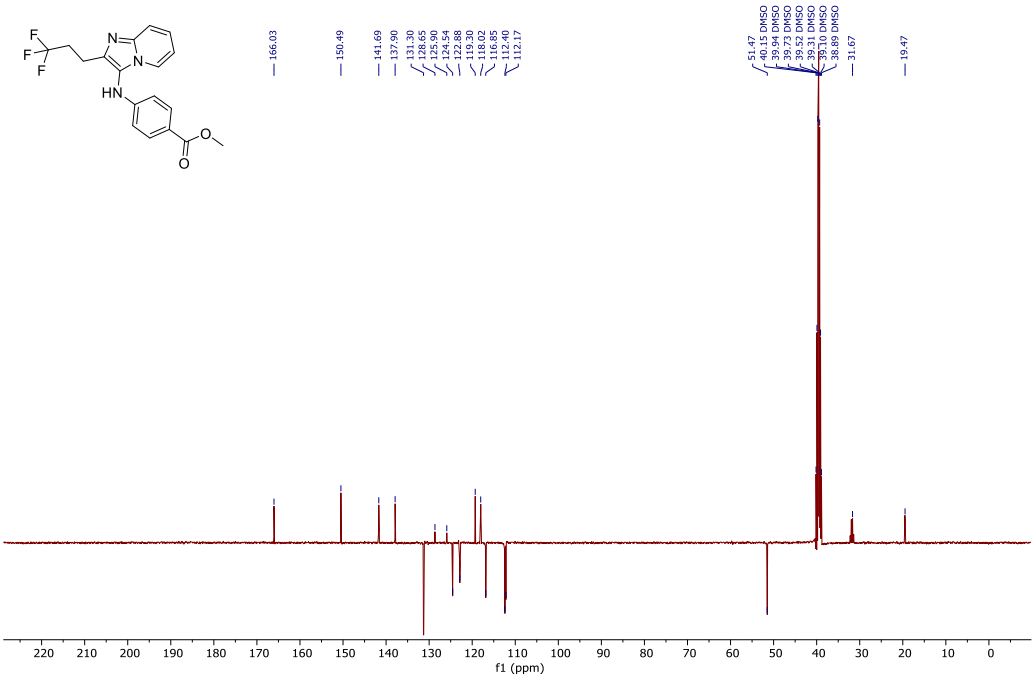
^{1}H-NMR (300 MHz, DMSO-d_6) of compound **7f**.



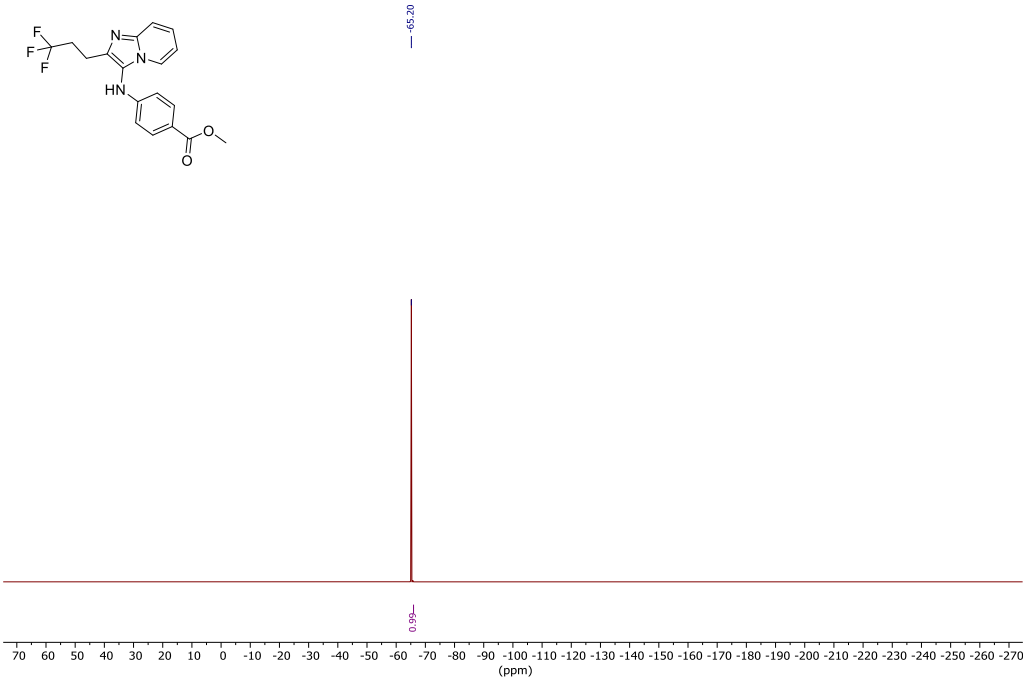
^{13}C-NMR (75 MHz, DMSO-d_6) of compound **7f**.



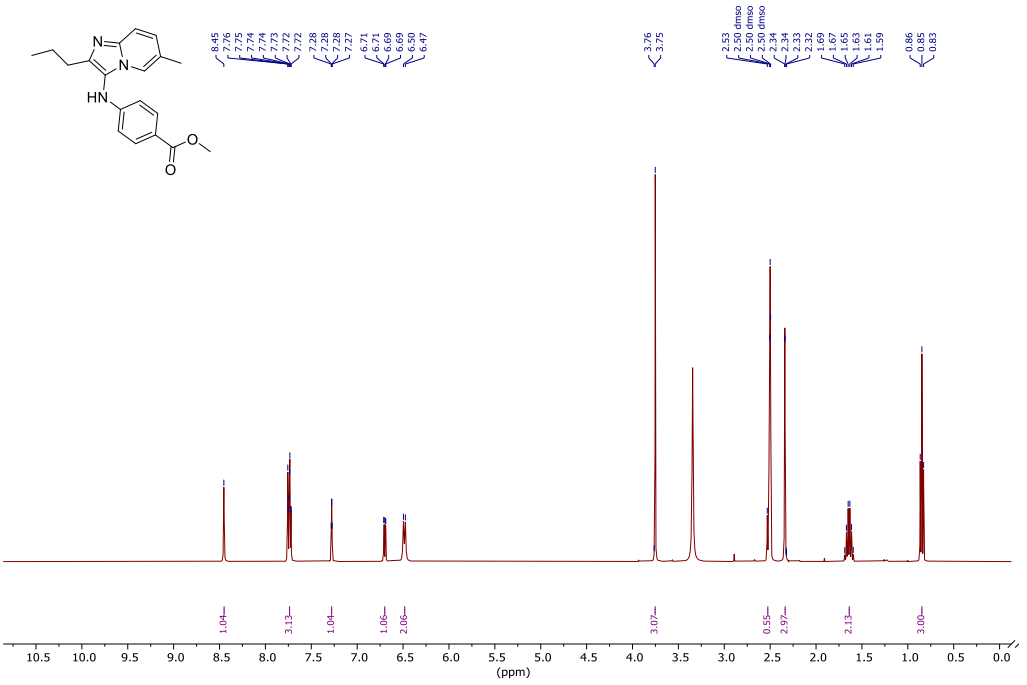
^{1}H-NMR (400 MHz, DMSO-d_6) of compound **7g**.



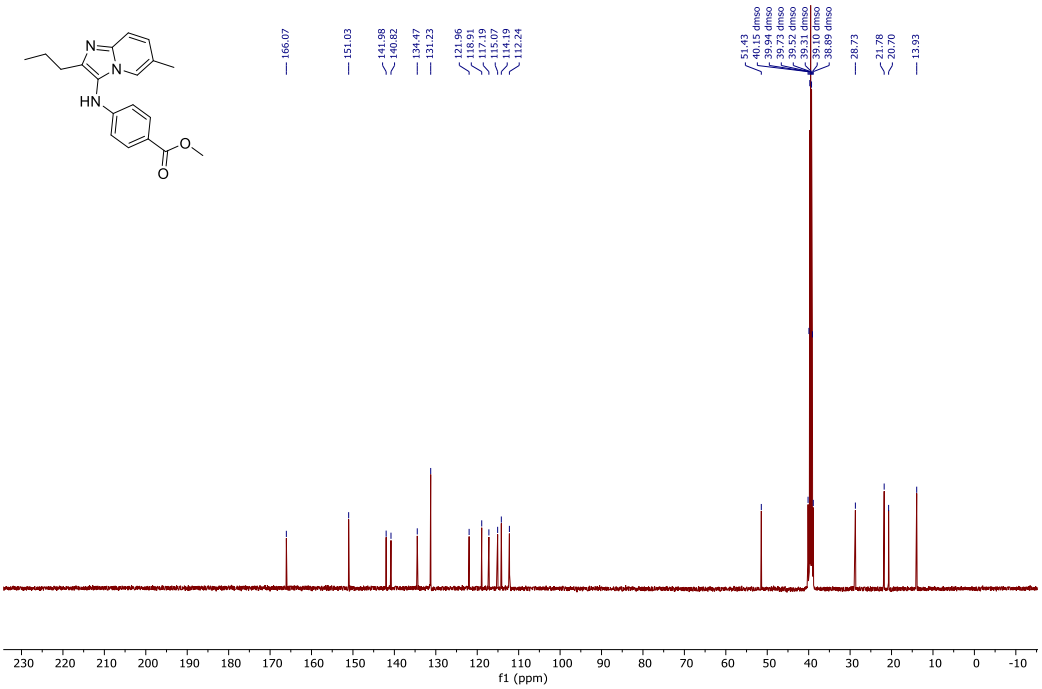
^{13}C-NMR APT (101 MHz, DMSO-d_6) of compound **7g**.



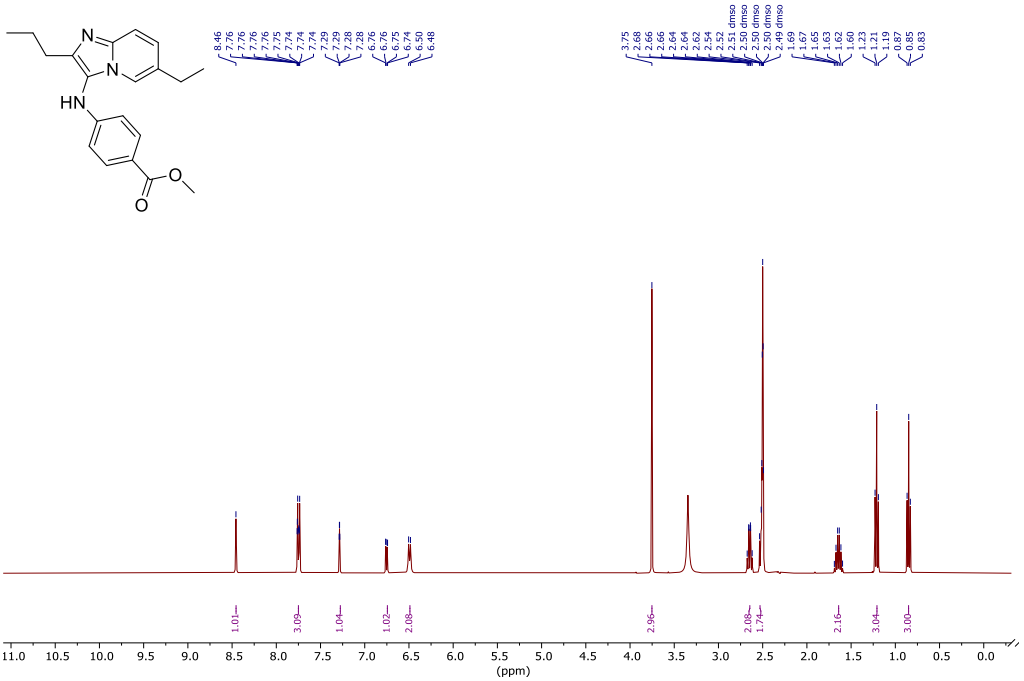
^{19}F-NMR (377 MHz, DMSO-d_6) of compound **7g**.



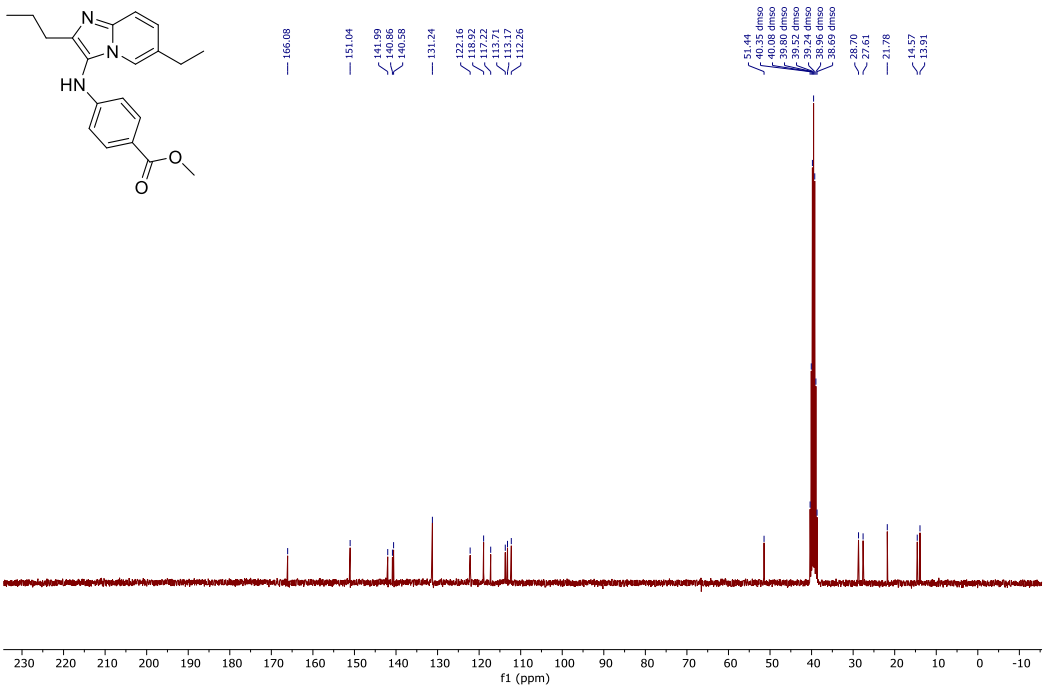
^{1}H-NMR (400 MHz, DMSO-d_6) of compound **7h**.



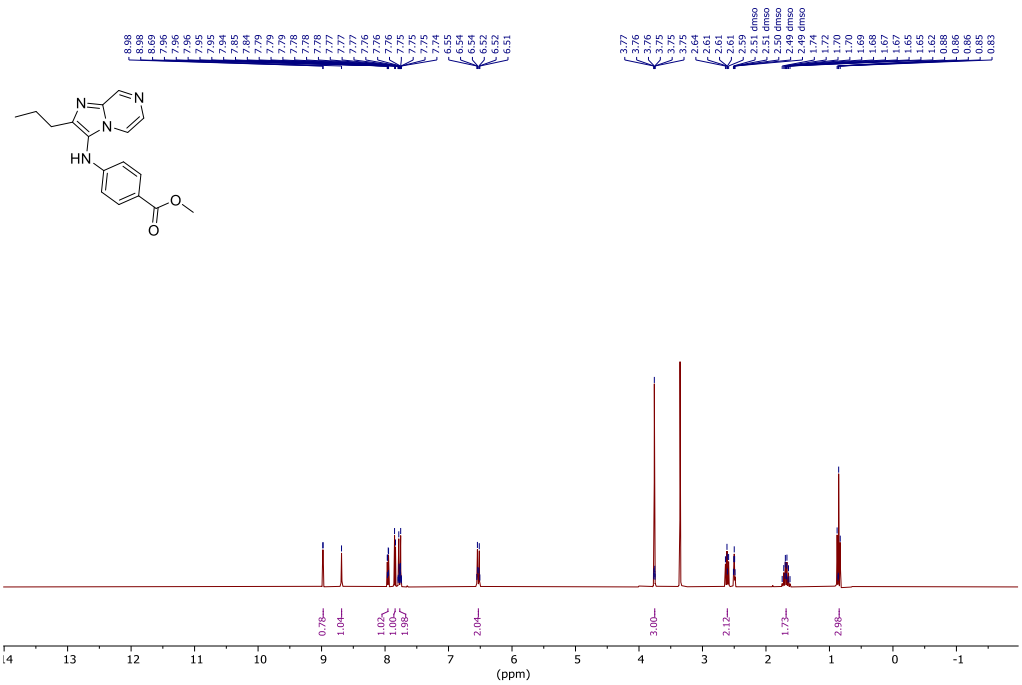
^{13}C-NMR (101 MHz, DMSO-d_6) of compound **7h**.



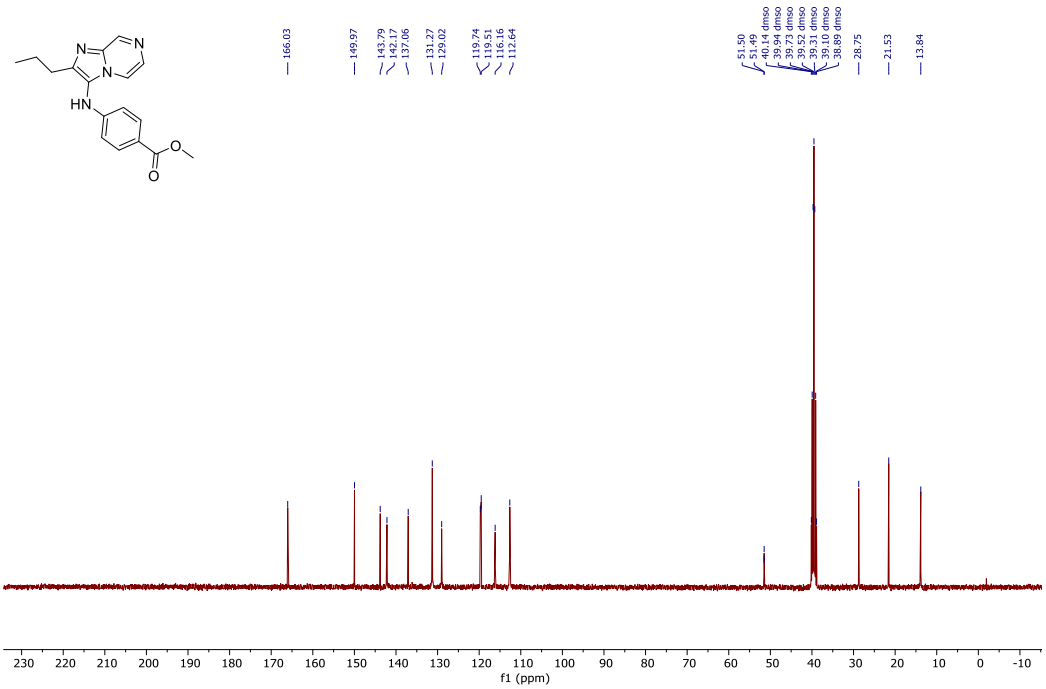
^{1}H-NMR (400 MHz, DMSO-d_6) of compound **7i**.



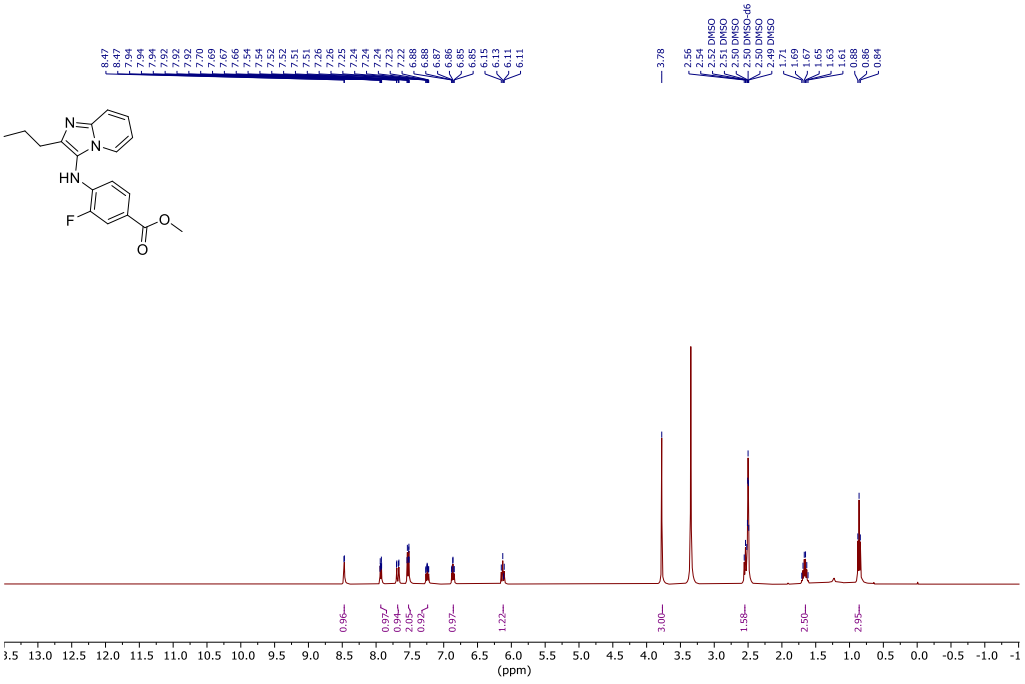
^{13}C-NMR (75 MHz, DMSO-d_6) of compound **7i**.



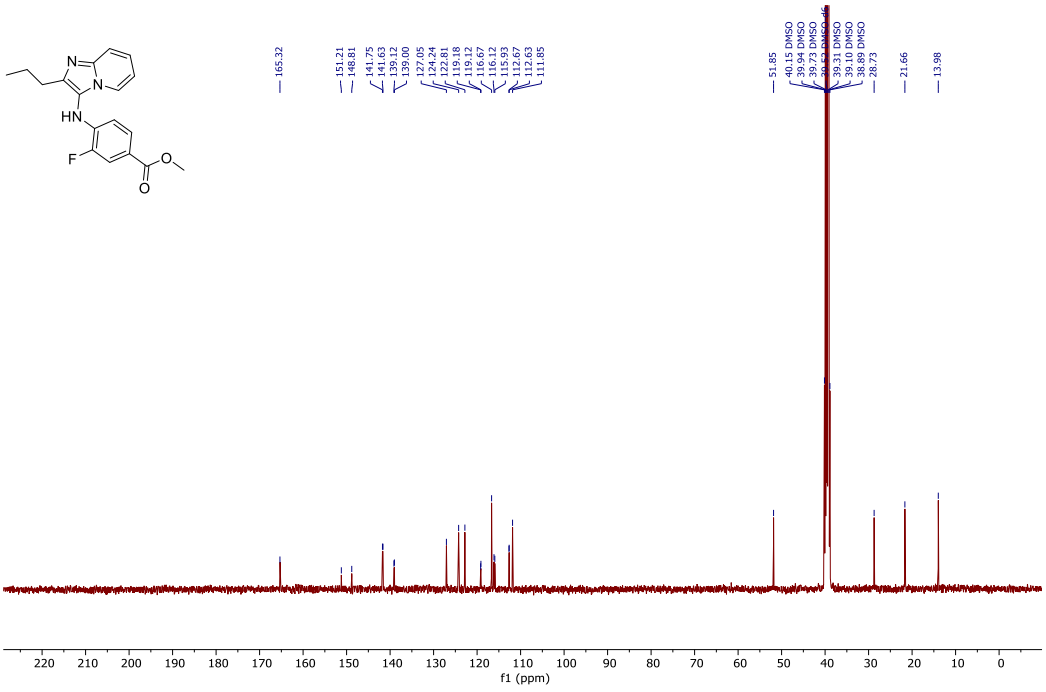
^{1}H-NMR (300 MHz, DMSO-d_6) of compound **7j**.



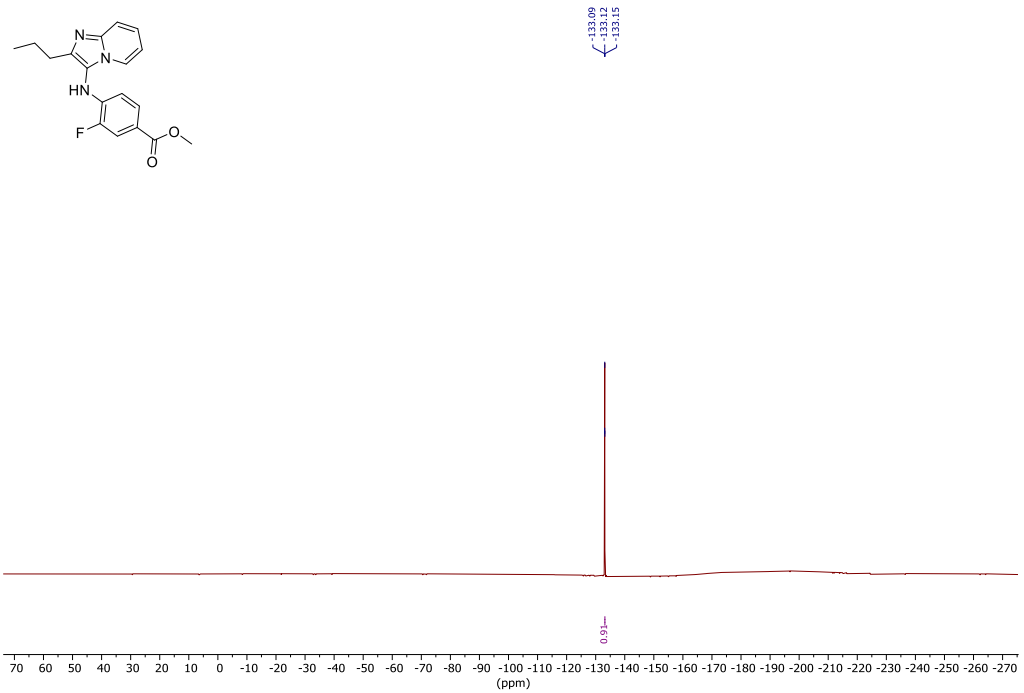
^{13}C-NMR (101 MHz, DMSO-d_6) of compound **7j**.



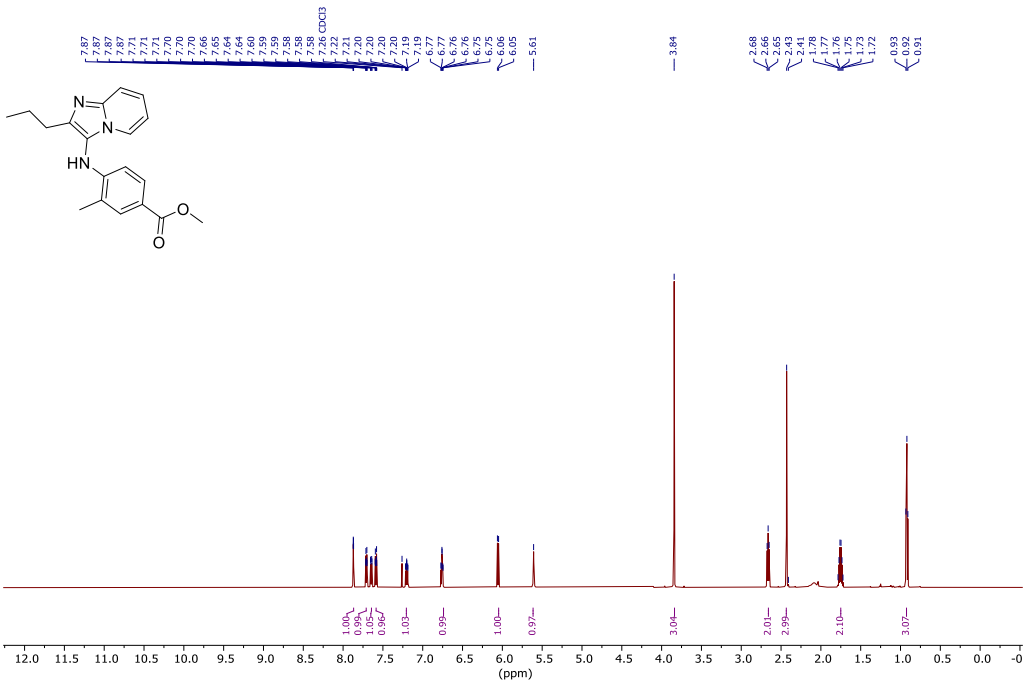
^{1}H-NMR (400 MHz, DMSO-d_6) of compound **7k**.



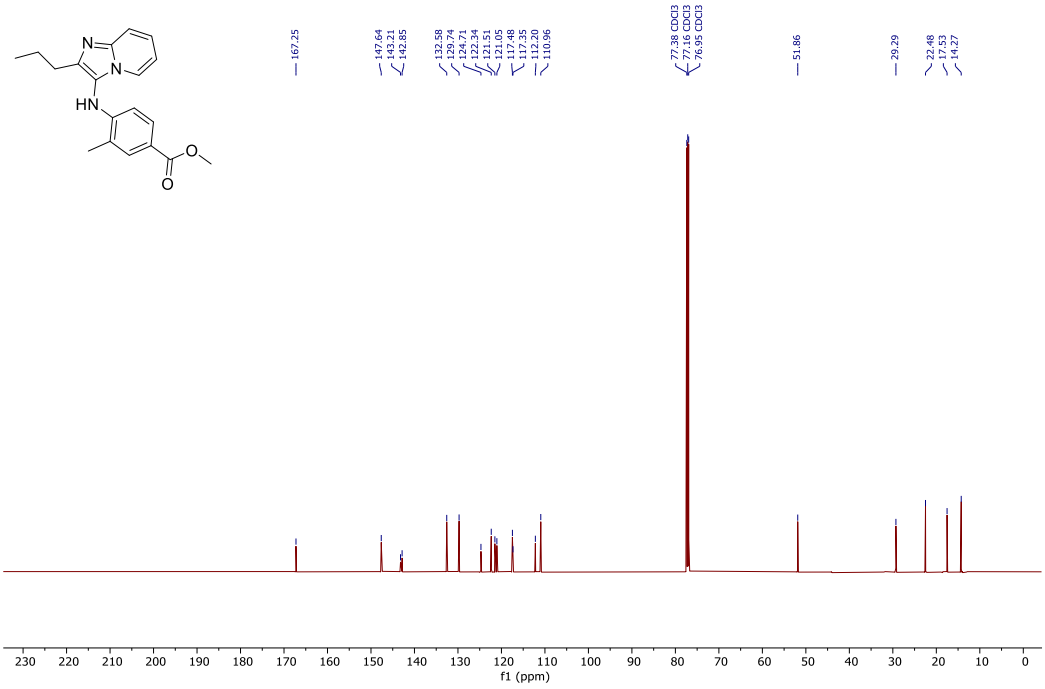
^{13}C-NMR (101 MHz, DMSO-d_6) of compound **7k**.



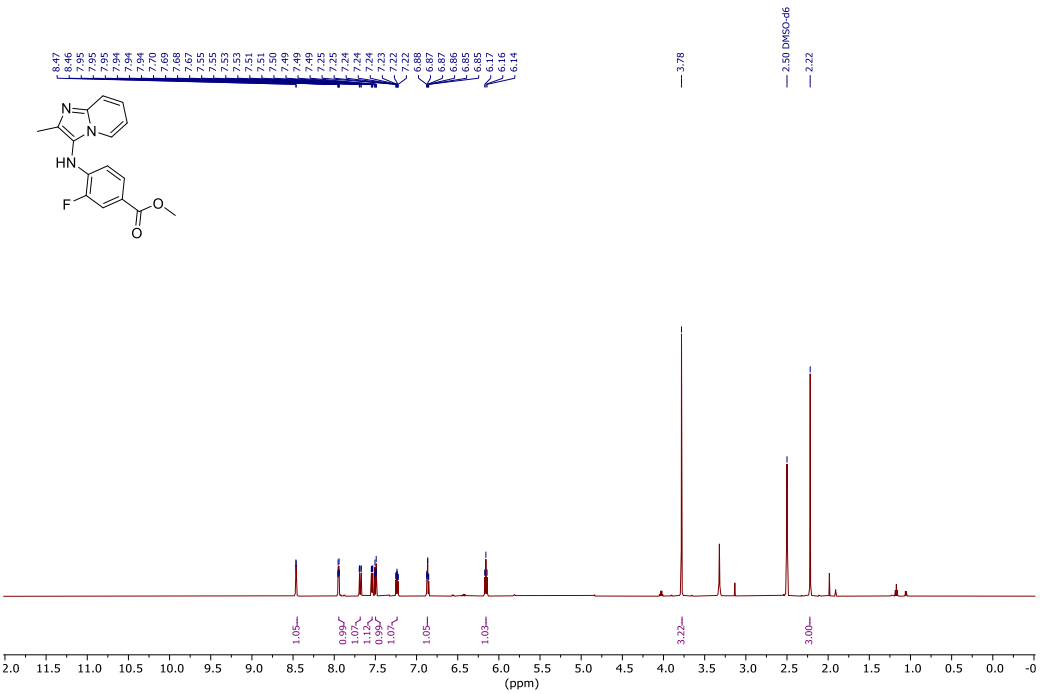
^{19}F-NMR (377 MHz, DMSO-d_6) of compound **7k**.



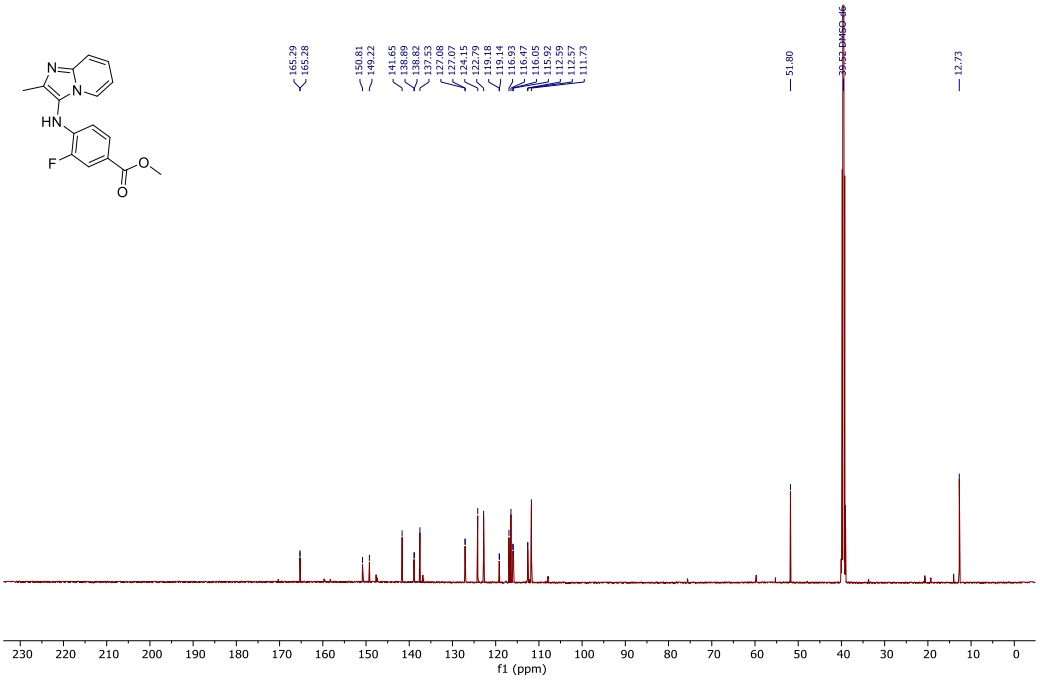
^{1}H-NMR (600 MHz, DMSO-d_6) of compound **7l**.



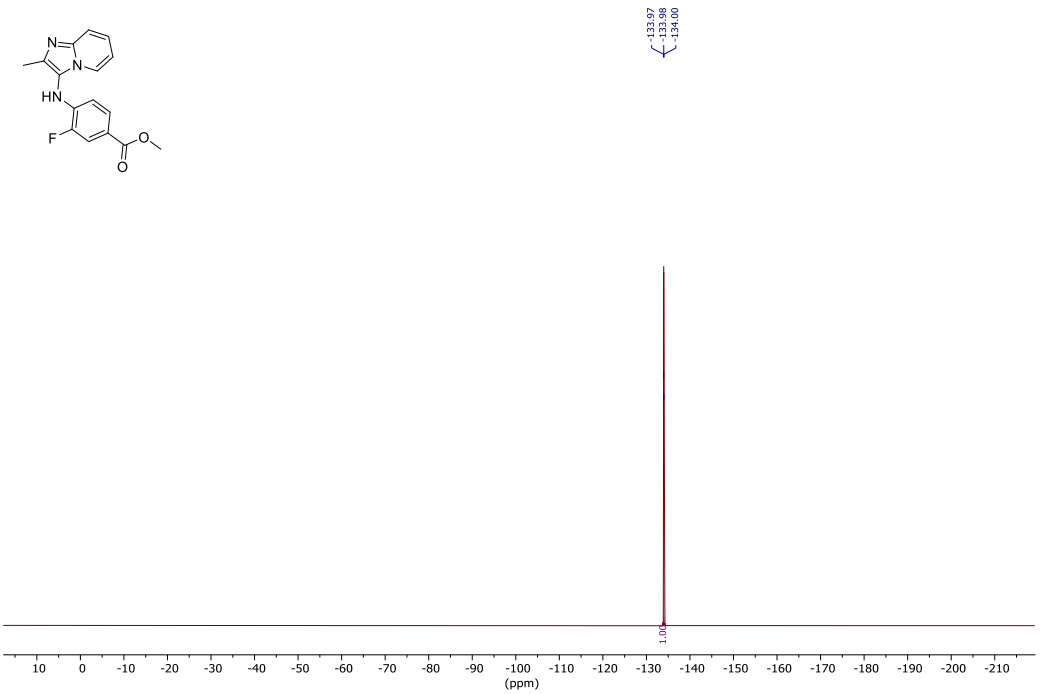
^{13}C-NMR (151 MHz, DMSO-d_6) of compound **7l**.



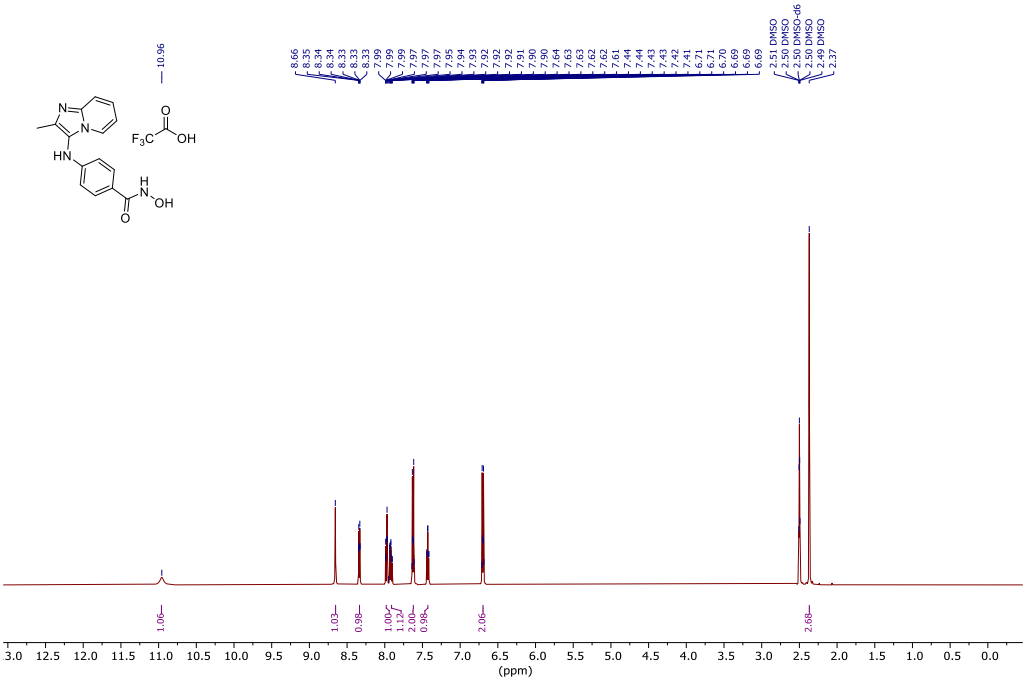
^{1}H-NMR (600 MHz, DMSO-d_6) of compound **7m**.



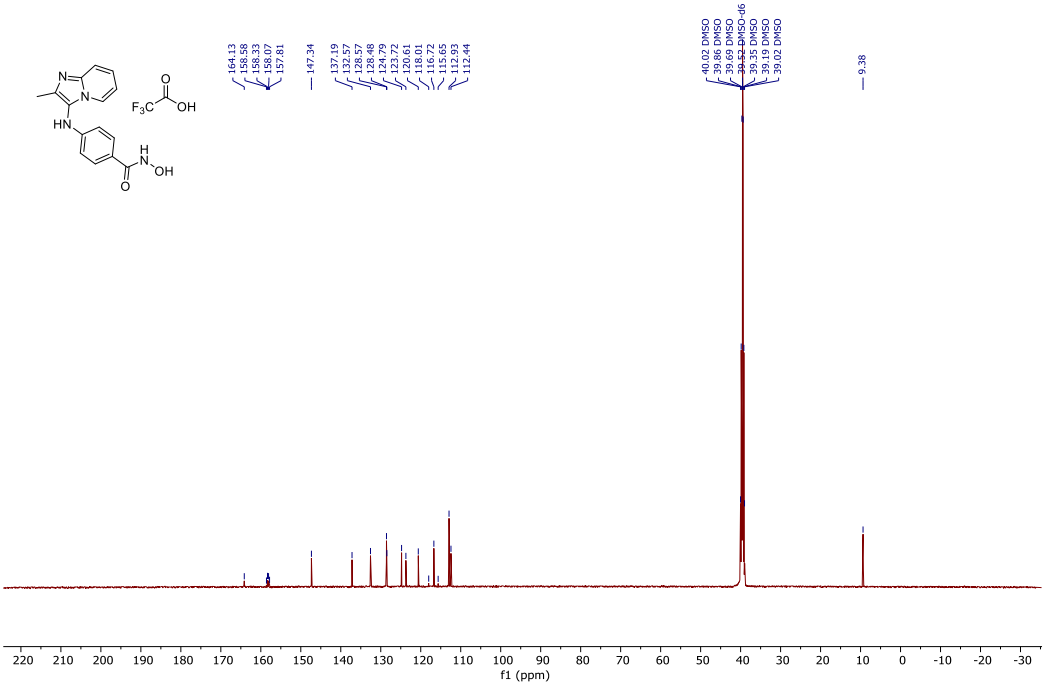
^{13}C-NMR (151 MHz, DMSO-d_6) of compound **7m**.



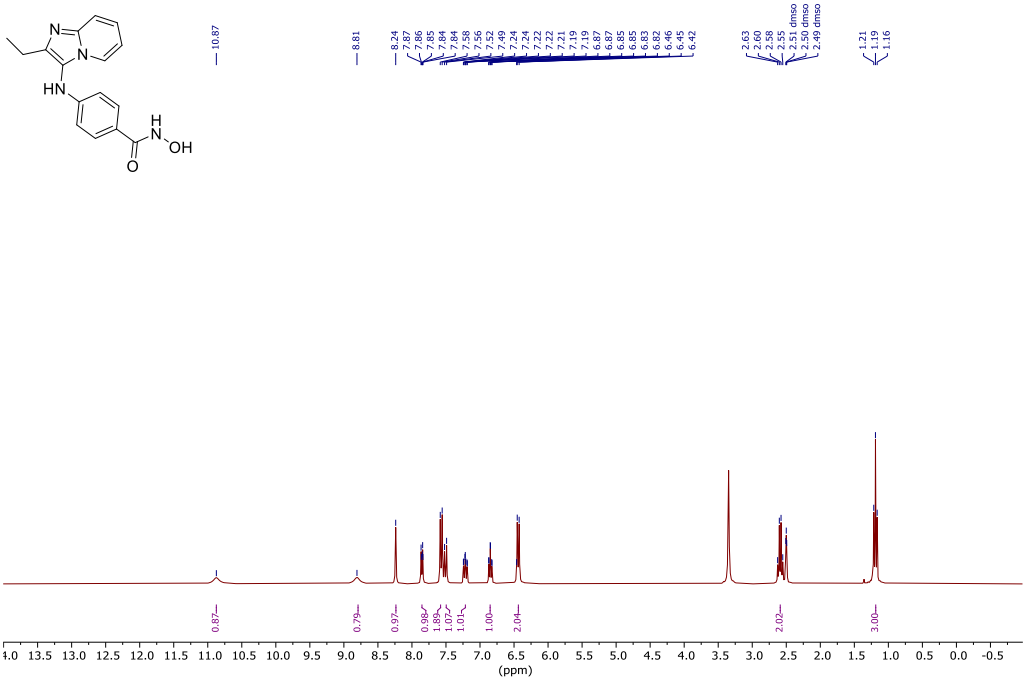
^{19}F-NMR (565 MHz, DMSO-d_6) of compound **7m**.



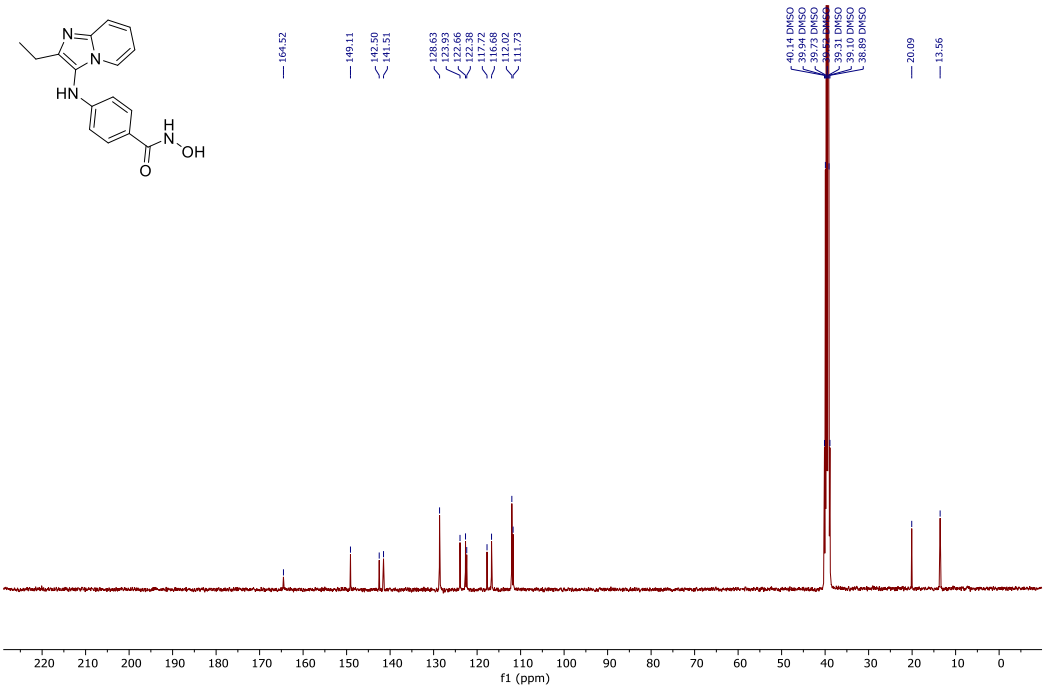
^{1}H-NMR (500 MHz, DMSO-d_6) of compound **8a**.



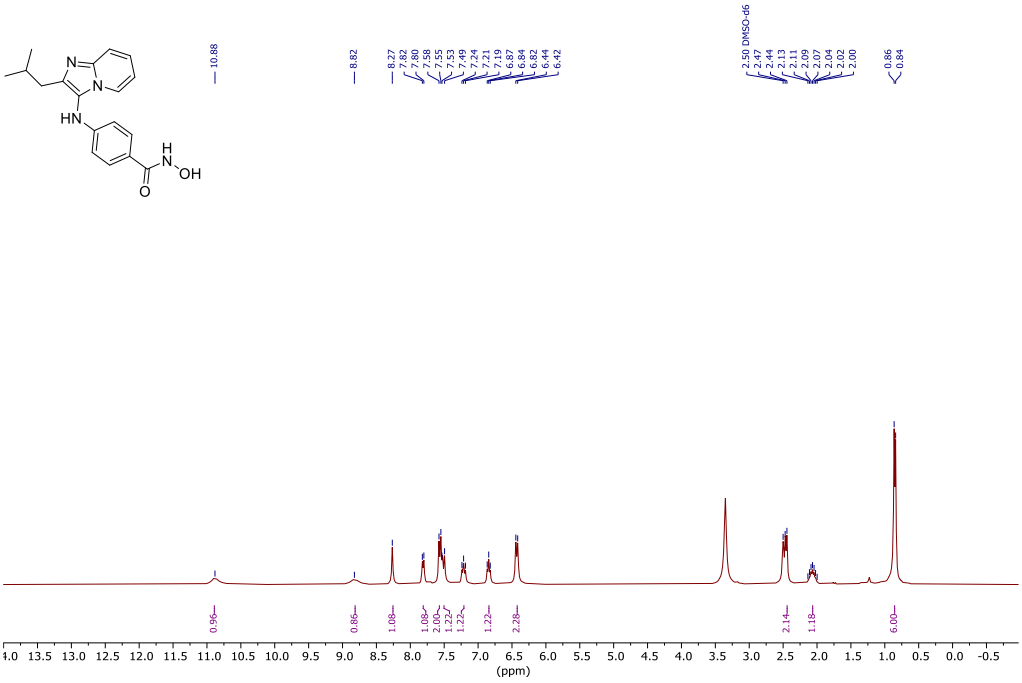
^{13}C-NMR (126 MHz, DMSO-d_6) of compound **8a**.



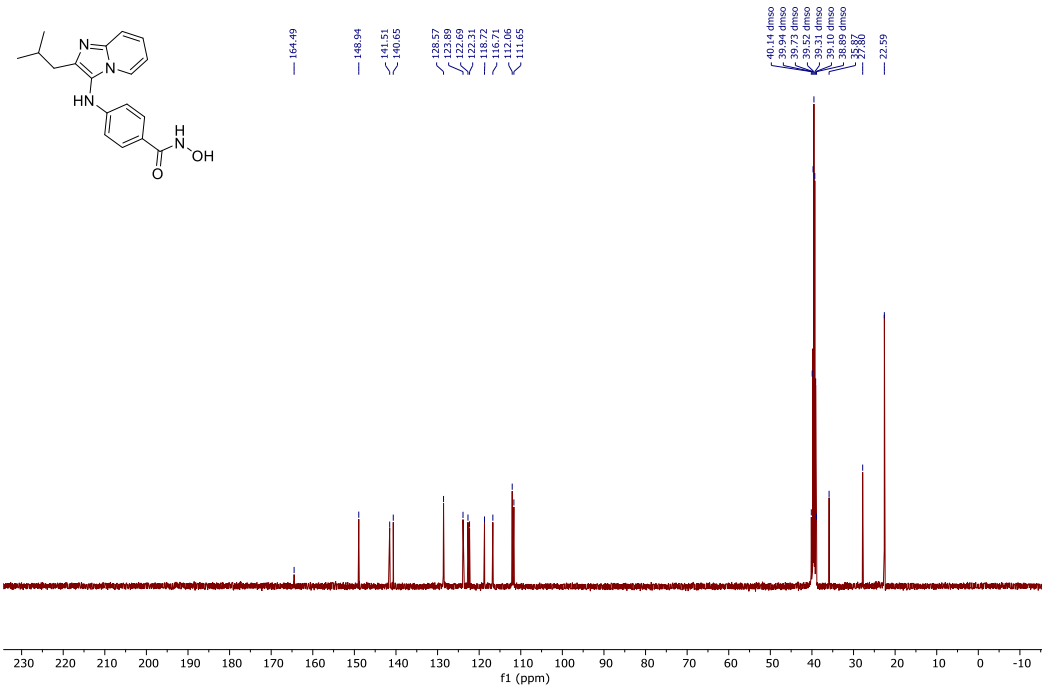
^{1}H-NMR (300 MHz, DMSO-d_6) of compound **8b**.



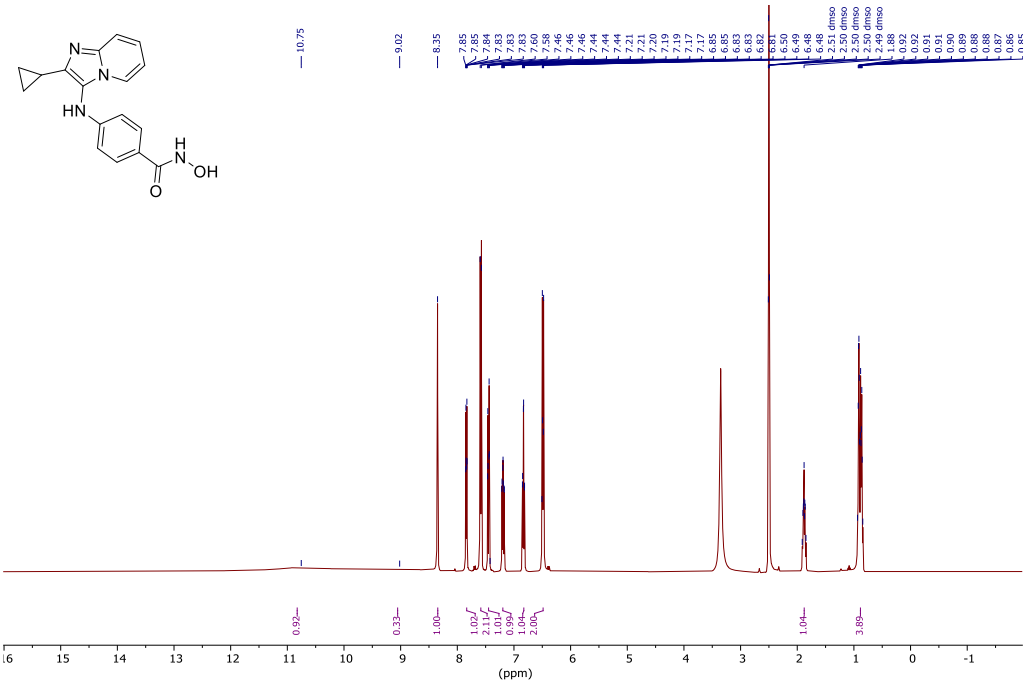
^{13}C-NMR (101 MHz, DMSO-d_6) of compound **8b**.



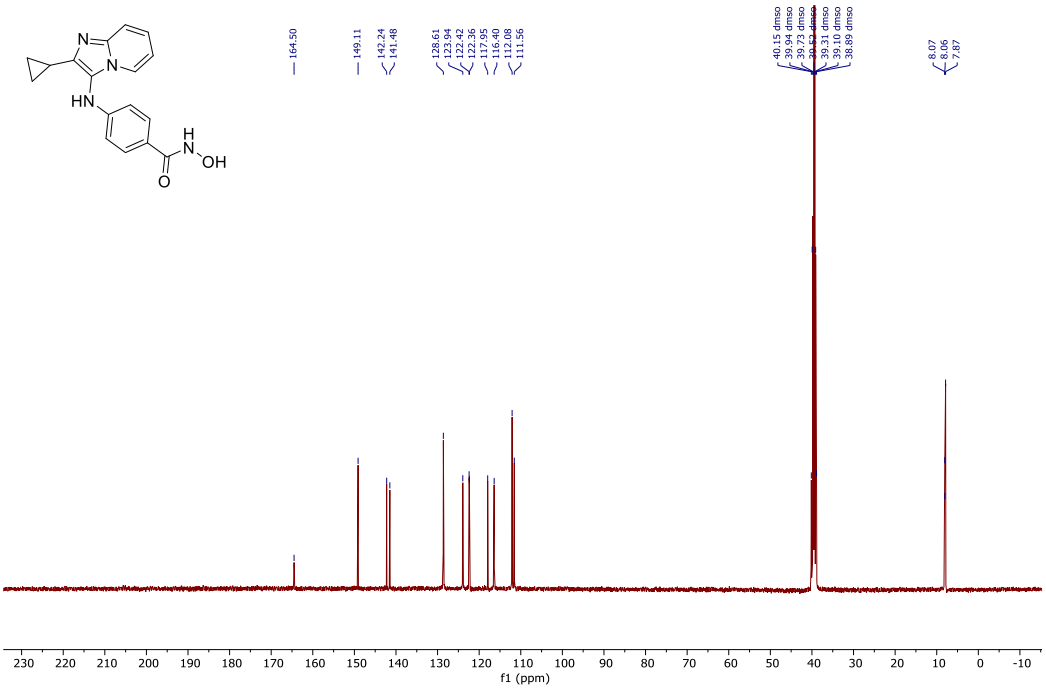
^{1}H-NMR (300 MHz, DMSO-d_6) of compound **8c**.



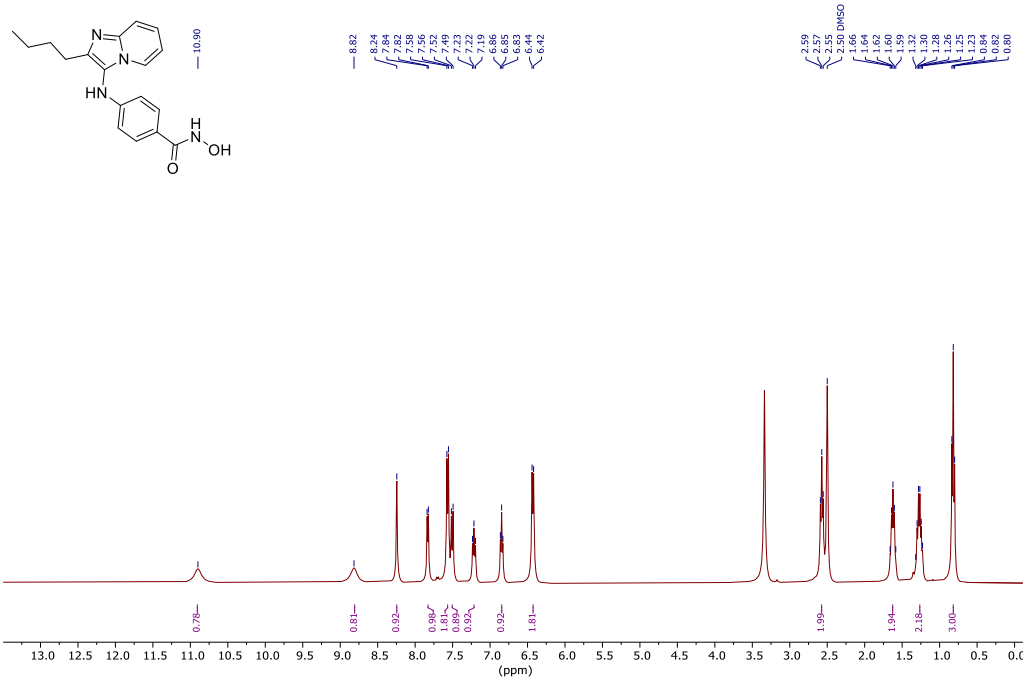
^{13}C-NMR (101 MHz, DMSO-d_6) of compound **8c**.



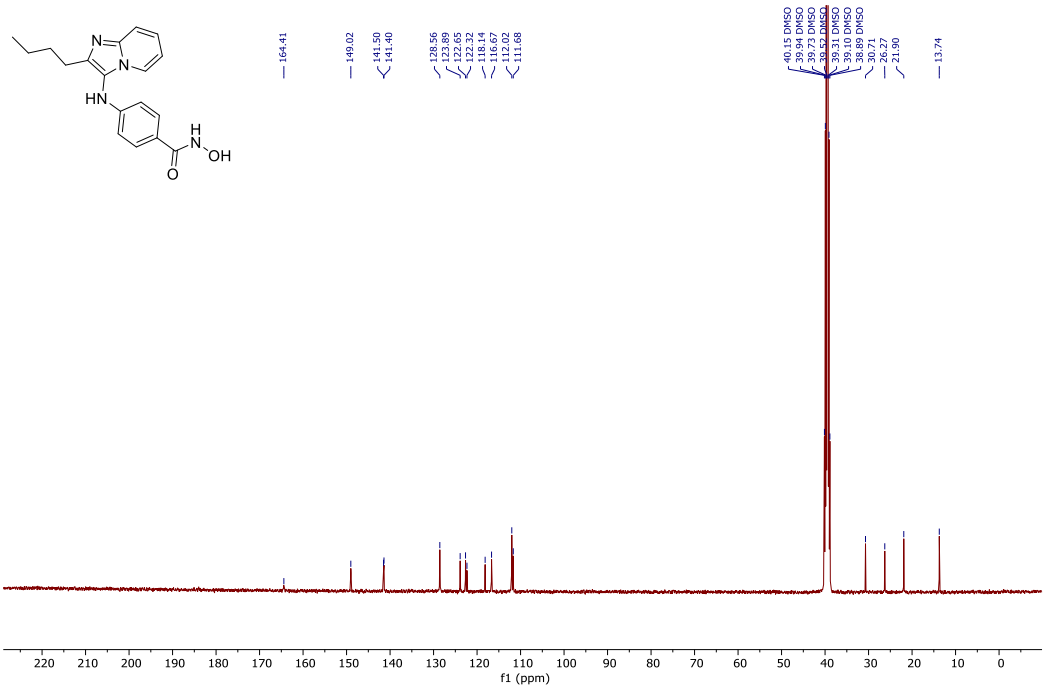
^{1}H-NMR (400 MHz, DMSO-d_6) of compound **8d**.



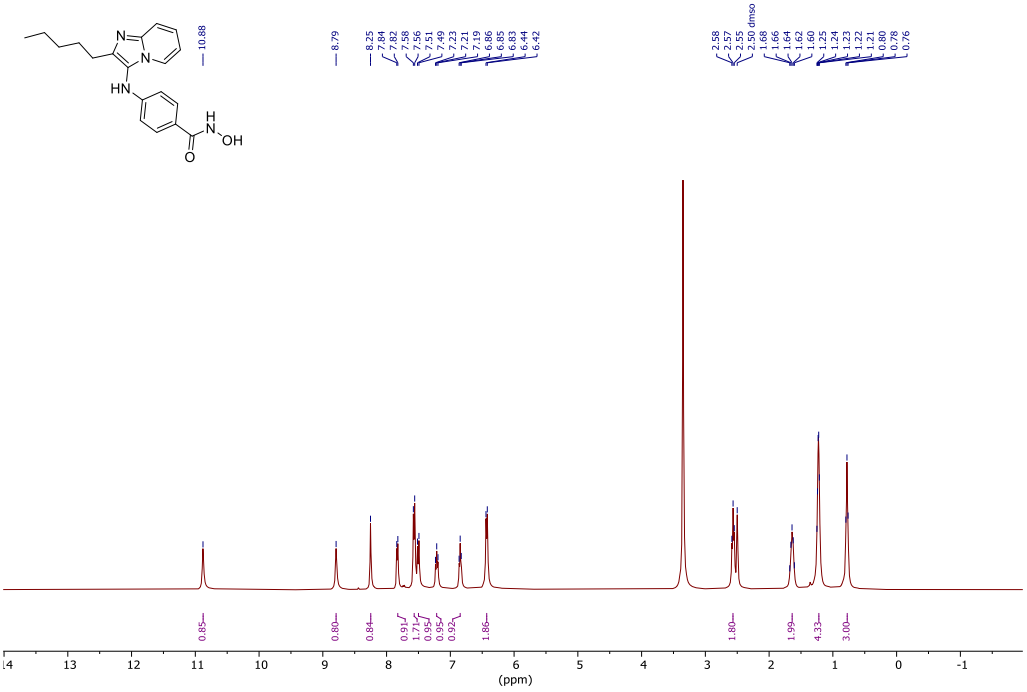
^{13}C-NMR (101 MHz, DMSO-d_6) of compound **8d**.



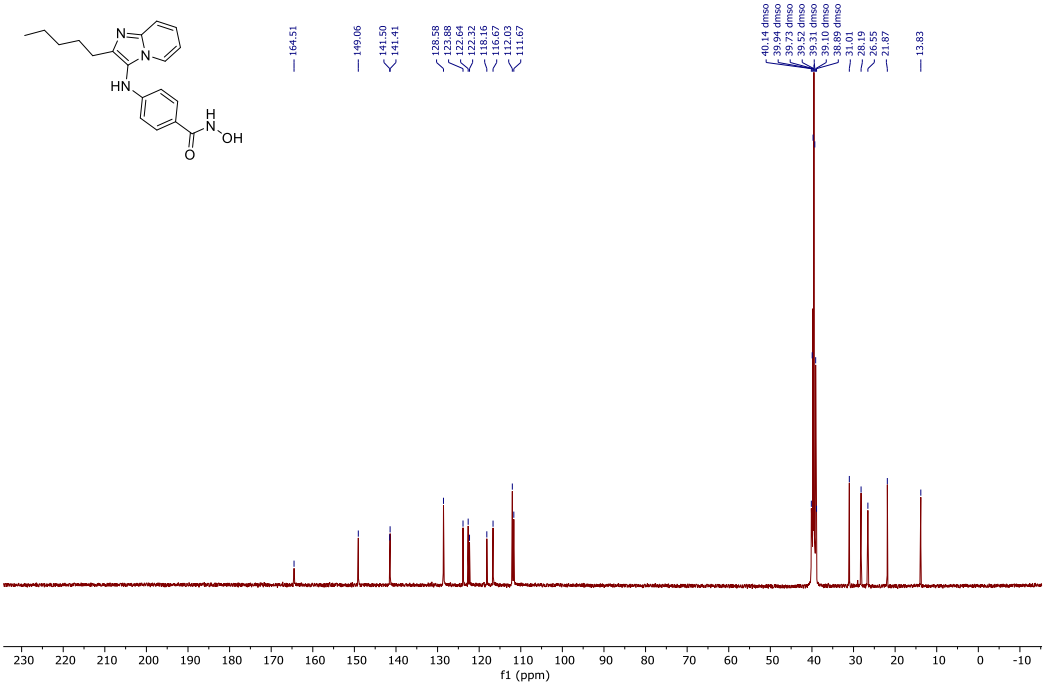
^{1}H-NMR (400 MHz, DMSO-d_6) of compound **8e**.



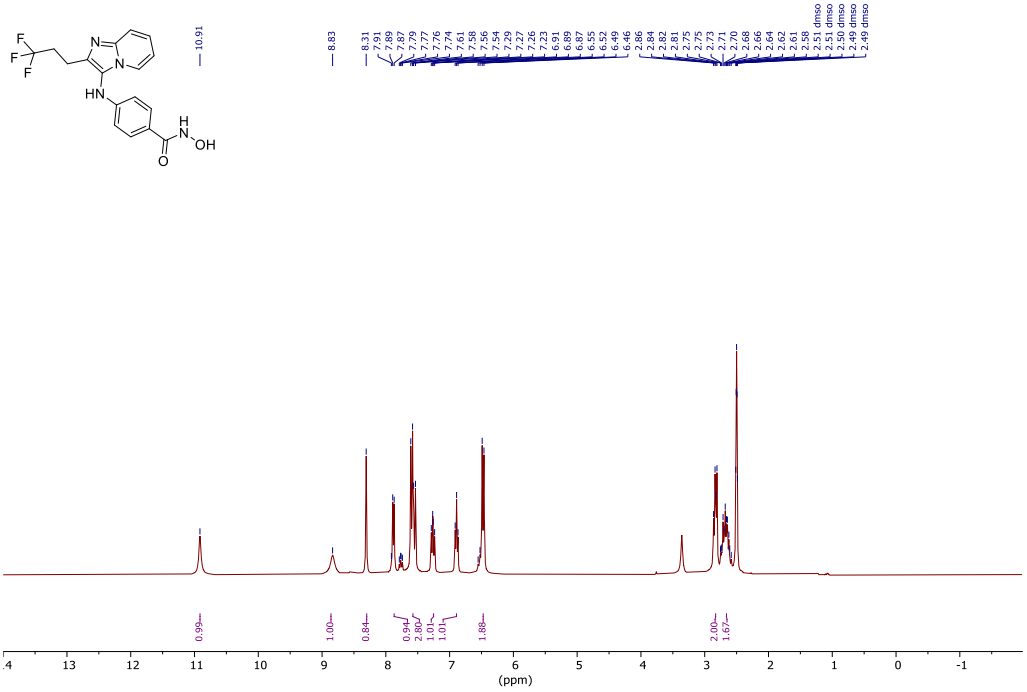
^{13}C-NMR (101 MHz, DMSO-d_6) of compound **8e.**



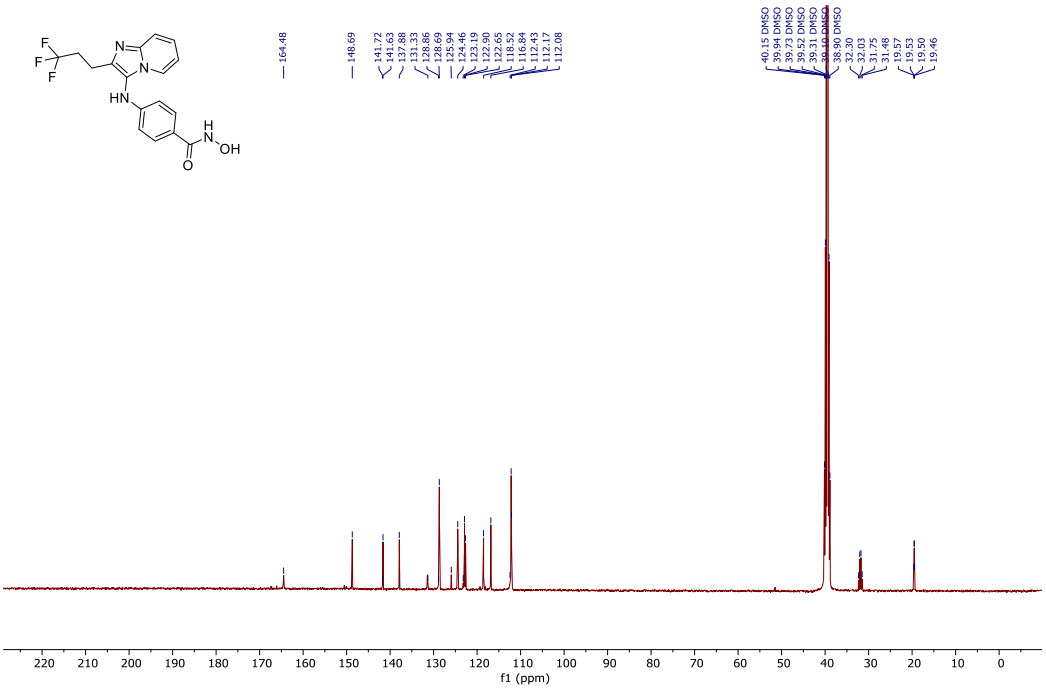
^{1}H-NMR (400 MHz, DMSO-d_6) of compound **8f**.



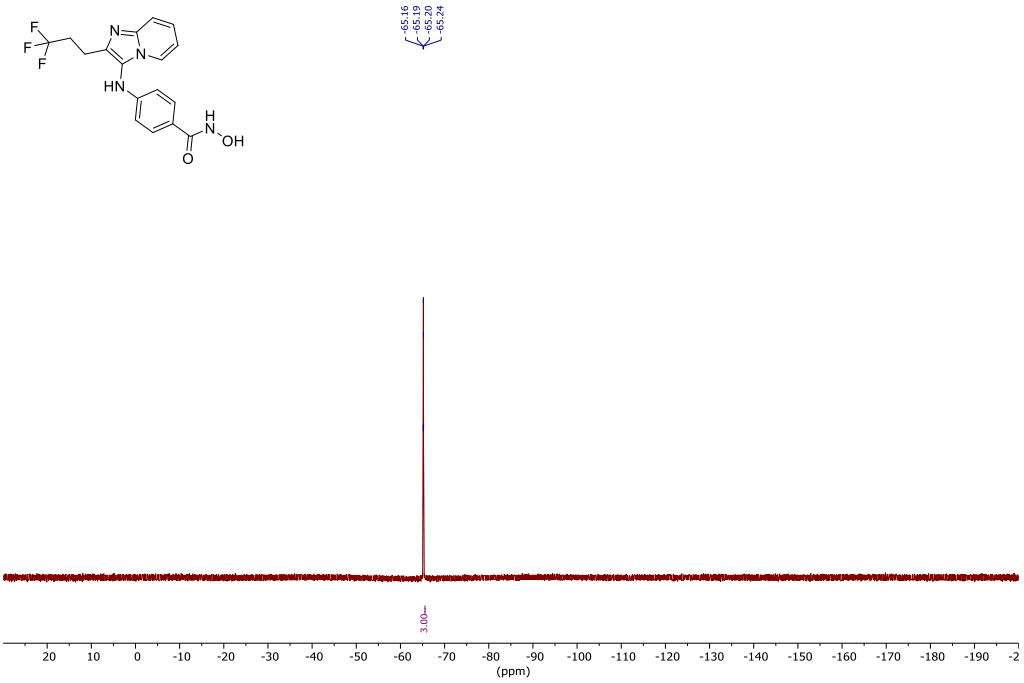
^{13}C-NMR (101 MHz, DMSO-d_6) of compound **8f**.



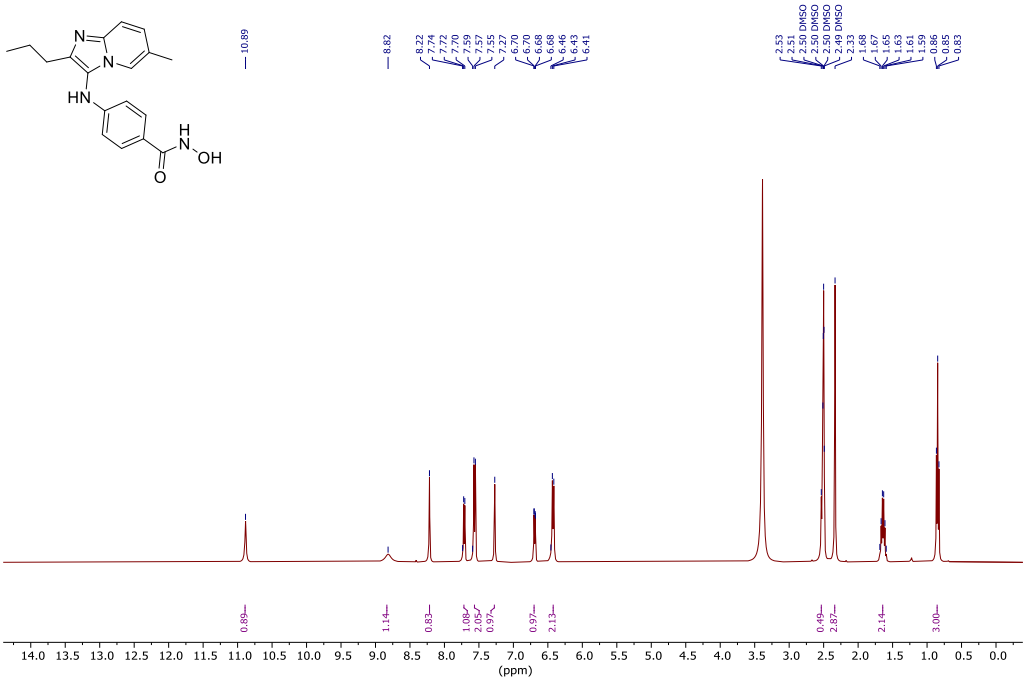
^{1}H-NMR (300 MHz, DMSO-d_6) of compound **8g**.



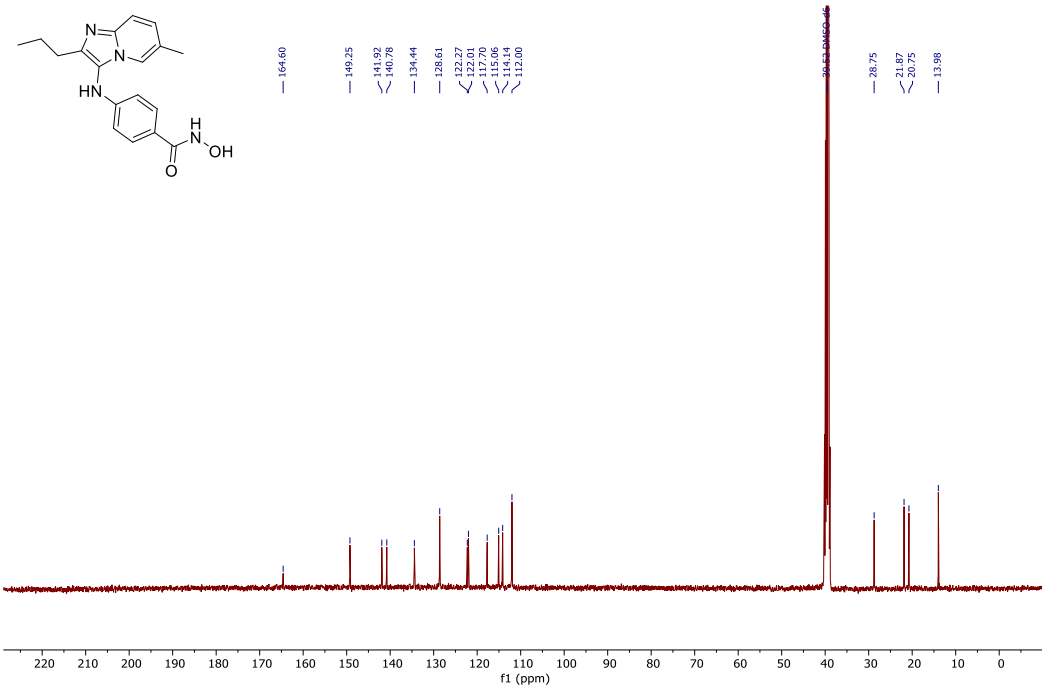
^{13}C-NMR (101 MHz, DMSO-d_6) of compound **8g**.



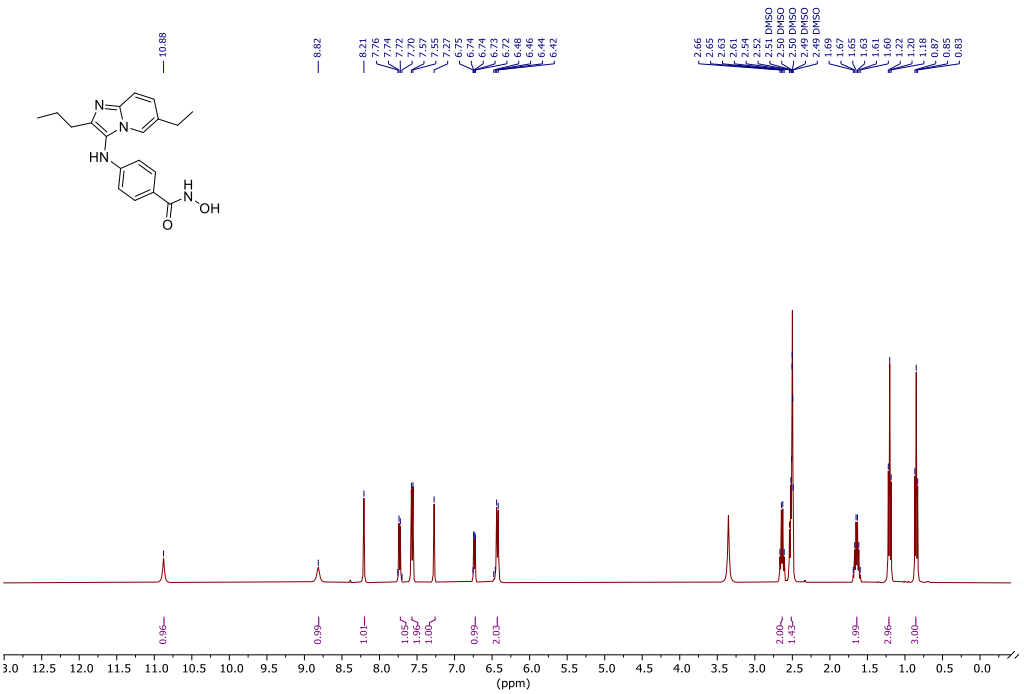
^{19}F-NMR (282 MHz, DMSO-d_6) of compound **8g**.



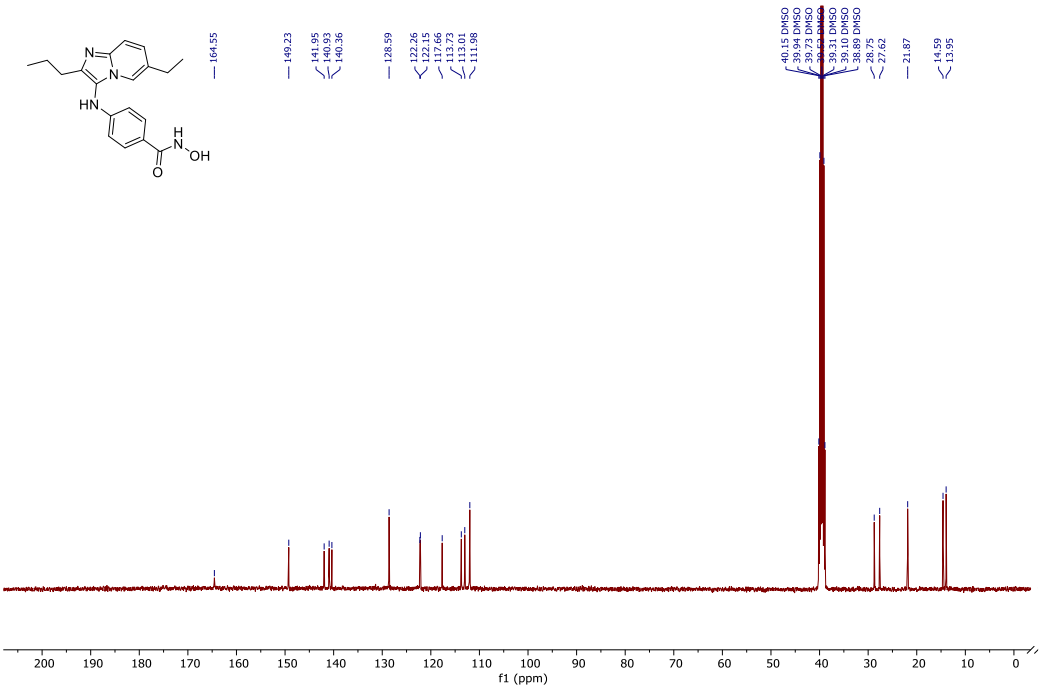
^{1}H-NMR (400 MHz, DMSO-d_6) of compound **8h**.



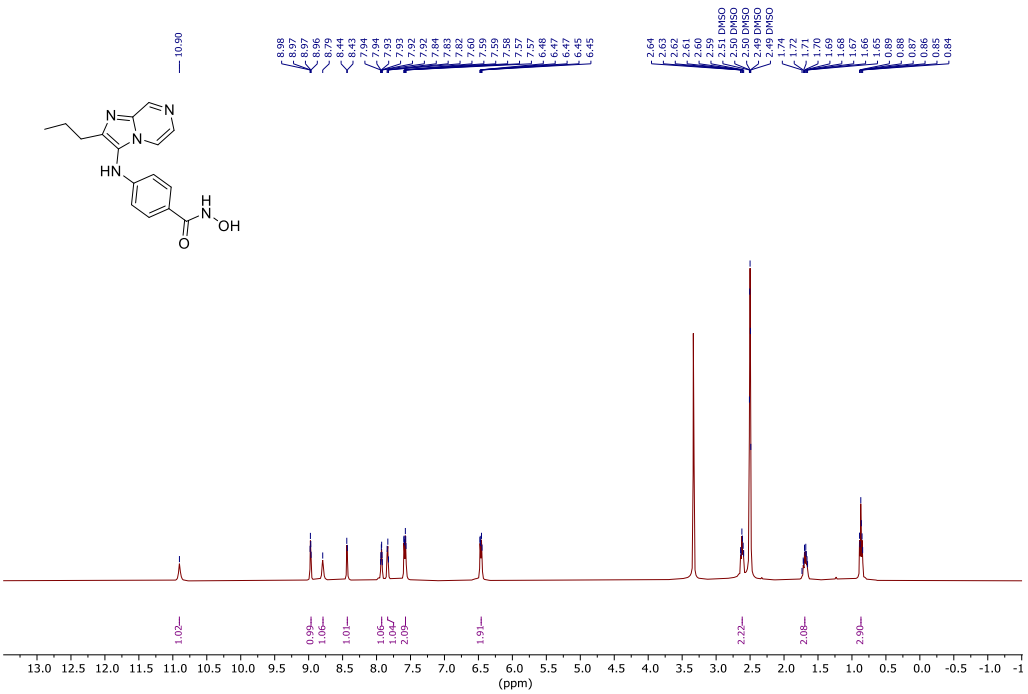
^{13}C-NMR (101 MHz, DMSO-d_6) of compound **8h**.



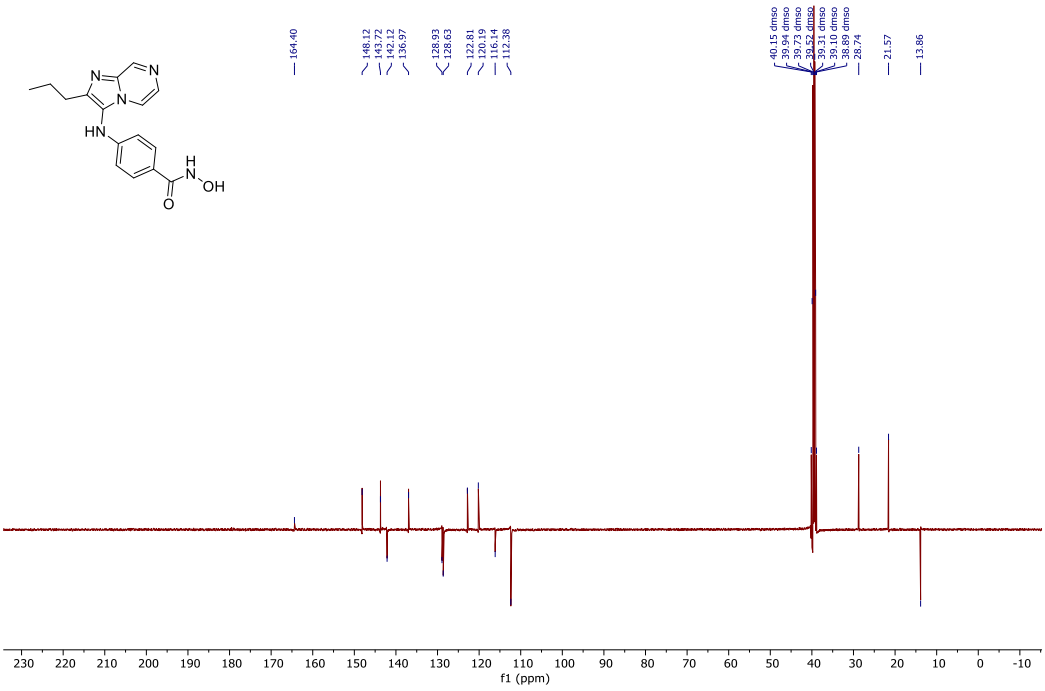
^{1}H-NMR (400 MHz, DMSO-d_6) of compound **8i**.



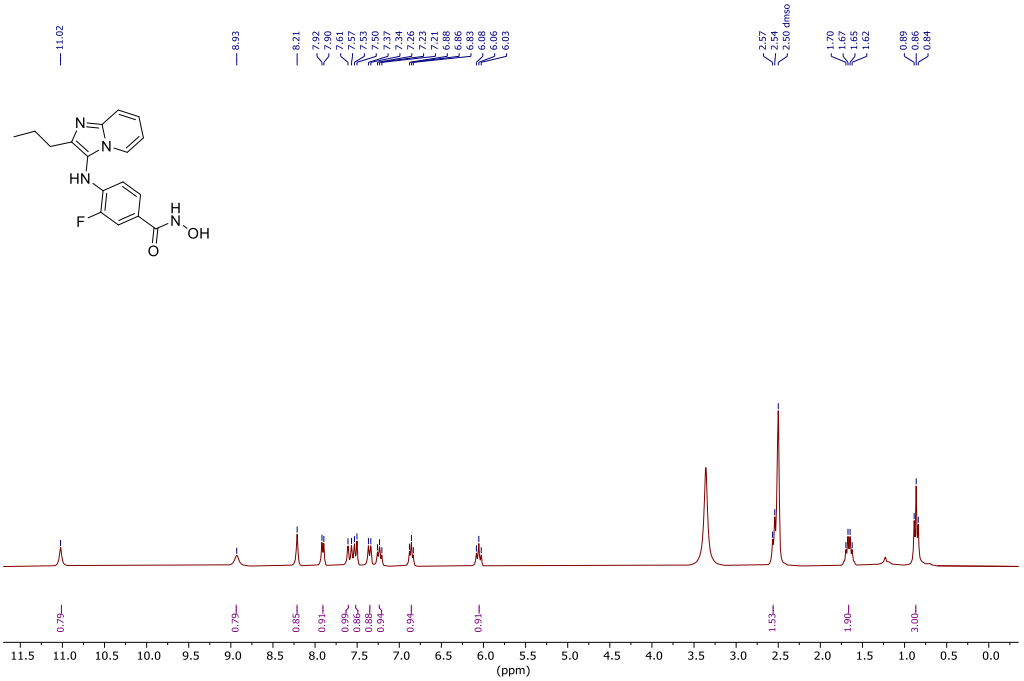
^{13}C-NMR (101 MHz, DMSO-d_6) of compound **8i**.



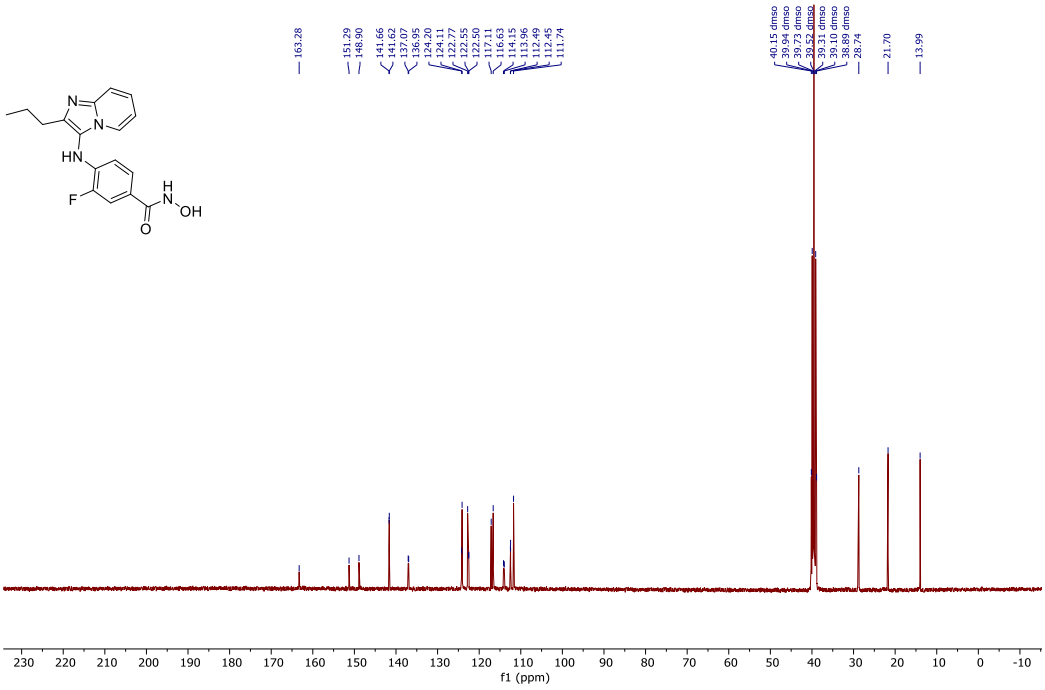
^{1}H-NMR (400 MHz, DMSO-d_6) of compound **8j**.



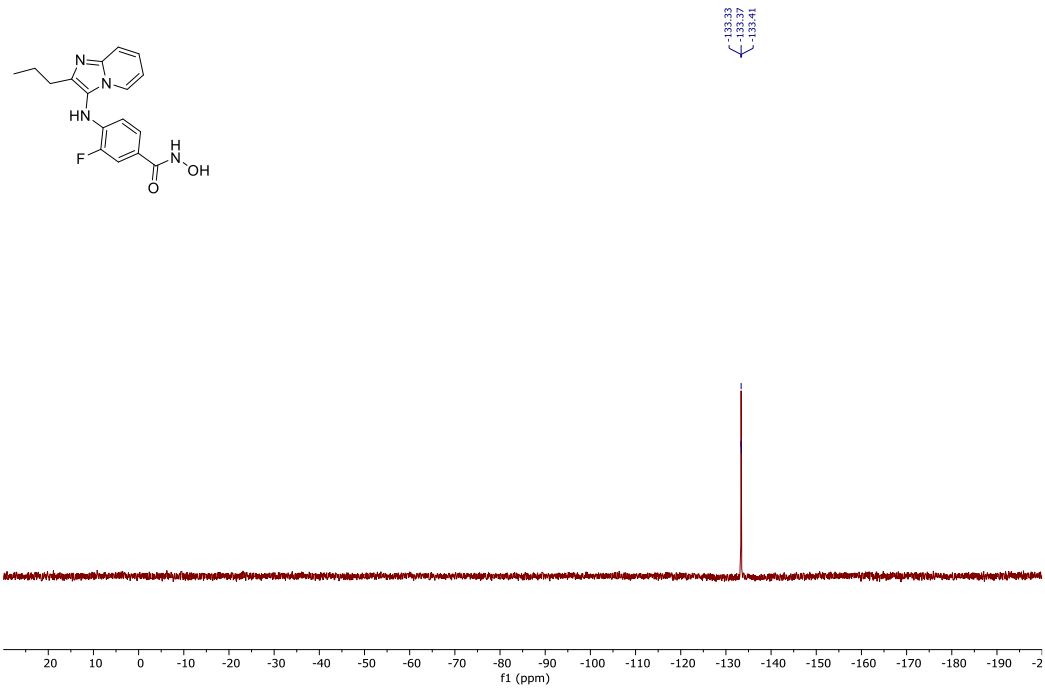
^{13}C-NMR APT (101 MHz, DMSO-d_6) of compound **8j**.



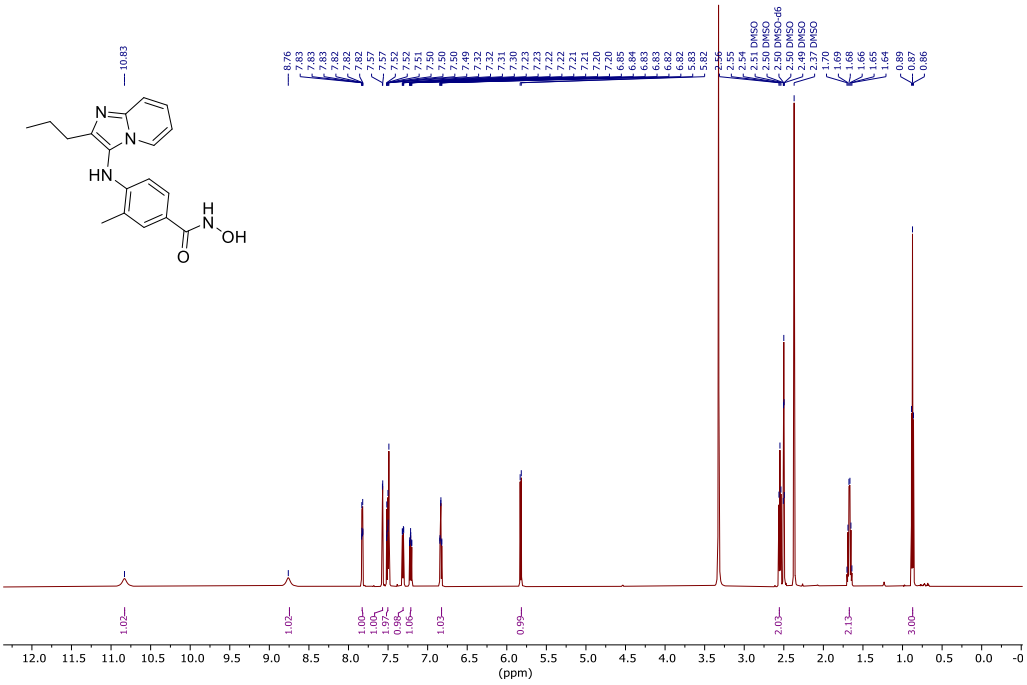
^{1}H-NMR (300 MHz, DMSO-d_6) of compound **8k**.



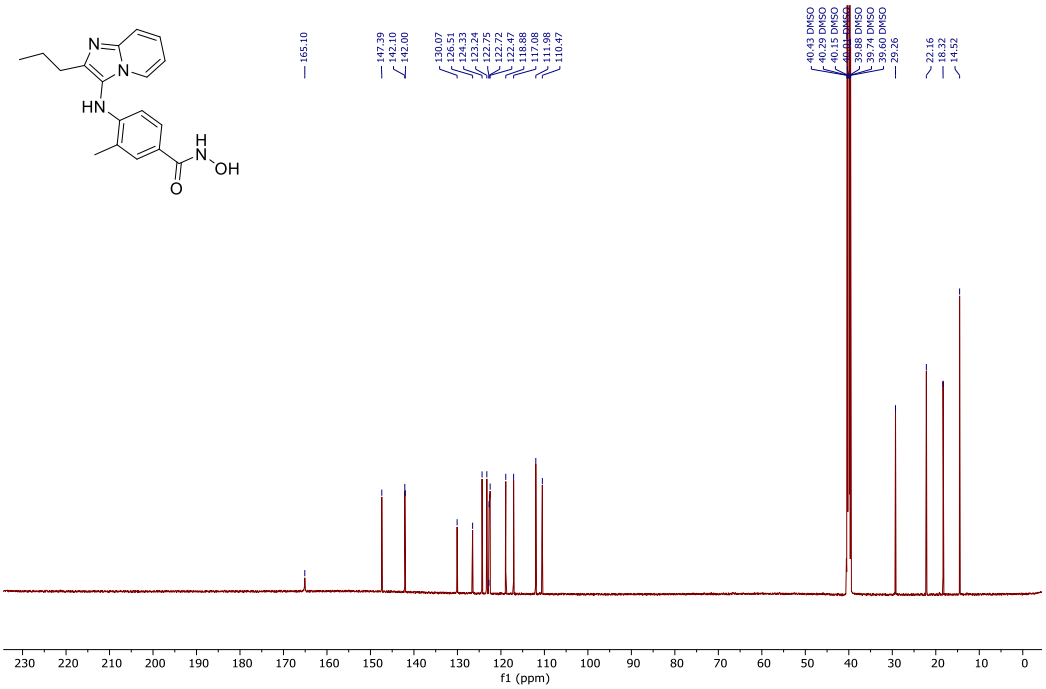
^{13}C-NMR (101 MHz, DMSO-d_6) of compound **8k**.



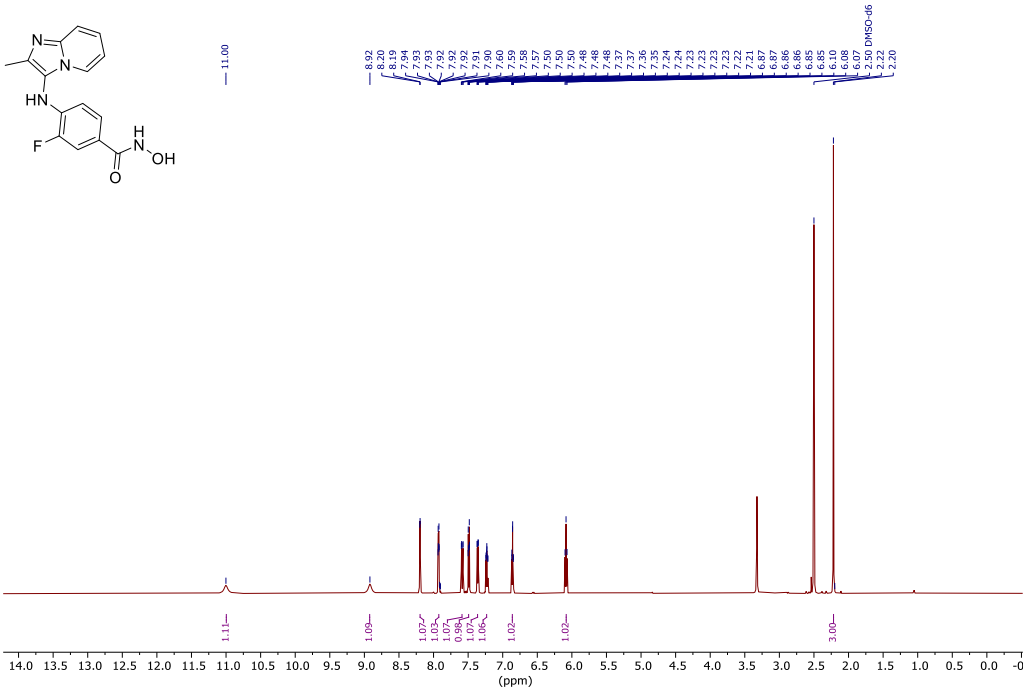
^{19}F-NMR (282 MHz, DMSO-d_6) of compound **8k**.



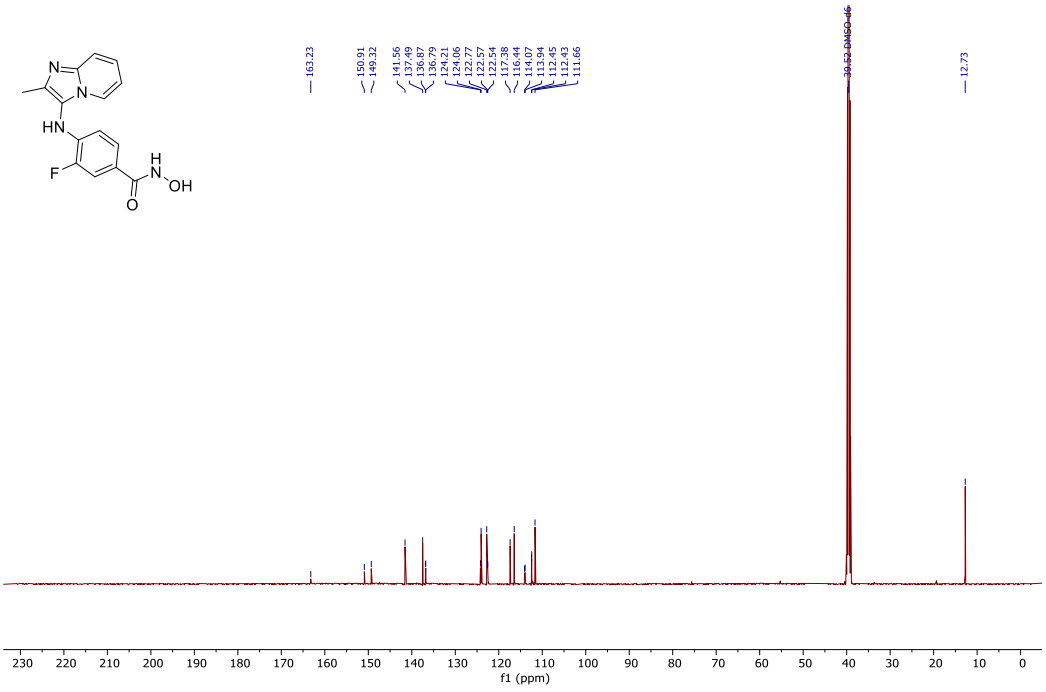
^{1}H-NMR (600 MHz, DMSO-d_6) of compound **8l**.



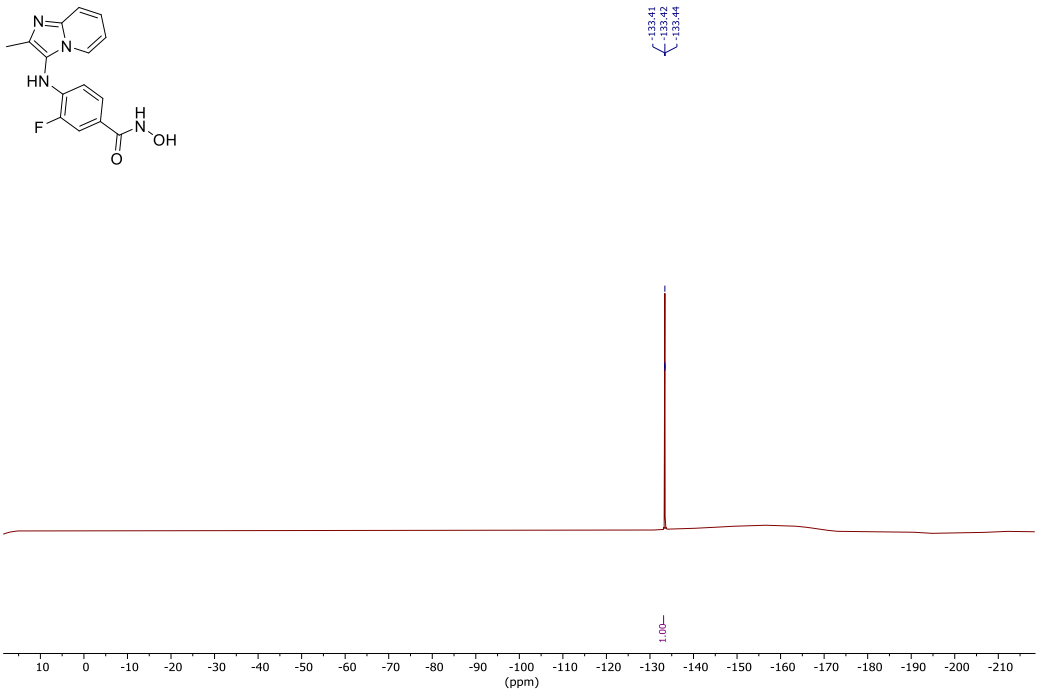
^{13}C-NMR (151 MHz, DMSO-d_6) of compound **8l.**



^{1}H-NMR (600 MHz, DMSO-d_6) of compound **8m**.

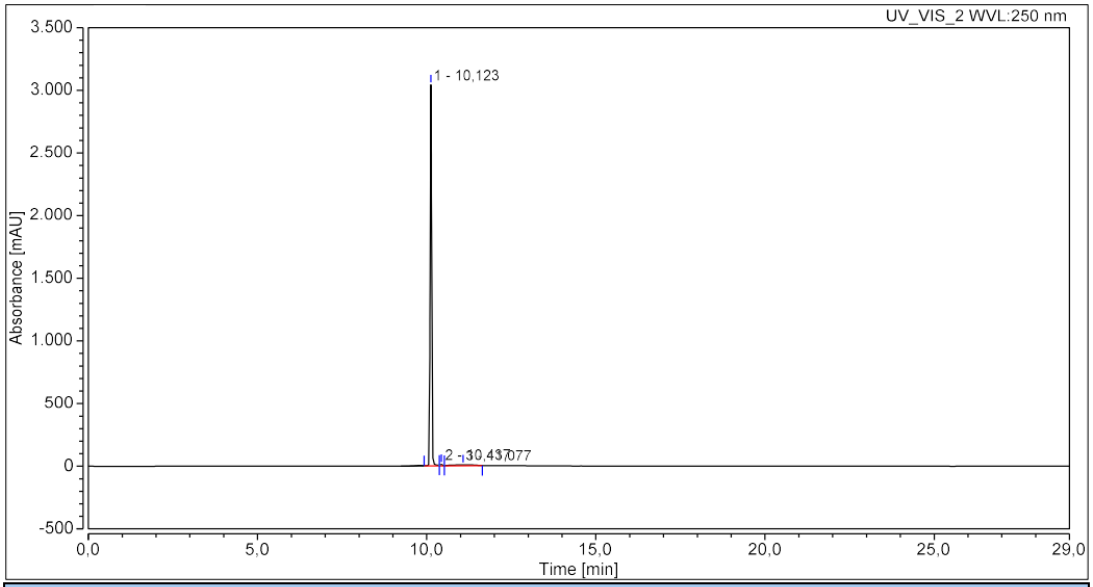


^{13}C-NMR (151 MHz, DMSO-d_6) of compound **8m**.



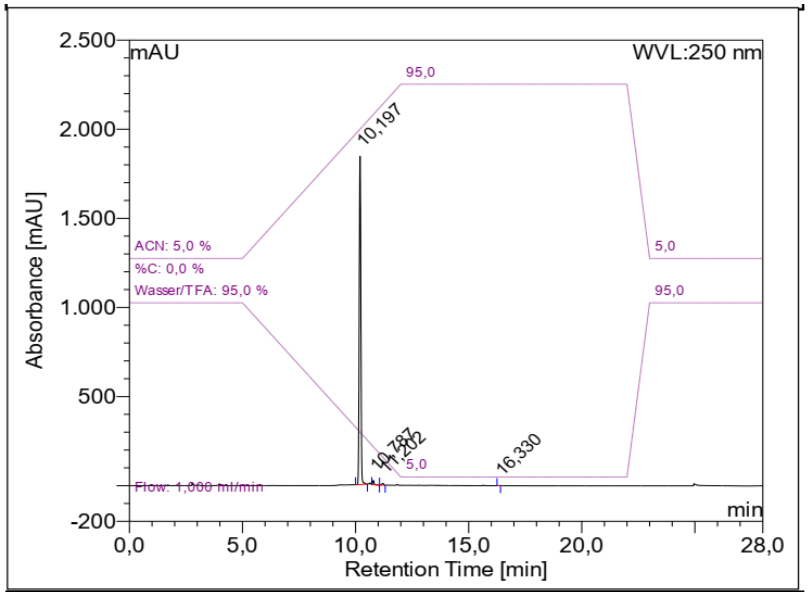
^{19}F-NMR (565 MHz, DMSO-d_6) of compound **8m**.

5 HPLC-Chromatograms



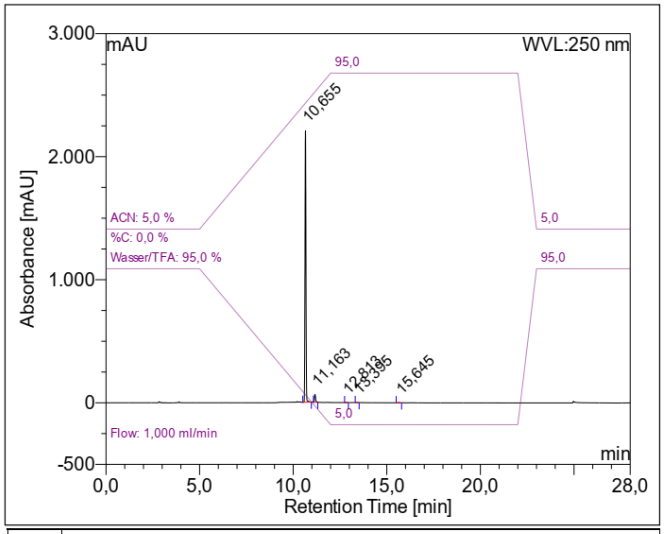
Integration Results							
No.	Peak Name	Retention Time min	Area mAU*min	Height mAU	Relative Area %	Relative Height %	Amount n.a.
1		10,123	151,116	3040,362	95,96	99,42	n.a.
2		10,437	1,002	11,286	0,64	0,37	n.a.
3		11,077	5,355	6,372	3,40	0,21	n.a.
Total:			**157,472**	**3058,021**	**100,00**	**100,00**	

HPLC chromatogram of compound **8a** (purity: 96.0%).



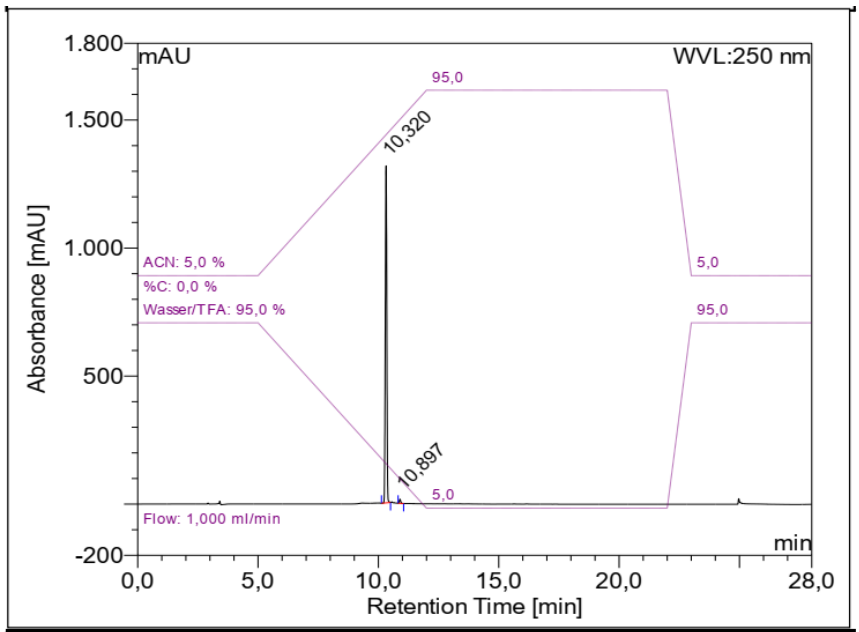
No.	Ret.Time min	Peak Name	Height mAU	Area mAU*min	Rel.Area %	Amount	Type
1	10,20	n.a.	#######	155,760	98,52	n.a.	BMB*
2	10,79	n.a.	23,354	1,475	0,93	n.a.	BMB*
3	11,20	n.a.	9,488	0,799	0,51	n.a.	BMB
4	16,33	n.a.	0,888	0,065	0,04	n.a.	BMB
Total:			#######	158,099	100,00	0,000	

HPLC chromatogram of compound **8b** (purity: 98.5%).



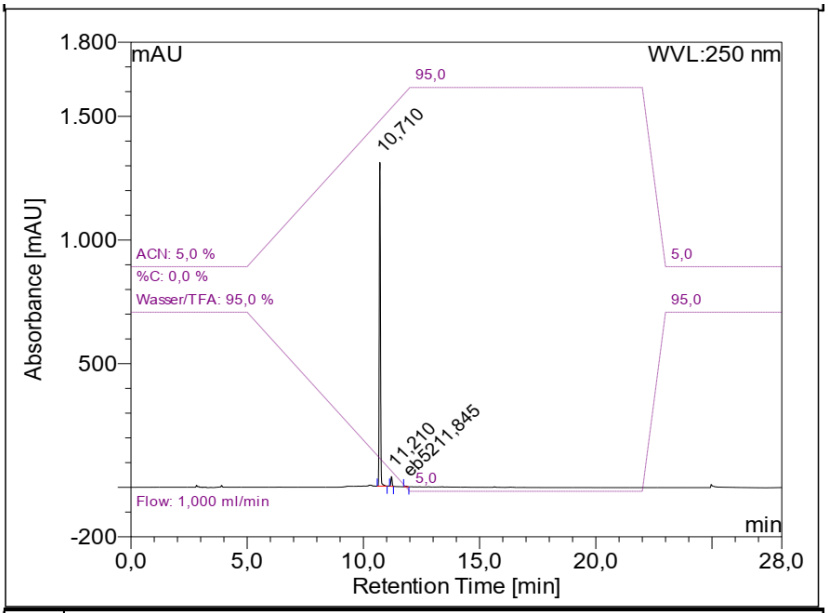
No.	Ret.Time min	Peak Name	Height mAU	Area mAU*min	Rel.Area %	Amount	Type
1	10,66	n.a.	#######	133,970	96,65	n.a.	BMB*
2	11,16	n.a.	63,205	4,349	3,14	n.a.	BMB*
3	12,81	n.a.	0,965	0,071	0,05	n.a.	BMB
4	13,40	n.a.	0,655	0,059	0,04	n.a.	BMB
5	15,65	n.a.	1,956	0,166	0,12	n.a.	BMB
Total:			#######	138,616	100,00	0,000	

HPLC chromatogram of compound **8c** (purity: 96.8%).



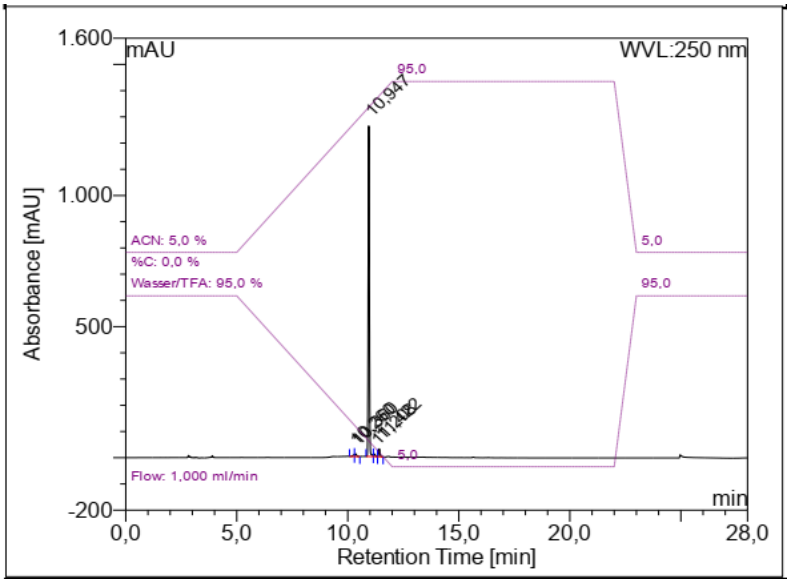
No.	Ret.Time min	Peak Name	Height mAU	Area mAU*min	Rel.Area %	Amount	Type
1	10,32	n.a.	#######	95,769	98,97	n.a.	BMB*
2	10,90	n.a.	15,982	1,001	1,03	n.a.	BMB
Total:			#######	96,770	100,00	0,000	

HPLC chromatogram of compound **8d** (purity: 99.0%).



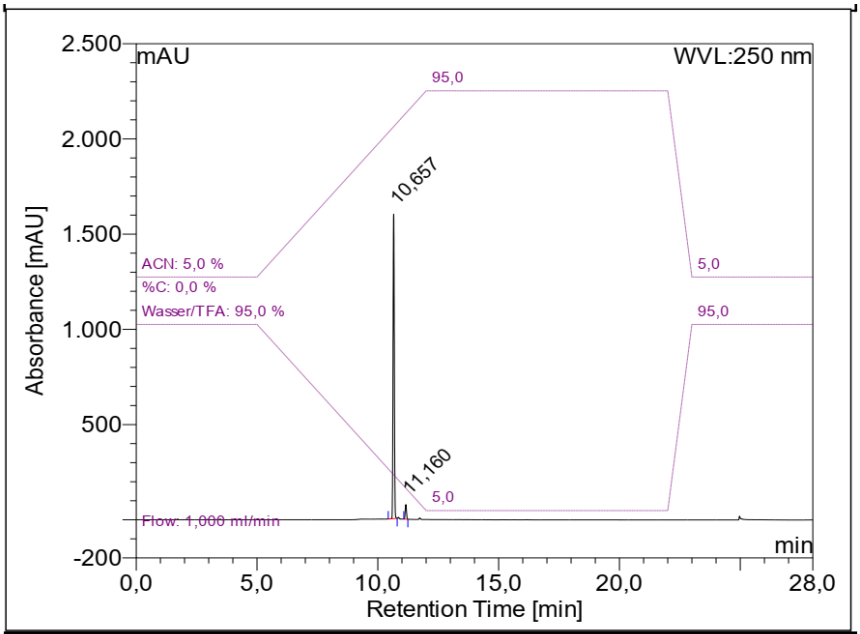
No.	Ret.Time min	Peak Name	Height mAU	Area mAU*min	Rel.Area %	Amount	Type
1	10,71	n.a.	########	80,031	96,79	n.a.	BMB
2	11,21	n.a.	39,665	2,421	2,93	n.a.	BMB
3	11,85	eb52	2,469	0,233	0,28	n.a.	BMB
Total:			#######	82,686	100,00	0,000	

HPLC chromatogram of compound **8e** (purity: 96.8%).



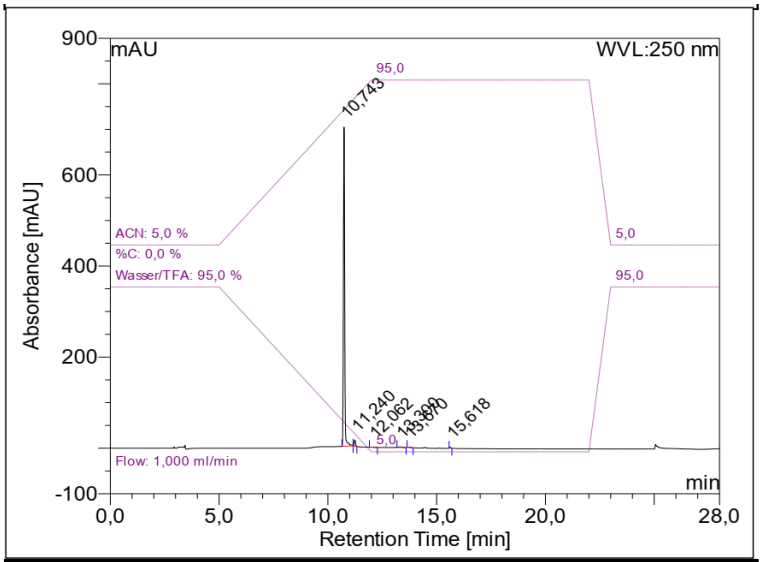
No.	Ret.Time min	Peak Name	Height mAU	Area mAU*min	Rel.Area %	Amount	Type
1	10,26	n.a.	6,447	0,556	0,68	n.a.	BM
2	10,36	n.a.	10,376	0,900	1,10	n.a.	MB
3	10,95	n.a.	#######	77,922	95,04	n.a.	BM
4	11,21	n.a.	9,569	0,715	0,87	n.a.	MB
5	11,42	n.a.	29,838	1,899	2,32	n.a.	BMB
Total:			#######	81,992	100,00	0,000	

HPLC chromatogram of compound **8f** (purity: 95.0%).



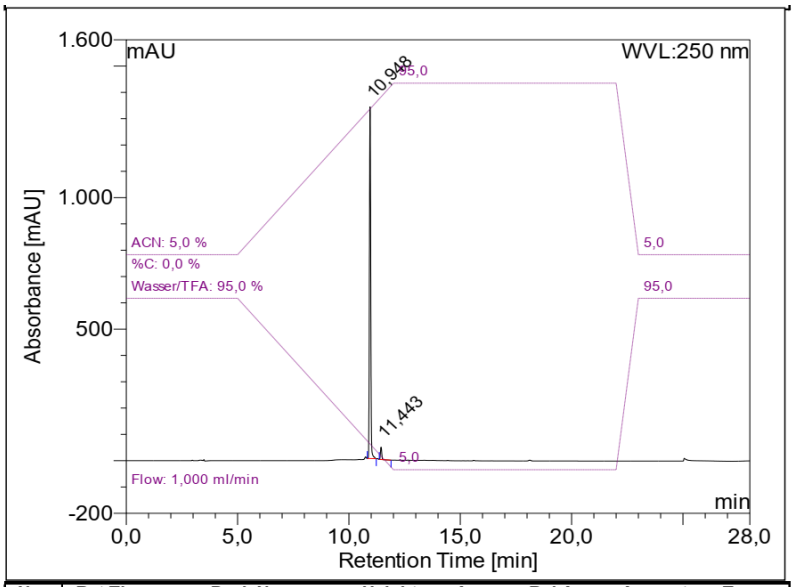
No.	Ret.Time min	Peak Name	Height mAU	Area mAU*min	Rel.Area %	Amount	Type
1	10,66	n.a.	#######	97,633	95,42	n.a.	BMB*
2	11,16	n.a.	76,602	4,691	4,58	n.a.	BMB
Total:			#######	102,324	100,00	0,000	

HPLC chromatogram of compound **8g** (purity: 95.4%).



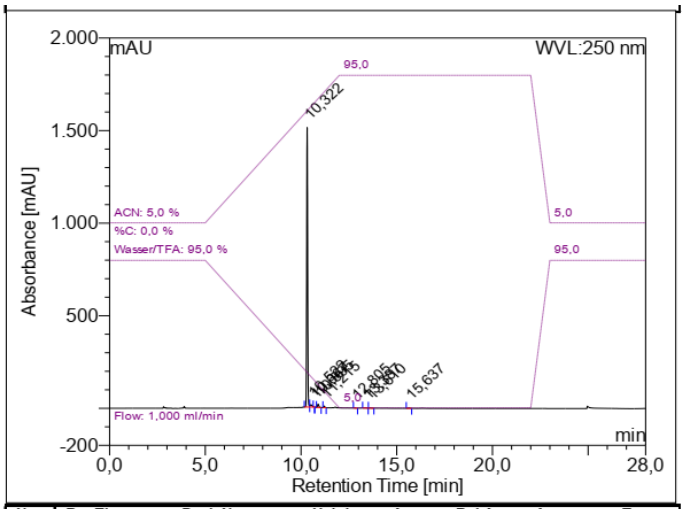
No.	Ret.Time min	Peak Name	Height mAU	Area mAU*min	Rel.Area %	Amount	Type
1	10,74	n.a.	700,562	47,730	97,38	n.a.	BMb
2	11,24	n.a.	13,188	0,894	1,82	n.a.	bMB
3	12,06	n.a.	0,305	0,020	0,04	n.a.	BMB*
4	13,30	n.a.	1,125	0,153	0,31	n.a.	BMB*
5	13,67	n.a.	0,317	0,089	0,18	n.a.	BMB*
6	15,62	n.a.	2,018	0,126	0,26	n.a.	BMB*
Total:			717,514	49,013	100,00	0,000	

HPLC chromatogram of compound **8h** (purity: 97.4%).



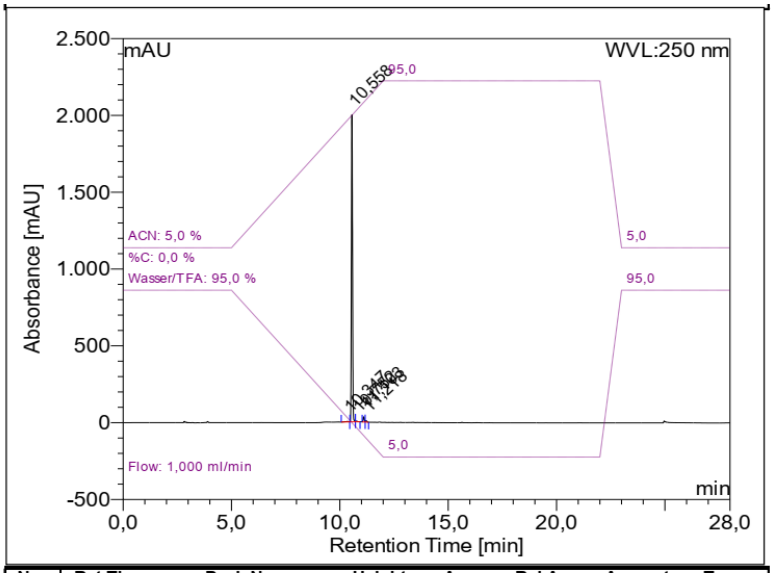
No.	Ret.Time min	Peak Name	Height mAU	Area mAU*min	Rel.Area %	Amount	Type
1	10,95	n.a.	########	91,455	96,79	n.a.	BMB*
2	11,44	n.a.	47,129	3,036	3,21	n.a.	BMB*
Total:			########	94,491	100,00	0,000	

HPLC chromatogram of compound **8i** (purity: 96.8%).



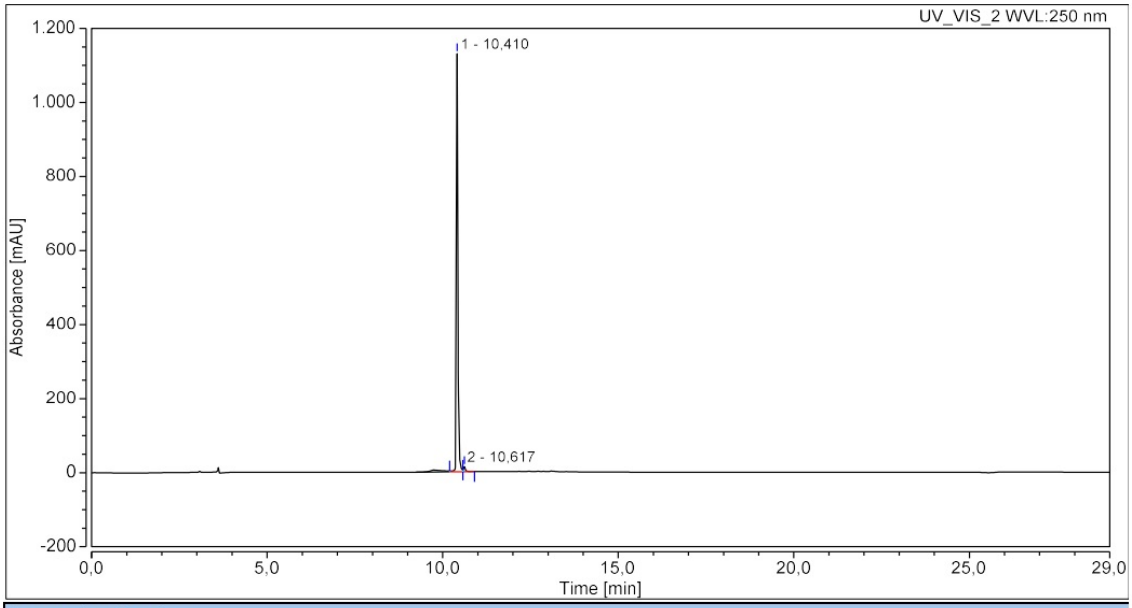
No.	Ret.Time min	Peak Name	Height mAU	Area mAU*min	Rel.Area %	Amount	Type
1	10,32	n.a.	#######	90,189	95,85	n.a.	BM
2	10,52	n.a.	13,076	1,523	1,62	n.a.	MB
3	10,67	n.a.	1,266	0,049	0,05	n.a.	Rd
4	10,90	n.a.	17,593	1,329	1,41	n.a.	BMB
5	11,22	n.a.	8,622	0,537	0,57	n.a.	BMB
6	12,81	n.a.	0,979	0,071	0,08	n.a.	BMB
7	13,39	n.a.	0,865	0,095	0,10	n.a.	BMB
8	13,61	n.a.	1,085	0,137	0,15	n.a.	BMB
9	15,64	n.a.	1,954	0,166	0,18	n.a.	BMB
Total:			#######	94,097	100,00	0,000	

HPLC chromatogram of compound **8j** (purity: 95.8%).



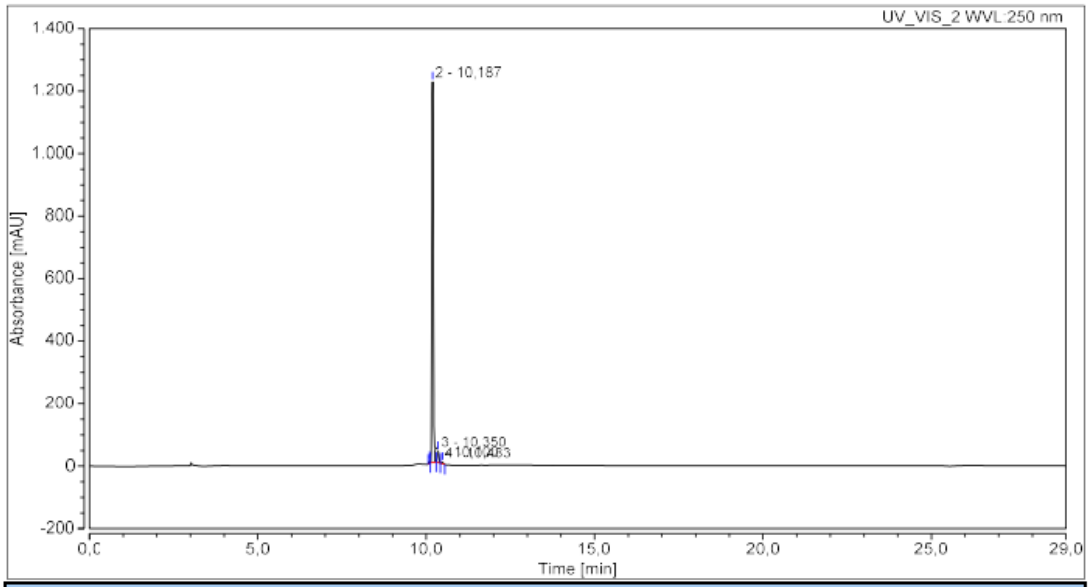
No.	Ret.Time min	Peak Name	Height mAU	Area mAU*min	Rel.Area %	Amount	Type
1	10,35	n.a.	3,327	0,489	0,39	n.a.	BMB
2	10,56	n.a.	#######	121,652	97,03	n.a.	BM
3	10,75	n.a.	5,510	0,508	0,40	n.a.	MB
4	11,10	n.a.	34,378	2,084	1,66	n.a.	BM
5	11,22	n.a.	9,197	0,647	0,52	n.a.	MB
Total:			#######	125,380	100,00	0,000	

HPLC chromatogram of compound **8k** (purity: 97.0%).



Integration Results							
No.	Peak Name	Retention Time min	Area mAU*min	Height mAU	Relative Area %	Relative Height %	Amount n.a.
1		10,410	57,491	1129,260	98,55	98,80	n.a.
2		10,617	0,845	13,717	1,45	1,20	n.a.
Total:			**58,336**	**1142,977**	**100,00**	**100,00**	

HPLC chromatogram of compound **8l** (purity: 98.6%).

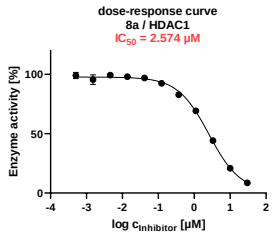


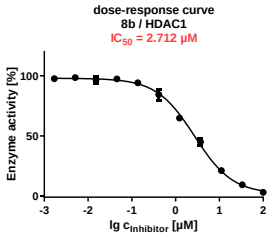
Integration Results

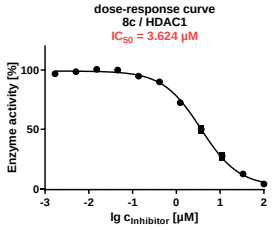
No.	Peak Name	Retention Time min	Area mAU*min	Height mAU	Relative Area %	Relative Height %	Amount n.a.
1		10,100	0,237	6,256	0,41	0,49	n.a.
2		10,187	55,066	1217,831	96,10	96,23	n.a.
3		10,350	1,702	36,241	2,97	2,86	n.a.
4		10,483	0,296	5,202	0,52	0,41	n.a.
Total:			**57,301**	**1265,530**	**100,00**	**100,00**	

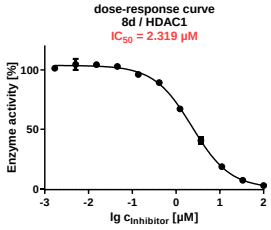
HPLC chromatogram of compound **8m** (purity: 96.1%).

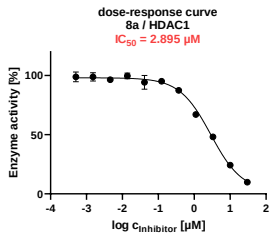
6 Dose-Response-Curves of the *In Vitro* HDAC Inhibition Assay

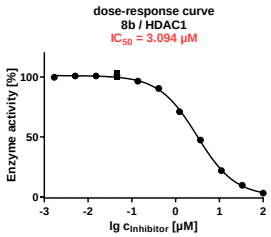


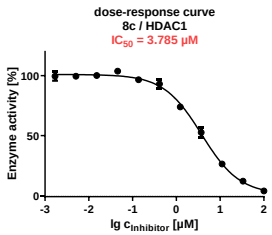


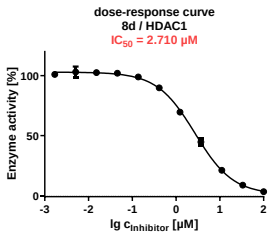


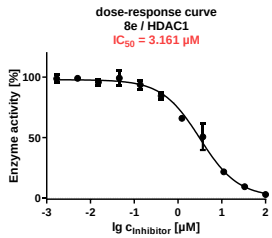


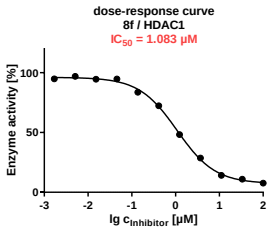


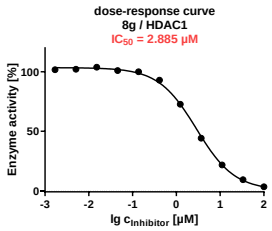


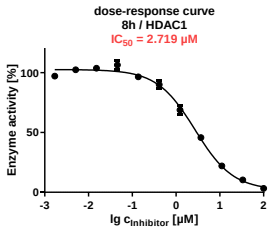


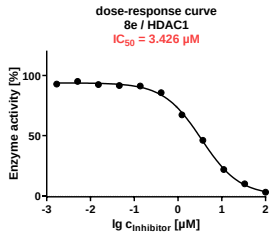


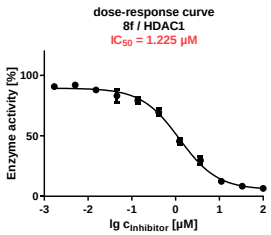


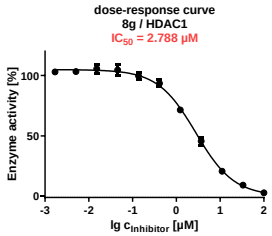


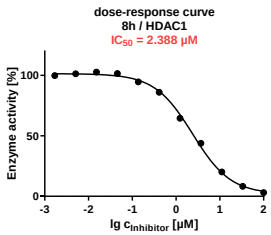


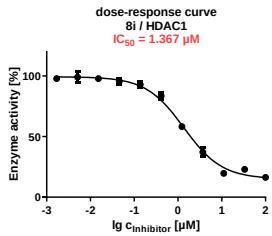


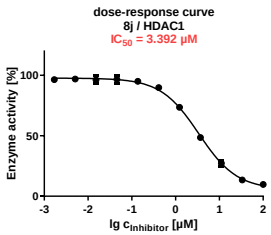


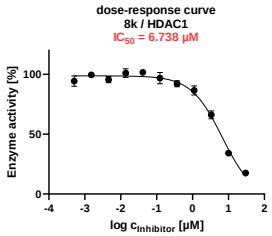


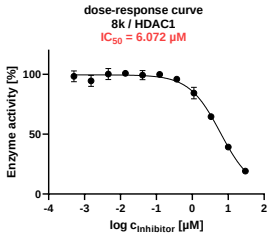


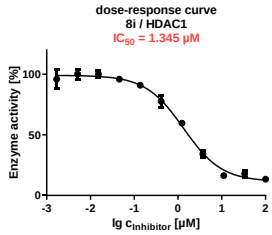


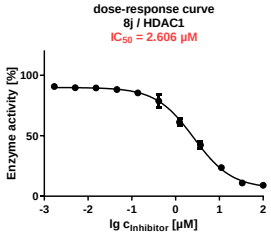


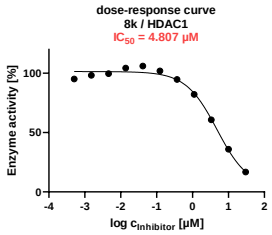


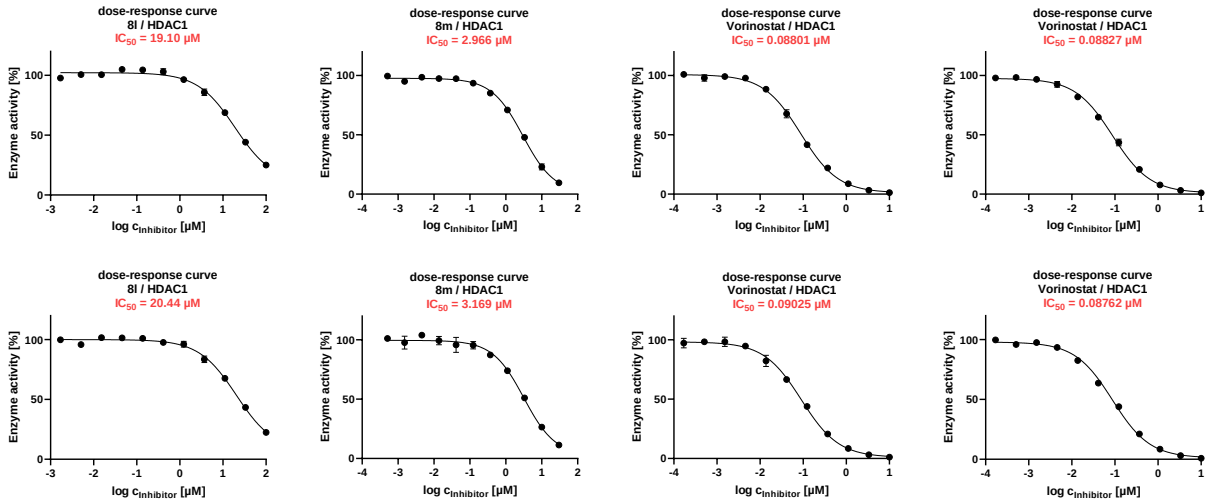




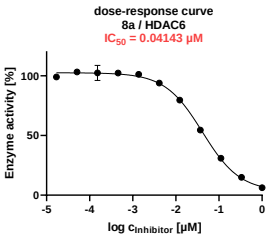


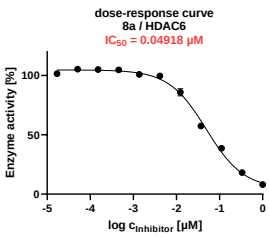


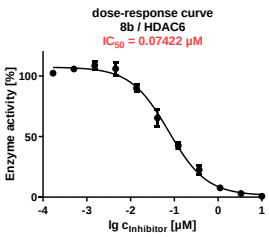


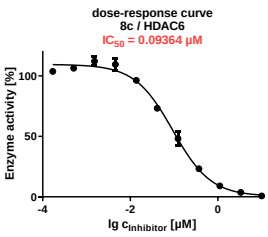


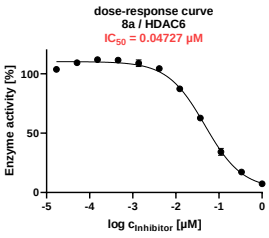
Normalized dose-response curves of the *in vitro* HDAC inhibition assay against HDAC1 for compounds **8a-m**. Data points are depicted as black dots including the respective error bars (standard deviation). In some cases, more than two experiments were performed. Additionally, depending on the plate layout and the quantity of the investigated compounds, not all compounds were investigated in one assay run. Vorinostat was included in every assay run as a control compound.

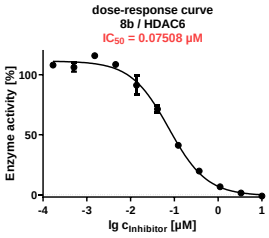

dose-response curve
8a / HDAC6
IC50 = 0.04143 µM
Enzyme activity [%]
log cInhibitor [µM]

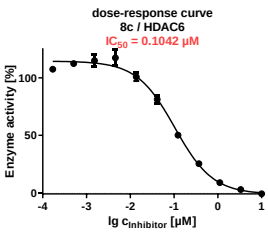

dose-response curve
8a / HDAC6
IC50 = 0.04918 µM
Enzyme activity [%]
log cInhibitor [µM]

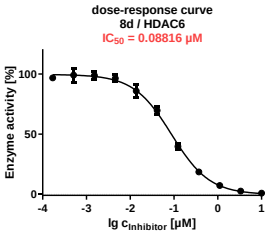

dose-response curve
8b / HDAC6
IC50 = 0.07422 µM
Enzyme activity [%]
lg cInhibitor [µM]

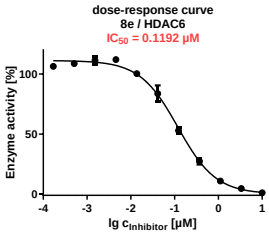

dose-response curve
8c / HDAC6
IC50 = 0.09364 µM
Enzyme activity [%]
lg cInhibitor [µM]

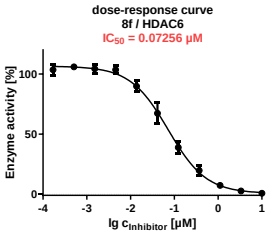

dose-response curve
8a / HDAC6
IC50 = 0.04727 µM
Enzyme activity [%]
log cInhibitor [µM]

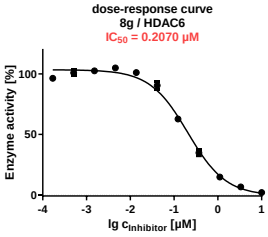

dose-response curve
8b / HDAC6
IC50 = 0.07508 µM
Enzyme activity [%]
lg cInhibitor [µM]

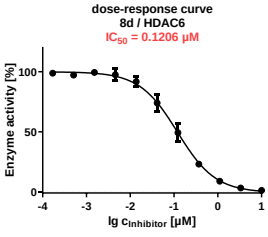

dose-response curve
8c / HDAC6
IC50 = 0.1042 µM
Enzyme activity [%]
lg cInhibitor [µM]

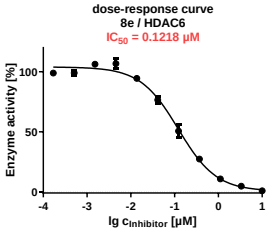

dose-response curve
8d / HDAC6
IC50 = 0.08816 µM
Enzyme activity [%]
lg cInhibitor [µM]

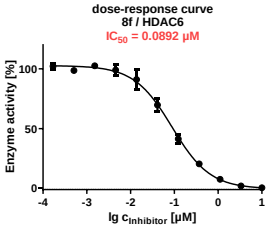

dose-response curve
8e / HDAC6
IC50 = 0.1192 µM
Enzyme activity [%]
lg cInhibitor [µM]

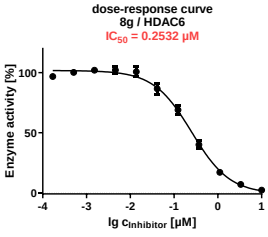

dose-response curve
8f / HDAC6
IC50 = 0.07256 µM
Enzyme activity [%]
lg cInhibitor [µM]

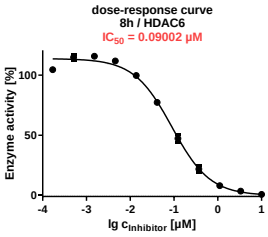

dose-response curve
8g / HDAC6
IC50 = 0.2070 µM
Enzyme activity [%]
lg cInhibitor [µM]

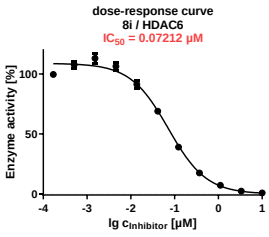

dose-response curve
8d / HDAC6
IC50 = 0.1206 µM
Enzyme activity [%]
lg cInhibitor [µM]

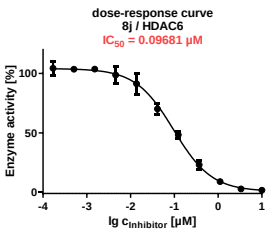

dose-response curve
8e / HDAC6
IC50 = 0.1218 µM
Enzyme activity [%]
lg cInhibitor [µM]

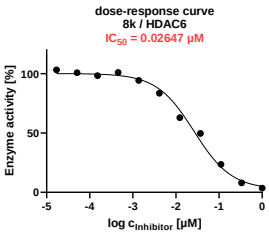

dose-response curve
8f / HDAC6
IC50 = 0.0892 µM
Enzyme activity [%]
lg cInhibitor [µM]

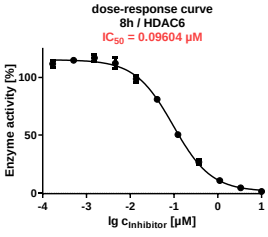

dose-response curve
8g / HDAC6
IC50 = 0.2532 µM
Enzyme activity [%]
lg cInhibitor [µM]

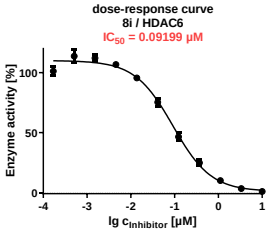

dose-response curve
8h / HDAC6
IC50 = 0.09002 µM
Enzyme activity [%]
lg cInhibitor [µM]

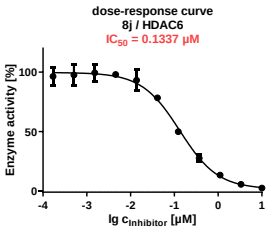

dose-response curve
8i / HDAC6
IC50 = 0.07212 µM
Enzyme activity [%]
lg cInhibitor [µM]

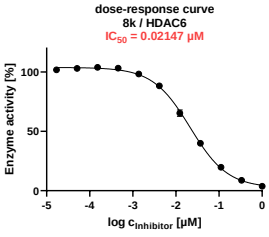

dose-response curve
8j / HDAC6
IC50 = 0.09681 µM
Enzyme activity [%]
lg cInhibitor [µM]

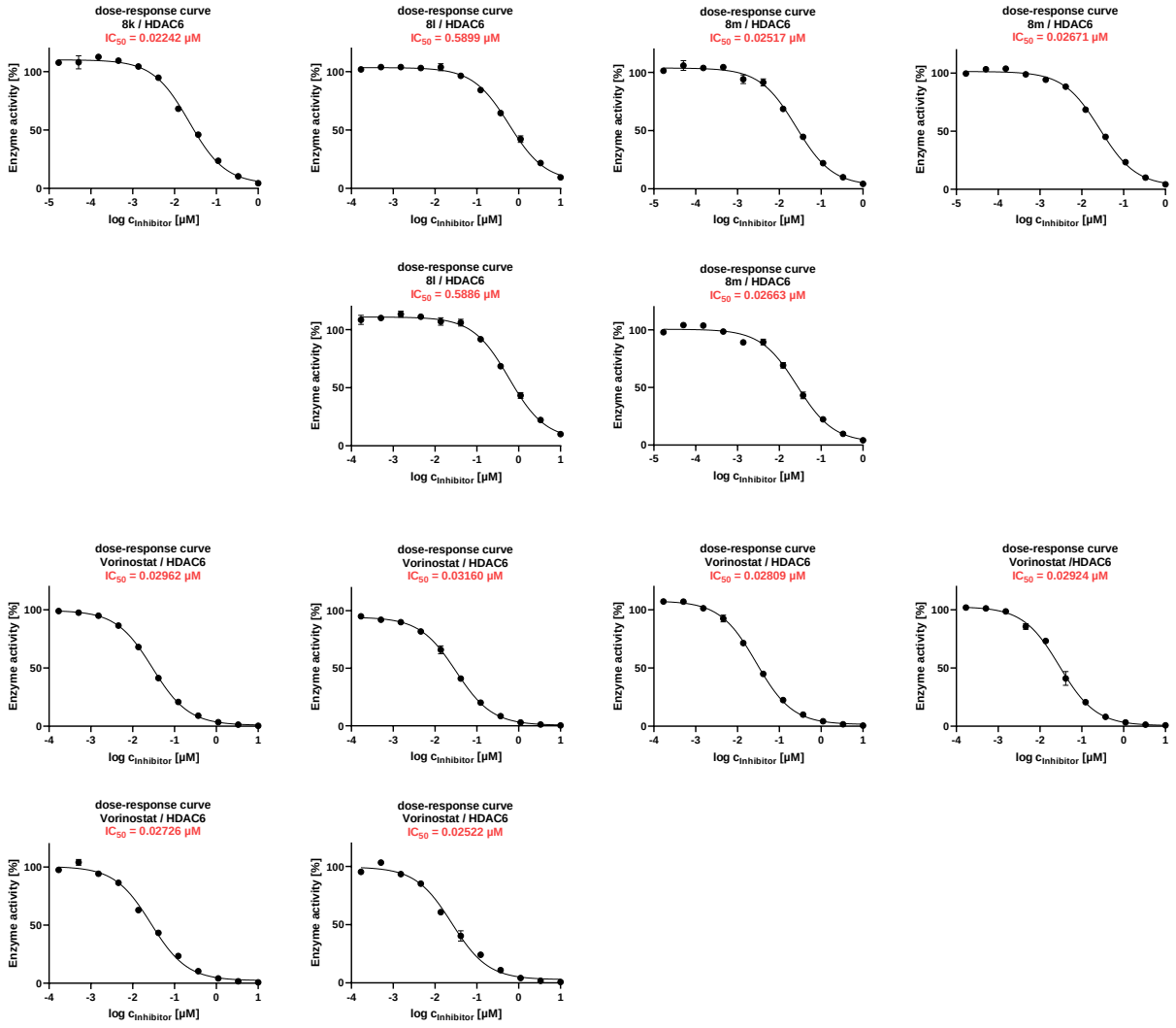

dose-response curve
8k / HDAC6
IC50 = 0.02647 µM
Enzyme activity [%]
log cInhibitor [µM]


dose-response curve
8h / HDAC6
IC50 = 0.09604 µM
Enzyme activity [%]
lg cInhibitor [µM]

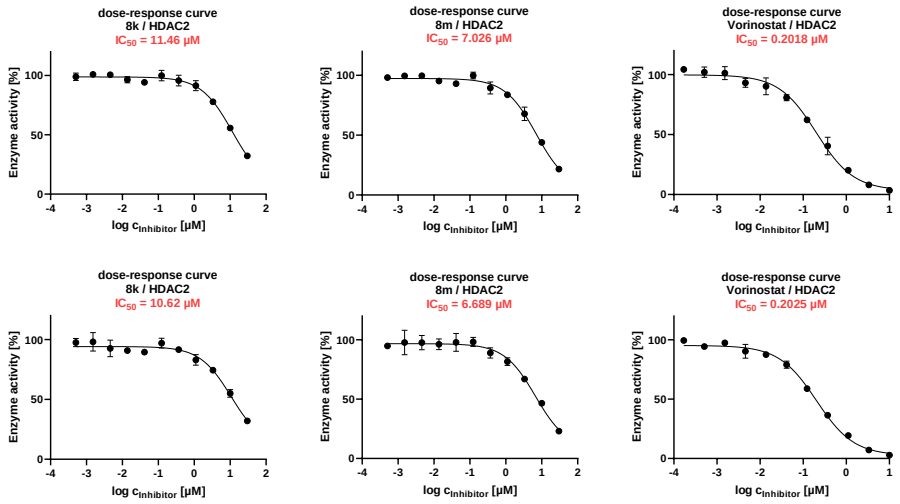

dose-response curve
8i / HDAC6
IC50 = 0.09199 µM
Enzyme activity [%]
lg cInhibitor [µM]


dose-response curve
8j / HDAC6
IC50 = 0.1337 µM
Enzyme activity [%]
lg cInhibitor [µM]

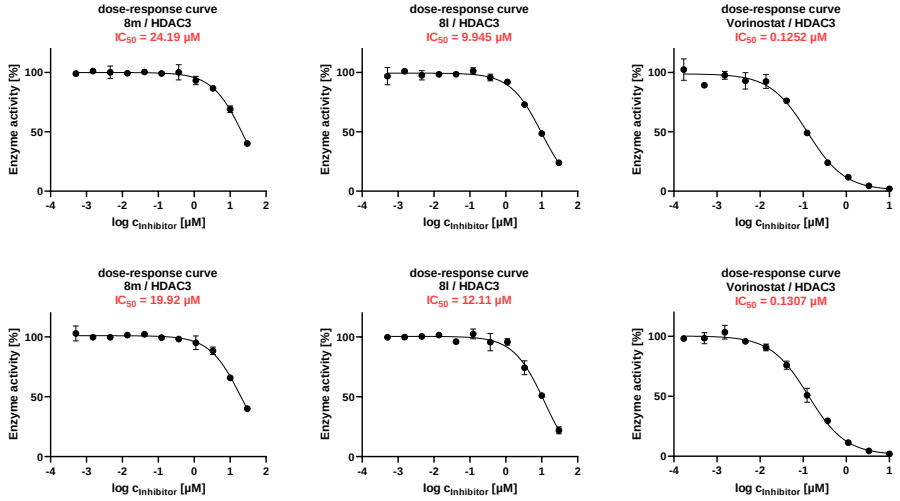

dose-response curve
8k / HDAC6
IC50 = 0.02147 µM
Enzyme activity [%]
log cInhibitor [µM]



Normalized dose-response curves of the *in vitro* HDAC inhibition assay against HDAC6 for compounds **8a-m**. Data points are depicted as black dots including the respective error bars (standard deviation). In some cases, more than two experiments were performed. Additionally, depending on the plate layout and the quantity of the investigated compounds, not all compounds were investigated in one assay run. Vorinostat was included in every assay run as a control compound.



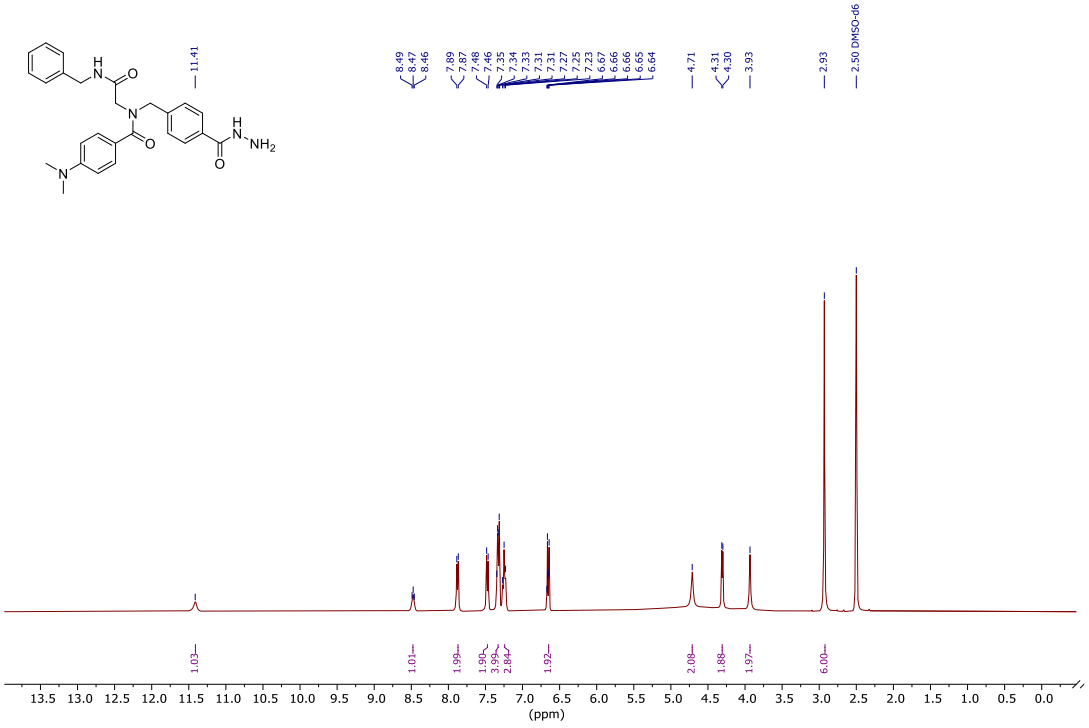
Normalized dose-response curves of the *in vitro* HDAC inhibition assay against HDAC2 for hit compounds **8k** and **8m**. Data points are depicted as black dots including the respective error bars (standard deviation). Vorinostat was included as a control compound.



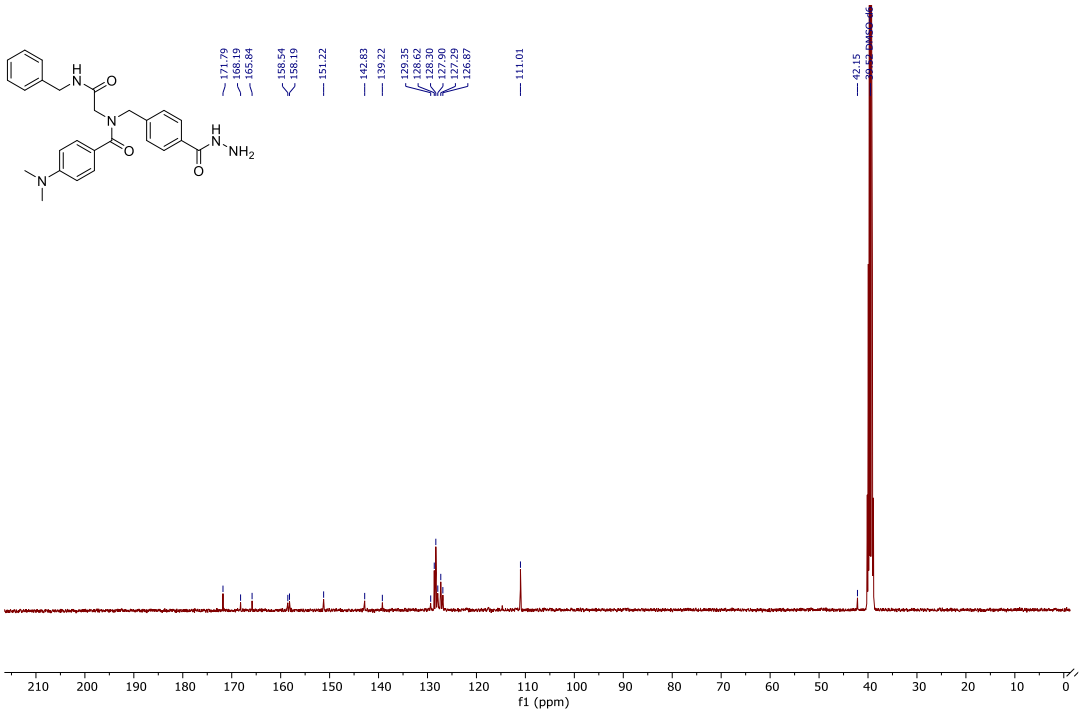
Normalized dose-response curves of the *in vitro* HDAC inhibition assay against HDAC3 for hit compounds **8k** and **8m**. Data points are depicted as black dots including the respective error bars (standard deviation). Vorinostat was included as a control compound.

8.2 Appendix II. Supporting Information of chapter 3 "Hydrazide-based class I HDAC inhibitors with HDAC3 preference completely reverse chemoresistance in a synergistic manner in platinum-resistant solid cancer cells"

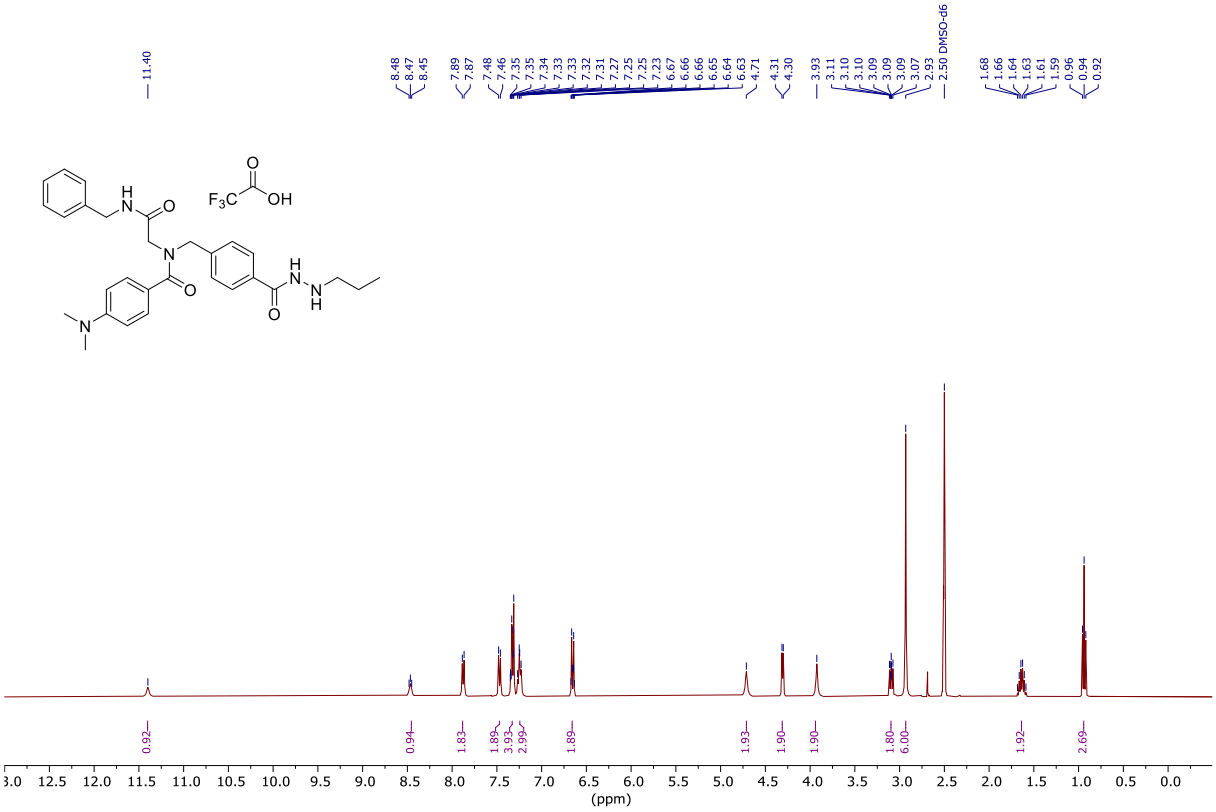
The following pages include ^{1}H-, ^{13}C-, and ^{19}F-NMR spectra of newly synthesized compounds and HPLC chromatograms of all final compounds reported in chapter 3.



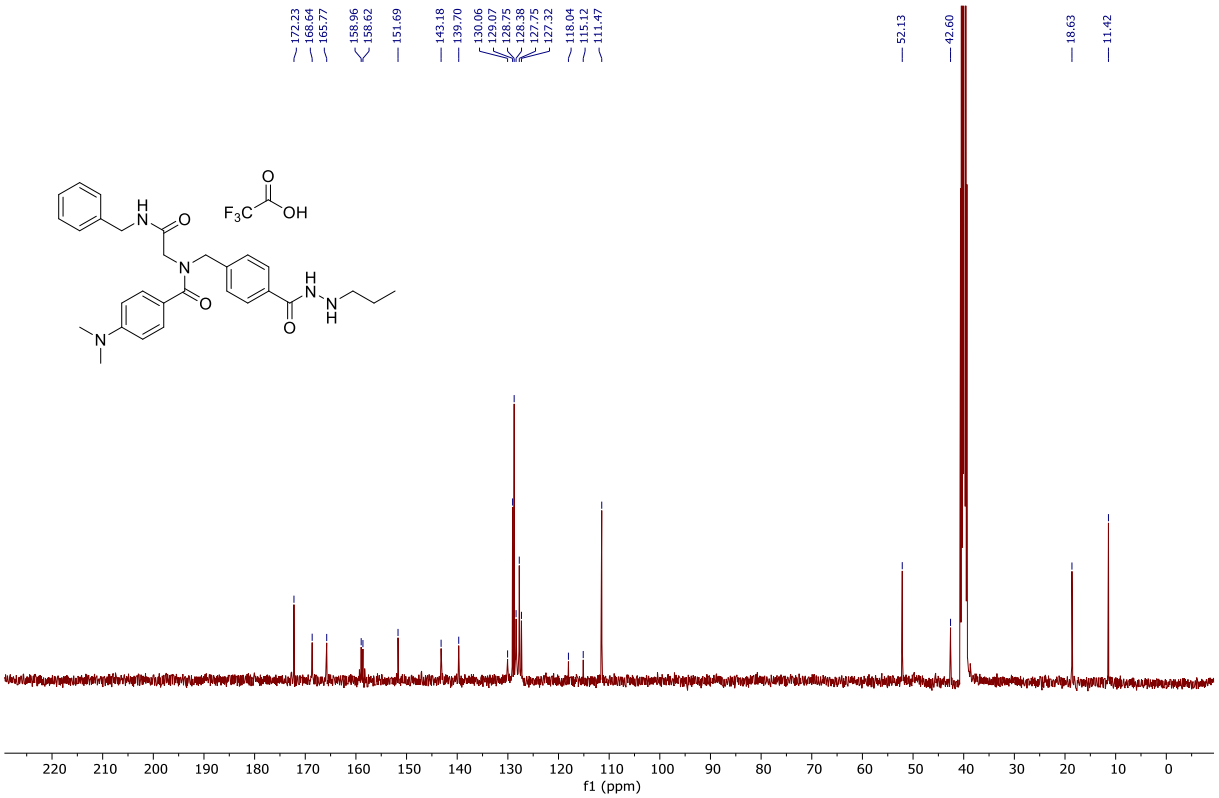
^{1}H-NMR (400 MHz, DMSO-d_6) of compound **4**.



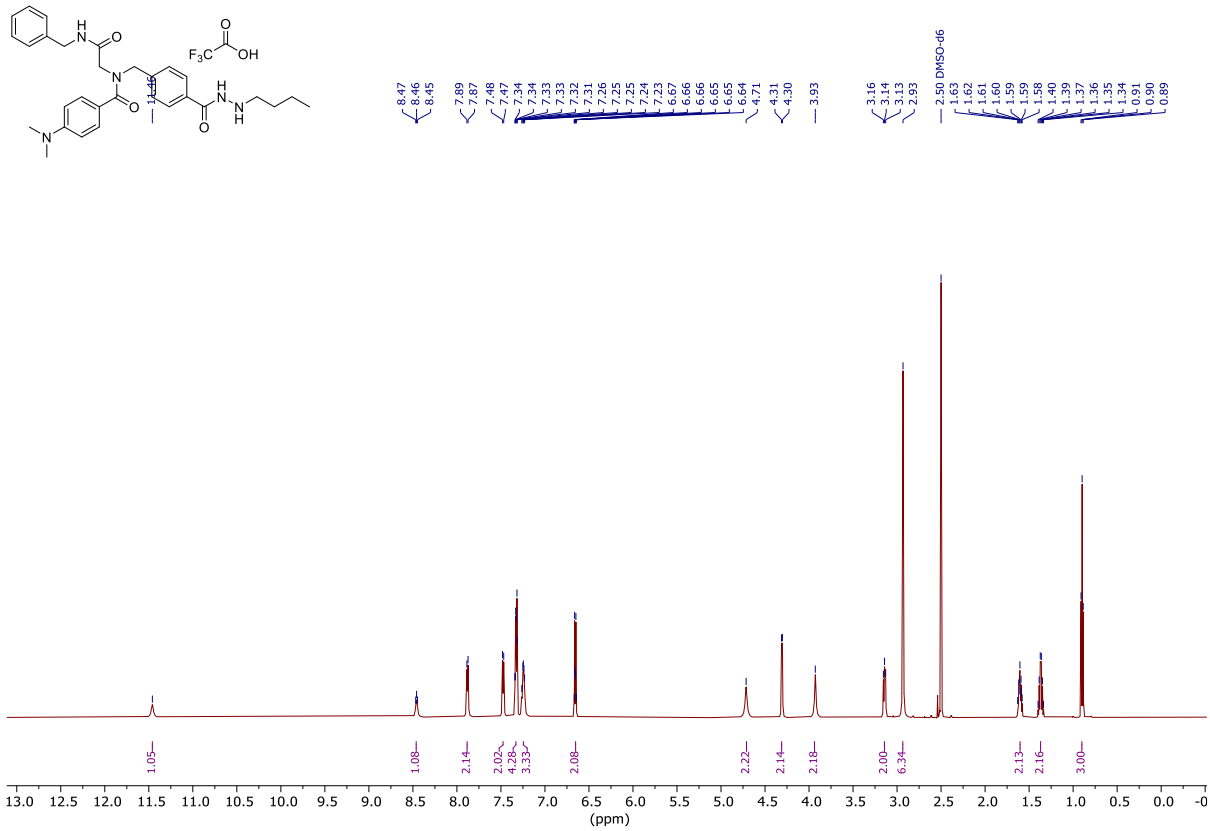
^{13}C-NMR (101 MHz, DMSO-d_6) of compound **4**.



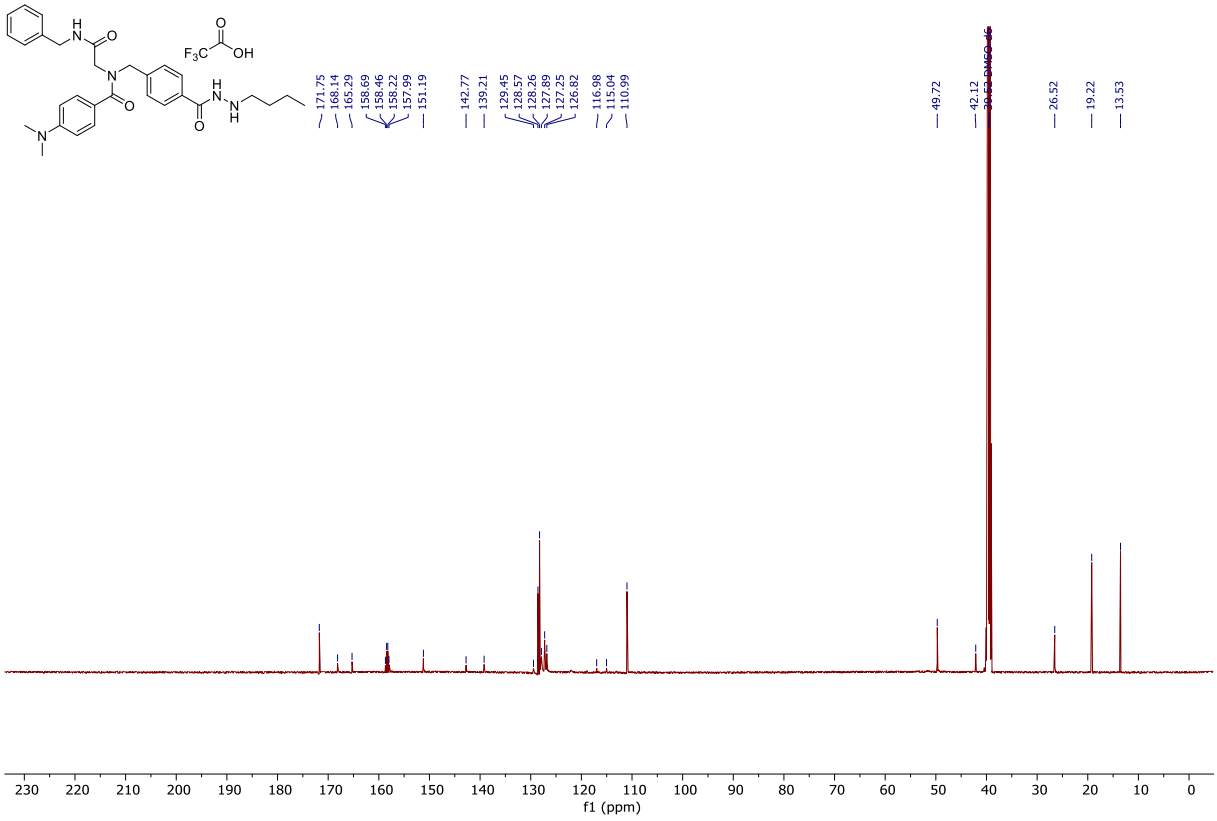
^{1}H-NMR (400 MHz, DMSO-d_6) of compound **5**.



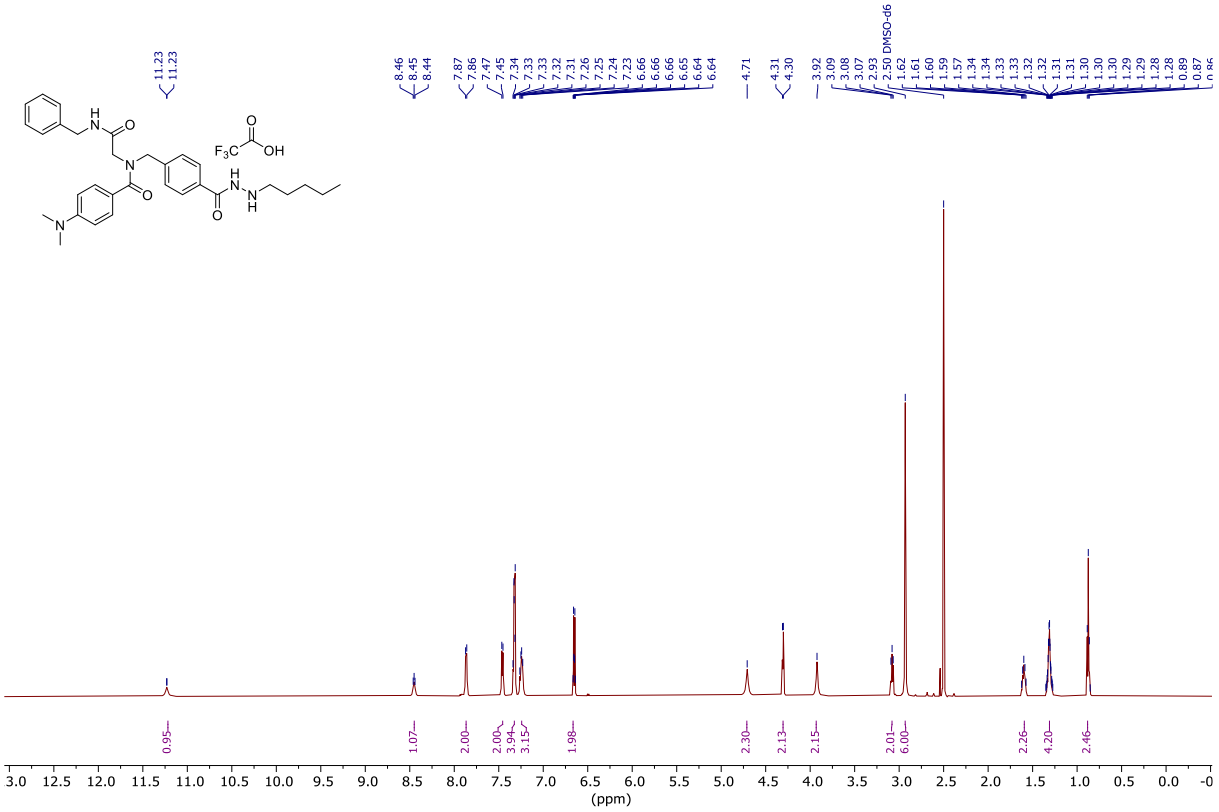
^{13}C-NMR (101 MHz, DMSO-d_6) of compound **5**.



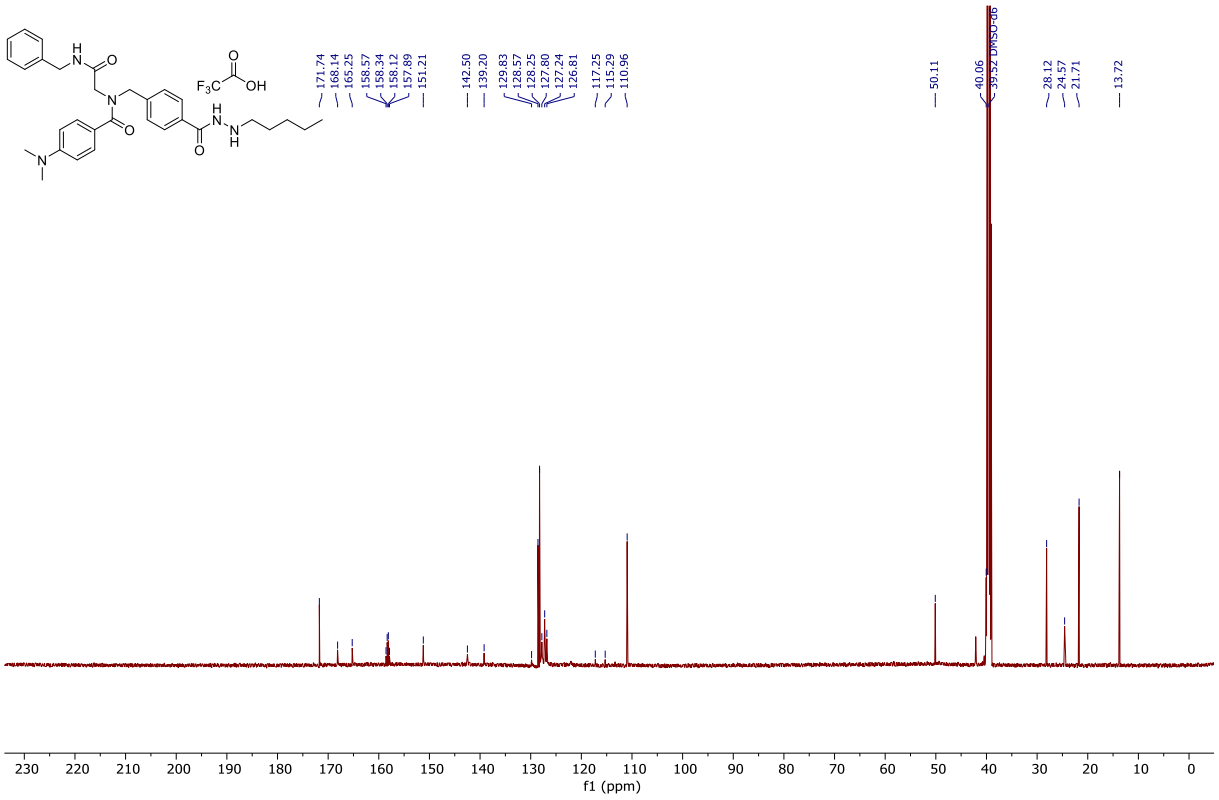
^{1}H-NMR (600 MHz, DMSO-d_6) of compound **6**.



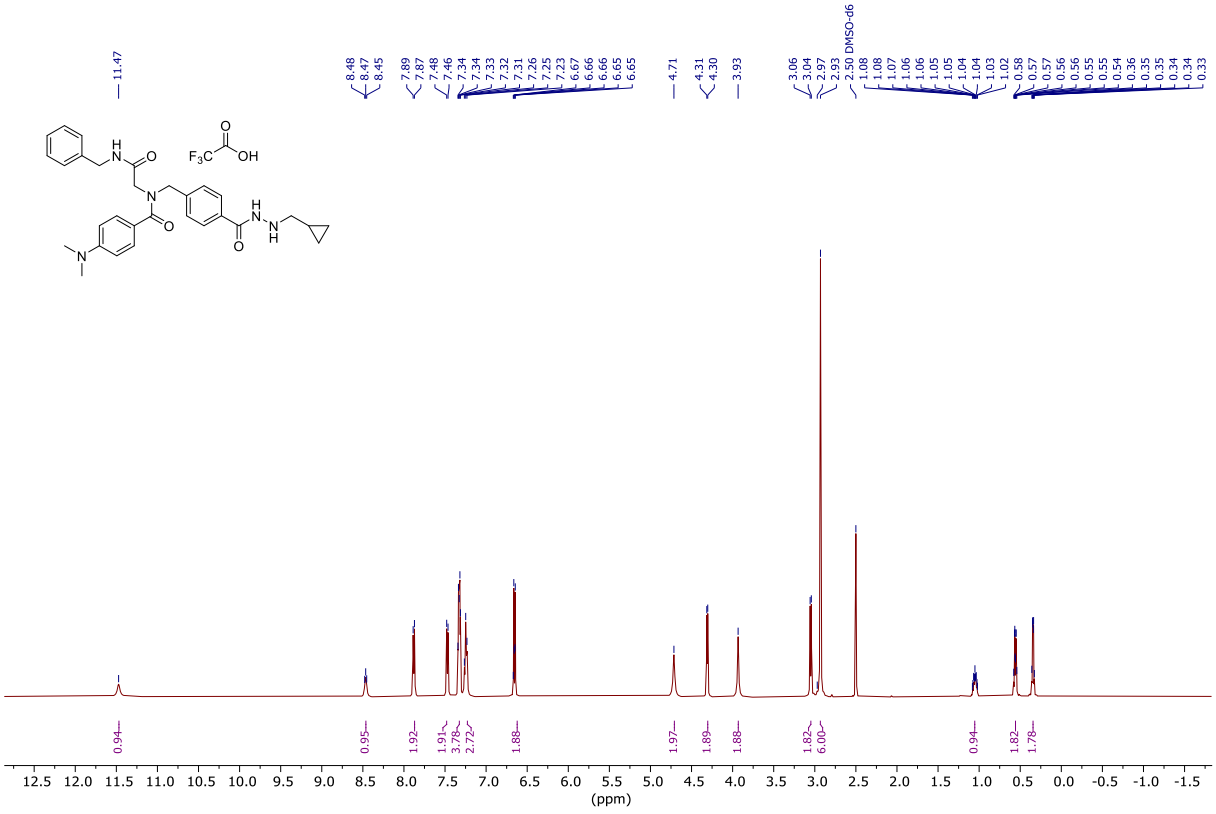
^{13}C-NMR (151 MHz, DMSO-d_6) of compound **6**.



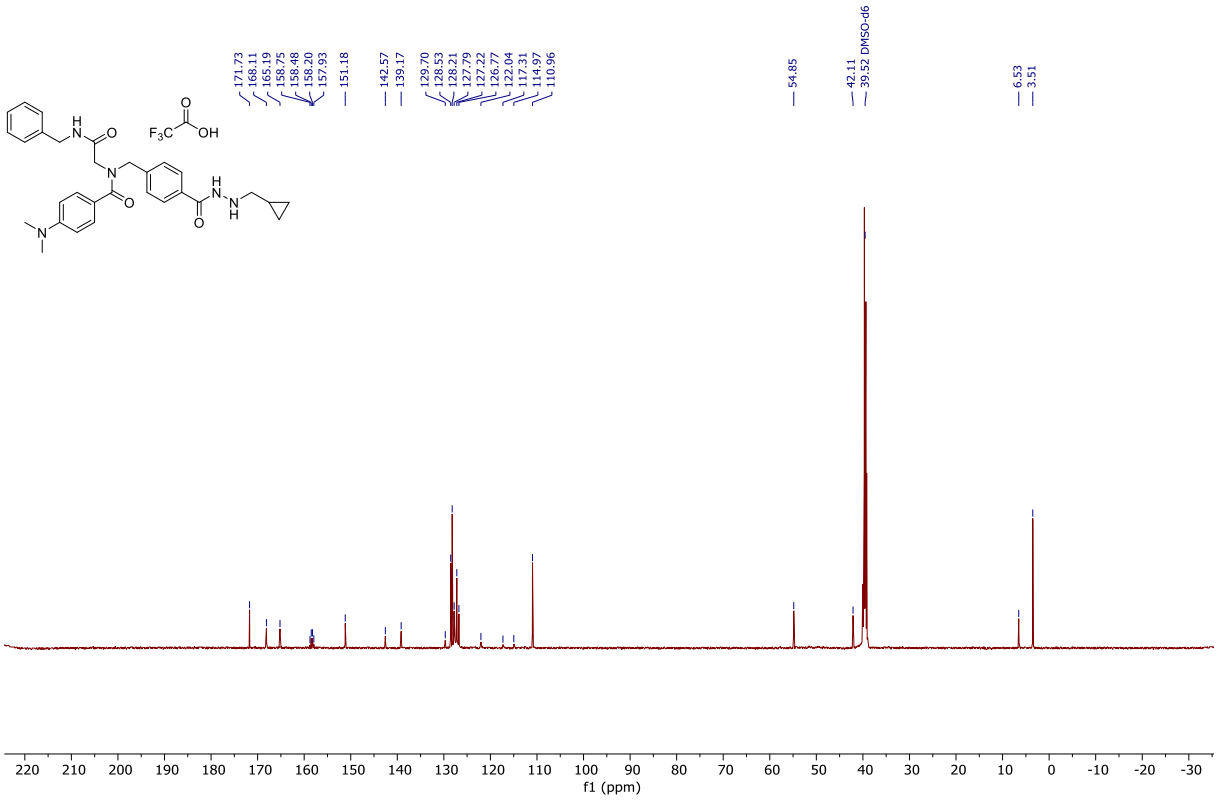
^{1}H-NMR (600 MHz, DMSO-d_6) of compound **7**.



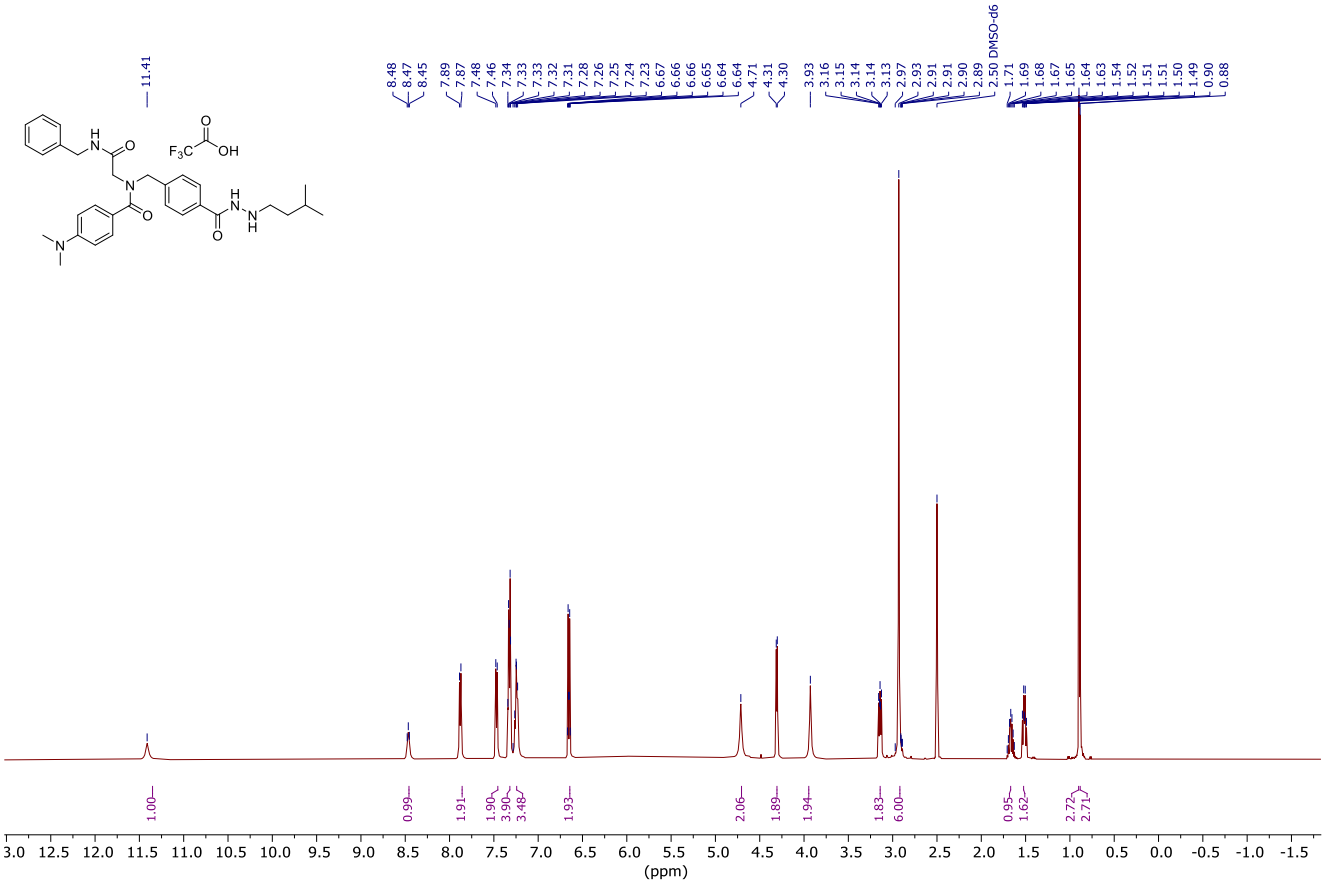
^{13}C-NMR (151 MHz, DMSO-d_6) of compound **7**.



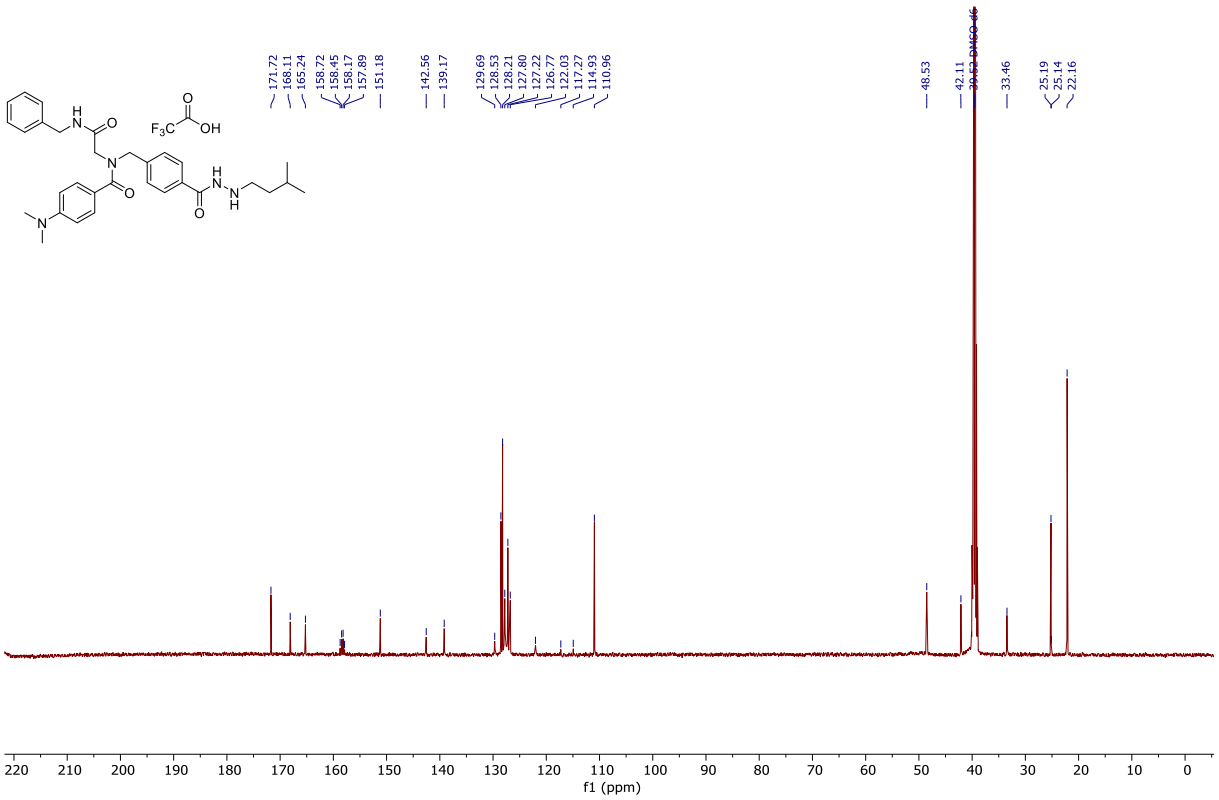
^{1}H-NMR (500 MHz, DMSO-d_6) of compound **8**.



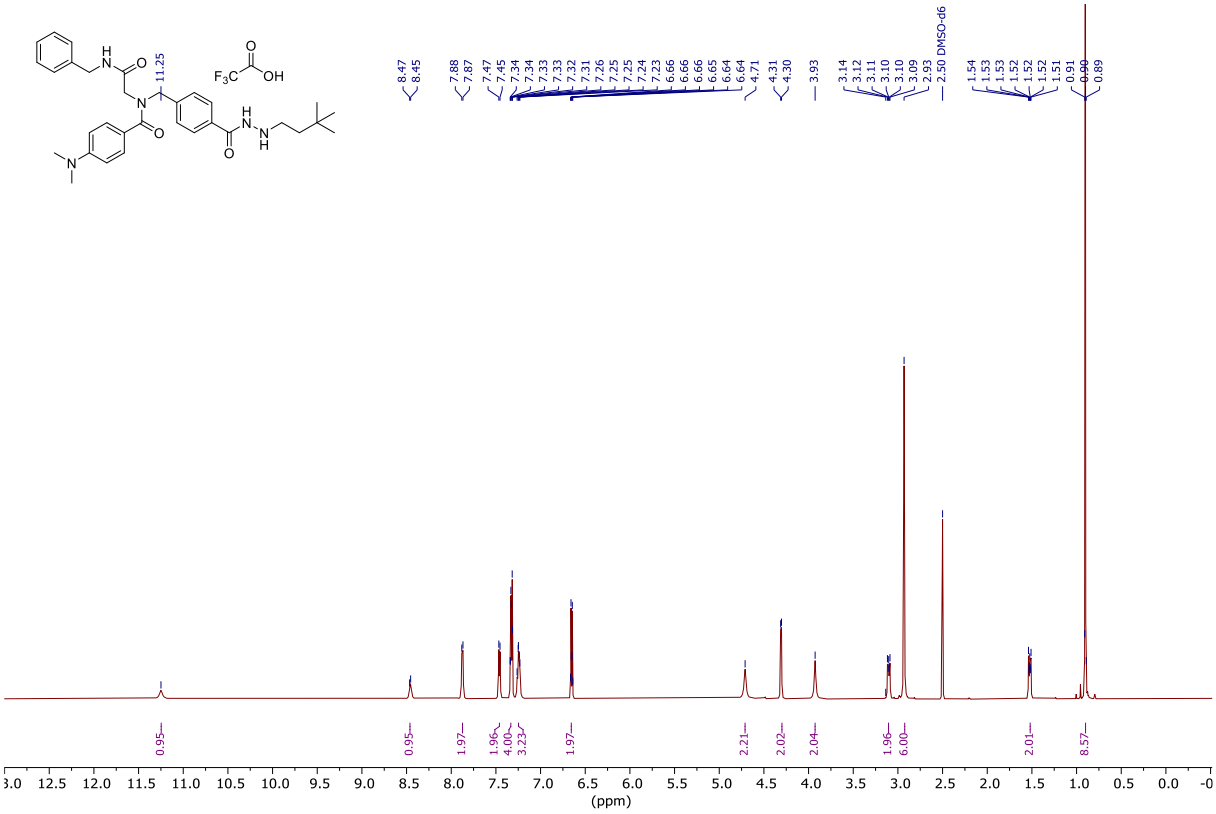
^{13}C-NMR (126 MHz, DMSO-d_6) of compound **8**.



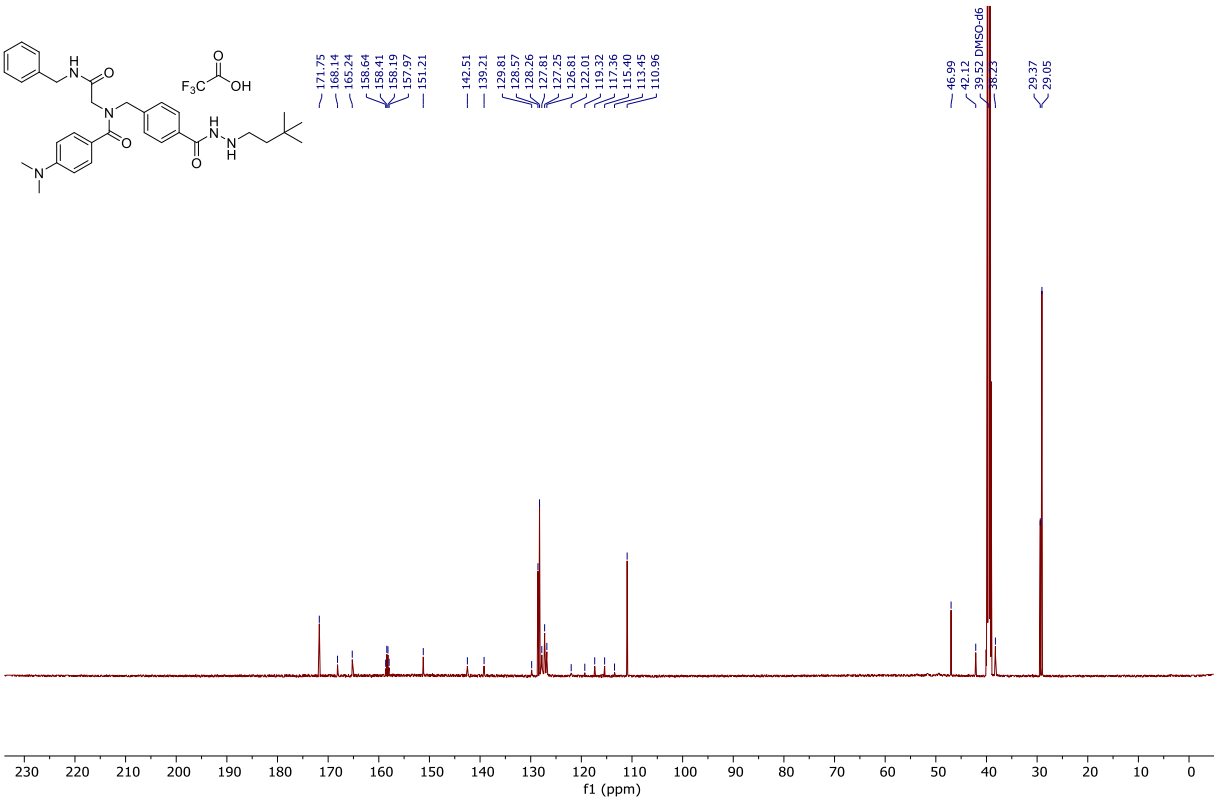
^{1}H-NMR (500 MHz, DMSO-d_6) of compound **9**.



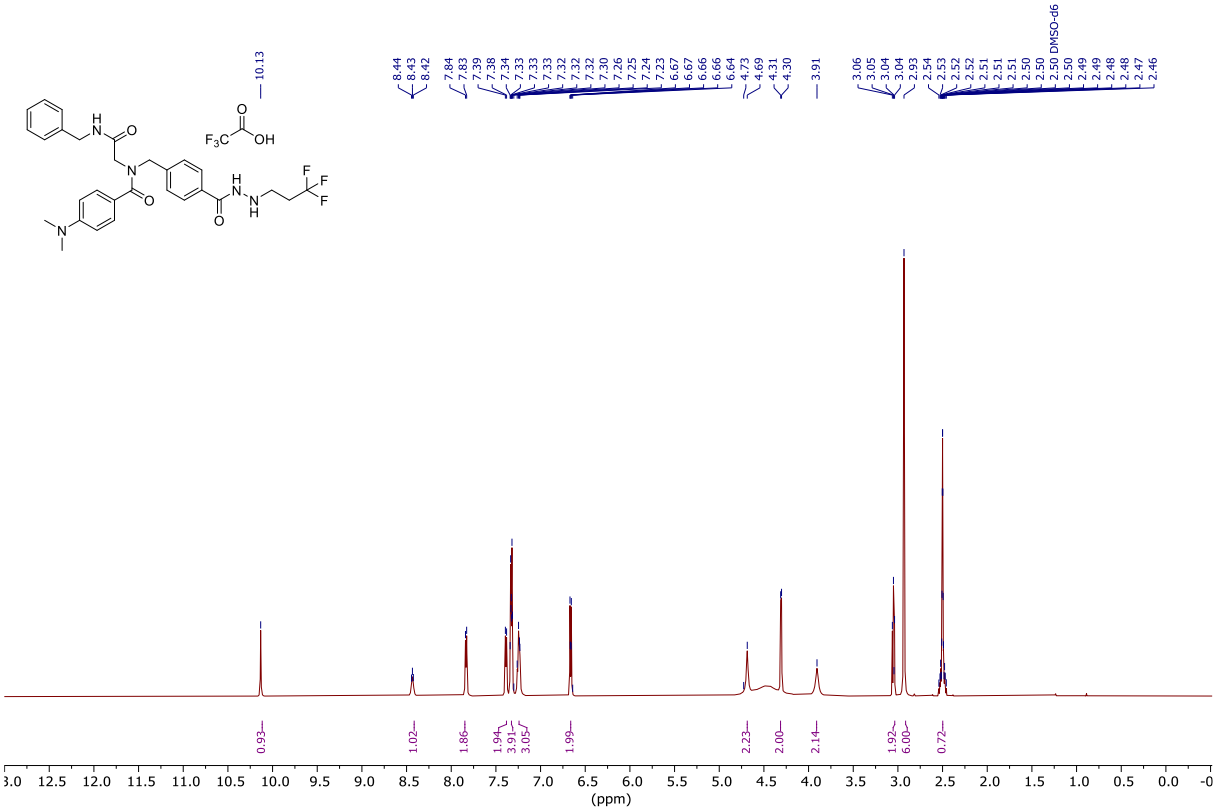
^{13}C-NMR (126 MHz, DMSO-d_6) of compound **9**.



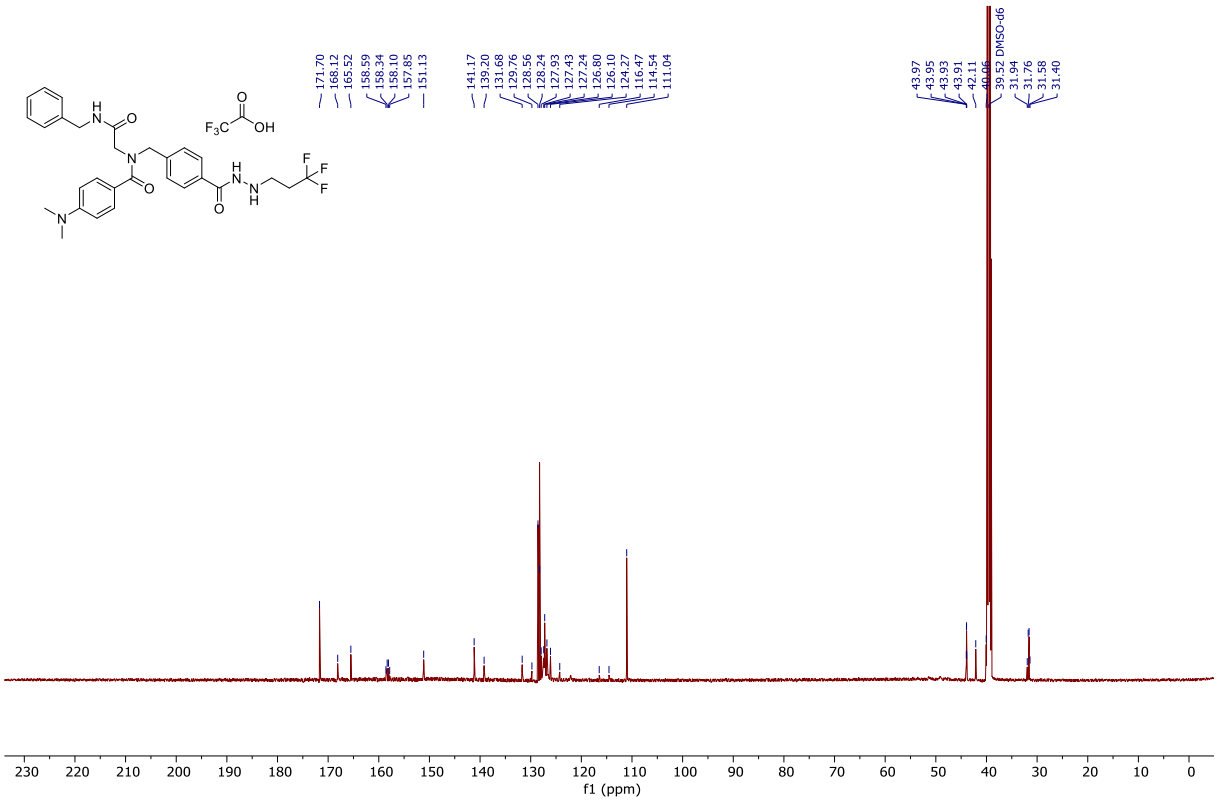
^{1}H-NMR (600 MHz, DMSO-d_6) of compound **10**.



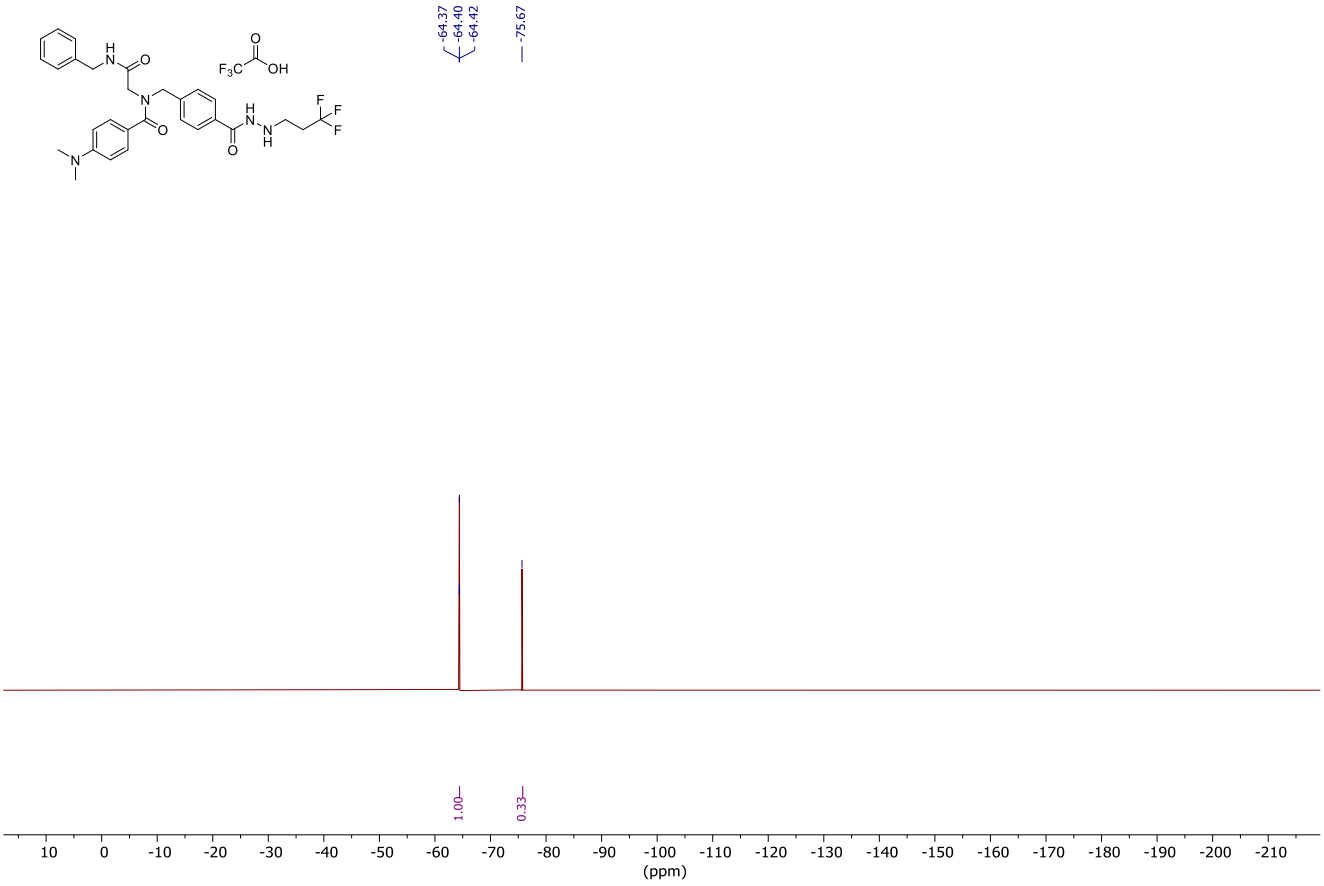
^{13}C-NMR (151 MHz, DMSO-d_6) of compound **10**.



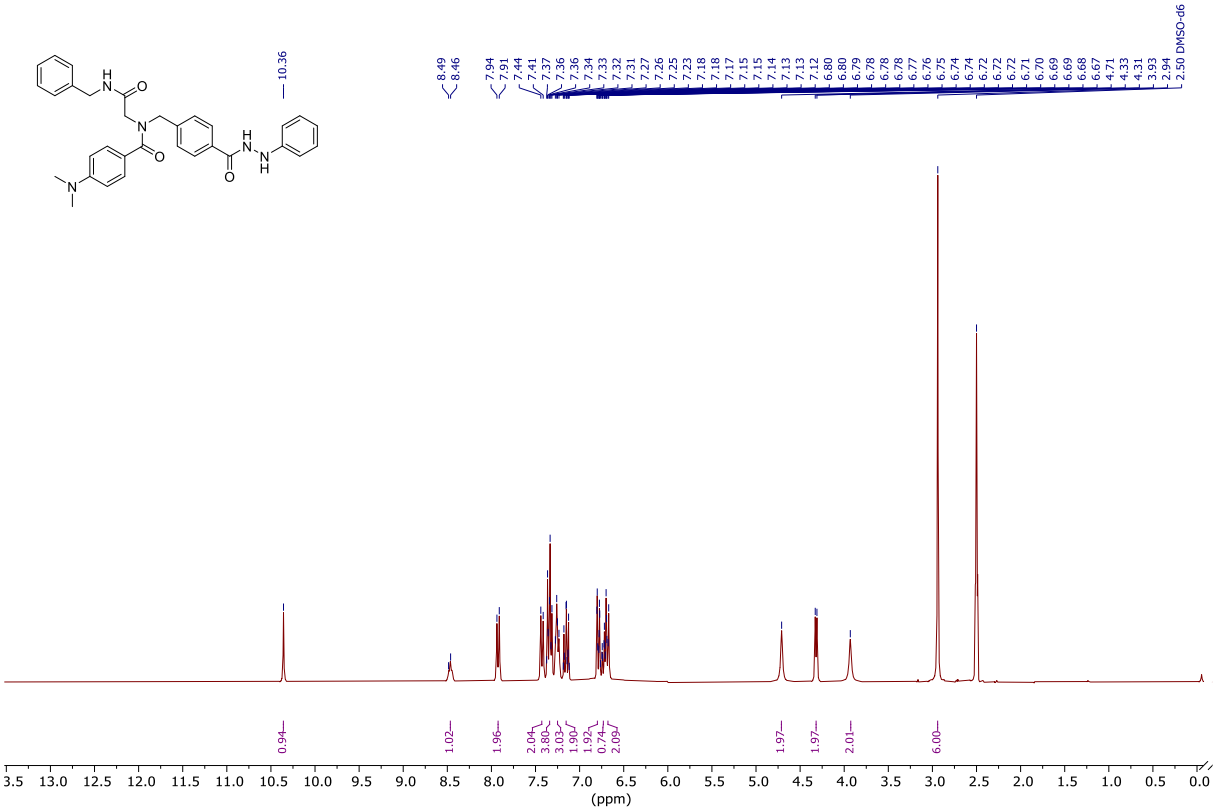
^{1}H-NMR (600 MHz, DMSO-d_6) of compound **11**.



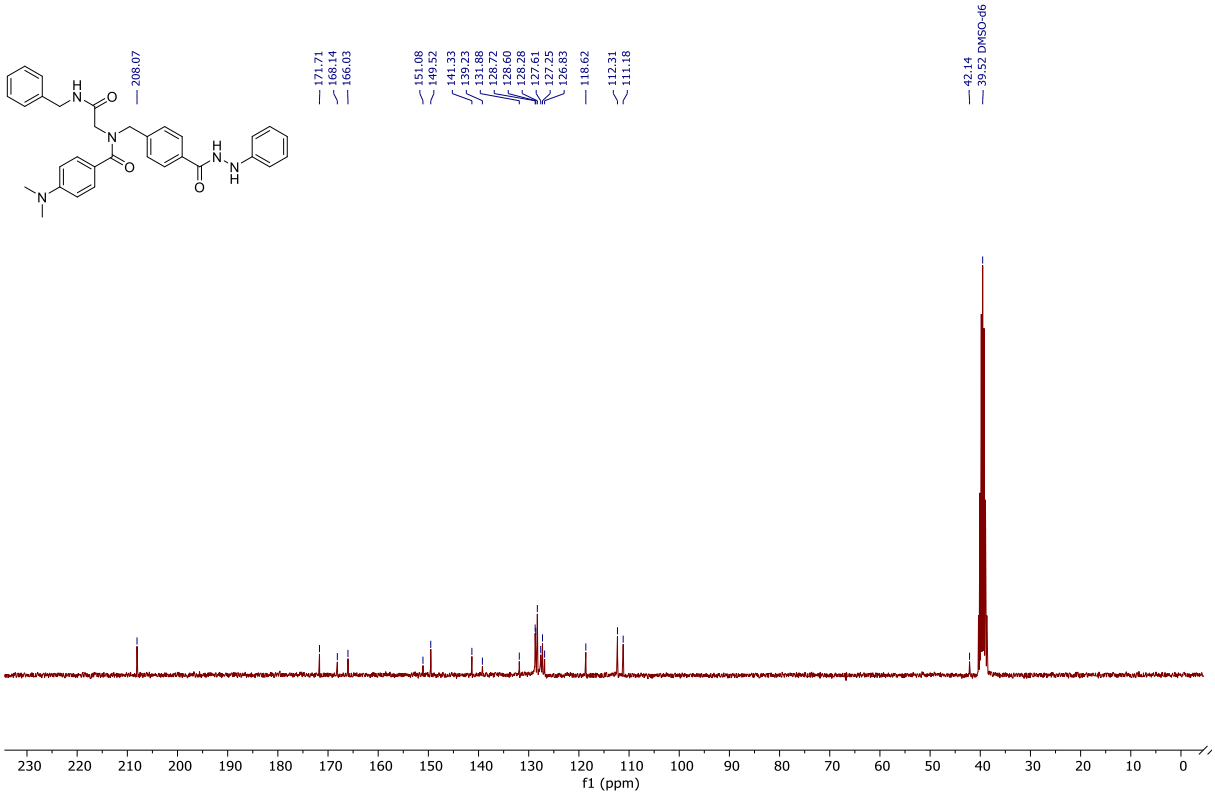
^{13}C-NMR (151 MHz, DMSO-d_6) of compound **11**.



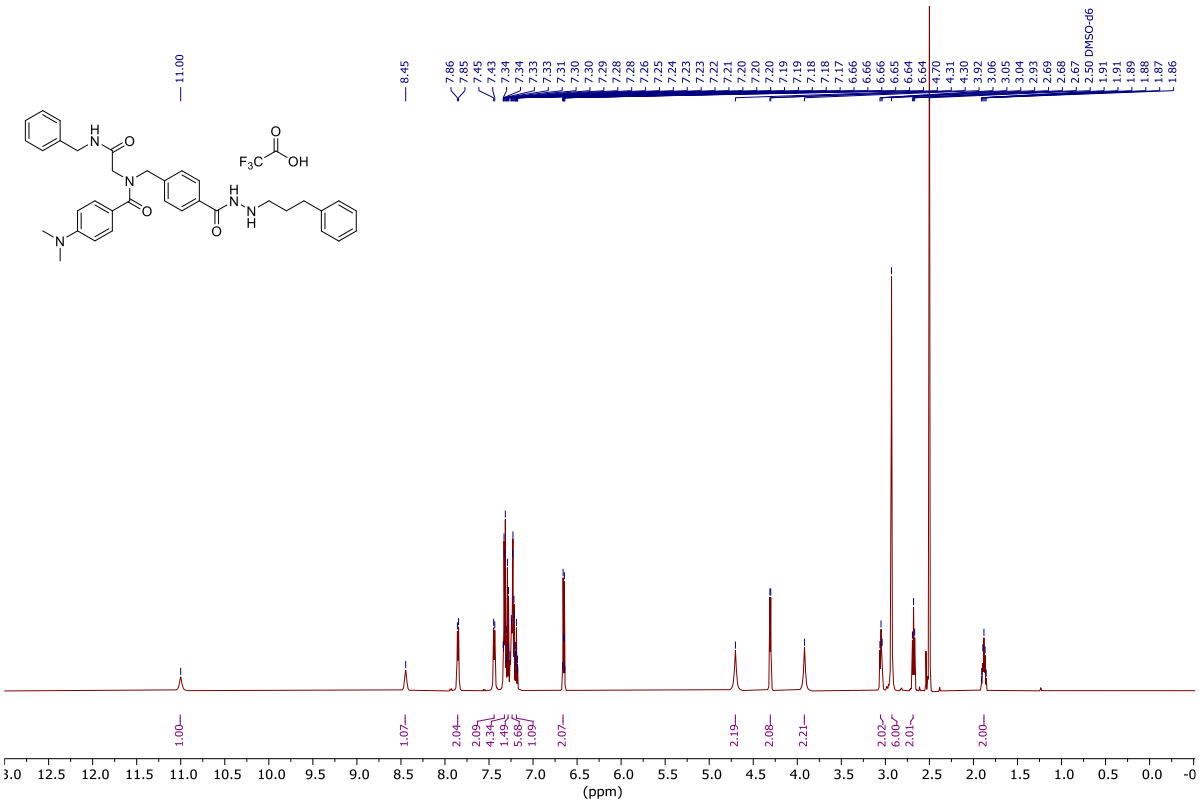
^{19}F-NMR (565 MHz, DMSO-d_6) of compound **11**.



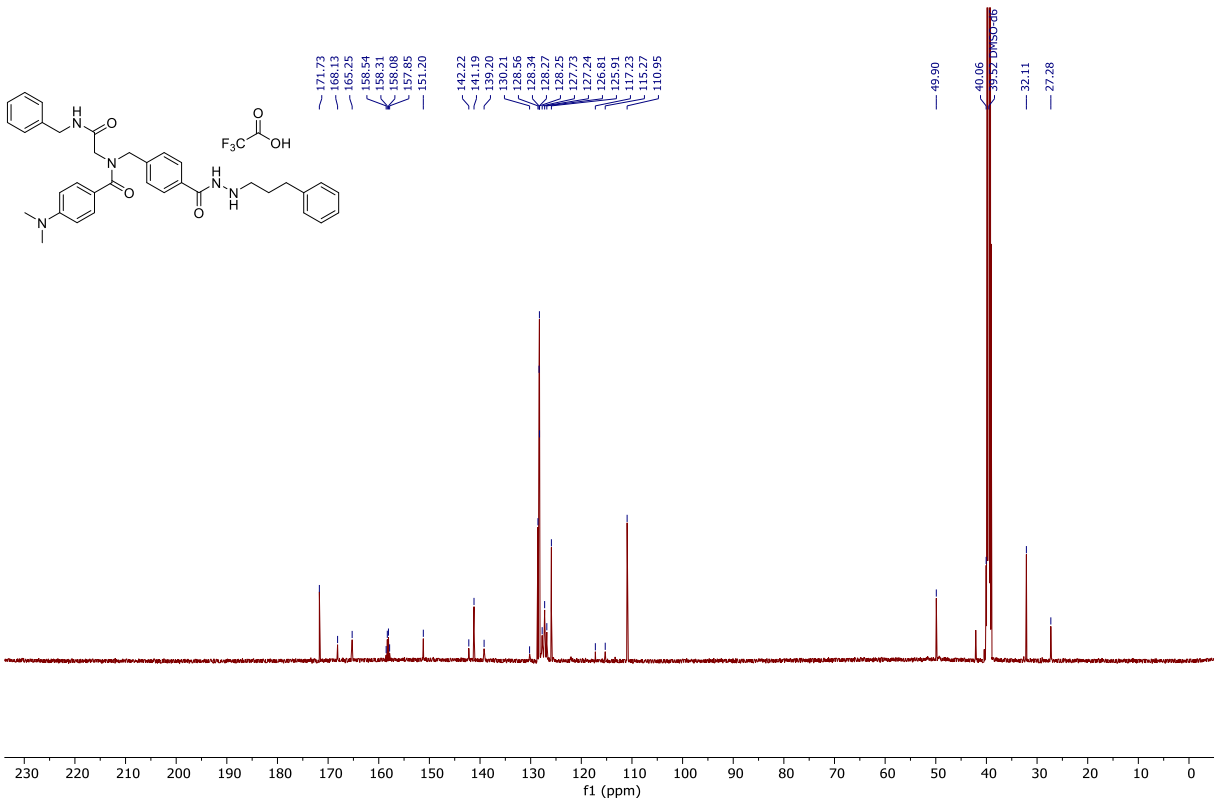
^{1}H-NMR (300 MHz, DMSO-d_6) of compound **12**.



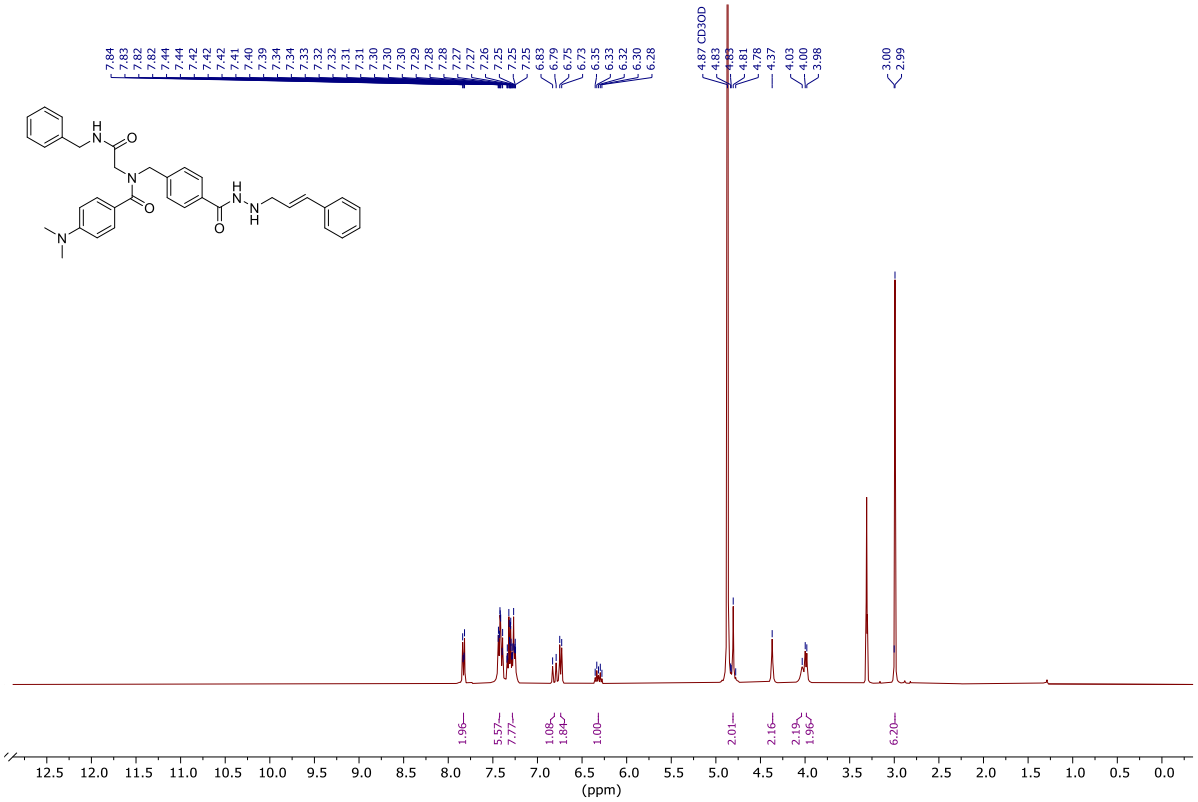
^{13}C-NMR (75 MHz, DMSO-d_6) of compound **12**.



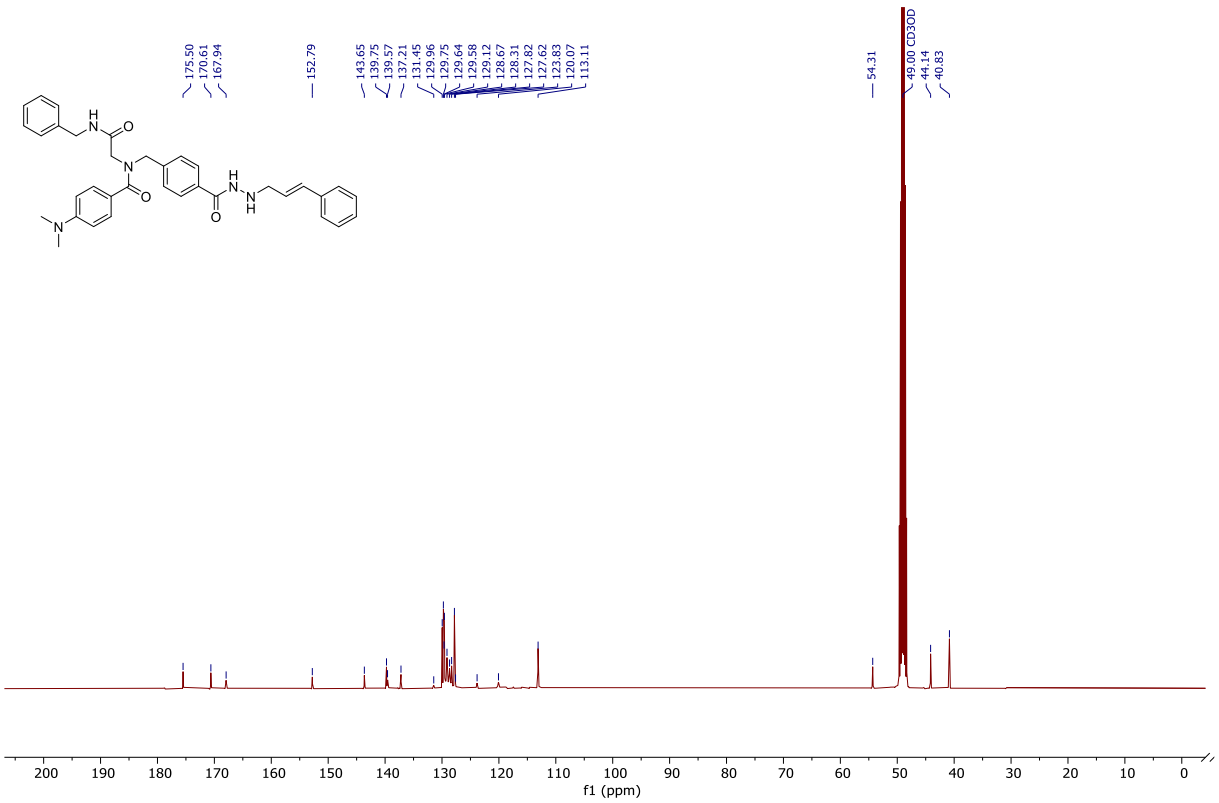
^{1}H-NMR (600 MHz, DMSO-d_6) of compound **13**.



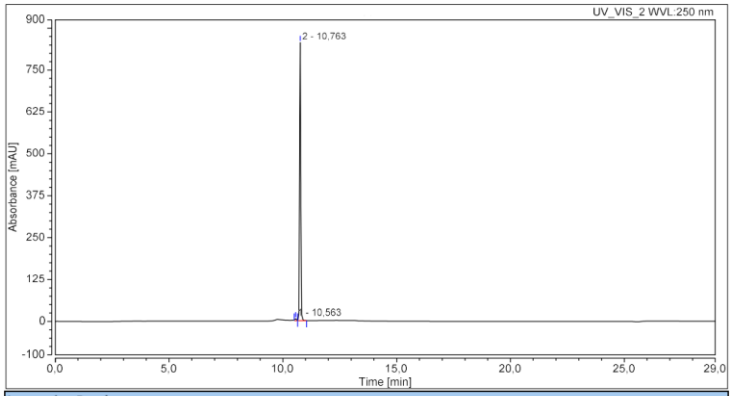
^{13}C-NMR (151 MHz, DMSO-d_6) of compound **13**.



^{1}H-NMR (400 MHz, MeOH-d_4) of compound **14**.



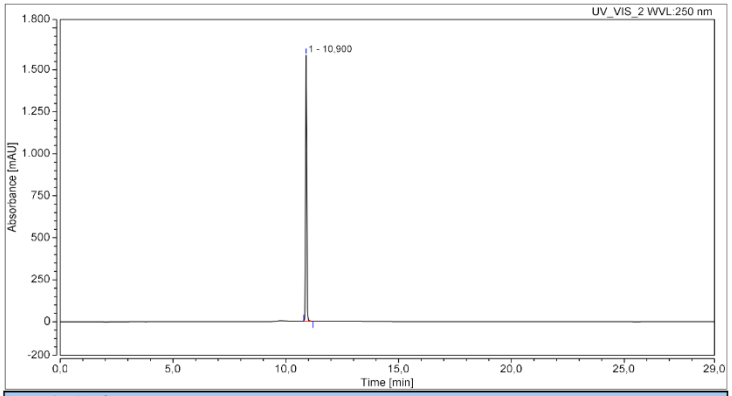
^{13}C-NMR (101 MHz, MeOH-d_4) of compound **14**.



Integration Results

No.	Peak Name	Retention Time min	Area mAU*min	Height mAU	Relative Area %	Relative Height %	Amount n.a.
1		10,563	0,459	5,585	0,92	0,67	n.a.
2		10,763	49,350	829,794	99,08	99,33	n.a.
Total:			**49,809**	**835,379**	**100,00**	**100,00**	

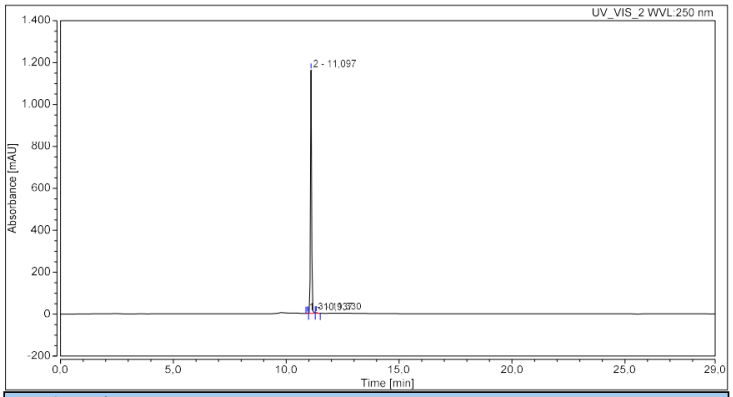
HPLC chromatogram of compound **5** (purity: 99.1%).



Integration Results

No.	Peak Name	Retention Time min	Area mAU*min	Height mAU	Relative Area %	Relative Height %	Amount n.a.
1		10,900	96,191	1584,431	100,00	100,00	n.a.
Total:			**96,191**	**1584,431**	**100,00**	**100,00**	

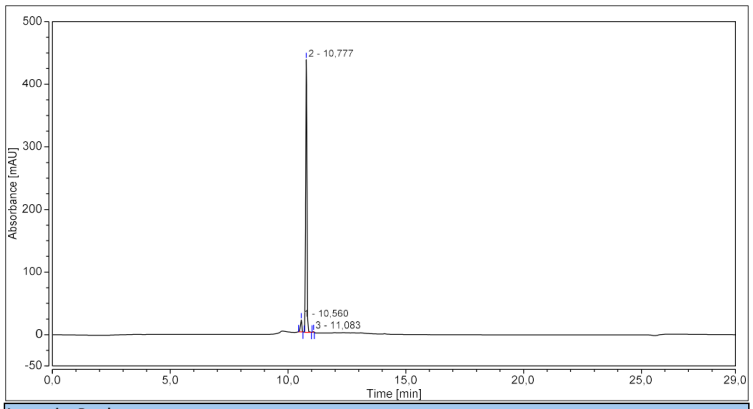
HPLC chromatogram of compound **6** (purity: > 99.9%).



Integration Results

No.	Peak Name	Retention Time min	Area mAU*min	Height mAU	Relative Area %	Relative Height %	Amount n.a.
1		10,937	0,104	1,615	0,15	0,14	n.a.
2		11,097	70,963	1160,416	99,45	99,60	n.a.
3		11,330	0,285	3,070	0,40	0,26	n.a.
Total:			**71,352**	**1165,101**	**100,00**	**100,00**	

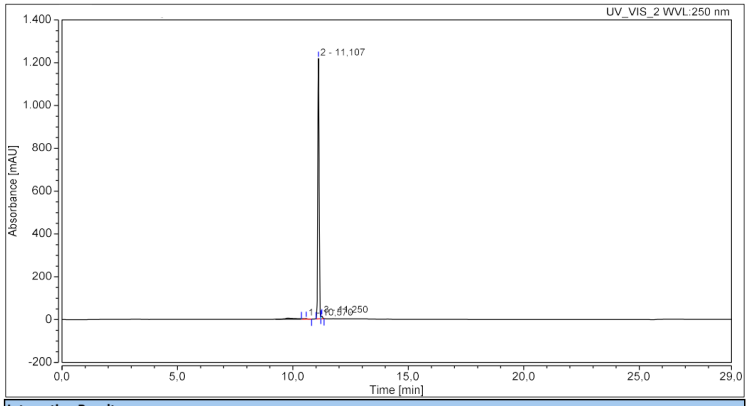
HPLC chromatogram of compound **7** (purity: 99.5%).



Integration Results

No.	Peak Name	Retention Time min	Area mAU*min	Height mAU	Relative Area %	Relative Height %	Amount n.a.
1		10,560	1,273	19,102	4,71	4,19	n.a.
2		10,777	25,733	435,288	95,11	95,59	n.a.
3		11,083	0,051	0,998	0,19	0,22	n.a.
Total:			**27,057**	**455,388**	**100,00**	**100,00**	

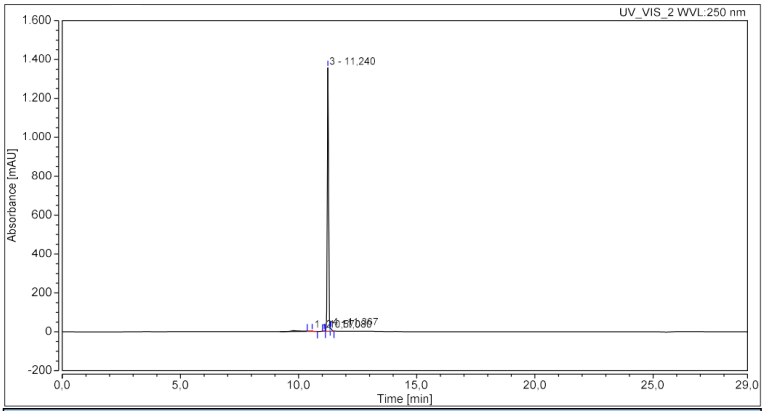
HPLC chromatogram of compound **8** (purity: 95.1%).



Integration Results

No.	Peak Name	Retention Time min	Area mAU*min	Height mAU	Relative Area %	Relative Height %	Amount n.a.
1		10,570	0,583	2,573	0,73	0,21	n.a.
2		11,107	78,563	1216,135	98,11	98,74	n.a.
3		11,250	0,928	12,940	1,16	1,05	n.a.
Total:			**80,074**	**1231,649**	**100,00**	**100,00**	

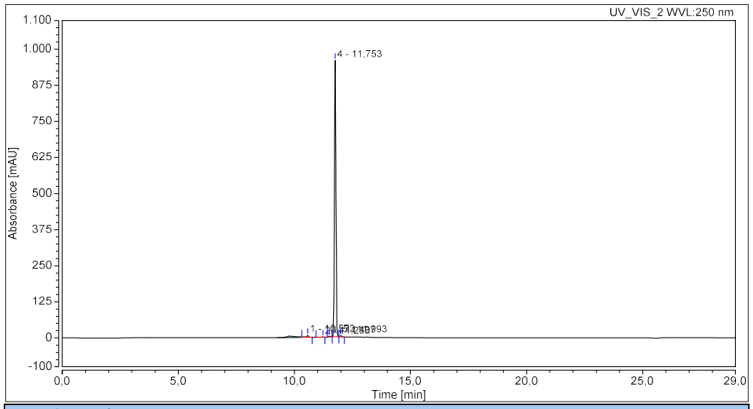
HPLC chromatogram of compound **9** (purity: 98.1%).



Integration Results

No.	Peak Name	Retention Time min	Area mAU*min	Height mAU	Relative Area %	Relative Height %	Amount n.a.
1		10,570	0,604	2,899	0,67	0,21	n.a.
2		11,080	0,179	2,431	0,20	0,18	n.a.
3		11,240	88,478	1355,048	98,00	98,51	n.a.
4		11,367	1,023	15,104	1,13	1,10	n.a.
Total:			**90,284**	**1375,482**	**100,00**	**100,00**	

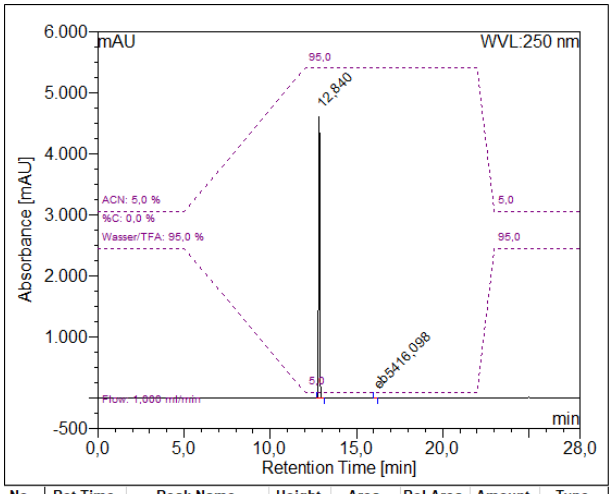
HPLC chromatogram of compound **10** (purity: 98.0%).



Integration Results

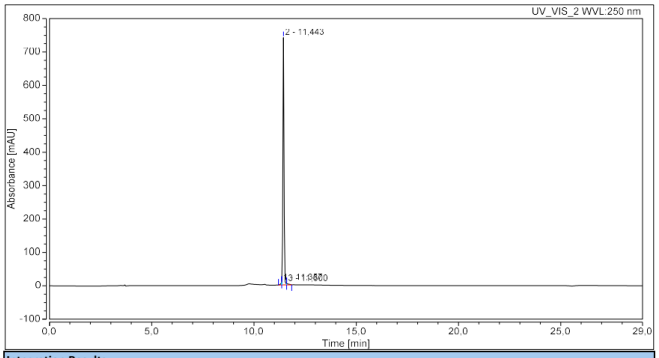
No.	Peak Name	Retention Time min	Area mAU*min	Height mAU	Relative Area %	Relative Height %	Amount n.a.
1		10,573	0,878	6,922	1,23	0,71	n.a.
2		11,233	0,145	1,443	0,20	0,15	n.a.
3		11,497	0,225	2,153	0,31	0,22	n.a.
4		11,753	69,888	957,334	97,67	98,46	n.a.
5		11,993	0,423	4,502	0,59	0,46	n.a.
Total:			**71,558**	**972,354**	**100,00**	**100,00**	

HPLC chromatogram of compound **11** (purity: 97.7%).



No.	Ret.Time min	Peak Name	Height mAU	Area mAU*min	Rel.Area %	Amount	Type
1	12,84	n.a.	#######	376,809	99,84	n.a.	BMB
2	16,10	eb54	7,346	0,601	0,16	n.a.	BMB
Total:			#######	377,409	100,00	0,000	

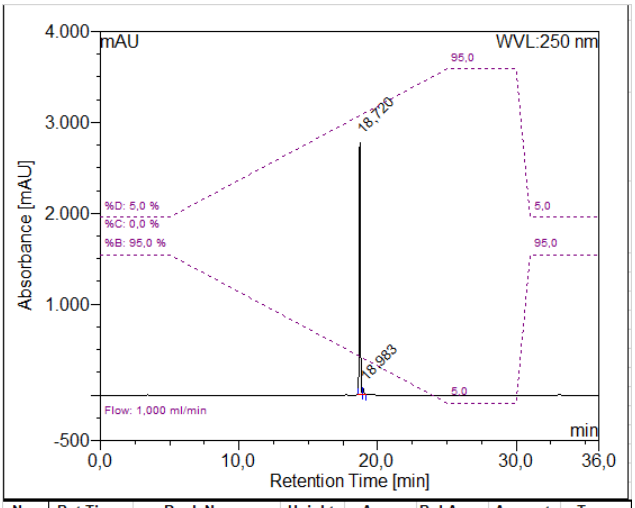
HPLC chromatogram of compound **12** (purity: 99.8%).



Integration Results

No.	Peak Name	Retention Time min	Area mAU*min	Height mAU	Relative Area %	Relative Height %	Amount n.a.
1		11,357	0,414	7,887	0,83	1,05	n.a.
2		11,443	48,871	740,607	98,24	98,45	n.a.
3		11,600	0,461	3,762	0,93	0,50	n.a.
Total:			**49,746**	**752,256**	**100,00**	**100,00**	

HPLC chromatogram of compound **13** (purity: 98.2%).

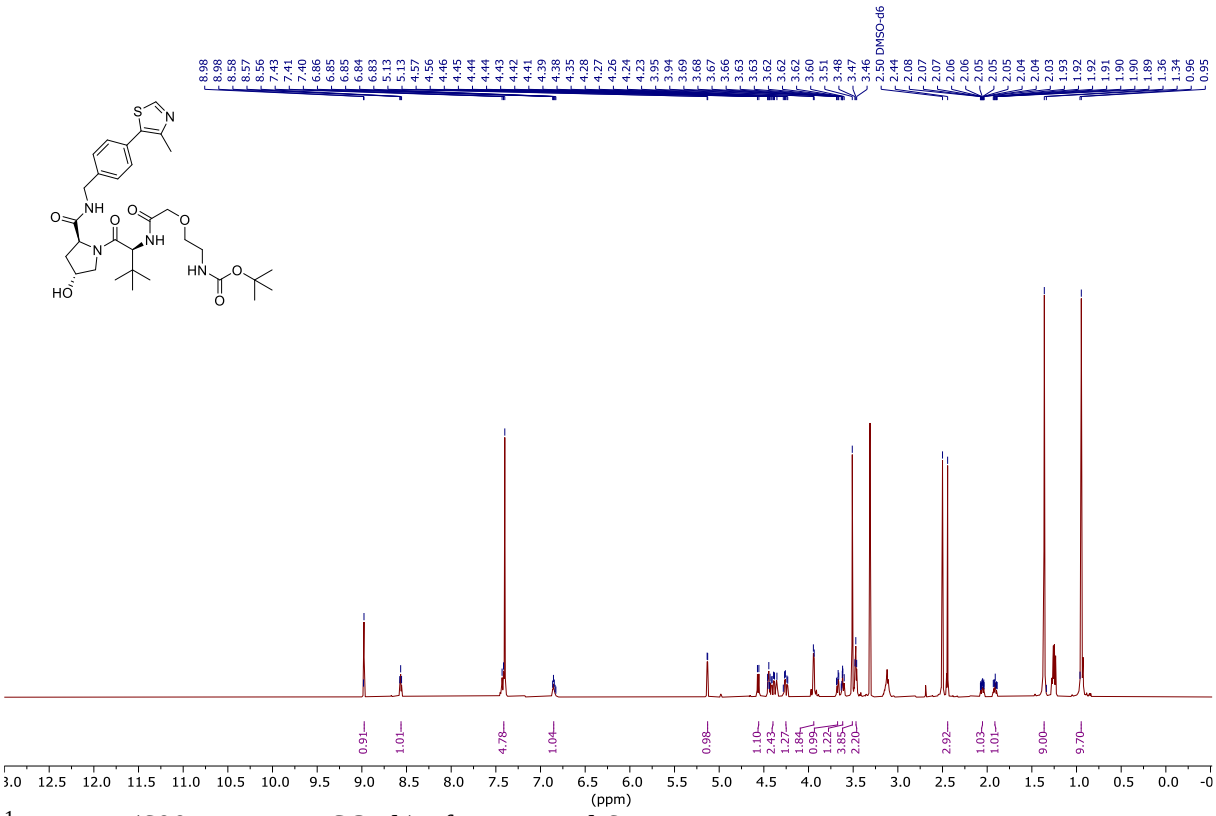


No.	Ret.Time min	Peak Name	Height mAU	Area mAU*min	Rel.Area %	Amount	Type
1	18,72	n.a.	#######	269,966	97,33	n.a.	BM *
2	18,98	n.a.	65,858	7,398	2,67	n.a.	MB*
Total:			#######	277,364	100,00	0,000	

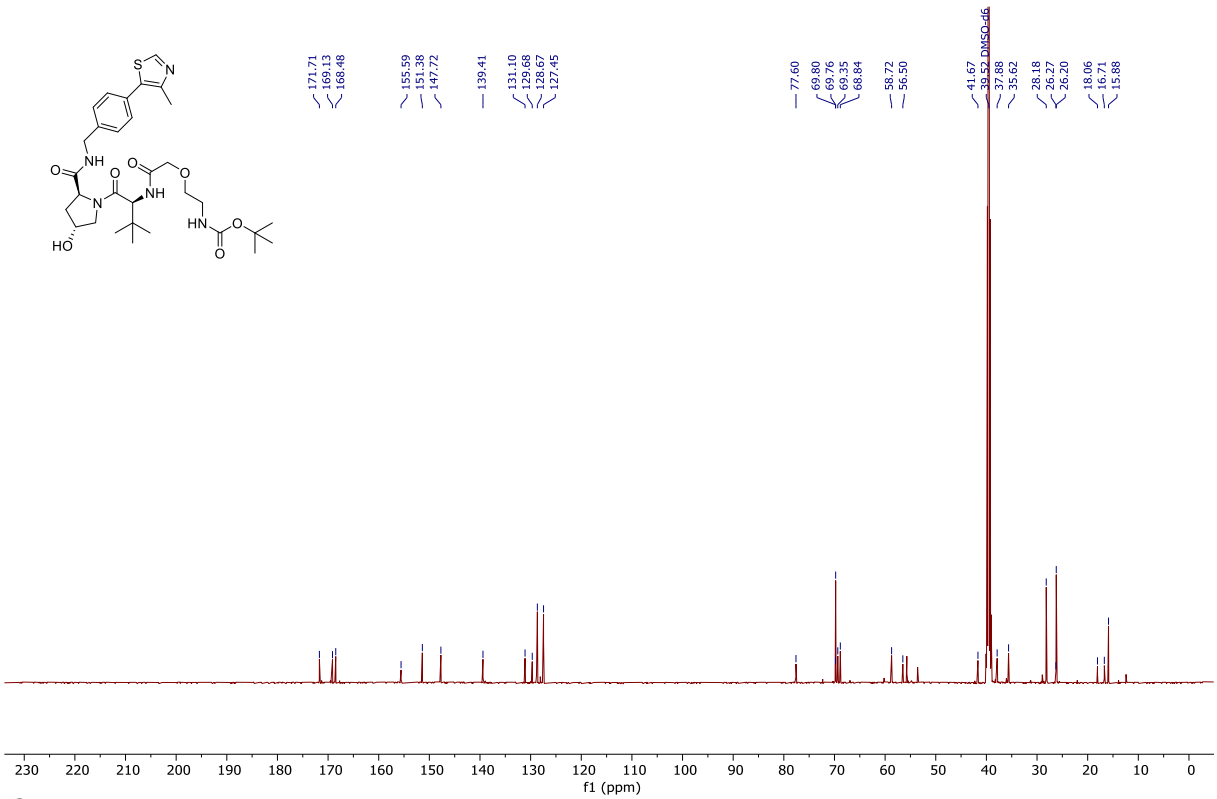
HPLC chromatogram of compound **14** (purity: 97.3%).

8.3 Appendix III. Supporting Information of chapter 4 “Development of HDAC class I selective PROTACs”.

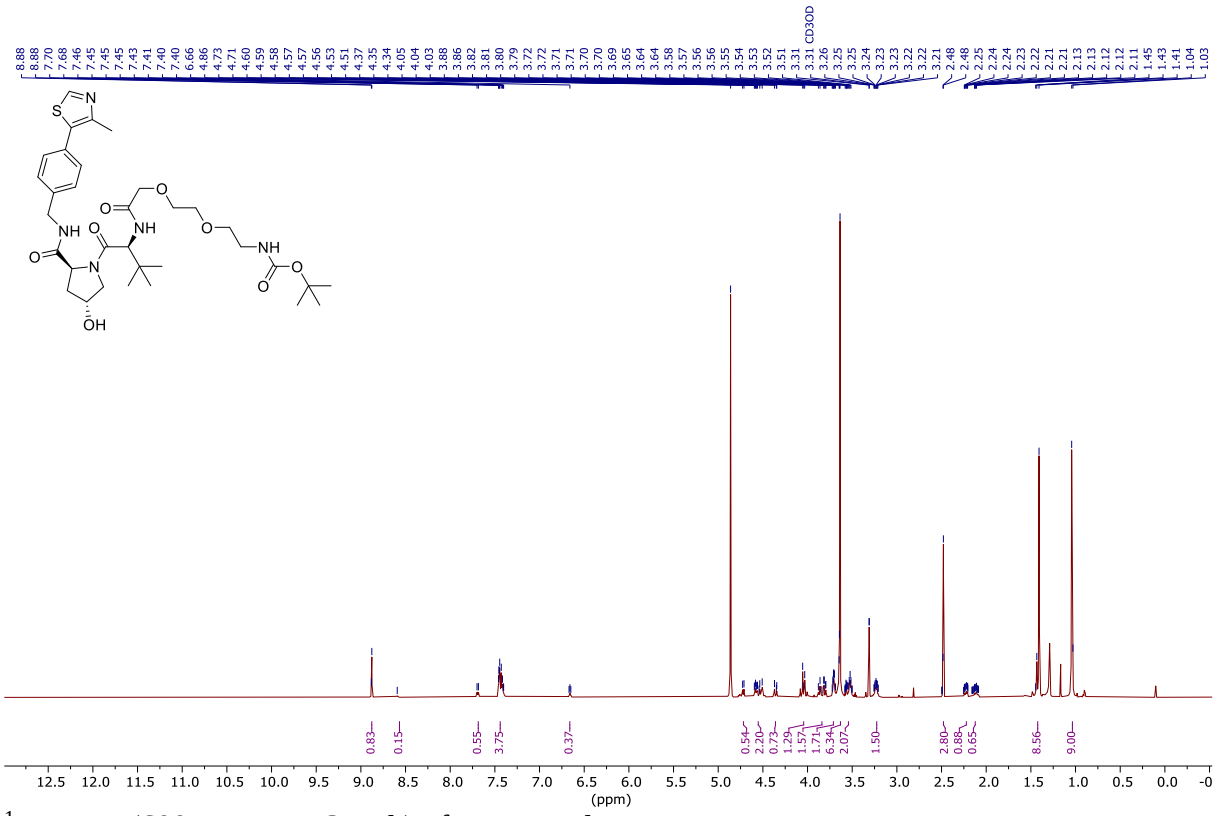
The following pages include ^{1}H- and ^{13}C-NMR spectra of newly synthesized compounds and HPLC chromatograms of all final compounds reported in chapter 4.



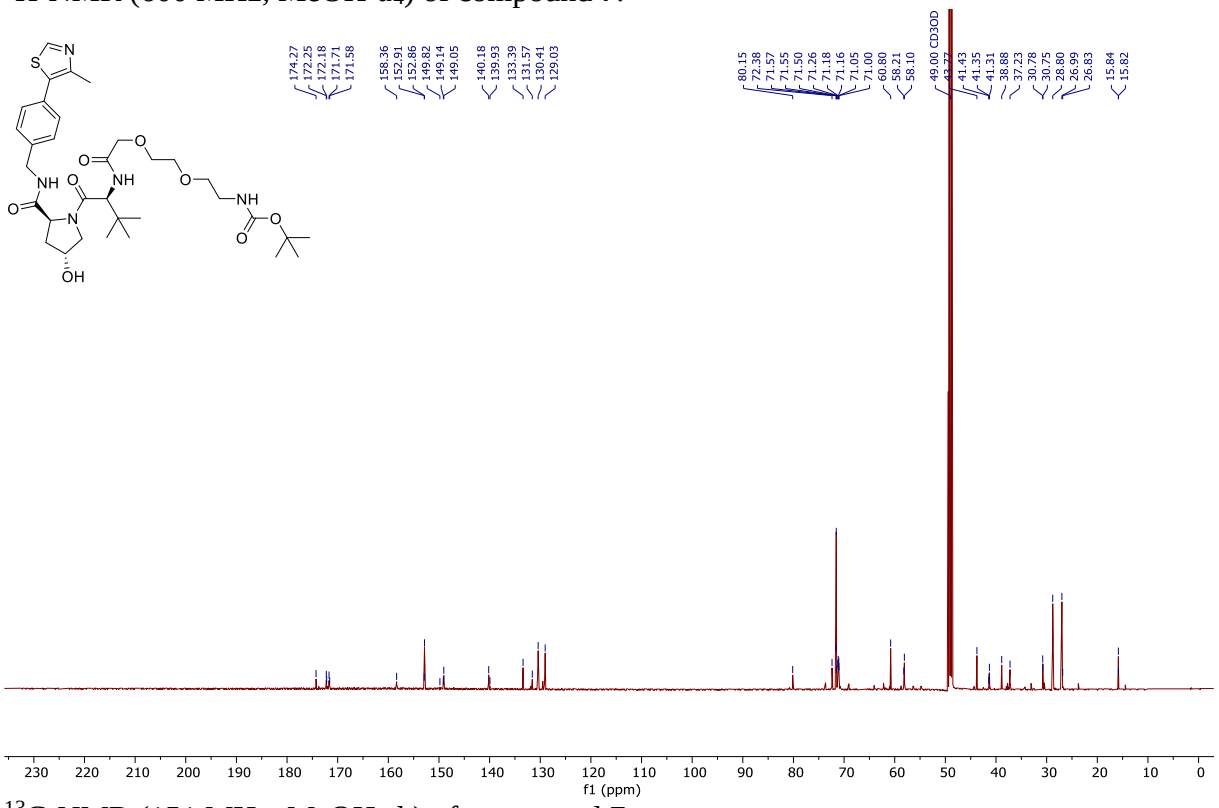
^{1}H-NMR (600 MHz, DMSO-d_6) of compound **6**.



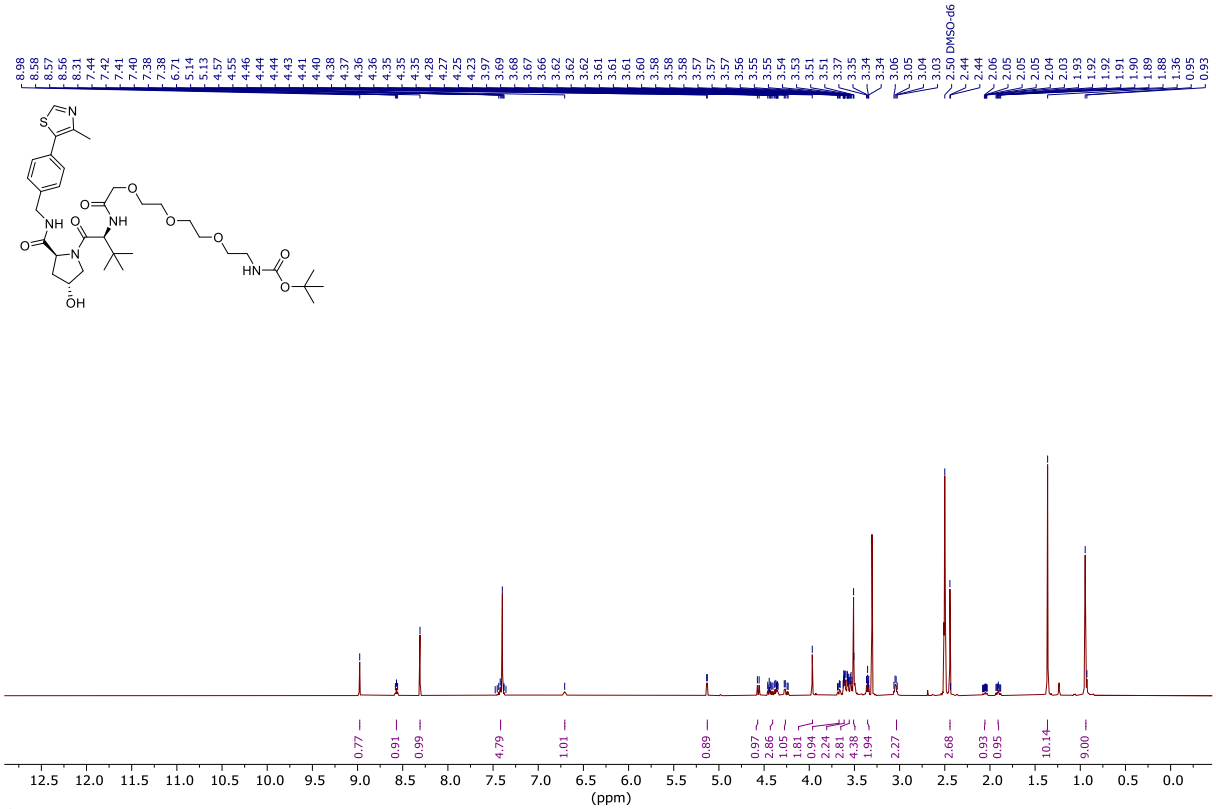
^{13}C-NMR (151 MHz, DMSO-d_6) of compound **6**.



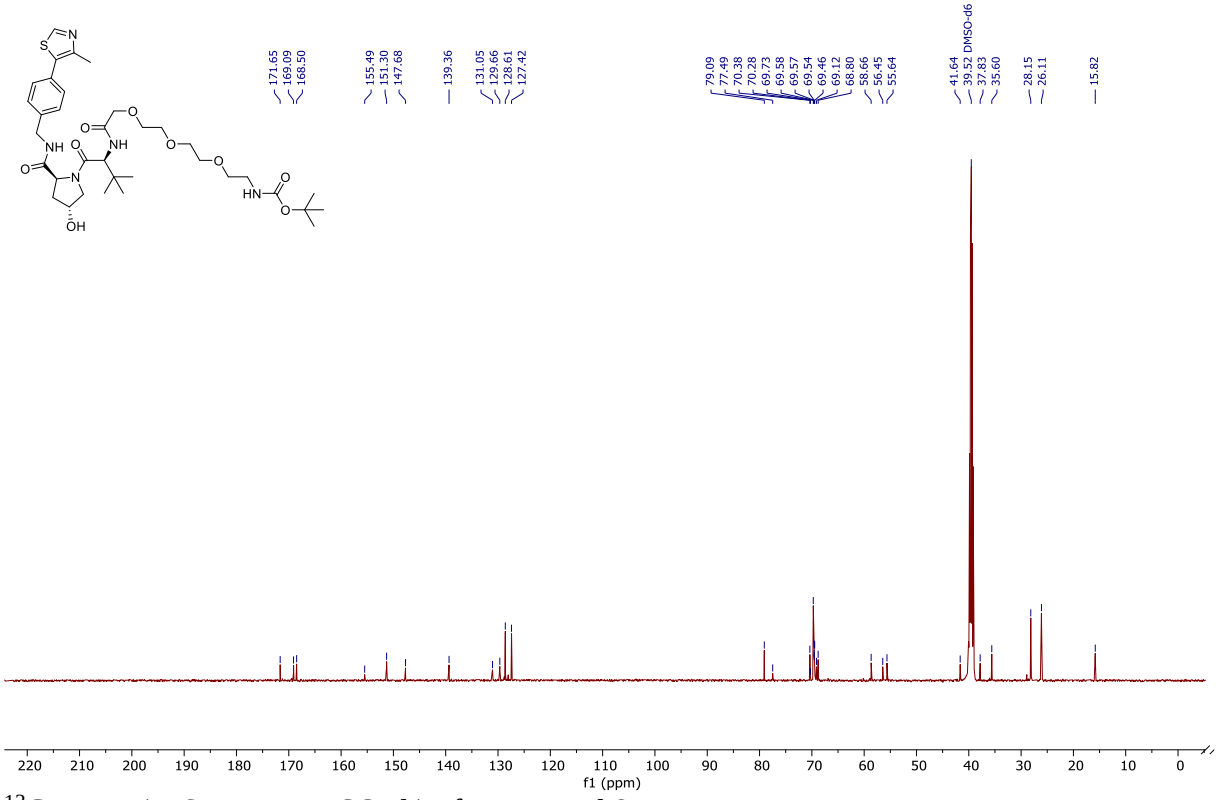
^{1}H-NMR (600 MHz, MeOH-d_4) of compound **7**.



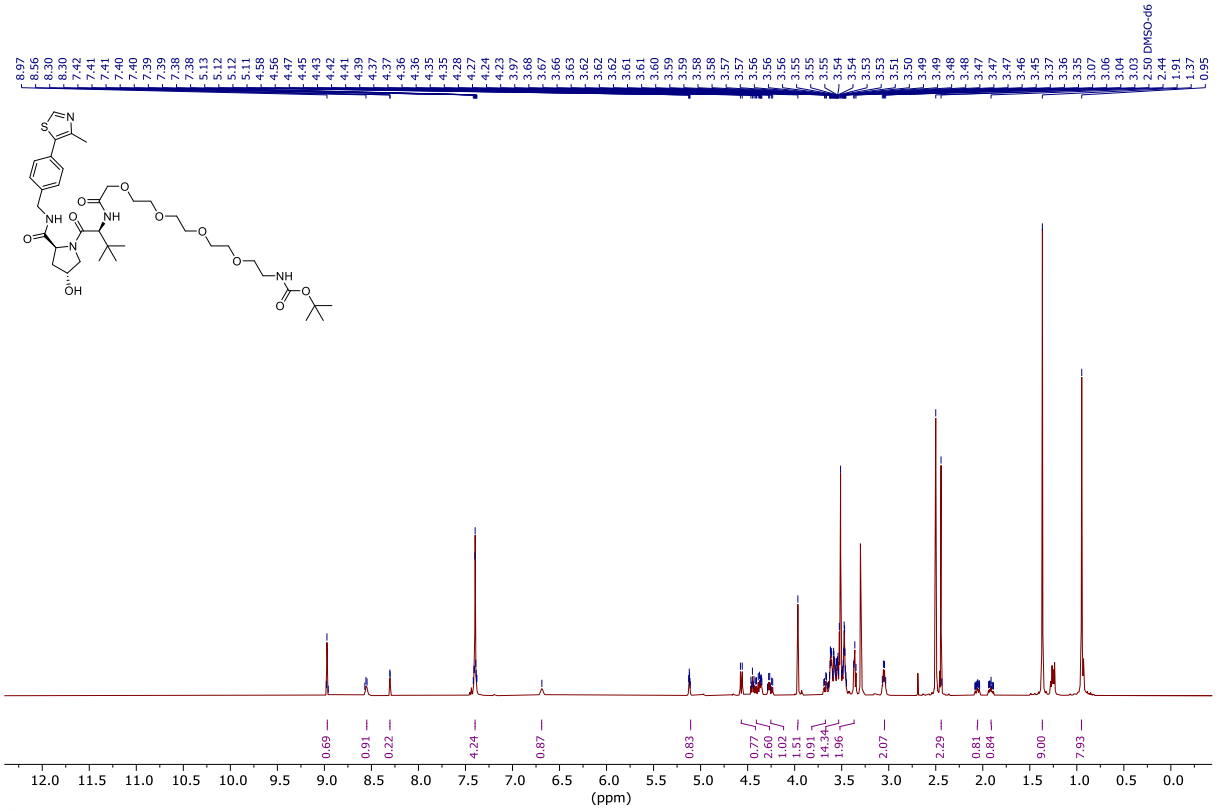
^{13}C-NMR (151 MHz, MeOH-d_4) of compound **7**.



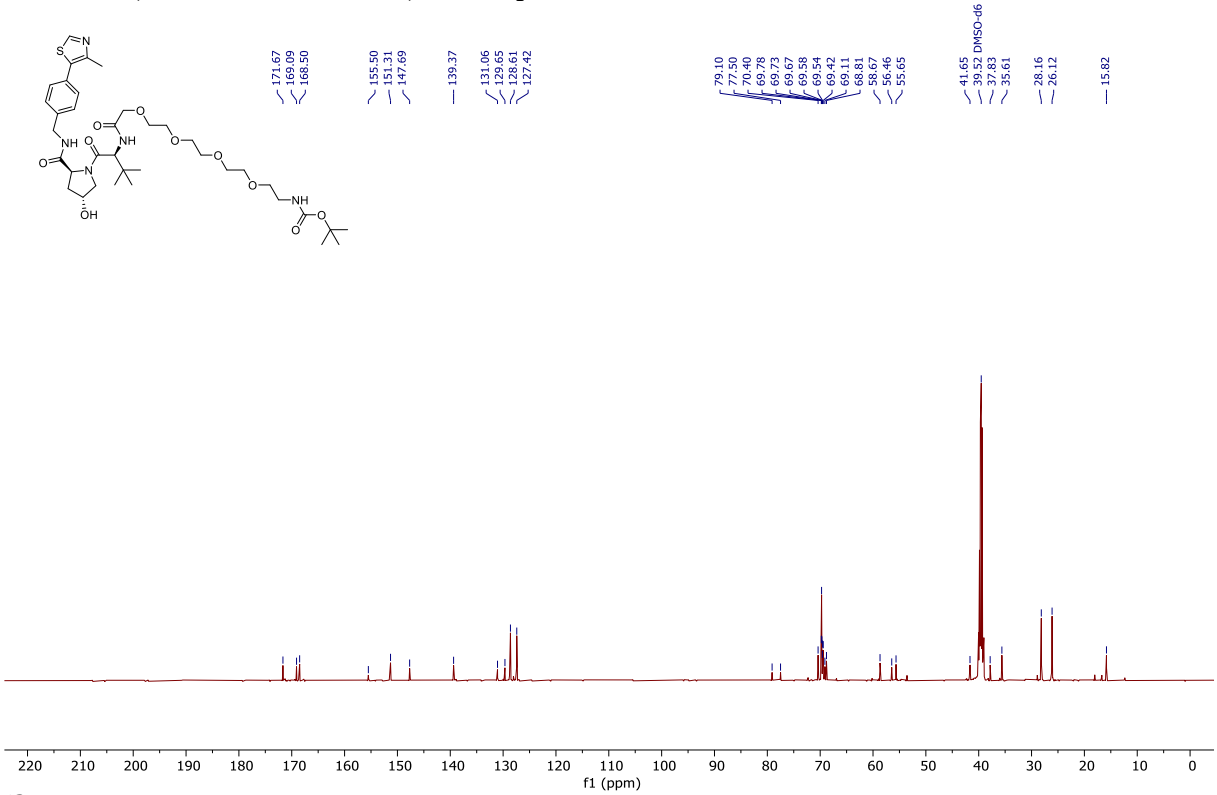
^{1}H-NMR (500 MHz, DMSO-d_6) of compound **8**.



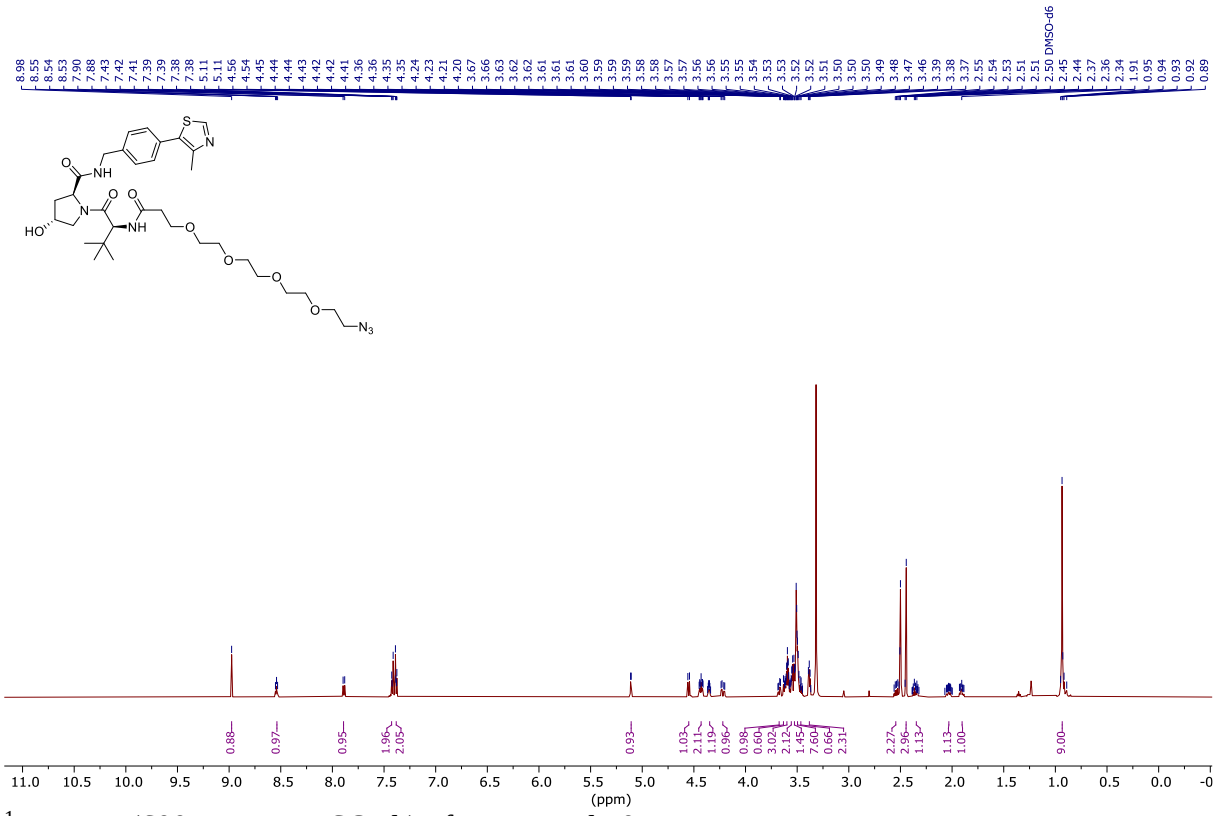
^{13}C-NMR (126 MHz, DMSO-d_6) of compound **8**.



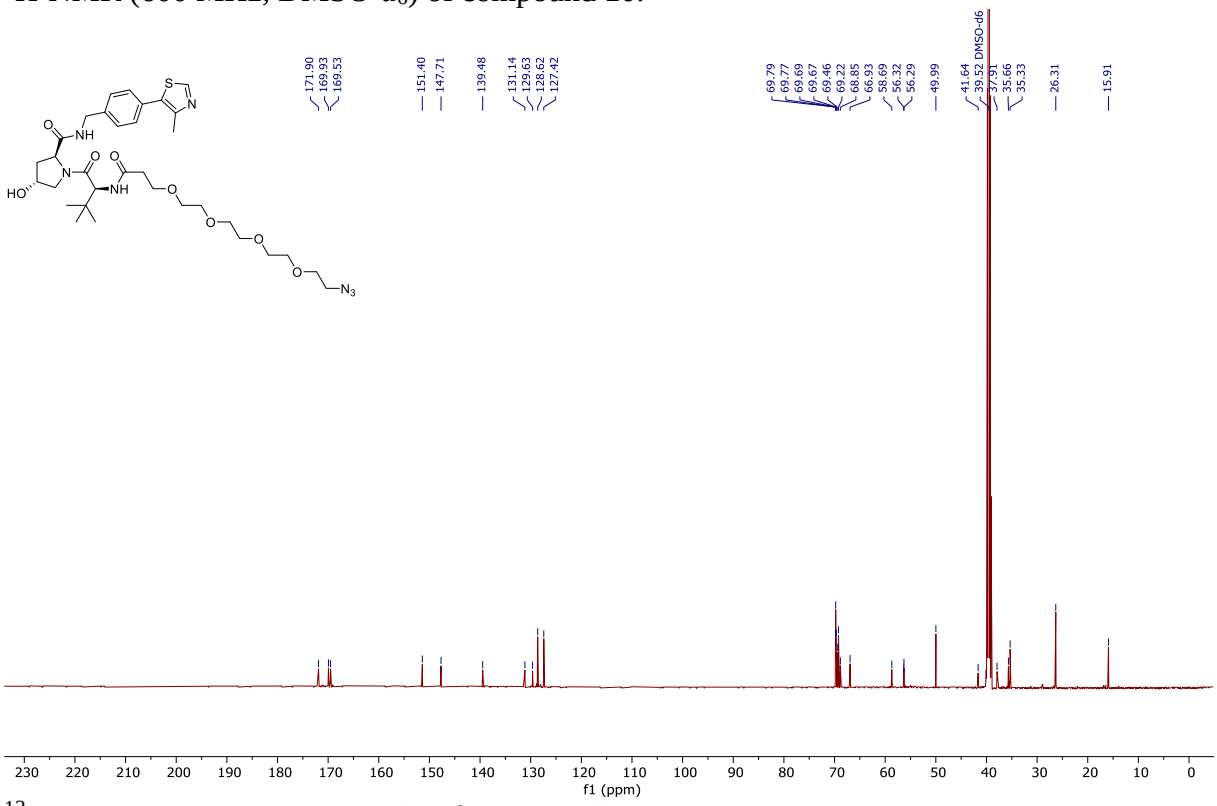
^{1}H-NMR (500 MHz, DMSO-d_6) of compound **9**.



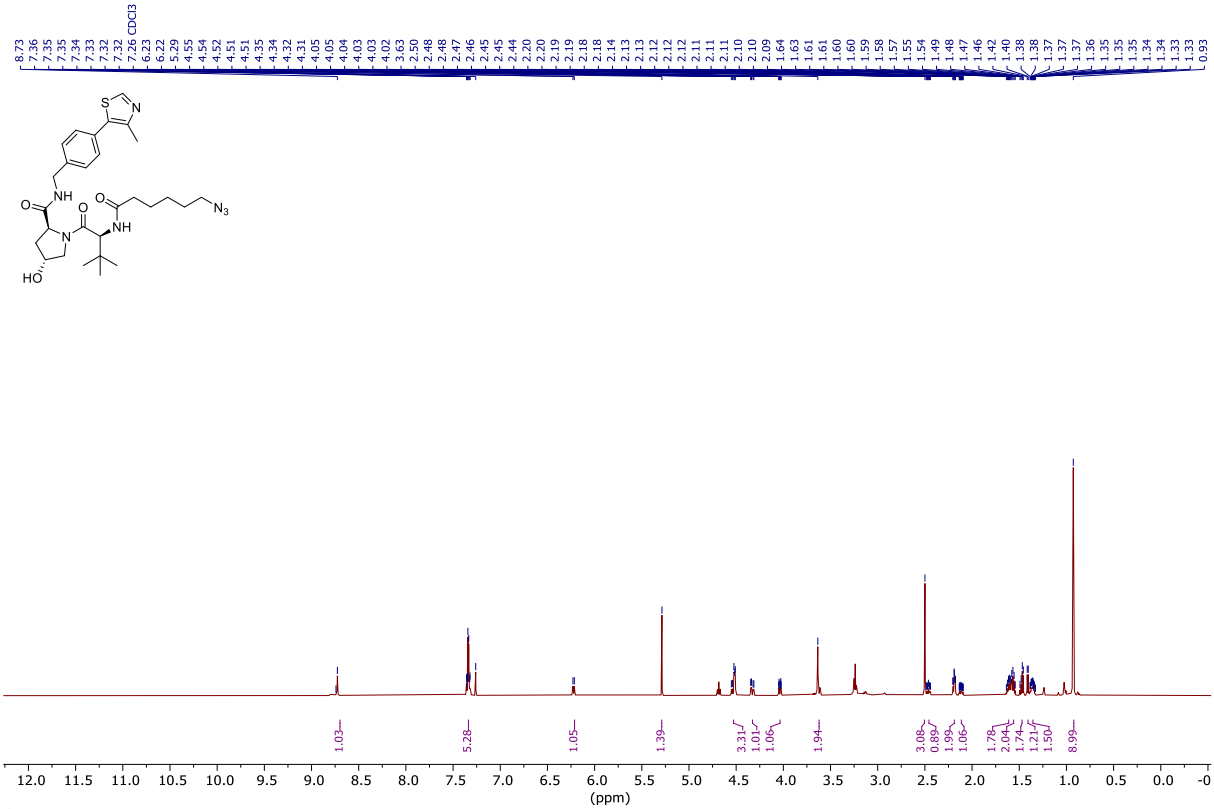
^{13}C-NMR (126 MHz, DMSO-d_6) of compound **9**.



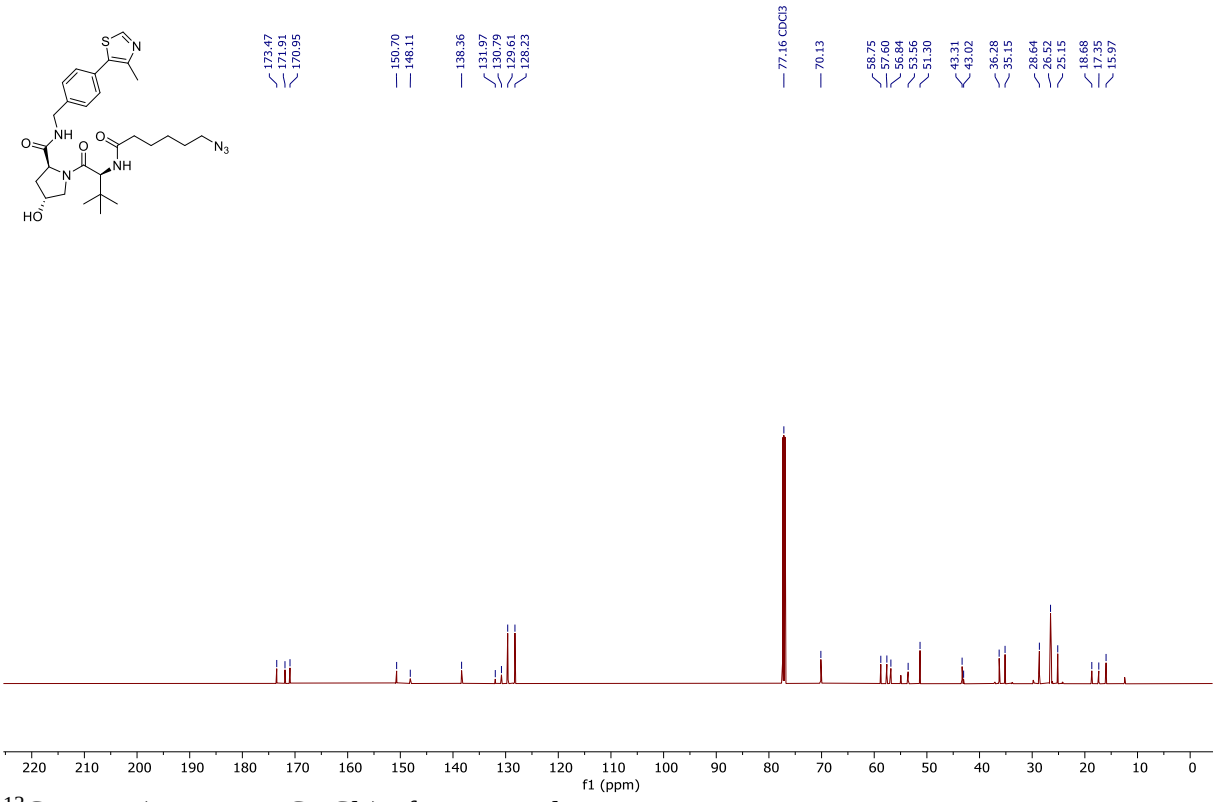
^{1}H-NMR (600 MHz, DMSO-d_6) of compound **10**.



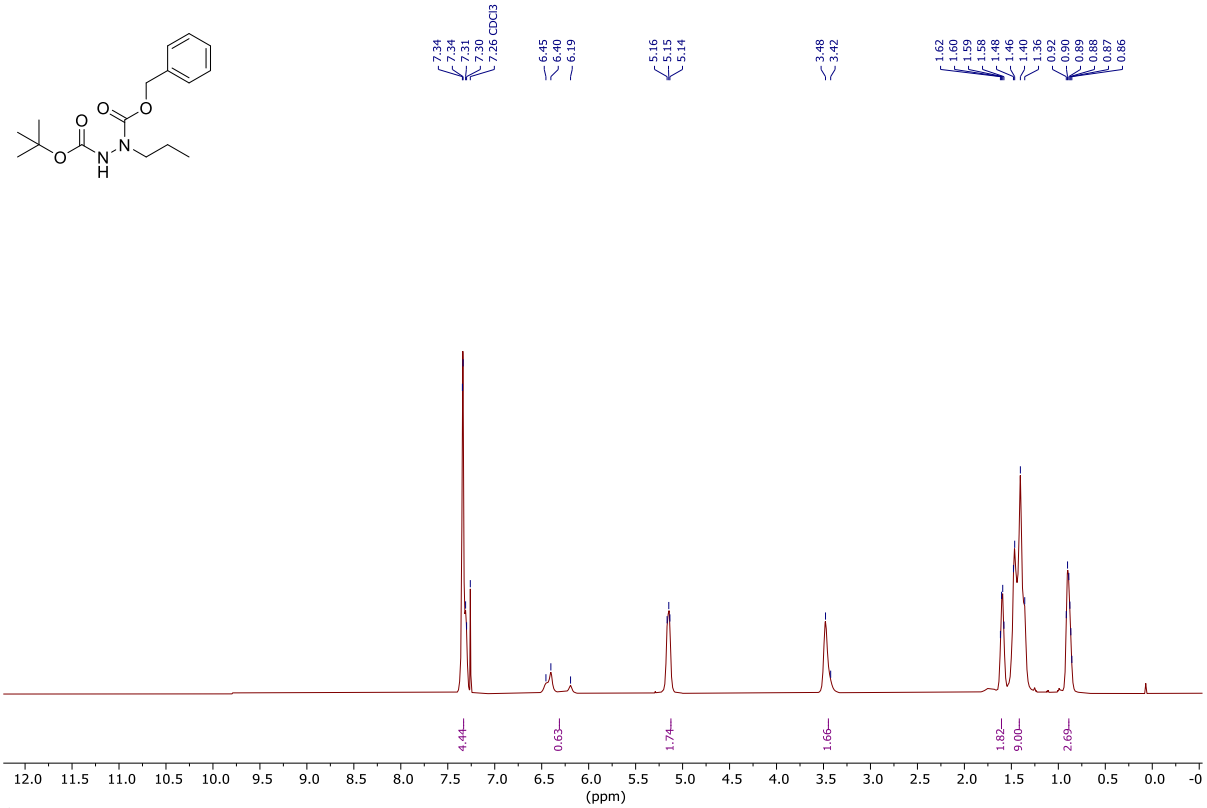
^{13}C-NMR (151 MHz, DMSO-d_6) of compound **10**.



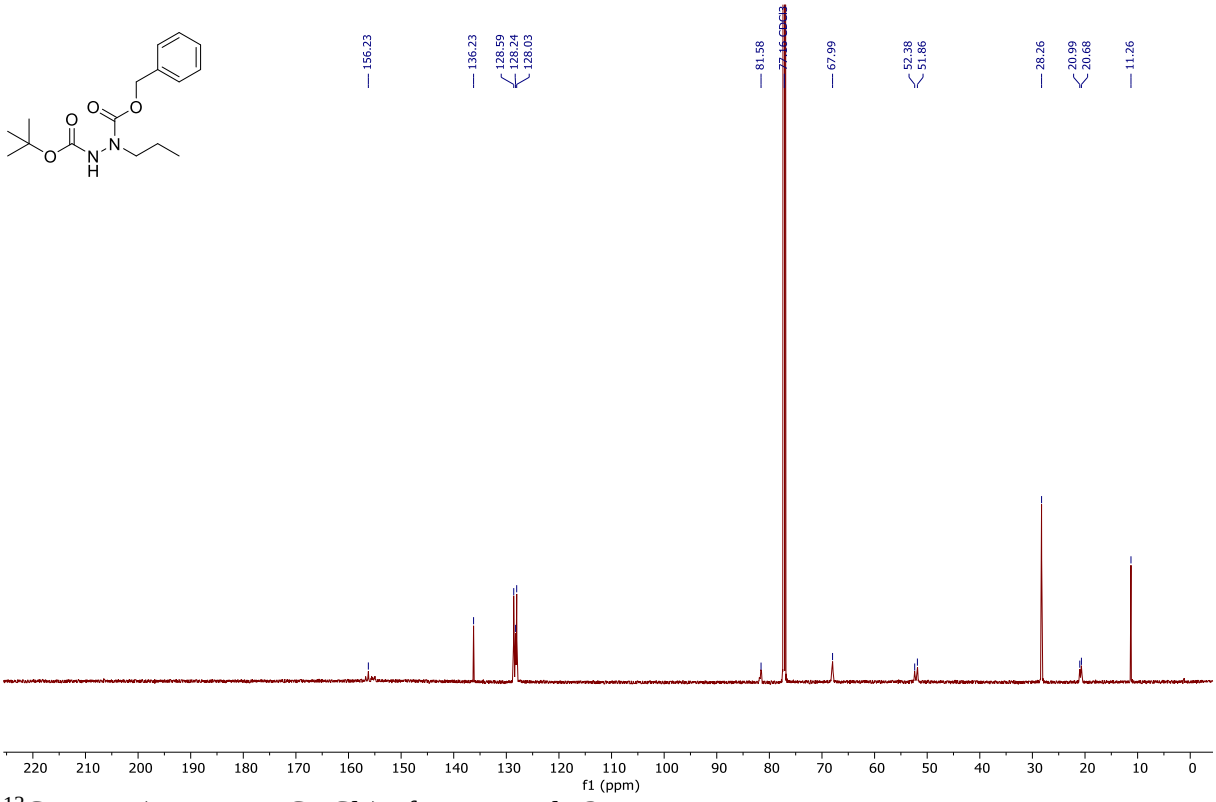
^{1}H-NMR (600 MHz, $CDCl_3$) of compound **11**.



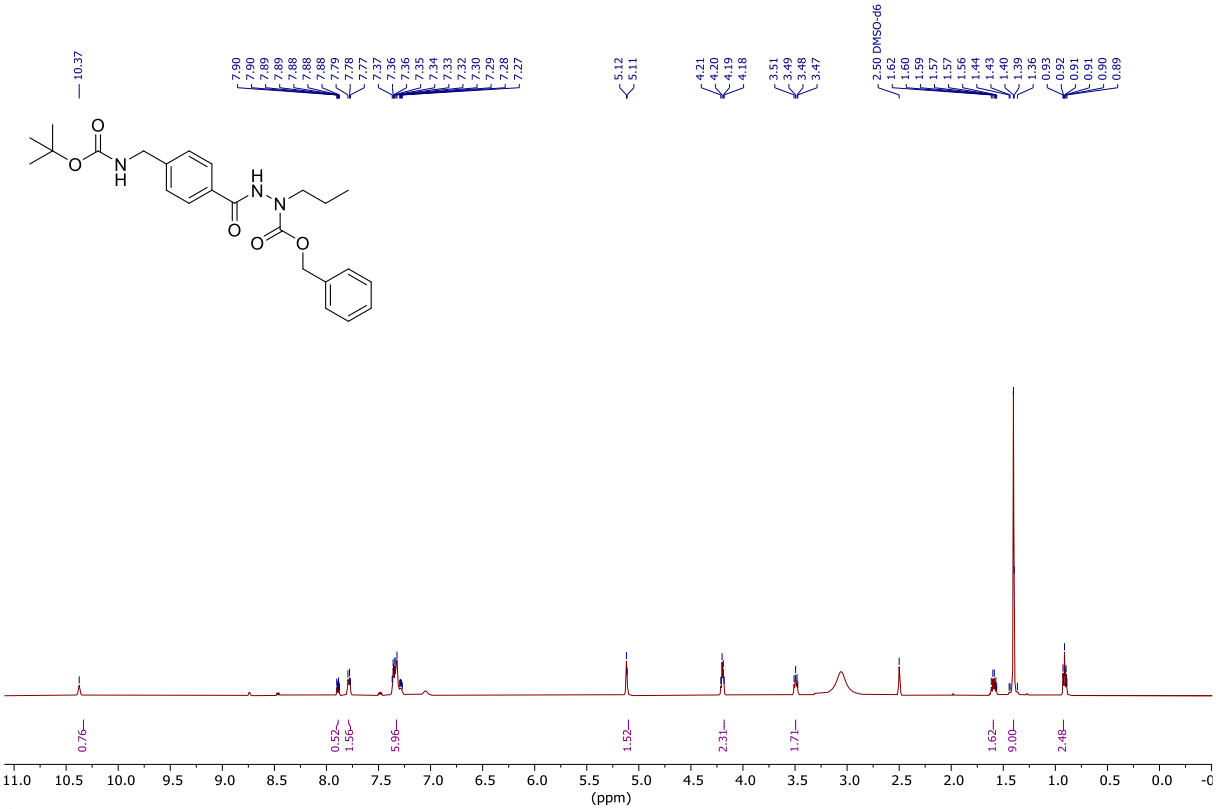
^{13}C-NMR (151 MHz, $CDCl_3$) of compound **11**.



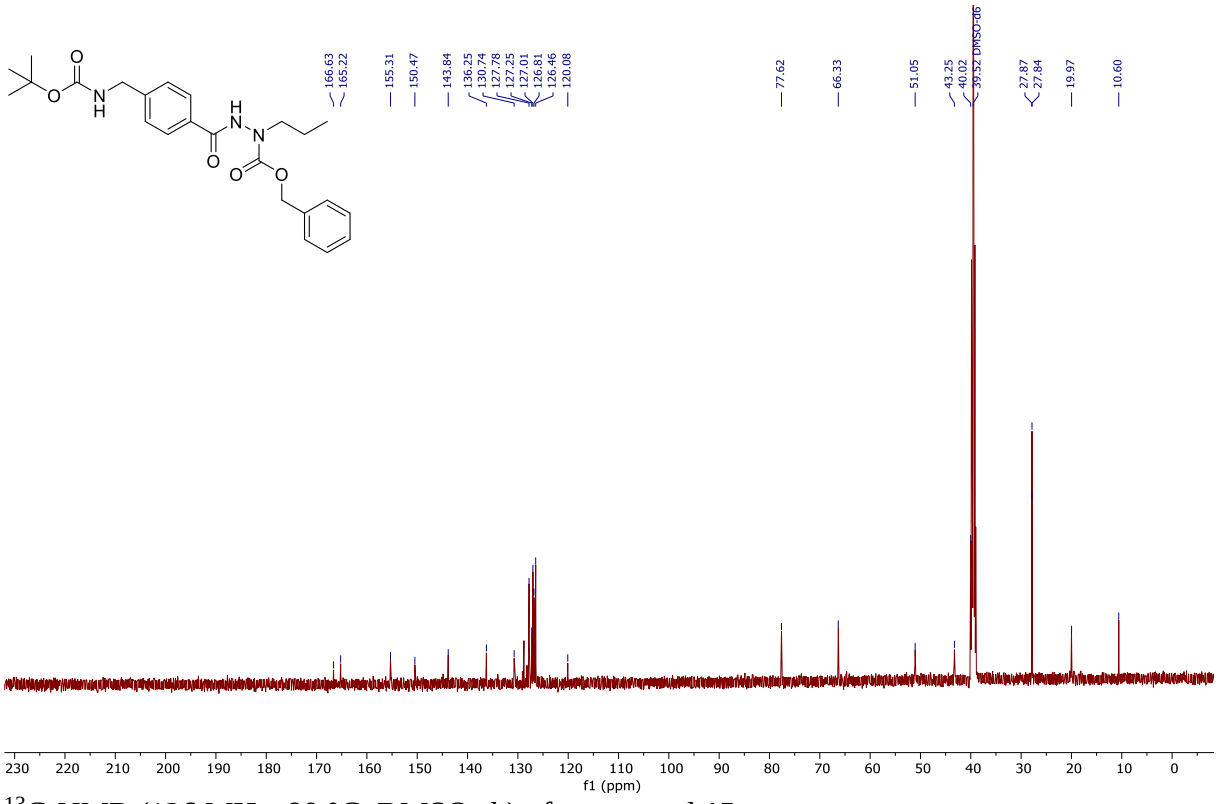
^{1}H-NMR (600 MHz, $CDCl_3$) of compound **13**.



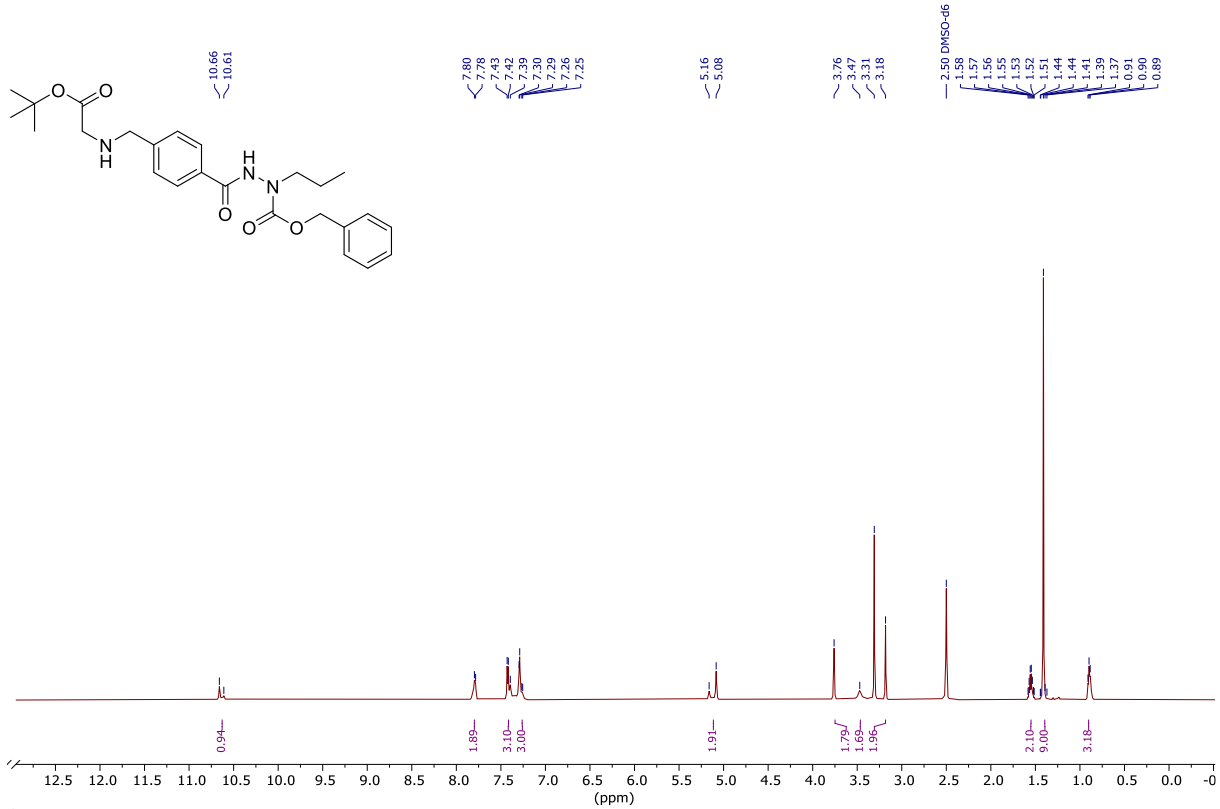
^{13}C-NMR (151 MHz, $CDCl_3$) of compound **13**.



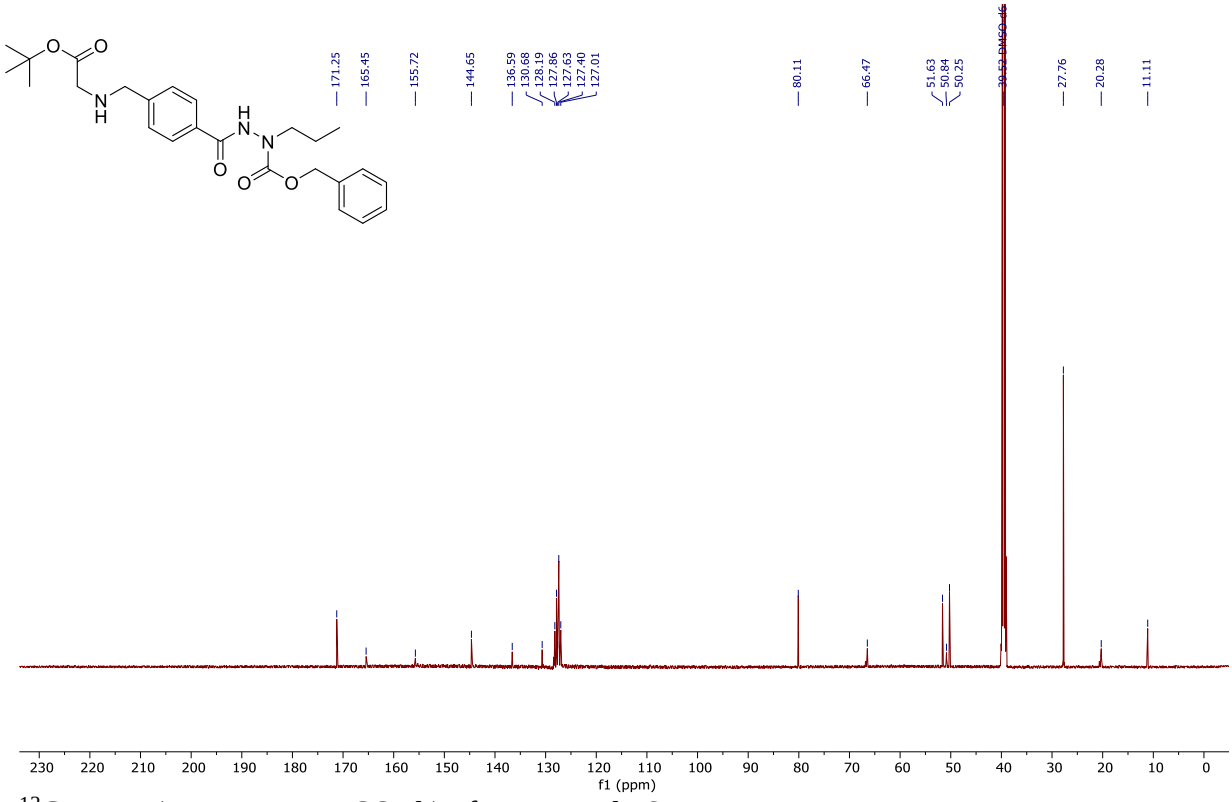
^{1}H-NMR (500 MHz, 90 °C, DMSO-d_6) of compound **15**.



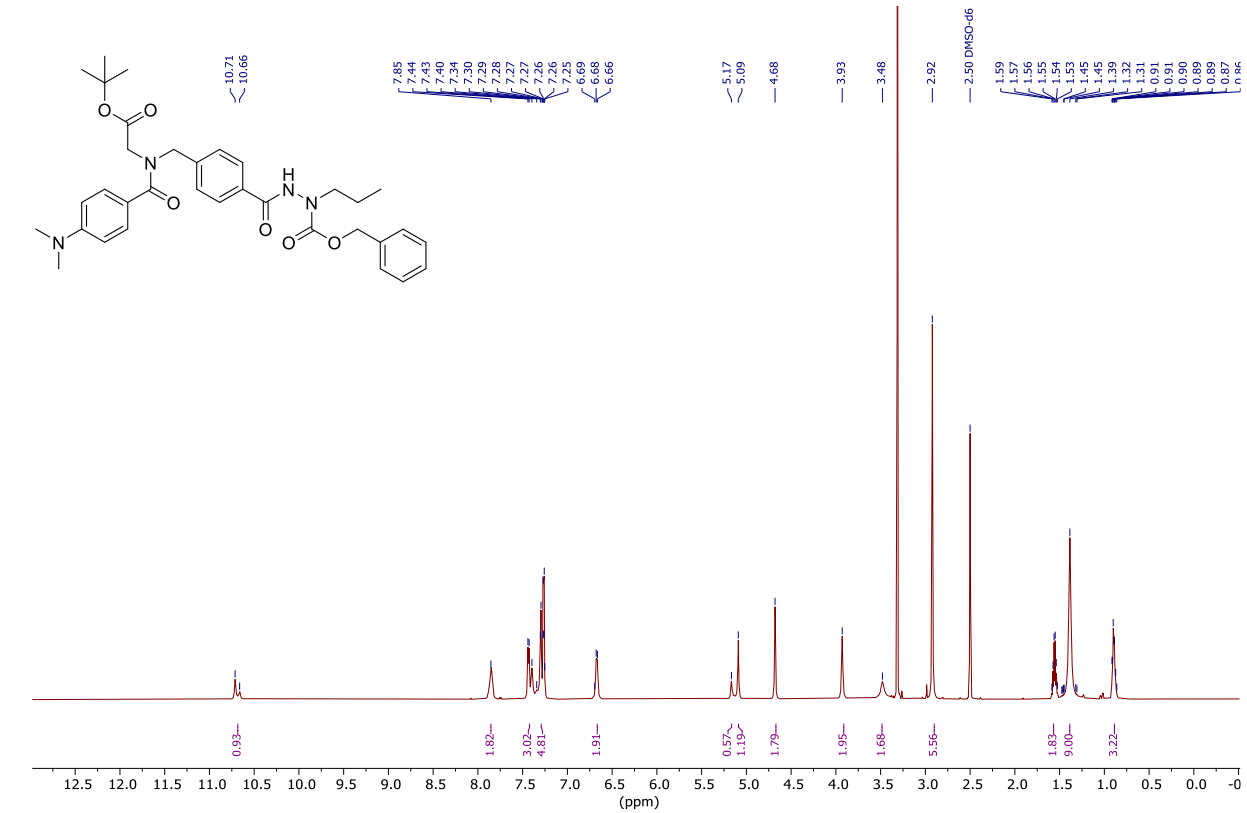
^{13}C-NMR (126 MHz, 90 °C, DMSO-d_6) of compound **15**.



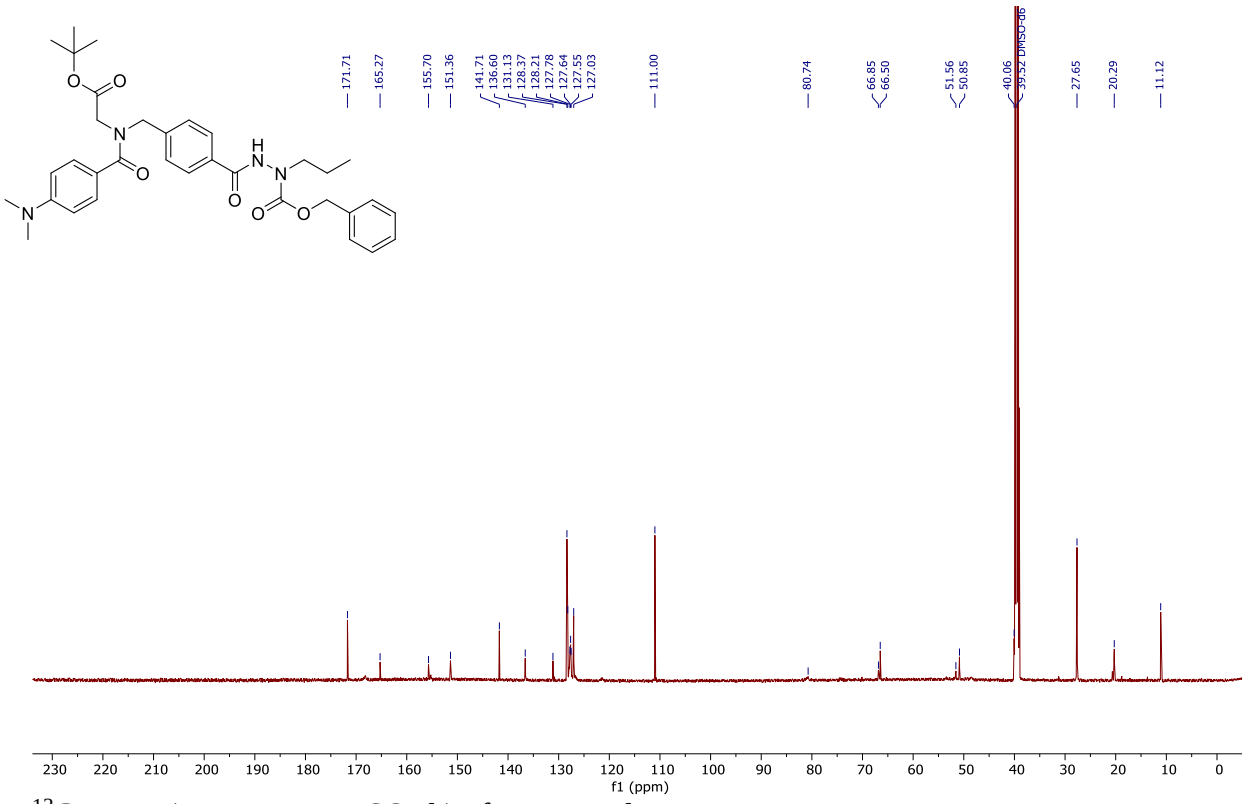
^{1}H-NMR (600 MHz, DMSO-d_6) of compound **16**.



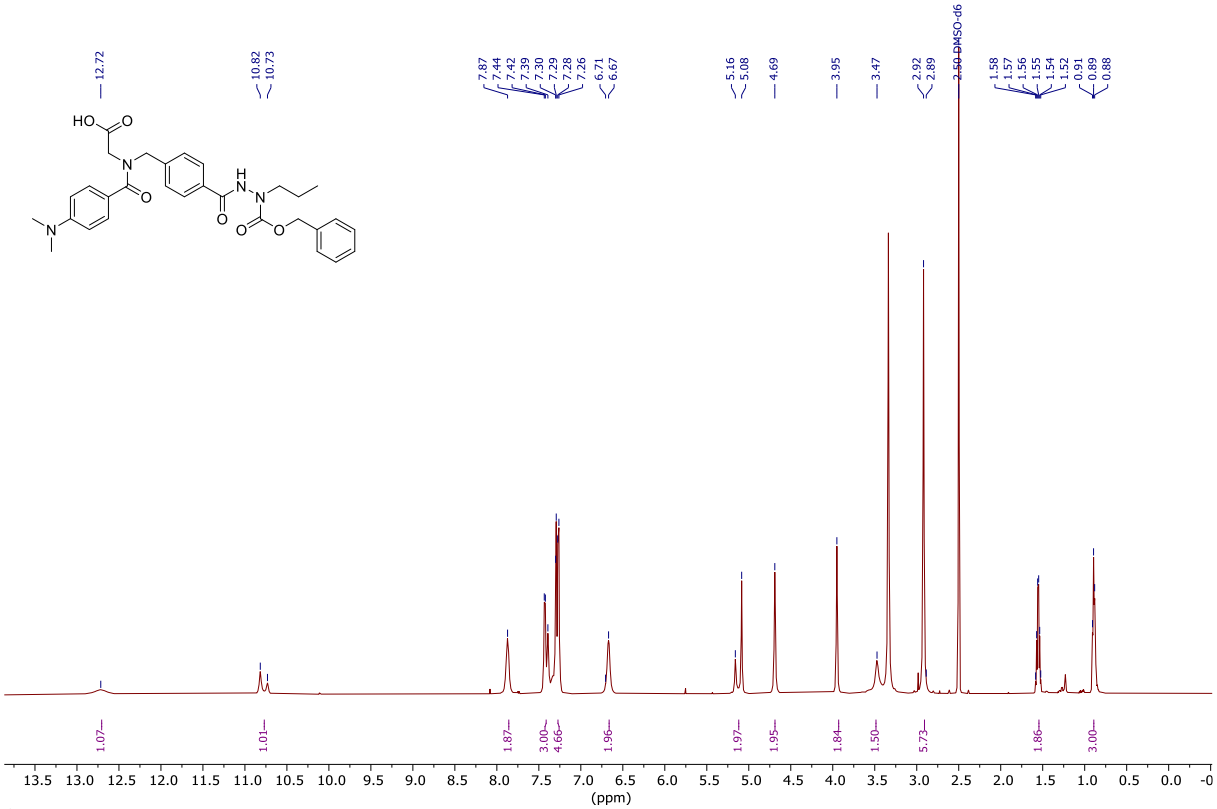
^{13}C-NMR (151 MHz, DMSO-d_6) of compound **16**.



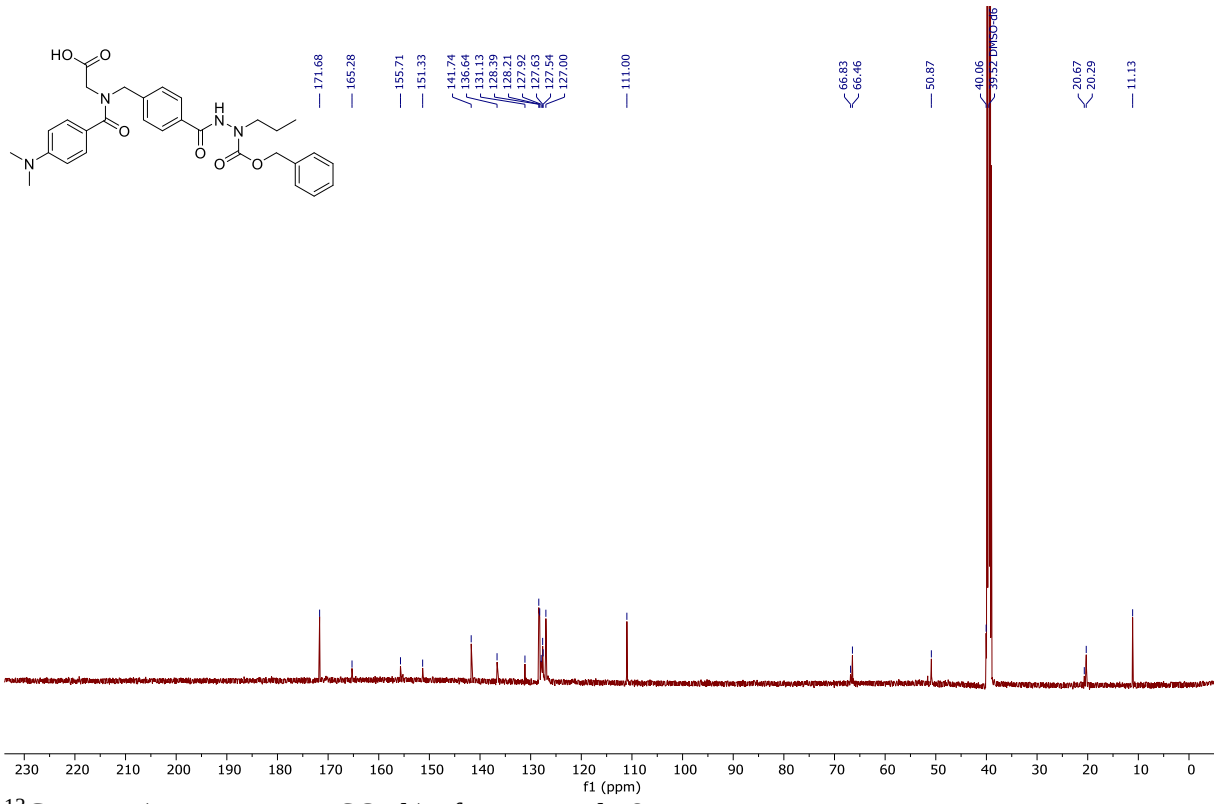
^{1}H-NMR (600 MHz, DMSO-d_6) of compound **17**.



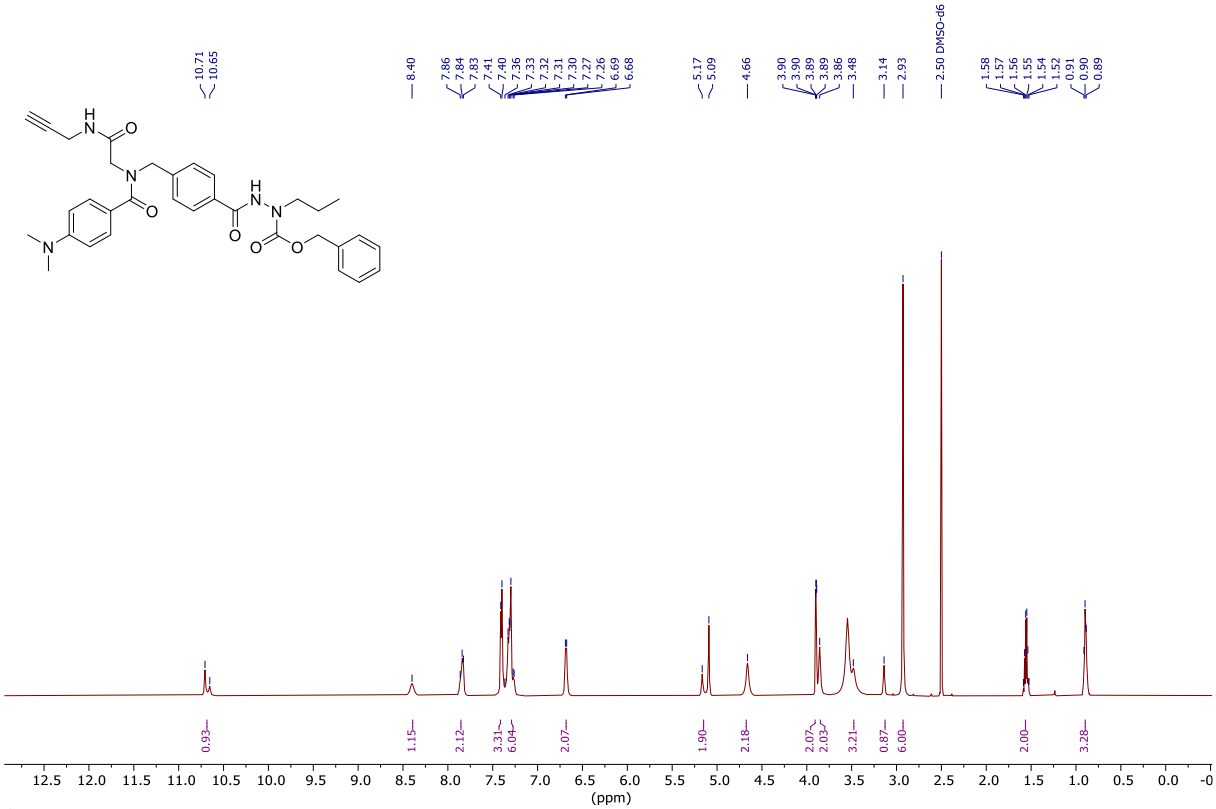
^{13}C-NMR (151 MHz, DMSO-d_6) of compound **17**.



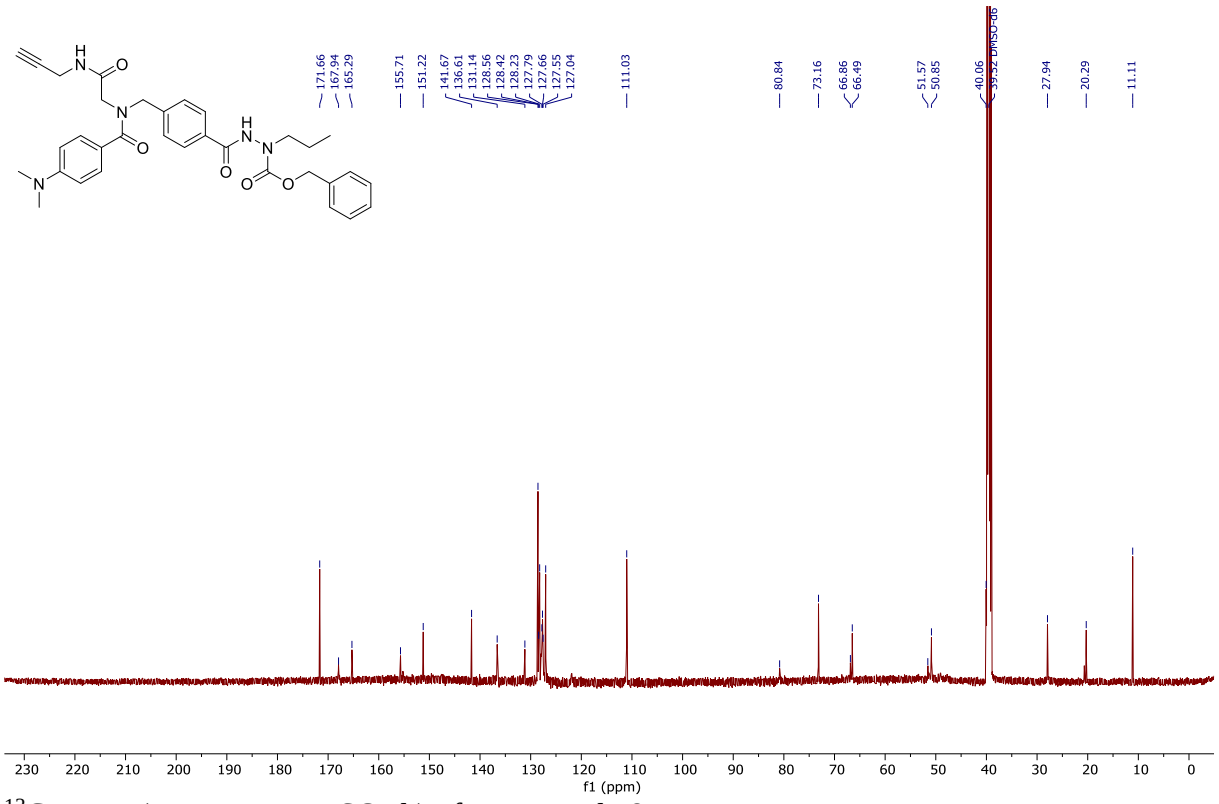
^{1}H-NMR (600 MHz, DMSO-d_6) of compound **18**.



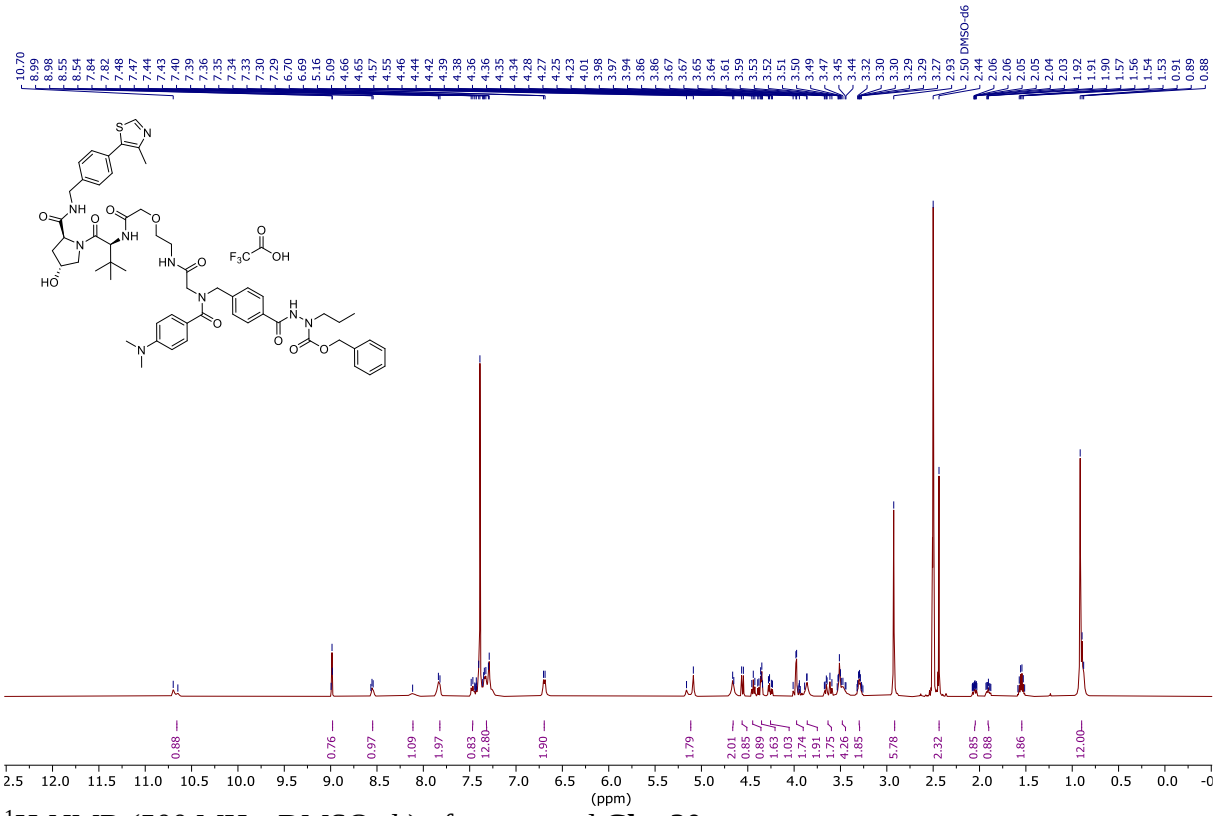
^{13}C-NMR (151 MHz, DMSO-d_6) of compound **18**.



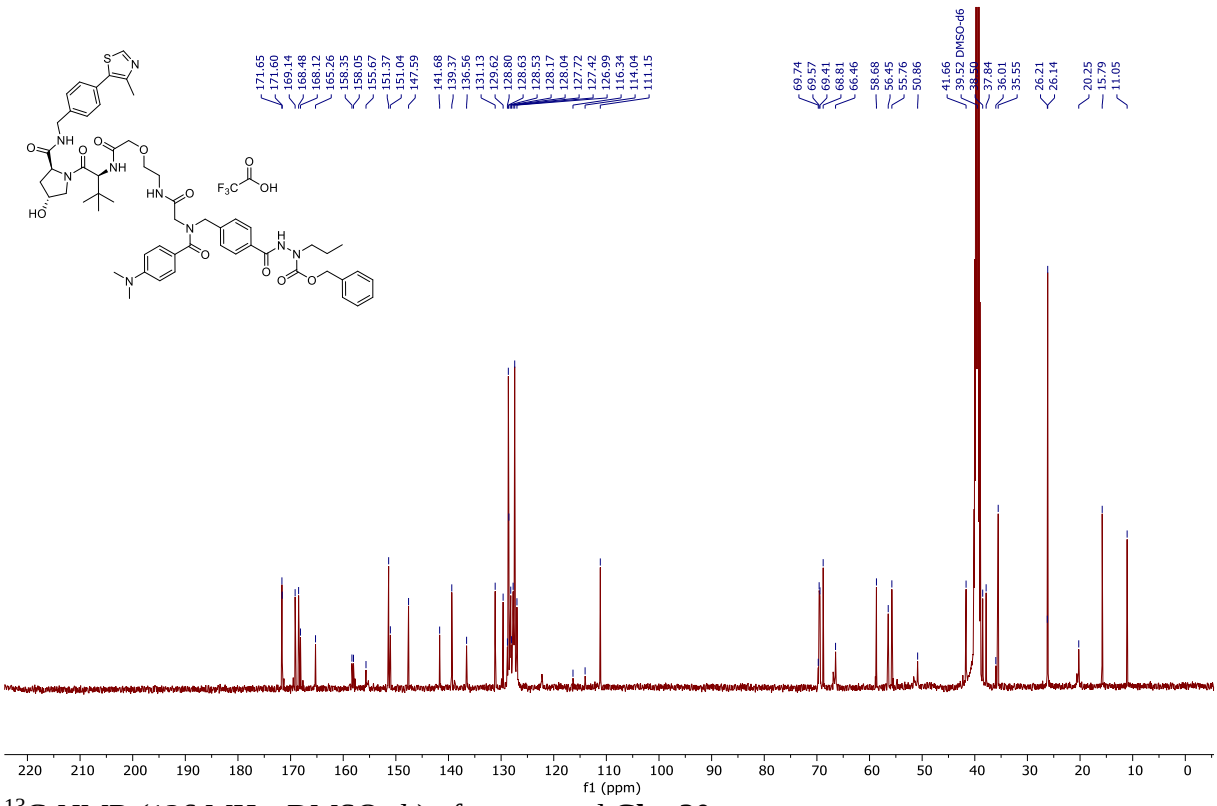
^{1}H-NMR (600 MHz, DMSO-d_6) of compound **19**.



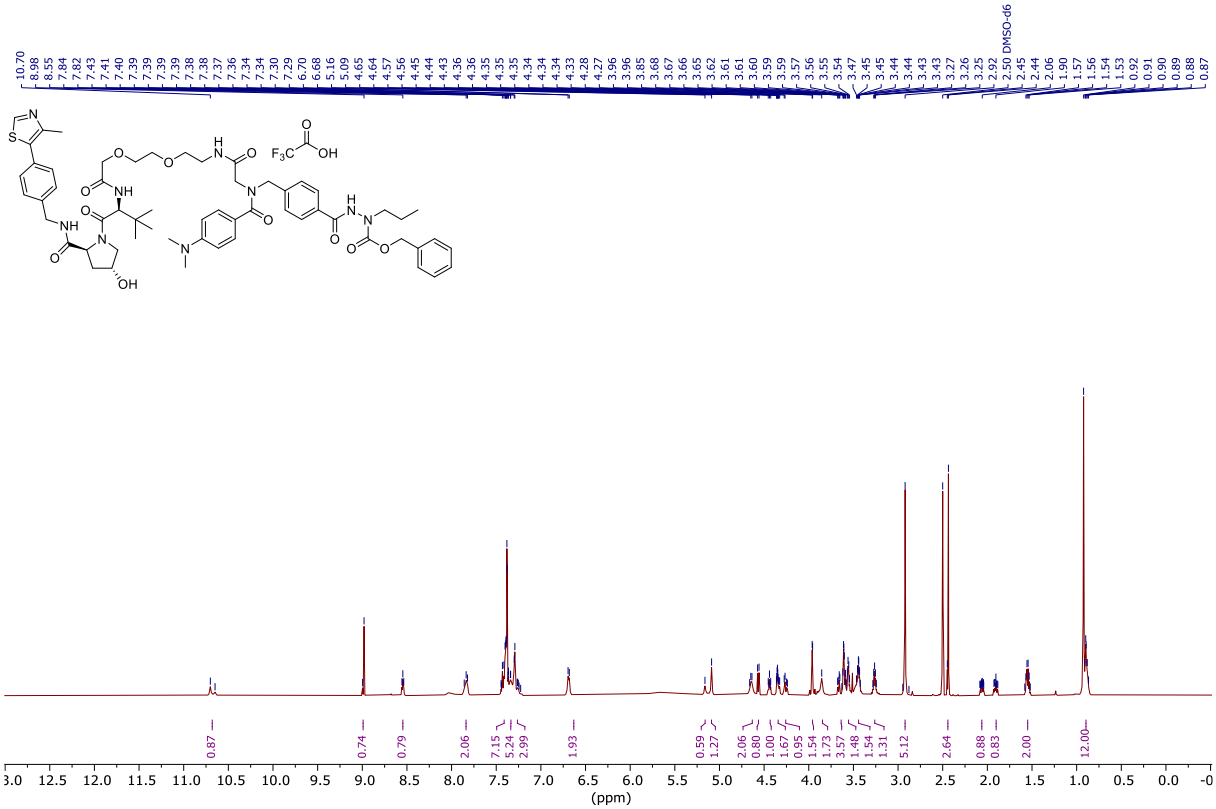
^{13}C-NMR (151 MHz, DMSO-d_6) of compound **19**.



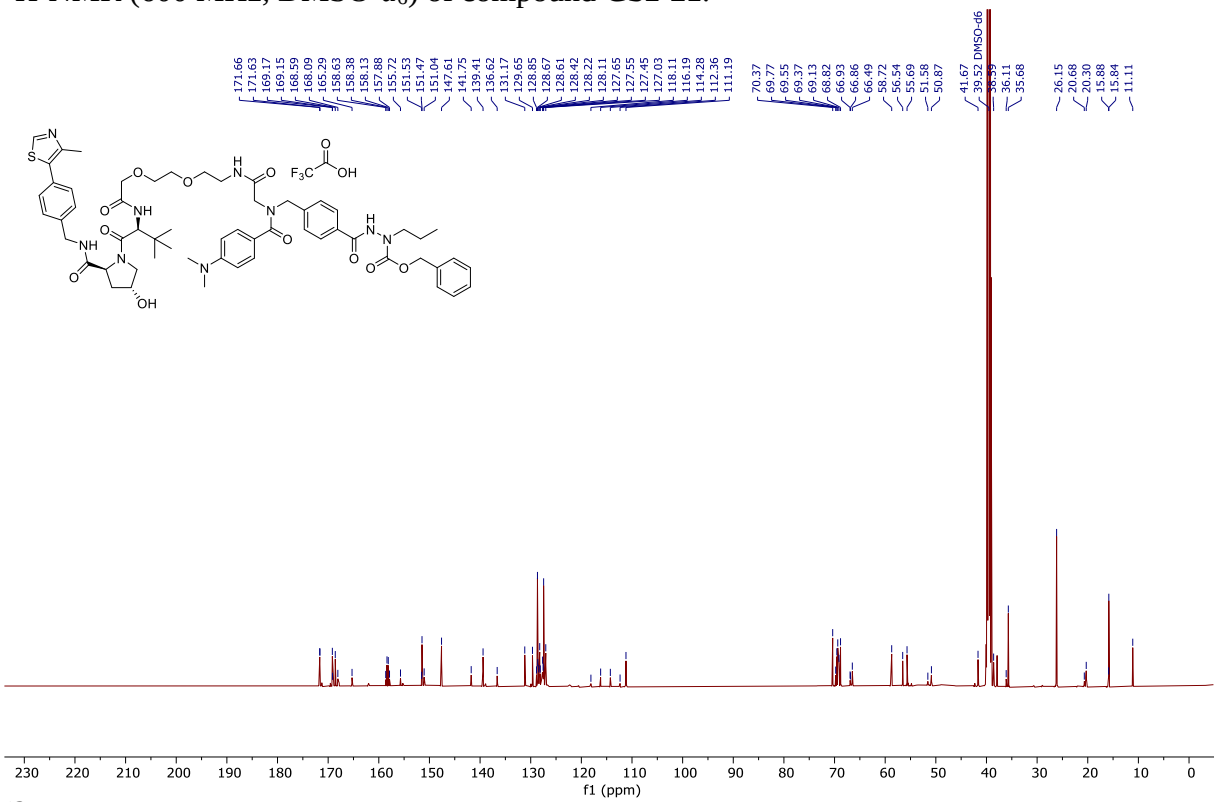
^{1}H-NMR (500 MHz, DMSO-d_6) of compound **Cbz-20**.



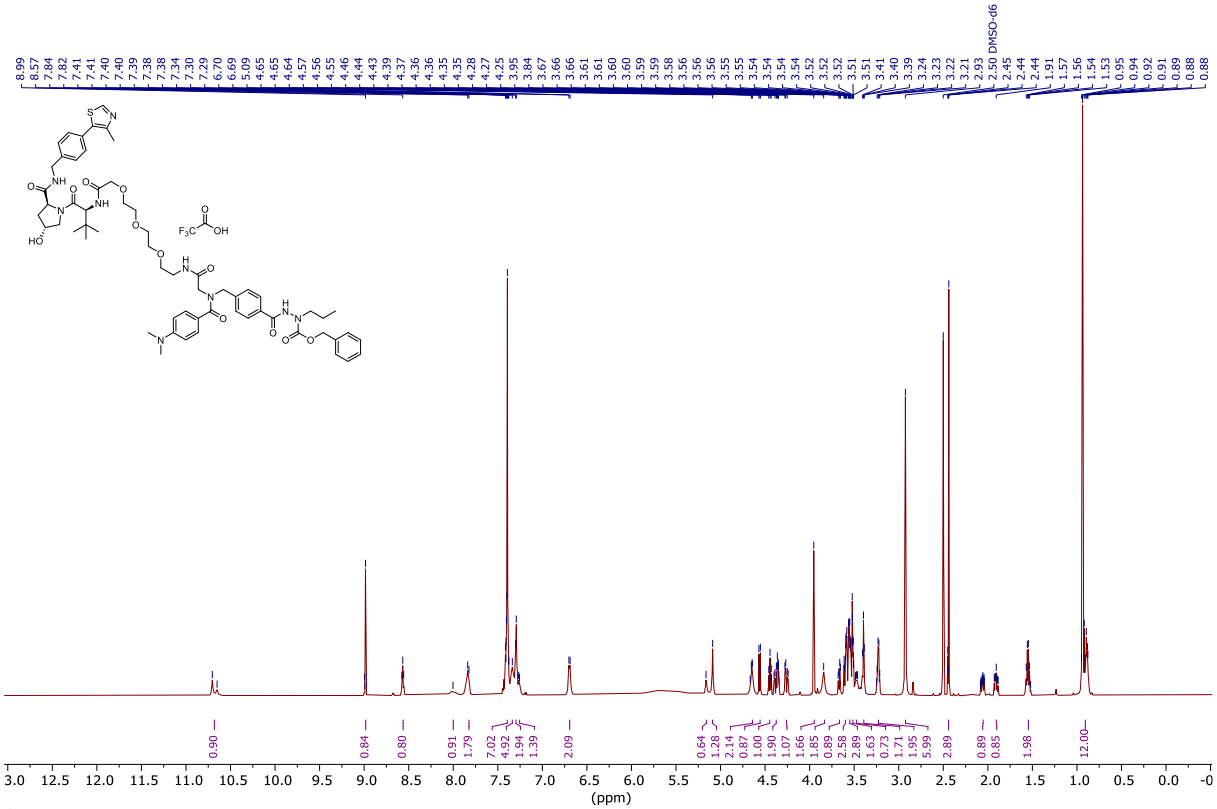
^{13}C-NMR (126 MHz, DMSO-d_6) of compound **Cbz-20**.



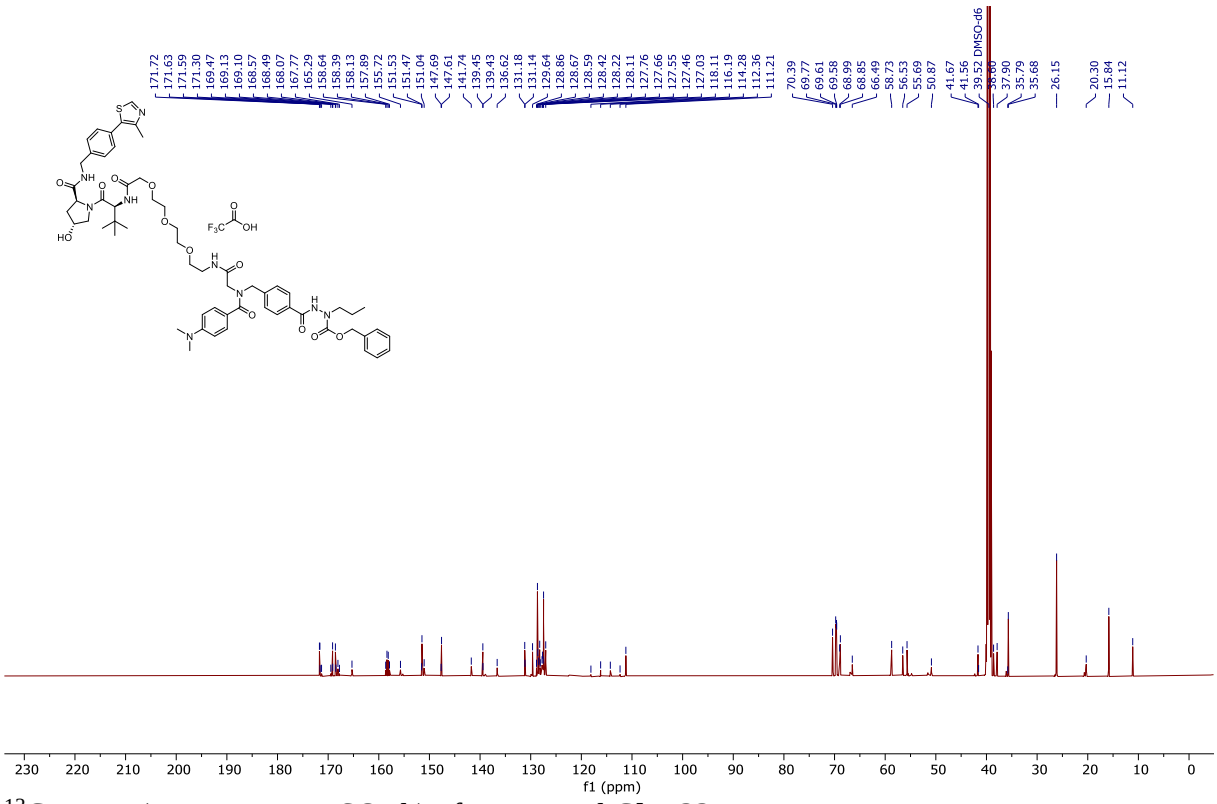
^{1}H-NMR (600 MHz, DMSO-d_6) of compound **Cbz-21**.



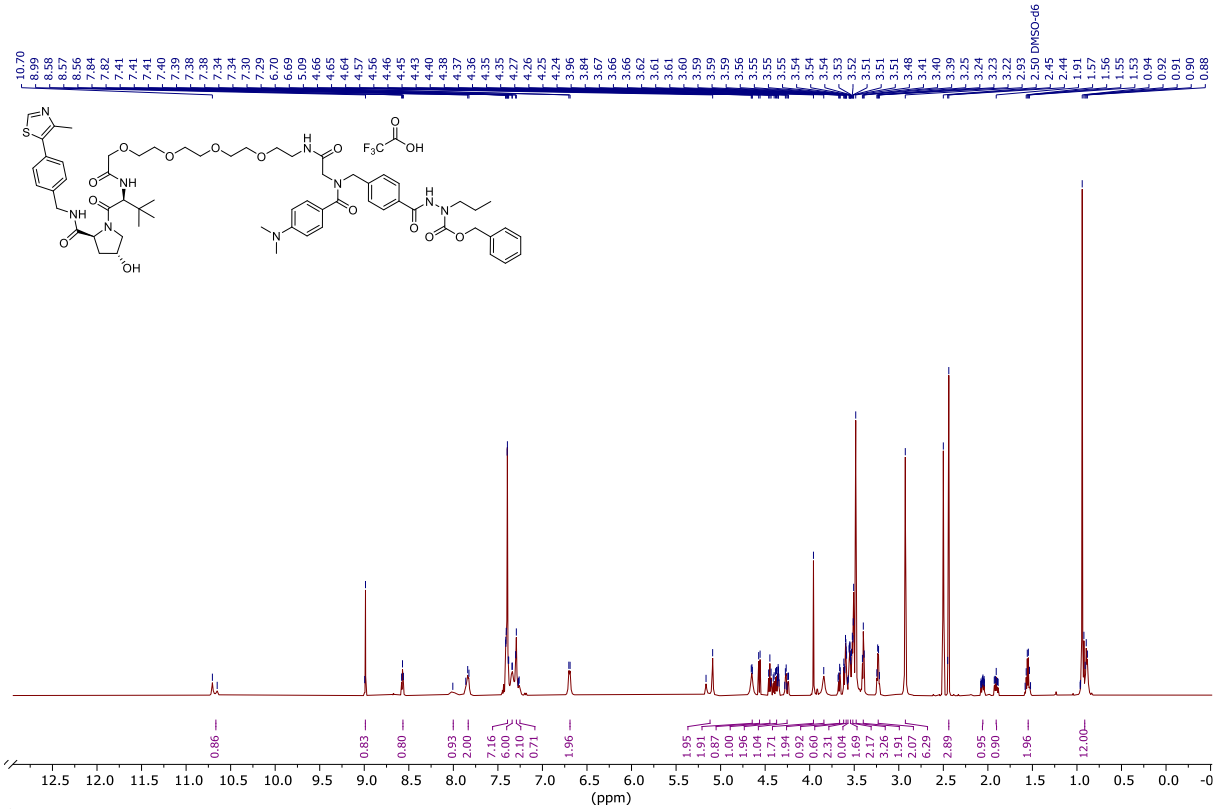
^{13}C-NMR (151 MHz, DMSO-d_6) of compound **Cbz-21**.



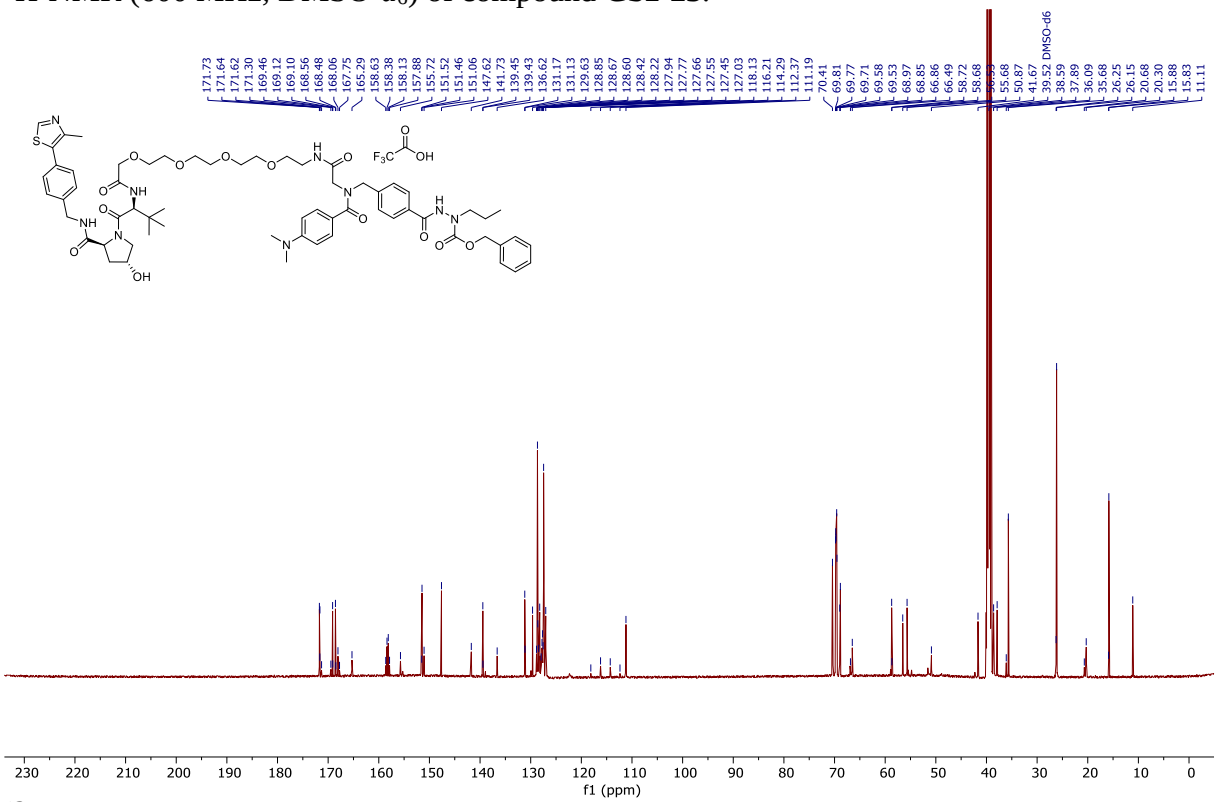
^{1}H-NMR (600 MHz, DMSO-d_6) of compound **Cbz-22**.



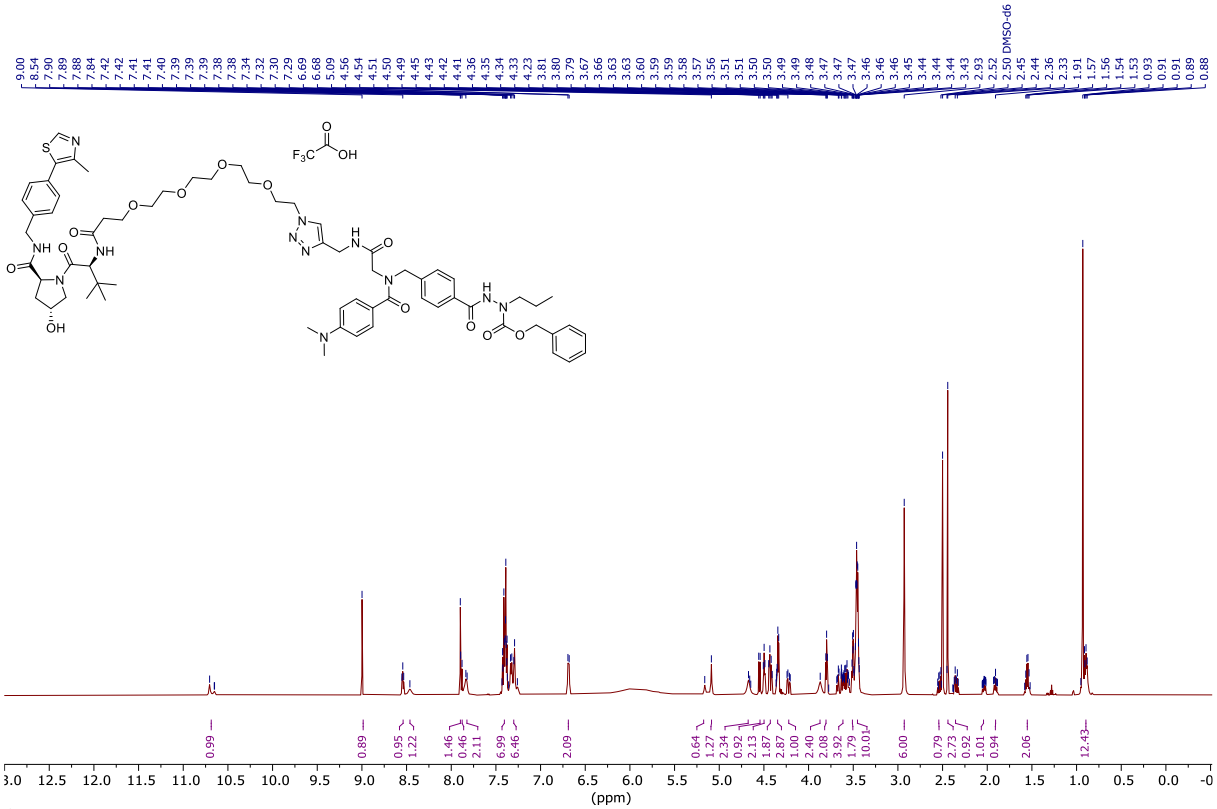
^{13}C-NMR (151 MHz, DMSO-d_6) of compound **Cbz-22**.



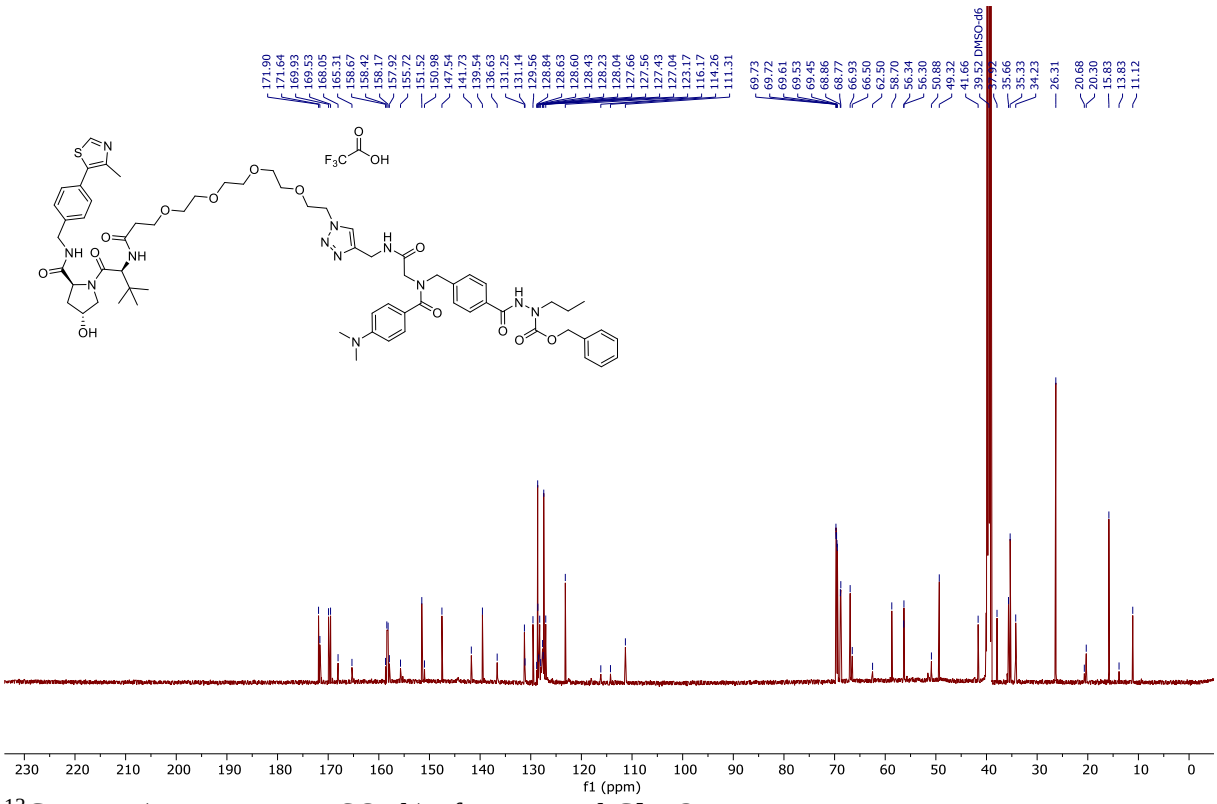
^{1}H-NMR (600 MHz, DMSO-d_6) of compound **Cbz-23**.



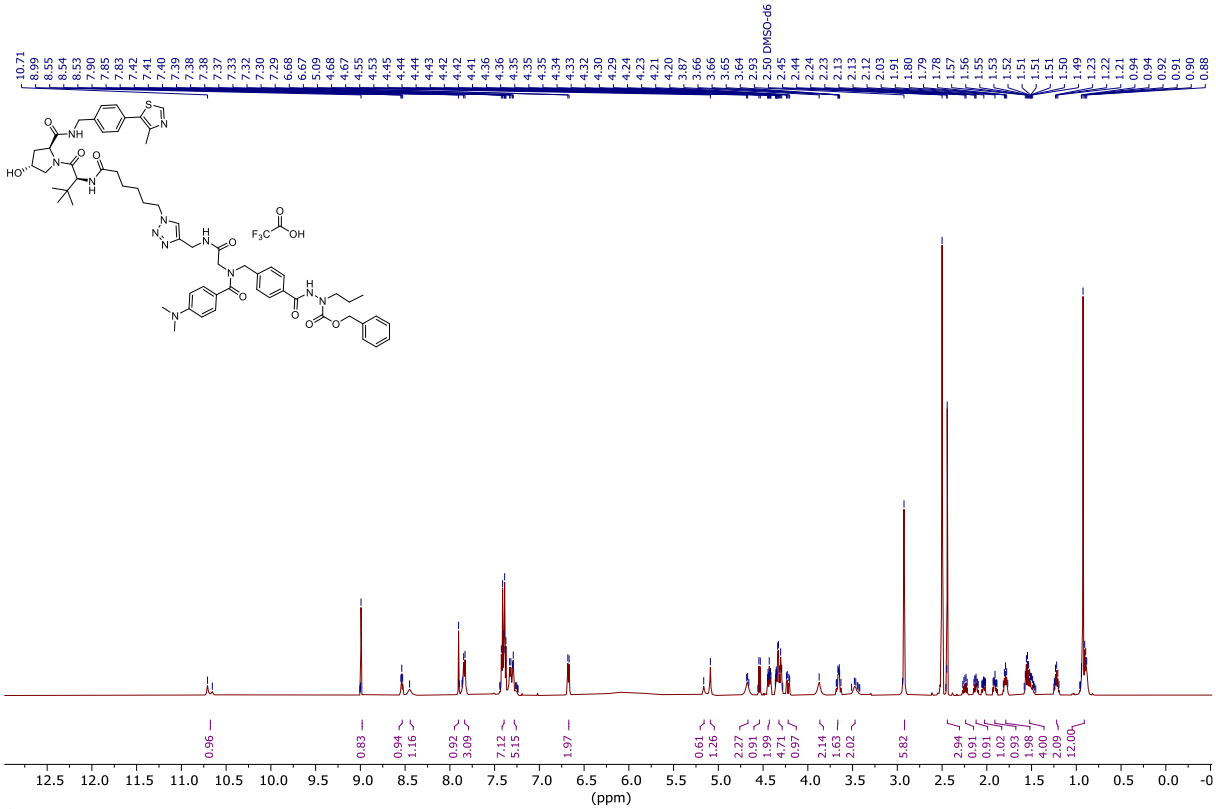
^{13}C-NMR (151 MHz, DMSO-d_6) of compound **Cbz-23**.



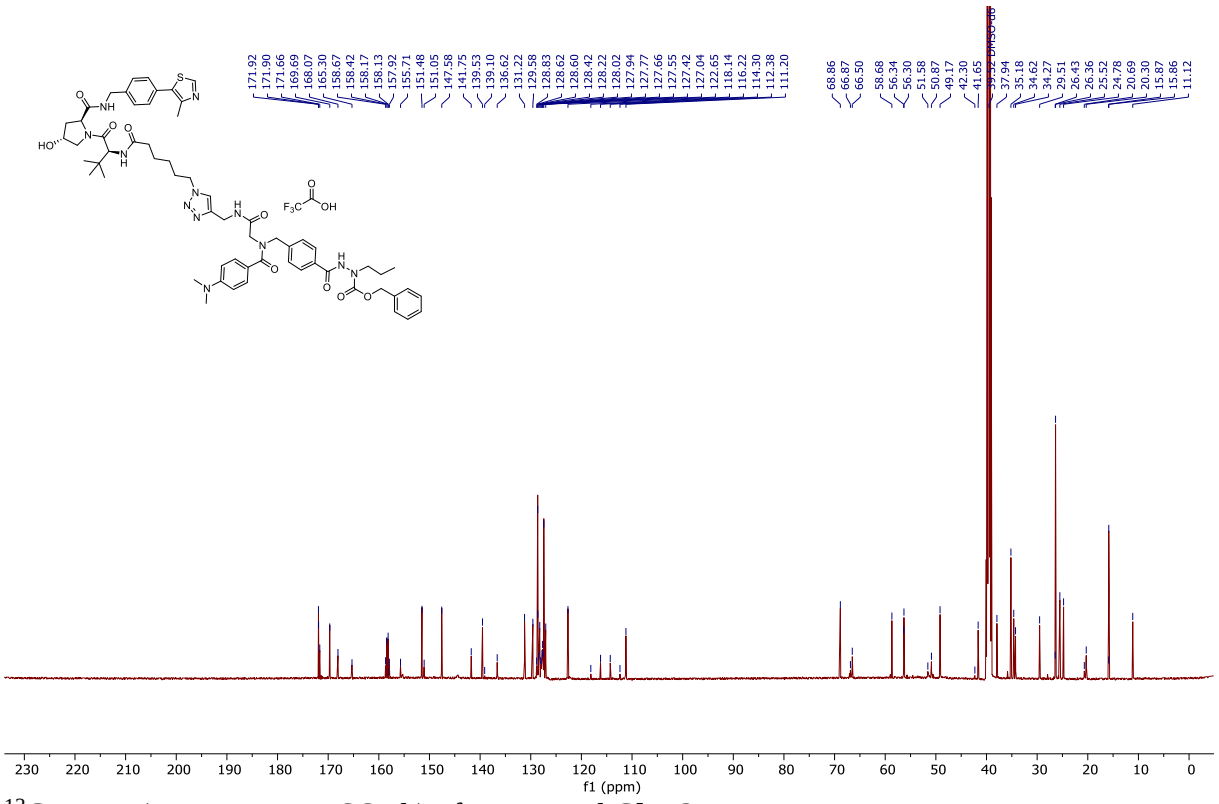
^{1}H-NMR (600 MHz, DMSO-d_6) of compound **Cbz-24**.



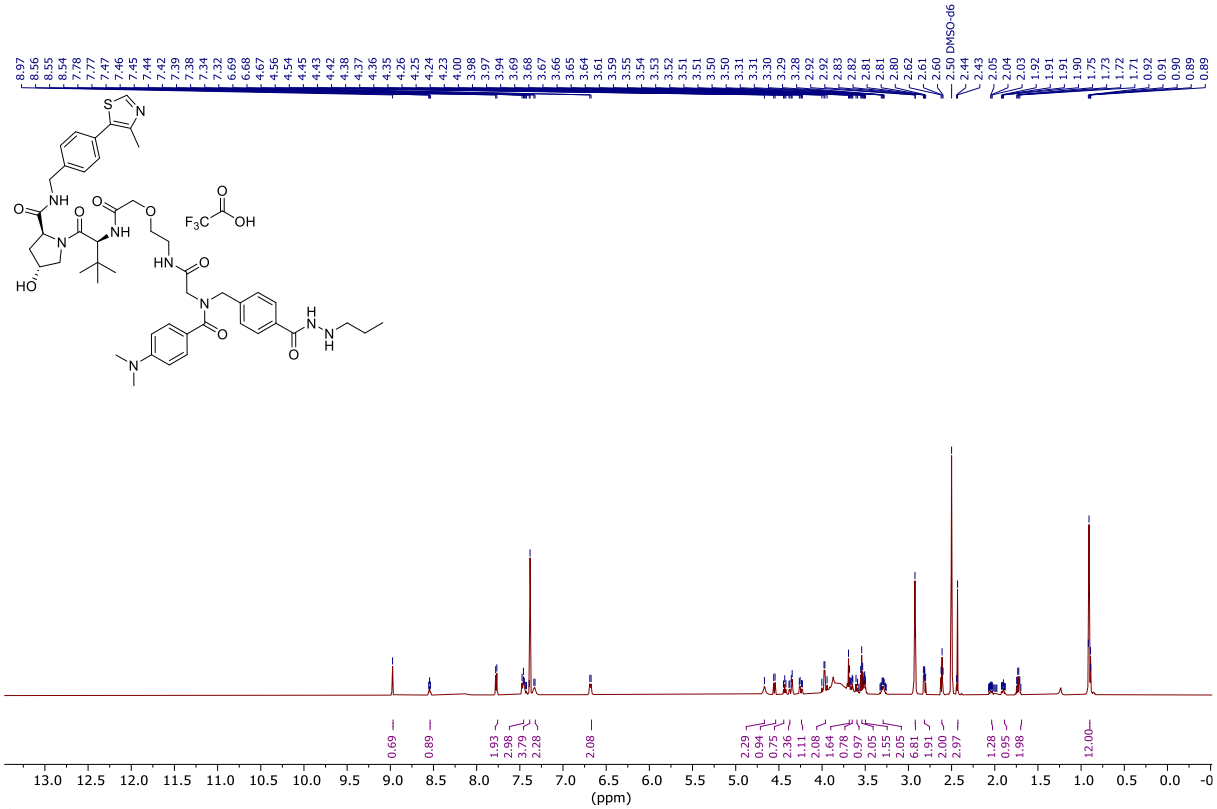
^{13}C-NMR (151 MHz, DMSO-d_6) of compound **Cbz-24**.



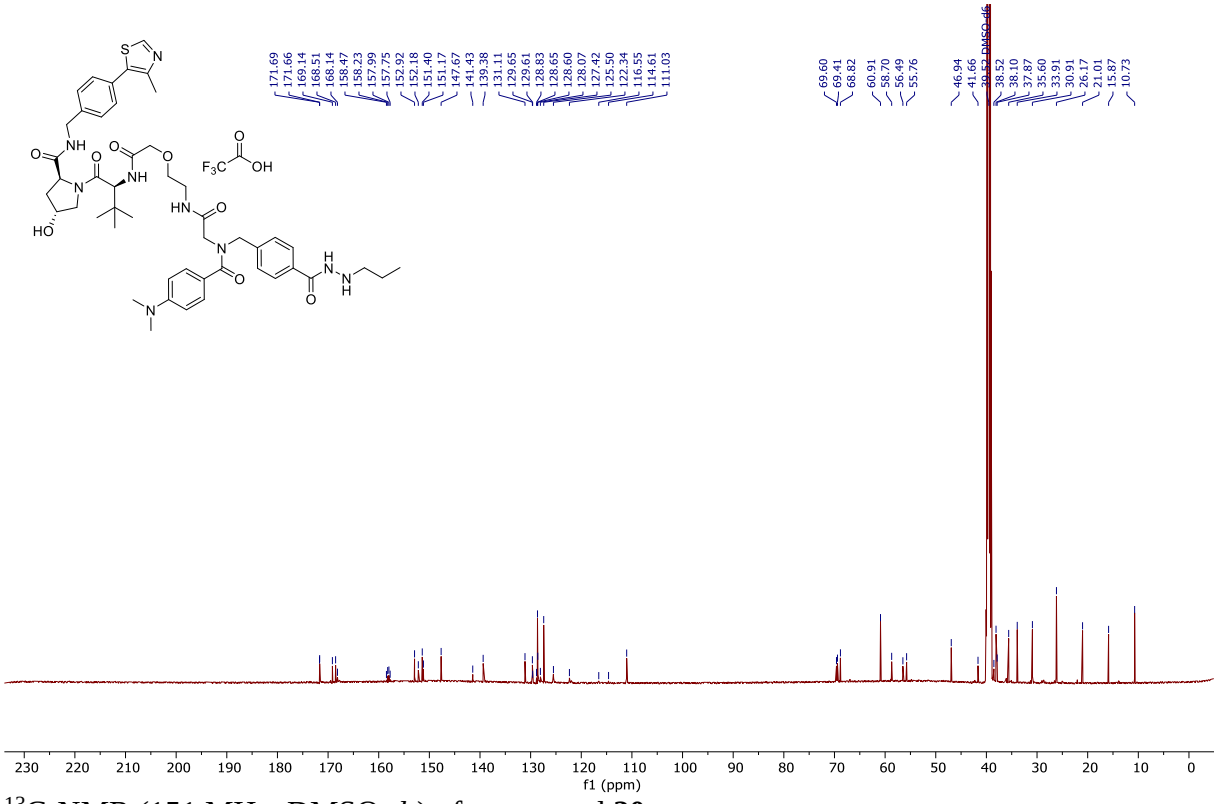
^{1}H-NMR (600 MHz, DMSO-d_6) of compound **Cbz-25**.



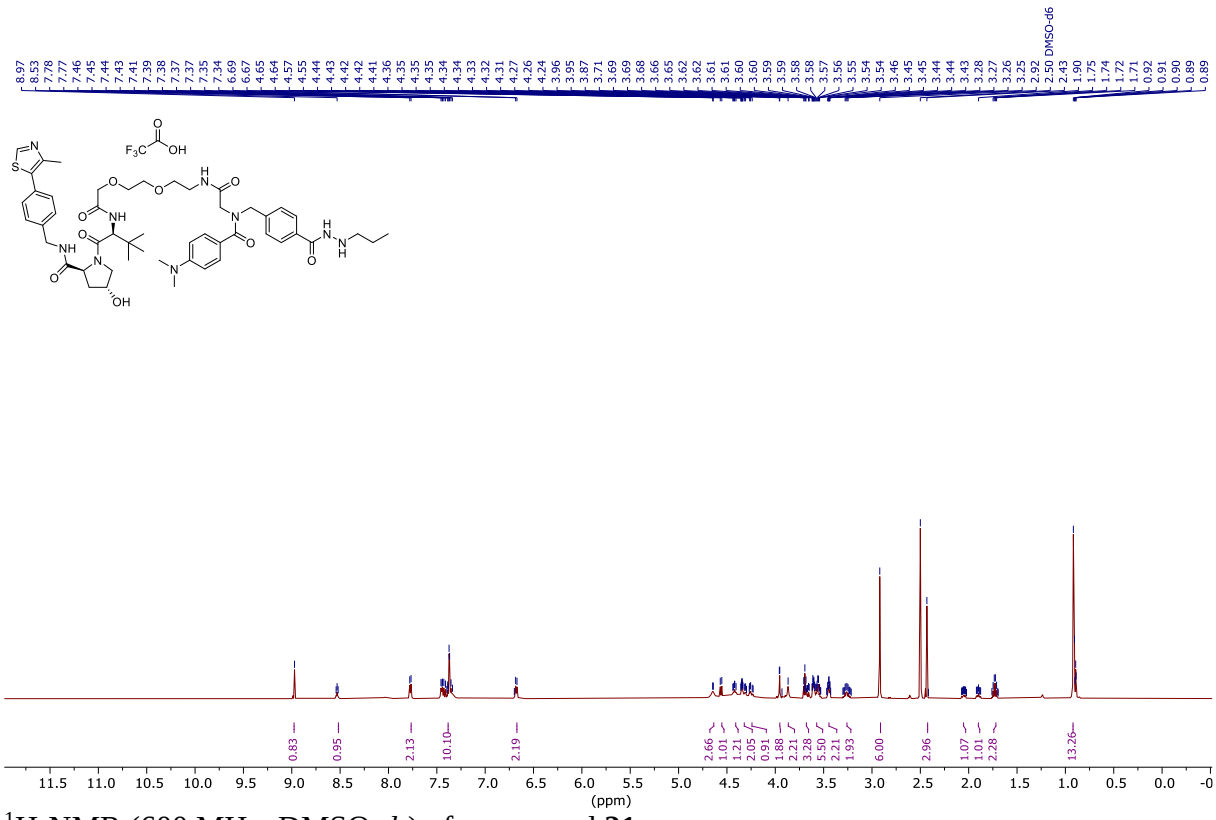
^{13}C-NMR (151 MHz, DMSO-d_6) of compound **Cbz-25**.



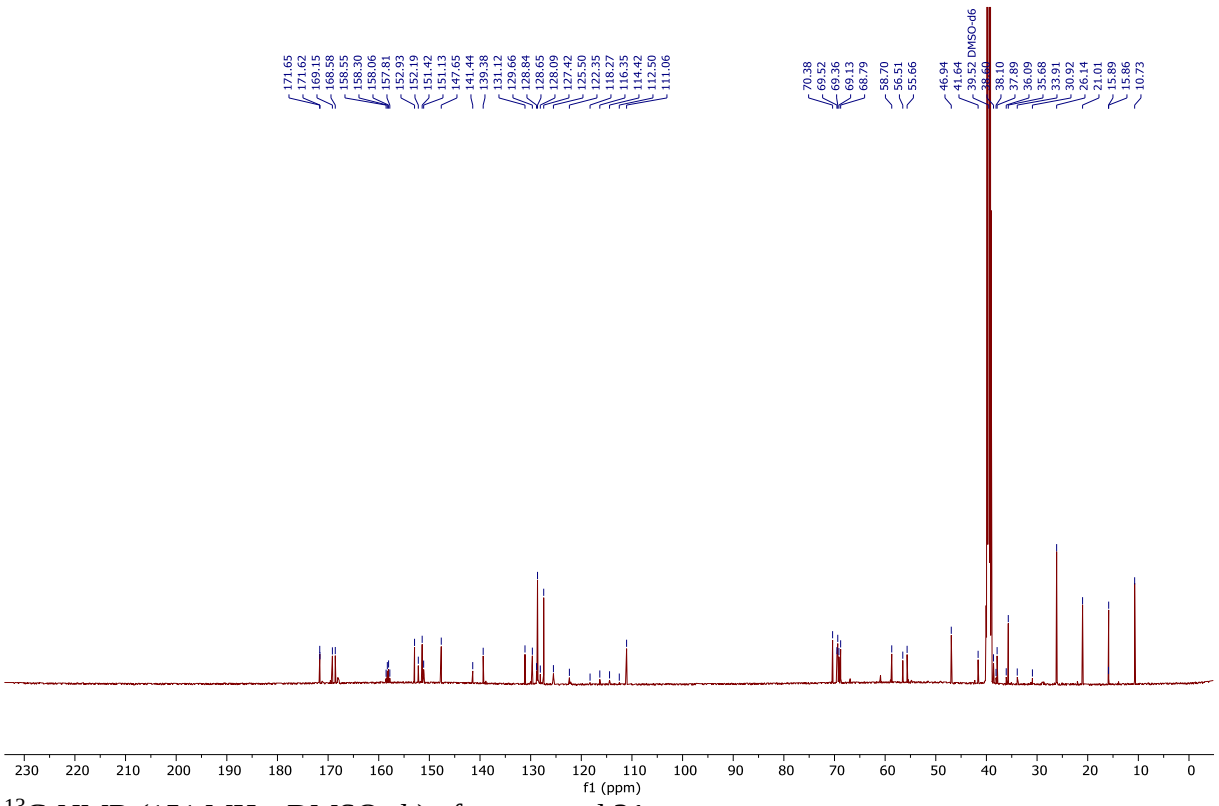
^{1}H-NMR (600 MHz, DMSO-d_6) of compound **20**.



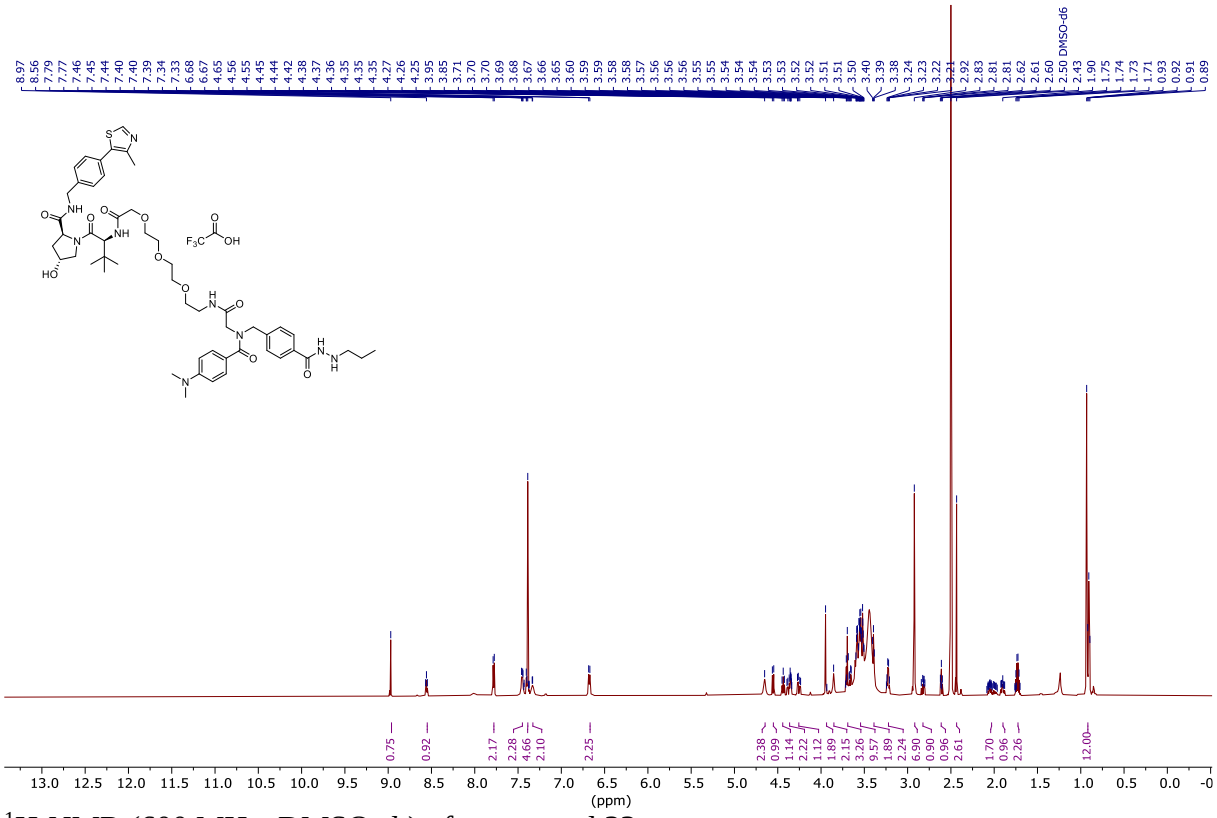
^{13}C-NMR (151 MHz, DMSO-d_6) of compound **20**.



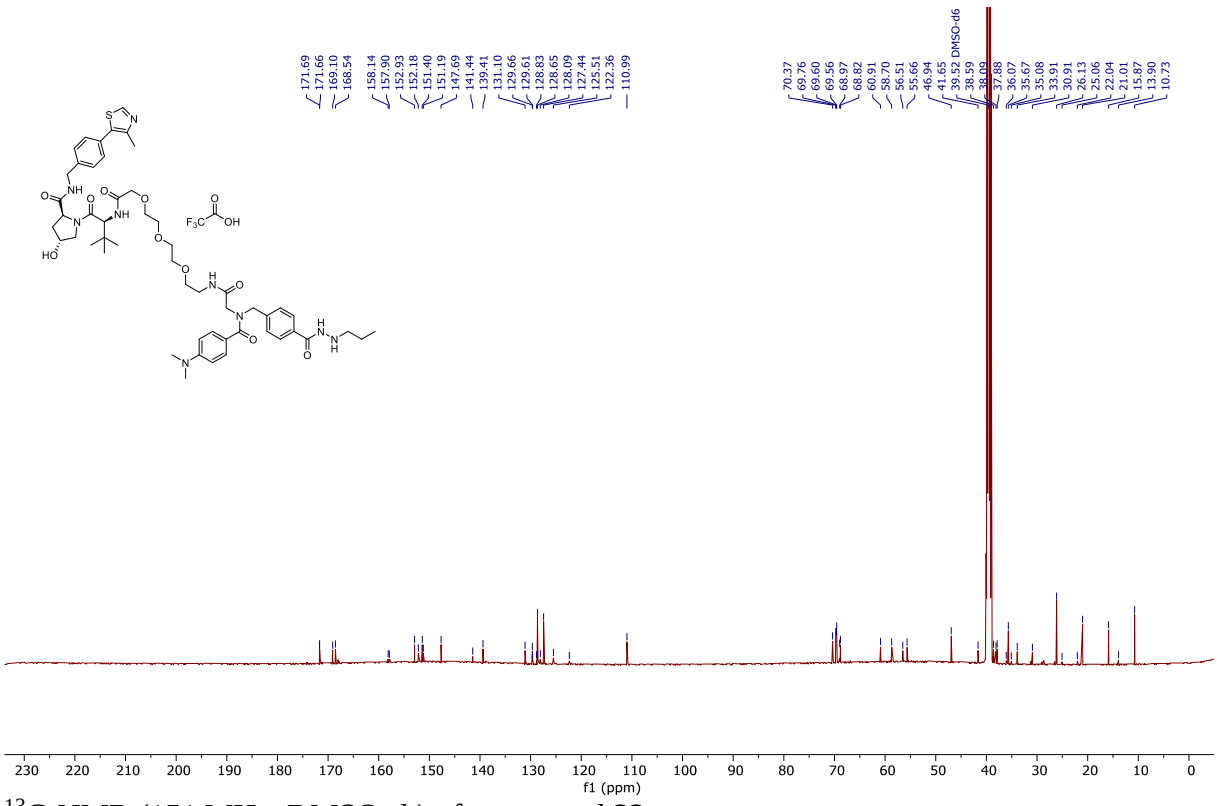
^{1}H-NMR (600 MHz, DMSO-d_6) of compound **21**.



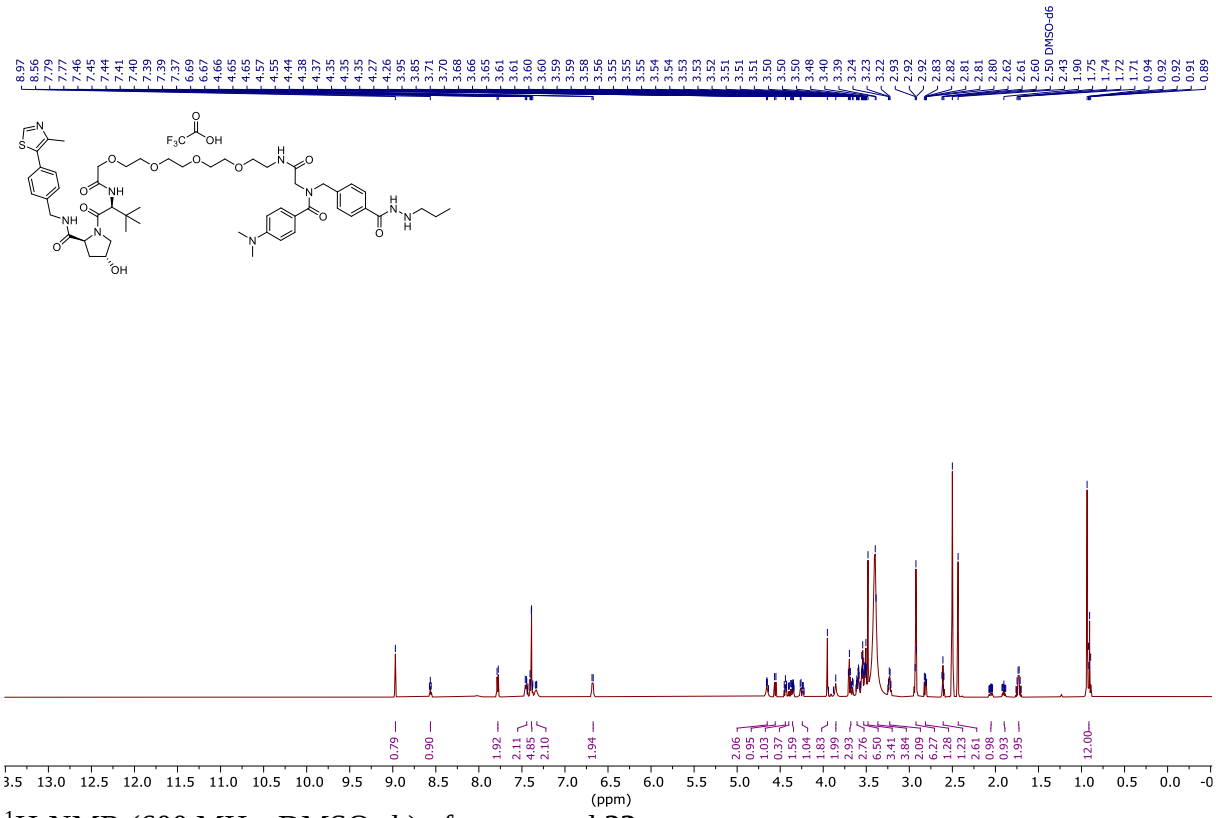
^{13}C-NMR (151 MHz, DMSO-d_6) of compound **21**.



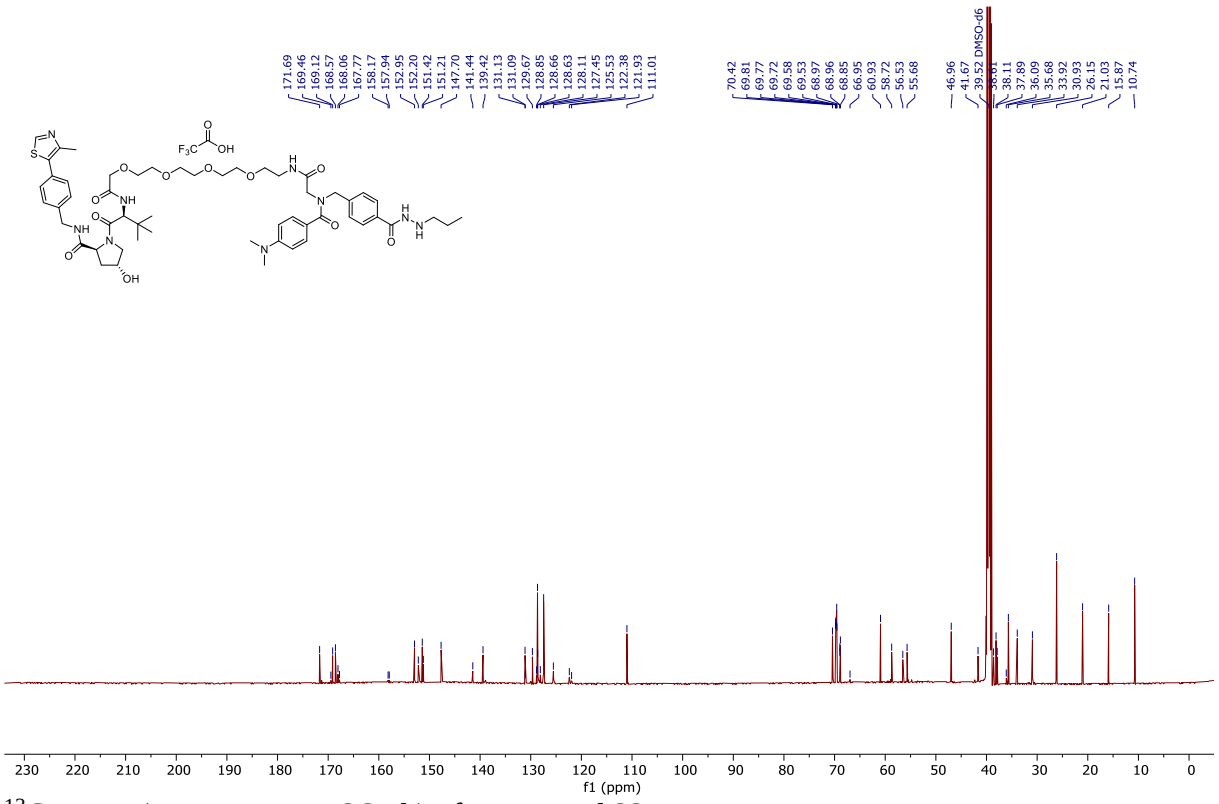
^{1}H-NMR (600 MHz, DMSO-d_6) of compound **22**.



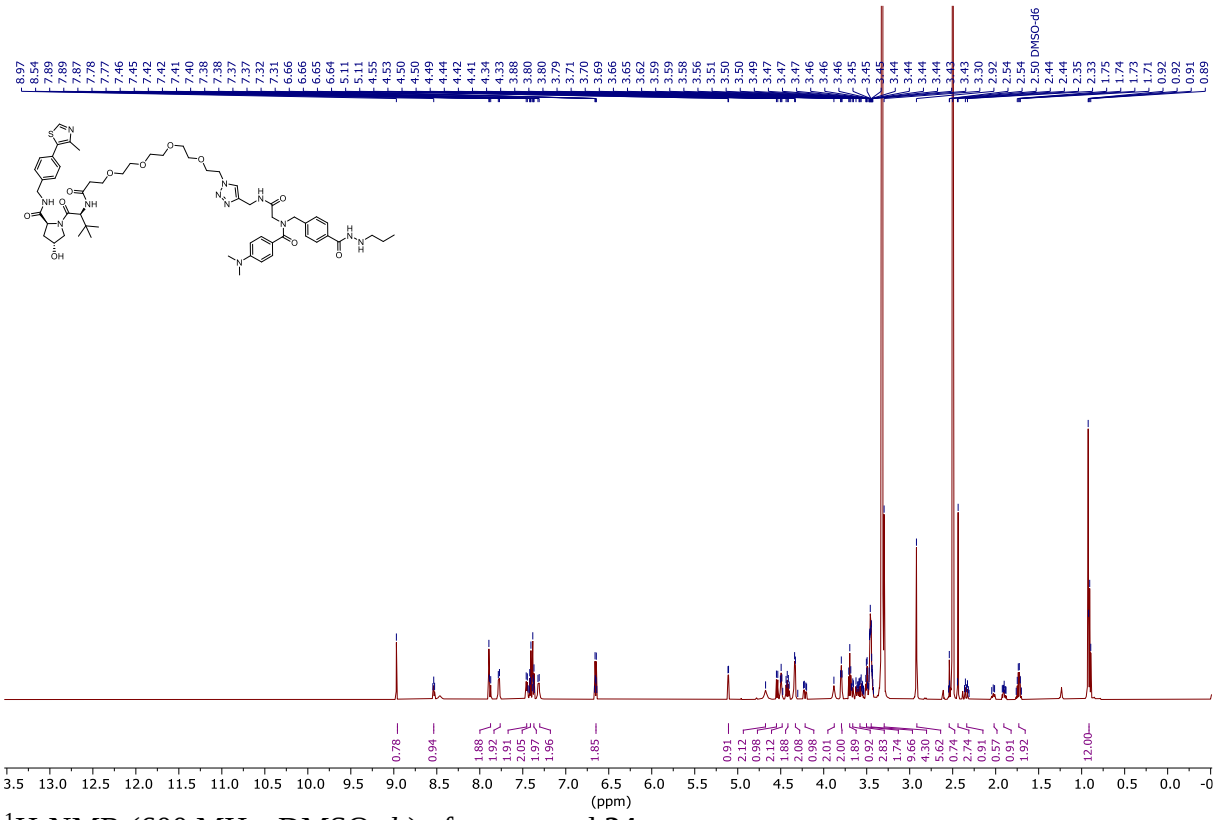
^{13}C-NMR (151 MHz, DMSO-d_6) of compound **22**.



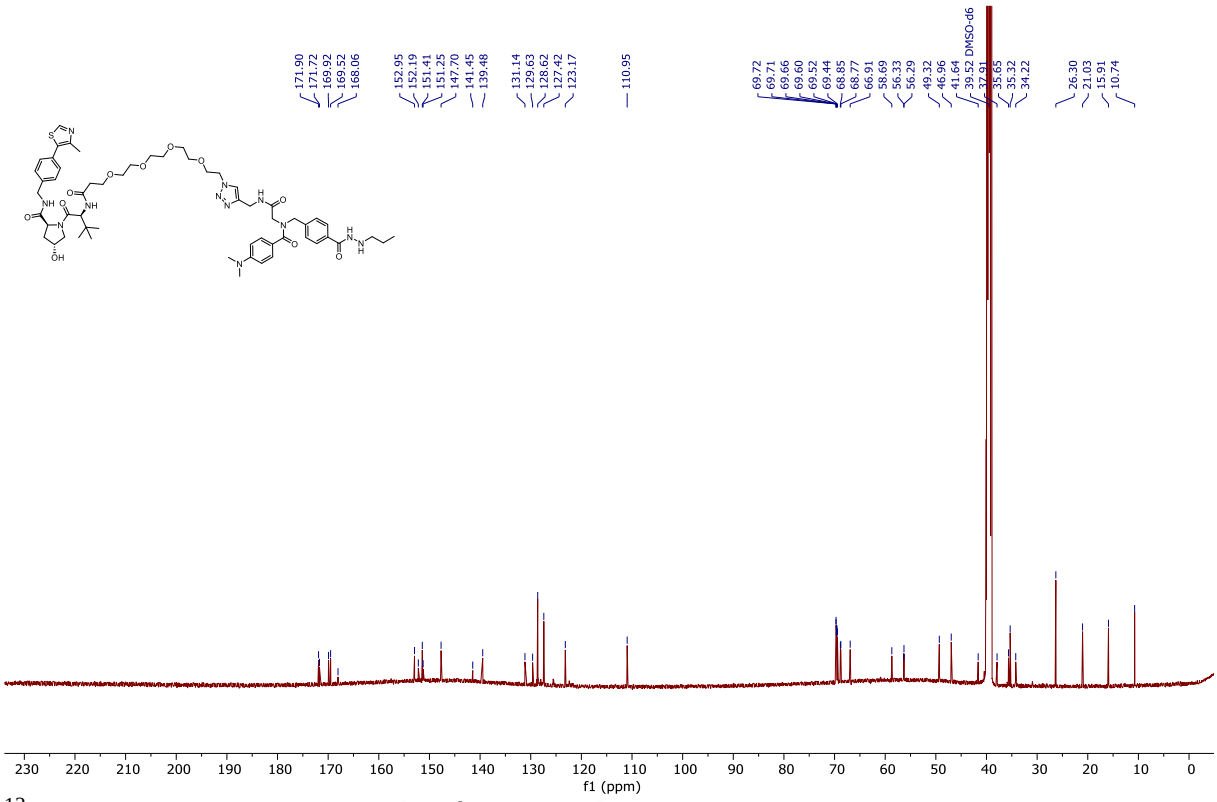
^{1}H-NMR (600 MHz, DMSO-d_6) of compound **23**.



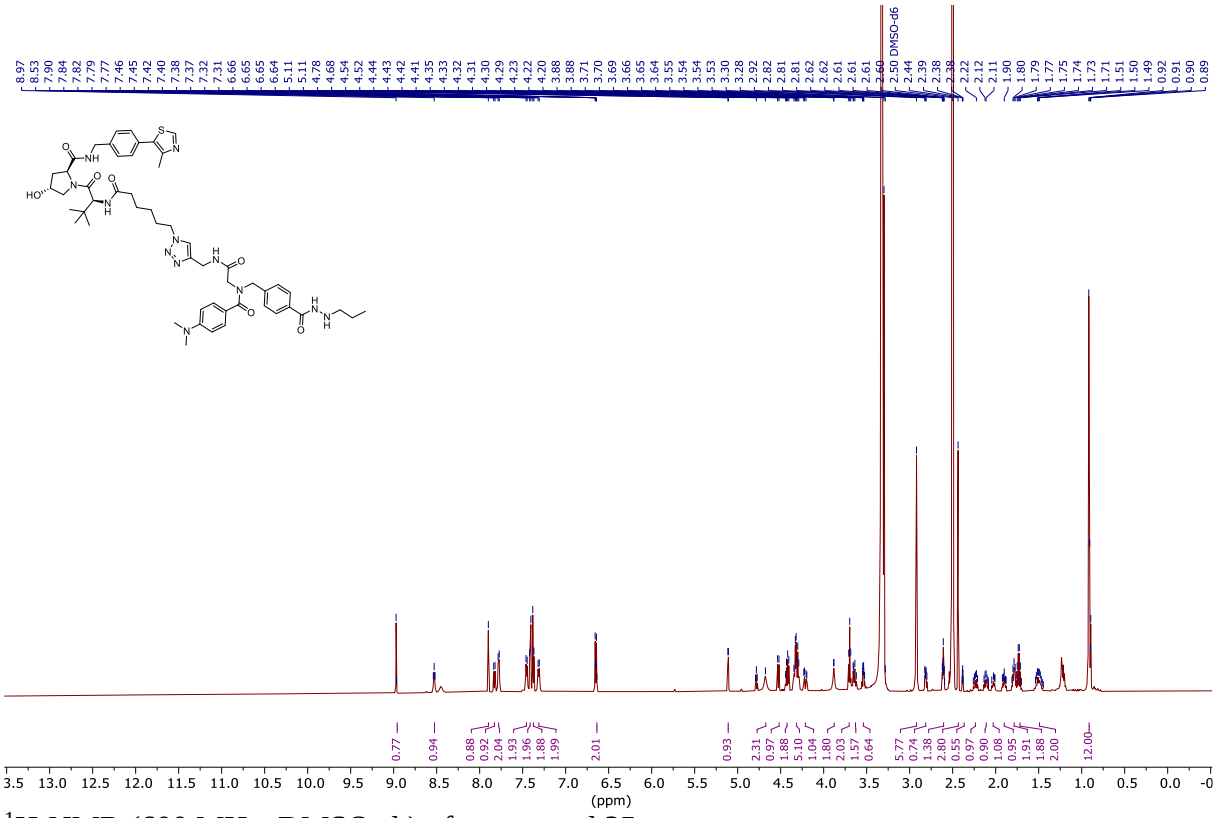
^{13}C-NMR (151 MHz, DMSO-d_6) of compound **23**.



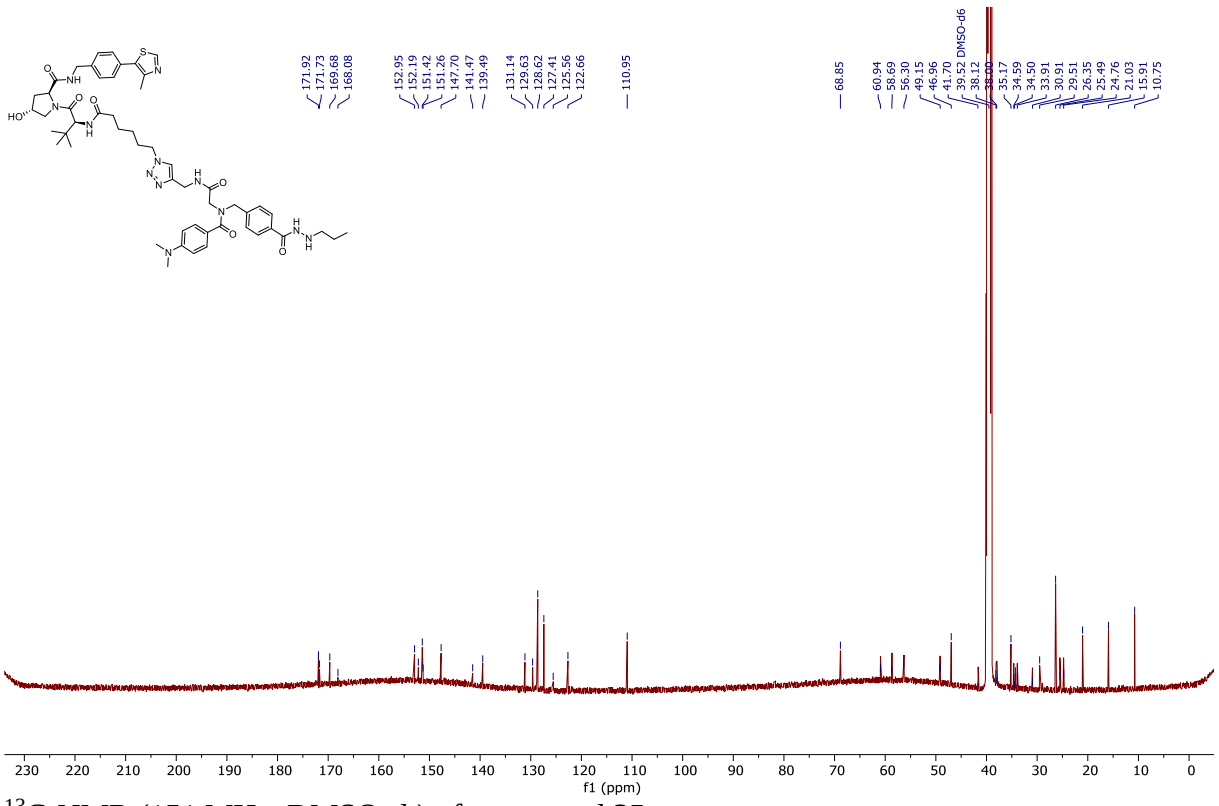
^{1}H-NMR (600 MHz, DMSO-d_6) of compound **24**.



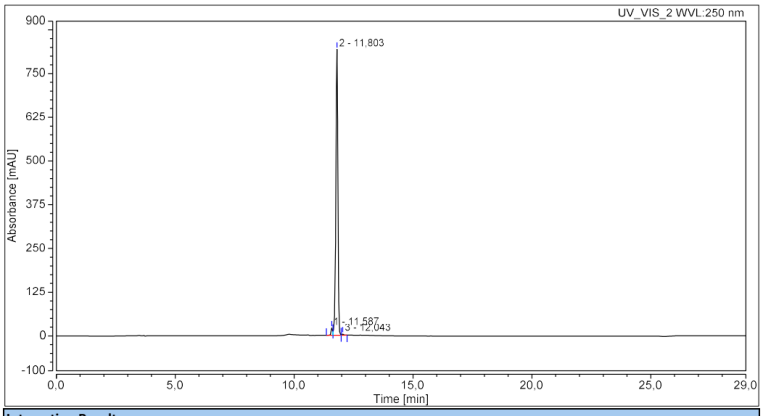
^{13}C-NMR (151 MHz, DMSO-d_6) of compound **24**.



^{1}H-NMR (600 MHz, DMSO-d_6) of compound **25**.



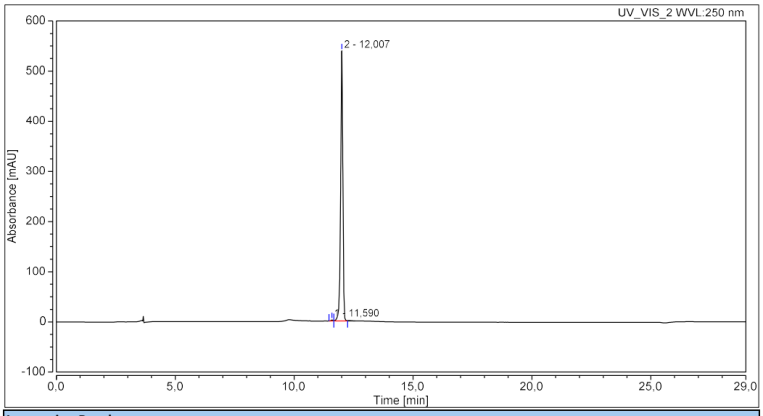
^{13}C-NMR (151 MHz, DMSO-d_6) of compound **25**.



Integration Results

No.	Peak Name	Retention Time min	Area mAU*min	Height mAU	Relative Area %	Relative Height %	Amount n.a.
1		11,587	1,442	20,748	1,78	2,46	n.a.
2		11,803	79,178	817,615	97,84	97,13	n.a.
3		12,043	0,307	3,396	0,38	0,40	n.a.
Total:			**80,926**	**841,759**	**100,00**	**100,00**	

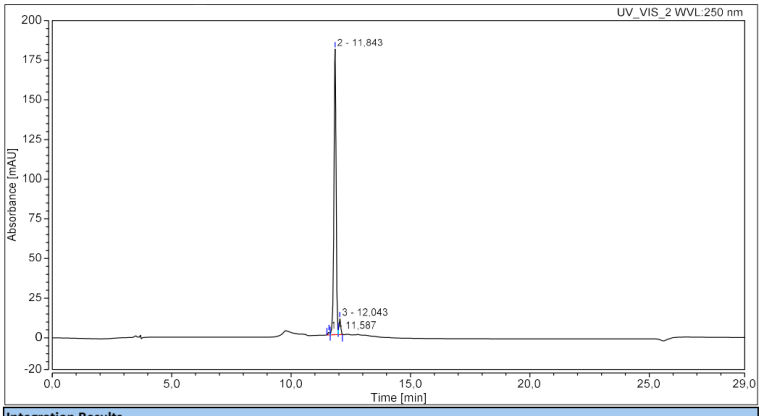
HPLC chromatogram of compound **20** (purity: 97.8%).



Integration Results

No.	Peak Name	Retention Time min	Area mAU*min	Height mAU	Relative Area %	Relative Height %	Amount n.a.
1		11,590	0,207	2,586	0,35	0,48	n.a.
2		12,007	58,163	538,528	99,65	99,52	n.a.
Total:			**58,370**	**541,115**	**100,00**	**100,00**	

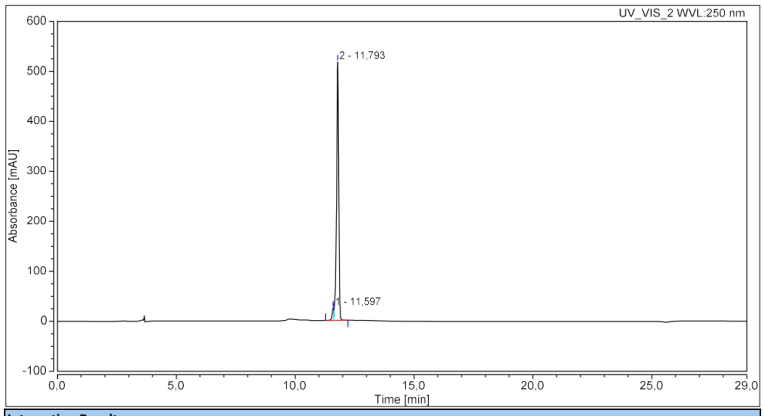
HPLC chromatogram of compound **21** (purity: 99.7%).



Integration Results

No.	Peak Name	Retention Time min	Area mAU*min	Height mAU	Relative Area %	Relative Height %	Amount n.a.
1		11,587	0,129	1,922	0,67	1,00	n.a.
2		11,843	18,383	180,071	95,00	93,83	n.a.
3		12,043	0,839	9,917	4,33	5,17	n.a.
Total:			**19,351**	**191,909**	**100,00**	**100,00**	

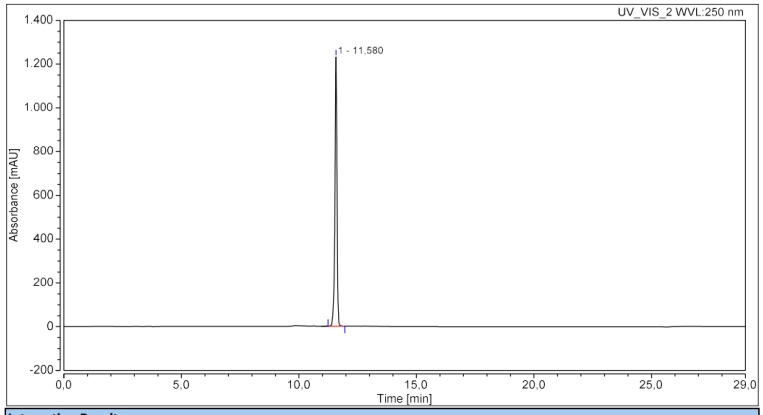
HPLC chromatogram of compound **22** (purity: 95.0%).



Integration Results

No.	Peak Name	Retention Time min	Area mAU*min	Height mAU	Relative Area %	Relative Height %	Amount n.a.
1		11,597	1,710	24,455	3,12	4,52	n.a.
2		11,793	53,171	516,557	96,88	95,48	n.a.
Total:			**54,881**	**541,012**	**100,00**	**100,00**	

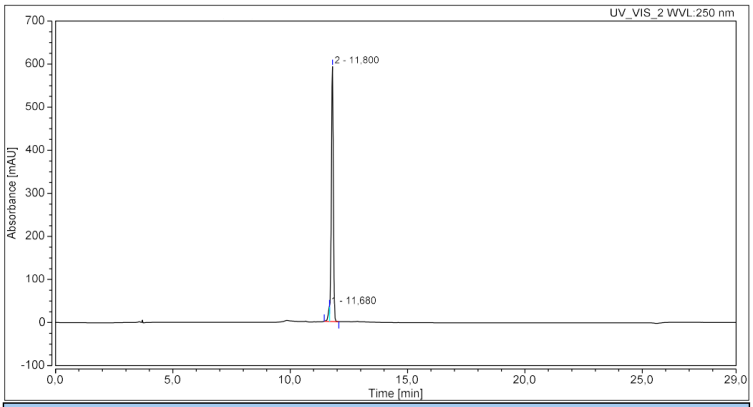
HPLC chromatogram of compound **23** (purity: 96.9%).



Integration Results

No.	Peak Name	Retention Time min	Area mAU*min	Height mAU	Relative Area %	Relative Height %	Amount n.a.
1		11,580	124,331	1229,995	100,00	100,00	n.a.
Total:			**124,331**	**1229,995**	**100,00**	**100,00**	

HPLC chromatogram of compound **24** (purity: > 99.9%).



Integration Results

No.	Peak Name	Retention Time min	Area mAU*min	Height mAU	Relative Area %	Relative Height %	Amount n.a.
1		11,680	2,260	33,986	3,77	5,43	n.a.
2		11,800	57,619	591,924	96,23	94,57	n.a.
Total:			**59,879**	**625,910**	**100,00**	**100,00**	

HPLC chromatogram of compound **25** (purity: 96.2%).

8.4 Appendix IV. Publication II: Photocaged Histone Deacetylase Inhibitors as Prodrugs in Targeted Cancer Therapy.

The following pages include the article “Photocaged Histone Deacetylase Inhibitors as Prodrugs in Targeted Cancer Therapy” as it was published in Pharmaceuticals by MDPI.

The article is reprinted with permission from:

Kraft, F. B.; Hanl, M.; Feller, F.; Schäker-Hübner, L.; Hansen, F. K. Photocaged Histone Deacetylase Inhibitors as Prodrugs in Targeted Cancer Therapy. *Pharmaceuticals* **2023**, *16* (3), 356.

Copyright 2023 by the authors.

pharmaceuticals

Article

Photocaged Histone Deacetylase Inhibitors as Prodrugs in Targeted Cancer Therapy

Fabian B. Kraft, Maria Hanl, Felix Feller, Linda Schäker-Hübner and Finn K. Hansen *

Department of Pharmaceutical and Cell Biological Chemistry, Pharmaceutical Institute, University of Bonn, An der Immenburg 4, 53121 Bonn, Germany
* Correspondence: finn.hansen@uni-bonn.de

Abstract: Histone deacetylases (HDACs) play a key role in the control of transcription, cell proliferation, and migration. FDA-approved histone deacetylase inhibitors (HDACi) demonstrate clinical efficacy in the treatment of different T-cell lymphomas and multiple myeloma. However, due to unselective inhibition, they display a wide range of adverse effects. One approach to avoiding off-target effects is the use of prodrugs enabling a controlled release of the inhibitor in the target tissue. Herein, we describe the synthesis and biological evaluation of HDACi prodrugs with photo-cleavable protecting groups masking the zinc-binding group of the established HDACi DDK137 (**I**) and VK1 (**II**). Initial decaging experiments confirmed that the photocaged HDACi **pc-I** could be deprotected to its parent inhibitor **I**. In HDAC inhibition assays, **pc-I** displayed only low inhibitory activity against HDAC1 and HDAC6. After irradiation with light, the inhibitory activity of **pc-I** strongly increased. Subsequent MTT viability assays, whole-cell HDAC inhibition assays, and immunoblot analysis confirmed the inactivity of **pc-I** at the cellular level. Upon irradiation, **pc-I** demonstrated pronounced HDAC inhibitory and antiproliferative activities which were comparable to the parent inhibitor **I**. Additionally, only phototreated **pc-I** was able to induce apoptosis in Annexin V/PI and caspase-Glo 3/7 assays, making **pc-I** a valuable tool for the development of light-activatable HDACi.

Keywords: histone deacetylase; prodrug; photo-activatable; epigenetics; cancer

check for updates

Citation: Kraft, F.B.; Hanl, M.; Feller, F.; Schäker-Hübner, L.; Hansen, F.K. Photocaged Histone Deacetylase Inhibitors as Prodrugs in Targeted Cancer Therapy. *Pharmaceuticals* **2023**, *16*, 356. https://doi.org/10.3390/ph16030356

Academic Editor: Valentina Onnis

Received: 20 January 2023
Revised: 21 February 2023
Accepted: 22 February 2023
Published: 25 February 2023

Copyright: © 2023 by the authors. Licensee MDPI, Basel, Switzerland. This article is an open access article distributed under the terms and conditions of the Creative Commons Attribution (CC BY) license (https://creativecommons.org/licenses/by/4.0/).

1. Introduction

Histone deacetylases are a group of enzymes that remove acyl groups from the ε-amino groups of lysine side chains [1]. Despite their name, the target range is not limited only to histone proteins, but also includes numerous non-histone proteins [2,3]. There are 18 known human HDAC isoforms, which can be roughly divided into two families according to their catalytic activities. Eleven isoforms possess a zinc ion in their catalytic domain, while the other seven, the so-called sirtuins, depend on the cofactor NAD^+. In accordance with their cellular localization and structural homology, the zinc-dependent isoforms are further classified into different groups: class I (HDAC 1, 2, 3, and 8), class IIa (HDAC 4, 5, 7, and 9), class IIb (HDAC 6 and 10), and class IV (HDAC 11) [4]. Through their direct influence on the chromatin structure, HDACs play a significant role in important processes such as transcription, as well as cell proliferation, differentiation, and migration [5]. Their high expression rates in different kinds of cancer have led to the development of numerous HDAC inhibitors (HDACi). As of now, four HDACi are approved by the FDA for the treatment of different T-cell lymphomas and multiple myeloma (Figure 1) [6]. Among them, the pan-HDACi vorinostat, belinostat, and panobinostat possess a hydroxamic acid as a zinc-binding group (ZBG), while the prodrug romidepsin binds via an in situ generated thiol.

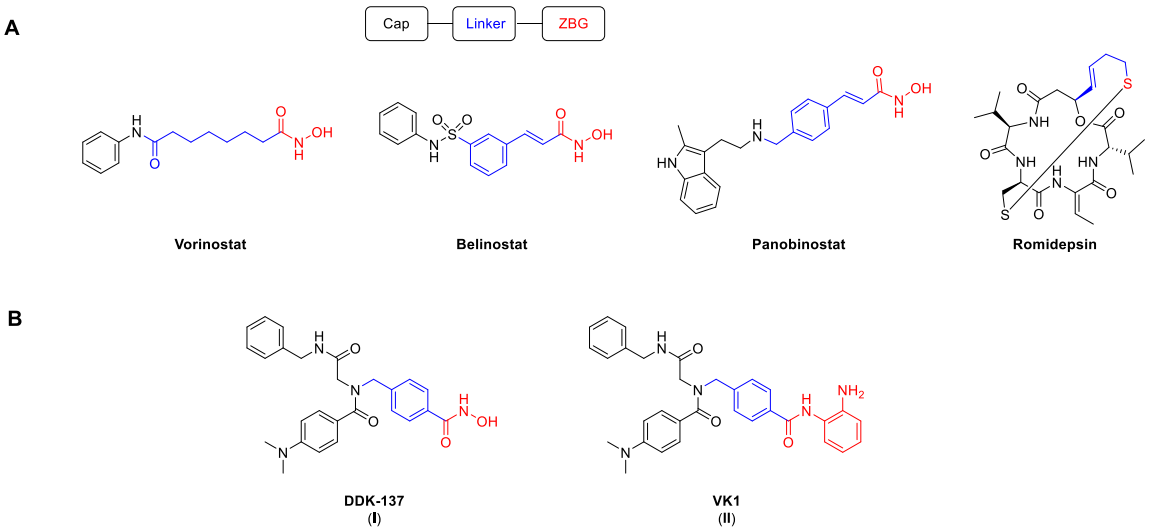


Figure 1. Selected HDACi, including the established HDAC pharmacophore model. Cap, linker, and ZBG are highlighted in black, blue, and red, respectively. (**A**) Structures of FDA-approved HDACi. (**B**) Structures of the peptoid-based HDACi **DDK-137** (**I**) and **VK1** (**II**) [7,8].

Although they are known to be possibly mutagenic, hydroxamic acids are among the most common ZBGs. Notably, vorinostat, panobinostat, and belinostat all show mutagenic activity in the Ames test and provoke chromosomal aberrations in rodent cells [9]. Another considerable issue with hydroxamic-acid-based HDACi is their relatively low metabolic stability in vivo [10]. In addition, all FDA-approved HDACi can cause severe hematological and gastrointestinal side effects, which are presumably caused by non-specific HDAC inhibition and frequently lead to treatment interruptions [11–13]. Therefore, the clinical use of unselective HDACi has so far been limited to a small number of cancer entities.

One approach to circumvent unwanted off-target effects while preserving the therapeutic efficacy is to release or activate the active drug in the target tissue [14]. Photodynamic therapy (PDT) is a classic example for the activation of a drug in the diseased tissue. The PDT principle relies on a photosensitizer, which, after exposure to light of a specific wavelength, produces radicals and/or reactive oxygen species [15,16]. Since the photosensitizer is only activated locally, most of the side effects can be avoided. In addition to the treatment of acne [17], PDT has shown increasing influence on cancer therapy [18,19]. In another approach to avoid unwanted side effects, the active drug can be converted into a prodrug and masked by a photocleavable (pc) protecting group, which allows the release of the parent drug in the target tissue with high tempo-spatial accuracy [14]. In 1977, *Engels* et al. described the photorelease of cAMP, the first biological application of a photoremovable protecting group (PPG) [20]. Today, *o*-nitrobenzyl derivatives are by far the most commonly used PPGs [21]. The main requirement for the application of light-induced treatments is the accessibility of the target tissue to the light source. Consequently, skin cancers are particularly suitable for photopharmacological approaches. Current modern treatments of malignant melanoma are based on BRAF inhibitors like vemurafenib [22] but are accompanied by severe side effects and fast development of resistance. *Pfeifer* and co-workers established a vemurafenib derivative with a PPG [23]. In vitro investigations showed the inactivity of the protected inhibitor, while irradiation with light restored the activity against kinases [23]. Additional recent examples of photocaged drugs in the field of cancer include phosphoinositide 3-kinase (PI3K) [24], mouse double minute 2 homolog (MDM2) [25], and proteasome inhibitors [26]. Furthermore, PPGs have been successfully utilized to transform proteolysis-targeting chimeras (PROTACs) into photo-activatable degraders of the bromodomain-containing protein 4 (BRD4) [27] and estrogen-related receptor α (ERRα) [28].

Eventually, it was discovered that drug-resistant malignant melanoma cells overexpress HDAC1-3, and the inhibition of these isoforms overcomes drug resistance via different mechanisms [29,30]. To minimize off-target effects, the photo-controlled release of HDACi in the target tissue is desirable. In 2016, *Gasser* and co-workers converted the ferrocene-containing HDACi Fc-SAHA into the photocaged analog p-Fc-SAHA. However, the insufficient physicochemical properties of p-Fc-SAHA prohibited the investigation of its properties in a cellular setting [31]. Recently, *Conway* and coworkers developed the panobinostat prodrug Zap-Pano utilizing a 4,5-dimethoxy-2-nitrobenzyl (DMNB) group attached to the hydroxamic acid oxygen. Through irradiation with light at 405 nm, they were able to release the parent inhibitor panobinostat under controlled conditions [32]. While they could completely suppress the HDAC inhibitory activity with their prodrug, another major side product, the corresponding amide Pano-NH_2, was released upon irradiation with light [32].

We previously reported the synthesis and biological evaluation of the highly potent pan-inhibitor **DDK-137** (**I**) [8,33] and the HDAC1-3 selective inhibitor **VK1** (**II**) [7]. Compound **I** displayed potent antiplasmodial activity against asexual blood stage and liver stage parasites and also submicromolar antiproliferative activity against the HepG2 cancer cell line [8]. The *ortho*-aminoanilide **II** revealed promising antiproliferative effects in the human ovarian cancer cell line A2780 and the human squamous carcinoma cell line Cal27. In addition, **II** demonstrated chemosensitizing properties and was capable of reversing cisplatin resistance in cisplatin-resistant Cal27CisR cells [7]. In this work, we describe the synthesis and biological evaluation of photocaged HDACi prodrugs for both inhibitors.

2. Results

2.1. Design and Synthesis of HDACi Prodrugs

The previously reported crystal structure of the non-selective HDACi **I** in complex with the second catalytic domain of zebrafish HDAC6 is depicted in Figure 2 [33]. The hydroxamic acid moiety coordinates to the Zn^{2+}-ion and the adjacent water molecule at the same time in a monodentate binding mode. Consequently, the inhibitory potential of **I** against Zn^{2+}-dependent HDAC enzymes should be diminished by masking the hydroxamic acid warhead.

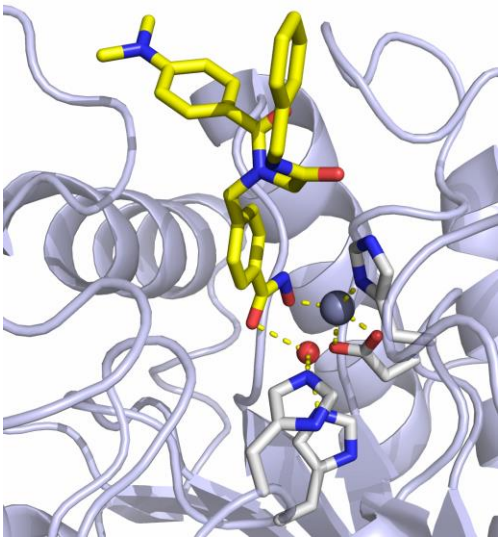
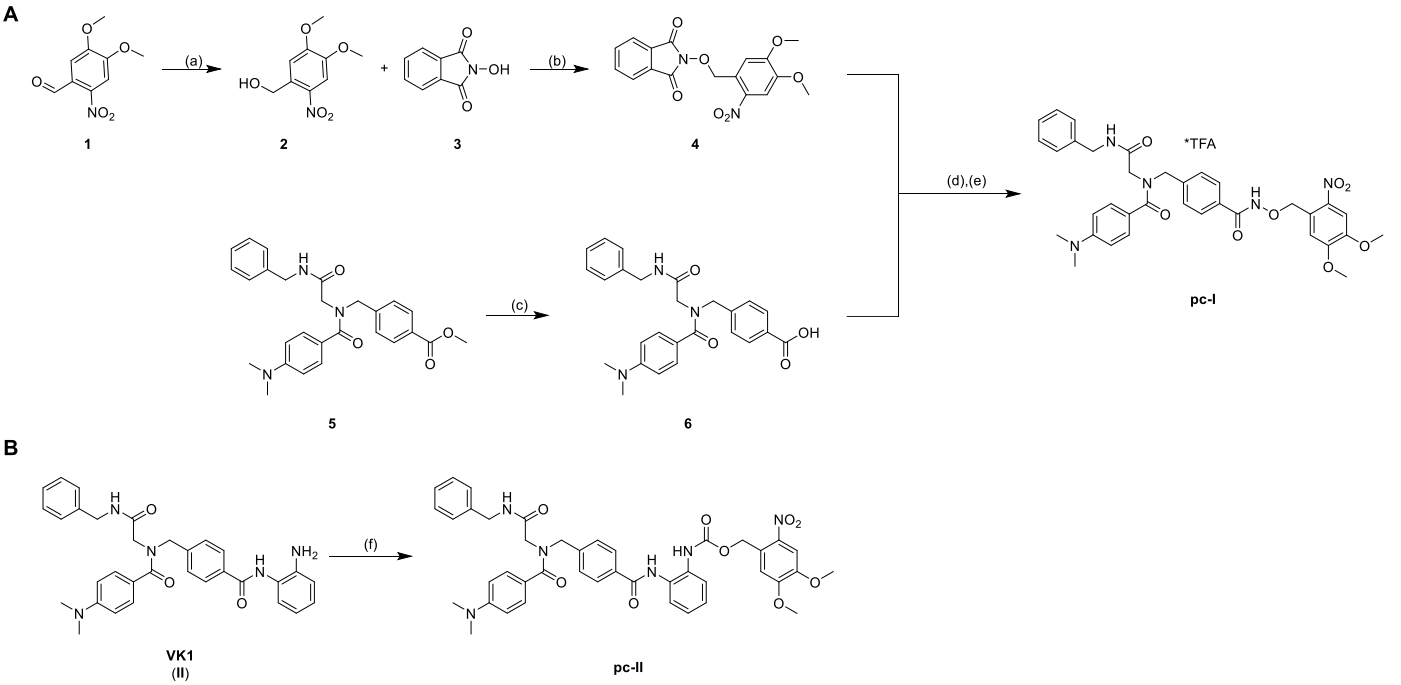


Figure 2. Crystal structure of **I** in complex with HDAC6 (PDB ID: 6DVN). The catalytic Zn^{2+}-ion appears as a gray, the water molecule as a red sphere. Metal coordination and hydrogen bond interactions are shown as dashed yellow lines [33].

To enable the optochemical control of HDAC inhibition with a high spatio-temporal accuracy, we attached a photocleavable DMNB moiety to the zinc-binding oxygen atom of the inhibitor. Additionally, we protected the previously reported *ortho*-aminoanilide **II** via a carbamate moiety with a DMNB group (Scheme 1) [7]. The syntheses of the parent inhibitors **I** and **II** were accomplished as previously published [7,8].



Scheme 1. Synthesis of the photocaged prodrugs **pc-I** (**A**) and **pc-II** (**B**). Reagents and conditions: (**a**) $NaBH_4$, CH_2Cl_2, rt, 30 min, 98%; (**b**) PPh_3, DIAD, THF, 0 °C to rt, 4 h, quant.; (**c**) 1.25 M $NaOH_{aq}$, THF/MeOH 10/1 *v*/*v*, 40 °C, 24 h, 97%; (**d**) NH_2NH_2*H_2O, CH_2Cl_2, rt, 4 h; (**e**) EDC*HCl, CH_2Cl_2, 0 °C to rt, 2 h, 16%; (**f**) NVOC-Cl, pyridine, 0 °C to rt, THF, 19 h, 51%.

The synthesis of the photocaged prodrugs **pc-I** and **pc-II** is summarized in Scheme 1. The *N*-phthalimide protected compound **4** was synthesized via a two-step protocol starting from commercially available 6-nitroverartraldehyde **1**. The reduction of **1** to the corresponding benzyl alcohol **2** was conducted in an excellent yield of 98%. Further on, the *Mitsunobu* reaction of **2** with *N*-hydroxyphthalimide **3** yielded the protected hydroxylamine **4** under mild conditions as a yellow solid. The HDACi precursor **6** was obtained in two steps according to our published protocol. Briefly, an *Ugi* four-component reaction afforded the intermediate **5**, which was hydrolyzed to generate **6**. The subsequent deprotection of **4** with hydrazine followed by an amide coupling with **6** provided the prodrug **pc-I** in a yield of 16% (Scheme 1A). Finally, the photocaged **VK1**-prodrug **pc-II** was prepared in 51% yield via the treatment of **II** with 6-nitroveratryl chloroformate (NVOC-Cl) in the presence of pyridine as a base (Scheme 1B).

2.2. Biological Evaluation of HDACi Prodrugs

Subsequently, the photo-uncaging of the two photocaged HDACi was investigated with high-performance liquid chromatography (HPLC) analysis. The photocleavage reaction of **pc-I** in DMSO after irradiation with light at a wavelength of 365 nm proceeded smoothly, and the HPLC chromatograms clearly showed the appearance of compound **I**. After treatment for 10 min, **pc-I** was deprotected to its parent inhibitor **I** in a yield of 82%, as determined by HPLC using a calibration curve. Compound **pc-II** decomposed under treatment with light and did not release the parent HDACi **II** in significant quantities (see Supporting Information). Thus, we focused our biological evaluation on the prodrug **pc-I**.

In the first step, **pc-I** was screened in fluorogenic assays for its in vitro inhibitory activity against HDAC1 (class I) and HDAC6 (class IIb) with or without UV irradiation (365 nm) (Table 1).

Table 1. Inhibitory activity of photocaged **pc-I** (with and without UV irradiation) and **I** against human HDAC1 and HDAC6 [a].

	pc-I	pc-I + UV	I	Vorinostat
IC_{50} (HDAC1) [nM]	824 ± 32.2	6.8 ± 1.2	12.7 ± 0.7	104 ± 6.2
IC_{50} (HDAC6) [nM]	794 ± 74.7	21.6 ± 2.8	13.1 ± 0.9	36.3 ± 2.8

[a] Reported mean IC_{50} values, including standard deviation, are calculated from at least two independent experiments. For primary data see Supporting Information Figure S1.

The photocaged prodrug pc-I showed low inhibitory activity against both isoforms. Upon irradiation with UV-light, we detected considerably increased inhibition of HDAC1 (121-fold) and HDAC6 (37-fold). Encouraged by these enzymatic data, we assessed our prodrug in a whole-cell HDAC assay using the melanoma cell line MV-3 (Figure 3). This cell line was selected because skin cancers are particularly suitable for the light-triggered release of photocaged drugs. Without UV irradiation, **pc-I** showed less than 25% inhibition at 25 µM. After irradiation for 10 min, **pc-I** (IC_{50}: 73 nM) demonstrated potent activity in the whole-cell HDAC inhibition assay, which was comparable to the parent compound **I** (IC_{50}: 91 nM).

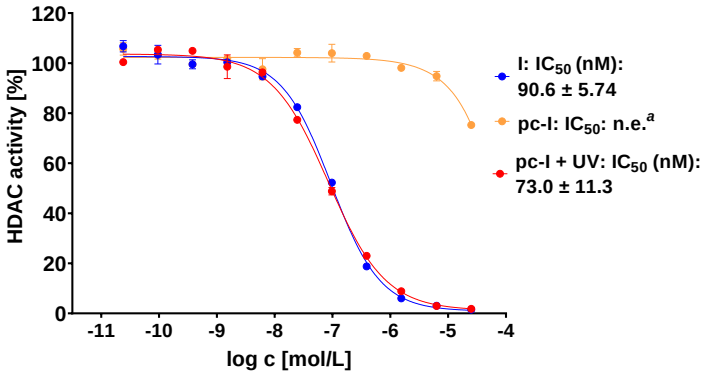


Figure 3. Representative concentration-effect curves of the whole-cell HDAC inhibition assays of **pc-I** and **I** in MV-3 cells. Stated IC_{50} values were determined from the mean of three independent experiments in duplicates. Irradiation with UV light was executed at 365 nm for 10 min. [a] n.e: no effect: <25% inhibition at 25 µM.

Next, we performed additional cellular target engagement assessment with immunoblot analysis with the MV-3 cell line (Figure 4). We chose acetyl-α-tubulin (a marker of HDAC6 inhibition) and acetyl-histone H3 (a marker of HDAC1-3 inhibition) as representative HDAC substrates. For **pc-I** without irradiation, no increased levels of acetylated α-tubulin were observed. The parent inhibitor **I** showed strong hyperacetylation, thus proving the inhibition of HDAC6. Similarly, activation of **pc-I** with UV light led to an increased level of acetyl-α-tubulin. The same tendency was observed for the acetylation levels of histone H3. After UV activation of **pc-I**, a higher amount of acetyl-histone-H3 was measured, confirming the inhibition of class I HDAC enzymes in a cellular environment.



Figure 4. Representative immunoblot analysis of acetylated α-tubulin and histone H3. MV-3 cells were incubated for 24 h with **I** and **pc-I** at a concentration of 3.1 μM. Afterward, cell lysates were immunoblotted with an anti-acetyl-α-tubulin and anti-acetyl-histone H3 antibody. GAPDH was used as loading control. (+): UV irradiation at 365 nm for 10 min. (−): no treatment with UV light.

Subsequently, we evaluated our compound with in vitro MTT cell viability assays against the MV-3 cell line and the ovarian cancer cell line A2780 (Figure 5, Table 2). In accordance with our previous data, **pc-I** showed <25% inhibition at 25 μM in both cell lines. As expected, upon light activation, pronounced antiproliferative activity was measured (MV-3 IC_{50}: 727 nM; A2780 IC_{50}: 428 nM). Thus, we confirmed the inactivity of our photocaged inhibitor in a cellular environment and the cell toxicity upon irradiation with light.

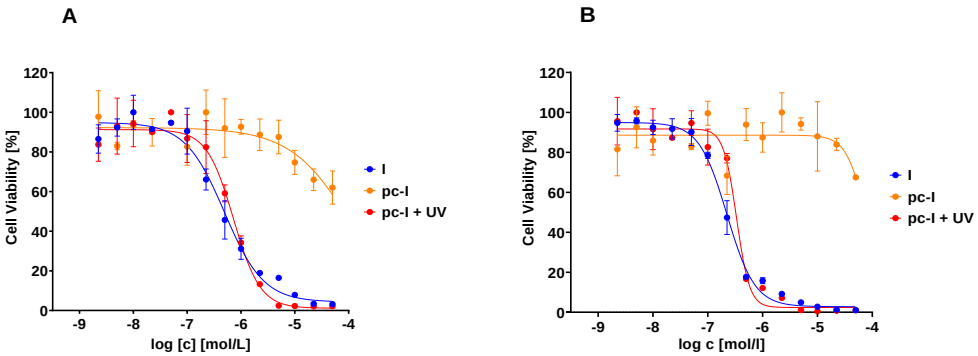


Figure 5. Representative concentration-effect curves of the MTT cell viability assays of **pc-I** and **I**. (**A**) MV-3 cell line, (**B**) A2780 cell line. UV irradiation was executed at 365 nm for 10 min.

Table 2. Inhibitory activity of photocaged **pc-I** (with and without UV irradiation) and **I** against the MV-3 and A2780 cell line [a].

	pc-I	pc-I + UV	I
IC_{50} (MV-3) [nM]	n.e. [b]	727 ± 133	616 ± 161
IC_{50} (A2780) [nM]	n.e. [b]	428 ± 62.5	249 ± 84.7

[a] Stated IC_{50} values were determined from the mean of three independent experiments in duplicates. UV irradiation was executed at 365 nm for 10 min. [b] n.e— no effect: <25% inhibition at 25 μM.

Encouraged by the promising antiproliferative activity of **pc-I** in the presence of light, we investigated whether **I** and **pc-I** are capable of inducing apoptosis. To this end, A2780 cells were treated for 48 or 72 h with 0.5 μM of **I** and **pc-I**, stained with annexin V/propidium iodide (PI), and afterwards analyzed with flow cytometry. The results are presented in Figure 6A,B. Treatment with **I** led to a significant increase in early and late apoptotic cells compared to the DMSO control, while **pc-I** in the absence of light showed no significant increase in early and late apoptosis. However, after light activation, **pc-I** also demonstrated increased apoptosis levels which were comparable to compound **I**.

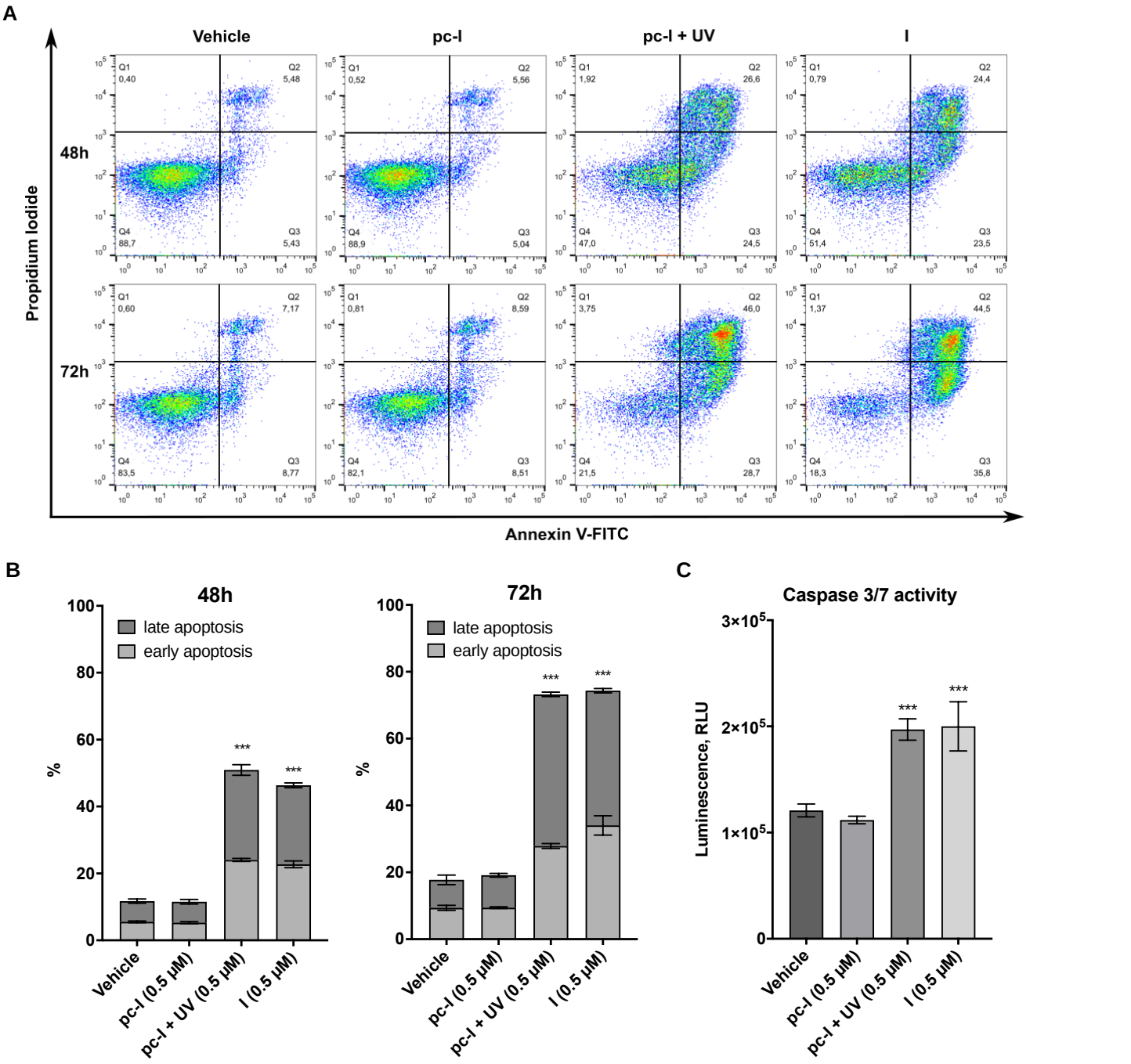


Figure 6. Results from apoptosis assays. A2780 cells were treated with 0.5 µM **pc-I**, **pc-I** + UV, **I** or vehicle (DMSO). (**A**) Cells were stained with annexin V and propidium iodide (PI) after 48 and 72 h. (**B**) Annexin-V-positive but PI-negative cells were classified as early apoptotic; annexin-V- and PI-positive cells were classified as late apoptotic. Statistical difference was calculated for annexin-V-positive cells compared to vehicle. (**C**) Cells were treated with the compounds and vehicle (DMSO) for 24 h, followed by incubation with caspase-Glo 3/7 substrate, and subsequently, luminescence was measured. For primary data, see Supporting Information Figure S2. Statistical analysis was performed with one-way ANOVA (*** $p < 0.001$).

Finally, we investigated whether the apoptosis induction of **I** and **pc-I** + UV is mediated in a caspase 3/7-dependent fashion by performing caspase-Glo 3/7 activation assays. The treatment of A2780 cells with **I** or **pc-I** + UV led to a significant activation of caspase 3/7, while **pc-I** was inactive in the absence of UV light (Figure 6C). Taken together, the results

demonstrate that light-activated **pc-I** can kill cancer cells via apoptosis induction and in a caspase 3/7-dependent fashion.

3. Discussion

In this work, we have designed and synthesized light-activatable prodrugs of our previously reported HDACi **DDK-137** (**I**) and **VK1** (**II**) by attaching a DMNB group to the zinc-binding moiety of both inhibitors. Through irradiation with light at 365 nm, **pc-I** showed fast deprotection and thereby conversion to its parent inhibitor **I,** while **pc-II** decomposed. In subsequent fluorogenic assays against human HDAC1 and HDAC6, **pc-I** showed only low inhibitory activity. After irradiation with light, the inhibitory activity of **pc-I** strongly increased against both isoforms (HDAC1: 121-fold; HDAC6: 37-fold), leading to IC_{50} values comparable to those observed for the parent inhibitor **I**.

For subsequent evaluation of **I** and phototreated **pc-I**, we used the melanoma cell line MV-3 and the ovarian cancer cell line A2780. The melanoma cell line was chosen since this cancer entity is easily accessible with light, while the ovarian cancer cell line was selected because we previously showed that A2780 cells are highly sensitive to our peptoid-based HDACi [7]. Both **I** and photoactivated **pc-I** demonstrated pronounced inhibition of cellular HDAC activity in a whole-cell HDAC inhibition assay in the melanoma cell line MV-3 and displayed IC_{50} values in the double-digit nanomolar concentration range; meanwhile, **pc-I** was inactive without irradiation with UV light. Similar results were observed when we studied intracellular HDAC inhibition with immunoblot analysis in the MV-3 cell line. Again, only **I** and photoactivated **pc-I**, but not **pc-I** in the absence of light, were capable of inducing a hyperacetylation of acetyl-α-tubulin (a marker of HDAC6 inhibition) and acetyl-histone H3 (a marker of HDAC1-3 inhibition). While the prodrug **pc-I** was inactive in MTT viability assays (MV-3 and A2780 cell lines) and annexin V/PI apoptosis assays (A2780 cells), phototreated **pc-I** showed antiproliferative activity and apoptosis induction comparable to that of the parent compound **I**. Caspase 3/7-activation assays in A2780 cells confirmed that **I** and light-activated **pc-I** can kill cancer cells via apoptosis induction in a caspase 3/7-dependent fashion.

Compared to previously published photocaged HDACi such as Zap-Pano and p-Fc-SAHA [32], which utilize the same DMNB caging group, our light-activatable HDACi **pc-I** features some important advantages. The treatment of Zap-Pano with light of the wavelength of 405 nm generated a significant amount of the corresponding amide Pano-NH_2 as a side product. In our decaging experiments, we did not observe this amide side product, thus indicating that **I** might be more suitable for photocaging than panobinostat. While the DMNB-caged ferrocene-containing HDACi p-Fc-SAHA showed encouraging decaging efficiency and activity in cell-free assays, insufficient aqueous solubility prevented the analysis of p-Fc-SAHA in a cellular environment [31].

To conclude, the prodrug **pc-I** presented in this study is a promising tool for the further development of new light-activatable HDACi prodrugs.

4. Materials and Methods

4.1. General Information and Chemistry

Chemicals were obtained from *abcr* GmbH (Karlsruhe, Germany), *Acros Organics* (Geel, Belgien), *Carbolution Chemicals* (Sankt Ingberg, Germany), *Sigma-Aldrich* (Steinheim, Germany,) *TCI Chemicals* (Eschborn, Germany) or *VWR* (Langenfeld, Germany) and used without further purification. Technical-grade solvents were distilled prior to use. For all HPLC purposes, acetonitrile in HPLC-grade quality (HiPerSolv CHROMANORM, *VWR*, Langenfeld, Germany) was used. Water was purified with a PURELAB flex® (*ELGA VEOLIA*, Celle, Germany). Thin-layer chromatography (TLC) was carried out on prefabricated plates (silica gel 60, F_{254}, *Merck*). Components were visualized either by irradiation with ultraviolet light (254 nm or 366 nm) or by staining appropriately. Column chromatography was carried out on silica gel (60 Å, 40–60 µm, *Acros Organics*, Geel, Belgien). If no solvent is stated, an aqueous solution was prepared with demineralized water. Mixtures of two

or more solvents are specified as "solvent A"/"solvent B", 3/1, *v*/*v*; meaning that 100 mL of the respective mixture consists of 75 mL of "solvent A" and 25 mL of "solvent B". The uncorrected melting points were determined using a *Büchi* (Essen, Germany) Melting Point M-560 apparatus.

Nuclear magnetic resonance spectroscopy (NMR): Proton (^{1}H) and carbon (^{13}C) NMR spectra were recorded either on a Bruker AVANCE 500 MHz at a frequency of 500 MHz (^{1}H) and 126 MHz (^{13}C), a Bruker AVANCE III HD 600 MHz at a frequency of 600 MHz (^{1}H) and 151 MHz (^{13}C), or a Bruker AVANCE III HD 400 MHz at a frequency of 400 MHz (^{1}H), 75 MHz (^{13}C). The chemical shifts are given in parts per million (ppm). As solvents, deuterated chloroform ($CDCl_3$), deuterated methanol (methanol-d_4) and deuterated dimethyl sulfoxide (DMSO-d_6) were used. The residual solvent signal ($CDCl_3$: ^{1}H NMR: 7.26 ppm, ^{13}C NMR: 77.1 ppm; DMSO-d_6: ^{1}H NMR: 2.50 ppm, ^{13}C NMR: 39.52 ppm; methanol-d_4: ^{1}H NMR: 3.31 ppm, 4.87 ppm, ^{13}C NMR: 49.00 ppm) was used for calibration. The multiplicity of each signal is reported as singlet (s), doublet (d), triplet (t), quartet (q), multiplet (m) or combinations thereof. Multiplicities and coupling constants are reported as measured and might disagree with the expected values.

Mass spectrometry: High-resolution electrospray-ionization mass spectra (HRMS-ESI) were acquired with Bruker Daltonik GmbH micrOTOF coupled to a an LC Packings Ultimate HPLC system and controlled by micrOTOFControl3.4 and HyStar 3.2-LC/MS, with a Bruker Daltonik GmbH ESI-qTOF Impact II coupled to a Dionex UltiMateTM 3000 UHPLC system and controlled by micrOTOFControl 4.0 and HyStar 3.2-LC/MS or with a micrOTOF-Q mass spectrometer (*Bruker*, Bremen, Germany) with ESI-source coupled with an HPLC Dionex UltiMate 3000 (*Thermo Scientific*, Heysham, United Kingdom). Low-resolution electrospray-ionization mass spectra (LRMS-ESI) were acquired with an *Advion* expression® compact mass spectrometer (CMS) coupled with an automated TLC plate reader Plate Express® (*Advion*, Ithaca, NY, USA).

High performance liquid chromatography (HPLC): A *Thermo Fisher Scientific* (Heysham, United Kingdom) UltiMate™ 3000 UHPLC system with a Nucleodur 100-5 C18 (250 × 4.6 mm, *Macherey Nagel*, Düren, Germany) with a flow rate of 1 mL/min and a temperature of 25 °C, or a 100-5 C18 (100 × 3 mm, Macherey Nagel, Düren, Germany) with a flow rate of 0.5 mL/min and a temperature of 25 °C with an appropriate gradient was used. For preparative purposes, an AZURA Prep. 500/1000 gradient system with a Nucleodur 110-5 C18 HTec (150 × 32 mm, *Macherey Nagel*, Düren, Germany) column with 20 mL/min was used. Detection was implemented with UV absorption measurement at wavelengths of λ = 220 nm and λ = 250 nm. Bidest. H_2O (A) and MeCN (B) were used as eluents with an addition of 0.1% TFA for eluent A. **Purity:** The purity of all final compounds was 95% or higher. Purity was determined via HPLC with the Nucleodur 100-5 C18 (250 × 4.6 mm, *Macherey Nagel*, Düren, Germany) at 250 nm. After column equilibration for 5 min, a linear gradient from 5% A to 95% B in 7 min, followed by an isocratic regime of 95% B for 10 min, was used.

The following compounds were synthesized according to literature and used without further purification: Methyl-4-({*N*-[2-(benzylamino)-2-oxoethyl]-4-(dimethylamino)-benzamido}-methyl)-benzoate (**5**), 4-({*N*-[2-(benzylamino)-2-oxoethyl]-4-(dimethylamino)-benzamido}-methyl)-benzoic acid (**6**), *N*-[2-(benzylamino)-2-oxoethyl]-4-(dimethylamino)-*N*-[4-(hydroxycarbamoyl)-benzyl]-benzamide (**DDK-137** (**I**)) [8], *N*-{4-[(2-aminophenyl)-carbamoyl]-benzyl}-*N*-[2-(benzylamino)-2-oxoethyl]-4-(dimethylamino)-benzamide (**VK1** (**II**)) [7].

4.2. Experimental Protocols

4.2.1. (4,5-Dimethoxy-2-nitrophenyl)-methanol (**2**)

6-Nitroveratraldehyde (0.845 g, 4.00 mmol, 1.00 eq.) was dissolved in CH_2Cl_2 (20 mL). $NaBH_4$ (0.303 g, 8.00 mmol, 2.00 eq.) was added, and the solution was stirred for 30 min at room temperature. After completion of the reaction, 1 M HCl (20 mL) was added and stirred for further 10 min. The resulting layers were separated, and the inorganic layer

was extracted with CH_2Cl_2 (3 × 20 mL). The combined organic layers were washed with sat. NaCl-solution (20 mL) and dried over Na_2SO_4. After removal of the solvent under reduced pressure, the alcohol **2** (0.835 g, 3.92 mmol, 98%) was isolated as a yellow solid. $\mathbf{R_f}$ (cyclohexane/ethyl acetate 1/1, *v*/*v*): 0.28; **mp.**: 141–143 °C; **^{1}H NMR** (600 MHz, $CDCl_3$) δ = 7.70 (d, *J* = 1.5 Hz, 1H), 7.18 (d, *J* = 1.5 Hz, 1H), 4.96 (d, *J* = 1.5 Hz, 2H), 4.02–3.99 (m, 3H), 3.97–3.94 (m, 3H), 2.41 (s, 1H); **^{13}C NMR** (151 MHz, $CDCl_3$) δ = 154.0, 148.1, 139.9, 132.4, 111.2, 108.3, 63.0, 56.6, 56.5; **LRMS-ESI (*m*/*z*):** $[M+Na]^+$ calcd for $C_9H_{11}NO_5$: 236.0, found: 236.0.

4.2.2. 2-[(4,5-Dimethoxy-2-nitrobenzyl)oxy]-isoindoline-1,3-dione (**4**)

Alcohol **2** (0.426 g, 2.00 mmol, 1.00 eq.), PPh_3 (0.603 g, 2.30 mmol, 1.15 eq.) and *N*-hydroxyphthalimide (0.375 g, 2.30 mmol, 1.15 eq.) were dissolved in THF (13 mL) and cooled to 0 °C. Over 15 min, DIAD (0.451 mL, 0.465 g, 2.30 mmol, 1.15 eq., 5 equal portions every 3 min) was added dropwise. The reaction was allowed to warm to room temperature and stirred for 4 h. After completion of the reaction, the solvent was removed under reduced pressure and the residue dissolved in CH_2Cl_2 (20 mL). The organic layer was washed with sat. Na_2CO_3 (20 mL) solution. The inorganic layer was extracted with CH_2Cl_2 (3 × 20 mL); the combined organic layers were washed with sat. NaCl-solution (20 mL) and dried over Na_2SO_4. After removal of the solvent under reduced pressure, the crude product was purified with column chromatography (cyclohexane/ethyl acetate 2/1 to 1/3, *v*/*v*) yielding **4** (0.716 g, 2.00 mol, quant.) as a yellow solid. $\mathbf{R_f}$ (cyclohexane/ ethyl acetate 2/1, *v*/*v*): 0.22; **mp.**: 104–106 °C; **^{1}H NMR** (500 MHz, DMSO-d_6) δ = 7.87–7.80 (m, 4H), 7.68 (s, 1H), 7.52 (s, 1H), 5.55 (s, 2H), 3.90 (s, 3H), 3.88 (s, 3H); **^{13}C NMR** (126 MHz, DMSO-d_6) δ = 163.0, 152.7, 148.3, 140.4, 134.7, 128.5, 124.9, 123.2, 112.9, 108.1, 75.5, 56.2, 56.1; **LRMS-ESI (*m*/*z*):** $[M+H]^+$ calcd for $C_{17}H_{14}N_2O_7$: 359.1, found: 359.0.

4.2.3. *N*-[2-(Benzylamino)-2-oxoethyl]-*N*-(4-{[(4,5-dimethoxy-2-nitrobenzyl)oxy]carbamoyl}benzyl)-4-(dimethylamino)benzamide (**pc-I**)

The synthesis was conducted in the dark as much as possible. Building block **4** (0.120 g, 0.335 mmol, 1.50 eq.) was dissolved in CH_2Cl_2 (2.2 mL). Hydrazine-monohydrate (50% in H_2O, 0.102 mL, 53.2 mg, 1.67 mmol, 7.50 eq.) was added and the solution stirred for 4 h at room temperature. The precipitate was removed by filtration and washed with CH_2Cl_2 (3 × 5 mL). The solvent was evaporated under reduced pressure. The remaining yellow solid was re-dissolved in CH_2Cl_2 (0.37 mL) and used without further purification (hydroxylamine solution).

In a separated vessel, carboxylic acid **6** (99.3 mg, 0.223 mmol, 1.00 eq) was dissolved in CH_2Cl_2 (0.37 mL). It was cooled to 0 °C before EDC*HCl (85.5 mg, 0.446 mmol, 2.00 eq.) was added and stirred for 10 min at this temperature, followed by the addition of the previously prepared hydroxylamine solution. The reaction mixture was stirred for a further 10 min at 0 °C followed by additional 2 h at room temperature. The solvent was removed under reduced pressure. The remaining oily residue was purified via preparative HPLC. **pc-I** (27.7 mg, 35.6 µmol, 16%) was isolated as a yellow lyophilizate. **^{1}H NMR** (600 MHz, DMSO-d_6) δ = 11.80 (s, 1H), 8.42 (t, *J* = 6.0 Hz, 1H), 7.71 (d, *J* = 7.9 Hz, 2H), 7.69 (s, 1H), 7.49 (s, 1H), 7.38 (d, *J* = 7.9 Hz, 2H), 7.34–7.29 (m, 4H), 7.27–7.20 (m, 3H), 6.70–6.62 (m, 2H), 5.32 (s, 2H), 4.67 (s, 2H), 4.30 (d, *J* = 5.9 Hz, 2H), 3.93 (s, 3H), 3.87 (s, 3H), 2.93 (s, 6H); **^{13}C NMR** (151 MHz, DMSO-d_6) δ = 172.2, 168.6, 158.8, 158.6, 153.7, 151.6, 148.3, 141.9, 140.3, 139.7, 131.4, 129.0, 128.7, 127.7, 127.3, 111.9, 111.6, 108.5, 73.8, 56.8, 56.6, 42.6; **HRMS-ESI (*m*/*z*):** $[M+H]^+$ calcd for $C_{35}H_{37}N_5O_8$: 656.2720, found: 656.2715; **HPLC**: t_R = 12.10 min (99.6% purity).

4.2.4. 4,5-Dimethoxy-2-nitrobenzyl-{2-[4-({*N*-[2-(benzylamino)-2-oxoethyl]-4-(dimethylamino)benzamido}methyl)benzamido]phenyl}carbamate (**pc-II**)

The synthesis was conducted in the dark as much as possible. **VK-1** (52.3 mg, 97.6 µg, 1.00 eq.) and pyridine (8.65 µL, 8.49 mg, 0.107 mmol, 1.10 eq.) were dissolved in THF

(1.2 mL) and cooled to 0 °C. NVOC-Cl (28.1 mg, 0.102 mmol, 1.05 eq.) was added, and the reaction mixture was stirred for 1 h at this temperature. The ice bath was removed, and the suspension was allowed to warm to room temperature and stirred for a further 18 h. The solvent was removed under reduced pressure and the residue dissolved in CH_2Cl_2 (10 mL). The solution was washed with sat. $NaHCO_3$ (10 mL), 1 M HCl (10 mL), and sat. NaCl (10 mL) solution. The organic layer was dried over Na_2SO_4 and the solvent removed under reduced pressure. The residue was suspended in acetonitrile (10 mL) and the precipitate isolated by filtration and washed with acetonitrile (3 × 10 mL). **pc-II** (38.6 mg, 49.8 µmol, 51%) was isolated as a yellow solid. **mp.**: 159-161 °C, **^{1}H NMR** (600 MHz, DMSO-d_6) δ = 9.83 (s, 1H), 9.19 (s, 1H), 8.45 (d, *J* = 6.2 Hz, 1H), 7.95 (d, *J* = 7.9 Hz, 2H), 7.70 (s, 1H), 7.61–7.55 (m, 2H), 7.44 (d, *J* = 7.9 Hz, 2H), 7.36–7.33 (m, 3H), 7.32 (s, 1H), 7.28–7.22 (m, 4H), 7.21–7.18 (m, 2H), 6.66 (d, *J* = 8.9 Hz, 2H), 5.48 (s, 2H), 4.73 (s, 2H), 4.32 (d, *J* = 5.9 Hz, 2H), 3.93 (s, 2H), 3.85 (s, 3H), 3.79 (s, 3H), 2.93 (s, 6H); **^{13}C NMR** (151 MHz, DMSO-d_6) δ = 171.7, 168.1, 165.2, 153.7, 153.3, 151.2, 147.8, 141.5, 139.4, 139.2, 133.1, 131.5, 130.2, 128.6, 128.3, 128.0, 127.2, 127.2, 126.8, 126.1, 125.7, 124.6, 122.0, 110.9, 110.7, 108.2, 62.9, 56.1, 42.1; **HRMS-ESI (*m*/*z*):** $[M+H]^+$ calcd for $C_{42}H_{42}N_6O_9$: 775.3092, found: 775.3086; **HPLC**: t_R = 12.75 min (97.2% purity).

4.2.5. Benzyl (*S*)-{6-acetamido-1-[(4-methyl-2-oxo-2*H*-chromen-7-yl)amino]-1-oxohexan-2-yl}carbamate (**ZMAL**)

Cbz-L-Lys-OH (0.500 g, 1.75 mmol, 1.00 eq.) was dissolved in acetonitrile/water (27.5 mL 9/1, *v*/*v*). Acetic anhydride (0.200 mL, 0.214 g, 2.10 mmol, 1.20 eq.) was added and the solution stirred for 2 h at room temperature. The solution was diluted with water (125 mL), and the solvent was removed by lyophilization. The crude product and DIPEA (0.893 mL (0.663 g, 5.25 mmol, 3.00 eq.) were dissolved in DMF (4.4 mL). HATU (0.996 g, 2.62 mmol, 1.50 eq.) and 7-amino-4-methylcumarine (0.613 g, 3.50 mmol, 2.00 eq.) were added and the solution stirred for 16 h at room temperature. The solvent was removed under reduced pressure and the residue dissolved in ethyl acetate (50 mL). The organic layer was washed with 1 M HCl (2 × 30 mL), sat. NaCl (30 mL) solution, and dried over Na_2SO_4. The solvent was removed under reduced pressure and the residue purified by column chromatography (ethyl acetate/MeOH 1/0 to 93/7, *v*/*v*), yielding the target compound (0.537 g, 1.12 mmol, 64%) as an off-white solid. **R_f** (ethyl acetate/ MeOH 95/5, *v*/*v*): 0.25; **^{1}H NMR** (400 MHz, DMSO-d_6) δ = 10.47 (s, 1H), 7.80 (t, J = 5.6 Hz, 1H), 7.77 (d, J = 2.0 Hz, 1H), 7.72 (d, J = 8.7 Hz, 1H,), 7.64 (d, J = 7.7 Hz, 1H), 7.49 (dd, J = 8.7, 2.1 Hz, 1H), 7.41–7.16 (m, 5H), 6.26 (d, J = 1.4 Hz,), 5.04 (s, 2H), 4.14 (td, J = 8.2, 5.0 Hz, 1H), 3.00 (td, J = 7.0, 3.4 Hz, 2H), 2.39 (d, J = 1.3 Hz, 3H), 1.76 (s, 3H), 1.73–1.56 (m, 2H), 1.45–1.23 (m, 4H). **^{13}C-NMR** (75 MHz, DMSO-d_6) δ = 179.2, 172.0, 169.0, 160.1, 156.2, 153.7, 153.1, 142.2, 128.4, 127.9, 127.8, 125.6, 115.8, 115.1, 112.3, 105.7, 65.5, 55.6, 38.3, 31.3, 28.9, 23.1, 22.6, 18.0; **HRMS-ESI (*m*/*z*):** $[M+Na]^+$ calcd for $C_{26}H_{29}N_3O_6$: 502.1954, found: 502.1962; **HPLC**: t_R = 12.85 min (98.9% purity (300 nm)). Reported data match the literature [34].

4.3. Photolysis of Photocaged HDAC Inhibitor Prodrugs

Photolysis (photo-uncaging) of photocaged HDACi prodrugs was performed at room temperature using a UVP CL-1000 Crosslinker (Analytik Jena GmbH, Jena, Germany) equipped with five UV-A tubes (F8T5/BL368; λ_{max} = 365 nm; Analytik Jena GmbH, Jena, Germany). Hereafter, this entire experimental set-up will be referred to as the "UV reactor".

Testing of Photo-Uncaging Efficiency

For the photo-uncaging efficiency testing, 10 µL of a 1.0 mM DMSO solution of the respective compound was irradiated for 10 min using the UV reactor described above. Subsequently, 90 µL acetonitrile was added, and the samples were analyzed via HPLC. The amount of photo-cleaved HDACi was determined by comparison with a five-point calibration curve of the respective parent inhibitor, using HPLC/UV detection at an appropriate wavelength (area under the curve; area mAu*min).

4.4. Biological Evaluation

4.4.1. HDAC Enzyme Inhibition Assays

First, predilutions (100-fold final assay concentration) of test compounds or reference inhibitors were prepared. To this end, 3-fold serial dilutions of the respective DMSO stock solutions were prepared in DMSO using clear V-bottom 96-well microplates (*Greiner Bio-One*, Greiner AG, Kremsmünster, Austria). Predilutions designated for photolysis were irradiated for 10 min using the UV reactor described above. Subsequently, all DMSO predilutions were further diluted 1:10 in assay buffer (50 mM Tris-HCl, pH 8.0, 137 mM NaCl, 2.7 mM KCl, 1 mM $MgCl_2$, 0.1 mg/mL BSA). Next, 5.0 µL of these serial dilutions in assay buffer were transferred into 96-well microplates (OptiPlate-96 Black, PerkinElmer, Waltham, MA, USA). Then, 35 µL of the fluorogenic substrate ZMAL (Z-Lys(Ac)-AMC (see Section 4.2.5); 21.43 µM in assay buffer) and 10 µL of human recombinant HDAC1 (BPS Bioscience Inc., San Diego, CA, USA, Catalog# 50051) or human recombinant HDAC6 (*BPS Bioscience* Inc., San Diego, CA, USA, Catalog# 50006) enzyme solution in assay buffer were added. The total assay volume (50 µL, 1% DMSO) was incubated at 37 °C for 90 min. Subsequently, 50 µL of trypsin (0.4 mg/mL) in trypsin buffer (50 mM Tris-HCl, pH 8.0, 100 mM NaCl) was added, followed by additional 30 min of incubation at 37 °C. Fluorescence (excitation: 355 nm, emission: 460 nm) was measured using a FLUOstar OPTIMA microplate reader (*BMG LABTECH* GmbH, Ortenberg, Germany). IC_{50} values were determined by generating normalized dose–response curves using the built-in *"log(inhibitor)* vs. *response (three parameters)"* equation provided by GraphPad Prism (GraphPad Prism 9.0, San Diego, CA, USA). All compounds were tested in duplicates; reported mean IC_{50} values, including standard deviation, were calculated from at least two independent experiments.

4.4.2. Cell Line and Cell Culture

The amelanotic melanoma cell line MV-3 was obtained from EPO GmbH Berlin-Buch. The human ovarian carcinoma cell line A2780 was obtained from the European Collection of Cell Cultures (*ECACC*, Salisbury, UK). The cell lines were cultivated in RPMI 1640 medium supplemented with 10% fetal bovine serum and 50 U/mL penicillin and 50 µg/mL streptomycin and incubated at 37 °C under humidified air with 5% CO_2 to 80–90% confluency before being used in further assays.

4.4.3. HDAC Whole-Cell Assay

The HDAC whole-cell assay is based on the assay established by *Ciossek* et al. [35] and *Bonfils* et al. [36], with minor changes. Melanoma cells MV-3 were seeded in concentration of 15×10^3 cells/well (total volume of 81 µL) in 96-well cell-culture microplates (Catalog# 655086, *Greiner Bio-One*, Frickenhausen, Germany) and cultured for 24 h. Aliquots of the DMSO stock solutions (10 mM) designated for photolysis were irradiated for 10 min with the UV reactor (see Section 4.3). The stock solutions processed with or without irradiation were used to perform a 4-fold serial dilution in PBS. Next, the cells were treated with 9 µL of the serial dilution for 18 h. For the analysis of the remaining HDAC activity, 10 µL of substrate solution, containing 3 mM Boc-Lys(ε-Ac)-AMC (Catalog# 233691-67-3, *BLD pharmatech* GmbH, Kaiserslautern, Germany) and 0.5% IGEPAL CA-630 (Catalog# J61055, *Alfa Aesar*, *Thermo Fisher Scientific*, Heysham, United Kingdom), was added and incubated for 3 h under cell culture conditions. The reaction was stopped with 100 µL of stop solution (50 mM Tris-HCl, 137 mM NaCl, 2.7 mM KCl, 1 mM $MgCl_2$, 1% IGEPAL CA-630, 10 µM vorinostat, 2.0 mg/mL trypsin) and developed for 1.5 h under cell culture conditions. The fluorescence signal was measured using a Spark multimode microplate reader (*Tecan* Group AG, Männedorf, Swiss) at excitation wavelength of λ = 355 nm and emission wavelength of λ = 460 nm. Concentration-effect curves were generated using the four-parameter logistic equation (GraphPad Prism 9.0, San Diego, CA, USA), and mean IC_{50} values were determined by nonlinear regression based on at least three independent experiments in duplicates.

4.4.4. MTT Cell Viability Assay

For this, 200-fold dilution series of the compounds of the respective stock solutions in DMSO (10 mM) were prepared in DMSO using clear U-bottom 96-well microplates (*Greiner Bio-One*, Greiner AG, Kremsmünster, Austria). Predilutions intended for photolysis experiments were irradiated for 10 min in the UV reactor described above. Thereafter, all predilutions were further diluted 1:200 in medium and provided in clear sterile F-bottom 96-well plates (*Starlab GmbH*, Hamburg, Germany). MV-3 cells were added at a density of 3000 cells/well and A2780 cells at a density of 8000 cells/well. The cells were added directly and without prior attachment. Final volume was 200 µL, and the final DMSO concentration was 0,5%. After 72 h, 40 µL MTT (3-(4,5-dimethylthiazol-2-yl)-2,5-diphenyltetrazolium bromide; *BioChemica*, Applichem GmbH, Darmstadt, Germany) solution (5 mg/mL in phosphate-buffered saline) was added to determine cell survival. The formazan dye was dissolved in DMSO (*Sigma-Aldrich*, Steinheim, Germany) after 1 h, and absorbance was measured at 570 nm and 690 nm using a Multiskan microplate photometer (*Thermo Fisher Scientific*, Waltham, MA, USA). Concentration-effect curves were generated using the four-parameter logistic equation (*GraphPad* Prism 9.0, San Diego, CA, USA), and mean IC_{50} values were determined by nonlinear regression based on at least three distinct experiments in duplicates.

4.4.5. Immunoblot

MV-3 cells were seeded to cell culture flasks and cultured for 48 h. Aliquots of the DMSO stock solution (10 mM) designated for photolysis were irradiated for 10 min with the UV reactor (see Section 4.3). The cells were treated with the stock solutions, processed with or without irradiation, of the indicated concentration or vehicle (DMSO) for 24 h. Cell lysis was performed with Cell Extraction Buffer (10 mM Tris, pH 7.4, 100 mM NaCl, 1 mM EDTA, 1 mM EGTA, 1 mM NaF, 20 mM $Na_4P_2O_7$, 2 mM Na_3VO_4, 1% Triton™ ×-100, 10% glycerol, 0.1% SDS, 0.5% deoxycholate; Catalog# FNN0011, *Thermo Fisher Scientific Inc*., Waltham, MA, USA) and addition of Halt Protease Inhibitor Cocktail (100×) (Catalog# 78429, *Life Technologies GmbH* Carlsbad, CA, USA) and phenylmethanesulfonyl fluoride (Catalog# 10837091001, *Sigma-Aldrich*, St. Louis, MO, USA) according to manufacturer instructions. Protein content was determined by Pierce™ BCA Protein Assay Kit (Catalog# 23225, *Thermo Fisher Scientific Inc*., Waltham, MA, USA) according to manufacturer guidelines. Samples were denatured by Laemmli 2× Concentrate (Catalog# S3401-10VL, *Sigma-Aldrich*, St. Louis, MO, USA), and Precision Plus Protein Unstained Standard was used as molecular weight marker (Catalog# 1610363, *Bio-Rad*, Hercules, CA, USA). SDS-PAGE was performed with 10% Mini-PROTEAN TGX Stain-Free Gel at 200 V for 50 min (Catalog# 458035, *Bio-Rad*, Hercules, CA, USA). Afterwards, proteins were transferred with the Trans-Blot Turbo Transfer System (Catalog# 1704150, *Bio-Rad*, Hercules, CA, USA) to Immobilon-FL PVDF membranes (Catalog# IPFL00005, *Millipore Merck*, Burlington, MA, USA) at 1.0 A for 30 min and incubated with 5% milk-powder solution for 1 h at room temperature under slight agitation. Subsequently, the membranes were incubated with anti-acetyl-histone H3 (Catalog# 9677S, *Cell Signaling Technology*, Denver, MA, USA), anti-acetyl-α-tubulin (Catalog#5335, *Cell Signaling Technology*, Denver, MA, USA), and anti-GAPDH (Catalog# T0004, *Affinity Biosciences*, Cincinnati, OH, USA) in 1:1000–1:10000 dilutions at 4 °C, overnight. Incubation with HRP-conjugated secondary anti-mouse (Catalog# sc-516102, *Santa Cruz*, Dallas, TX, USA) and anti-rabbit (Catalog# HAF008, *R&D Systems, Inc*., Minneapolis, MN, USA) was performed for 1.5 h, and membranes were developed with clarity western ECL substrate (Catalog# 1705061, *Bio-Rad*, Hercules, CA, USA). ChemiDoc XRS+ System (Catalog# 1708265, *Bio-Rad*, Hercules, CA, USA) was used for detection and Image Lab Software 6.1 (*Bio-Rad*, Hercules, CA, USA) for analyses.

4.4.6. Annexin V/PI Assay

A2780 cells (4×10^4 cells/mL) were seeded in 6-well plates (*Starlab GmbH*, Hamburg, Germany) and allowed to attach. First, dilutions (500 µM) in DMSO were prepared from the

respective stock solutions in DMSO (10 mM). Predilutions for photolysis experiments were irradiated in clear U-bottom 96-well microplates (*Greiner Bio-One*, Greiner AG, Kremsmünster, Austria) for 10 min in the UV reactor described above. Subsequently, vehicle control (DMSO) or compounds, at a concentration of 0.5 µM, were added to the cells and incubated for 48 h and 72 h, respectively. The final volume was 3 mL, and the final DMSO concentration was 0.1%. Staining was performed in triplicate in two separate experiments using annexin V and propidium iodide and analyzed by flow cytometry (*Guava*® easyCyte™, Luminex, Austin, TX, USA), according to the manufacturer's protocol (*BioLegend*, San Diego, CA, USA).

Results were expressed as mean with standard deviation (SD). Statistical analysis was performed using GraphPad Prism (*GraphPad* Software, San Diego, CA, USA). Normality of the data was analyzed using the Shapiro–Wilk's test. Statistical significance was assessed using one-way analysis of variance (ANOVA) with Tukey's multiple comparison test. Differences were considered statistically significant at * $p < 0.05$, ** $p < 0.01$, *** $p < 0.001$.

4.4.7. Caspase-Glo 3/7 Assay

A2780 cells (8000 cells/well) were seeded in white sterile 96-well plates (*ThermoFisher Scientific*, Waltham, MA, USA, #136102). Dilutions (500 µM) in DMSO were prepared from the respective stock solutions in DMSO (10 mM). Predilutions used for photolysis experiments were irradiated in clear U-bottom 96-well microplates (*Greiner Bio-One*, Greiner AG, Kremsmünster, Austria) for 10 min in the UV reactor described above. Vehicle control (DMSO) or compounds, at a concentration of 0.5 µM, were added to the cells. The cells were then incubated for 24 h under standard culture conditions. The final volume was 100 µL, and the final DMSO concentration was 0.1%. After 24 h, cells were subsequently incubated with Caspase-Glo 3/7 substrate (*Promega*, Madison, WI, USA, #G8091) for 1 h at 25 °C, according to the manufacturer´s protocol. Luminescence was detected at 25 °C using a Spark microplate reader (*Tecan* Group AG, Maennedorf, Swiss). Two independent experiments were performed in triplicates.

GraphPad Prism (*GraphPad* Software, San Diego, CA, USA) was used to perform statistical analysis. Normality of the data was assessed using Shapiro–Wilk's and Kolmogorov–Smirnov tests. To determine statistical differences between means, a one-way analysis of variance (ANOVA) was performed. If the difference was significant ($p < 0.05$), the mean of each column was compared to the mean of the control and corrected for multiple comparisons using Dunnett's post-hoc test. Differences were considered statistically significant at * $p < 0.05$, ** $p < 0.01$, *** $p < 0.001$.

Supplementary Materials: The following Supporting Information can be downloaded at https://www.mdpi.com/article/10.3390/ph16030356/s1: Figure S1. Normalized dose–response curves of the in vitro HDAC inhibition assays against HDAC1 and HDAC6; Figure S2. Caspase-Glo 3/7 assays; Figure S3. Original images of acetylated α-tubulin immunoblots. Figure S4. Original images of acetylated histone H3 immunoblots. Figure S5. Calibration curve of DDK-137 (I).; HPLC traces and ^{1}H and ^{13}C NMR spectra of final compounds.

Author Contributions: Compound design and synthesis was performed by F.B.K.; M.H. performed MTT, apoptosis, and Caspase-Glo 3/7 assays. F.F. performed whole-cell HDAC inhibition assays and immunoblot experiments. L.S.-H. performed biochemical HDAC inhibition assays. F.B.K. and F.K.H. designed the study and analyzed data. F.B.K. wrote the paper with input from all authors. All authors have read and agreed to the published version of the manuscript.

Funding: This work was supported by the Open Access Publication Fund of the University of Bonn.

Institutional Review Board Statement: Not applicable.

Informed Consent Statement: Not applicable.

Data Availability Statement: Data is contained within the article and Supplementary Material.

Conflicts of Interest: The authors declare no conflict of interest.

References

1. Roche, J.; Bertrand, P. Inside HDACs with more selective HDAC inhibitors. *Eur. J. Med. Chem.* **2016**, *121*, 451–483. [CrossRef]
2. Kouzarides, T. Chromatin modifications and their function. *Cell* **2007**, *128*, 693–705. [CrossRef] [PubMed]
3. Dancy, B.M.; Cole, P.A. Protein lysine acetylation by p300/CBP. *Chem. Rev.* **2015**, *115*, 2419–2452. [CrossRef] [PubMed]
4. Park, S.-Y.; Kim, J.-S. A short guide to histone deacetylases including recent progress on class II enzymes. *Exp. Mol. Med.* **2020**, *52*, 204–212. [CrossRef]
5. Peng, X.; Liao, G.; Sun, P.; Yu, Z.; Chen, J. An Overview of HDAC Inhibitors and their Synthetic Routes. *Curr. Med. Chem.* **2019**, *19*, 1005–1040. [CrossRef] [PubMed]
6. Cappellacci, L.; Perinelli, D.R.; Maggi, F.; Grifantini, M.; Petrelli, R. Recent Progress in Histone Deacetylase Inhibitors as Anticancer Agents. *Curr. Med. Chem.* **2020**, *27*, 2449–2493. [CrossRef] [PubMed]
7. Krieger, V.; Hamacher, A.; Cao, F.; Stenzel, K.; Gertzen, C.G.W.; Schäker-Hübner, L.; Kurz, T.; Gohlke, H.; Dekker, F.J.; Kassack, M.U.; et al. Synthesis of Peptoid-Based Class I-Selective Histone Deacetylase Inhibitors with Chemosensitizing Properties. *J. Med. Chem.* **2019**, *62*, 11260–11279. [CrossRef]
8. Mackwitz, M.K.W.; Hesping, E.; Antonova-Koch, Y.; Diedrich, D.; Woldearegai, T.G.; Skinner-Adams, T.; Clarke, M.; Schöler, A.; Limbach, L.; Kurz, T.; et al. Structure-Activity and Structure-Toxicity Relationships of Peptoid-Based Histone Deacetylase Inhibitors with Dual-Stage Antiplasmodial Activity. *ChemMedChem* **2019**, *14*, 912–926. [CrossRef]
9. Shen, S.; Kozikowski, A.P. Why Hydroxamates May Not Be the Best Histone Deacetylase Inhibitors–What Some May Have Forgotten or Would Rather Forget? *Chem. Med. Chem.* **2016**, *11*, 15–21. [CrossRef] [PubMed]
10. Fan, W.; Zhang, L.; Jiang, Q.; Song, W.; Yan, F.; Zhang, L. Histone deacetylase inhibitor based prodrugs. *Eur. J. Med. Chem.* **2020**, *203*, 112628. [CrossRef]
11. Eleutherakis-Papaiakovou, E.; Kanellias, N.; Kastritis, E.; Gavriatopoulou, M.; Terpos, E.; Dimopoulos, M.A. Efficacy of Panobinostat for the Treatment of Multiple Myeloma. *J. Oncol.* **2020**, *2020*, 7131802. [CrossRef]
12. San-Miguel, J.F.; Hungria, V.T.M.; Yoon, S.-S.; Beksac, M.; Dimopoulos, M.A.; Elghandour, A.; Jedrzejczak, W.W.; Günther, A.; Nakorn, T.N.; Siritanaratkul, N.; et al. Panobinostat plus bortezomib and dexamethasone versus placebo plus bortezomib and dexamethasone in patients with relapsed or relapsed and refractory multiple myeloma: A multicentre, randomised, double-blind phase 3 trial. *Lancet Oncol.* **2014**, *15*, 1195–1206. [CrossRef] [PubMed]
13. Adhikari, N.; Jha, T.; Ghosh, B. Dissecting Histone Deacetylase 3 in Multiple Disease Conditions: Selective Inhibition as a Promising Therapeutic Strategy. *J. Med. Chem.* **2021**, *64*, 8827–8869. [CrossRef]
14. Rautio, J.; Meanwell, N.A.; Di, L.; Hageman, M.J. The expanding role of prodrugs in contemporary drug design and development. *Nat. Rev. Drug. Discov.* **2018**, *17*, 559–587. [CrossRef] [PubMed]
15. Huang, Z. A review of progress in clinical photodynamic therapy. *Technol. Cancer Res. Treat.* **2005**, *4*, 283–293. [CrossRef]
16. Josefsen, L.B.; Boyle, R.W. Photodynamic therapy and the development of metal-based photosensitisers. *Met. Based Drugs* **2008**, *2008*, 276109. [CrossRef] [PubMed]
17. Keyal, U.; Bhatta, A.K.; Wang, X.L. Photodynamic therapy for the treatment of different severity of acne: A systematic review. *Photodiagnosis Photodyn. Ther.* **2016**, *14*, 191–199. [CrossRef]
18. Biel, M.A. Photodynamic therapy treatment of early oral and laryngeal cancers. *Photochem. Photobiol.* **2007**, *83*, 1063–1068. [CrossRef]
19. Ong, Y.H.; Kim, M.M.; Finlay, J.C.; Dimofte, A.; Singhal, S.; Glatstein, E.; Cengel, K.A.; Zhu, T.C. PDT dose dosimetry for Photofrin-mediated pleural photodynamic therapy (pPDT). *Phys. Med. Biol.* **2017**, *63*, 15031. [CrossRef]
20. Engels, J.; Schlaeger, E.J. Synthesis, structure, and reactivity of adenosine cyclic 3′,5′-phosphate benzyl triesters. *J. Med. Chem.* **1977**, *20*, 907–911. [CrossRef] [PubMed]
21. Klán, P.; Šolomek, T.; Bochet, C.G.; Blanc, A.; Givens, R.; Rubina, M.; Popik, V.; Kostikov, A.; Wirz, J. Photoremovable protecting groups in chemistry and biology: Reaction mechanisms and efficacy. *Chem. Rev.* **2013**, *113*, 119–191. [CrossRef] [PubMed]
22. Yeon, M.; Kim, Y.; Jung, H.S.; Jeoung, D. Histone Deacetylase Inhibitors to Overcome Resistance to Targeted and Immuno Therapy in Metastatic Melanoma. *Front. Cell Dev. Biol.* **2020**, *8*, 486. [CrossRef] [PubMed]
23. Horbert, R.; Pinchuk, B.; Davies, P.; Alessi, D.; Peifer, C. Photoactivatable Prodrugs of Antimelanoma Agent Vemurafenib. *ACS Chem. Biol.* **2015**, *10*, 2099–2107. [CrossRef] [PubMed]
24. Zhang, K.; Ji, M.; Lin, S.; Peng, S.; Zhang, Z.; Zhang, M.; Zhang, J.; Zhang, Y.; Wu, D.; Tian, H.; et al. Design, Synthesis, and Biological Evaluation of a Novel Photocaged PI3K Inhibitor toward Precise Cancer Treatment. *J. Med. Chem.* **2021**, *64*, 7331–7340. [CrossRef] [PubMed]
25. Hansen, M.J.; Feringa, F.M.; Kobauri, P.; Szymanski, W.; Medema, R.H.; Feringa, B.L. Photoactivation of MDM2 Inhibitors: Controlling Protein-Protein Interaction with Light. *J. Am. Chem. Soc.* **2018**, *140*, 13136–13141. [CrossRef] [PubMed]
26. Uhl, E.; Wolff, F.; Mangal, S.; Dube, H.; Zanin, E. Light-Controlled Cell-Cycle Arrest and Apoptosis. *Angew. Chem. Int. Ed.* **2021**, *60*, 1187–1196. [CrossRef] [PubMed]
27. Kounde, C.S.; Shchepinova, M.M.; Saunders, C.N.; Muelbaier, M.; Rackham, M.D.; Harling, J.D.; Tate, E.W. A caged E3 ligase ligand for PROTAC-mediated protein degradation with light. *Chem. Commun.* **2020**, *56*, 5532–5535. [CrossRef]
28. Naro, Y.; Darrah, K.; Deiters, A. Optical Control of Small Molecule-Induced Protein Degradation. *J. Am. Chem. Soc.* **2020**, *142*, 2193–2197. [CrossRef]

29. Krumm, A.; Barckhausen, C.; Kücük, P.; Tomaszowski, K.-H.; Loquai, C.; Fahrer, J.; Krämer, O.H.; Kaina, B.; Roos, W.P. Enhanced Histone Deacetylase Activity in Malignant Melanoma Provokes RAD51 and FANCD2-Triggered Drug Resistance. *Cancer Res.* **2016**, *76*, 3067–3077. [CrossRef]
30. Gallagher, S.J.; Gunatilake, D.; Beaumont, K.A.; Sharp, D.M.; Tiffen, J.C.; Heinemann, A.; Weninger, W.; Haass, N.K.; Wilmott, J.S.; Madore, J.; et al. HDAC inhibitors restore BRAF-inhibitor sensitivity by altering PI3K and survival signalling in a subset of melanoma. *Int. J. Cancer* **2018**, *142*, 1926–1937. [CrossRef]
31. Leonidova, A.; Mari, C.; Aebersold, C.; Gasser, G. Selective Photorelease of an Organometallic-Containing Enzyme Inhibitor. *Organometallics* **2016**, *35*, 851–854. [CrossRef]
32. Troelsen, K.S.; Calder, E.D.D.; Skwarska, A.; Sneddon, D.; Hammond, E.M.; Conway, S.J. Zap-Pano: A Photocaged Prodrug of the KDAC Inhibitor Panobinostat. *ChemMedChem* **2021**, *16*, 3691–3700. [CrossRef] [PubMed]
33. Porter, N.J.; Osko, J.D.; Diedrich, D.; Kurz, T.; Hooker, J.M.; Hansen, F.K.; Christianson, D.W. Histone Deacetylase 6-Selective Inhibitors and the Influence of Capping Groups on Hydroxamate-Zinc Denticity. *J. Med. Chem.* **2018**, *61*, 8054–8060. [CrossRef]
34. Heltweg, B.; Dequiedt, F.; Verdin, E.; Jung, M. Nonisotopic substrate for assaying both human zinc and NAD+-dependent histone deacetylases. *Anal. Biochem.* **2003**, *319*, 42–48. [CrossRef]
35. Ciossek, T.; Julius, H.; Wieland, H.; Maier, T.; Beckers, T. A homogeneous cellular histone deacetylase assay suitable for compound profiling and robotic screening. *Anal. Biochem.* **2008**, *372*, 72–81. [CrossRef] [PubMed]
36. Bonfils, C.; Kalita, A.; Dubay, M.; Siu, L.L.; Carducci, M.A.; Reid, G.; Martell, R.E.; Besterman, J.M.; Li, Z. Evaluation of the pharmacodynamic effects of MGCD0103 from preclinical models to human using a novel HDAC enzyme assay. *Clin. Cancer Res.* **2008**, *14*, 3441–3449. [CrossRef] [PubMed]

Disclaimer/Publisher's Note: The statements, opinions and data contained in all publications are solely those of the individual author(s) and contributor(s) and not of MDPI and/or the editor(s). MDPI and/or the editor(s) disclaim responsibility for any injury to people or property resulting from any ideas, methods, instructions or products referred to in the content.

Electronic Supplementary Information

Photocaged histone deacetylase inhibitors as prodrugs in targeted cancer therapy

Fabian B. Kraft [1], Maria Hanl [1], Felix Feller [1], Linda Schäker-Hübner [1] and Finn K. Hansen [1,]*

[1] Pharmaceutical Institute, Department of Pharmaceutical and Cell Biological Chemistry, University of Bonn, An der Immenburg 4, D-53121 Bonn, Germany

*Correspondence: finn.hansen@uni-bonn.de

Table of Contents

1. Supplemental Figures S3

2. Photouncaging Experiments S6

3. HPLC Chromatograms S8

4. ^{1}H and ^{13}C NMR Spectra S9

1. Supplemental Figures

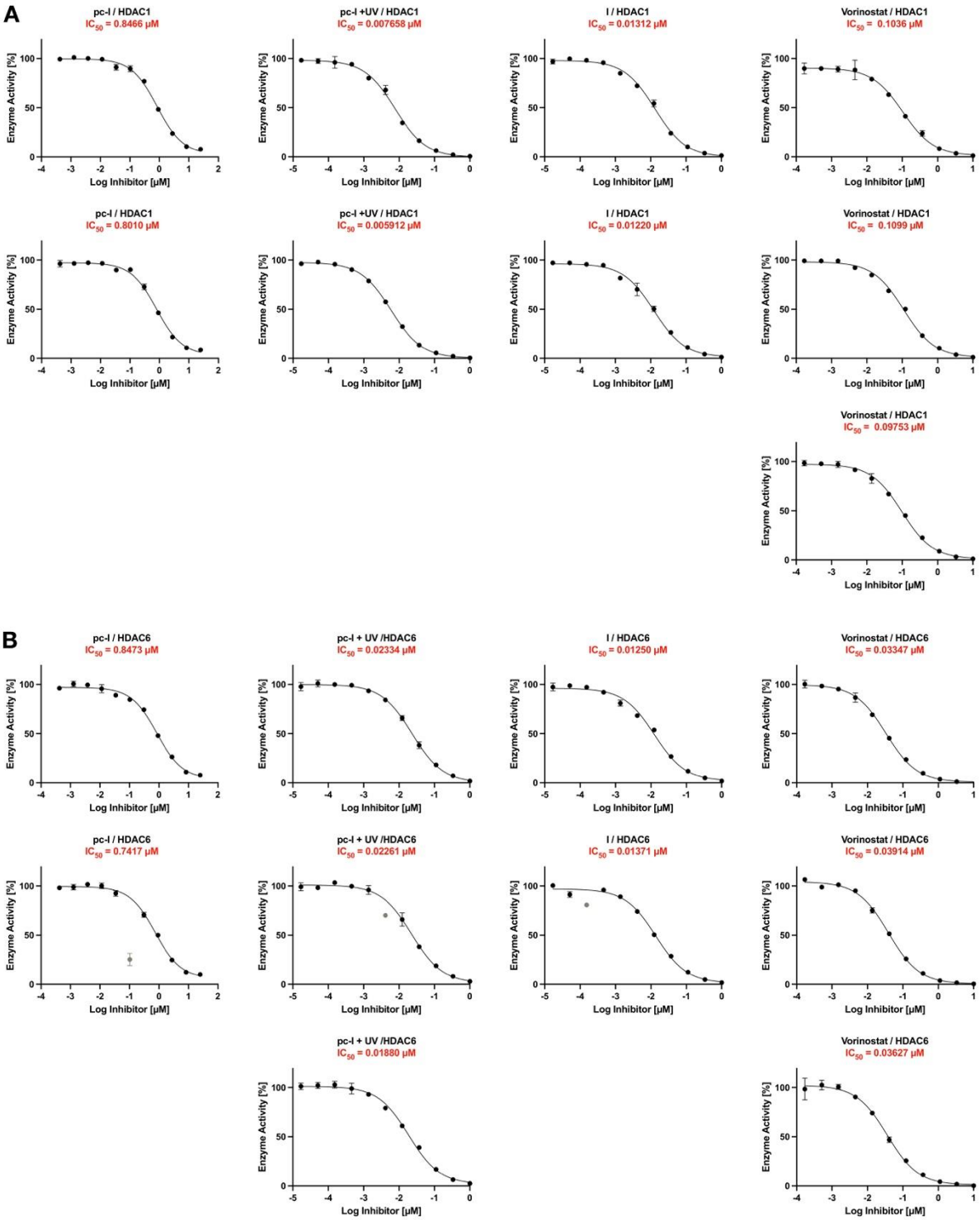


Figure S1. Normalized dose-response curves of the *in vitro* HDAC inhibition assays against HDAC1 (**A**) and HDAC6 (**B**). Data points which were used to calculate the IC_{50} values are depicted as black dots including the respective error bars (standard deviation). Excluded data points are depicted in grey. In some cases, more than two experiments were performed. Additionally, depending on the plate layout and the quantity of the investigated compounds, not all compounds were investigated in one assay run. Vorinostat was included in every assay run as a control compound.

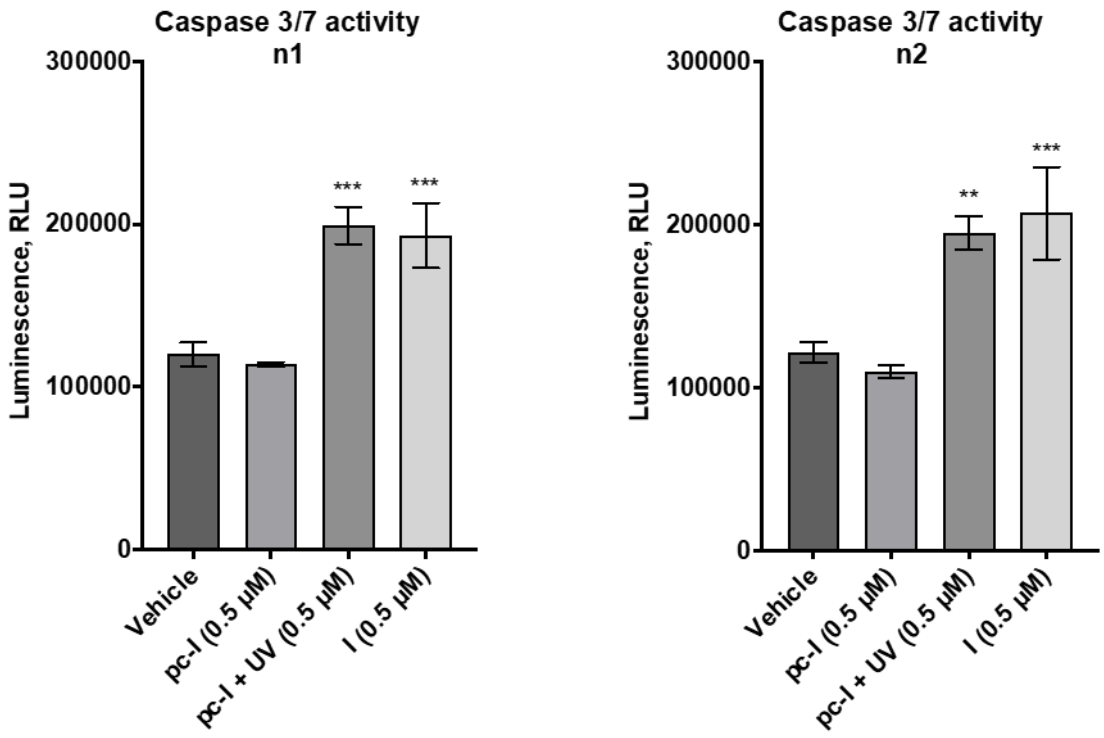


Figure S2. A2780 cells were treated with the indicated concentrations of pc-I, pc-I + UV, I and vehicle (DMSO) for 24h. Afterwards cells were incubated with Caspase-Glo 3/7 substrate and luminescence was determined. The assay was performed in two independent experiments (n1 and n2). Statistical analysis was calculated by one-way ANOVA (*p<0.05, **p<0.01, ***p<0.001).

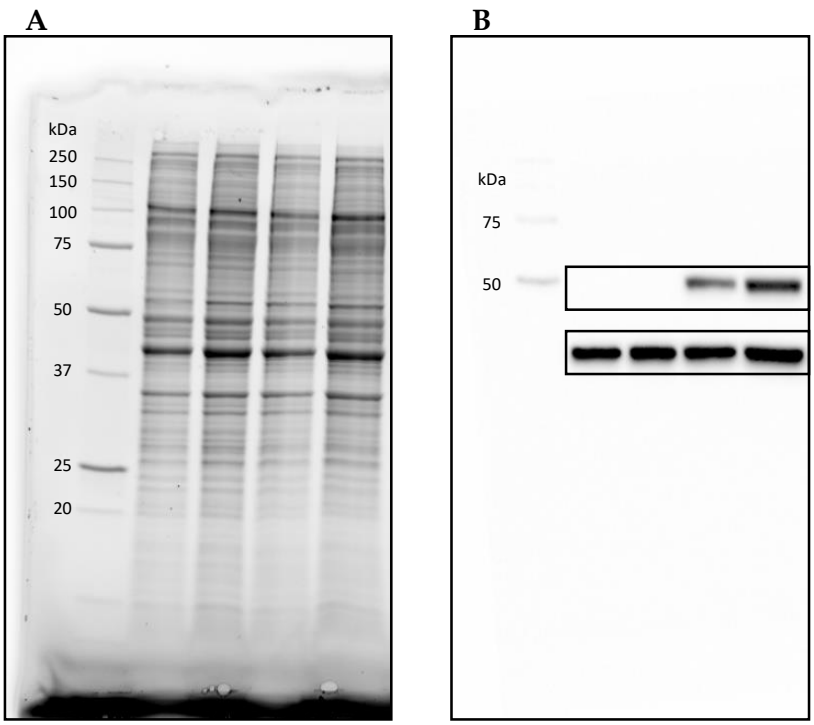


Figure S3. Original images of acetylated α-tubulin immunoblots. **A** shows the stain free detection image of the gel. **B** shows the image of the visualization of the selected acetylated α-tubulin and GAPDH bands.

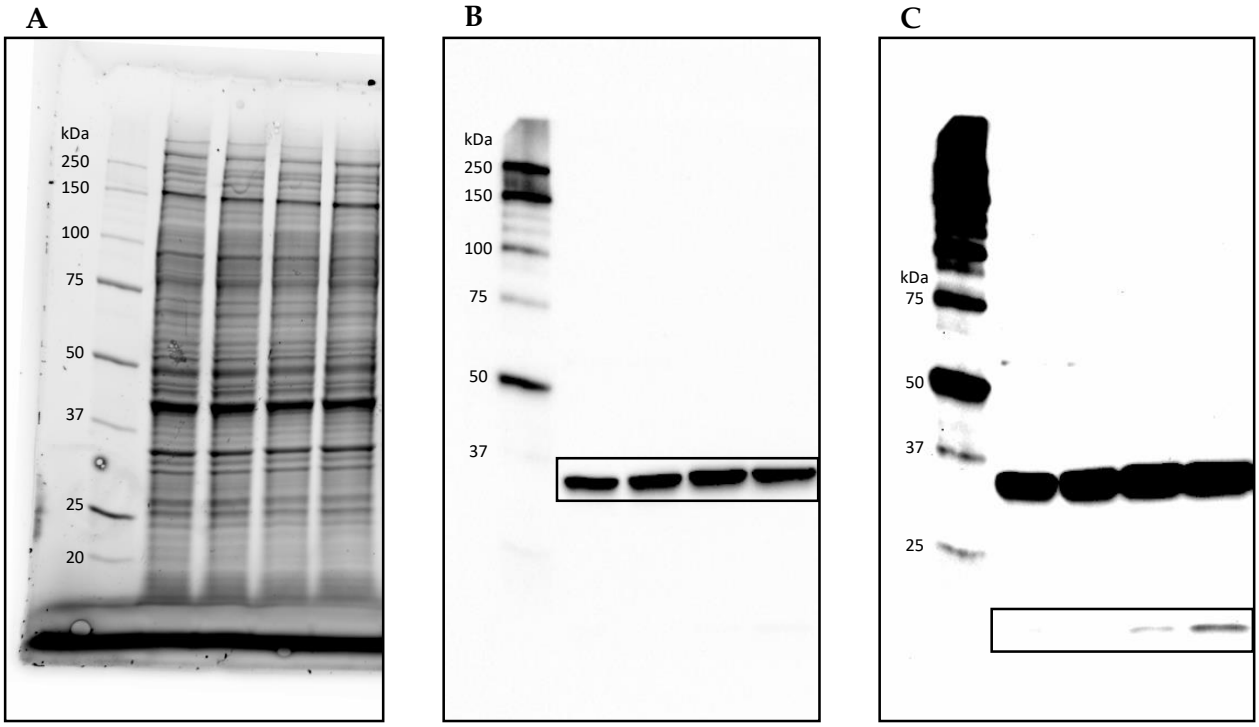


Figure S4. Original images of acetylated histone H3 immunoblots. **A** shows the stain free detection image of the gel. **B** shows the image of the visualization of the GAPDH band. **C** shows the image of the selected acetylated histone H3 band after longer visualization time.

2. Photouncaging Experiments

Photolysis (photouncaging) of photocaged HDACi prodrugs was performed at room temperature using an UVP CL-1000 Crosslinker (Analytik Jena GmbH, Jena, Germany) equipped with five UV-A tubes (F8T5/BL368; λmax = 365 nm; Analytik Jena GmbH, Jena, Germany). Hereafter, this entire experimental set-up will be referred to as the "UV-reactor".
For the deprotection experiments 10 µL of a 1.0 mM DMSO-solution of the respective compound were irradiated for 10 min using the UV-reactor described above. Subsequently, 90 µL acetonitrile were added and the samples were analyzed via HPLC. The amount of photo-cleaved HDACi was determined by comparison with a five-point calibration curve of the respective parent inhibitor using HPLC/UV detection at an appropriate wavelength (area under the curve; area mAu*min).

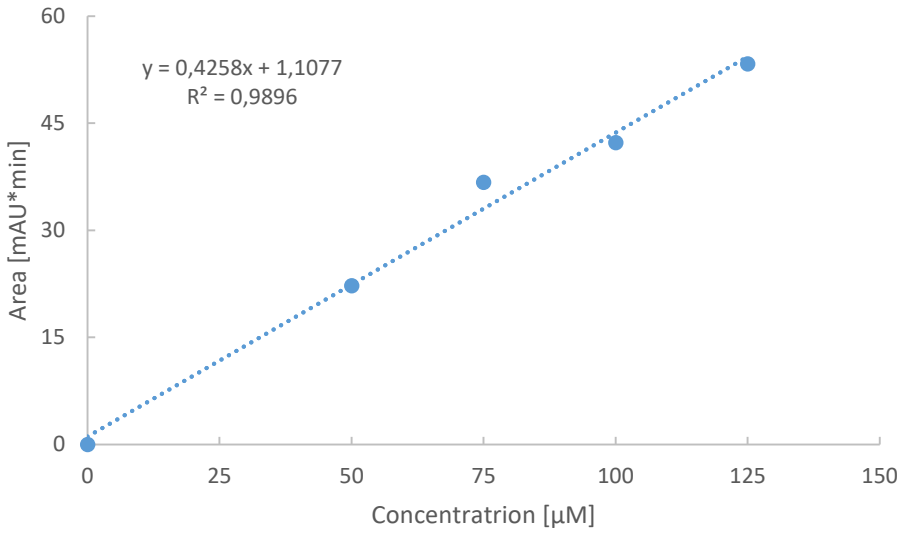
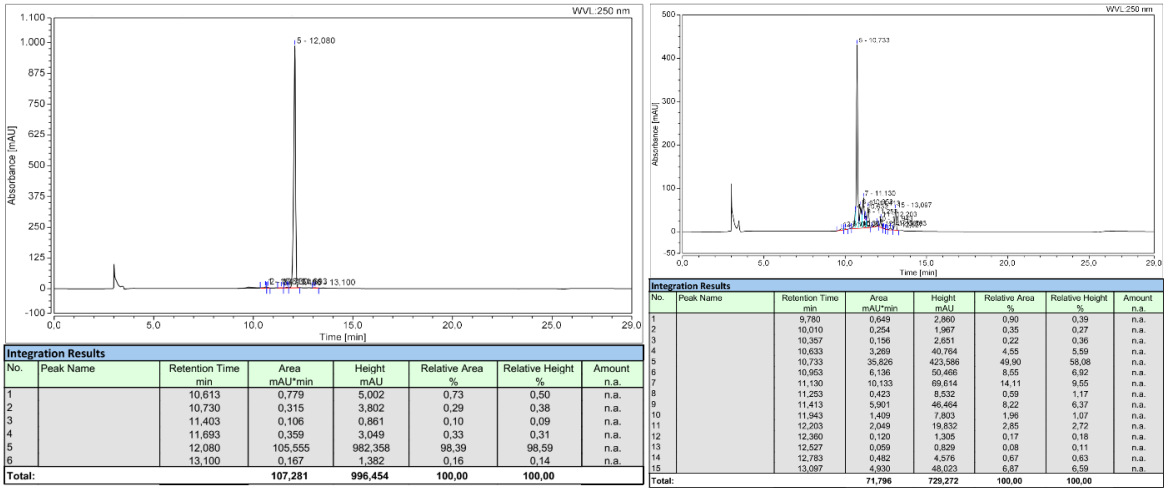


Figure S5. Calibration curve of **DDK-137** (**I**).



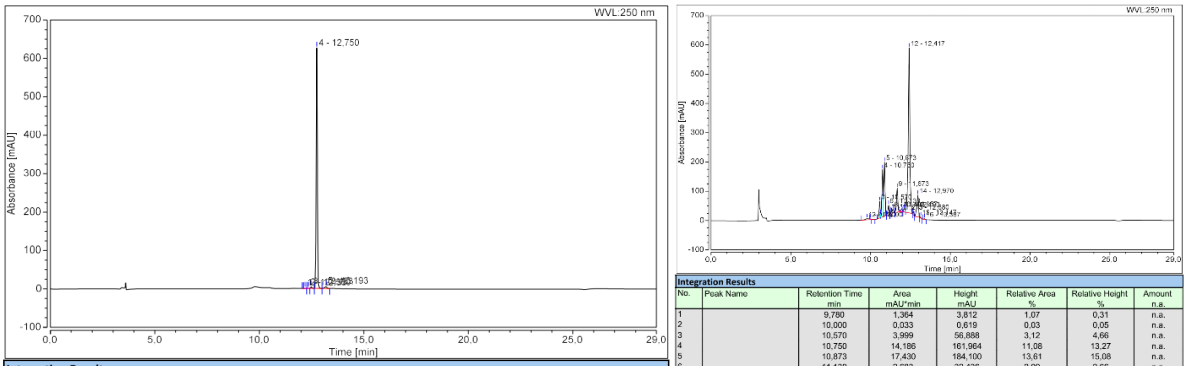
Integration Results

No.	Peak Name	Retention Time min	Area mAU*min	Height mAU	Relative Area %	Relative Height %	Amount n.a.
1		10,613	0,779	5,002	0,73	0,50	n.a.
2		10,730	0,315	3,802	0,29	0,38	n.a.
3		11,403	0,106	0,861	0,10	0,09	n.a.
4		11,693	0,359	3,049	0,33	0,31	n.a.
5		12,080	105,555	982,358	98,39	98,59	n.a.
6		13,100	0,167	1,382	0,16	0,14	n.a.
Total:			107,281	996,454	100,00	100,00	

Integration Results

No.	Peak Name	Retention Time min	Area mAU*min	Height mAU	Relative Area %	Relative Height %	Amount n.a.
1		9,780	0,649	2,860	0,90	0,39	n.a.
2		10,010	0,254	1,967	0,35	0,27	n.a.
3		10,357	0,156	2,651	0,22	0,36	n.a.
4		10,633	3,269	40,764	4,55	5,59	n.a.
5		10,733	35,826	423,586	49,90	58,08	n.a.
6		10,953	6,136	50,466	8,55	6,92	n.a.
7		11,130	10,133	69,614	14,11	9,55	n.a.
8		11,253	0,423	8,532	0,59	1,17	n.a.
9		11,413	5,901	46,464	8,22	6,37	n.a.
10		11,943	1,409	7,803	1,96	1,07	n.a.
11		12,203	2,049	19,832	2,85	2,72	n.a.
12		12,360	0,120	1,305	0,17	0,18	n.a.
13		12,527	0,059	0,829	0,08	0,11	n.a.
14		12,783	0,482	4,576	0,67	0,63	n.a.
15		13,097	4,930	48,023	6,87	6,59	n.a.
Total:			71,796	729,272	100,00	100,00	

Figure S5. Representative chromatograms of **pc-I** before irradiation (left) and after 10 min of irradiation (right) with light at 365 nm. Initial concentration of **pc-I**: 100 μM. Concentration of photo-released **I** (t_R = 10.73 min) after irradiation: 81.5 μM (82%).



Integration Results

No.	Peak Name	Retention Time min	Area mAU*min	Height mAU	Relative Area %	Relative Height %	Amount n.a.
1		12,193	0,045	0,551	0,10	0,09	n.a.
2		12,350	0,048	0,762	0,11	0,12	n.a.
3		12,483	0,503	4,429	1,13	0,70	n.a.
4		12,750	43,189	625,677	97,23	98,23	n.a.
5		13,193	0,637	5,533	1,43	0,87	n.a.
Total:			44,421	636,953	100,00	100,00	

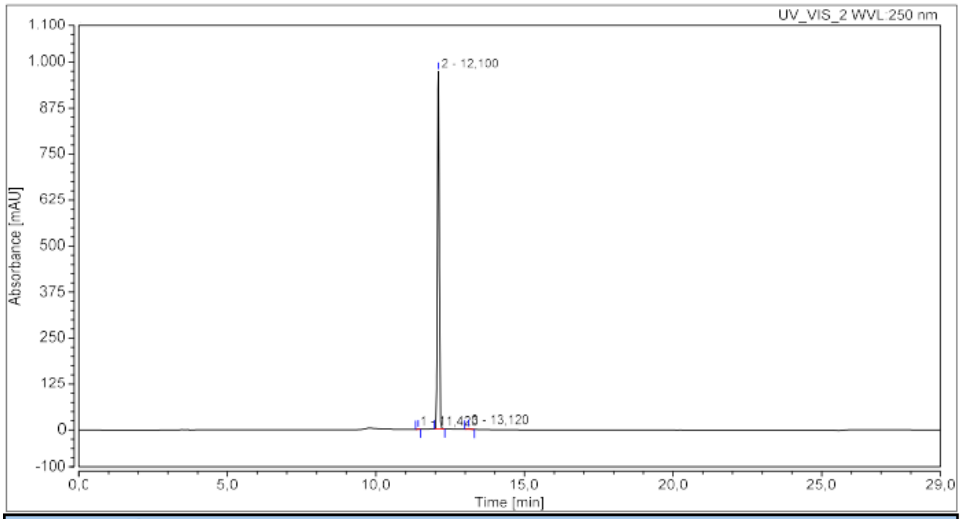
Integration Results

No.	Peak Name	Retention Time min	Area mAU*min	Height mAU	Relative Area %	Relative Height %	Amount n.a.
1		9,780	1,364	3,812	1,07	0,31	n.a.
2		10,000	0,033	0,619	0,03	0,05	n.a.
3		10,570	3,999	56,888	3,12	4,66	n.a.
4		10,750	14,186	161,964	11,06	13,27	n.a.
5		10,873	17,430	184,100	13,61	15,08	n.a.
6		11,130	2,683	32,436	2,09	2,66	n.a.
7		11,273	0,608	8,022	0,47	0,66	n.a.
8		11,403	1,574	14,799	1,23	1,21	n.a.
9		11,673	8,184	82,353	6,39	6,75	n.a.
10		11,957	1,036	9,493	0,81	0,78	n.a.
11		12,100	1,222	10,286	0,95	0,84	n.a.
12		12,417	65,931	563,877	51,48	46,20	n.a.
13		12,680	0,746	11,133	0,58	0,91	n.a.
14		12,970	8,518	74,743	6,65	6,12	n.a.
15		13,147	0,321	3,678	0,25	0,30	n.a.
16		13,387	0,229	2,370	0,18	0,19	n.a.
Total:			128,064	1220,573	100,00	100,00	

Figure S6. Representative chromatograms of **pc-II** before irradiation (left) and after 10 min of irradiation (right) with light at 365 nm. Initial concentration of **pc-II**: 100 μM. Concentration of photo-released **II** (t_R = 10.89 min) after irradiation: not detected.

3. HPLC Chromatograms

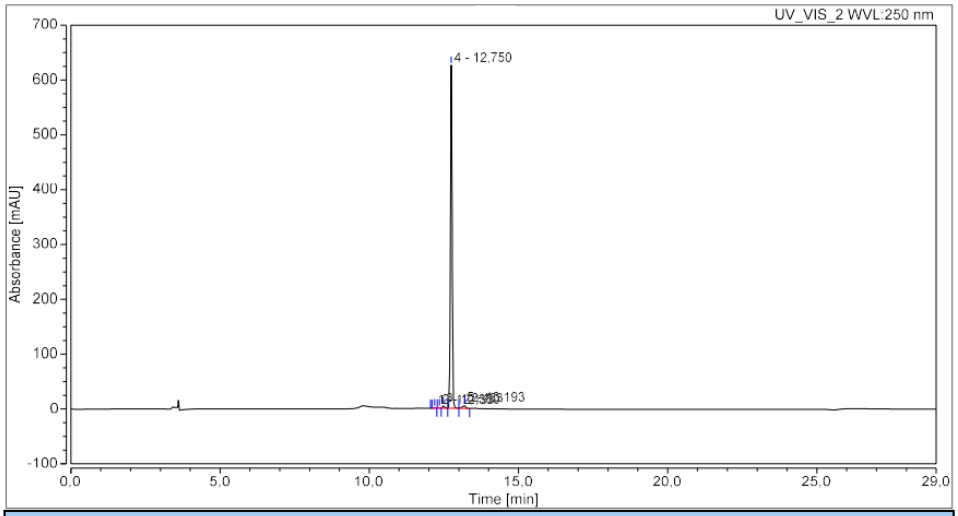
HPLC chromatogram of **pc-I** (purity: 99.6 %)



Integration Results

No.	Peak Name	Retention Time min	Area mAU*min	Height mAU	Relative Area %	Relative Height %	Amount n.a.
1		11,420	0,052	0,756	0,08	0,08	n.a.
2		12,100	66,624	971,696	99,57	99,69	n.a.
3		13,120	0,233	2,249	0,35	0,23	n.a.
Total:			**66,909**	**974,701**	**100,00**	**100,00**	

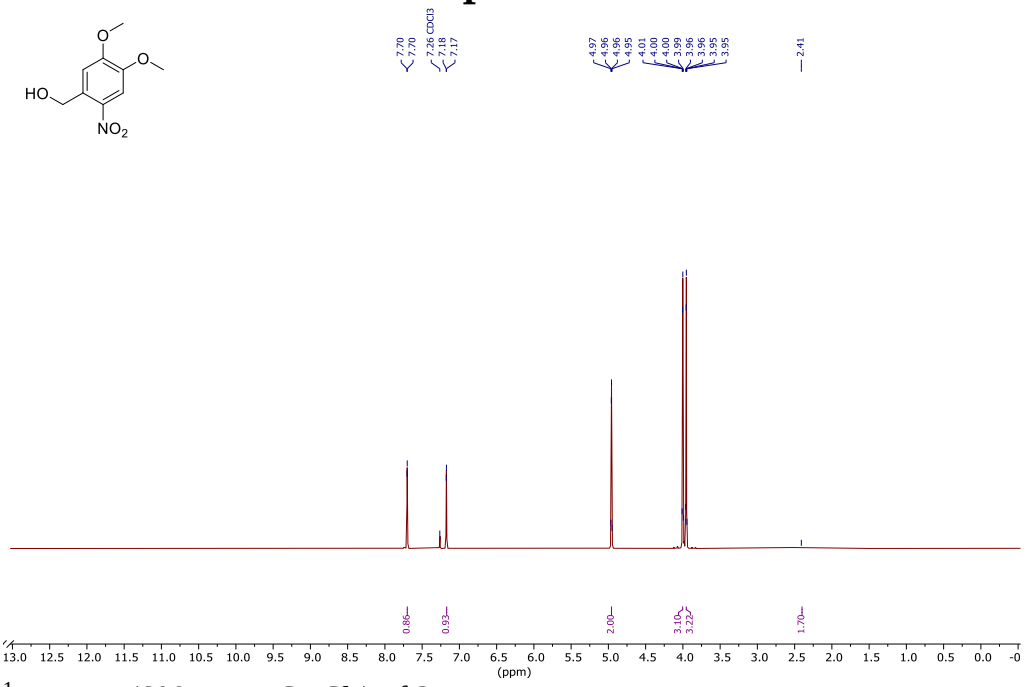
HPLC chromatogram of **pc-II** (purity: 97.2 %).



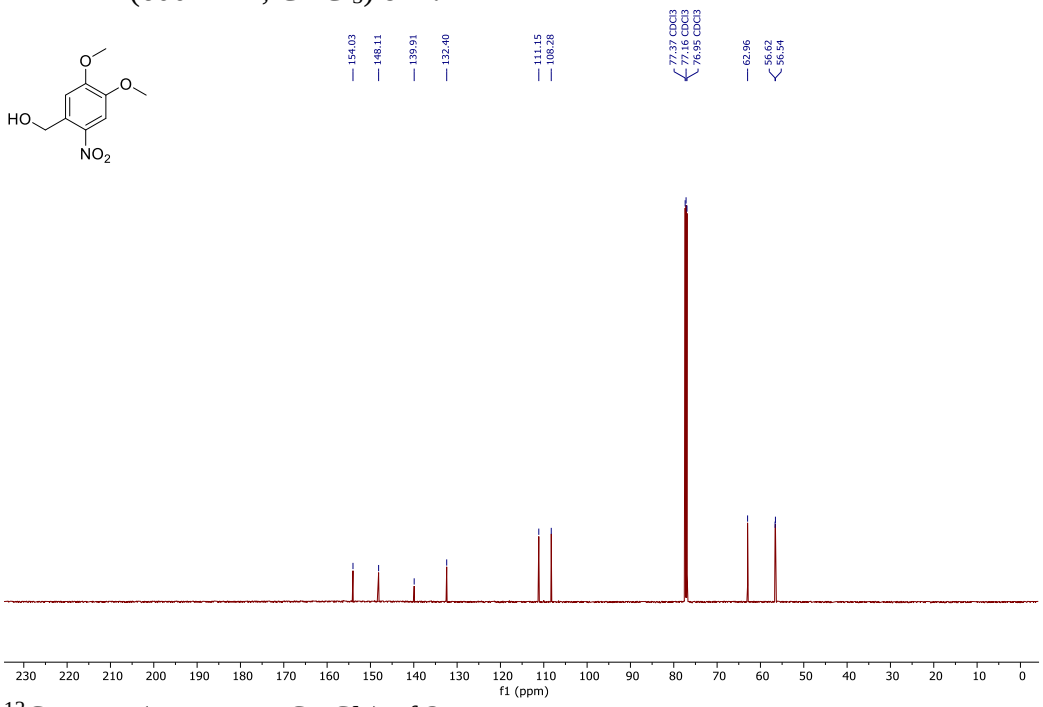
Integration Results

No.	Peak Name	Retention Time min	Area mAU*min	Height mAU	Relative Area %	Relative Height %	Amount n.a.
1		12,193	0,045	0,551	0,10	0,09	n.a.
2		12,350	0,048	0,762	0,11	0,12	n.a.
3		12,483	0,503	4,429	1,13	0,70	n.a.
4		12,750	43,189	625,677	97,23	98,23	n.a.
5		13,193	0,637	5,533	1,43	0,87	n.a.
Total:			**44,421**	**636,953**	**100,00**	**100,00**	

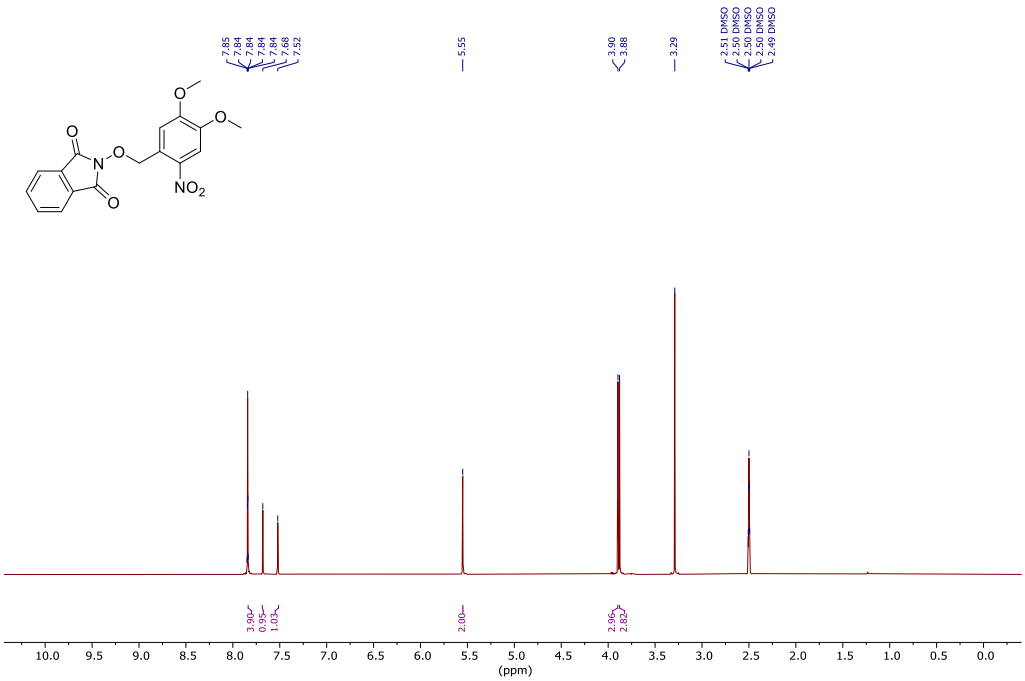
4. ^{1}H and ^{13}C NMR Spectra



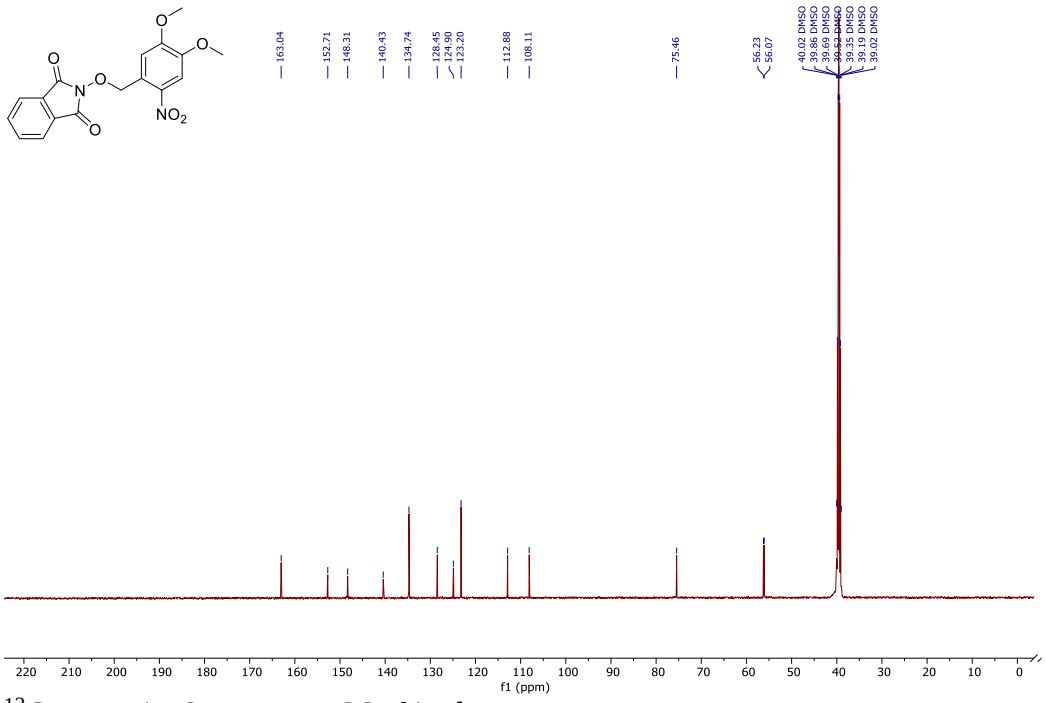
^{1}H-NMR (600 MHz, $CDCl_3$) of **2.**



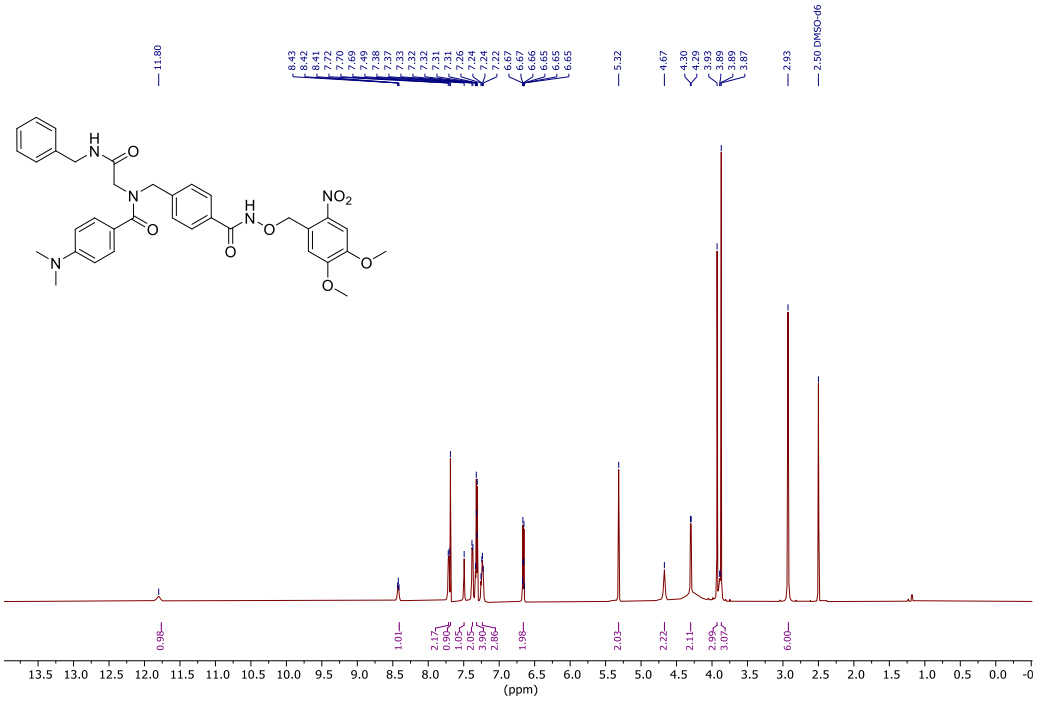
^{13}C-NMR (151 MHz, $CDCl_3$) of **2.**



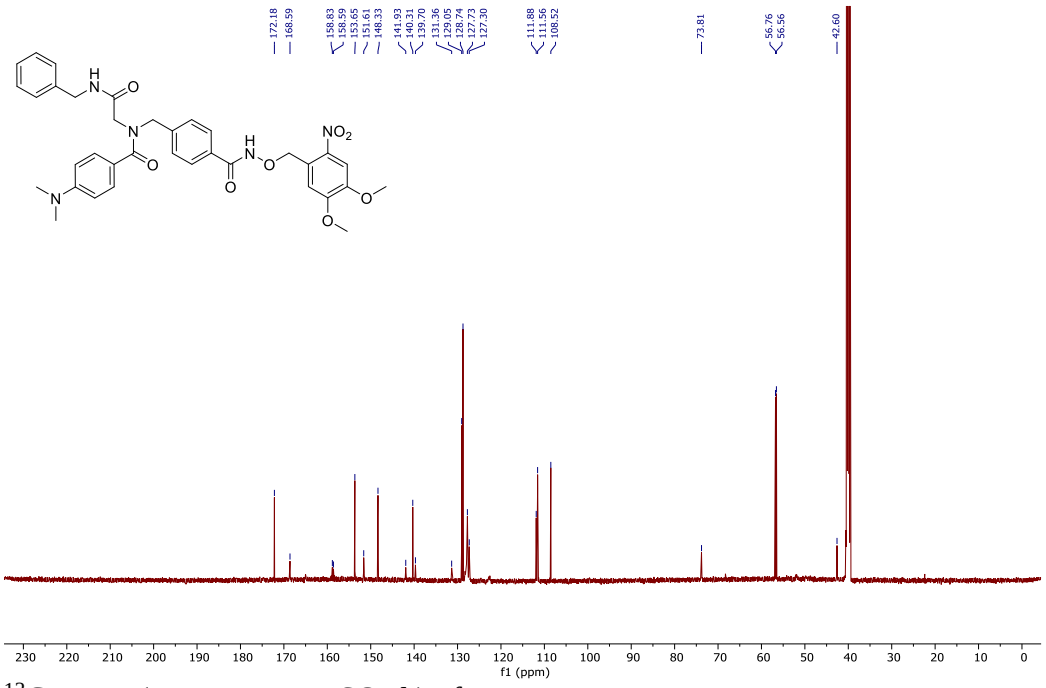
^{1}H-NMR (500 MHz, DMSO-d_6) of **4**.



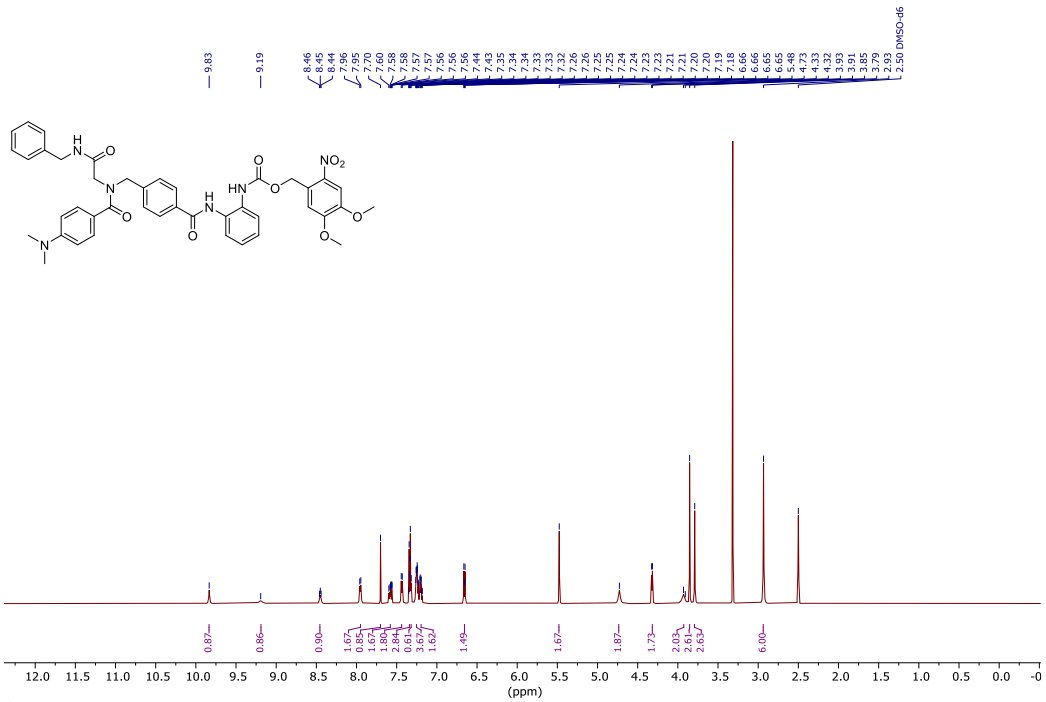
^{13}C-NMR (126 MHz, DMSO-d_6) of **4**.



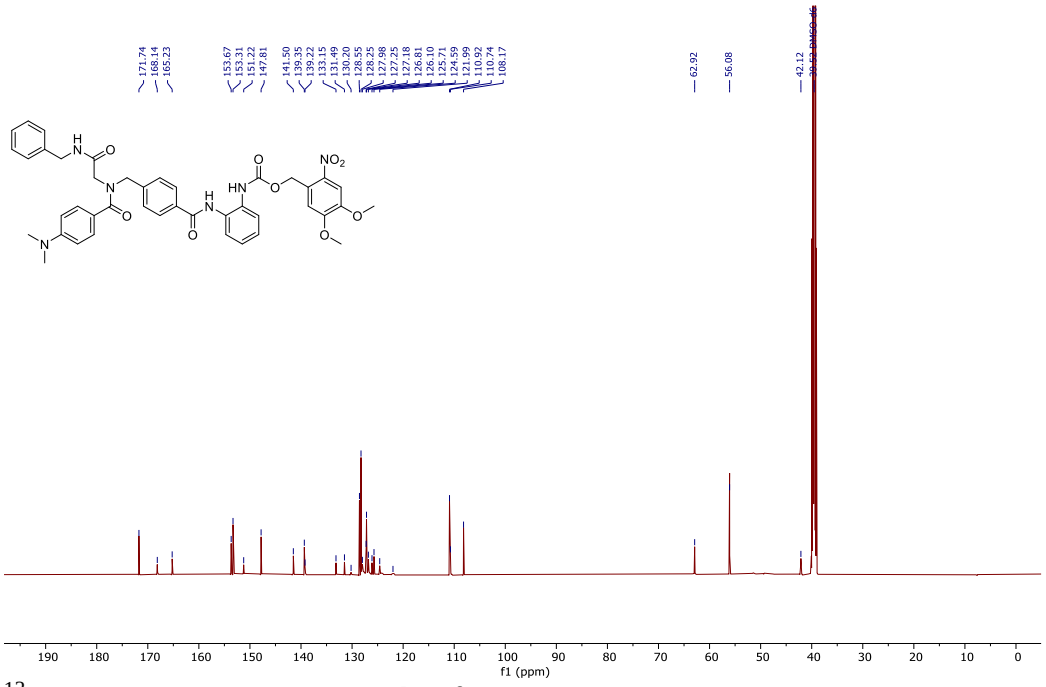
^{1}H-NMR (500 MHz, DMSO-d_6) of **pc-I.**



^{13}C-NMR (151 MHz, DMSO-d_6) of **pc-I.**



^{1}H-NMR (600 MHz, DMSO-d_6) of **pc-II**.



^{13}C-NMR (151 MHz, DMSO-d_6) of **pc-II**.

Danksagung

Ich möchte mich an dieser Stelle herzlich bei all jenen bedanken, die mir die Anfertigung dieser Dissertation ermöglicht haben oder mich in dieser Zeit begleitet und unterstützt haben.

An erster Stelle möchte ich mich besonders bei Herr Prof. Dr. Finn K. Hansen für die Aufnahme in seinen Arbeitskreis, das überlassene Themengebiet sowie das entgegengebrachte Vertrauen während meiner gesamten Promotionszeit bedanken. Weiterhin möchte ich mich für das aufgeschlossene und produktive Arbeitsklima und die stets engagierte Betreuung bedanken.

Prof. Dr. Gerd Bendas möchte ich herzlich für die Übernahme des zweiten Gutachtens danken. Ich bedanke mich außerdem bei allen Kooperationspartner aus den Arbeitskreisen von Prof. Dr. Weindl, Prof. Dr. Meiler und Prof. Dr. Kassack, ohne deren Unterstützung die interdisziplinären Projekte nicht zustande gekommen wären. Insbesondere möchte ich mich hierbei bei Jana Enns, Jonas Engelhardt, Shannon Smith und Lukas Biermann für die gute Zusammenarbeit bedanken. Den Mitarbeiter*innen in den Abteilungen der NMR- und Massenspektrometrie an der Universität Leipzig sowie Marion Schneider und Christiane Bous an der Universität Bonn danke ich sehr für die immer zuverlässige Zusammenarbeit und Hilfestellungen zu Fragen der Strukturaufklärung.

Den Mitgliedern des Arbeitskreis Bendas und den Betreuern des Erstsemester Praktikums danke ich für die unkomplizierte Arbeit und das angenehme Klima. Außerdem möchte ich mich bei Iris Jusen und Dieter Baumert bedanken. Ohne euch würde das gesamte Institut in reinem Chaos versinken.

Ganz herzlich möchte ich mich bei allen ehemaligen und aktuellen Kollegen des „alten“ und „neuen“ AK Hansen bedanken. Insbesondere möchte ich meiner langjährigen Labor- und Bürokollegin Dr. Linda Schäker-Hübner für unsere unzähligen fachlichen und persönlichen Gespräche und unverhältnismäßig vielen Korrekturen von Manuskripten danken. Beate König danke ich für die unersetzliche Hilfe bei der Renovierung der Laborräume und dem Aufbau einer funktionierenden Infrastruktur. Ohne deine fortlaufende Unterstützung und immerwährenden Optimismus würde ich heute noch Glasgeräte bestellen. Darüber hinaus danke ich Daniel Stopper, Felix Feller und Dr. Kathrin Tan für die freundschaftliche Atmosphäre und eure anhaltenden Motivation und Rückendeckung.

Mein größter Dank gilt meiner Familie. Eure dauerhafte Unterstützung, stetige Ermutigungen und absolutes Vertrauen in meine Entscheidungen haben diese Arbeit erst ermöglicht.